RETRIEVAL OF STRATOSPHERIC OZONE AND NITROGEN DIOXIDE PROFILES FROM ODIN OPTICAL SPECTROGRAPH AND INFRARED IMAGER SYSTEM (OSIRIS) LIMB-SCATTERED SUNLIGHT MEASUREMENTS

CRAIG STUART HALEY

A DISSERTATION SUBMITTED TO THE FACULTY OF GRADUATE STUDIES
IN PARTIAL FULFILMENT OF THE REQUIREMENTS
FOR THE DEGREE OF

DOCTOR OF PHILOSOPHY

GRADUATE PROGRAM IN EARTH AND SPACE SCIENCE
YORK UNIVERSITY
TORONTO, ONTARIO

NOVEMBER 2008

Your file Votre référence
ISBN: 978-0-494-52156-4
Our file Notre référence
ISBN: 978-0-494-52156-4

Retrieval of Stratospheric Ozone and Nitrogen Dioxide Profiles from Odin Optical Spectrograph and Infrared Imager System (OSIRIS) Limb-Scattered Sunlight Measurements

By **Craig S. Haley**

a dissertation submitted to the Faculty of Graduate Studies of York University in partial fulfillment of the requirements for the degree of

DOCTOR OF PHILOSOPHY

Abstract

Key to understanding and predicting the effects of global environmental problems such as ozone depletion and global warming is a detailed understanding of the atmospheric processes, both dynamical and chemical. Essential to this understanding are accurate global data sets of atmospheric constituents with adequate temporal and spatial (vertical and horizontal) resolutions. For this purpose the Canadian satellite instrument OSIRIS (Optical Spectrograph and Infrared Imager System) was launched on the Odin satellite in 2001. OSIRIS is primarily designed to measure minor stratospheric constituents, including ozone (O_3) and nitrogen dioxide (NO_2), employing the novel limb-scattered sunlight technique, which can provide both good vertical resolution and near global coverage.

This dissertation presents a method to retrieve stratospheric O_3 and NO_2 from the OSIRIS limb-scatter observations. The retrieval method incorporates an a posteriori optimal estimator combined with an intermediate spectral analysis, specifically differential optical absorption spectroscopy (DOAS). A detailed description of the retrieval method is presented along with the results of a thorough error analysis and a geophysical validation exercise. It is shown that OSIRIS limb-scatter observations successfully

produce accurate stratospheric O_3 and NO_2 number density profiles throughout the stratosphere, clearly demonstrating the strength of the limb-scatter technique.

The OSIRIS observations provide an extremely useful data set that is of particular importance for studies of the chemistry of the middle atmosphere. The long OSIRIS record of stratospheric ozone and nitrogen dioxide may also prove useful for investigating variability and trends.

To my wife Stacey and my daughter Eden, for their support and inspiration.

"The human brain now holds the key to our future. We have to recall the image of the planet from outer space: a single entity in which air, water and continents are interconnected. That is our home."

Dr. David Suzuki

Acknowledgements

This dissertation would not have been possible without the help and support of many people. I would first like to express my gratitude to my graduate supervisor, Prof. Ian McDade, for his committed support through the long process of completing this dissertation. I would also like to acknowledge the hard work and dedication of the Odin and OSIRIS teams that brought about an extremely successful mission, in particular the tireless efforts of the Odin Aeronomy Mission Scientist, Prof. Donal Murtagh, and the OSIRIS Principal Investigator, Prof. Ted Llewellyn.

I have worked closely with many colleagues in producing this work, and I would especially like to acknowledge the contributions of Samuel Brohede, Erik Griffioen, Nick Lloyd, Chris McLinden, Chris Sioris and Christian von Savigny. I would also like to express my thanks to my supervisory committee members, Dr. Brian Solheim, Prof. Kim Strong and Prof. Jack McConnell, for their guidance, to Sally Marshall and Vladka Soltesz, for guiding me through the York University bureaucracy, and to Chris McLinden and Stella Melo, for their helpful comments on this dissertation.

I would also like to acknowledge the Natural Sciences and Engineering Research Council (Canada) and the Canadian Space Agency for their financial support.

Table of Contents

List of Tables

List of Figures

Chapter 1

Introduction

Although the problem of stratospheric ozone depletion was recognized in the early 1980s, our understanding of the problem is still not complete. The decline in global stratospheric ozone that was seen over the past decades appears to have halted due to the Montreal Protocol controls on ozone depleting substances (ODS). However, the predicted pace and extent of a recovery continue to have large degrees of uncertainty since many factors are at play, including the behaviour of the ozone depleting substances, dynamical, volcanic and solar variability, and climate change (e.g. *Intergovernmental Panel on Climate Change*, 2005; *World Meteorological Organization*, 2007). Key to improving our understanding of these issues is the knowledge of the concentration, distribution and time evolution of stratospheric constituents.

Measurements of the stratosphere are made with instruments on the ground (e.g. *Friess et al.*, 2005; *Kerr and McElroy*, 1995), balloons (e.g. *Pommereau et al.*, 1994; *Thompson et al.*, 2003), rockets (e.g. *Hilsenrath*, 1983; *Watanabe et al.*, 2001), aircraft (e.g. *Livingston et al.*, 2005; *Proffitt et al.*, 1989) and satellites (e.g. *McPeters et al.*,

1998; *Russell et al.*, 1993), using both in situ and remote techniques. Satellite instruments have an advantage in that they can provide a global picture. However, satellite measurements can be limited in vertical resolution, global coverage and temporal resolution or sampling, with the specific limitations depending on the measurement technique employed.

Satellite instruments measuring the stratosphere have historically used a number of measurement techniques, primarily nadir (backscatter or thermal emission), solar occultation and limb thermal emission. Nadir-measuring instruments, such as the Ozone Monitoring Instrument (OMI) on Aura (*Levelt et al.*, 2006) and the Scanning Imaging Absorption Spectrometer for Atmospheric Chartography (SCIAMACHY) on Envisat (*Bovensmann et al.*, 1999), generally provide good global coverage and horizontal resolution, but give limited or no vertical information. Solar occultation instruments, including the Atmospheric Chemistry Experiment (ACE) (*Bernath et al.*, 2005) and Measurements of Aerosol Extinction in the Stratosphere and Troposphere Retrieved by Occultation (MAESTRO) (*McElroy et al.*, 2007) instruments on Scisat, provide good vertical resolution, but provide sparse coverage and limited horizontal resolution. Limb thermal emission instruments, such as the Submillimetre and Millimetre Radiometer (SMR) on the Odin satellite (*Frisk et al.*, 2003), the Michelson Interferometer for Passive Atmospheric Sounding (MIPAS) on Envisat (*Fischer and Oelhaf*, 1996) and the Microwave Limb Sounder (MLS) on Aura (*Waters et al.*, 2006), provide good global coverage and vertical resolution, but have limited horizontal resolution and can be affected by poor sensitivity in the upper troposphere and lower stratosphere.

A novel measurement technique with the potential of providing vertical profiles of stratospheric minor constituents with high vertical resolution (1-3 km) and global coverage involves observations of sunlight scattered by the Earth's atmosphere in the limb-viewing geometry, known as the limb-scatter technique. A limitation of the technique is that measurements are restricted to daylight conditions. The limb-scatter technique was pioneered by *Cunnold et al.* (1973), who used limb-scatter observations from a high altitude aircraft to measure stratospheric ozone and aerosol, and *McElroy* (1988), who used limb-scatter observations from a high altitude balloon to measure stratospheric nitrogen dioxide. Early theoretical studies were carried out by *Malchow and Whitney* (1977) and *Aruga and Heath* (1982). The first satellite to employ the limb-scatter technique was the Solar Mesosphere Explorer (SME) (*Thomas et al.*, 1980), where an ultraviolet spectrometer was used to measure mesospheric ozone (*Rusch et al.*, 1983, 1984) and a visible spectrometer was used to measure upper stratospheric nitrogen dioxide (*Mount et al.*, 1983, 1984). The Shuttle Ozone Limb Scattering Experiment (SOLSE) and Limb Ozone Retrieval Experiment (LORE) instrument package that flew on NASA's Space Shuttle also used the limb-scatter technique to successfully derive stratospheric ozone profiles (*Flittner et al.*, 2000; *McPeters et al.*, 2000).

Although the first limb-scatter instruments demonstrated the potential of the measurement technique, a number of instrument and analysis limitations restricted the vertical range, global coverage and quality of the measurements, preventing a complete evaluation of the technique. However, based on the demonstrated potential, a new generation of limb-scatter satellite instruments was developed, including

two satellite instruments that are currently in operation, namely the Optical Spectrograph and Infrared Imager System (OSIRIS) instrument on the Odin satellite (*Llewellyn et al.*, 2004) and SCIAMACHY. SAGE (Stratospheric Aerosol and Gas Experiment) III, which flew on the Meteor-3M spacecraft (*McCormick et al.*, 1991), was primarily a solar occultation instrument, but also included a limb-scatter capability and measured stratospheric O_3 (e.g. *Rault*, 2005). GOMOS (Global Ozone Measurement by Occultation of Stars) on Envisat (*Bertaux et al.*, 1991), although primarily a stellar occultation instrument, makes limb-scatter measurements to aid in the interpretation of the daytime occultation measurements. This new generation of limb-scatter instruments were designed with significant care towards stray light effects (in the case of SCIAMACHY and OSIRIS) and measure broad spectral regions with high spectral resolution. These improved measurements, combined with the use of sophisticated radiative transfer models that account for multiple scattering within a spherical atmosphere, have largely addressed the inadequacies of the early instruments and allow for improved retrievals of stratospheric minor constituents.

The successful demonstration of the limb scatter technique, primarily by OSIRIS, led to the inclusion of a limb-scatter instrument in the Ozone Mapping and Profiler Suite (OMPS) on the NPOESS (National Polar-Orbiting Operational Environmental Satellite System) Preparatory Project (NPP) (*Seftor et al.*, 2003), due to be launched in 2010, that will provide stratospheric O_3 profiles on an operational basis. Also, a follow-on OSIRIS instrument is planned for the STEP (Stratosphere-Troposphere Exchange Processes) mission that is currently under development (D.A. Degenstein, personal communication), with a focus on the upper troposphere/lower stratosphere

(UTLS) region.

This dissertation presents a method for retrieving stratospheric ozone and nitrogen dioxide number density profiles from limb-scattered sunlight observations from OSIRIS limb-scattered sunlight measurements. The retrieval of stratospheric information from the OSIRIS limb-scatter observations is not trivial, requiring the use of a spectral analysis technique and the solving of a non-linear inverse problem within a complicated radiative transfer environment. A number of methods for retrieving stratospheric minor species profiles from OSIRIS and SCIAMACHY limb-scatter observations have been proposed, including methods that retrieve information directly from the observations (*Auvinen et al.*, 2002; *Kaiser*, 2001) and methods that apply a spectral analysis technique to simplify the problem (*Flittner et al.*, 2000; *McDade et al.*, 2002; *Rozanov*, 2001; *Sioris et al.*, 2003; *Strong et al.*, 2002). The initial OSIRIS O_3 retrievals were undertaken by *von Savigny et al.* (2003), using an adaptation of the retrieval method used for the SOLSE/LORE instrument package (*Flittner et al.*, 2000) that involves measurements at three wavelengths in the Chappuis band of O_3 combined with an optimal estimation (OE) inversion approach (*Rodgers*, 2000). The initial OSIRIS NO_2 retrievals were carried out by *Sioris et al.* (2003) using differential optical absorption spectroscopy (DOAS) (*Platt*, 1994) combined with a Chahine-type inversion approach (*Chahine*, 1970). The retrieval method presented in this dissertation combines DOAS with an OE approach, more specifically the maximum a posteriori (MAP) estimator, with a forward model that uses the multiple scattering, pseudo-spherical radiative transfer model LIMBTRAN (*Griffioen and Oikarinen*, 2000).

This dissertation is based on the work contained in the following papers, referred to by Roman numerals in the text:

I. McDade, I.C., K. Strong, C.S. Haley, J. Stegman, D.P. Murtagh, and E.J. Llewellyn, **A method for recovering stratospheric minor species densities from the Odin OSIRIS scattered sunlight measurements**, *Can. J. Phys.*, 80(4), 395-408, doi:10.1139/P01-152, 2002.

II. Sioris, C.E., C.S. Haley, C.A. McLinden, C. von Savigny, I.C. McDade, J.C. McConnell, W.F.J. Evans, N.D. Lloyd, E.J. Llewellyn, K.V. Chance, T.P. Kurosu, D.P. Murtagh, U. Frisk, K. Pfeilsticker, H. Bösch, F. Weidner, K. Strong, J. Stegman, and G. Mégie, **Stratospheric profiles of nitrogen dioxide observed by Optical Spectrograph and Infrared Imager System on the Odin satellite**, *J. Geophys. Res.*, 108(D7), 4215-4234, doi:10.1029/2002JD002672, 2003.

III. Haley, C.S., C. von Savigny, S. Brohede, C.E. Sioris, I.C. McDade, E.J. Llewellyn, and D.P. Murtagh, **A comparison of methods for retrieving stratospheric ozone profiles from OSIRIS limb-scatter measurements**, *Adv. Space Res.*, 34(4), 769-774, doi:10.1016/j.asr.2003.08.058, 2004.

IV. Haley, C.S., S.M. Brohede, C.E. Sioris, E. Griffioen, D.P. Murtagh, I.C. McDade, P. Eriksson, E.J. Llewellyn, A. Bazureau, and F. Goutail, **Retrieval of stratospheric O_3 and NO_2 profiles from Odin Optical Spectrograph and Infrared Imager System (OSIRIS) limb-scattered sunlight measurements**, *J. Geophys. Res.*, 109, D16303, doi:10.1029/2004JD004588, 2004.

V. McLinden, C.A., C.S. Haley, and C.E. Sioris, **Diurnal effects in limb scatter observations**, *J. Geophys. Res.*, 111, D14302, doi:10.1029/2005JD006628, 2006.

VI. Brohede, S.M., C.S. Haley, C.A. McLinden, C.E. Sioris, D.P. Murtagh, S.V. Petelina, E.J. Llewellyn, A. Bazureau, F. Goutail, C.E. Randall, J.D. Lumpe, G. Taha, L.W. Thomasson, and L.L. Gordley, **Validation of Odin/OSIRIS stratospheric NO_2 profiles**, *J. Geophys. Res.*, 112, D07310, doi:10.1029/2006JD007586, 2007.

VII. Haley, C.S. and S. Brohede, **Status of the Odin/OSIRIS stratospheric O_3 and NO_2 data products**, *Can. J. Phys.*, 85(11), 1177-1194, doi:10.1139/P07-114, 2007.

Paper I describes the application of DOAS combined with an iterative least-squares (ILS) inversion approach to simulated OSIRIS limb-scatter radiances. **Paper II** is a presentation of the first retrievals of stratospheric NO_2 from OSIRIS measurements using DOAS combined with a Chahine-type inversion approach. **Paper III** presents the first application of the retrieval method presented in this work (DOAS combined with OE) to OSIRIS measurements to retrieve stratospheric O_3 and NO_2. **Paper IV** is a comprehensive study of the application of the retrieval method of this work to OSIRIS limb-scatter radiances, including a detailed error analysis. **Paper V** studies the error in the retrieved NO_2 profiles due to horizontal variations caused by photochemistry. **Paper VI** is a detailed validation study of the OSIRIS stratospheric NO_2 profiles. **Paper VII** presents an overview of the retrieval method as it is being

applied in the OSIRIS operational retrievals.

The following papers are related to the retrieval method presented here but are not explicitly discussed as part of this dissertation.

1. von Savigny, C., C.S. Haley, C.E. Sioris, I.C. McDade, E.J. Llewellyn, D. Degenstein, W.F.J. Evans, R.L. Gattinger, E. Griffioen, N.D. Lloyd, J.C. McConnell, C.A. McLinden, D. Murtagh, B. Solheim, and K. Strong, **Stratospheric ozone profiles retrieved from limb scattered sunlight radiance spectra measured by the OSIRIS instrument on the Odin satellite**, *Geophys. Res. Lett.*, 30(14), 1755-1758, doi:10.1029/2002GL016401, 2003.

2. McLinden, C.A., C.S. Haley, and E.J. Llewellyn, **Derivation of polarization from Odin/OSIRIS limb spectra**, *Geophys. Res. Lett.*, 31(7), L20112, doi:10.1029/2004GL020825, 2004.

3. Krecl, P., C.S. Haley, J. Stegman, S.M. Brohede, and G. Berthet, **Retrieving the vertical distribution of stratospheric OClO from Odin/OSIRIS limb-scattered sunlight measurements**, *Atmos. Chem. Phys.*, 6, 1879-1894, 2006.

4. McLinden, C.A. and C.S. Haley, **Odin/OSIRIS observations of stratospheric NO_3 through sunrise and sunset**, *Atmos. Chem. Phys.*, 8, 5529-5534, 2008.

This dissertation is presented as follows. Chapter 2 gives a brief synopsis of the dynamics and chemistry of the stratosphere, including the problem of ozone depletion.

Chapter 3 is an introduction to remote sounding of the atmosphere using limb-scatter measurements, including an overview of the measurement geometry and the radiative transfer. Chapters 4 and 5 present the DOAS spectral analysis technique and the OE inversion approach used in this work, respectively. Chapter 6 describes the Odin mission and the OSIRIS instrument. Chapter 7 presents the retrieval of stratospheric O_3 and NO_2 number density profiles from OSIRIS measurements of limb-scattered sunlight. Finally, Chapter 8 states the main conclusions and outlook.

Chapter 2

The Stratosphere

The stratosphere is the region of the Earth's atmosphere situated between 8-16 km (the tropopause) and 50 km (the stratopause) above the surface. In this region the temperature increases with altitude, a so-called 'temperature inversion'. This is in contrast to the troposphere (and mesosphere), where the temperature generally decreases with altitude. The temperature inversion is due to the absorption of solar ultraviolet (UV) radiation by ozone, which heats the upper layers of the stratosphere. The temperature inversion makes the stratosphere stable to vertical perturbations. Radiative, chemical and dynamical processes are all important in the stratosphere where, due to the vertical stability, horizontal mixing of gaseous components proceeds much more rapidly than does vertical mixing. The stratosphere and the accompanying ozone layer are extremely important for life on Earth as we know it, providing a shield from potentially harmful UV-B (280-315 nm) and UV-C (180-280 nm) solar radiation and contributing to the greenhouse effect of the atmosphere.

This chapter describes the basic dynamics and chemistry of the stratosphere as

well as the problem of ozone depletion and the impact of climate change. More detailed information can be found in *Dessler* (2000), *Brasseur and Solomon* (2005) and *World Meteorological Organization* (2007).

2.1 Dynamics of the Stratosphere

2.1.1 Stratospheric Transport

Stratospheric transport is largely governed by the Brewer-Dobson circulation (*Brewer*, 1949; *Dobson*, 1956). The stratospheric Brewer-Dobson circulation consists of an upwelling in the tropics and a descent in the extratropics, with a general poleward flow (see Figure 2.1).

The Brewer-Dobson circulation is primarily driven by forcing from the dissipation of planetary-scale waves in the stratosphere. These planetary waves are generated in the troposphere by topographic and thermal forcing, and by synoptic meteorology (large-scale weather systems). Vertical propagation of planetary waves into the stratosphere occurs primarily during winter, and this seasonality in wave forcing accounts for a winter maximum in the Brewer-Dobson circulation. Also, since planetary wave activity is stronger in the Northern Hemisphere (NH) due to the more variable topography, the Brewer-Dobson circulation is stronger there.

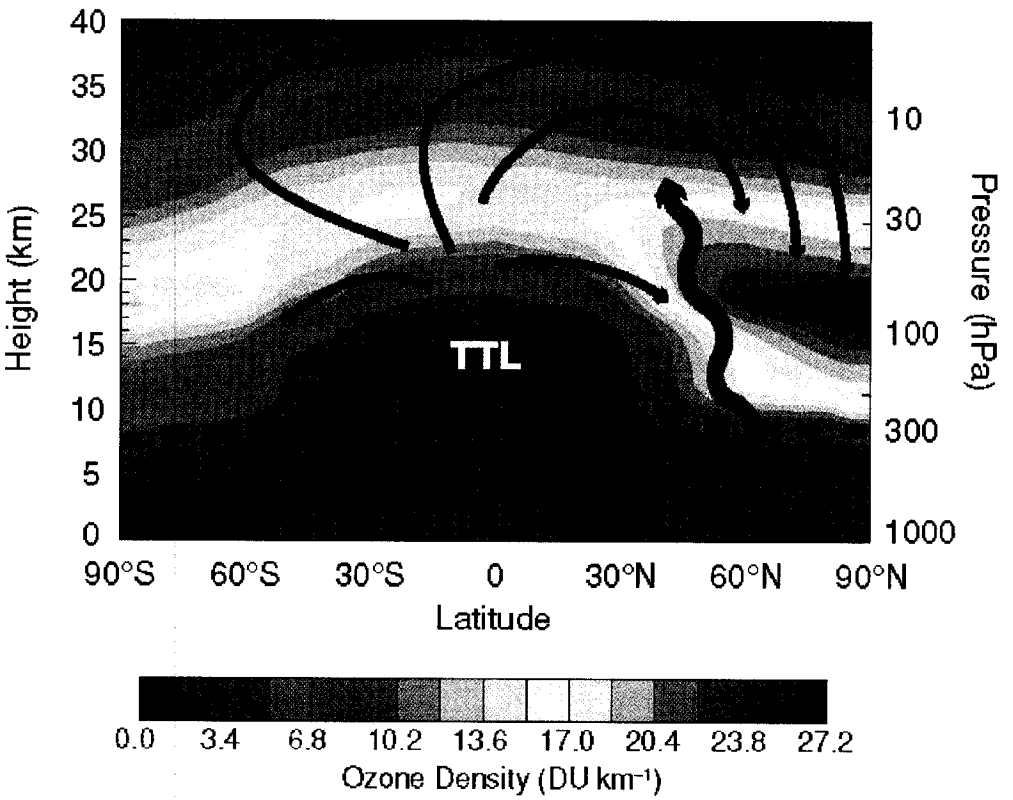

Figure 2.1: Meridional cross-section of the atmosphere showing ozone density (colour contours; in Dobson units (DU) per km) during Northern Hemisphere (NH) winter (January to March). The dashed line denotes the tropopause, and TTL stands for tropical tropopause layer, a region of characteristics intermediate to those of the troposphere and stratosphere. The black arrows indicate the Brewer-Dobson circulation during NH winter, and the red arrow represents planetary waves that propagate from the troposphere into the winter stratosphere. Source: *Intergovernmental Panel on Climate Change* (2005, Box 1.2 Fig.).

2.1.2 The Polar Vortex

A polar night zonal westerly jet develops in response to the meridional temperature gradient that is created by atmospheric heating (cooling). In the Antarctic, the jet effectively isolates the polar vortex from the southern midlatitudes by preventing any mixing between air inside and outside the vortex. Because the vortex is dynamically isolated, no heat is delivered, and the vortex cools radiatively, causing temperatures within the Antarctic polar vortex to reach as low as 180 K. The Arctic polar night jet is not as effective in isolating the northern polar region from the warmer, ozone-rich midlatitude air due to the increased planetary wave activity. As a result, the Arctic polar vortex is less stable and the minimum temperatures within the vortex are generally warmer.

2.1.3 The Quasi-Biennial Oscillation

In the tropical stratosphere there is a quasi-periodic oscillation of the equatorial zonal winds from easterlies to westerlies with a period ranging from 24 to 30 months (*Reed et al.*, 1961). The alternating wind regimes of this 'quasi-biennial oscillation' (QBO) propagate downward from the top of the lower stratosphere (~30 km) to the tropical tropopause at a rate of about one km per month and arise from the interaction of the zonal mean flow and vertically propagating equatorial waves (*Lindzen and Holton*, 1968). The easterly phase of the QBO is generally stronger, with zonal mean winds of up to 40 m/s. The westerly phase is characterized by winds of up to 20 m/s. See *Baldwin et al.* (2001) for a detailed review.

2.1.4 The Semi-Annual Oscillation

Another dynamical feature of the stratosphere is the 'semi-annual oscillation' (SAO) of the zonal winds near the equatorial stratopause (~50 km) (*Reed*, 1962, 1966). The SAO has a period of six months related to the seasonal variation in solar heating. The SAO has peak zonal mean winds of about 30 m/s, eastward at the equinoxes and westward at the solstices. See *Hirota* (1980) for a detailed review.

2.2 Chemistry of the Stratosphere

2.2.1 Odd-Oxygen Chemistry

Chapman (1930) first described the chemistry of stratospheric O_3 through a cycle of 'Chapman reactions'. The cycle begins with the photolysis of molecular oxygen:

$$O_2 + h\nu \rightarrow O + O \qquad \text{(R2.1)}$$

The resulting atomic oxygen then rapidly combines with O_2 to form O_3:

$$O + O_2 + M \rightarrow O_3 + M \qquad \text{(R2.2)}$$

where M is a third body that is required to stabilize the reaction (generally N_2 or O_2). During the day, O_3 is quickly photolysed:

$$O_3 + h\nu \rightarrow O_2 + O \qquad \text{(R2.3)}$$

and also reacts with O:

$$O_3 + O \rightarrow O_2 + O_2 \qquad \text{(R2.4)}$$

An additional reaction is part of the original Chapman reactions:

$$O + O + M \rightarrow O_2 + M \qquad \text{(R2.5)}$$

but is now known to be insignificant in the stratosphere. Reactions (R2.2) and (R2.3) form a rapid photochemical equilibrium between O_3 and O, together referred to as 'odd oxygen', O_x.

Due to the larger amount of actinic flux, O_3 is created predominantly at tropical latitudes and then is transported to the polar regions by the Brewer-Dobson circulation, leading to the latitudinal distribution shown in Figure 2.1, with the largest concentrations (number densities) generally located in the polar regions, in particular the winter poles. The ascent in the tropics and descent at the poles also causes the altitude of the peak O_3 concentration to vary with latitude, with the peak occurring at about 25 km in the tropics and near 15 km in the polar regions.

The loss of O_3 by Reaction (R2.4) alone is not sufficient to account for the O_3 concentrations found in the stratosphere, predicting concentrations that are significantly higher than are observed. Additional loss mechanisms, loss through catalytic destruction, occur:

$$X + O_3 \rightarrow XO + O_2 \qquad \text{(R2.6)}$$

$$XO + O \rightarrow X + O_2 \qquad \text{(R2.7)}$$

$$\text{NET} : O + O_3 \rightarrow 2O_2$$

where X is the catalyst that is preserved in the cycle. The net result of this catalytic cycle is equivalent to Reaction (R2.4). In the stratosphere the primary catalysts in this cycle are hydrogen (H, OH) (*Bates and Nicolet*, 1950), nitrogen oxides (NO)

(*Crutzen*, 1970; *Johnston*, 1971) and halogens (Cl, Br) (*Molina and Rowland*, 1974; *Stolarski and Cicerone*, 1974; *Wofsy and McElroy*, 1974; *Wofsy et al.*, 1975). In the middle stratosphere (20-40 km), catalytic destruction by NO_x ($NO+NO_2$) dominates over ClO_x (Cl+ClO), HO_x (HO_2+OH+H) and loss from the Chapman cycle (O_x), as is shown in Figure 2.2. BrO_x (Br+BrO) also contributes to O_3 loss, but the contribution is small except in the lowest stratosphere (below ~20 km).

The above catalytic cycle is limited by Reaction (R2.7), and as a result is dependant on the availability of atomic oxygen. Since the concentration of O increases with altitude through the stratosphere, the O_3 loss due to this cycle is greatest in the middle and upper stratosphere. Other catalytic cycles that are not limited by atomic oxygen, such as:

$$OH + O_3 \rightarrow HO_2 + O_2 \qquad \text{(R2.8)}$$

$$HO_2 + O_3 \rightarrow OH + 2O_2 \qquad \text{(R2.9)}$$

$$\text{NET} : 2O_3 \rightarrow 3O_2$$

are important in regions of low atomic oxygen concentrations (e.g. the lower stratosphere).

In the polar regions during winter and early spring, the low temperatures, particularly in the Antarctic due to the strong and stable vortex, allow for the formation of polar stratospheric clouds (PSCs). Three types of PSCs exist:

- Type Ia (crystalline): nitric acid trihydrate (NAT), at temperatures less than 195 K

- Type Ib (liquid): supercooled ternary solutions (STS) of HNO_3, H_2O and H_2SO_4, at temperatures less than 195 K

- Type II: water ice crystals, at temperatures less than 185 K

Heterogenous reactions on the PSC particle surfaces lead to a greatly enhanced concentrations of ClO (see Section 2.3.2), allowing two additional catalytic cycles to contribute to O_3 loss. The first is the ClO dimer cycle (*Molina and Molina*, 1987):

$$ClO + ClO + M \rightarrow Cl_2O_2 + M \quad \text{(R2.10)}$$

$$Cl_2O_2 + h\nu \rightarrow ClO_2 + Cl \quad \text{(R2.11)}$$

$$ClO_2 + M \rightarrow Cl + O_2 + M \quad \text{(R2.12)}$$

$$2(Cl + O_3 \rightarrow ClO + O_2) \quad \text{(R2.13)}$$

$$\text{NET} : 2O_3 \rightarrow 3O_2$$

The second is the ClO-BrO cycle (*McElroy et al.*, 1986; *Tung et al.*, 1986):

$$ClO + BrO \rightarrow BrCl + O_2 \quad \text{(R2.14)}$$

$$BrCl + h\nu \rightarrow Br + Cl \quad \text{(R2.15)}$$

$$Cl + O_3 \rightarrow ClO + O_2 \quad \text{(R2.16)}$$

$$Br + O_3 \rightarrow BrO + O_2 \quad \text{(R2.17)}$$

$$\text{NET} : 2O_3 \rightarrow 3O_2$$

These cycles are also not limited by atomic oxygen.

The catalytic cycles are limited by the formation of reservoir species, most importantly HCl, $ClONO_2$ and HNO_3:

$$Cl + CH_4 \rightarrow HCl + CH_3 \quad \text{(R2.18)}$$

$$ClO + NO_2 + M \rightarrow ClONO_2 + M \quad \text{(R2.19)}$$

$$OH + NO_2 + M \rightarrow HNO_3 + M \quad \text{(R2.20)}$$

that store the reactive species in less reactive forms.

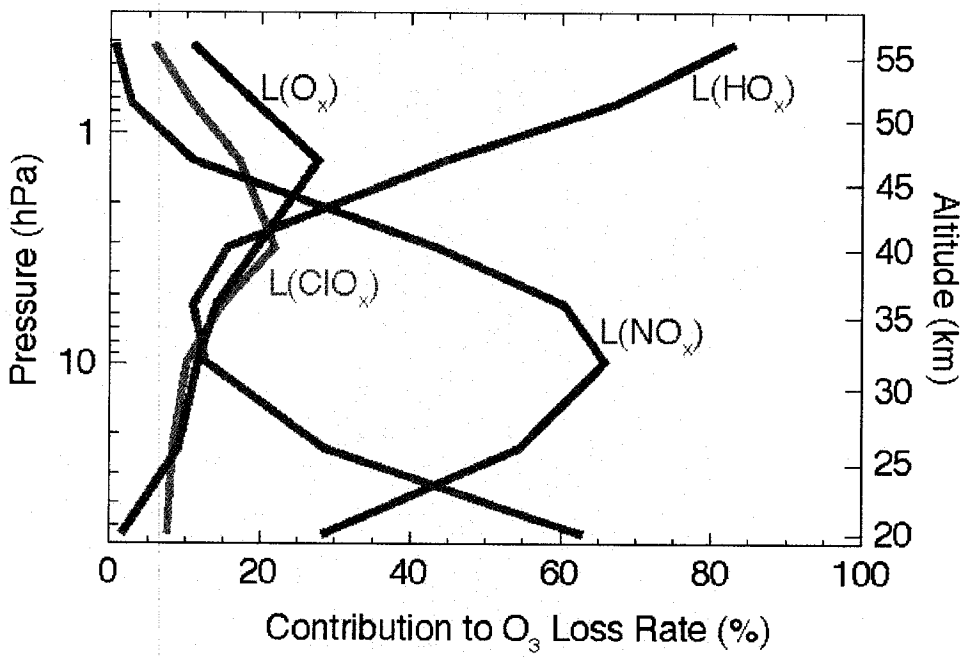

Figure 2.2: The vertical distribution of the relative importance of the contributions to O_3 loss by the HO_x, ClO_x and NO_x cycles as well as the Chapman loss cycle (O_x). Source: *Intergovernmental Panel on Climate Change* (2005, Fig. 1.11).

2.2.2 Nitrogen Chemistry

Reactive nitrogen species, known collectively as NO_y ($N+NO+NO_2+NO_3+HNO_3+2\times N_2O_5+ClONO_2+BrONO_2+HO_2NO_2$), play an important role in stratospheric O_3 chemistry. Reactive nitrogen species are the largest contributors to O_3 destruction in the middle stratosphere, primarily through catalytic cycles involving NO and NO_2, as mentioned in Section 2.2.1. In the lower stratosphere, NO_y also indirectly affects O_3 through its influence on the partitioning of the HO_x, ClO_x and BrO_x families.

The primary source of stratospheric NO_y is the oxidation of N_2O:

$$N_2O + O(^1D) \rightarrow NO + NO \qquad \text{(R2.21)}$$

where $O(^1D)$ is an excited state of atomic oxygen. This competes with other N_2O loss processes:

$$N_2O + h\nu \rightarrow N_2 + O \qquad \text{(R2.22)}$$

$$N_2O + h\nu \rightarrow NO + N \qquad \text{(R2.23)}$$

$$N_2O + O(^1D) \rightarrow N_2 + O_2 \qquad \text{(R2.24)}$$

with Reaction (R2.22) being dominant in the stratosphere. Reaction (R2.23) also produces NO_y, but is much less important than Reaction (R2.21). The source of N_2O is a combination of natural and anthropogenic surface sources. A much smaller and more sporadic source of NO_y is downward transport from the mesosphere of NO created by the precipitation of energetic particles in the auroral zones in the polar night.

The main loss of stratospheric NO_y is transport into the troposphere. In the upper stratosphere NO_y is lost through:

$$N + NO \rightarrow N_2 + O \qquad \text{(R2.25)}$$

NO_y can also be removed from the gas phase by sequestering HNO_3 in stratospheric aerosols ('denoxification'):

$$N_2O_5(g) + H_2O(s) \rightarrow 2HNO_3(s) \qquad \text{(R2.26)}$$

where (g) and (s) refer to gas phase and solid phase, respectively. The sedimentation of these aerosols can lead to the permanent removal of NO_y from the lower stratosphere ('denitrification'). These processes occur on PSCs in the winter polar stratosphere (*Crutzen and Arnold*, 1986; *Molina et al.*, 1987) and can also occur at midlatitudes at times when the aerosol loading is high, for example after major volcanic eruptions. Stratospheric 'renitrification' can occur if the aerosols sublimate as they descend or due to an intrusion of warmer air (e.g. in the polar spring).

As discussed in Section 2.2.1, the term NO_x refers to the sum of NO and NO_2, and is used due to the strong interaction and short-lived nature of these species, with:

$$NO_2 + h\nu \rightarrow NO + O \qquad \text{(R2.27)}$$

$$NO_2 + O \rightarrow NO + O_2 \qquad \text{(R2.28)}$$

$$NO + O_3 \rightarrow NO_2 + O_2 \qquad \text{(R2.29)}$$

$$NO + ClO \rightarrow NO_2 + Cl \qquad \text{(R2.30)}$$

$$NO + HO_2 \rightarrow NO_2 + OH \qquad \text{(R2.31)}$$

NO_3 is also short-lived, but is often not included in NO_x. The NO_x species are photochemically active, and their relative abundances are primarily determined by the availability of solar radiation. During daytime, the balance is pushed toward NO. As the sun sets the NO_2 concentration rapidly increases (see Figure 2.3).

During nighttime, NO_x is converted to NO_y through the production of N_2O_5 (and NO_3):

$$NO_2 + O_3 \rightarrow NO_3 + O_2 \quad \text{(R2.32)}$$

$$NO_3 + NO_2 + M \rightarrow N_2O_5 + M \quad \text{(R2.33)}$$

which is photolysed during daytime to recreate NO_x:

$$N_2O_5 + h\nu \rightarrow NO_2 + NO_3 \quad \text{(R2.34)}$$

$$NO_3 + h\nu \rightarrow NO_2 + O \quad \text{(R2.35)}$$

$$NO_3 + h\nu \rightarrow NO + O_2 \quad \text{(R2.36)}$$

The NO_3 is photolysed rapidly at sunrise, while N_2O_5 is more slowly photolysed, creating a positive gradient in NO_2 during the day. This is shown in Figure 2.3, which illustrates the diurnal variation of NO_2 at different altitudes.

NO_x can be converted to reservoir species via the following reactions:

$$OH + NO_2 + M \rightarrow HNO_3 + M \quad \text{(R2.37)}$$

$$ClO + NO_2 + M \rightarrow ClONO_2 + M \quad \text{(R2.38)}$$

$$BrO + NO_2 + M \rightarrow BrONO_2 + M \quad \text{(R2.39)}$$

and can be released from the reservoir species by:

$$N_2O_5 + M \rightarrow NO_2 + NO_3 + M \quad \text{(R2.40)}$$

$$NO_3 + NO \rightarrow NO_2 + NO_2 \quad \text{(R2.41)}$$

$$HNO_3 + h\nu \rightarrow OH + NO_2 \quad \text{(R2.42)}$$

and the photolysis of $ClONO_2$ and $BrONO_2$.

2.3 Ozone Depletion

Over the past few decades the amount of O_3 in the stratosphere has been slowly declining at midlatitudes, while in the polar regions a severe springtime depletion has been occurring, particularly over Antarctica. A brief introduction to these issues and the future of stratospheric O_3 is presented below.

2.3.1 Global Ozone

The depletion of stratospheric O_3 at midlatitudes was first reported by *Reinsel et al.* (1982) and has been taking place since the early 1970s. As an example, Figure 2.4 shows column O_3 variations in the 60°N to 60°S latitude band measured using ground-based instruments over the past few decades. As is illustrated, many factors affect the O_3 abundance, including the annual cycle, solar cycle, QBO and volcanic activity. However, when these effects are removed from the measurements, a clear trend emerges, reaching a maximum O_3 depletion of about 10 DU, or 3%, in the late 1990s relative to the pre-1970 values. This trend is attributed to O_3 destruction from an

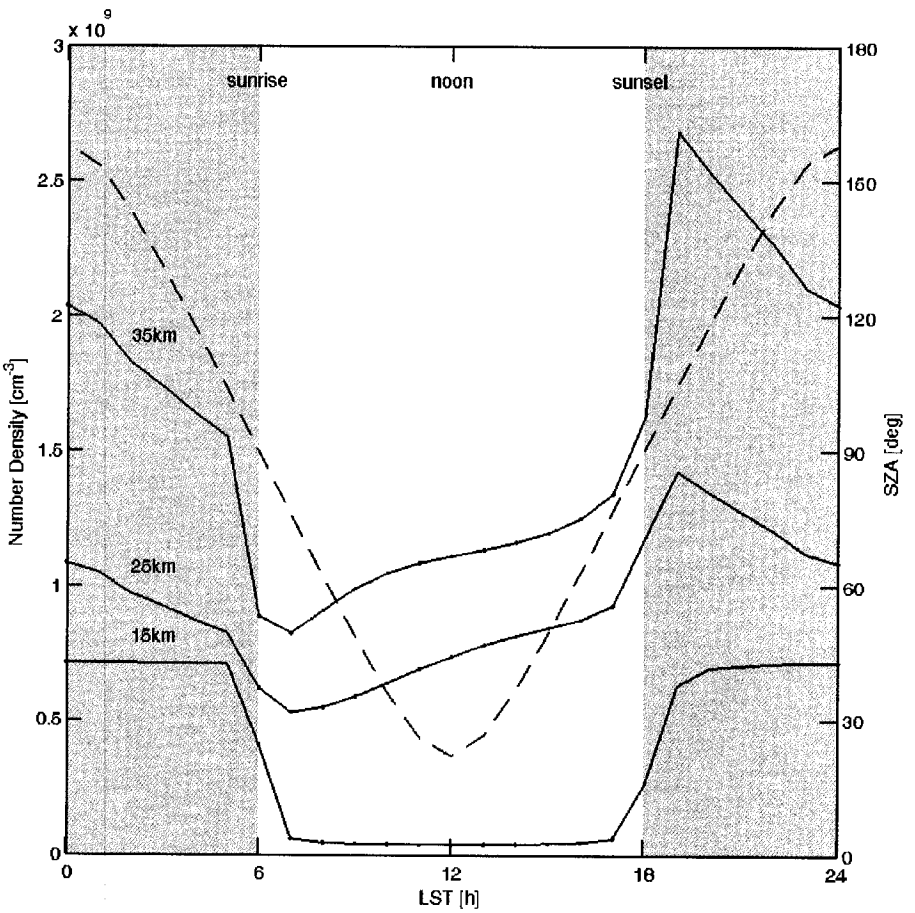

Figure 2.3: NO_2 concentrations (solid lines) and solar zenith angle (SZA) (dashed line) as a function of local solar time (LST) and altitude based on simulations from the University of California, Irvine photochemical box model (*McLinden et al.*, 2000; *Prather*, 1992) for equatorial conditions (1 June, albedo = 0.2). The NO_2 concentrations drop rapidly at sunrise due to photolysis and increase similarly at sunset as NO_2 reforms from NO reacting with O_3.

increase in particular anthropogenic trace gases. The primary contributor is reactive chlorine released from anthropogenic halocarbons, in particular chlorofluorocarbons (CFCs). CFCs were in widespread use in the 1970s and 1980s as refrigerants and propellants because of their non-toxic and inert chemical structure. When released into the atmosphere (in the manufacturing process or though use or leakage) CFCs prove difficult to remove, with no appreciable short-term loss mechanism in the troposphere. As a result, CFCs released into the troposphere are transported into the stratosphere where they are photolysed, releasing chlorine atoms. A secondary contributor is reactive bromine released from halons, which are long-lived halocarbons used in fumigants and fire extinguishers. Other contributors are carbon tetrachloride (CCl_4), methyl bromide (CH_3Br), methyl chloroform (CH_3CCl_3), bromochloromethane (CH_2BrCl) and hydrobromofluorocarbons (HBFCs). The short-term replacements for CFCs, hydrochlorofluorocarbons (HCFCs), also lead to O_3 depletion, though significantly less than CFCs.

In recent years, a leveling-off or possibly the beginnings of an O_3 recovery has begun to appear due primarily to the controls over halocarbon emissions (see Section 2.3.3) that have reduced the equivalent effective stratospheric chlorine (EESC) in the atmosphere, as shown in Figure 2.5. EESC is a measure of the destructive potential of all of the ODS in the stratosphere.

2.3.2 Polar Ozone

Farman et al. (1985) made measurements of column O_3 in the springtime Antarctic

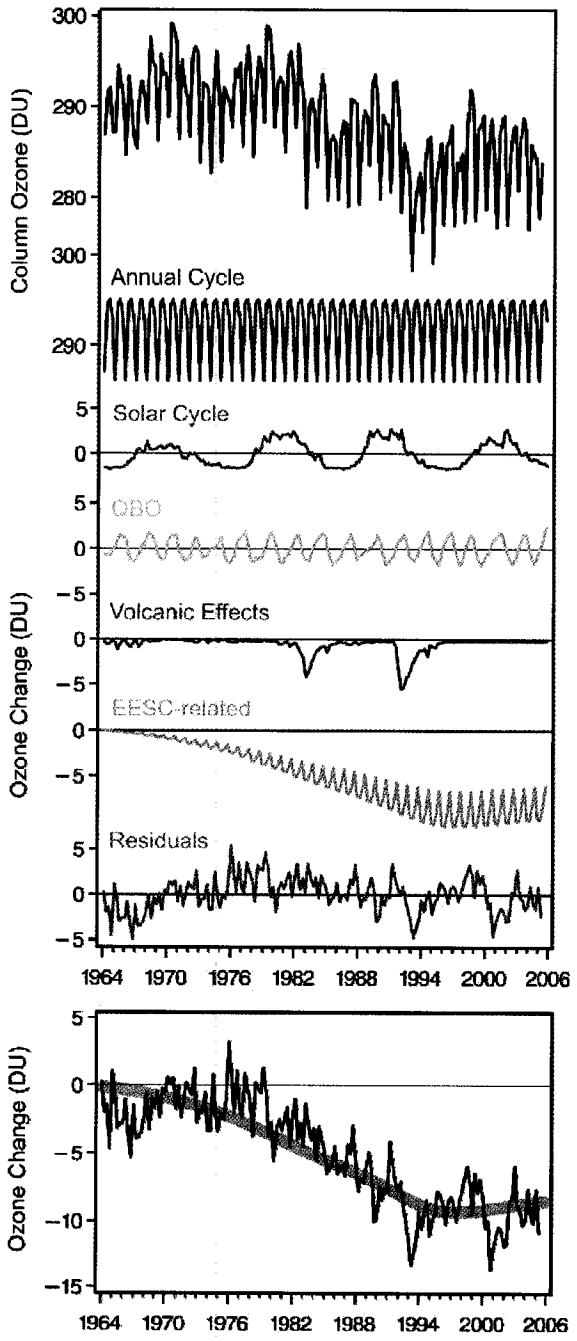

Figure 2.4: Top: Ozone variations for 60°S-60°N estimated from ground-based data and individual components that comprise ozone variations. Bottom: Deseasonalized, area-weighted total ozone deviations estimated from ground-based adjusted for solar, volcanic and QBO effects, for 60°S-60°N. The thick yellow line represents the EESC (equivalent effective stratospheric chlorine) curve scaled to fit the data from 1964-2005. Source: *World Meteorological Organization* (2007, Fig. 3-1).

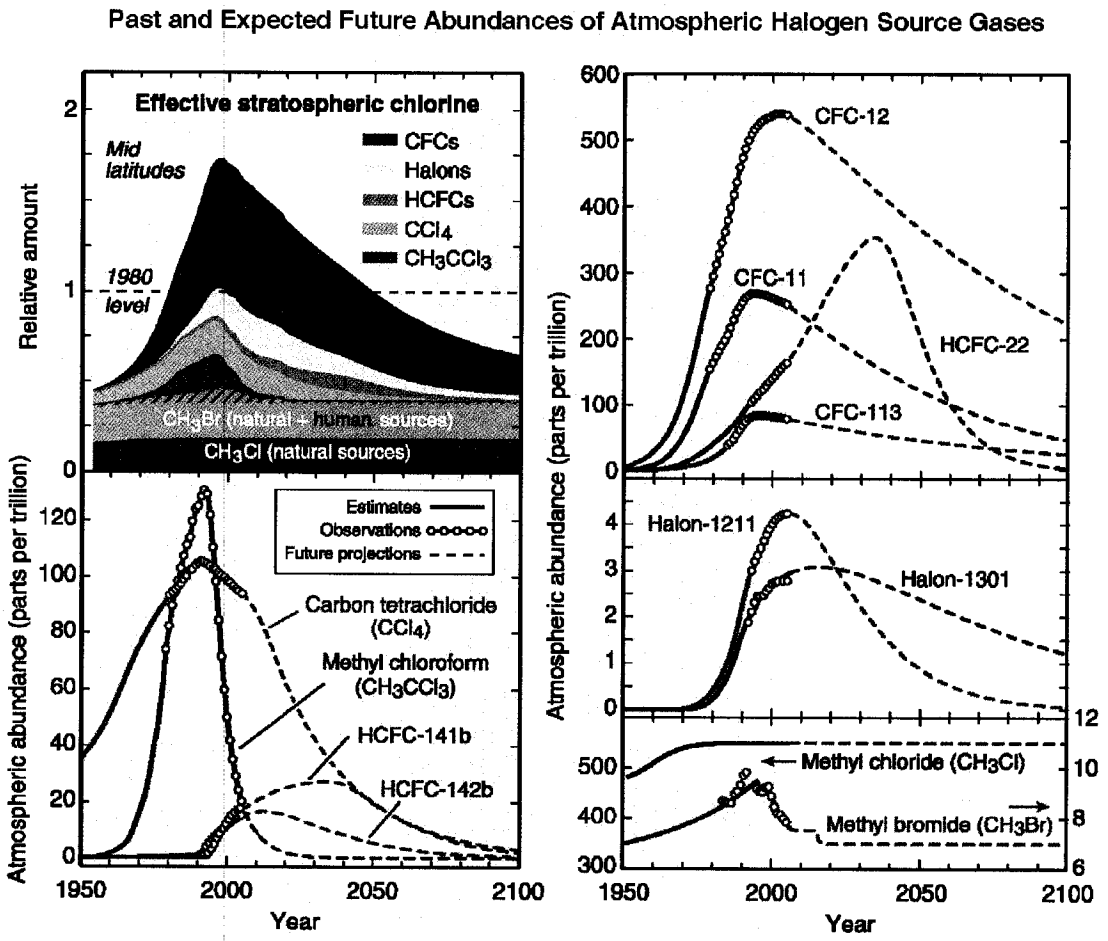

Figure 2.5: Halogen source gas changes. Source: *World Meteorological Organization* (2007, Fig. Q16-1).

vortex that showed considerably less O_3 than had been measured previously. This was later confirmed with satellite measurements by *Stolarski et al.* (1986). This was the first recognition of the Antarctic 'ozone hole'. The series of maps of total O_3 (vertical columns) for the Southern Hemisphere (SH) in October covering the period from 1979 to 2003 in Figure 2.6 and the time series of average total O_3 in Figure 2.7 show the extent of the Antarctic O_3 depletion.

The severe depletion is due to a combination of the cold temperatures within the polar vortex and the springtime release of ODS, primarily reactive chlorine from CFCs (*Solomon et al.*, 1986). As discussed in Section 2.2.1, at the low stratospheric temperatures within the winter polar vortex, PSCs are formed. The cloud particles provide surfaces for a number of heterogeneous reactions to take place:

$$ClONO_2(g) + HCl(s) \rightarrow Cl_2(g) + HNO_3(s) \quad \text{(R2.43)}$$

$$ClONO_2(g) + H_2O(s) \rightarrow HOCl(g) + HNO_3(s) \quad \text{(R2.44)}$$

$$HOCl(g) + HCl(s) \rightarrow Cl_2(g) + H_2O(s) \quad \text{(R2.45)}$$

The Cl_2 and HOCl accumulated through these processes during the polar night are photolysed when the sun rises in the spring, releasing Cl atoms:

$$Cl_2 + h\nu \rightarrow Cl + Cl \quad \text{(R2.46)}$$

$$HOCl + h\nu \rightarrow OH + Cl \quad \text{(R2.47)}$$

that are subsequently converted to ClO:

$$Cl + O_3 \rightarrow ClO + O_2 \quad \text{(R2.48)}$$

This process is known as 'chlorine activation', releasing chlorine from the reservoir species HCl and $ClONO_2$. The ClO is then available to catalytically destroy O_3 as described in Section 2.2.1. Furthermore, the denoxification and denitrification of the lower stratosphere by PSCs (in particular Type II PSCs) limits the amount of NO_2 available to react with ClO to produce $ClONO_2$.

Ozone depletion in the Arctic has also been observed, as is shown in Figures 2.7 and 2.8, but is generally not as severe or consistent due to dynamical conditions - as mentioned earlier, the Arctic polar vortex is not as stable as the Antarctic vortex largely because of the more variable topography, which leads to warmer temperatures and less PSC formation.

2.3.3 The Future of Stratospheric Ozone

The recognition of the severe polar O_3 depletion due to CFCs led to the *Vienna Convention for the Protection of the Ozone Layer* in 1985 and the subsequent *Montreal Protocol on Substances that Deplete the Ozone Layer* in 1987. The Montreal Protocol (and amendments) placed controls on the production of the halocarbons that contribute to ozone depletion. As a result, the concentrations of a number of halocarbons are now decreasing in the atmosphere, with the EESC predicted to reach its pre-1980 level by 2050, as is shown in Figure 2.5.

Figure 2.9 shows that atmospheric models that account for expected changes in halogen gases and other atmospheric parameters predict a full ozone recovery (to pre-1980 values) in the midlatitudes by 2030. The recovery in the Antarctic stratosphere

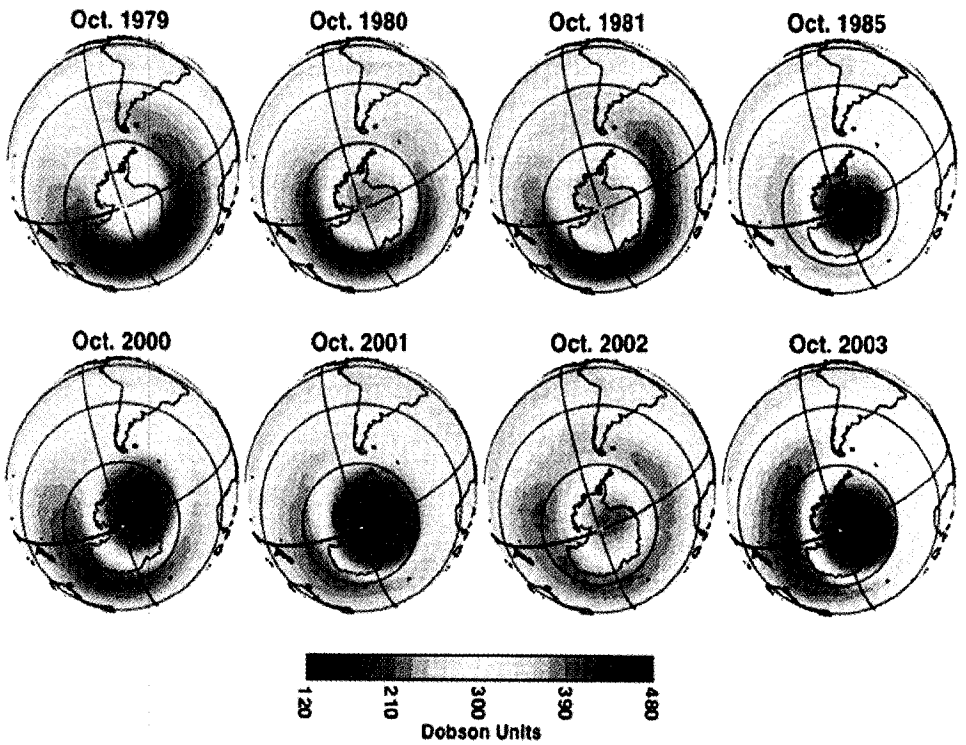

Figure 2.6: October monthly-averaged total ozone for the Southern Hemisphere derived from the Nimbus-7 Total Ozone Mapping Spectrometer (TOMS) (1979-1981 and 1985) and the Earth Probe TOMS (2000-2003). Source: Courtesy of P. Newman.

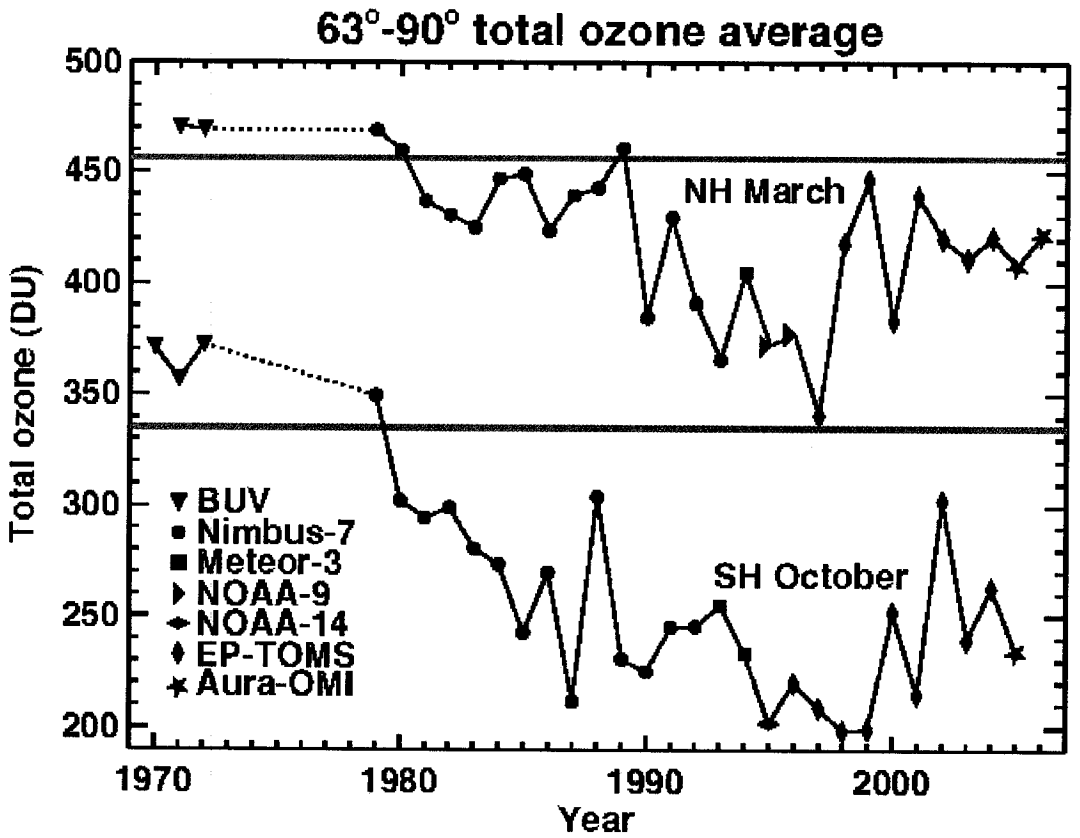

Figure 2.7: Total ozone average of 63° to 90° latitude in March (NH) and October (SH). Symbols indicate the satellite data that have been used in different years. The horizontal gray lines represent the average total ozone in March and October for the years prior to 1983 for the NH and SH. Source: *World Meteorological Organization* (2007, Fig. 4-7).

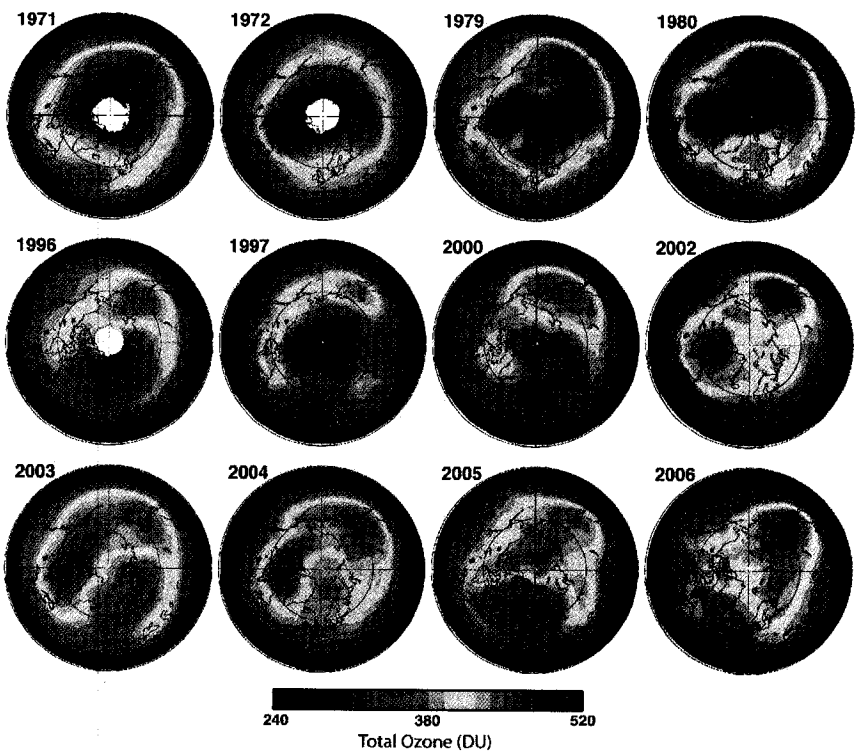

Figure 2.8: March monthly averaged total ozone for the Northern Hemisphere. The 1971 and 1972 images are from the Nimbus-4 Backscatter Ultraviolet (BUV) instrument; the 1979 and 1980 images are from the Nimbus-7 TOMS instrument; the 1996 image is from the NOAA-9 Solar BUV instrument (SBUV/2); the 1997, 2000, 2002, 2003 and 2004 images are from the Earth Probe TOMS instrument; and the 2005 and 2006 images are from OMI. Source: *World Meteorological Organization* (2007, Fig. 4-6).

is expected to occur later due to the older age of air compared to the lower latitudes, with a return to 1980 levels occurring around 2050 (or later). The range of model predictions shown in Figure 2.9 is from the use of a number of different models of the future atmosphere (*World Meteorological Organization*, 2007). Note that the range of model calculations is significantly larger than the range of observations.

2.4 Climate Change

It is well established that radiative forcing from increased concentrations of anthropogenic greenhouse gases is causing a 'global warming' phenomenon in global surface temperatures. The observed surface temperature increase is shown in Figure 2.10 along with the associated rise in sea level and decrease in snow cover. Many factors contribute to the positive radiative forcing causing the global warming, as is shown in Figure 2.11, with the primary contributor being the anthropogenic increase in the greenhouse gases CO_2, CH_4, N_2O, halocarbons and tropospheric O_3 (*Intergovernmental Panel on Climate Change*, 2007a). The primary concern with respect to global warming is the increase in the temperature of the surface and oceans and the related consequences (*Intergovernmental Panel on Climate Change*, 2007b). However, the effects on the stratosphere are also of concern.

In the stratosphere, the combined influence of increased greenhouse gases and ozone depletion has been a cooling, as shown in Figure 2.12. In the upper stratosphere, this cooling can lead to increased levels of ozone through the reduction of the rates of gas phase ozone destruction. However, in the polar lower stratosphere the

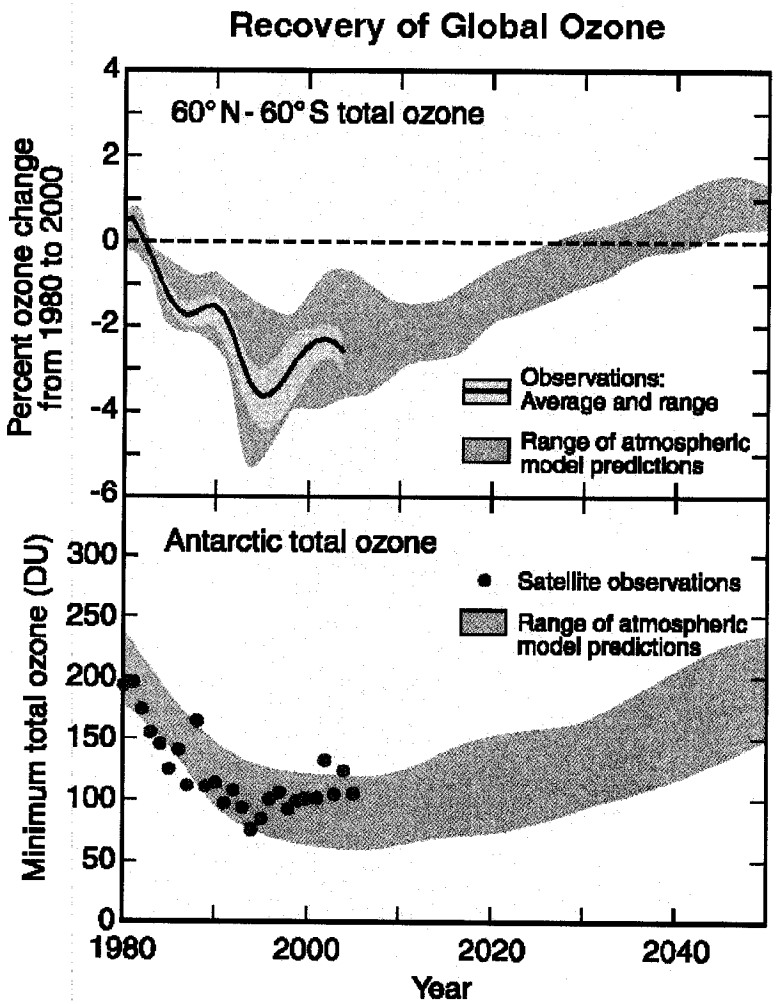

Figure 2.9: Observed midlatitude total ozone (top panel) and September-October minimum total ozone values over Antarctica (bottom panel) along with the range of model predictions. Also plotted in the top panel is the pre-1980 average total ozone value as a baseline for global ozone recovery. Source: *World Meteorological Organization* (2007, Fig. Q20-1).

cooler temperatures can lead to increased PSC formation and potentially more O_3 depletion, at least until EESC decreases further. Additional increases in greenhouse gases are expected to cool the upper stratosphere further (*Intergovernmental Panel on Climate Change*, 2007a), although any O_3 recovery will mitigate this effect. The temperature changes may also affect the stratospheric circulation, complicating the ability to accurately predict O_3 recovery.

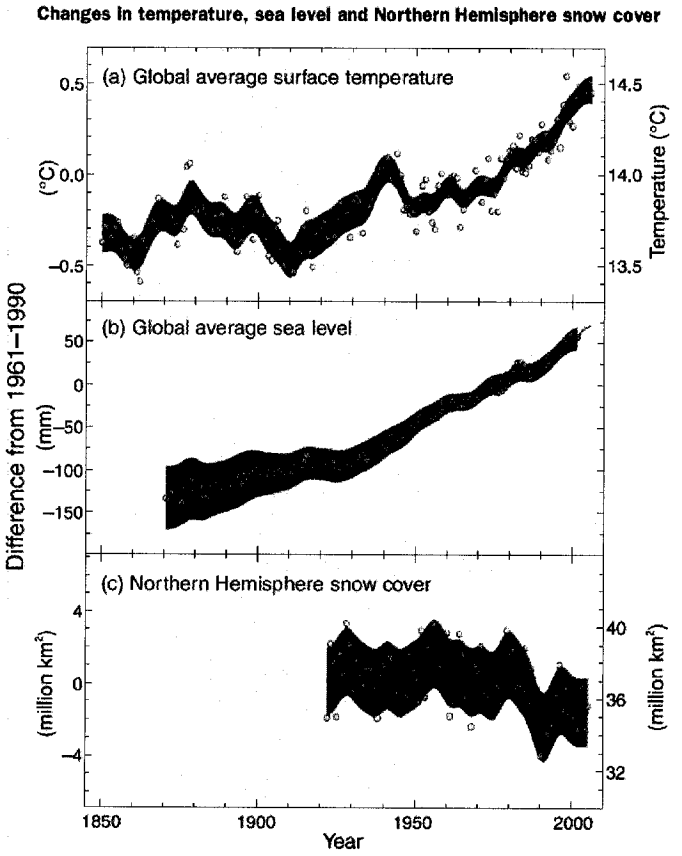

Figure 2.10: Observed changes in (a) global average surface temperature; (b) global average sea level from tide gauge (blue) and satellite (red) data; and (c) Northern Hemisphere snow cover for March-April. All differences are relative to corresponding averages for the period 1961-1990. Smoothed curves represent decadal averaged values while circles show yearly values. The shaded areas are the uncertainty intervals estimated from a comprehensive analysis of known uncertainties (a and b) and from the time series (c). Source: *Intergovernmental Panel on Climate Change* (2007a, Fig. SPM.3).

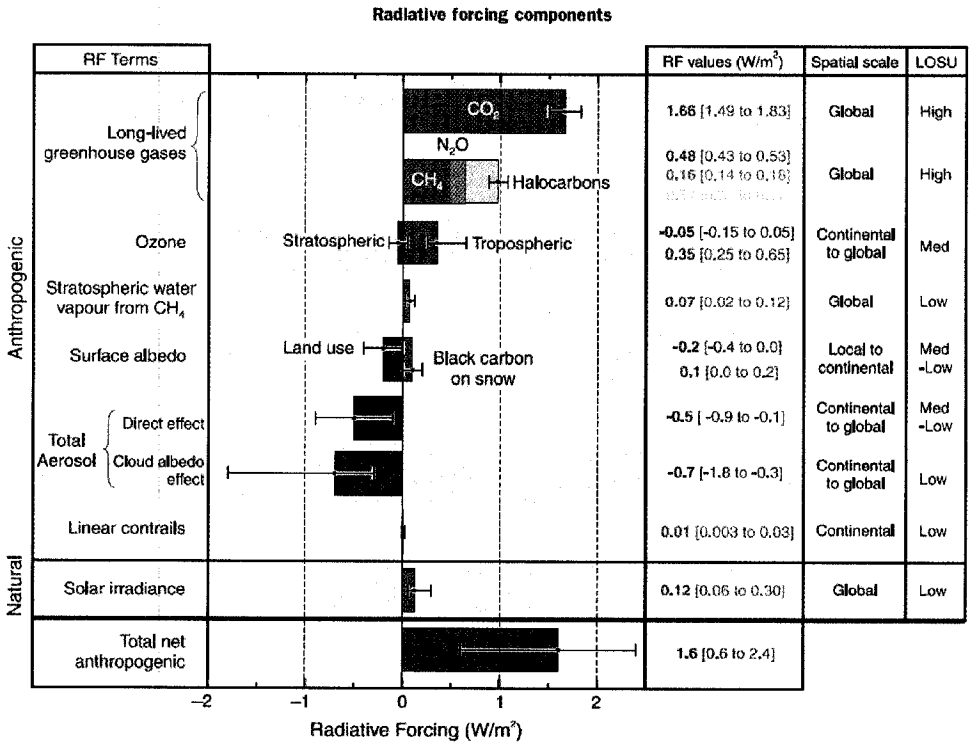

Figure 2.11: Global average radiative forcing (RF) in 2005 (best estimates and 5 to 95% uncertainty ranges) with respect to 1750 for CO_2, CH_4, N_2O and other important agents and mechanisms, together with the typical geographical extent (spatial scale) of the forcing and the assessed level of scientific understanding (LOSU). Aerosols from explosive volcanic eruptions contribute an additional episodic cooling term for a few years following an eruption. The range for linear contrails does not include other possible effects of aviation on cloudiness. Source: *Intergovernmental Panel on Climate Change* (2007a, Fig. SMP.2).

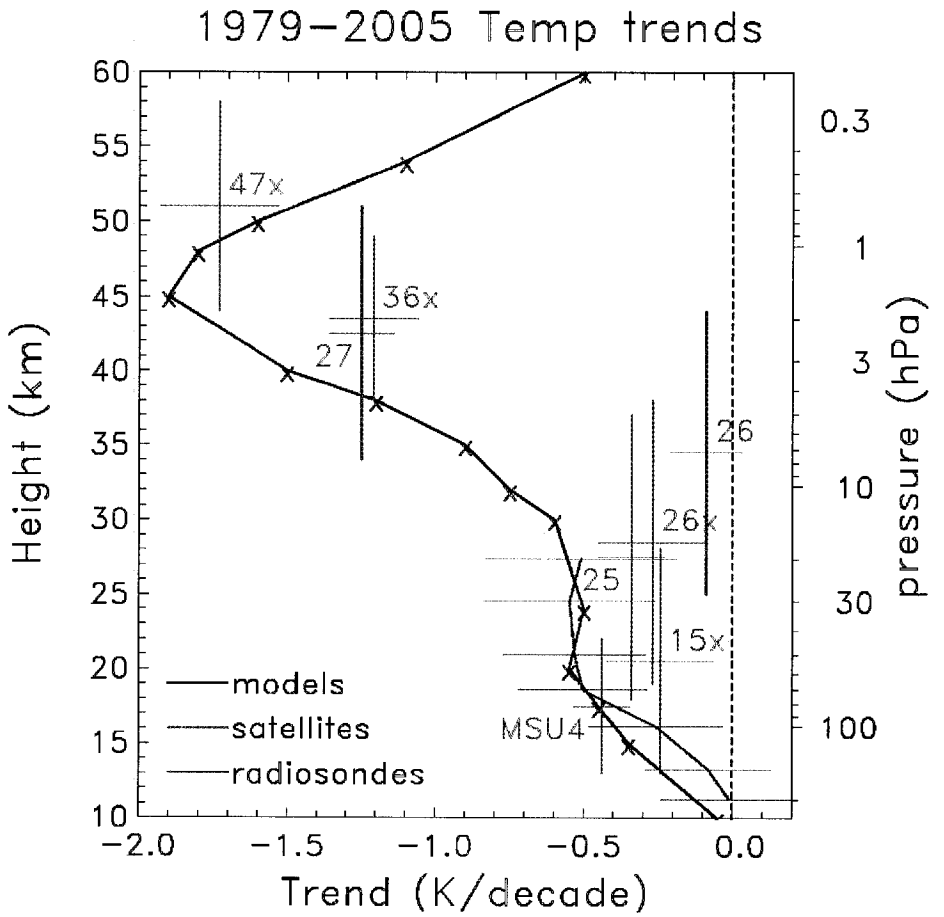

Figure 2.12: Vertical profile of temperature trends derived from satellite and radiosonde data over 60°N-60°S for the period 1979-2005, together with a synthesis of model results. The satellite data are from a number of fundamental (26, 26, 27) and synthetic (15x, 26x, 36x, 47x) channels from the Stratospheric Sounding Unit (SSU) and one channel (MSU4) from the Microwave Sounding Unit (MSU), instruments that have flown on a number of operational satellites. Source: *World Meteorological Organization* (2007, Fig. 5-6).

Chapter 3

Sounding the Atmosphere Using Limb-Scattered Sunlight

The limb-scatter technique involves passive remote measurements of UV/visible/near-infrared (IR) sunlight scattered by molecules and particles from the limb of the atmosphere. This chapter provides an introduction to the limb-scatter observation geometry and radiative transfer, followed by a presentation of some existing radiative transfer models (RTMs), including sample limb-scatter calculations.

3.1 Limb-Scatter Geometry

The limb-scatter viewing geometry is illustrated in Figures 3.1 and 3.2. A limb-scatter observation is defined by the tangent height (TH) and the SZA, θ_0, and single scattering angle (SSA), Θ, at the tangent point along the observation line of sight (LOS). Alternatively, the difference in azimuth angle (dAZ),$\Delta\phi$, can be used instead

of the SSA, where the two are related by:

$$\cos(\Theta) = \cos(\theta_0) * \cos(\theta) + \sin(\theta_0) * \sin(\theta) * \cos(\Delta\phi) \tag{3.1}$$

where the zenith angle θ is, by definition, 90° at the tangent point for limb measurements. Forward scattering is defined as $\Delta\phi < 90°$, while backward scattering is defined as $\Delta\phi > 90°$.

As is shown in Figure 3.2, the total limb-scatter radiance contains contributions from single scattering (SS), albedo scattering (AS) and multiple scattering (MS), causing a complicated radiative transfer environment.

3.2 Limb-Scatter Radiative Transfer

This section describes the radiative transfer of limb-scattered sunlight in the atmosphere, beginning with a brief introduction to the radiative transfer equation (RTE) and its application to limb-scatter for both singly- and multiply-scattered light. Approaches to the problem for spherical geometries are then presented. More complete treatments of atmospheric radiation and radiative transfer can be found in *Goody and Yung* (1989) and *Thomas and Stamnes* (1999).

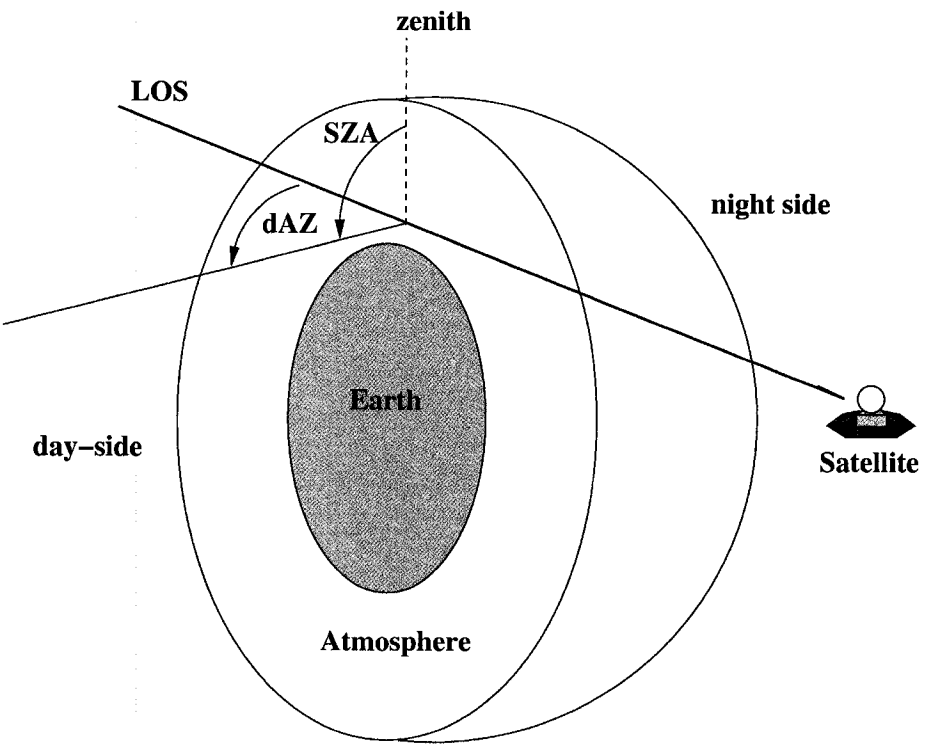

Figure 3.1: Limb-scatter geometry. Source: Courtesy of S. Brohede.

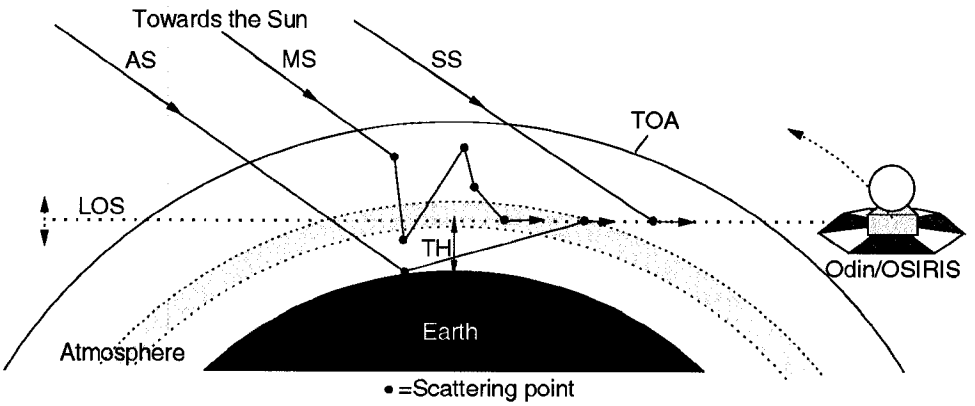

Figure 3.2: Limb-scatter viewing geometry illustrating the contribution of SS, AS and MS to the measurements. TOA is the top of the atmosphere. Source: *Haley et al.* (2004, Fig. 1).

3.2.1 The Radiative Transfer Equation

The radiation field of the atmosphere, including polarization, can be described using the Stokes vector:

$$\mathbf{I} = \begin{pmatrix} I \\ Q \\ U \\ V \end{pmatrix} \tag{3.2}$$

The four Stokes components describe the polarization properties of the electromagnetic radiation. I describes the total radiance (intensity) of the radiation, Q and U describe the linear polarization, and V describes the circular polarization. If the radiation is assumed to be unpolarized (i.e. $Q = U = V = 0$), I is the so-called

'scalar approximation'. The unit of energy used in this work is the spectral radiance (or spectral intensity). The spectral radiance is the flux of energy in a given direction per second per unit wavelength range per unit solid angle per unit area perpendicular to the given direction, for example photons/(cm^2·s·nm·sr). In the presentation of the radiative transfer equation below, the radiances are assumed to be unpolarized for simplicity. However, in some applications, in particular when an accurate calculation of the absolute radiance is required or when the quantity of interest has a significant dependence on the degree of polarization of the atmosphere, the more thorough treatment is required.

The radiative transfer equation for unpolarized monochromatic radiation in an isotropic medium can be expressed as (e.g. *Chandrasekhar*, 1960):

$$\frac{dI(\mathbf{r},\mathbf{\Omega})}{ds} = -k_e(\mathbf{r})I(\mathbf{r},\mathbf{\Omega}) + J(\mathbf{r},\mathbf{\Omega}) \tag{3.3}$$

with corresponding boundary conditions, where $\mathbf{r}$ and $\mathbf{\Omega}$ are the position of the observer and the direction of light propagation, respectively, and J is the source function, describing the sources of radiation within the atmosphere. The extinction coefficient, k_e, is given by the sum of the scattering coefficient, k_s, and the absorption coefficient, k_a (i.e. $k_e = k_s + k_a$). The coefficients are related to the extinction cross section, σ_e, scattering cross section, σ_s, and absorption cross section, σ_a, by $k_{(e,s,a)}(z) = n(z)\sigma_{(e,s,a)}$, where $n(z)$ is the number density at altitude z. When a number of different molecules and aerosols, denoted by i, contribute to the extinction, the total extinction coefficient is given by:

$$k_e(z) = \sum_i n_i(z)\sigma_{e,i} = \sum_i n_i(z)\left(\sigma_{s,i} + \sigma_{a,i}\right) \tag{3.4}$$

The integral form of Equation (3.3) is:

$$I(\mathbf{r}(s), \mathbf{\Omega}) = I(\mathbf{r}(0), \mathbf{\Omega}) \exp\left[-\tau(0, s)\right] + \int_0^s J(s', \mathbf{\Omega}) \exp\left[-\tau(s', s)\right] ds' \tag{3.5}$$

and describes the radiance observed at position $\mathbf{r}$ (point s) along a path (or LOS) in the propagation direction $\mathbf{\Omega}$. $I(\mathbf{r}(0), \mathbf{\Omega})$ represents the radiance at the end of the path (point zero). $\tau(s_a, s_b)$ is the 'optical depth' between the points s_a and s_b:

$$\tau(s_a, s_b) = \int_{s_a}^{s_b} k_e(s) ds \tag{3.6}$$

3.2.2 Radiative Transfer in a Scattering Atmosphere

In a scattering atmosphere and in the absence of thermal emission (e.g. measurements in the UV/visible/near-IR spectral region), the source function at point s is:

$$J(s, \mathbf{\Omega}) = \frac{k_s(s)}{4\pi} \int_{4\pi} \Phi(s, \mathbf{\Omega}', \mathbf{\Omega}) I(s, \mathbf{\Omega}') d\mathbf{\Omega}' \tag{3.7}$$

where Φ is the scattering phase function, describing the angular dependence of the light scattering.

In order to understand the scattering source function it is useful to separate the radiance field into its direct, I_{dir}, and diffuse (indirect), I_{diff}, components. The direct component is given by:

$$I_{dir}(s, \mathbf{\Omega}) = \pi F_0 \delta\left(\mathbf{\Omega} - \mathbf{\Omega}_0\right) \exp\left[-\tau(s_{TOA}, s)\right] \tag{3.8}$$

where πF_0 is the (unpolarized) solar flux per unit area incident in the direction $\mathbf{\Omega}_0$, δ is the Dirac delta function, and s_{TOA} is the point at the top of the atmosphere on

the path specified by $\mathbf{\Omega}_0$ and s. Using Equation (3.5), the diffuse component can be expressed as:

$$\begin{aligned} I_{diff}(s,\mathbf{\Omega}) &= I_{diff}(0,\mathbf{\Omega})\exp\left[-\tau(0,s)\right] + \\ &\int_0^s \left[J_{SS}(s',\mathbf{\Omega}) + J_{MS}(s',\mathbf{\Omega})\right]\exp\left[-\tau(s',s)\right]ds' \end{aligned} \tag{3.9}$$

I_{diff} is clearly more complex because of its dependence on the local source function, which also has a diffuse component (i.e. the radiative transfer is not localized). J_{SS} and J_{MS} are the single scattering and multiple scattering parts of the source function, respectively:

$$J_{SS}(s,\mathbf{\Omega}) = \frac{k_s(s)}{4\pi}\Phi(s,\mathbf{\Omega}_0,\mathbf{\Omega})I_{dir}(s,\mathbf{\Omega}) \tag{3.10}$$

$$J_{MS}(s,\mathbf{\Omega}) = \frac{k_s(s)}{4\pi}\int_{4\pi}\Phi(s,\mathbf{\Omega}',\mathbf{\Omega})I_{diff}(s,\mathbf{\Omega}')d\mathbf{\Omega}' \tag{3.11}$$

3.2.2.1 Boundary Conditions

Two boundary conditions are required in the solution of Equation (3.3): the inward radiance at the top of the atmosphere and upward radiance at the bottom of the atmosphere. In the UV/visible/near-IR spectral region considered here, the diffuse radiance at the top of the atmosphere is zero. The diffuse source at the bottom of the atmosphere can arise from reflection off of the surface. The normal (and simplest) approach is to treat the surface as Lambertian (isotropic), with its reflectivity expressed in terms of the surface albedo A, which is the ratio of the total up-welling irradiance to the total down-welling irradiance.

3.2.2.2 Solution

If only single scattering is considered, the solution to Equation (3.3) is:

$$I(\mathbf{r}(s), \mathbf{\Omega}) = \tag{3.12}$$
$$I(\mathbf{r}(0), \mathbf{\Omega}) \exp\left[-\tau(0, s)\right] +$$
$$\frac{F_0}{4} \int_0^s k_s(s) \Phi(s', \mathbf{\Omega}_0, \mathbf{\Omega}) \exp\left[-\tau(s_{TOA}, s')\right] \exp\left[-\tau(s', s)\right] ds'$$

If the path intersects with the ground, the radiance at the end of the path is given by:

$$I(\mathbf{r}(0), \mathbf{\Omega}) = A F_0 \exp\left[-\tau(s_{TOA}, 0)\right] \cos\left[\theta_0(0)\right] \tag{3.13}$$

where $\theta_0(0)$ is the solar zenith angle at the ground intersection point. If the path does not intersect the ground, as is the case for limb measurements, the radiance at the end of the path is zero:

$$I(\mathbf{r}(0), \mathbf{\Omega}) = 0 \tag{3.14}$$

with the exception being when the observation direction is directly towards the sun (solar occultation) or another extra-terrestrial source, cases that are not considered here.

The solution for higher-order scattering is significantly more complicated due to the dependence of the diffuse radiance radiance field on scattering at other locations, with the entire atmosphere acting as a coupled system, and requiring sophisticated methods to determine the local diffuse radiation. A thorough review of scattering theory and methods for computing the multiple scattering is given in *Hansen and Travis* (1974) and *Lenoble* (1985).

3.2.3 The Spherical Atmosphere

When dealing with limb observations, the spherical nature of the atmosphere must be considered and multiple scattering (often) can not be ignored (*Oikarinen et al.*, 1999). A number of methods for solving the RTE for limb-scattering in a spherical and multiply-scattering atmosphere are discussed below.

3.2.3.1 Monte Carlo Approach

The complicated nature of the radiative transfer in a three-dimensional, inhomogeneous, spherical atmosphere means that no complete analytical solution exists other than a Monte Carlo approach (*Marchuk et al.*, 1980). In this approach the RTE is not solved explicitly. Instead, the paths of model photons through the atmosphere are simulated numerically in a random fashion. The accuracy of the calculation depends on the number of photons simulated. Although there are a number of approaches to minimize the computationally expensive nature of the calculations, the Monte Carlo approach is still prohibitive for application to large data sets. However, Monte Carlo models are very useful for evaluating the approaches of approximate models (e.g. *Griffioen and Oikarinen*, 2000; *Loughman et al.*, 2004; *Rozanov et al.*, 2001).

3.2.3.2 Plane-Parallel Approximation

For many problems of radiative transfer in the atmosphere it is appropriate to assume that the atmosphere is 'plane-parallel', that is, one-dimensional planar with all quantities invariant in the horizontal direction. Under the plane-parallel approximation

the RTE is expressed in terms of the vertical optical depth, $\tau(z)$:

$$\tau(z) = \int_{z}^{z_{TOA}} k_e(z)dz \tag{3.15}$$

which is stated as τ for simplicity, and spherical polar coordinates (a zenith angle θ and an azimuth angle ϕ):

$$\mu \frac{dI(\tau,\mu,\phi)}{d\tau} = I(\tau,\mu,\phi) - J(\tau,\mu,\phi) \tag{3.16}$$

where $\mu = |\cos(\theta)|$.

For upward propagating radiance streams ($+\mu$), the integral expression is:

$$I(\tau,+\mu,\phi) = I(\tau_t,+\mu,\phi)\exp\left(-\frac{\tau_t-\tau}{\mu}\right) + \int_{\tau_t}^{\tau} J(\tau',\mu,\phi)\exp\left(-\frac{\tau'-\tau}{\mu}\right)\frac{d\tau'}{\mu} \tag{3.17}$$

where τ_t is the total vertical optical depth of the atmosphere. For downward propagating radiance streams ($-\mu$) the expression is:

$$I(\tau,-\mu,\phi) = I(0,-\mu,\phi)\exp\left(-\frac{\tau}{\mu}\right) + \int_{0}^{\tau} J(\tau',-\mu,\phi)\exp\left(-\frac{\tau-\tau'}{\mu}\right)\frac{d\tau'}{\mu} \tag{3.18}$$

As mentioned in Section 3.2.2.1, for UV/visible/near-IR radiation, $I(0,-\mu,\phi) = 0$ (assuming that there is no direct source). $I(\tau_t,\mu,\phi)$ is the source from reflection of the solar beam by the surface:

$$I(\tau_t,+\mu,\phi) = AF_0\mu_0\mu\exp(-\tau_s) \tag{3.19}$$

where μ_0 is the cosine of the solar zenith angle and τ_s is the optical depth along the solar beam to τ_t (the surface). The solar beam direction is defined as $(-\mu_0,\phi_0)$.

The plane-parallel scattering source function is given by:

$$\begin{aligned} J(\tau,\mu,\phi) &= \frac{\tilde{\omega}(\tau)}{4\pi}\int_0^{2\pi}\int_{-1}^{1} I(\tau,\mu',\phi')\Phi(\tau,\mu',\phi',\mu,\phi)d\mu'd\phi' + \\ &\quad \frac{\tilde{\omega}(\tau)}{4}F_0\Phi(\tau,-\mu_0,\phi_0,\mu,\phi)\exp(-\tau_s) \end{aligned} \tag{3.20}$$

where $\tilde{\omega}$ is the 'single scattering albedo', representing the ratio of extinction by scattering to the total extinction:

$$\tilde{\omega} = \frac{k_s}{k_e} = \frac{k_s}{k_s + k_a} \tag{3.21}$$

The first term on the right in Equation (3.20) represents the multiply-scattered radiation and the second term represents the singly-scattered radiation.

In a pure plane-parallel approach, τ_s in Equations (3.19) and (3.20) is calculated as:

$$\tau_s = \frac{\tau}{\mu_0} \tag{3.22}$$

However, at large SZAs (larger than about 75°), the plane-parallel calculations overestimate the attenuation of the solar beam since as μ_0 tends toward zero, the plane-parallel enhancement, $1/\mu_0$, becomes infinite. To improve the accuracy at large SZAs, a calculation of the optical depth along the solar beam in spherical geometry using the 'Chapman function' is required (e.g. *Dahlback and Stamnes*, 1991):

$$\tau_s = \sum_{j=1}^{p} \Delta\tau_j \left(\frac{\Delta s_j}{\Delta z_j}\right) \tag{3.23}$$

where p is the number of spherical layers above the scattering point at altitude z, Δz_j is the vertical thickness of layer j and Δs_j is spherically-corrected path through layer j. For $\theta_0 < 90°$, the path enhancement is given by:

$$\Delta s_j = \sqrt{(r_j + \Delta z_j)^2 - r_p^2 \sin^2\theta_0} - \sqrt{r_j^2 - r_p^2 \sin^2\theta_0} \tag{3.24}$$

where r_p and r_j are the distance from the centre of the Earth to the scattering point τ and the bottom of layer j, respectively.

By including the spherical correction to the solar beam, plane parallel calculations produce accurate radiances for near-nadir and near-zenith viewing geometries. However, as the observation geometry departs from nadir or zenith (i.e. as $\mu \rightarrow 0$), the plane-parallel approximation begins to break down. Most importantly, in the plane-parallel approximation the limb observation geometry, where the LOS crosses through the atmosphere (θ=90° or $\mu = 0$ at the tangent point), is not defined.

Note that the plane-parallel approximation tends to overestimate the multiple scattering contribution to the radiances, particularly at high altitudes, since the upwelling diffuse source for a plane-parallel atmosphere is larger than for a truly spherical atmosphere (there is no limb-dimming).

3.2.3.3 Pseudo-Spherical Approximation

As noted above, the plane-parallel approximation is not valid for limb observations. As a result, some treatment of the spherical nature of the atmosphere, beyond its consideration in the attenuation of the incoming solar beam, is required. One approach is to treat the atmosphere as 'pseudo-spherical'. In the pseudo-spherical approximation, the singly-scattered light is calculated assuming spherical geometry, both in the attenuation of the incoming solar beam and in the integration of the single scattering source function along the LOS. For the multiply-scattered light, the spherical nature of the atmosphere is approximated by calculating the multiple scattering source function under the plane-parallel approximation, where the diffuse radiances, I_{diff}, are calculated as described in Section 3.2.3.2 (with a spherical correction to the incoming solar beam) at a number of points along the LOS for the local SZA. The number of

points, and in some implementations the positions of the points, are varied depending on the desired accuracy. The integration of the approximate multiple scattering source functions along the LOS is then carried out assuming a spherical atmosphere.

Although the pseudo-spherical approximation is generally a good representation of the spherical atmosphere, it tends to overestimate the radiance even when a large number of SZA points are used since the plane-parallel approximation overestimates the multiple scattering source functions, as mentioned in Section 3.2.3.2 (*Griffioen and Oikarinen*, 2000; *Loughman et al.*, 2004). This error increases with increasing altitude as the curvature becomes more important. Also, in the application of the approximation it can be difficult to determine the appropriate number (and position) of the SZA points at which the source function calculations are carried out since the impact of the selection depends on the viewing and solar conditions (and optical depth).

3.2.3.4 Spherical Approaches

A number of approaches have been devised to allow for the sphericity of the atmosphere in the determination of the diffuse field in a more accurate fashion. The approaches can be classed into two types: 'approximately spherical' and 'fully spherical'. The approximately spherical approaches generally expand on the pseudo-spherical approximation to give a better representation of the spherical atmosphere. One approach is to use the pseudo-spherical approximation to determine the diffuse field at a number of points along the LOS, thereby effectively calculating the first two orders of scattering in spherical geometry and higher orders in plane-parallel. Fully-spherical

approaches calculate the diffuse radiance in a fully spherical geometry, but tend to be computationally expensive and usually only the most important contributions to the limb radiance (e.g. the first and second orders of scattering at UV/visible/near-IR wavelengths in a cloud-free atmosphere) are calculated explicitly in a spherical atmosphere. Higher orders of scattering are either ignored or are approximated to make the calculations computationally efficient. The contribution from the third order of scattering is generally small (<15%), with higher orders contributing even less (*Bourassa et al.*, 2008). However, the contribution is a function of the wavelength as well as the solar, viewing and atmospheric conditions, including the effective albedo and optical depth.

Spherical approaches are generally in better agreement than pseudo-spherical calculations with Monte Carlo results (*Bourassa et al.*, 2008; *Loughman et al.*, 2004).

3.3 Radiative Transfer Models

A number of radiative transfer models for limb-scatter observations have been developed. Following the approaches for addressing the spherical atmosphere discussed in Section 3.2.3, the RTMs can be divided into three types: Monte Carlo models, pseudo-spherical models and spherical models. Available Monte Carlo models include Siro (*Oikarinen*, 2001, 2002; *Oikarinen et al.*, 1999) and MCC++ (Monte Carlo C++) (*Postylyakov*, 2004a,b,c). Available pseudo-spherical models include LIMBTRAN (*Griffioen and Oikarinen*, 2000), CDI (Combined Differential-Integral) (*Rozanov et al.*, 2000), and VECTOR (Vector Orders-of-Scattering Radiative Trans-

fer Model) (*McLinden et al.*, 2002a). Available spherical models include CDIPI (Combined Differential-Integral Picard Iterative) (*Rozanov et al.*, 2001), SCIARAYS (*Kaiser*, 2001), SASKTRAN (*Bourassa et al.*, 2008), and GSLS (Gauss-Seidel Limb Spherical) (*Loughman et al.*, 2004). Note that CDI and CDIPI are implemented in the radiative transfer package SCIATRAN (*Rozanov et al.*, 2005). Table 3.1 summarizes the models and their features. A detailed intercomparison of a number of the limb-scatter RTMs can be found in *Loughman et al.* (2004).

3.3.1 Sample Calculations

Figure 3.3 shows limb-scattered sunlight radiances calculated using the LIMBTRAN radiative transfer model (*Griffioen and Oikarinen*, 2000). The calculations were carried out for a tangent height of 20 km with a SZA and SSA (defined at the tangent point) of 70° and 90°, respectively, in an aerosol-free atmosphere with the ground approximated as a Lambertian surface with an albedo of 0.3. The figure illustrates the contributions of singly- and multiply-scattered light to the total radiance over the UV/visible/near-IR spectral region, and includes absorption by O_3 and NO_2. The figure shows that the limb-scatter radiances resemble a Rayleigh-trended solar spectrum, with the predominant spectral features due to Fraunhofer lines in the solar spectrum. The sharp cut-off from absorption by the O_3 Hartley and Huggins bands below 330 nm and the broad absorption feature between 500 nm and 700 nm from the O_3 Chappuis band are clearly evident. Additional spectral features in limb-scatter spectra will be discussed in more detail in Section 6.2.

Name	Type	vector	refrac	SS	MS
Siro	Monte Carlo	yes	yes	statistical	statistical
MCC++	Monte Carlo	yes	yes	analytic	statistical
CDI	pseudo-sph.	no	yes	analytic	plane parallel
LIMBTRAN	pseudo-sph.	no	no	analytic	plane parallel
VECTOR	pseudo-sph.	yes	no	analytic	plane parallel
GSLS	spherical	yes	no	analytic	approx. sph.
CDIPI	spherical	no	yes	analytic	approx. sph.
SCIARAYS	spherical	no	no	analytic	analytic†
SASKTRAN	spherical	no	no	analytic	analytic‡

Table 3.1: Summary of limb-scatter radiative transfer models. Here 'vector' indicates whether the model can account for the polarization of the scattered radiance; 'refrac' indicates whether refraction can be included in the model; 'SS' indicates whether the single scattering calculation is done statistically (in the Monte Carlo case) or analytically (by direct integration of the SS source function); and 'MS' indicates the method employed for the multiple scattering source function calculation. †SCIARAYS only includes two orders of scattering. ‡SASKTRAN uses an approximation for the third and higher orders of scattering.

Figure 3.4 shows the fractional contribution of MS to the total limb-scatter radiances for the same conditions as Figure 3.3, but over a range of tangent heights. Since the single scattering calculations (by definition) do not include an albedo contribution, the calculations assumed a surface albedo of zero to clearly illustrate the impact of multiple scattering. The contribution of multiple scattering generally increases with shorter wavelengths, as is expected by the increased Rayleigh scattering, with multiple scattering accounting for 30-40% of the total radiance at 350 nm. Note the almost complete attenuation of the upwelling diffuse radiance by O_3 absorption at the shortest wavelengths, where the total radiance is dominated by single scattering.

The ratio of total limb-scatter radiance calculations at two albedos (0.6 and 0.3) is shown in Figure 3.5. As is expected, the effect of an increased albedo depends on the transparency of the atmosphere, and the enhancement in total radiance increases with increasing wavelength (as the Rayleigh extinction of the upwelling radiation decreases). At the shortest wavelengths, the strong O_3 absorption effectively eliminates the sensitivity of the limb-scatter radiances to the surface albedo.

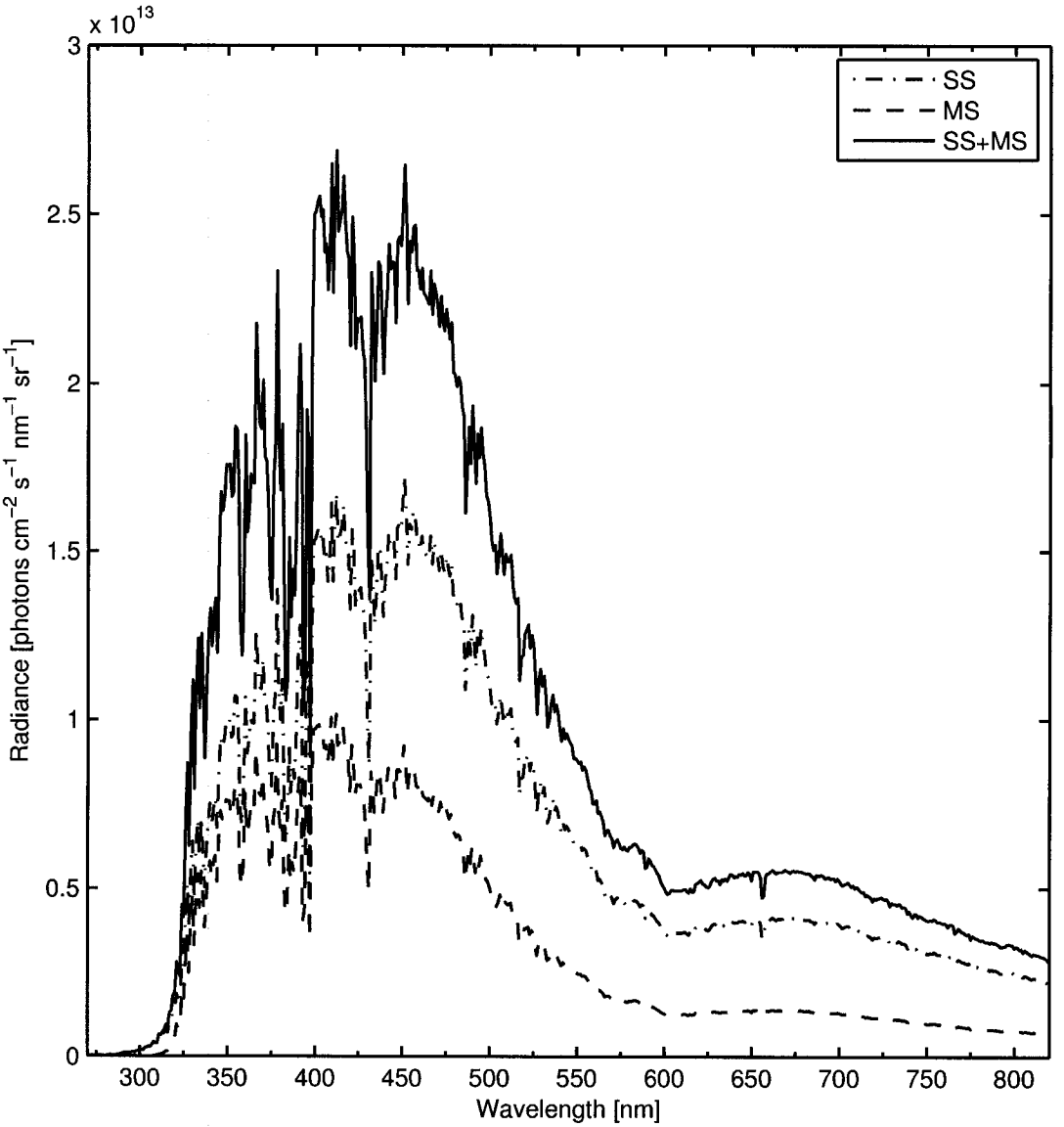

Figure 3.3: Limb-scatter radiances at 20 km tangent height calculated using the LIMBTRAN model and illustrating the contributions of single and multiple scattering to the total radiance for SZA=70°, SSA=90° and albedo=0.3 in an aerosol free atmosphere with absorption by O_3 and NO_2.

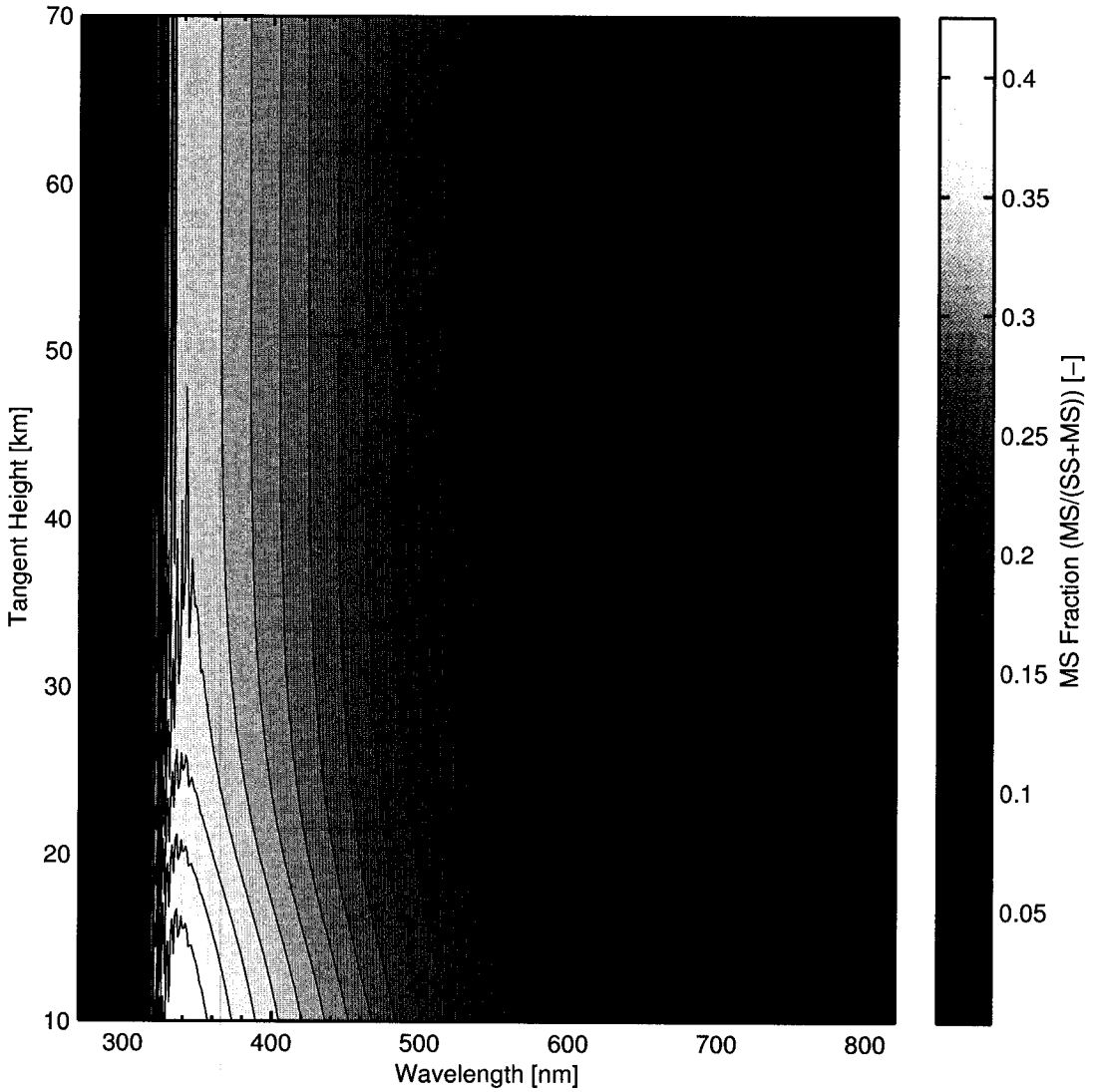

Figure 3.4: Fractional contribution of multiply-scattered light to the total limb-scatter radiance, calculated using the LIMBTRAN model at a series of tangent heights for the same conditions as Figure 3.3, except at albedo=0.

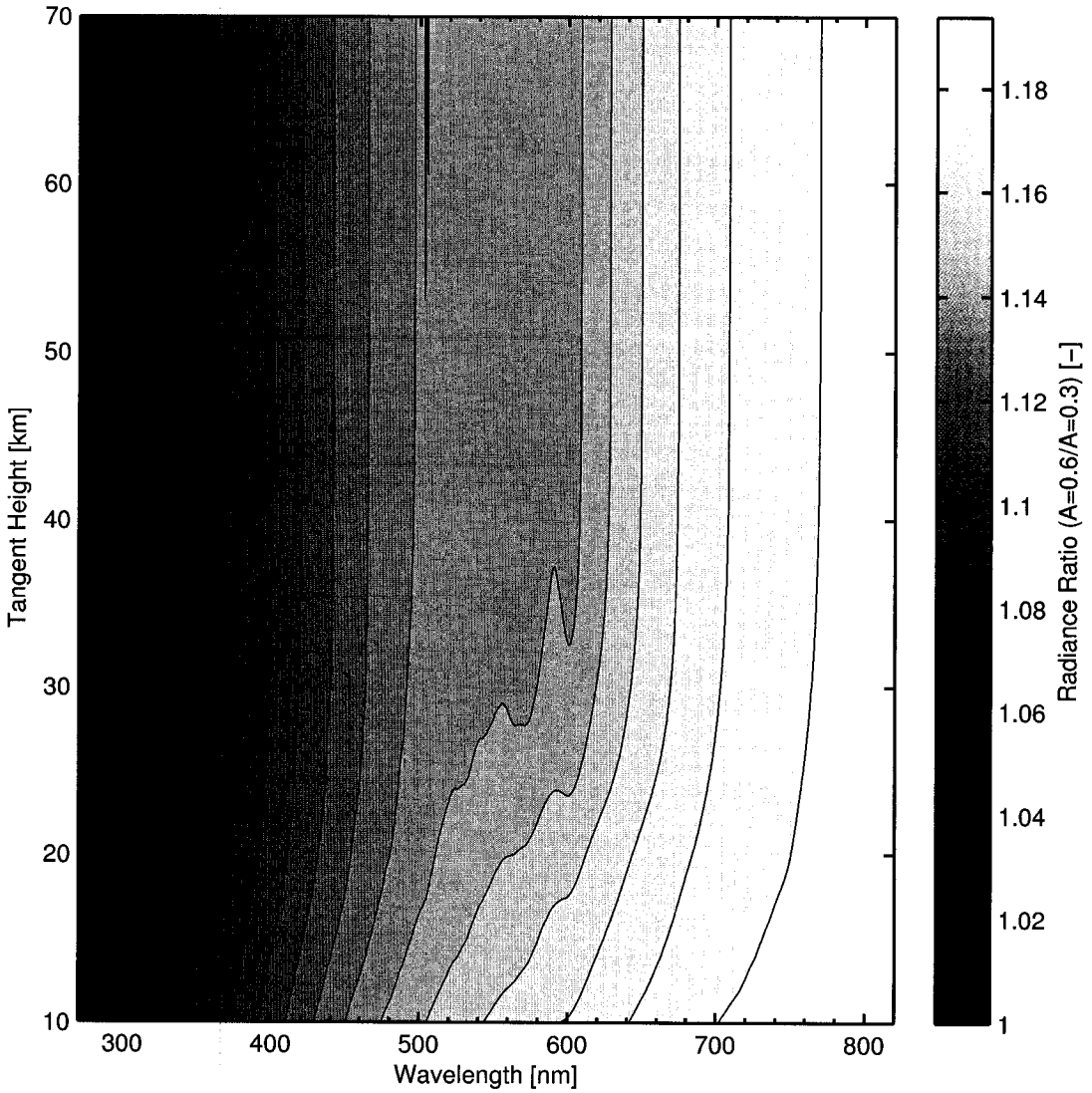

Figure 3.5: Ratio of limb-scatter total radiances at a series of tangent heights for albedo=0.6 and albedo=0.3, calculated using the LIMBTRAN model for the same conditions as Figure 3.3.

Chapter 4

Differential Optical Absorption Spectroscopy

Retrieving stratospheric minor species concentrations directly from absolute limb-scattered radiance observations is challenging. This is largely due to the strong sensitivity of the observed signal to many parameters, including neutral density, aerosol, albedo and instrument calibration. A direct retrieval may also require more detailed forward model calculations, possibly making it impractical for use on large data sets or in an operational setting.

To aid in the interpretation it can be advantageous to apply an initial spectral analysis on the observed radiances. The analysis technique used in this work is differential optical absorption spectroscopy, first described by *Noxon* (1975), *Noxon et al.* (1979), *Platt et al.* (1979), *Perner and Platt* (1979) and *Perner and Platt* (1980). In general, DOAS is a spectral fitting technique, analysing broadband spectra of UV/visible/near-IR light that has been transmitted through long paths. Different

atmospheric species leave their absorption 'fingerprints' in the spectra, from which concentrations can be derived. DOAS has been used in ground, balloon, aircraft and satellite applications, with both active and passive instruments (e.g. *Axelsson et al.*, 1990; *Burrows et al.*, 1999; *Pfeilsticker et al.*, 2001). Advantages of the DOAS technique include:

- A minimized sensitivity to broad extinction features such as Rayleigh and Mie extinction.
- No requirement for measuring or estimating the unattenuated spectrum (when it contains no high-frequency structure).
- The opportunity of simultaneously measuring multiple species.
- A high sensitivity due to long pathlengths.
- A high specificity due to broad spectral bands.

Disadvantages of the technique include:

- Limited to species that exhibit relatively narrow absorption features.
- Measurements can be affected (or prevented) by strong attenuation sources (e.g. rain, snow, fog and clouds).

This chapter describes the general DOAS technique. A detailed discussion of the technique can be found in *Platt* (1994), *Stutz and Platt* (1996) and *Platt and Stutz* (2008). A presentation of the application of DOAS to limb-scatter observations can be found in Chapter 7.

4.1 The Beer-Lambert Law

The basic equation of absorption spectroscopy is the Beer-Lambert Law, where the local attenuation of radiation is described by:

$$\frac{dI(s,\lambda)}{ds} = -k(s,\lambda)I(s,\lambda) \tag{4.1}$$

where $dI(s,\lambda)$ is the change in radiance $I(s,\lambda)$ at wavelength λ after passing a distance ds through a medium with absorption coefficient $k(s,\lambda)$, where the subscript a has been removed for clarity. In the case of a single absorber in a homogeneous medium of length L, the integration of Equation (4.1) gives:

$$I(\lambda) = I_0(\lambda)\exp\left[-Lk(\lambda)\right] \tag{4.2}$$

where $I_0(\lambda)$ is the incident (unattenuated) radiance and $I(\lambda)$ is the attenuated radiance. The extinction coefficient is the product of the absorption cross section, $\sigma(\lambda)$, where the subscript a has been removed for clarity, and the concentration of the absorber, n, and Equation (4.2) can be stated as:

$$I(\lambda) = I_0(\lambda)\exp\left[-L\sigma(\lambda)n\right] \tag{4.3}$$

The product $L\sigma(\lambda)n$ is referred to as the optical depth of the medium, $\tau(\lambda)$, which can also be expressed as:

$$\tau(\lambda) = \ln\left[\frac{I_0(\lambda)}{I(\lambda)}\right] \tag{4.4}$$

and the concentration of the absorber can be determined from:

$$n = \frac{\tau(\lambda)}{L\sigma(\lambda)} \tag{4.5}$$

It should be noted that the Beer-Lambert law as expressed above is not strictly valid for averaged (convolved) spectra unless the medium is optically thin (i.e. $\tau \ll 1$).

4.2 The Beer-Lambert Law in the Atmosphere

In the atmosphere, Rayleigh and Mie scattering contribute to the radiation extinction. By scattering light away from the line of sight these phenomena act like absorption processes. Also, several atmospheric species can have significant absorption that must be considered. The various sources of extinction can simply be added, and the total atmospheric absorption through a homogeneous path of length L can be expressed as:

$$I(\lambda) = I_0(\lambda) \exp\left\{-L\left[\sum_i \sigma_i(\lambda) n_i + k_R(\lambda) + k_M(\lambda)\right]\right\} \tag{4.6}$$

where $k_R(\lambda)$ and $k_M(\lambda)$ are the Rayleigh and Mie scattering coefficients, respectively, and n_i and $\sigma_i(\lambda)$ are the concentration and absorption cross section of absorbing species i, respectively.

However, for atmospheric measurements the medium is generally not homogeneous, with the absorber concentrations usually varying along the measurement path. As a result, instead of number density, an integral quantity referred to as the 'column density' or 'slant column density', c, is necessary, with:

$$c = \int n(s) ds \tag{4.7}$$

However, this terminology is only appropriate when the path is direct from I_0 (e.g. occultation measurements). When I_0 is diffuse, as is the case for scattered sunlight

measurements, the term 'effective column density' (ECD) (also sometimes referred to as 'apparent column density') is more appropriate, indicating that $I(\lambda)$ contains contributions from different routes through the atmosphere and that the measurement path is not well defined. In this case the relationship between the ECD and the absorber concentration requires a detailed understanding of the radiative transfer processes.

The temperature and pressure also usually vary along the measurement path, and this can impact $\sigma_i(\lambda)$ since the absorption cross sections can have a temperature and pressure dependence. For clarity this will not be considered here.

Modifying Equation (4.6) for a non-homogeneous medium gives:

$$I(\lambda) = I_0(\lambda) \exp\left\{ -\left[\sum_i \sigma_i(\lambda) c_i + \tau_R(\lambda) + \tau_M(\lambda) \right] \right\} \tag{4.8}$$

where c_i is the ECD of absorber i. $\tau_R(\lambda)$ is the Rayleigh scattering optical depth, which is the product of the Rayleigh scattering cross section, $\sigma_R(\lambda)$, and the ECD of air, c_{air}. Similarly, the Mie optical depth, $\tau_M(\lambda)$, corresponds to $\sigma_M(\lambda) c_{aer}$, where c_{aer} is the ECD of aerosol and $\sigma_M(\lambda)$ is the Mie scattering cross section.

Determining the absorber concentrations in Equation (4.6) or the effective column densities in Equation (4.8) can be difficult because all of the contributions to the radiances must be modeled and a direct measure of $I_0(\lambda)$ (a measurement of $I(\lambda)$ with no absorbers in the path) is often not available.

4.3 Differential Optical Absorption Spectroscopy

The key principle of DOAS is the separation of the total cross section, $\sigma(\lambda)$, into two components, one slowly varying with wavelength, $\sigma^s(\lambda)$, and another rapidly varying one, $\sigma'(\lambda)$:

$$\sigma(\lambda) = \sigma^s(\lambda) + \sigma'(\lambda) \tag{4.9}$$

The slowly varying component describes the general shape while the rapidly varying component, referred to as the differential cross section, corresponds to the difference between $\sigma^s(\lambda)$ and $\sigma(\lambda)$ (see Figure 4.1). The use of the terms "slowly" and "rapidly" is somewhat subjective and depends on the nature of the cross section. What is important, and becomes more evident in the discussion below, is that the slowly varying component addresses the relatively broad spectral features, with the rapidly varying component containing information that is more unique to the absorbers.

Combining Equations (4.6) and (4.9) and separating the slowly and rapidly varying components gives:

$$I(\lambda) = \tag{4.10}$$
$$I_0(\lambda) \exp\left[-L \sum_i \sigma'_i(\lambda) n_i\right] \exp\left\{-L\left[\sum_i \sigma^s_i(\lambda) n_i + k_R(\lambda) + k_M(\lambda)\right]\right\}$$

Note that the Rayleigh and Mie extinction coefficients both vary slowly with wavelength. If a measurement or accurate estimate of $I_0(\lambda)$ exists, the optical depth can, like the absorption cross sections, be separated into its slowly, $\tau^s(\lambda)$, and rapidly, $\tau'(\lambda)$, varying components:

$$\tau(\lambda) = \tau^s(\lambda) + \tau'(\lambda) \tag{4.11}$$

The rapidly varying component can be assigned to the rapidly varying term of Equation (4.10), giving the expression for the differential optical depth (DOD):

$$\tau'(\lambda) = \left\{ \ln \left[\frac{I_0(\lambda)}{I(\lambda)} \right] \right\}' = L \sum_i \sigma_i'(\lambda) n_i \tag{4.12}$$

where $\tau'(\lambda)$ is determined by calculating the differential component of the natural logarithm of the ratio of $I_0(\lambda)$ and $I(\lambda)$. The concentrations can then be determined, for example through a least squares (LSQ) fit of Equation (4.12), finding the minimum of the norm of the residuals:

$$\| \tau'(\lambda) - L \sum_i \sigma_i'(\lambda) n_i \|^2 \tag{4.13}$$

with respect to the concentrations, n_i. Note that the number of wavelengths should greatly exceed the number of fitted species concentrations.

When ECDs are considered, Equation (4.12) simply becomes:

$$\tau'(\lambda) = \sum_i \sigma_i'(\lambda) c_i \tag{4.14}$$

and c_i can be determined as in Equation (4.13).

If the true $I_0(\lambda)$ is not available but is known to vary slowly with wavelength, an analogous quantity can be defined using Equation (4.10):

$$I_0^s(\lambda) = I_0(\lambda) \exp \left\{ -L \left[\sum_i \sigma_i^s(\lambda) n_i + k_R(\lambda) + k_M(\lambda) \right] \right\} \tag{4.15}$$

where $I_0^s(\lambda)$ is the radiance in the absence of any differential absorption. $I_0^s(\lambda)$ can be estimated from $I(\lambda)$, for example, by interpolating using measurements made near narrow absorption lines. Other options include approximating $I_0^s(\lambda)$ by a polynomial fit to $I(\lambda)$ or a smoothed (filtered) version of $I(\lambda)$. Figure 4.2 illustrates the determination of $I_0^s(\lambda)$.

Using Equations (4.10) and (4.15), the differential optical depth can be expressed as:

$$\tau'(\lambda) = \ln\left[\frac{I_0^s(\lambda)}{I(\lambda)}\right] = L\sum_i \sigma_i'(\lambda)n_i \tag{4.16}$$

and the concentrations (or analogously ECDs) can be determined.

Note that a differential approach can be advantageous even when the true $I_0(\lambda)$, or an adequate approximation, is available. Such an approach has two particular benefits: (1) it reduces the need to model all of the contributions to $I(\lambda)$ explicitly, with slowly varying components effectively eliminated through the differential technique, and (2) it places the focus on the rapidly varying components of the spectra, which can be advantageous when studying minor absorbers.

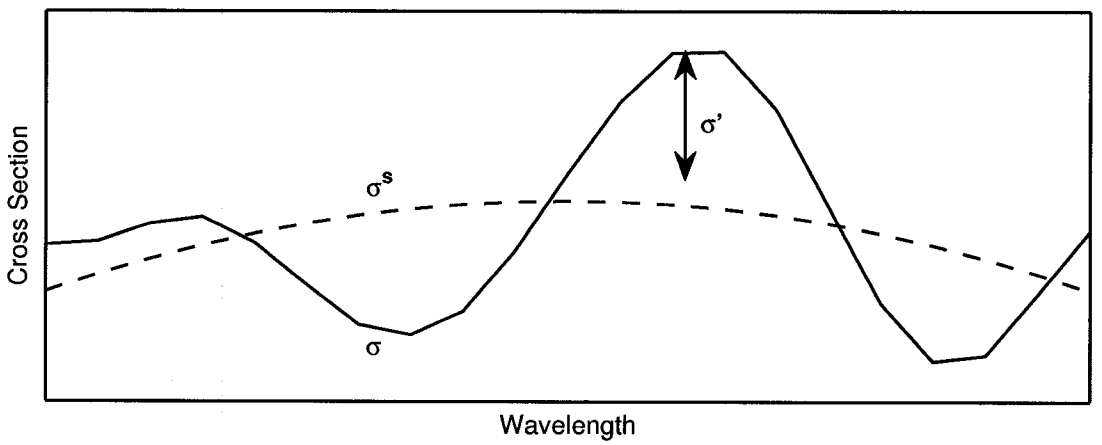

Figure 4.1: The differential cross section, $\sigma'(\lambda)$, calculated as the difference between the total cross section, $\sigma(\lambda)$, and the slowly varying component, $\sigma^s(\lambda)$

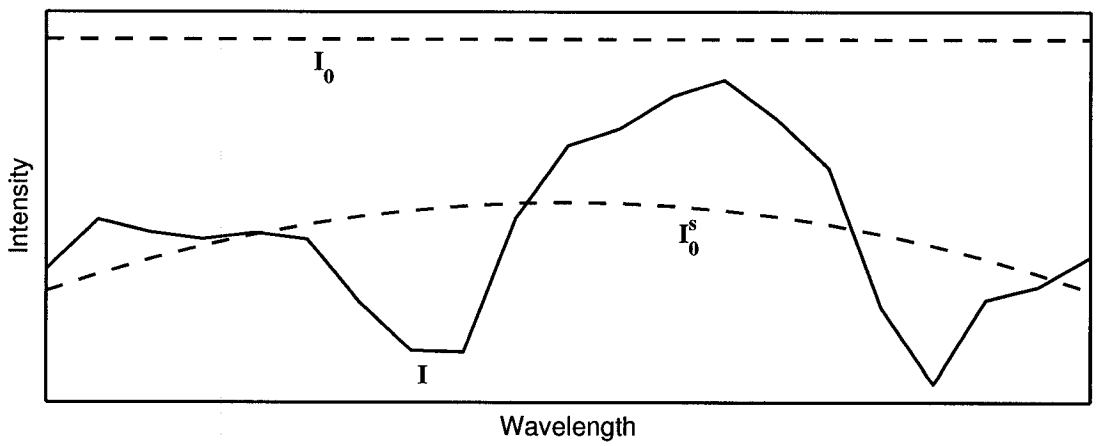

Figure 4.2: The determination of $I_0^s(\lambda)$, a proxy for the (slowly varying) unattenuated reference radiance, $I_0(\lambda)$, and calculated from $I(\lambda)$.

Chapter 5

Inversion Theory

The general problem to be solved is the inversion of measurements of the atmosphere to atmospheric state parameters. The inversion method used in this work is optimal estimation, or more specifically the maximum a posteriori estimator for moderately non-linear problems (*Rodgers*, 1976, 1990). The MAP estimator is a Bayesian approach that gives the most likely solution based on the measurements and a priori information, along with the associated covariances. The advantages of the MAP approach are that it is statistically-based, makes intuitive sense as a weighted combination of the measurements and a priori information, and provides an estimate of the associated uncertainties. Also, the MAP approach provides useful diagnostics, including a measure of the effective resolution and degree of a priori contamination. Disadvantages of the approach include the need for well characterized a priori information and the assumption of Gaussian statistics. This chapter gives a summary of the inversion problem, solution, characterisation and error analysis formalism. A detailed description of the MAP estimator and derivations of the presented formulae

can be found in *Rodgers* (2000).

5.1 The Inversion Problem

The inversion problem is first addressed by recognizing that the measurement, $\mathbf{y}$, is a function of some unknown state, $\mathbf{x}$:

$$\mathbf{y} = \mathbf{f}(\mathbf{x}, \mathbf{b}) + \boldsymbol{\epsilon} \tag{5.1}$$

where $\mathbf{f}$ is a forward function that describes the physics of the measurement, $\mathbf{b}$ is a set of known parameters of the function and $\boldsymbol{\epsilon}$ is the measurement noise, with covariance $\mathbf{S}_\epsilon$. The forward function must be replaced with a numerical forward model, $\mathbf{F}$:

$$\mathbf{F}(\mathbf{x}, \mathbf{b}) \simeq \mathbf{f}(\mathbf{x}, \mathbf{b}, \mathbf{b}') \tag{5.2}$$

where $\mathbf{b}'$ are the parameters of the forward function not included in $\mathbf{F}$. The problem can now be stated as:

$$\mathbf{y} \simeq \mathbf{F}(\mathbf{x}, \mathbf{b}) + \boldsymbol{\epsilon}_y \tag{5.3}$$

where $\boldsymbol{\epsilon}_y$ is the total error in the measurement relative to the forward model (i.e. including errors in the representation of $\mathbf{f}$ by $\mathbf{F}$). The contributions to $\boldsymbol{\epsilon}_y$ will be discussed in Section 5.4 and $\boldsymbol{\epsilon}_y$ will be ignored in the following discussion for clarity.

It is useful to linearize Equation (5.3) about an initial guess, $\mathbf{x}_L$, to account for non-linearities in the relationship between $\mathbf{x}$ and $\mathbf{y}$. This is accomplished through a Taylor expansion:

$$\mathbf{y} \simeq \mathbf{F}(\mathbf{x}_L, \mathbf{b}) + \frac{\delta \mathbf{F}(\mathbf{x}, \mathbf{b})}{\delta \mathbf{x}}\Big|_{\mathbf{x}=\mathbf{x}_L} * (\mathbf{x} - \mathbf{x}_L) + \cdots \tag{5.4}$$

Neglecting the higher-order terms gives:

$$\mathbf{y} \simeq \mathbf{F}(\mathbf{x}_L, \mathbf{b}) + \mathbf{K}_L(\mathbf{x} - \mathbf{x}_L) \tag{5.5}$$

where $\mathbf{K}$ is the so-called weighting function matrix or Jacobian, and $\mathbf{K}_L$ is $\mathbf{K}$ evaluated at $\mathbf{x} = \mathbf{x}_L$.

When measurement noise and the measurement conditions are considered, it is clear that Equation (5.5) is ill-posed, meaning that a unique solution does not exist (there are an infinite number of states that can give the same measurement, within the measurement uncertainty). The inversion method must estimate or retrieve the solution in some fashion.

5.2 The Maximum A Posteriori Solution

In the MAP approach the prior knowledge and the measurement are quantified as probability density functions (PDFs) over the state and measurement space, respectively. Bayes' theorem describes how the measurement PDF maps into state space using the a priori information:

$$P(\mathbf{x}|\mathbf{y}) = \frac{P(\mathbf{y}|\mathbf{x})P(\mathbf{x})}{P(\mathbf{y})} \tag{5.6}$$

where $P(\mathbf{x})$ is the a priori PDF, or the PDF of the state before the measurement is made, $P(\mathbf{y})$ is the PDF of the measurement before it is made, $P(\mathbf{y}|\mathbf{x})$ is the conditional PDF of $\mathbf{y}$ given $\mathbf{x}$, and $P(\mathbf{x}|\mathbf{y})$ is the conditional PDF of $\mathbf{x}$ given $\mathbf{y}$, or the PDF of the state after the measurement is made. $P(\mathbf{x}|\mathbf{y})$ is the desired quantity from the inversion, denoted the posterior PDF.

Applying Gaussian formalism (normal distribution) for vectors and expressing $P(\mathbf{x})$ in terms of the difference from the a priori gives:

$$-2\ln P(\mathbf{x}) + c_1 = (\mathbf{x} - \mathbf{x}_a)^T \mathbf{S}_a^{-1} (\mathbf{x} - \mathbf{x}_a) \tag{5.7}$$

where $\mathbf{x}_a$ is the a priori state vector, $\mathbf{S}_a$ is the covariance matrix of $\mathbf{x}_a$ and c_1 is a constant. Using Equation (5.5), $P(\mathbf{y}|\mathbf{x})$ can be expressed as:

$$\begin{aligned} &-2\ln P(\mathbf{y}|\mathbf{x}) + c_2 = \\ &\quad [\mathbf{y} - \mathbf{F}(\mathbf{x}_L, \mathbf{b}) - \mathbf{K}_L(\mathbf{x} - \mathbf{x}_L)]^T \mathbf{S}_\epsilon^{-1} [\mathbf{y} - \mathbf{F}(\mathbf{x}_L, \mathbf{b}) - \mathbf{K}_L(\mathbf{x} - \mathbf{x}_L)] \end{aligned} \tag{5.8}$$

where c_2 is a constant. No prior information about the quantity $\mathbf{y}$ is assumed, so $P(\mathbf{y})$ = constant. The posterior PDF, $P(\mathbf{x}|\mathbf{y})$, can be determined by substituting Equations (5.7) and (5.8) into Bayes' theorem, Equation (5.6), and rearranging:

$$\begin{aligned} &-2\ln P(\mathbf{x}|\mathbf{y}) + c_3 = \\ &\quad (\mathbf{x} - \mathbf{x}_a)^T \mathbf{S}_a^{-1} (\mathbf{x} - \mathbf{x}_a) + \\ &\quad [\mathbf{y} - \mathbf{F}(\mathbf{x}_L, \mathbf{b}) - \mathbf{K}_L(\mathbf{x} - \mathbf{x}_L)]^T \mathbf{S}_\epsilon^{-1} [\mathbf{y} - \mathbf{F}(\mathbf{x}_L, \mathbf{b}) - \mathbf{K}_L(\mathbf{x} - \mathbf{x}_L)] \end{aligned} \tag{5.9}$$

where c_3 is a constant.

Equation (5.9) shows that $P(\mathbf{x}|\mathbf{y})$ is normally distributed and can be analogously expressed in terms of the MAP expected value, $\hat{\mathbf{x}}$, and covariance, $\hat{\mathbf{S}}$:

$$-2\ln P(\mathbf{x}|\mathbf{y}) + c_4 = (\mathbf{x} - \hat{\mathbf{x}})^T \hat{\mathbf{S}}^{-1} (\mathbf{x} - \hat{\mathbf{x}}) \tag{5.10}$$

where c_4 is a constant. $\hat{\mathbf{x}}$ is the $\mathbf{x}$ at which $P(\mathbf{x}|\mathbf{y})$ reaches its maximum:

$$\hat{\mathbf{x}} = \max_{\mathbf{x}} [P(\mathbf{x}|\mathbf{y})] \tag{5.11}$$

Finding the maximum in Equation (5.11) is equivalent to finding the minimum of the right hand side of Equation (5.9), which is referred to as the cost function, C. To find the minimum, the first-order derivatives of C with respect to $\mathbf{x}$, denoted $\mathbf{g}(\mathbf{x})$, are required:

$$\mathbf{g}(\mathbf{x}) = -\left[\nabla_{\mathbf{x}}\mathbf{F}(\mathbf{x}_L, \mathbf{b})\right]^T \mathbf{S}_\epsilon^{-1}\left[\mathbf{y} - \mathbf{F}(\mathbf{x}_L, \mathbf{b}) - \mathbf{K}_L(\mathbf{x} - \mathbf{x}_L)\right] + \mathbf{S}_a^{-1}(\mathbf{x} - \mathbf{x}_a) \quad (5.12)$$

The quantity $\nabla_{\mathbf{x}}\mathbf{F}(\mathbf{x}_L, \mathbf{b})$ is recognized as equivalent to $\mathbf{K}_L$ in Equation (5.5), giving the final expression of $\mathbf{g}(\mathbf{x})$:

$$\mathbf{g}(\mathbf{x}) = -\mathbf{K}_L^T\mathbf{S}_\epsilon^{-1}\left[\mathbf{y} - \mathbf{F}(\mathbf{x}_L, \mathbf{b}) - \mathbf{K}_L(\mathbf{x} - \mathbf{x}_L)\right] + \mathbf{S}_a^{-1}(\mathbf{x} - \mathbf{x}_a) \quad (5.13)$$

and finding $\hat{\mathbf{x}}$ is identical to finding the $\mathbf{x}$ for which $\mathbf{g}(\mathbf{x}) = 0$.

5.2.1 The Linear Case

If the problem is linear, with $\mathbf{y} = \mathbf{F}(\mathbf{x}, \mathbf{b}) = \mathbf{K}\mathbf{x}$, the solution to Equation (5.11) can be expressed as:

$$\hat{\mathbf{x}} = \mathbf{x}_a + \mathbf{S}_a\mathbf{K}^T(\mathbf{K}\mathbf{S}_a\mathbf{K}^T + \mathbf{S}_\epsilon)^{-1}(\mathbf{y} - \mathbf{K}\mathbf{x}_a) \quad (5.14)$$

5.2.2 The Nearly-Linear Case

If the problem is nearly-linear, where Equation (5.5) is a good approximation given a sensible choice of $\mathbf{x}_L$, the solution to Equation (5.11) can be expressed as:

$$\hat{\mathbf{x}} = \mathbf{x}_a + \mathbf{S}_a\mathbf{K}_L^T(\mathbf{K}_L\mathbf{S}_a\mathbf{K}_L^T + \mathbf{S}_\epsilon)^{-1}\left[\mathbf{y} - \mathbf{F}(\mathbf{x}_L, \mathbf{b}) + \mathbf{K}_L(\mathbf{x}_L - \mathbf{x}_a)\right] \quad (5.15)$$

A common choice for the linearisation point is $\mathbf{x}_a$.

5.2.3 The Moderately Non-Linear Case

If the problem is moderately non-linear, the solution to Equation (5.15) will not minimize the cost function C, but in many cases will give a result that produces a smaller C than when evaluated at $\mathbf{x}_L$. In this case an iterative approach can be employed, where $\mathbf{x}_L$ is updated at each iteration using the result from the previous iteration. What is required is an iterative technique that guides the iterations towards the result that minimizes C.

5.2.3.1 Gauss-Newton Iteration

A popular option for finding the minimum of the cost function is Gauss-Newton (GN) iteration, which utilizes Newton's method:

$$\mathbf{x}_{i+1} = \mathbf{x}_i - \left[\nabla_{\mathbf{x}}\mathbf{g}(\mathbf{x}_i)\right]^{-1}\mathbf{g}(\mathbf{x}_i) \tag{5.16}$$

where $\nabla_{\mathbf{x}}\mathbf{g}(\mathbf{x}_i)$, known as the Hessian, is equal to:

$$\nabla_{\mathbf{x}}\mathbf{g}(\mathbf{x}_i) = \mathbf{S}_a^{-1} + \mathbf{K}_i^T\mathbf{S}_\epsilon^{-1}\mathbf{K}_i - \left(\nabla_{\mathbf{x}}\mathbf{K}_i^T\right)\mathbf{S}_\epsilon^{-1}\left[\mathbf{y} - \mathbf{F}(\mathbf{x}_i, \mathbf{b})\right] \tag{5.17}$$

with $\mathbf{x}_L$ replaced by $\mathbf{x}_i$ and $\mathbf{K}_i$ representing $\mathbf{K}$ evaluated at $\mathbf{x}_i$. Computing the Hessian involves the time-consuming and cumbersome calculation of the second-order derivative of the forward model, $\nabla_{\mathbf{x}}\mathbf{K}_i^T$. Fortunately, the third term on right hand side of Equation (5.17) is small for moderately non-linear problems and can be ignored. Inserting Equations (5.17) and (5.13) into Equation (5.16) and rearranging gives the Gauss-Newton iterative solution to Equation (5.11):

$$\mathbf{x}_{i+1} = \mathbf{x}_a + \mathbf{S}_a\mathbf{K}_i^T(\mathbf{K}_i\mathbf{S}_a\mathbf{K}_i^T + \mathbf{S}_\epsilon)^{-1}\left[\mathbf{y} - \mathbf{F}(\mathbf{x}_i, \mathbf{b}) + \mathbf{K}_i(\mathbf{x}_i - \mathbf{x}_a)\right] \tag{5.18}$$

Note that $\mathbf{x}_a$ is not updated. The starting value, $\mathbf{x}_0$, can be anything, but it is common to use $\mathbf{x}_a$.

5.2.3.2 Levenberg-Marquardt Iteration

For some moderately non-linear problems, Gauss-Newton iteration will fail if the starting value, $\mathbf{x}_0$, is not close enough to the true state. A solution to this is to employ the Levenberg-Marquardt (LM) algorithm, which combines the method of steepest descent with Newton's method:

$$\mathbf{x}_{i+1} = \mathbf{x}_i - \left[\gamma + \nabla_{\mathbf{x}}\mathbf{g}(\mathbf{x}_i)\right]^{-1}\mathbf{g}(\mathbf{x}_i) \tag{5.19}$$

The parameter γ controls the step size in the descent.

Following Section 5.2.3.1, the Levenberg-Marquardt iterative solution to Equation (5.11) can be expressed as:

$$\mathbf{x}_{i+1} = \mathbf{x}_i + \left[(1+\gamma)\mathbf{S}_a^{-1} + \mathbf{K}_i^T\mathbf{S}_\epsilon^{-1}\mathbf{K}_i\right]^{-1}\left\{\mathbf{K}_i^T\mathbf{S}_\epsilon^{-1}\left[\mathbf{y} - \mathbf{F}(\mathbf{x}_i, \mathbf{b})\right] - \mathbf{S}_a^{-1}(\mathbf{x}_i - \mathbf{x}_a)\right\} \tag{5.20}$$

Note that Equation (5.20) with $\gamma = 0$ is identical to the Gauss-Newton solution.

The standard approach to using the Levenberg-Marquardt method is as follows. If C decreases after a particular step, γ is decreased and the next iteration is begun. If C is instead found to increase after a step, γ is increased and $\mathbf{x}_{i+1}$ is recalculated, with this process repeated until C decreases.

The Gauss-Newton algorithm generally converges more quickly than does the Levenberg-Marquardt algorithm when the problem is well-behaved and the starting

value, $\mathbf{x}_0$, is reasonable. However, the Levenberg-Marquardt algorithm is more versatile and able to handle more difficult problems and cases where the starting value is far away from the true state.

5.2.3.3 Determining Convergence

Equations (5.18) and (5.20) are considered to have converged to $\hat{\mathbf{x}}$, with corresponding $\hat{\mathbf{S}}$, when:

$$(\mathbf{x}_{i+1} - \mathbf{x}_i)^T \hat{\mathbf{S}}^{-1} (\mathbf{x}_{i+1} - \mathbf{x}_i) \ll p \tag{5.21}$$

where p is the number of elements in $\mathbf{x}$ and with:

$$\hat{\mathbf{S}}^{-1}(\mathbf{x}_{i+1} - \mathbf{x}_i) \simeq \mathbf{K}_i^T \mathbf{S}_\epsilon^{-1} \left[\mathbf{y} - \mathbf{F}(\mathbf{x}_i, \mathbf{b})\right] - \mathbf{S}_a^{-1}(\mathbf{x}_i - \mathbf{x}_a) \tag{5.22}$$

Correct convergence is determined from a χ^2 test:

$$\chi^2_{inv} = \left[\mathbf{y} - \mathbf{F}(\hat{\mathbf{x}}, \mathbf{b})\right]^T \mathbf{S}_{\delta\hat{\mathbf{y}}}^{-1} \left[\mathbf{y} - \mathbf{F}(\hat{\mathbf{x}}, \mathbf{b})\right] \simeq q \tag{5.23}$$

where $\mathbf{S}_{\delta\hat{\mathbf{y}}} = \mathbf{S}_\epsilon(\hat{\mathbf{K}}\mathbf{S}_a\hat{\mathbf{K}}^T + \mathbf{S}_\epsilon)^{-1}\mathbf{S}_\epsilon$, $\hat{\mathbf{K}}$ is $\mathbf{K}$ evaluated at $\hat{\mathbf{x}}$ and q is the number of elements in $\mathbf{y}$.

5.2.4 The Grossly Non-Linear Case

If the problem being addressed is grossly non-linear, a significantly more sophisticated, and usually problem-dependent, approach is required. Grossly non-linear problems are generally difficult to solve and have unpredictable outcomes.

5.2.5 The Covariance Matrix

In both the nearly-linear and the moderately non-linear cases the covariance of $\hat{\mathbf{x}}$ is the same as for the purely linear solution:

$$\hat{\mathbf{S}} = \mathbf{S}_a - \mathbf{S}_a\hat{\mathbf{K}}^T(\hat{\mathbf{K}}\mathbf{S}_a\hat{\mathbf{K}}^T + \mathbf{S}_\epsilon)^{-1}\hat{\mathbf{K}}\mathbf{S}_a \tag{5.24}$$

5.3 Solution Characterization

The MAP solution can be restated as:

$$\hat{\mathbf{x}} = (\mathbf{1}_p - \mathbf{A})\,\mathbf{x}_a + \mathbf{A}\mathbf{x} + \mathbf{G}_y\boldsymbol{\epsilon}_y \tag{5.25}$$

where $\mathbf{1}_p$ is the $p \times p$ identity matrix, $\mathbf{G}_y$ is the gain matrix, or the sensitivity of the retrieval to the measurement:

$$\mathbf{G}_y = \frac{\delta\hat{\mathbf{x}}}{\delta\mathbf{y}} = \mathbf{S}_a\hat{\mathbf{K}}^T(\hat{\mathbf{K}}\mathbf{S}_a\hat{\mathbf{K}}^T + \mathbf{S}_\epsilon)^{-1} \tag{5.26}$$

$\mathbf{A}$ is the averaging kernel matrix, or the sensitivity of the retrieval to the true state:

$$\mathbf{A} = \frac{\delta\hat{\mathbf{x}}}{\delta\mathbf{x}} = \mathbf{G}_y\hat{\mathbf{K}} \tag{5.27}$$

From Equation (5.25) it can be seen that in the case of the retrieval of a profile the rows of $\mathbf{A}$ are effectively smoothing functions. The resolution of a profile retrieval is usually defined as the width of the averaging kernels (the rows of $\mathbf{A}$). A quantity called spread (*Backus and Gilbert*, 1970), denoted w, can be used to determine this width:

$$w(z_0) = 12\frac{\int(z_0 - z')^2\left[\mathbf{A}(z_0, z')\right]^2 dz'}{\left[\int \mathbf{A}(z_0, z')dz'\right]^2} \tag{5.28}$$

where z_0 is the nominal altitude of the peak of the related averaging kernel.

The sums of the rows of $\mathbf{A}$ give the response of the retrieval to the state vector, or the relative contribution of the measurement and a priori information to $\hat{\mathbf{x}}$.

5.4 Error Estimation

The total error in $\hat{\mathbf{x}}$ can be expressed as:

$$\hat{\mathbf{x}} - \mathbf{x} = (\mathbf{A} - \mathbf{1}_p)(\mathbf{x} - \mathbf{x}_a) + \mathbf{G}_y \boldsymbol{\epsilon}_y \tag{5.29}$$

with:

$$\boldsymbol{\epsilon}_y = \mathbf{K}_b(\mathbf{b} - \hat{\mathbf{b}}) + [\mathbf{f}(\mathbf{x}, \mathbf{b}, \mathbf{b}') - \mathbf{F}(\mathbf{x}, \mathbf{b})] + \boldsymbol{\epsilon} \tag{5.30}$$

where $\mathbf{K}_b$ are weighting functions representing the sensitivity of the forward model to the forward model parameters ($\delta\mathbf{F}/\delta\mathbf{b}$) and $\hat{\mathbf{b}}$ is the best estimate of the forward model parameters. The total error can thus be expressed as:

$$\hat{\mathbf{x}} - \mathbf{x} = (\mathbf{A} - \mathbf{1}_p)(\mathbf{x} - \mathbf{x}_a) + \mathbf{G}_y\mathbf{K}_b(\mathbf{b} - \hat{\mathbf{b}}) + \mathbf{G}_y\left[\mathbf{f}(\mathbf{x}, \mathbf{b}, \mathbf{b}') - \mathbf{F}(\mathbf{x}, \mathbf{b})\right] + \mathbf{G}_y\boldsymbol{\epsilon} \tag{5.31}$$

The first term on the right hand side of Equation (5.31) is referred to as the smoothing error, or the error due to the limited resolution of the retrieval compared to the true state. The second term is the forward model parameter (FMP) error, or the error due to uncertainties in the various input parameters of the forward model. The third term is the forward model (FM) error, or the error due to approximations or inadequacies in the forward model. Finally, the fourth term is the measurement error, which is the measurement noise propagated through the retrieval process.

The covariance of the smoothing error is given by:

$$\mathbf{S}_s = (\mathbf{A} - \mathbf{1}_p)\mathbf{S}_a(\mathbf{A} - \mathbf{1}_p)^T \tag{5.32}$$

assuming that $\mathbf{S}_a$ is a good approximation of the covariance of the ensemble of states about the mean state. The covariance of the measurement error is given by:

$$\mathbf{S}_m = \mathbf{G}_y\mathbf{S}_\epsilon\mathbf{G}_y^T \tag{5.33}$$

Combining Equations (5.32) and (5.33) gives the covariance matrix related to the retrieval, or the retrieval error, which is identical to the covariance of the solution, Equation (5.24):

$$\hat{\mathbf{S}} = \mathbf{S}_s + \mathbf{S}_m \tag{5.34}$$

This error represents the error in the retrievals under the assumption of a complete and accurate forward model and perfect knowledge of all of the forward model input parameters.

The forward model error covariance, $\mathbf{S}_f$, and forward model parameter error covariance, $\mathbf{S}_b$, are more difficult to determine and are obviously specific to the forward model used in the retrieval. For the former, a true forward function (containing the complete physics and no approximations) is required, while for the latter, knowledge of the uncertainty in each of the forward model parameters, $\mathbf{b}$, is required.

The total error covariance, $\mathbf{S}_{tot}$ is the sum of the four error covariances:

$$\mathbf{S}_{tot} = \mathbf{S}_s + \mathbf{S}_m + \mathbf{S}_f + \mathbf{S}_b \tag{5.35}$$

Chapter 6

The Odin/OSIRIS Instrument

6.1 The Odin Mission

Odin is a small satellite mission sponsored by Sweden (Swedish National Space Board), Canada (Canadian Space Agency), France (Centre National d'Études Spatiales), and Finland (National Technology Agency of Finland). Since May 2007 Odin has also received support as an European Space Agency Third Party Mission. Odin was launched in February 2001 into a 610 km circular sun-synchronous near-terminator orbit with an inclination of 97.8° and an ascending node at 18:00 hours LST. The characteristics of the Odin satellite are summarized in Table 6.1. The Odin satellite is shown in Figures 6.1 and 6.2 and the launch is shown in Figure 6.3.

6.1.1 Scientific Objectives

The Odin mission is shared between astronomy and aeronomy objectives, with initially with approximately 50% of the scientific operations time spent on each discipline

Characteristic	Specification
Launch date	20 February 2001
Launch vehicle	Start-1 rocket from Svobodny, Russia
Altitude	610 km, circular
Inclination	97.8°
Ascending node	18:00 LST
Platform	3-axis stabilized
Size	2 m high, 1.1 m wide
	(3.8 m wide with solar panels extended)
Mass	250 kg
Power	340 W
Designed lifetime	2 years

Table 6.1: The Odin satellite characteristics.

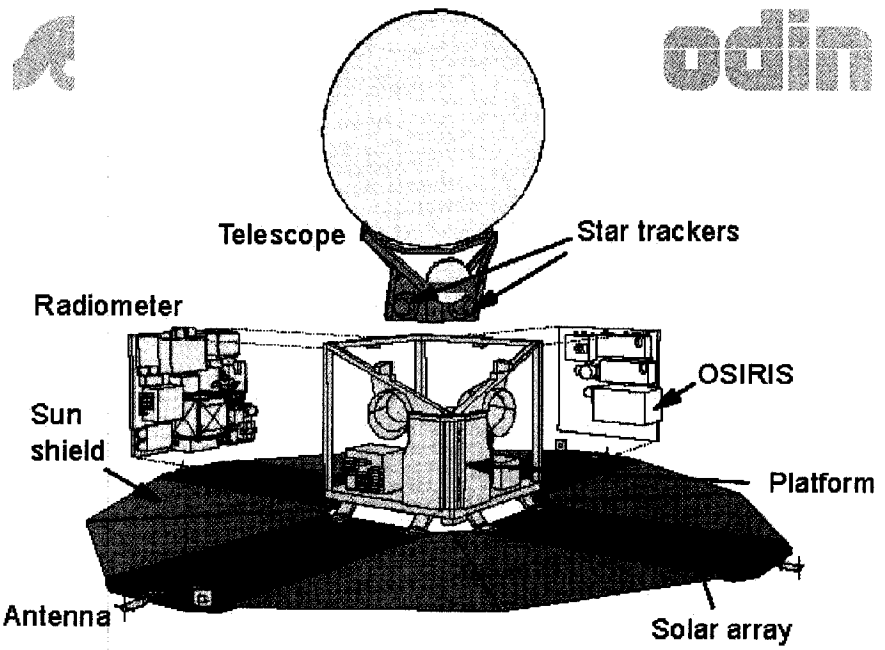

Figure 6.1: Exploded diagram of the Odin spacecraft. Source: *Murtagh et al.* (2002, Fig. 1).

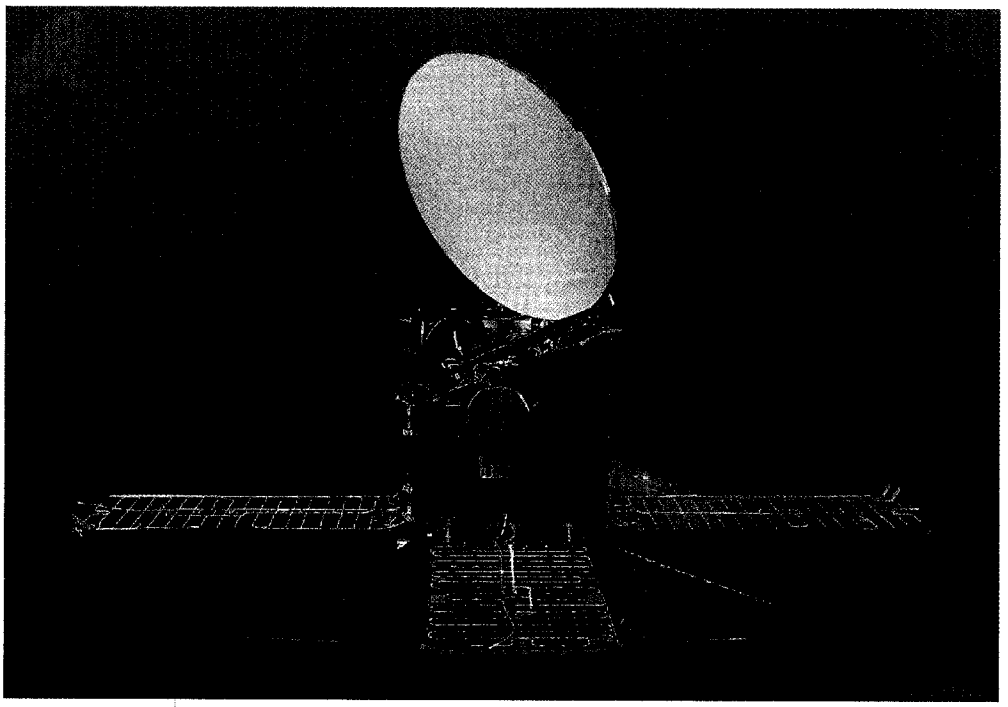

Figure 6.2: The Odin spacecraft. Source: Courtesy of Saab Ericsson Space.

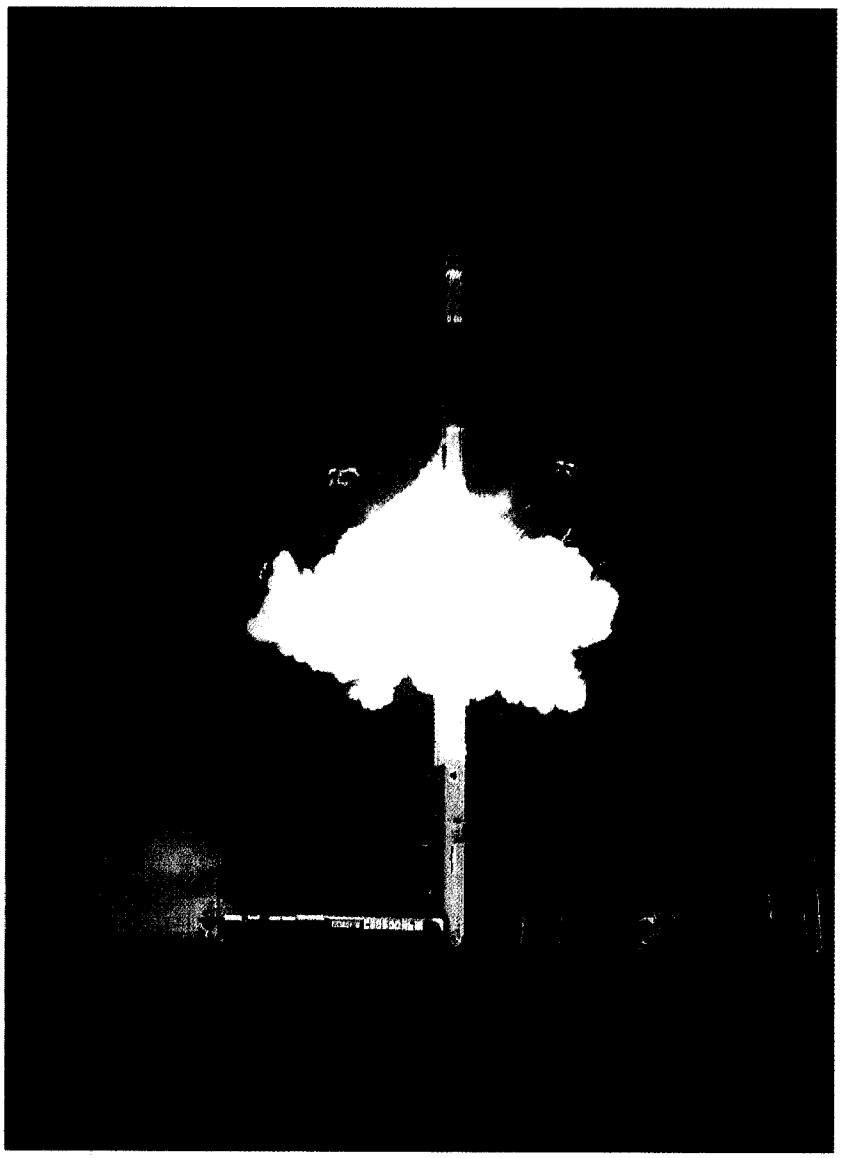

Figure 6.3: The launch of Odin on 20 February 2001 from Svobodny, Russia with a Start-1 rocket. Source: Courtesy of the Swedish Space Corporation.

(*Murtagh et al.*, 2002; *Nordh et al.*, 2003) (see Figure 6.4). Since May 2007 most of the scientific operations time is spent in aeronomy mode.

The Odin astronomy scientific objectives are (*von Schéele*, 1996):

1. **Interstellar clouds and star formation**: To enhance our understanding of the chemical conditions and the cooling mechanisms in molecular clouds leading to star formation.

2. **Composition of comets**: To study the surface properties and chemistry of comets.

3. **Composition and dynamics of the atmospheres of the giant planets**: To investigate the chemical composition, the structure and the dynamics of the atmospheres of Jupiter, Saturn, Neptune and Uranus.

The Odin aeronomy scientific objectives are (*Murtagh et al.*, 2002):

1. **Stratospheric ozone science**: To elucidate the geographical extent of and mechanisms responsible for ozone depletion in the ozone hole region and to study dilution effects and possible heterogeneous chemistry even outside of the polar regions due to sulphate aerosols.

2. **Mesospheric ozone science**: To establish the relative role of odd hydrogen chemistry and the effects of ordered and turbulent transport and corpuscular radiation.

3. **Summer mesosphere science**: To establish the variability of mesospheric

water vapour including an assessment of the required fluxes for aerosol formation in the polar mesosphere.

4. **Coupling of atmospheric regions**: To study some of the mechanisms that provide coupling between the upper and lower atmosphere, for example downward transport of aurorally-enhanced NO with its effects on ozone photochemistry and the vertical exchange of minor species such as odd oxygen, CO and H_2O.

More specifically, the aeronomy scientific objectives related to the Canadian contribution include (*Llewellyn et al.*, 1995):

- The demonstration of the use and full applicability of limb-scattered spectra for remote sensing.
- The measurement of polar ozone depletion.
- The detection and mapping of polar stratospheric clouds and polar mesospheric clouds.
- The measurement and global mapping of the ozone concentration profile in the stratosphere and mesosphere.
- The measurement and global mapping of the temperature profile throughout the stratosphere and mesosphere.
- Improved radiative transfer codes for twilight conditions on a spherical Earth.

- Improved 3-D chemical models that will validate the satellite measurements and advance our understanding of stratospheric and mesospheric processes.

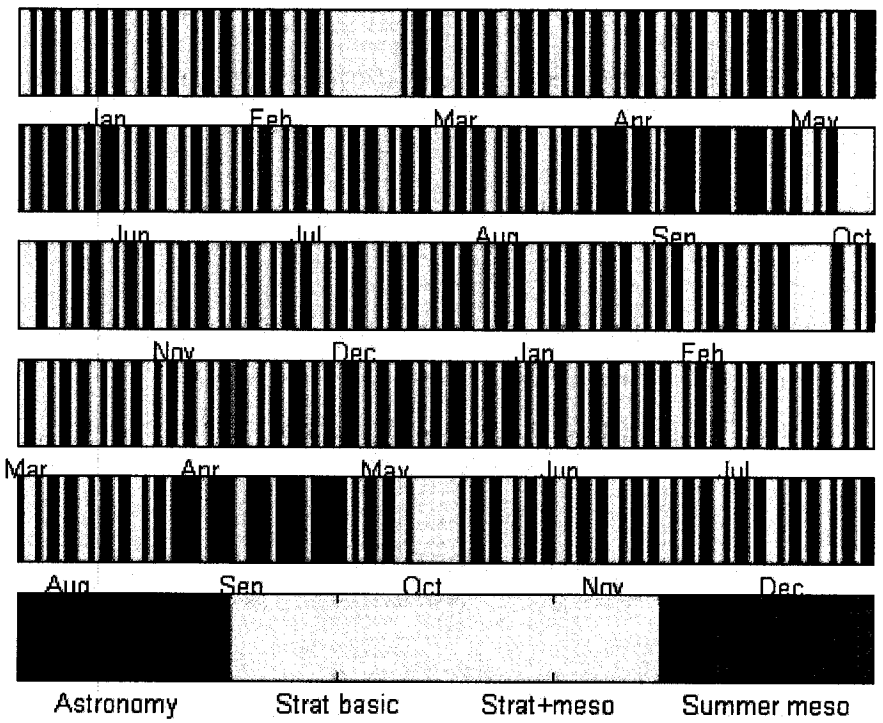

Figure 6.4: The distribution of observing time between the aeronomy and astronomy programs. Source: *Murtagh et al.* (2002, Fig. 4).

6.1.2 Instrument Complement

Odin contains two scientific instruments: SMR (*Frisk et al.*, 2003) and OSIRIS (*Llewellyn et al.*, 2004). The SMR is used for both astronomy and aeronomy studies

while OSIRIS is dedicated to aeronomy studies. The SMR measures in the 118.25-119.25, 486-504 and 541-581 GHz frequency ranges. OSIRIS, the main Canadian contribution to Odin, is essentially two instruments with separate optics and common electronics: the Optical Spectrograph (OS) and the Infrared Imager (IRI). The IRI is a camera that vertically images the atmosphere in three spectral channels, one at 1.53 μm and two near 1.27 μm. The OS is a grating spectrograph that measures spectra of scattered sunlight and airglow emission features in the atmospheric limb between 275 nm and 815 nm at a spectral resolution of about 1 nm, sampled at 0.4 nm intervals. The OS is the focus of this study and is discussed in detail in Section 6.2. The Odin instruments are co-aligned and scan the limb of the atmosphere in the orbit plane over a tangent height range of 7 km to 70 km in approximately 85 seconds in a sawtooth pattern during the normal stratospheric (strat) mode operations through controlled nodding of the spacecraft. Other modes include a mesospheric (meso) mode, in which the scanning covers 60-110 km, and a stratosphere-mesosphere (strat-meso) mode, in which the scanning covers 7-110 km.

6.1.3 Data Products

The SMR provides profiles of O_3, N_2O, ClO and HNO_3 (*Urban et al.*, 2005) as well as CO (*Dupuy et al.*, 2004) and H_2O (*Lautié et al.*, 2004). H_2CO (*Ricaud et al.*, 2007) and NO (J. Urban, personal communication) have also been retrieved from the SMR measurements.

The IRI provides high resolution 2-D measurements of the O_2 and OH nightglow

during local night and the O_2 dayglow and limb-scattered sunlight during local day through a tomographic retrieval technique (*Degenstein et al.*, 2003, 2004). The O_2 measurements can be used to derive mesospheric O_3 profiles (*Khabibrakhmanov et al.*, 2002). The IRI measurements have also been used to derive subvisual cirrus properties (*Bourassa et al.*, 2005).

The OS measurements have been used to produce a number of operational and research (off-line) data products. The current operational data products are stratospheric O_3, NO_2 and aerosol extinction. O_3 is produced using the so-called Chappuis triplet approach combined with OE (*Haley and Brohede*, 2007; *von Savigny et al.*, 2003). NO_2 is produced using the DOAS approach combined with OE, as described in this work. Stratospheric aerosol is recovered using an iterative multiplicative algebraic reconstruction technique (SaskMART) (*Bourassa et al.*, 2007). Alternative processing algorithms for stratospheric O_3 and NO_2 have been developed at the University of Saskatchewan (*Degenstein et al.*, 2006, 2008; *Roth et al.*, 2007) and the Finnish Meteorological Institute (*Auvinen et al.*, 2002; *Tukiainen et al.*, 2008). Off-line analyses have produced a number of additional stratospheric products, including BrO (*Freedman*, 2005), OClO (*Krecl et al.*, 2006) and NO_3 (*McLinden and Haley*, 2008). Additional analyses of OS measurements have produced polar mesospheric cloud (PMC) information (e.g. *Karlsson and Gumbel*, 2005; *Petelina et al.*, 2006), mesospheric Na (*Gumbel et al.*, 2007), mesospheric OH (*Gattinger et al.*, 2006) and polarization information (*McLinden et al.*, 2004). Table 6.2 summarizes the primary Odin data products.

Instrument	Data Products
SMR	O_3, N_2O, ClO, HNO_3, CO, H_2O
OS	O_3, NO_2, BrO, OClO, aerosol, PMC cloud properties
IRI	O_2 and OH airglow, mesospheric O_3, subvisual cirrus properties

Table 6.2: Summary of the Odin mission primary data products.

6.2 The Optical Spectrograph

A brief description of the OS design, Level 1 data processing and data characteristics is presented below, with a focus on the OS daytime measurements. The characteristics of the OS are summarized in Table 6.3.

6.2.1 Instrument Design

Detailed descriptions of the OSIRIS instrument can be found in *Warshaw et al.* (1998) and *Llewellyn et al.* (2004) and only an overview is presented here. Figure 6.5 shows a schematic of the OSIRIS instrument and Figure 6.6 shows a picture of the OSIRIS instrument.

The OS has a 36 mm by 36 mm square aperture with truncated corners. Light enters the entrance port, goes through a series of baffles and vanes and then is reflected by an off-axis parabolic objective mirror onto a flat folding mirror. The light then passes through the input slit and is reflected off of a fold mirror, followed by a second off-axis parabolic mirror that illuminates a blazed aspheric reflective grating. The first-order light reflected off of the grating is directed out of the main optical plane

Characteristic	Specification
Size	200 mm x 426 mm x 485 mm
Mass	12 kg
Power	15-20 W
Spectral range	275-815 nm
Spectral resolution	~1 nm
Spectral sampling interval	0.4 nm
Instantaneous vertical resolution	1 km
Instantaneous horizontal resolution	40 km
Integration time	0.01-2 s
Tangent height range	7-70 km (strat mode)
	7-110 km (strat-meso mode)
	60-110 km (meso mode)
Scan rate	0.75 km/s
Pointing accuracy	±500 m

Table 6.3: The Optical Spectrograph characteristics.

by a camera mirror in combination with a field-flattener/order-sorter/prism (FOP) element onto a charge-coupled device (CCD) detector (EEV model CCD26). The aspheric grating, produced by SA/Jobin-Yvon, has a density of 600 lines/mm, is blazed at 400 nm and operates in first-order. Second-order radiation that overlaps with the first-order is removed with a filter that blocks radiation with wavelengths shorter than 455 nm. This filter is incorporated into the FOP between the prism and the exit lens, and is positioned starting at the location of ~500 nm dispersed light. The CCD detector has an active imaging area of 1353 by 143 pixels, each having a size of 20 by 27 μm, and is passively cooled to a temperature of approximately -20°C in orbit.

The spectrally dispersed image of the slit is projected onto the CCD. The slit is oriented perpendicular to the orbit plane (horizontally) so that the horizontal field of view (FOV) is imaged over 32 rows and the light is dispersed in wavelength over 1353 columns, covering the wavelength range 275 nm to 815 nm (*Sioris and Haley*, 2001). Under normal operations the 32 rows are binned onboard. The spectral resolution, specified as the FWHM (full-width at half maximum) of the approximately Gaussian instrument function, ranges from 0.78 to 1.26 nm (see Figure 6.7) (*Brohede*, 2003; *Stegman*, 1998), giving a sampling ratio of about 2.5 pixels per FWHM. The spectral resolution was found to have some dependence on the temperature of the optical bench, with the optics de-focussing as the optical bench temperature decreases (*Llewellyn and Gattinger*, 2000).

The instantaneous vertical resolution is about 1 km and the horizontal (cross-track) resolution is about 40 km at the tangent point. The OS operates with a pseudo

auto-exposure technique, where the detector exposure times are varied autonomously to account for the extreme change in limb-scatter radiance with tangent height (see Figure 6.14). Due to the varying exposure times ($\sim$0.01 seconds at 10 km increasing to $\sim$2 seconds at 70 km) combined with the nodding motion of the spacecraft, the effective vertical resolution of the limb-scatter measurements varies from about 1 km at 7 km to 2.5 km at 70 km.

As is the case with all instruments utilizing a diffraction grating, the OS exhibits some wavelength-dependent sensitivity to the polarization (*Hutley*, 1982). The grating efficiencies for the OS were measured during the pre-launch characterization campaign (*McLinden et al.*, 2002b) and are shown in Figure 6.8. The relationship between the grating efficiencies and the diffracted radiance is discussed in Section 6.2.2.1.

The baffles and vanes are used to reduce both internal and external stray light, while the optical design, in which there are no obstructions in the optical path and where there is only one refractive element (the FOP), provides for a low level of internal stray light. Internal stray light arises from the scattering of unwanted light inside the optics unit (cross talk between light wavelengths which are separated in the spectrograph) and external stray light is unwanted light from outside the instrument FOV (e.g. from the bright limb or the Earth surface that is not adequately prevented from entering the instrument). The internal stray light is important at the short wavelengths and at low tangent heights (*Evans and Alfred*, 1999; *Haley et al.*, 2001; *Lloyd*, 2005b). The external stray light is a significant contaminant at the long wavelengths and at high tangent heights (*Llewellyn et al.*, 1998). An example of the

contamination due to external stray light is shown in Figure 6.9.

In the region of the edge of the order-sorting filter (~477-530 nm), there is some uncertainty about the characteristics of the OS, in particular the spectral resolution and responsivity. As a result the measurements in this spectral region are not retained during the normal operations, resulting in a gap in the OS spectra.

Another issue that affects the OS data is physical contamination of the slit that was discovered just prior to launch. This contamination is believed to be related to the gas purge of the instrument while it was stored awaiting integration on the satellite (*Llewellyn et al.*, 2001). A picture of the contaminated slit is shown in Figure 6.10. The impact on the OS radiances can be seen in Figure 6.11, where a full-field (32 row) OS image is shown. The spatial structure seen in the radiances is due to the contamination of the slit. The primary impact of the contamination is on the instrument responsivity. To compensate for this the responsivity measured during the pre-launch characterization campaign (*Stegman*, 1999) is adjusted at each wavelength by a factor determined under the assumption that the brightest row is free of contamination (N. Lloyd, personal communication).

6.2.2 OS Level 1 Data Processing

An important part of interpreting the OS data is understanding the various processing steps that are taken to convert the raw (Level 0) data to calibrated (Level 1) radiances. Equally important is an understanding of the estimated error in the measurements.

The OS Level 0 data is provided in data numbers (DN) and is influenced by the

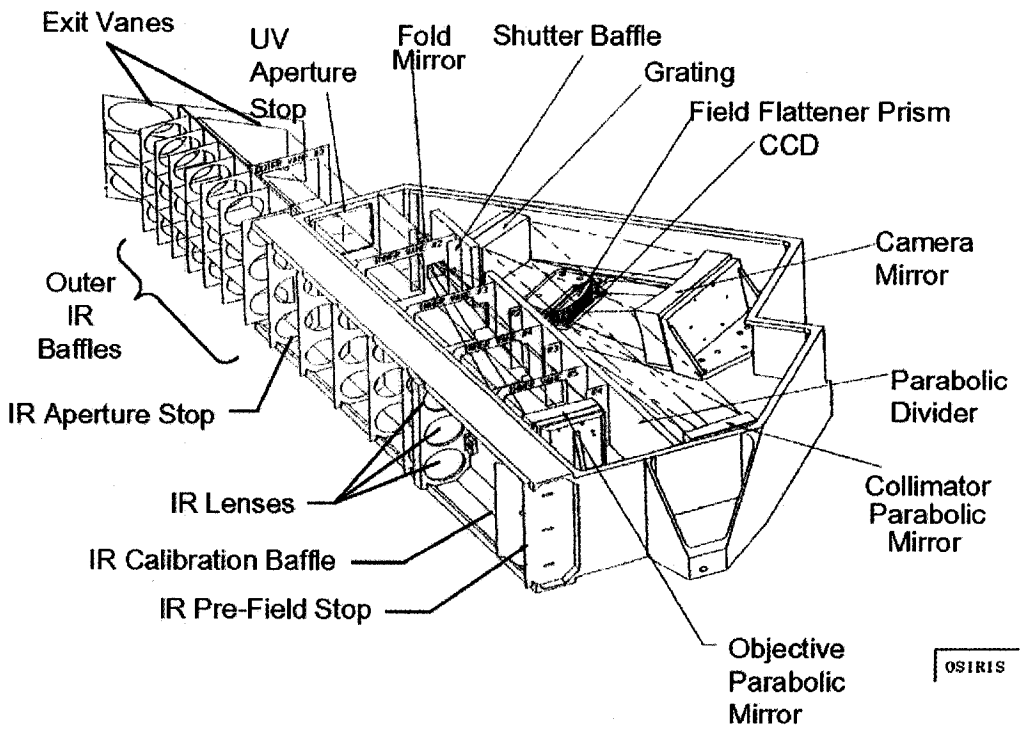

Figure 6.5: Schematic drawing of the OSIRIS instrument. Source: *Llewellyn et al.* (2004, Fig. 2a).

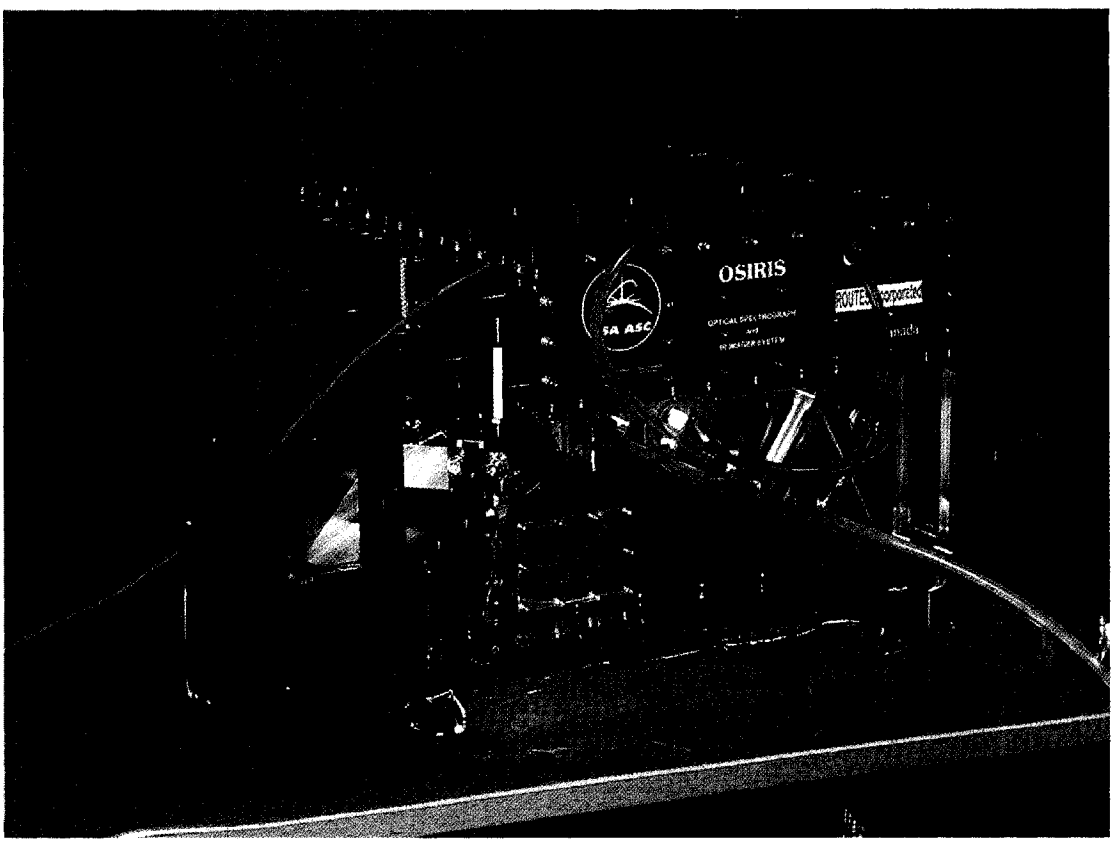

Figure 6.6: The OSIRIS instrument. Source: Courtesy of E.J. Llewellyn and L. Piché.

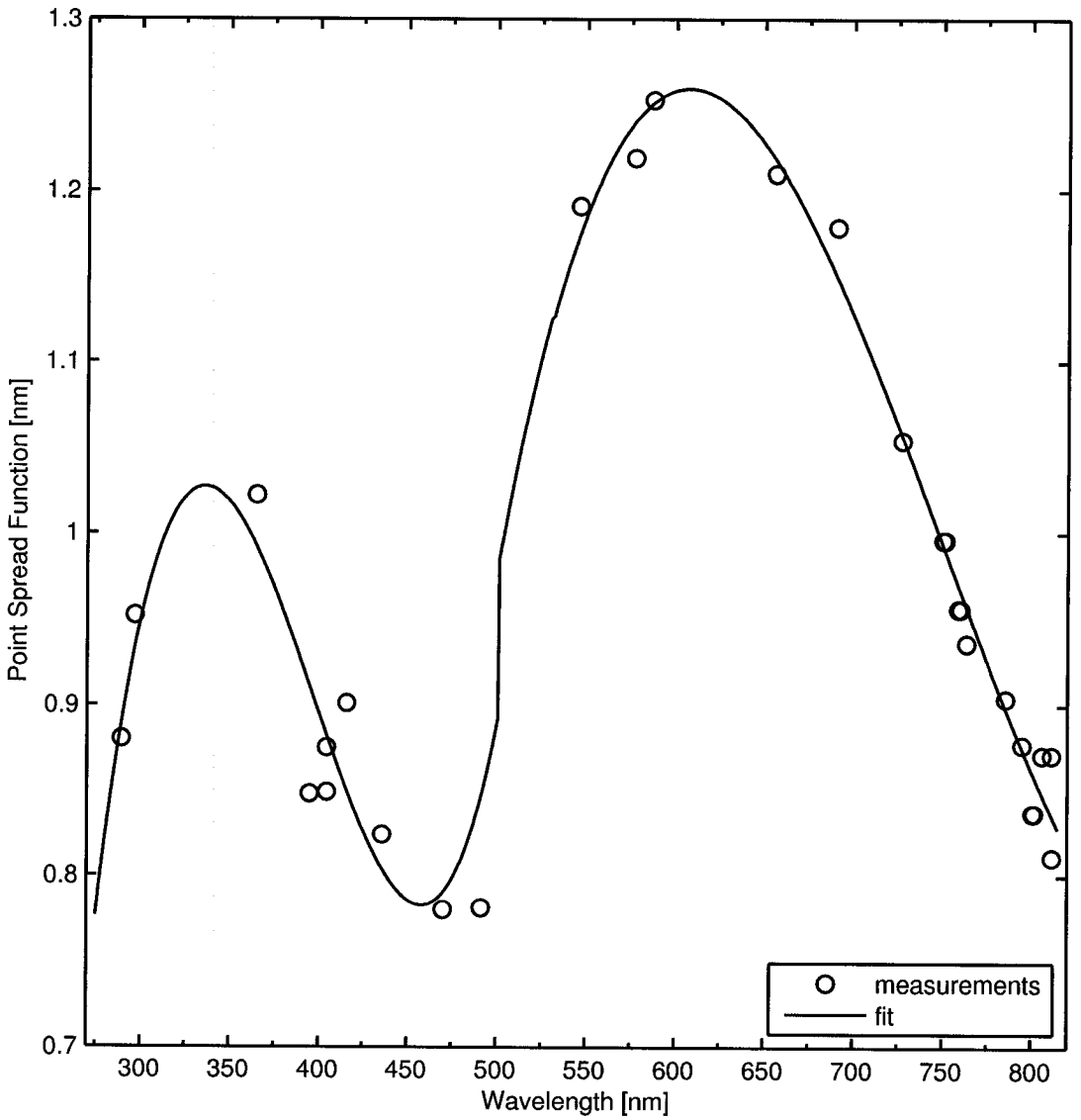

Figure 6.7: The OS point spread function (spectral resolution), defined as the FWHM of a Gaussian function from *Stegman* (1998).

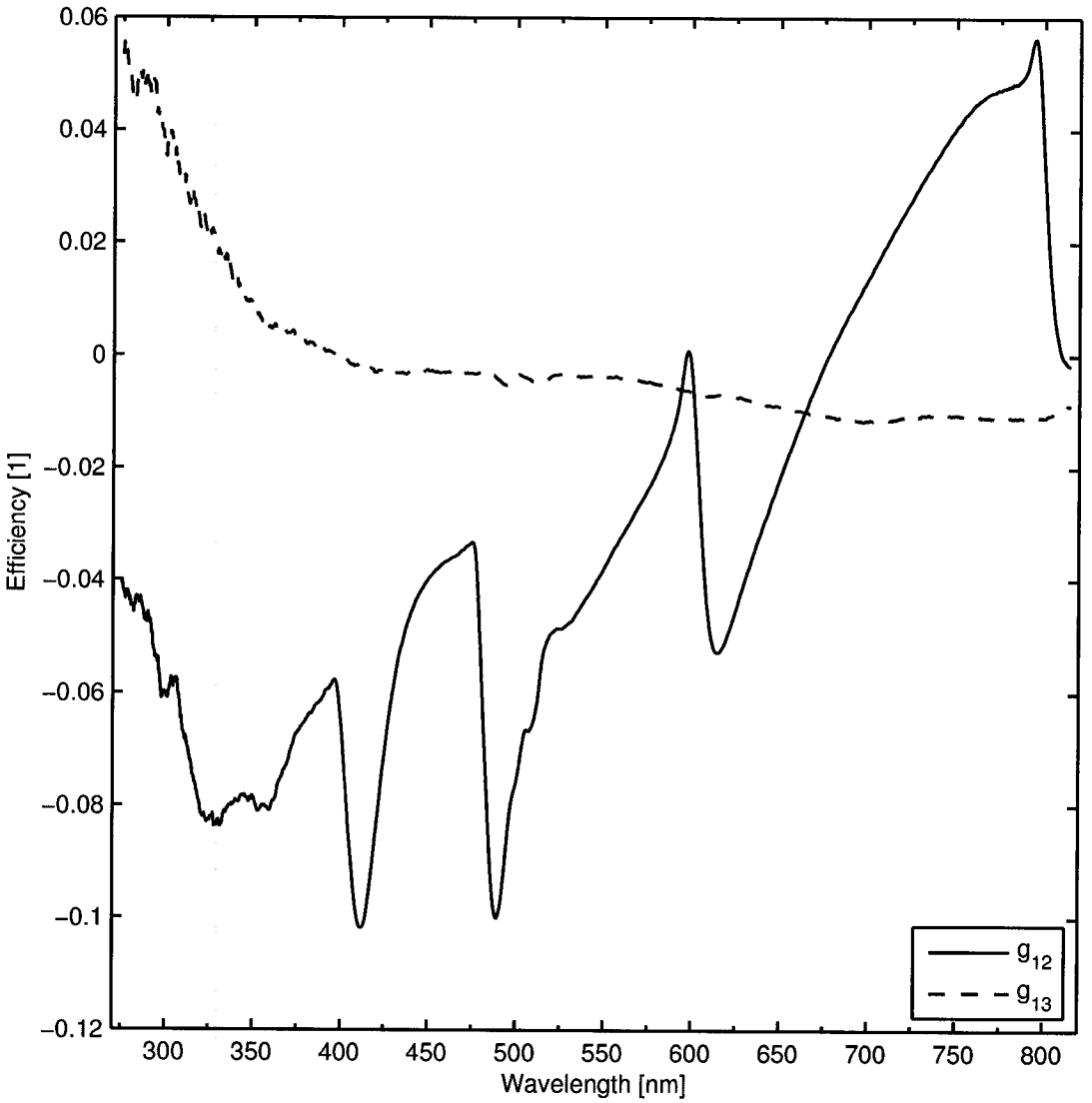

Figure 6.8: The OS polarization (grating) efficiencies from *McLinden et al.* (2002b).

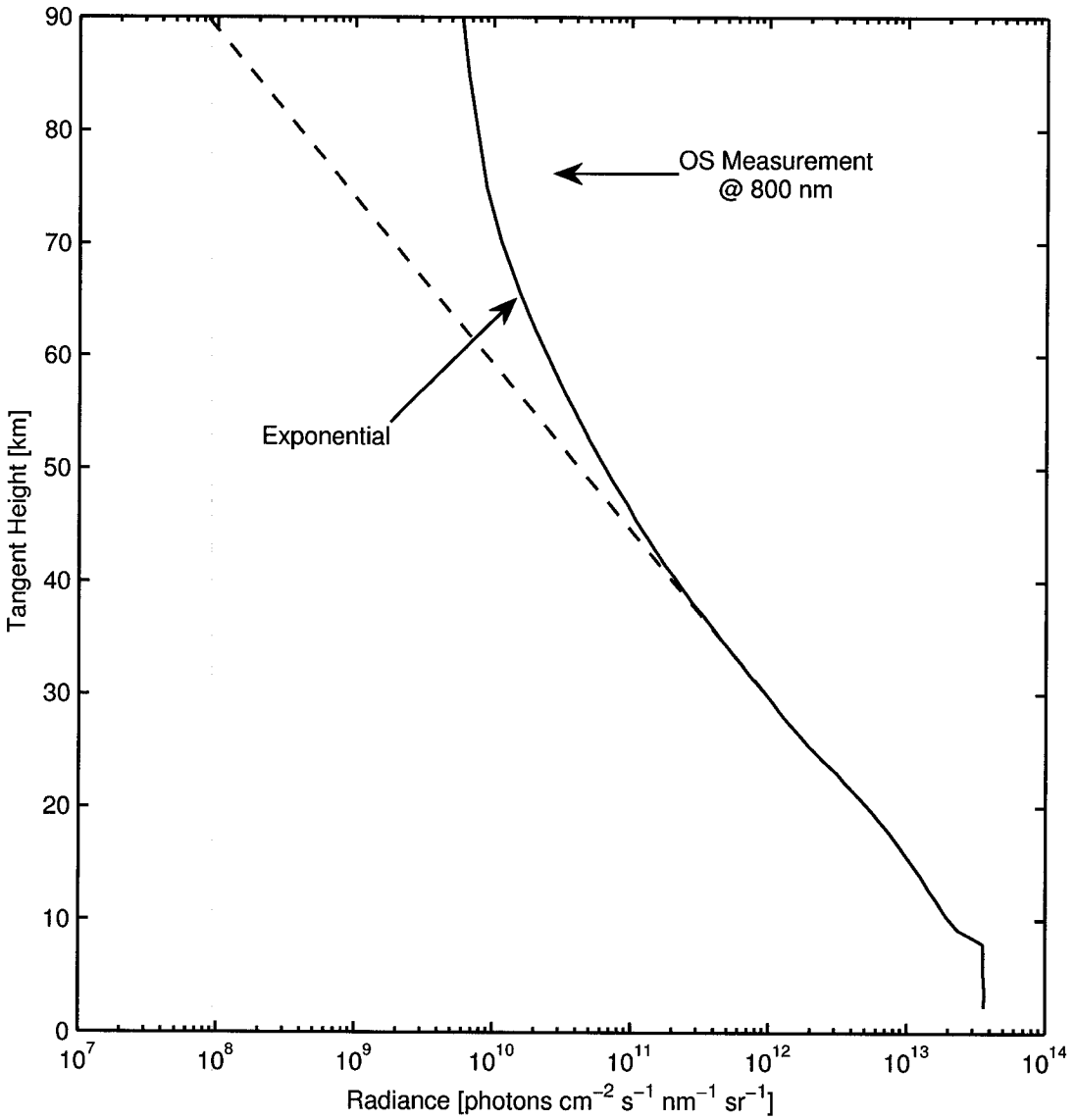

Figure 6.9: External stray light (baffle-scatter) contamination for a typical OS limb scan (scan 6045012) at a wavelength of 800 nm. The deviation from an exponentially-decreasing radiance profile is due to contamination from outside of the instrument FOV.

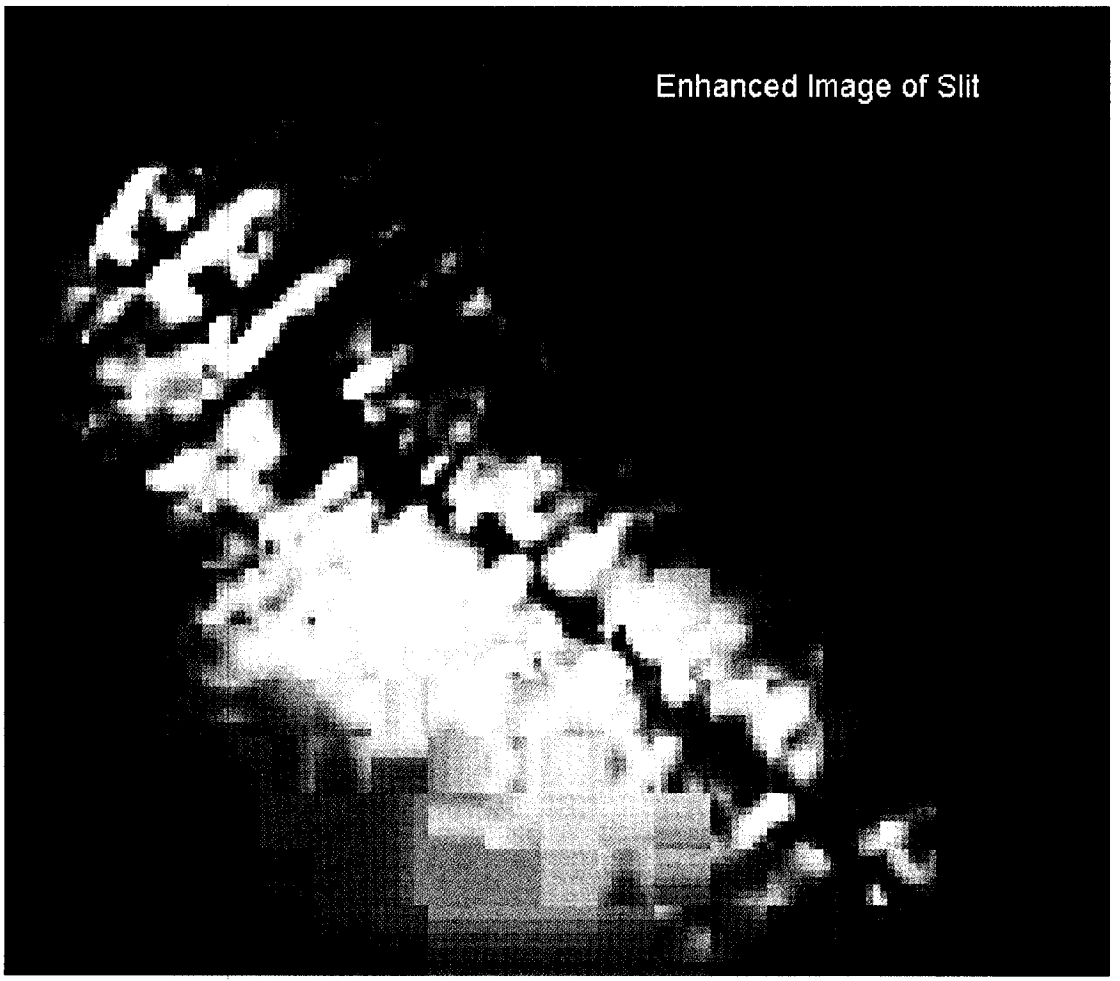

Figure 6.10: Picture of the contaminated OS input slit. Source: *Llewellyn et al.* (2001).

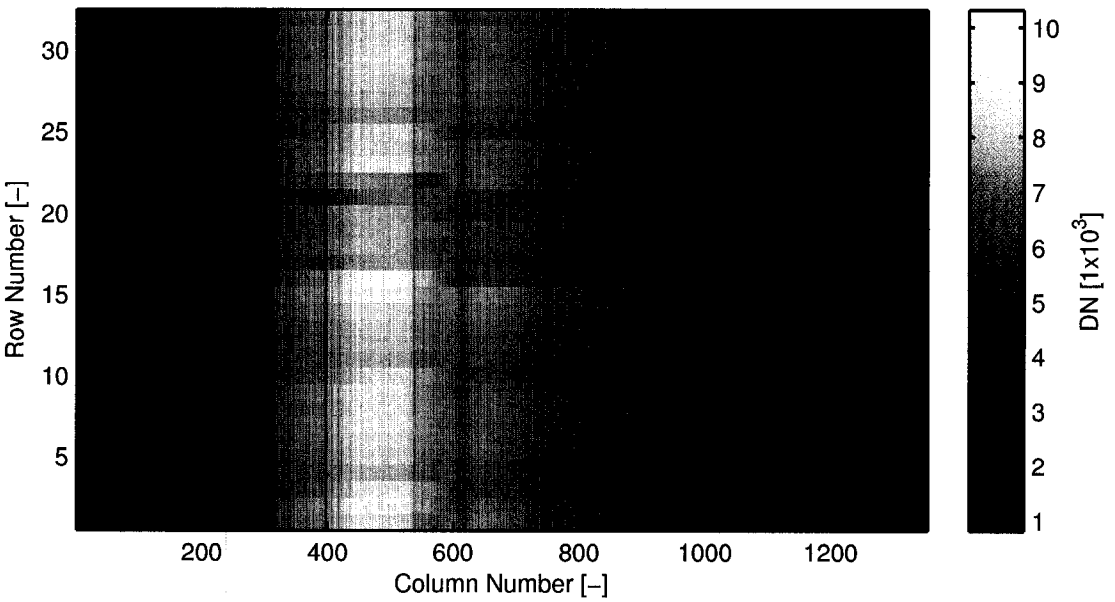

Figure 6.11: A full-field OS image (Level 0), with the structure in the vertical (spatial) dimension clearly showing the impact of the contaminated slit.

operating mode of the instrument as well as the instrument characteristics at the time of the measurement. OS Level 1 data is given in absolute radiance units. As is discussed below, the OS Level 1 data processing does not account for all of the instrument characteristics. Some issues, including polarization sensitivity and baffle (out-of-field) scatter, must be included in further (Level 2) processing, if necessary.

6.2.2.1 Level 0 Corrections

As described in *Haley and Sioris* (2001), the calibrated limb radiance, $I(\lambda)$, in photons/(cm^2·s·nm·sr), is calculated from the OS Level 0 data (in DN) through the following steps:

(1) Determine the normalized signal - DN/pixel/s):

$$I(\lambda)' = \frac{\frac{S(i)}{N_{off}} - B(i)}{N_{on} * t_{exp}} - D(i) \tag{6.1}$$

(2) Correct for internal stray light:

$$I(\lambda)'' = I(\lambda)' - \psi * \sum I(\lambda)' \tag{6.2}$$

(3) Convert to absolute radiance units - photons/(cm^2·s·nm·sr):

$$I(\lambda) = \frac{I(\lambda)''}{R(i)} \tag{6.3}$$

where $S(i)$ is the Level 0 measurement in DN for pixel i corresponding to wavelength λ. N_{off} is the off-chip binning, $B(i)$ is the bias correction in DN for pixel i, N_{on} is the number of pixels binned on-chip, $D(i)$ is the dark current correction for pixel i ($\sim 1-4$ DN/pixel/s) (*Lloyd*, 2005a), t_{exp} is the exposure or integration time ($0.01-2$

s), ψ is the internal stray light correction factor ($1.6 - 3.4 \times 10^{-6}$) (*Haley et al.*, 2001; *Lloyd*, 2005b) and $R(i)$ is the flat-field responsivity of pixel i ($0.1 - 0.8 \times 10^{-8}$ DN per photon/cm^2/sr/nm) (*Lloyd*, 2007; *Stegman*, 1999).

As discussed in Section 6.2.1, the OS has some sensitivity to polarized light, and the measured (polarized) radiances should be converted to equivalent unpolarized radiances, I_{unpol}, using the OS grating efficiency parameters g_{12} and g_{13} (*McLinden et al.*, 2002b):

$$I_{unpol}(\lambda) = \frac{I(\lambda)}{1 + LP(\lambda)\left[g_{12}(\lambda)\cos 2\chi(\lambda) + g_{13}(\lambda)\sin 2\chi(\lambda)\right]} \tag{6.4}$$

where LP is the degree of linear polarization:

$$LP(\lambda) = \frac{\sqrt{Q(\lambda)^2 + U(\lambda)^2}}{I(\lambda)} \tag{6.5}$$

and χ is the angle of polarization:

$$2\chi(\lambda) = \tan^{-1}\left[\frac{U(\lambda)}{Q(\lambda)}\right] \tag{6.6}$$

The V component of the Stokes vector can be ignored for the terrestrial atmosphere (*McLinden et al.*, 2002b). The calculation of the Stokes parameters Q and U requires assumptions about the state of the atmosphere and a radiative transfer model. This is beyond the scope of the Level 1 data processing.

Another issue that is not addressed in the Level 1 processing is that of external stray light (discussed in Section 6.2.1). To date no suitable correction for this effect has been discovered, and any correction for this effect would likely require knowledge of the source. As a result, no correction is included in the Level 1 data processing.

A sample calibrated Level 1 OS limb scan is shown in Figure 6.12.

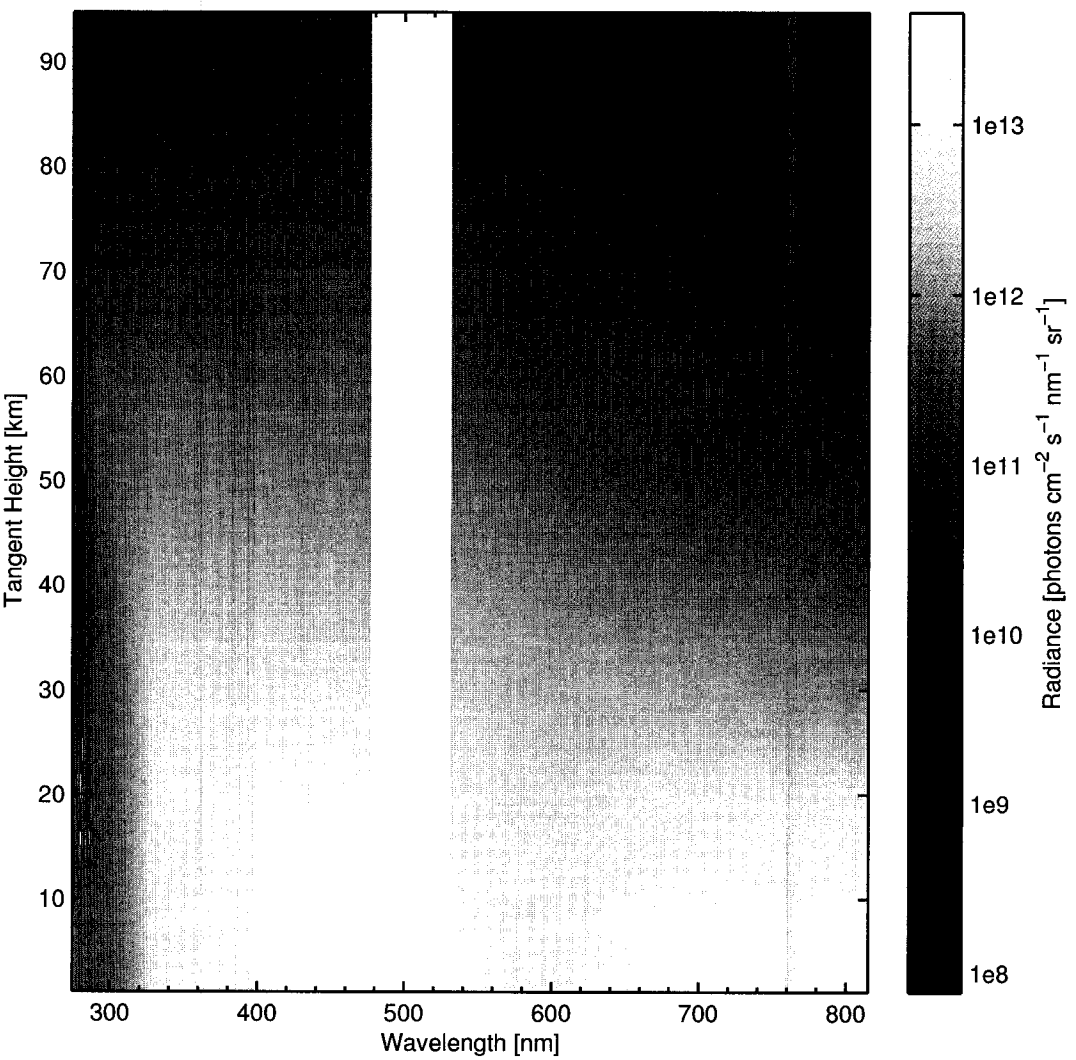

Figure 6.12: A sample calibrated Level 1 OS limb scan (scan 6045012).

6.2.2.2 Error Approximation

A key element of the Level 1 data product is an estimation of the error in the measured radiances. There are a number of sources of error that must be taken into account, including:

- photon shot noise from the source at the detector
- shot noise due to the detector dark current
- detector readout noise
- the impact of digitization

The error due to these sources is assumed to be random with a mean of zero, and the standard deviation (STD) of the error in the Level 0 data at pixel i, $\varepsilon_S(i)$, is approximated as:

$$\varepsilon_S(i) \simeq \sqrt{\left[\frac{\frac{S(i)}{N_{off}} - B(i)}{G} + \varepsilon_{ROE}^2 + \left(\frac{1}{2}\right)^2\right] * N_{off}} \tag{6.7}$$

where G is the reciprocal effective gain (14.3 electrons/DN) and ε_{ROE} is the readout electronics (ROE) noise (1.2 DN). When the Level 1 processing discussed in Section 6.2.2.1 is applied to the Level 0 data, the estimated STD of the error in $I(\lambda)$, $\varepsilon_I(\lambda)$, is calculated as follows:

$$\varepsilon_I(\lambda)' = \sqrt{\frac{\left[\frac{\varepsilon_S(i)}{N_{off}}\right]^2 + [\varepsilon_B(i)]^2}{(N_{on} * t_{exp})^2} + [\varepsilon_D(i)]^2} \tag{6.8}$$

$$\varepsilon_I(\lambda)'' = \sqrt{[\varepsilon_I(\lambda)']^2 + \left[\varepsilon_\psi * \sum I(\lambda)'\right]^2} \tag{6.9}$$

$$\varepsilon_I(\lambda) = I(\lambda) * \sqrt{\left[\frac{\varepsilon_I(\lambda)''}{I(\lambda)''}\right]^2 + \left[\frac{\varepsilon_R(i)}{R(i)}\right]^2} \tag{6.10}$$

where $\varepsilon_B(i)$, $\varepsilon_D(i)$, ε_ψ and $\varepsilon_R(i)$ are the standard deviations of the errors in $B(i)$, $D(i)$, ψ and $R(i)$, respectively. Note that the current OS Level 1 processing assumes no uncertainty in R. A complete derivation of the above equations can be found in *Haley and Sioris* (2001).

The signal-to-noise ratio (SNR) for a typical OS limb scan is shown in Figure 6.13.

6.2.3 Data Characteristics

Spectra from a typical OS limb scan are shown in Figure 6.14. The spectra in this plot resemble the 20 km tangent height modeled spectrum shown in Figure 3.3. However, a number of differences are evident. There is a gap in the measured spectra near 500 nm discussed in Section 6.2.1. Also, there are a number of spectral features present in the measured spectra that are not shown in the modeled spectra, including a number of absorption features from molecules not included in the model calculations: the O_2 A-band (758-771 nm), the O_2 b-band (685-693 nm), the O_2 γ-band (623-634 nm) and water vapour (H_2O(g)) (720-740 nm). A number of airglow emissions are also visible in the measured spectra at high tangent heights, including the green and red lines of atomic oxygen (557.7 nm and 630.0 nm, respectively) and the Na doublet (~589.0 nm). Note that the Na and O_2 A-band features appear as absorption features at low tangent heights and emission features at high tangent heights. The Na doublet is also a Fraunhofer feature, accounting for this behaviour (i.e. the airglow fills in and then

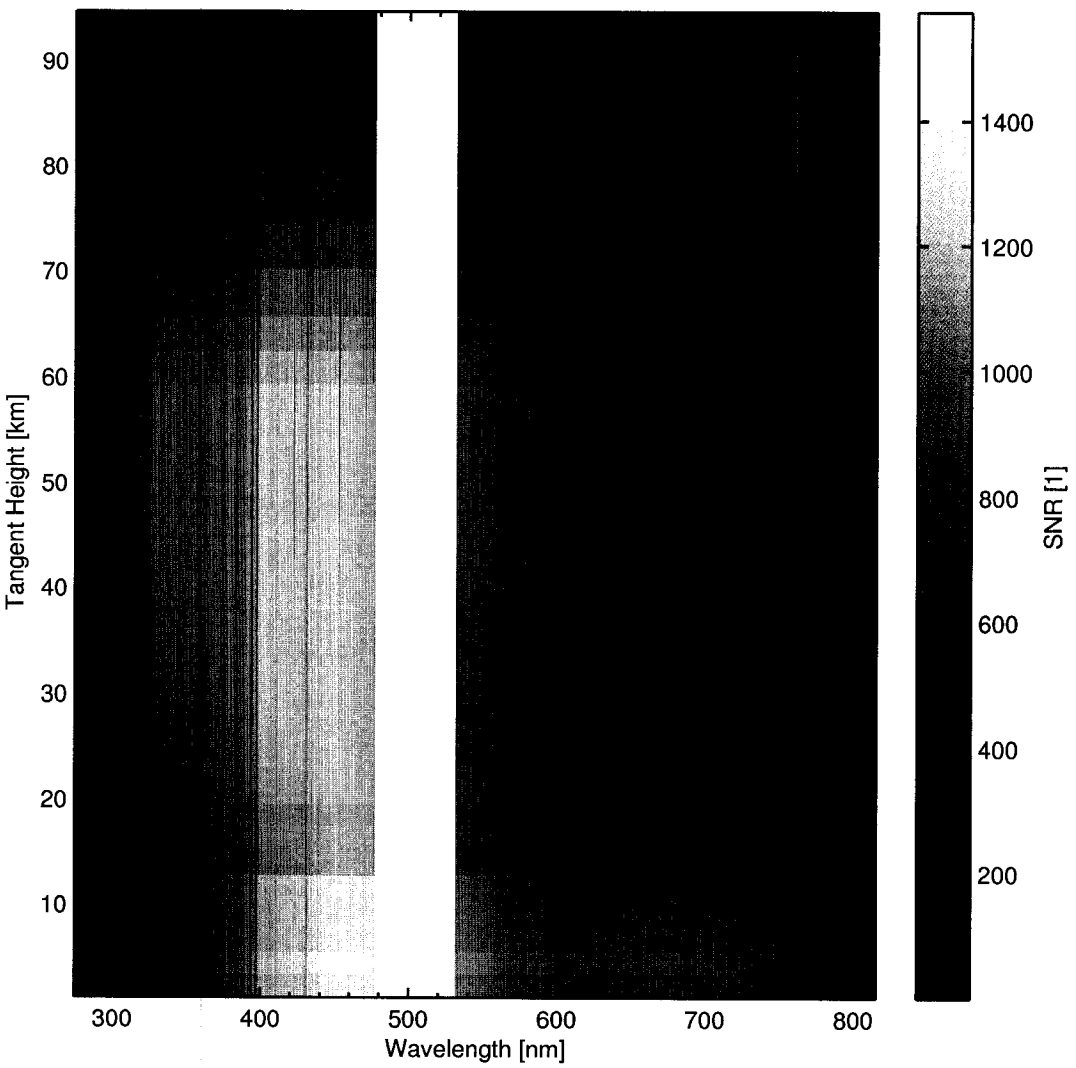

Figure 6.13: Signal-to-noise ratio for a typical OS limb scan (scan 6045012).

dominates the Fraunhofer feature as the tangent height increases). For the O_2 A-band, the strong absorption by O_2 in the lower atmosphere decreases with increasing tangent height while the A-band airglow emission increases. Also note that at high tangent heights the O_2 b-band and H_2O(g) features are unexpectedly still present in the spectra, primarily due to contamination by external stray light that causes a reddening of the high TH spectra and contains these lower atmosphere signatures. The measurement noise is also apparent in the measured spectra, in particular in the UV and and at high tangent heights.

Since the Odin spacecraft is in a near-terminator orbit, the limb-scatter measurements (which are normally made in the orbit plane) are hemispheric in nature, with the Northern Hemisphere sampled between mid-February and mid-October and the Southern Hemisphere sampled between mid-October and mid-February. There are short periods in February and October where near-global coverage is obtained (82.2°N to 82.2°S) when the are made along the terminator (terminator days). Figure 6.15 illustrates the Odin orbit orientation. Scheduled out-of-plane pointing manoeuvres provide measurements all the way to the pole in the Southern Hemisphere at certain time periods. The latitude coverage for a true near-terminator orbit, including the related SZAs, is shown in Figure 6.16. The actual latitude coverage of the OS from November 2001 (the start of nominal OSIRIS operations) to December 2007 is shown in Figure 6.17, with the associated SZAs and SSAs shown in Figure 6.18 and LSTs shown in Figure 6.19. The impact of the precession of the Odin orbit away from a true near-terminator orbit through the mission is clear in the figures, leading to better coverage in the sunrise (AM) portion of the orbit and poorer coverage in the sunset

(PM) portion.

6.2.4 Tangent Height Registration

An important issue for limb-viewing instruments is pointing or tangent height registration accuracy. From an orbit altitude of 600 km, a pointing error of only 0.01° corresponds to an approximately 500 m at the tangent point and can introduce significant errors in retrieved minor species profiles (e.g. *Haley et al.*, 2004; *Loughman et al.*, 2005; *von Savigny et al.*, 2005). The original design for the Odin spacecraft required pointing knowledge of ±0.04° or 2 km vertically on the limb for aeronomy measurements. Fortunately, the Odin attitude control system is designed for astronomical work as well, requiring very accurate pointing information (±8 arcseconds). Significant work was done by the Swedish Space Corporation to improve the aeronomy pointing accuracy, including providing improved GPS and star tracker information and making a number of aeronomy-specific improvements to the attitude reconstruction software. In addition, the relative alignment of the OS field of view was measured in-flight using measurements of Jupiter and determined to an accuracy of about 3 arcseconds, which translates to ~50 m vertically on the limb (N. Lloyd, personal communication). *McLinden et al.* (2007) confirmed that the current tangent height registration has a random variation of approximately 400 m and a positive systematic offset of about 100 m. Although the current pointing information is generally very accurate, there are infrequent periods of poor pointing, primarily caused by GPS position errors. A pointing issue (~200-500 m negative offset) in the Odin

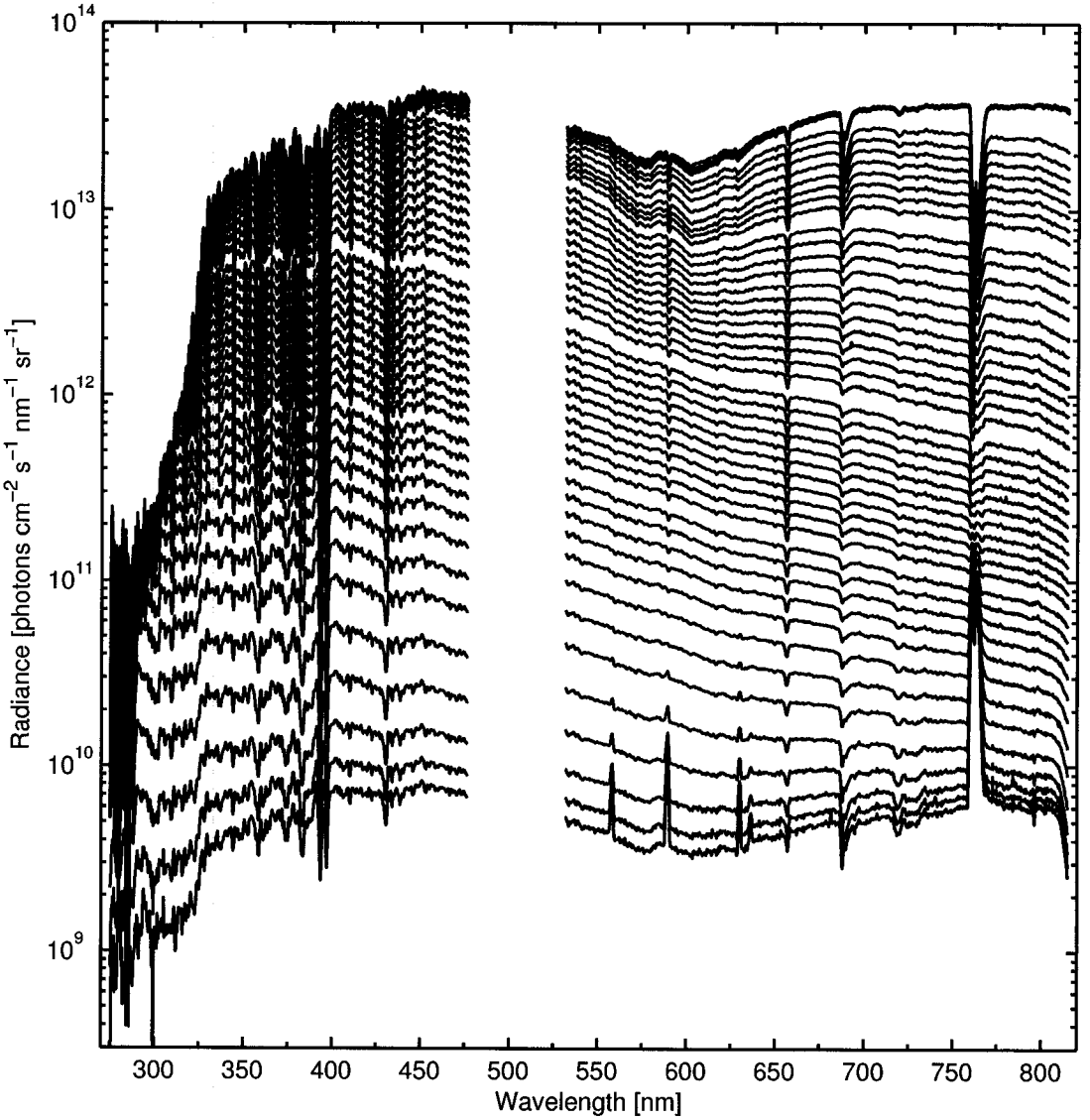

Figure 6.14: Limb-scatter radiance spectra from typical OS limb scan (scan 6045012), covering tangent heights from 2 km to 90 km. The data gap near 500 nm is in the region of the order-sorter where the data are not recorded in normal operations.

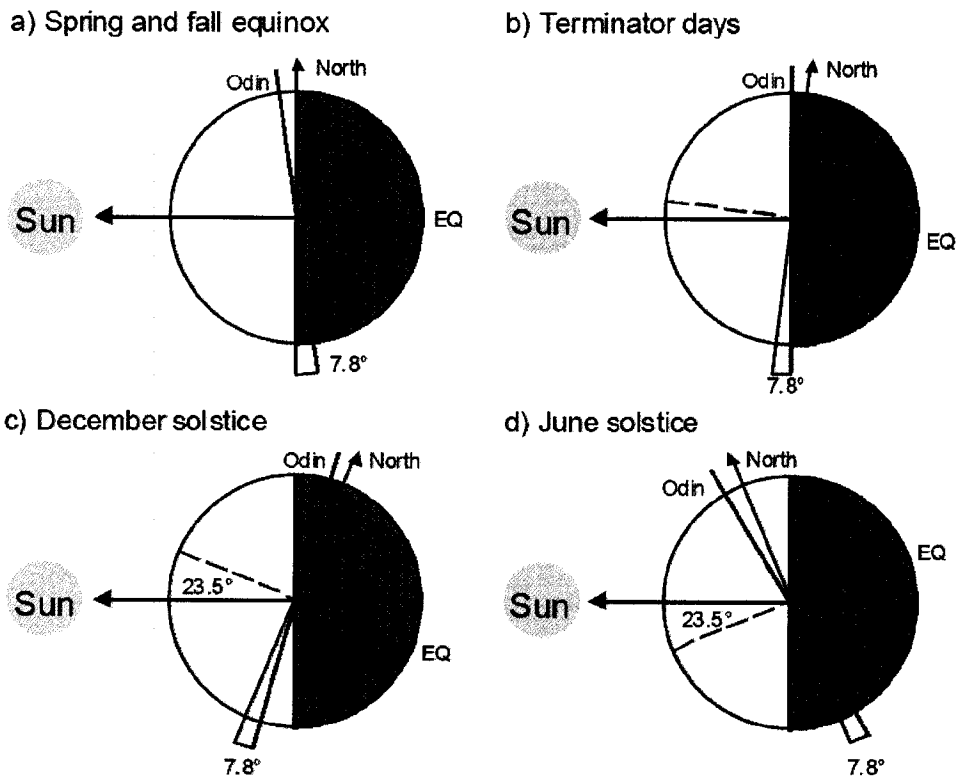

Figure 6.15: The orientation of the Odin orbit throughout the year. Source: *von Savigny* (2002, Fig. 3.4).

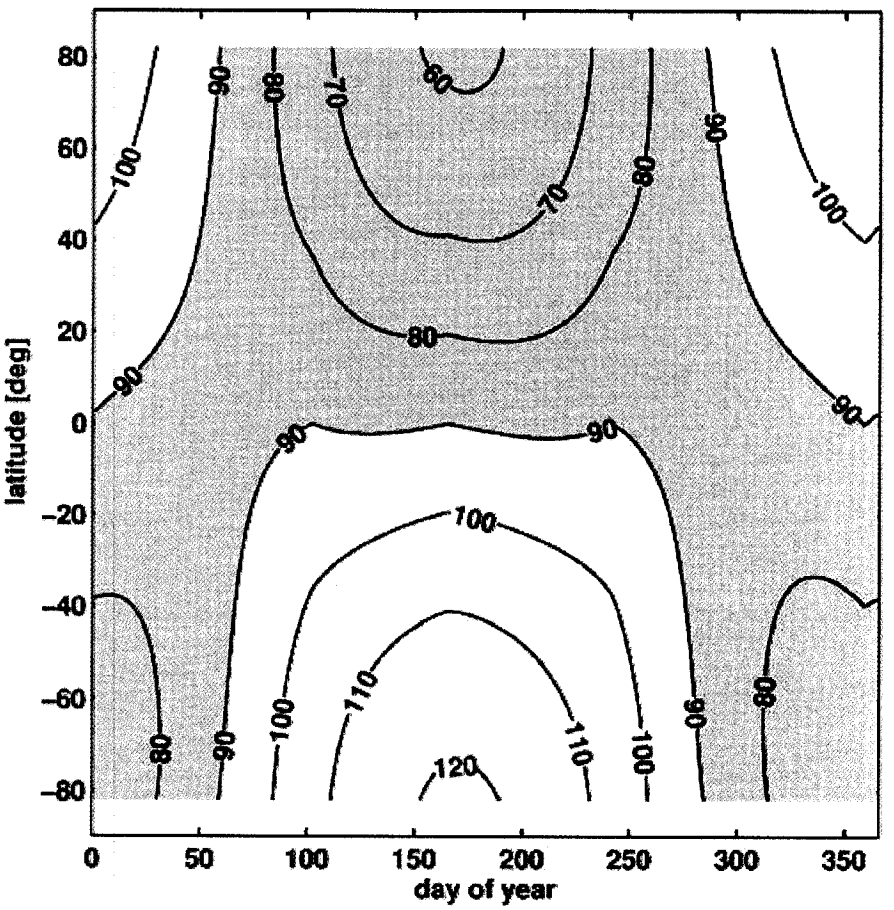

Figure 6.16: The expected latitude coverage of the OS limb-scatter measurements for a true near-terminator orbit (shaded) and the associated SZAs (contours). Source: *Haley et al.* (2004, Fig. 2).

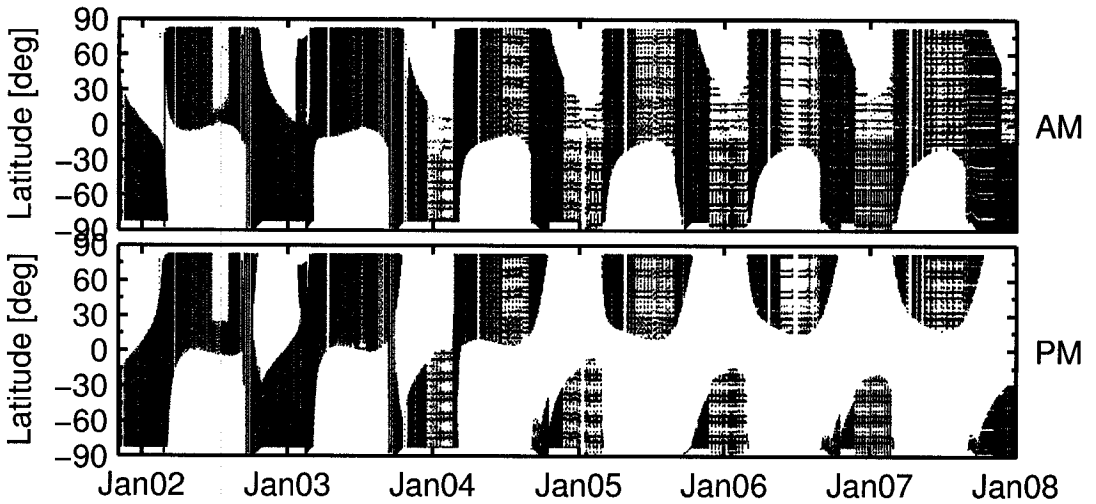

Figure 6.17: The latitude and temporal coverage of the OSIRIS version 3.0 NO_2 data product from November 2001 to December 2007, where sunrise measurements (AM) are shown in the upper panel and sunset measurements (PM) are shown in the lower panel. White regions indicate no measurements. Full global coverage is achieved near the equinoxes and hemispheric (summer hemisphere) coverage is achieved elsewhere. Note the gradual loss of PM measurements as the equator crossing time of the Odin orbit drifts over time.

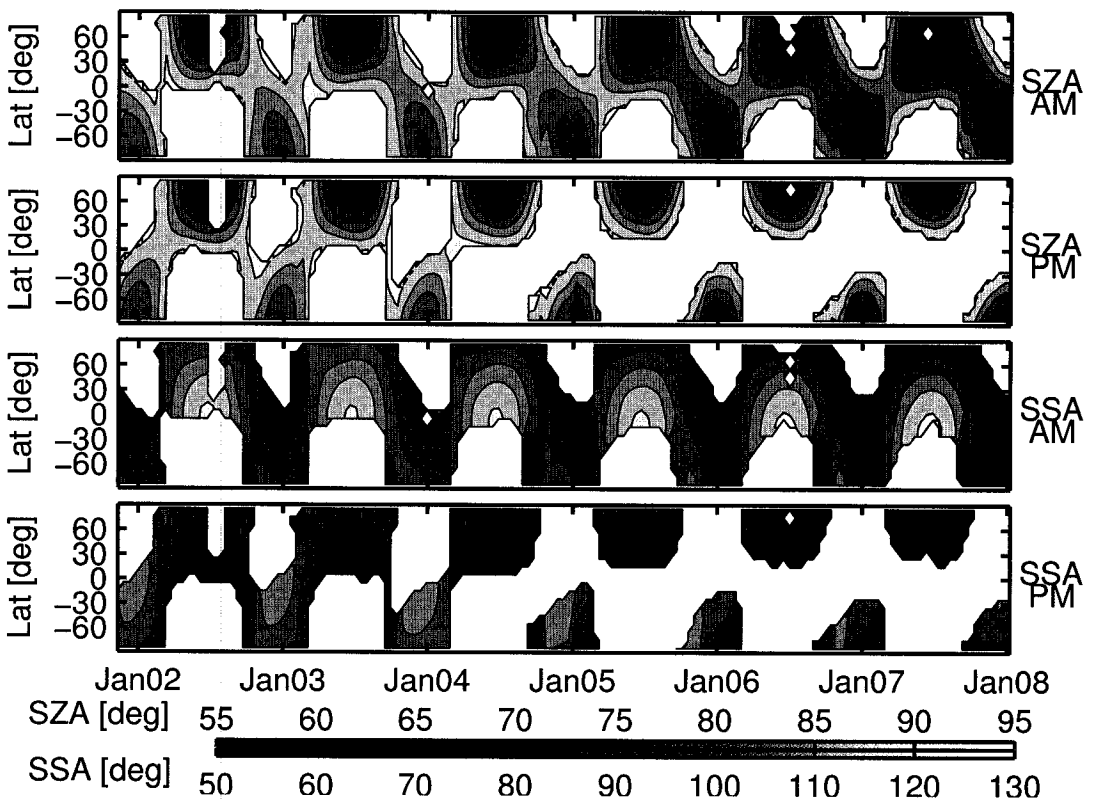

Figure 6.18: The SZA and SSA conditions of the OSIRIS version 3.0 NO_2 data product from November 2001 to December 2007, where sunrise measurements (AM) are shown in the upper panels and sunset measurements (PM) are shown in the lower panels. White regions indicate no measurements. The smallest SZAs are found in high latitude summer conditions, whereas the SZA is close to 90° for all latitudes at the equinoxes. The SSA deviates furthest from 90° in the equatorial region in the Northern Hemisphere summer.

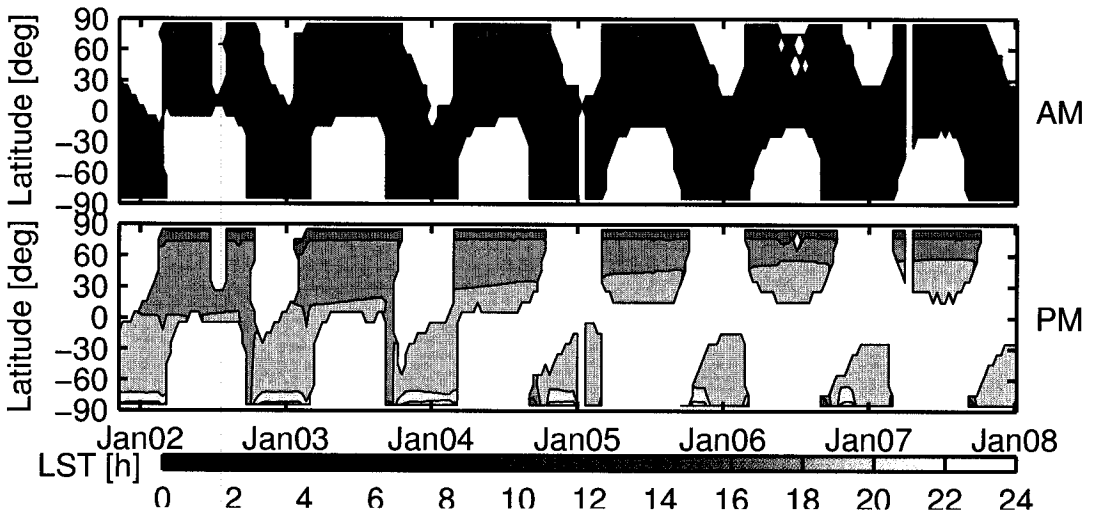

Figure 6.19: The LST of the OSIRIS version 3.0 NO_2 data product from November 2001 to December 2007, where sunrise measurements (AM) are shown in the upper panel and sunset measurements (PM) are shown in the lower panel. The AM node corresponds to a LST of about 06:00 hours for most latitudes and the PM node to about 18:00 hours. At high latitudes the LST rapidly sweeps through noon (12:00 hours) in the Northern Hemisphere and midnight (00:00 or 24:00 hours) in the Southern Hemisphere.

eclipse season (May-July) has also been discovered (*McLinden et al.*, 2007) and is likely caused by thermal distortions of the spacecraft during this period.

Chapter 7

Retrieval of Stratospheric O_3 and NO_2 from OSIRIS

The retrieval theory presented in the preceding chapters has been extended and applied to the retrieval of stratospheric O_3 and NO_2 number density profiles from limb-scatter measurements made by OSIRIS. This chapter presents an overview of the results published in **Papers I-VII**. The retrieval method described here is currently being applied to the OS data to produce the operational stratospheric NO_2 data product (version 3.0).

7.1 Minor Species Retrieval

Paper I and *Strong et al.* (2002) present the first applications of DOAS to simulated OS limb-scatter radiances for the retrieval of stratospheric species. **Paper II** presents the first application of DOAS to on-orbit OS data to retrieve stratospheric NO_2.

Paper III presents an early application of the method used in this work to OS data. **Paper IV** gives a detailed description of the retrieval method used in this work for retrieving stratospheric O_3 and NO_2 number density profiles from OS limb-scatter measurements, including the application of DOAS to the OS limb measurements and the inversion of the derived effective column densities to number density vertical profiles.

Some modifications to the retrieval algorithm presented in **Paper IV** have been made and are discussed in the following sections. The main changes are a widening of the O_3 fitting window, the use of a tangent height dependent tilt pseudo-absorber, a lower reference tangent height for O_3 and a smaller a priori standard deviation for NO_2. In addition, the H_2O and O_4 cross sections have been updated and a LM retrieval is carried out following a failed GN retrieval. Some of the changes are discussed in **Paper VII**.

Figure 7.1 shows an overview of the retrieval method applied to the OS observations. Table 7.1 summarizes the retrieval configuration for the O_3 and NO_2 retrievals.

7.1.1 Level 1 Data Evaluation

All OS Level 1 data (see Section 6.2.2) in which the SZA at the tangent point is less than 92° are selected for further processing. A large amount of data verification and filtering is carried out on the Level 1 data prior to further processing, as described in **Paper VII**. In particular, each scan is checked for large pointing offsets (*Sioris et al.*, 2001) and clouds in the FOV (*Sioris et al.*, 2007). A first-order correction for

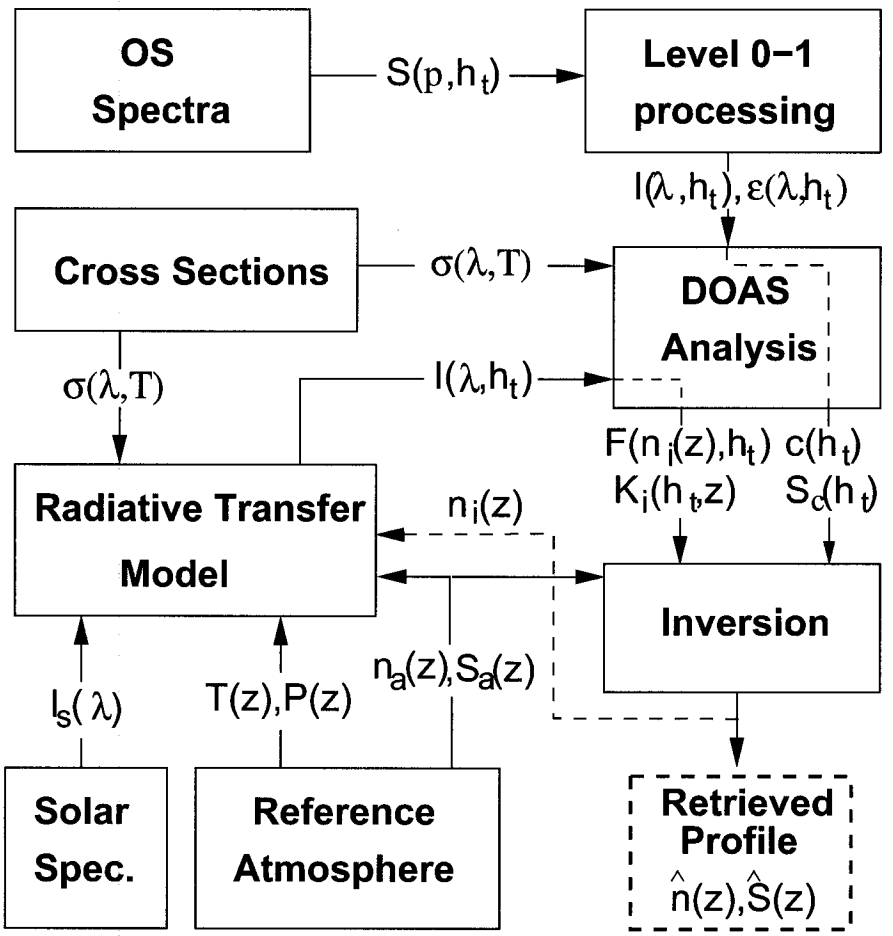

Figure 7.1: Overview of the retrieval process. Source: Adapted from *Haley et al.* (2004, Fig. 4).

	O_3	NO_2
Wavelengths	562-623 nm	435-451 nm
Fitted species	O_3,NO_2,O_4,H_2O, Rayleigh	O_3,NO_2,O_4, Rayleigh
Corrections	Polarization	Tilt,I_0,λ-shift
Retrieval range	10-46 km†	10-46 km†
Reference height	nearest above 46 km	46-65 km average
Estimating **F**	4 nm grid	2 nm grid
Estimating **K**	2-λ,SS,no aerosol	2-λ,SS,no aerosol
Response > 0.75	$\sim$12-44 km	$\sim$12-44 km
Resolution @ 25 km	$\sim$2 km	$\sim$2 km
Total error @ 25 km	$\sim$8%	$\sim$10%

Table 7.1: Summary of the configuration settings used for O_3 and NO_2 retrievals. †If no cloud is detected, otherwise the cloud top is used to set the lower limit.

the effect of refraction of the tangent heights is also applied.

7.1.2 The Application of DOAS to OS Measurements

When applying the DOAS technique described in Chapter 4 to the OS measurements (and to limb-scatter measurements in general), a number of issues must be considered. These include the selection of a method for determining the differential quantities, the inclusion of measurement noise, the choice of a reference, the selection of a spectral window and absorption cross sections, and a number of corrections to the ideal spectral fitting approach described previously. **Papers I-III** consider some of these issues, while a comprehensive treatment of the application of DOAS to the OS measurements can be found in **Paper IV**. Below is a summary of the issues and an brief presentation of typical results.

7.1.2.1 Determining the Differential Quantities

A number of options exist for determining the differential quantities $\tau'(\lambda)$ and $\sigma'(\lambda)$ to use in the spectral fitting. A common approach is to use a filter function (often a boxcar, or running average) to remove any slowly varying features. In this case the width of the boxcar must be chosen such that it is narrow enough to properly remove the low frequency component and identify the differential structure, but wide enough as to not remove a significant portion of that structure (thereby reducing the effective signal-to-noise ratio). A disadvantage of using a filter function is that measurements (most importantly, simulated measurements) outside of the desired spectral fitting

window are required. An alternative approach is to fit a low-order polynomial to the spectra. Again, the order of the polynomial must be chosen carefully, but in this case only measurements within the spectral window are required. Also, since the entire spectral window is considered in the fit, the calculation is less sensitive to measurement noise.

In this work an alternative approach is used. Instead of explicitly determining $\tau'(\lambda)$ and $\sigma'(\lambda)$, a polynomial function is included in the spectral fit, with $\tau(\lambda)$ expressed as:

$$\tau(\lambda) = \ln\left[\frac{I_0(\lambda)}{I(\lambda)}\right] = \sum_i \sigma_i(\lambda)c_i + \sigma_R(\lambda)c_{air} + \sigma_M(\lambda)c_{aer} + \sum_j a_j\lambda^j \qquad (7.1)$$

where a_j are the coefficients of the polynomial. The effective column densities and polynomial coefficients are then determined through a least squares fit. This approach is equivalent to fitting a polynomial of the same order to each of the quantities separately to determine the differential values, and then performing the fit. The advantage of fitting the polynomial simultaneously is the consistency with respect to the errors since the error related to the differential calculation is implicitly included in the results.

In this work a second-order polynomial is used. The wavelength dependence of the aerosol extinction depends on the Ångström coefficient, α, where $\sigma_M(\lambda) \propto \lambda^{-\alpha}$. For background stratospheric aerosol, $\alpha \sim 2$ (e.g. *Lenoble and Pruvost*, 1983) and the wavelength dependence can be approximated by a second-order polynomial over short intervals. Thus, the aerosol component can be neglected from the fits. The Rayleigh extinction has wavelength dependence $\sigma_R(\lambda) \propto \lambda^{-4}$ and is not adequately

removed with a second-order polynomial, and thus must be included in the fits.

7.1.2.2 Including Measurement Noise

In the application of DOAS to the OS limb-scatter measurements, made at a sequence of tangent heights, h_t, the error (noise) in the measured optical depths must be considered. Recalling that $\tau(\lambda, h_t) = \ln[I_0(\lambda)/I(\lambda, h_t)]$ (now including the TH notation), the standard deviation of this error, $\varepsilon_\tau(\lambda, h_t)$, can be estimated as:

$$\varepsilon_\tau(\lambda, h_t) = \sqrt{\left[\frac{\varepsilon_{I_0}(\lambda)}{I_0(\lambda)}\right]^2 + \left[\frac{\varepsilon_I(\lambda, h_t)}{I(\lambda, h_t)}\right]^2} \tag{7.2}$$

where $\varepsilon_{I_0}(\lambda)$ is the standard deviation of the error in $I_0(\lambda)$ and $\varepsilon_I(\lambda, h_t)$ is the standard deviation of the error in $I(\lambda, h_t)$, both determined as described in Section 6.2.2.2. Note that if differential optical depth is considered (as opposed to including a polynomial directly in the fit) an additional error contribution due to the technique used to determine the differential optical depth is required.

It is useful to express Equation (7.1), including noise, as a matrix equation for each tangent height:

$$\boldsymbol{\tau} = \mathbf{B}\mathbf{c} + \boldsymbol{\epsilon}_\tau \tag{7.3}$$

where $\boldsymbol{\tau}$ is the optical depth vector, $\mathbf{B}$ is the basis function matrix, $\mathbf{c}$ is a vector containing the ECDs (and polynomial coefficients) and $\boldsymbol{\epsilon}_\tau$ is a vector of the errors in $\boldsymbol{\tau}$, with covariance $\mathbf{S}_\tau$. The basis functions include the absorption cross sections of all significant absorbers, the Rayleigh cross section and the polynomial components. The ECDs (and the polynomial coefficients) are determined through a least-squares fit of

Equation (7.3) with respect to $\mathbf{c}$. The LSQ solution with a known error covariance matrix of the optical depth, $\mathbf{S}_\tau$, is given by:

$$\mathbf{c}_{lsq} = \left[\mathbf{B}^T\mathbf{S}_\tau^{-1}\mathbf{B}\right]^{-1}\mathbf{B}^T\mathbf{S}_\tau^{-1}\boldsymbol{\tau} \tag{7.4}$$

$$\mathbf{S}_{lsq} = \left[\mathbf{B}^T\mathbf{S}_\tau^{-1}\mathbf{B}\right]^{-1} \tag{7.5}$$

$$\mathbf{r}_{lsq} = \boldsymbol{\tau} - \mathbf{B}\mathbf{c}_{lsq} \tag{7.6}$$

where $\mathbf{c}_{lsq}$ is the least-squares estimation of $\mathbf{c}$, $\mathbf{S}_{lsq}$ is the covariance matrix of the errors in $\mathbf{c}_{lsq}$, and $\mathbf{r}_{lsq}$ is the fitting residual vector. A separate fit is carried out for each tangent height. The *lsq* notation is omitted in further discussions for clarity. Note that $\mathbf{S}_\tau$ is a diagonal matrix due to an assumed independence of the errors in $\boldsymbol{\tau}$, with values calculated using Equation (7.2).

The quality of the fits is evaluated using a χ^2 test:

$$\chi^2_{doas}(h_t) = \sum_{j=1}^{\eta}\left[\frac{r(\lambda_j, h_t)}{\varepsilon_\tau(\lambda_j, h_t)}\right]^2 \simeq d \tag{7.7}$$

where r is the residual, d is the number of degrees of freedom (the number of pixels in the spectral window minus the number of parameters in the fit), and η is the number of pixels in the fitting window. Tangent heights with $\chi^2_{doas}/d > 4$ are excluded from further analysis.

7.1.2.3 Choice of I_0

If a measurement of the radiance of the unattenuated reference spectrum, $I_0(\lambda)$, is not available, as is the case for the OS, either a limb-scatter measurement from another tangent height or a modeled or measured exoatmospheric spectrum can be used.

Using another OS limb-scatter spectrum from the same scan is preferable because it removes the need for absolute calibration. In addition, it is measured under similar conditions (e.g. SZA and surface reflectivity), minimizing the impact of issues such as the Ring-effect (see Section 7.1.2.6.5) and surface albedo sensitivity. However, a measurement at a reference tangent height, h_t^{ref}, will contain some absorption from minor species as well as some Rayleigh (and possibly Mie) extinction. Replacing $I_0(\lambda)$ with $I(\lambda, h_t^{ref})$ leads to a modified expression for the optical depth:

$$\begin{aligned}\tau(\lambda, h_t) &= \ln\left[\frac{I(\lambda, h_t^{ref})}{I(\lambda, h_t)}\right] \\ &= \sum_i \sigma_i(\lambda)\left[c_i(h_t) - c_i(h_t^{ref})\right] + \sigma_R(\lambda)\left[c_{air}(h_t) - c_{air}(h_t^{ref})\right] + \\ &\quad \sum_j a_j(h_t)\lambda^j \end{aligned} \tag{7.8}$$

where $\tau(\lambda, h_t)$ is now the optical depth between h_t^{ref} and h_t. In this formulation Equations (7.4) to (7.6) still hold, where the ECD elements of $\mathbf{c}$ are now interpreted as the effective column densities relative to the reference tangent height. It is generally desirable to choose a limb-scatter spectrum from a high tangent height (containing minimal absorption) as the reference in order to maximize the differential structure, hence maximizing the signal-to-noise ratio.

In this work the measurement closest to 46 km is chosen as the reference for the O_3 retrievals, while the average of measurements between 46 km and 65 km is used as the reference for the NO_2 retrievals to reduce noise. No averaging is carried out for the O_3 reference due to potential contamination from external stray light (baffle scattering) at high tangent heights, as discussed in Section 6.2.1. For the same reason the reference for O_3 was lowered from 50 km used in **Paper IV**.

7.1.2.4 Fitting Window Selection

Although it is possible to retrieve multiple species simultaneously from the same fitting window using DOAS, it is often unsuitable to do so. To decrease uncertainties it is usually advantageous to use a separate window for each target species. The fitting window must be selected carefully, with the target species being (preferably) the dominant absorber and having highly structured absorption features in the region, with interfering species avoided as much as possible. In addition, the differential absorption of the target species must be strong enough to achieve a high signal-to-noise ratio, but the total absorption must be weak enough to avoid large optical depths. The selected windows for O_3 and NO_2 are specified in Table 7.1 and illustrated in Figures 7.2 and 7.3.

For O_3, the spectral fitting window is 562-623 nm in the Chappuis region. This is selected to avoid the strong temperature dependence of the O_3 cross section in the Huggins and Wulf bands. Measurements in the region of the Na Fraunhofer/airglow feature (13 pixels centred around ~590 nm) are not included in the spectral fitting. For this fitting window, absorption cross sections of NO_2, the O_2 dimer (O_4) and H_2O(g), and the Rayleigh cross section are included along with O_3. The window has been modified slightly from that used in **Paper IV**, where a narrower window of 571-617 nm was used. Note that the selected O_3 window is not ideal for a DOAS analysis due to the broad nature of the spectral features and the potential interference from O_4 and polarization (see Section 7.1.2.6.6). A more suitable window that provides sufficiently large differential structure while also avoiding regions of strong O_3 cross

section temperature dependence is near 500 nm. However, as mentioned in Section 6.2.1 the OS data in this spectral region is not recorded.

The fitting window selected for NO_2 is 435-451 nm. In this window the NO_2 differential absorption cross section is large compared to that of O_3 and there are no strong Fraunhofer features. For this fitting window, absorption cross sections of O_3 and O_4, and the Rayleigh cross section are included along with NO_2.

7.1.2.5 Absorption Cross Sections

No useful measurements of O_3, NO_2, O_4 or H_2O(g) absorption cross sections were conducted with the OS, and thus the cross sections used in the DOAS analysis must be taken from the literature. These cross sections, usually highly resolved, must be convolved to the OS resolution. The procedure for this convolution is presented in **Paper IV**.

The following high resolution and temperature dependent cross sections are used in this work:

O_3: *Bogumil et al.* (2003) at temperatures 293 K, 273 K, 243 K, 223 K and 203 K with quadratic interpolation. Resolution (FWHM): 0.47 nm at 600 nm and 0.52 nm at 440 nm.

NO_2: *Vandaele et al.* (1998) at temperatures 294 K and 220 K with linear interpolation. Resolution (FWHM): 2 cm^{-1} (0.072 nm at 600 nm and 0.039 nm at 440 nm).

O_4: C. Hermans, Belgian Institute for Space Aeronomy (unpublished data, `http:`

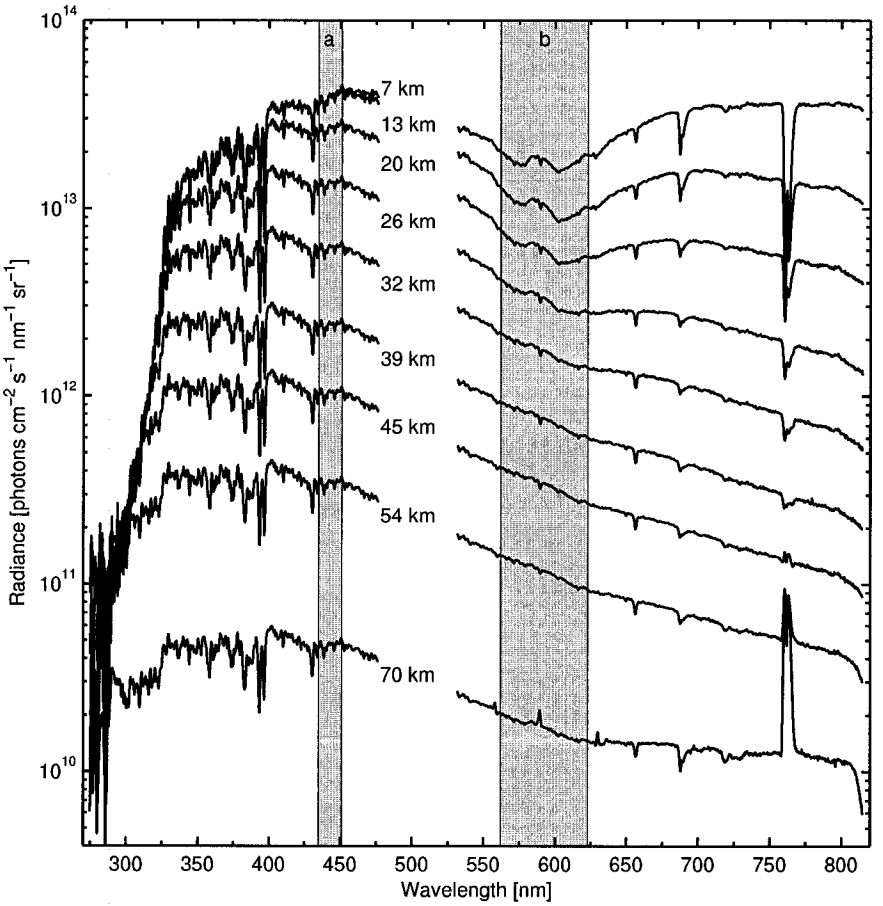

Figure 7.2: A sample of limb-scatter radiances at different tangent heights as measured by the OS for a typical limb scan (scan 6045012). Shaded area (a) is the NO_2 fitting window and (b) is the O_3 window.

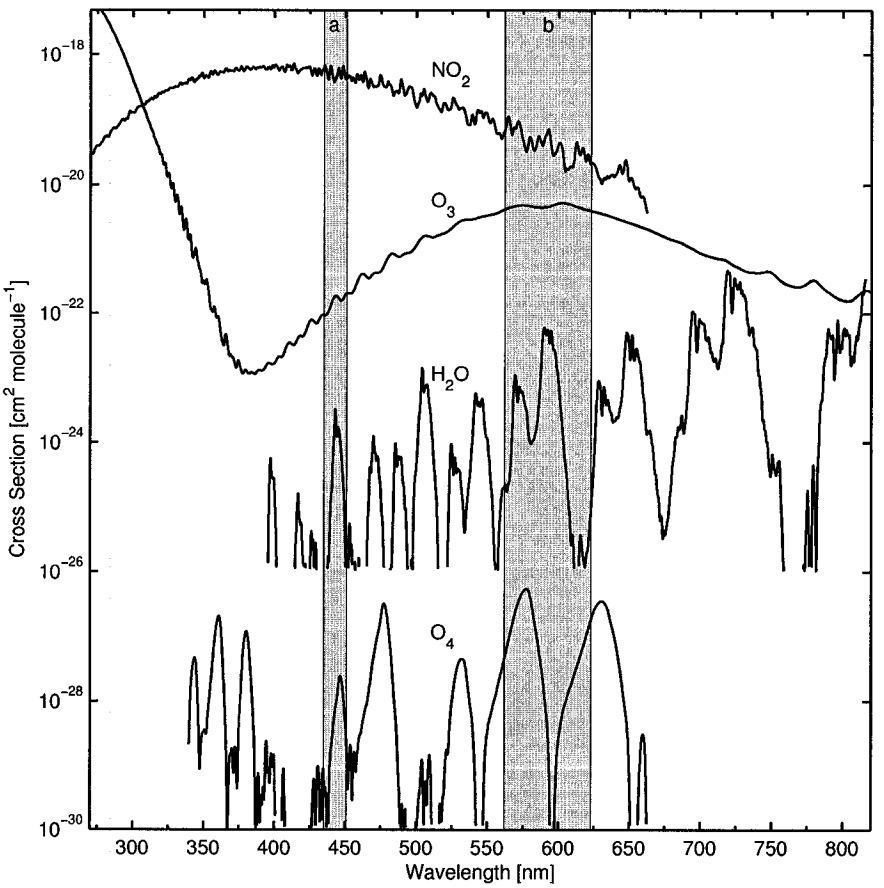

Figure 7.3: Cross sections of O_3 (*Bogumil et al.*, 2003), NO_2 (*Vandaele et al.*, 1998), O_4 (C. Hermans, unpublished data) and H_2O (*Rothman et al.*, 2005) convolved to the OS resolution. The H_2O cross sections have been multiplied by 100 for clarity. Shaded area (a) is the NO_2 fitting window and (b) is the O_3 window.

//www.aeronomie.be/spectrolab/o2.htm) at temperature 296 K. Resolution (FWHM): 2 cm^{-1} (0.072 nm at 600 nm and 0.039 nm at 440 nm).

H_2O(g): HITRAN 2004 (*Rothman et al.*, 2005) line-by-line calculation at pressure 500 hPa, temperature 246 K and partial water vapor pressure 0.03 hPa.

The O_4 and H_2O cross sections have been updated compared to those used in **Paper IV**. The new O_4 cross sections cover a wider wavelength range and are at a higher spectral resolution. The new H_2O cross sections take advantage of updates to the HITRAN database.

The above cross sections convolved to the OS resolution are shown in Figure 7.3. The Rayleigh cross section is taken from *Bates* (1984).

7.1.2.6 Corrections

In order to correctly apply the DOAS analysis to determine ECDs of atmospheric species like O_3 and NO_2 for the OS spectra, some corrections are required (e.g. *Platt et al.*, 1997). The effects of instrument resolution and sampling, polarization response, wavelength shifts, cross section temperature dependence and Ring contributions are briefly described in the following sections. Table 7.1 summarizes the corrections applied in each fitting window.

7.1.2.6.1 The I_0-Effect

The limited spectral resolution of the OS (approximately 1 nm FWHM) can lead to the interference of highly structured Fraunhofer features in the limb-scatter spectra

with the absorption cross sections. Dividing measured spectra with I_0, as in the DOAS analysis, can therefore lead to interfering spectral structure. This effect is usually referred to as the I_0-effect because it results from structure in the I_0 spectrum (*Aliwell et al.*, 2002). To deal with the I_0-effect, the convolution of absorption cross sections to the OS resolution must include structures in a highly resolved reference. This process is described in **Paper IV**.

The I_0-effect is not important in regions lacking deep Fraunhofer lines and highly structured differential cross sections. Thus, the I_0-effect is taken into account in the NO_2 window, but is not necessary in the O_3 window. Figure 7.4 shows that in the NO_2 fitting window the difference between the uncorrected and corrected NO_2 cross sections is up to 2%.

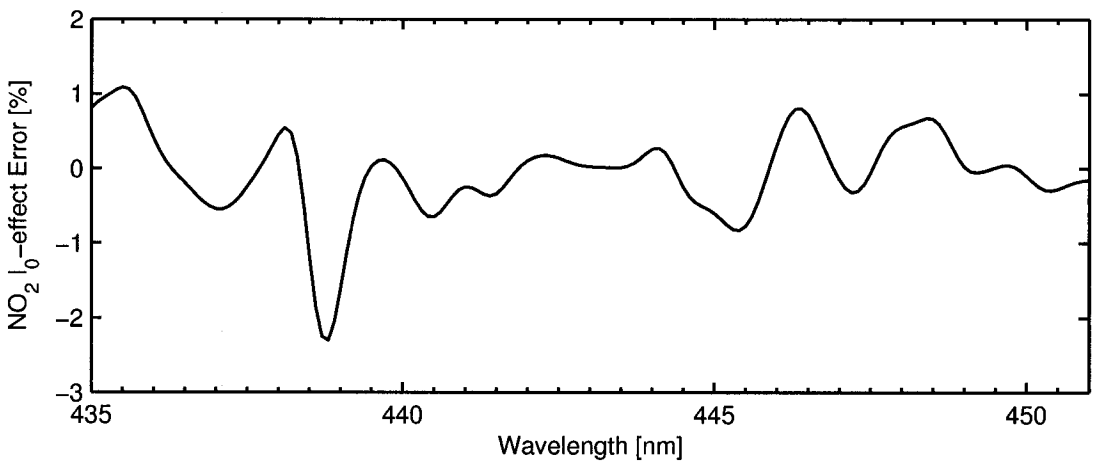

Figure 7.4: The difference in the cross sections of NO_2 (*Vandaele et al.*, 1998) in the NO_2 window when convolved to the OS spectral resolution and sampling with and without accounting for the I_0-effect.

7.1.2.6.2 The Tilt-Effect

Undersampling of Fraunhofer structures in combination with different slopes (tilts) of the reference and measurement spectra can lead to a skewed partitioning of the wings of Fraunhofer lines. The slope differences are primarily due to Rayleigh extinction. As described in **Paper II**, the effect, denoted tilt-effect, was discovered when the locations (pixels) of Fraunhofer minima in the OS spectra were found to vary with tangent height, leading to additional structures in the derived optical depths when a high tangent height measurement is used as the reference in the DOAS fit. The strongest influences from the tilt-effect are found in regions of strong Fraunhofer lines and in the blue part of the spectrum due to Rayleigh (and Mie) trending. Hence, the tilt-effect is negligible in the O_3 window but can be important in the NO_2 window.

In **Paper II** the tilt pseudo-absorber was calculated by subtracting a quadratic function from the ratio of two modeled limb radiance spectra (convolved to the OS resolution and sampling) at a high and low tangent height for a non-absorbing atmosphere. **Paper IV** proposed two modifications to the original approach. The first modification was to remove the trending in the ratio of the convolved and sampled radiances using the ratio of the modeled high resolution radiances at a high and at a low tangent height rather than using a quadratic polynomial. The second change was to employ the logarithm of the radiance ratios to be consistent with the DOAS treatment.

In **Paper IV**, limb radiances modeled at 10 km and 50 km were used to create a fixed tilt pseudo-absorber that was used at all tangent heights. *Krecl et al.* (2006)

expanded on this by simulating limb radiance spectra at a series of tangent heights to create a tangent height dependent tilt pseudo-absorber. This approach was found to produce better results (smaller residuals) compared to a fixed tilt pseudo-absorber.

In this work a set of tilt pseudo-absorbers was calculated with limb-scatter radiances from LIMBTRAN at tangent heights 10-48 km (2 km intervals) with a 50 km reference tangent height. The tilt pseudo-absorber for a specific tangent height is then linearly interpolated from this set of pre-calculated tilt pseudo-absorbers. The fixed 50 km reference tangent height simplifies the calculations and adequately represents the effective reference used for the measurements. Figure 7.5 shows the tilt pseudo-absorber at a tangent height of 10 km in the NO_2 window.

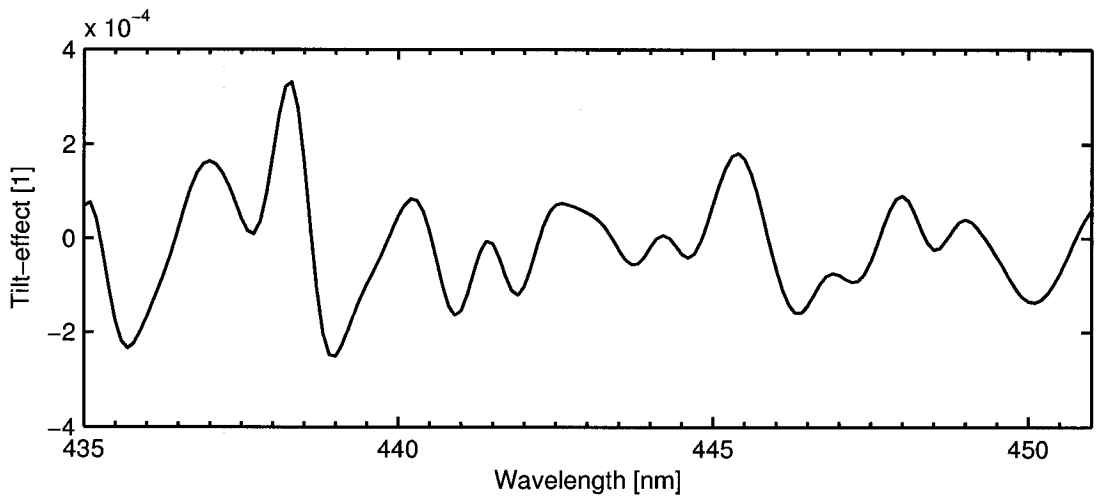

Figure 7.5: The tilt pseudo-absorber calculated for the NO_2 window for a tangent height of 10 km.

7.1.2.6.3 Wavelength Shifts

Wavelength calibration discrepancies between the measured spectra and the cross sections can affect the spectral fitting. A shift in wavelength of the measured spectra relative to the cross sections is accounted for through non-linear iterations of Equation (7.3) with respect to a wavelength shift, similar to the approach of *Stutz and Platt* (1996) and as described in **Paper IV**.

Ozone retrievals are insensitive to wavelength shift errors due to the relatively broad cross section features in the chosen window and no wavelength shift approach is required. However, due to the fine structure in the NO_2 cross section, the NO_2 retrievals are somewhat sensitive to wavelength shifts. It is not expected that the OS pixel wavelengths vary during the duration of a scan due to the short time period and the temperature stability of the OS. As such, the non-linear approach is only used to derive the wavelength shift at the lowest tangent height in each scan and the derived shift is then applied to all measurements in the scan.

An analysis of the wavelength shifts derived from NO_2 spectral fits for the entire OSIRIS data set has found a shift in the wavelengths (in the NO_2 fitting window) of about 0.1 nm (approximately one quarter of a pixel) towards shorter wavelengths at the beginning of the data set, decreasing approximately linearly to a zero shift in the current data. The source of this behaviour is unknown. The spectral fits have also been analyzed for a possible squeeze or stretch in the wavelength registration, but this was found to be negligible (in the NO_2 window).

7.1.2.6.4 Temperature Dependence

Any temperature dependence of the absorption cross sections can affect the DOAS fit since the derived ECDs depend on the specific cross sections used in the spectral fit. If there is a significant temperature dependence, the cross sections $\sigma_i(\lambda)$ in Equation (7.1) should be denoted $\sigma_i(\lambda, T_{h_t})$, where T_{h_t} is the temperature appropriate to measurements at tangent height h_t. However, since limb radiances contain information from many heights (temperatures), T_{h_t} is not well defined.

Fortunately, the temperature dependence of the O_3 cross section in the chosen windows is small, and the temperature dependence can be ignored in the DOAS fits, with the absorption cross section for one temperature, 223 K from *Bogumil et al.* (2003), used in all cases. The NO_2 cross section exhibits some temperature dependence in the selected window (see Figure 7.6) and this can lead to errors in the derived ECDs. However, as is discussed in Section 7.1.3.2, a forward model is utilized in the inversion of the ECDs. If the technique used to determine T_{h_t} for the measurements is also applied in the forward model, errors resulting from the choice of T_{h_t} are minimized. In other words, any systematic error in the ECDs derived from the measurements resulting from an incorrect T_{h_t} will be compensated for when ECDS are derived from the model radiances, providing that the radiative transfer model within the forward model properly accounts for the temperature dependence through the use of both the correct atmospheric temperature profile and the correct (temperature dependent) cross sections. As a result, it is also appropriate to select a cross section at one temperature for all cases in the NO_2 fits, and the 220 K cross

section from *Vandaele et al.* (1998) is used.

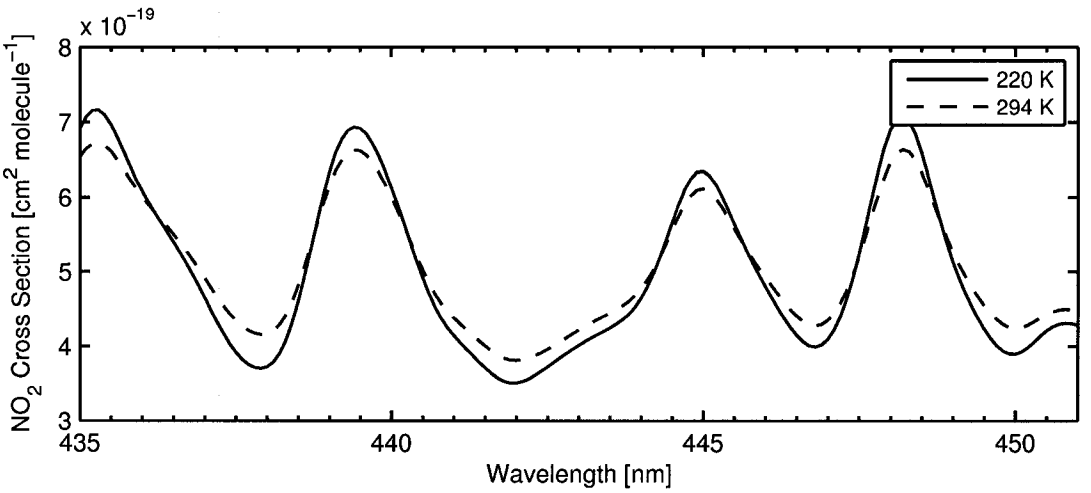

Figure 7.6: Cross sections of NO_2 in the NO_2 fitting window at temperatures 220 K and 294 K from *Vandaele et al.* (1998). The maximum difference between the two temperatures is about 10% in this window.

7.1.2.6.5 The Ring-Effect

The Ring-effect refers to the 'filling-in' (broadening and reduction of depth) of spectral features compared to the unattenuated spectrum (*Grainger and Ring*, 1962). The impact of the Ring-effect on the OS limb-scatter spectra varies with tangent height, and as a result Fraunhofer structures in the radiances do not cancel out entirely in a ratio of two limb-scatter spectra from different tangent heights, creating some residual structure that may interfere with the fit (*Sioris and Evans*, 1999). In addition, the filling-in of O_3 and NO_2 features can affect the derived ECDs.

The Ring-effect is negligible in the O_3 window due to the broad absorption features and lack of strong Fraunhofer structures. However, the impact is potentially important in the NO_2 window, where the difference between the limb radiances with and without accounting for the Ring-effect can be up to 0.5% at 15 km tangent height, for example (see Figure 7.7). In **Paper IV** it was found that accounting for the Ring-effect did not result in improved fits, likely due to a combination of the lack of strong Fraunhofer lines in the selected NO_2 window, imperfections in the method used to account for the Ring-effect and the use of a high tangent height spectrum from each scan as the reference.

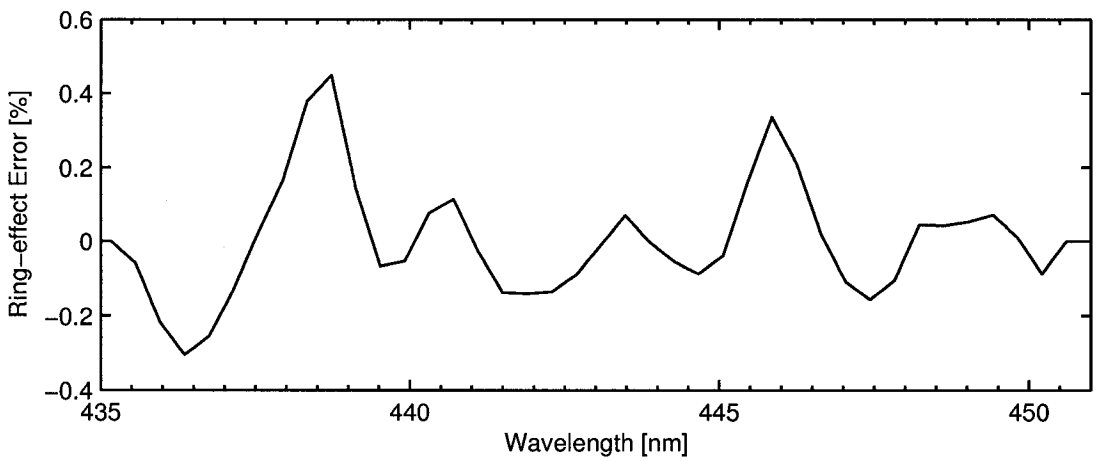

Figure 7.7: Difference between limb radiances at a tangent height of 15 km with and without correcting for the Ring-effect using the method of *Sioris et al.* (2002).

7.1.2.6.6 Polarization

The presentation of DOAS to this point has assumed unpolarized light. When linearly polarized light is considered the differential structure in the grating efficiency must be taken into account since it can lead to interference in the DOAS fits. As described in *McLinden et al.* (2002b) and **Paper IV**, a polarization pseudo-absorber can be introduced in the DOAS fit to account for the polarization features, where the pseudo-absorber is the OS g_{12} grating efficiency parameter (see Section 6.2.1) and the resulting fit coefficient is a measure of the degree of linear polarization (*McLinden et al.*, 2004).

In the NO_2 fitting window, g_{12} varies slowly with wavelength and the polarization pseudo-absorber can be neglected. However, in the O_3 window the differential structure of g_{12} is significant (see Figure 7.8) and can interfere with the spectral fitting and thus the polarization pseudo-absorber must be included.

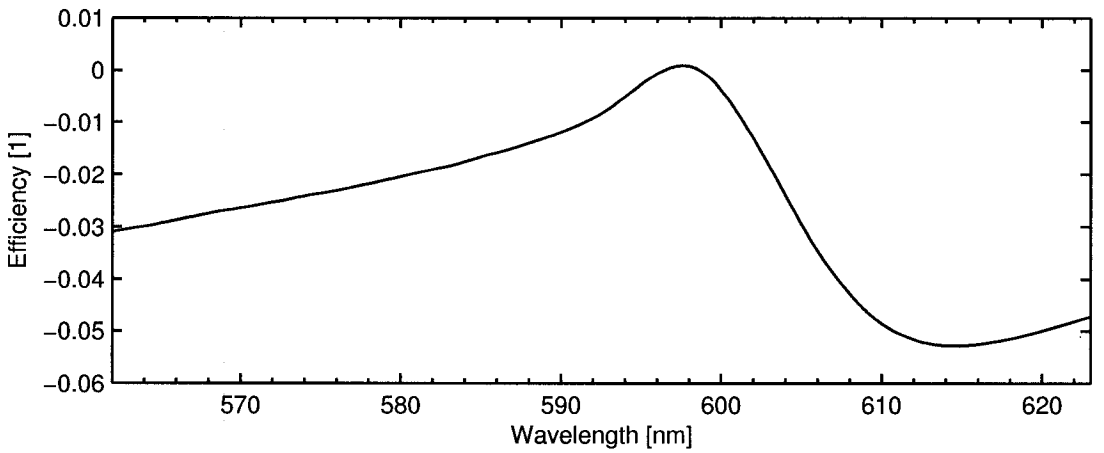

Figure 7.8: The OS grating efficiency parameter g_{12} in the O_3 window from *McLinden et al.* (2002b).

7.1.2.7 Sample Results

Sample spectral fits in the O_3 and NO_2 windows for a typical OS measurement at a 10 km tangent height are shown in Figures 7.9 and 7.10, respectively. In these figures the differential components of the fit are shown and compared to the measurements (fit component plus residual). The total measured differential optical depth is also plotted against the final fit. The differential quantities are shown to illustrate the components of the fits more clearly.

Figure 7.11 shows retrieved O_3 and NO_2 effective column densities plotted against tangent height for a typical OS scan. Also shown are the reduced χ^2 of the fits (χ^2_{doas}/d) and the root-mean-square (RMS) residuals. The RMS residuals are given by:

$$r_{rms}(h_t) = \sqrt{\frac{\sum_{j=1}^{\eta} [r(\lambda_j, h_t)]^2}{\eta}} \tag{7.9}$$

Residuals from the DOAS fits are typically less than $3\text{x}10^{-3}$ RMS for the O_3 window and less than $1\text{x}10^{-3}$ RMS for the NO_2 window. These residuals represent approximately 3% and 7% of the peak differential optical depths in the O_3 and NO_2 windows, respectively.

Figure 7.12 shows the ECDs calculated for a typical orbit. The variation in ECD is a result of both the variation in the species concentrations and the changing observing conditions (SZA/LST) over the orbit, making the ECDs difficult to interpret directly and necessitating an inversion.

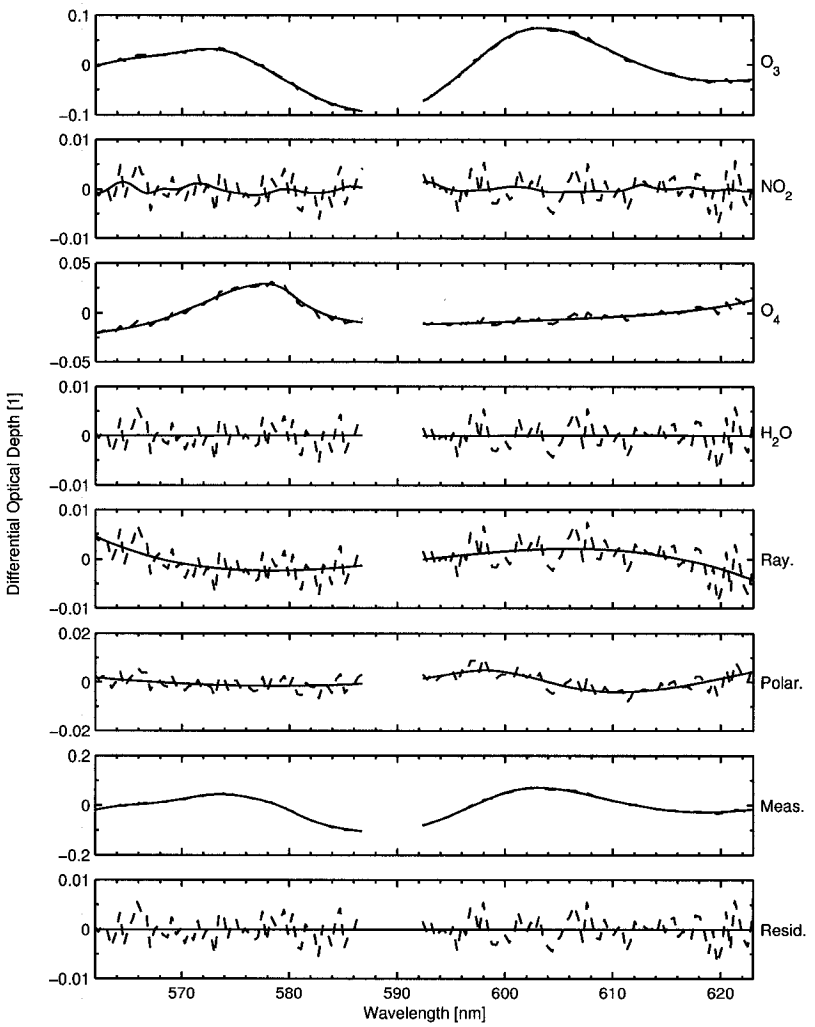

Figure 7.9: Typical example of the measured (blue lines) and fitted (red lines) differential optical depths of: O_3, NO_2, O_4, H_2O, Rayleigh and polarization in the O_3 window. The measured DODs are determined from the fit plus the residual. The total measured and fitted total DODs, and the residuals from the fit are shown in the bottom panels. The corresponding OS measurement was performed at the 10 km tangent height of scan 6045012.

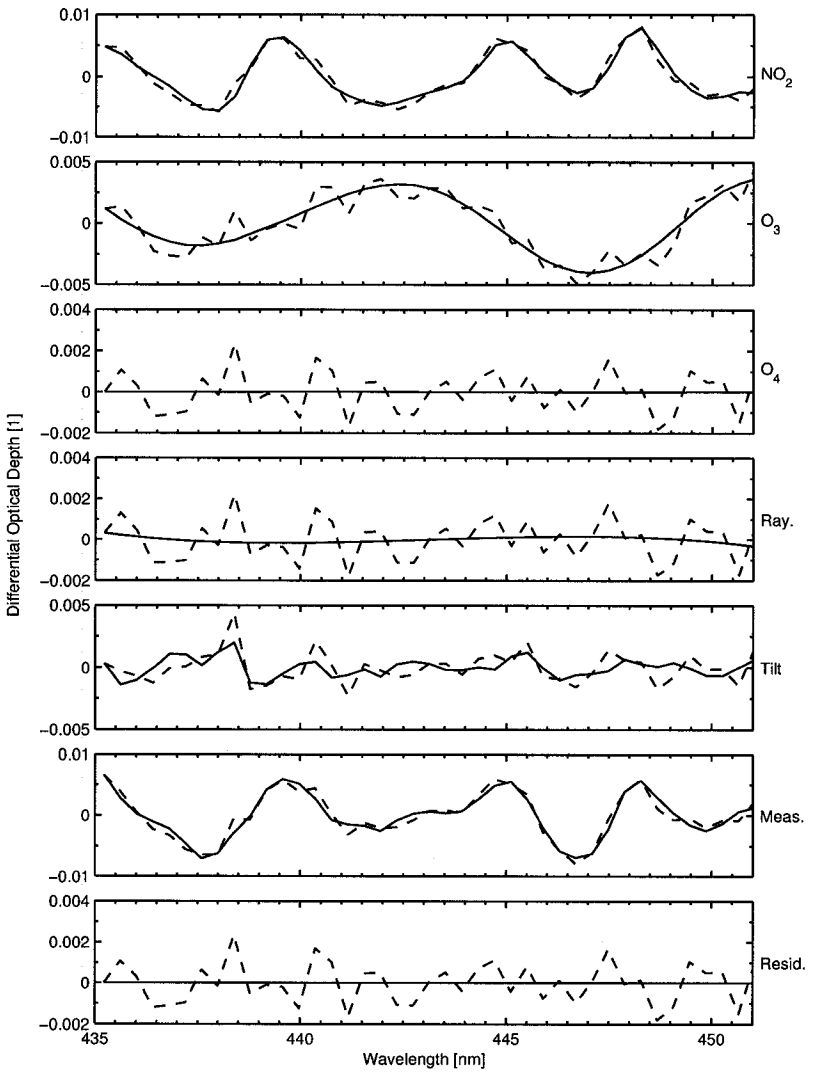

Figure 7.10: Same as Figure 7.9, but for the NO_2 fitting window.

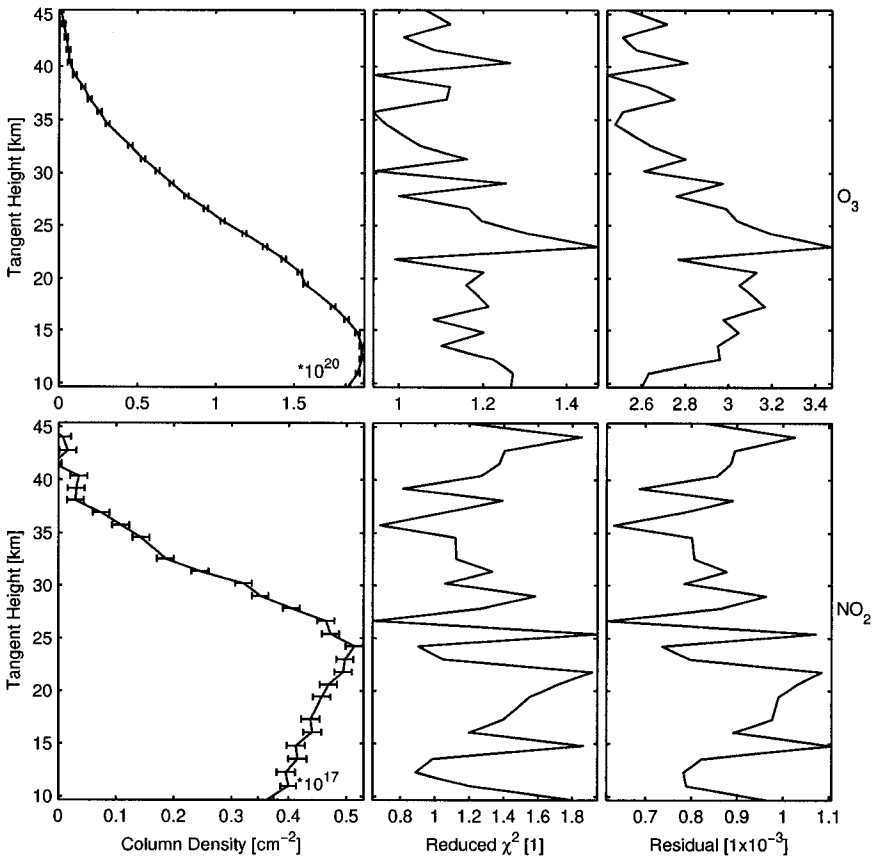

Figure 7.11: Typical DOAS fit results for O_3 (upper panels) and NO_2 (lower panels) from a typical OS scan (scan 6045012). The left panels show the derived ECDs as a function of tangent height, with the error bars giving the 1-STD uncertainties from the LSQ fit. The middle panels show the reduced χ^2 of the fits (χ^2_{doas}/d) and the right panels show the RMS residuals.

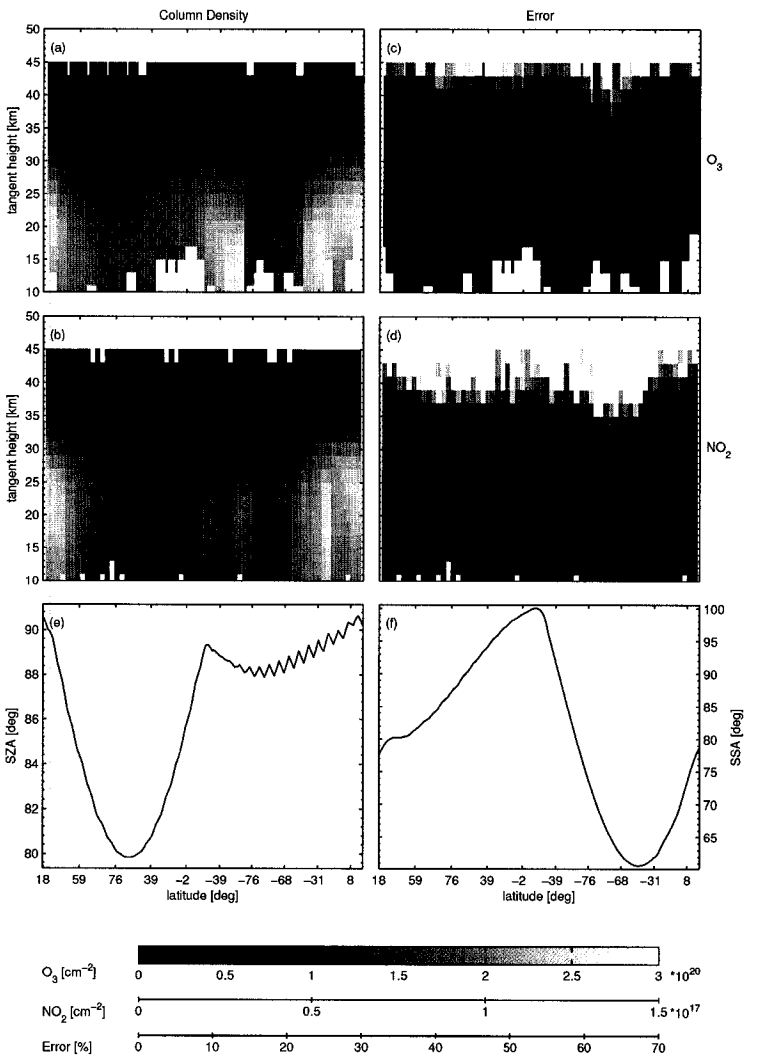

Figure 7.12: ECD profiles of O_3 (a) and NO_2 (b) for Odin orbit 14013 on 20 September 2003 as a function of latitude, with corresponding 1-STD ECD uncertainties, (c) and (d). Also plotted is the SZA and SSA for each scan versus latitude (panels e and f, respectively).

7.1.3 Inversion of OS Effective Column Densities

Effective column densities of the target species from the DOAS fit (O_3 or NO_2) need to be converted to number densities as a function of altitude. This conversion is an inverse problem, which uses a forward model, the measured quantities and some a priori information.

7.1.3.1 Inversion Algorithm

The inversion algorithm used in this work is the maximum a posteriori estimator from *Rodgers* (2000) described in Chapter 5. Cast in terms of the vector of ECDs for the target species, $\mathbf{c}$, and the number density vector of that species, $\mathbf{n}$, the LM solution from Equation (5.20) becomes:

$$\mathbf{n}_{i+1} = \mathbf{n}_i + \left[(1+\gamma)\mathbf{S}_a^{-1} + \mathbf{K}_i^T\mathbf{S}_c^{-1}\mathbf{K}_i\right]^{-1}\left\{\mathbf{K}_i^T\mathbf{S}_c^{-1}\left[\mathbf{c} - \mathbf{F}(\mathbf{n}_i, \mathbf{b})\right] - \mathbf{S}_a^{-1}(\mathbf{n}_i - \mathbf{n}_a)\right\} \tag{7.10}$$

where $\mathbf{n}_a$ is the a priori number density vector and $\mathbf{S}_c$ is the covariance matrix of the target species ECD errors. In this study the iteration is started at $\mathbf{n}_0 = \mathbf{n}_a$ and the retrieval (altitude) grid is chosen to be a 2 km grid from 10 km to 46 km for both O_3 and NO_2.. As described by *Krecl et al.* (2006), a GN approach (Equation (7.10) with $\gamma = 0$) is first attempted since the GN method generally converges more quickly. Cases where the GN iterations fail to converge or converge to a solution with an unacceptable χ^2 are subjected to the LM approach. Convergence is evaluated as discussed in Section 5.2.3.3, with a criterion of $0.001 * p$. Profiles that have not converged after ten iterations or that have converged with $\chi^2_{inv}/q > 4$ are discarded.

The target species ECD errors are assumed to be uncorrelated in tangent height, making $\mathbf{S}_c$ a diagonal matrix with elements taken from the diagonal component of $\mathbf{S}_{lsq}$ from Equation (7.5) for the target species at each tangent height. However, some correlation is expected due to the use of a fixed reference spectrum in the calculation of the optical depths. A more thorough approach would fit all tangent heights simultaneously in order to determine the correlations, but this has not been considered in this work. Also, not all of the noise in the measurements is truly random, with, for example, dark current correction errors expected to be largely consistent over all tangent heights in a particular scan. In other words, some portion of the residual spectral structure will be similar for all tangent heights.

As discussed in **Papers IV and VI**, a positive constraint is applied to the retrievals by inverting the natural logarithm of $\mathbf{n}$ instead of $\mathbf{n}$ directly, under the assumption that $\mathbf{n}$ follows a log-normal distribution. The relation between the log-normal and normal distributions is given by:

$$n_{log}(z) = \ln\left[\frac{n_{lin}(z)^2}{\sqrt{n_{lin}(z)^2 + \varepsilon_{lin}(z)^2}}\right] \tag{7.11}$$

$$\varepsilon_{log}(z) = \sqrt{\ln\left[1 + \frac{\varepsilon_{lin}(z)^2}{n_{lin}(z)^2}\right]} \tag{7.12}$$

where ε_{lin} and ε_{log} are the normal and log-normal standard deviations, respectively. Note that the positive constraint necessitates a non-linear retrieval.

7.1.3.2 Forward Model

A radiative transfer model is used to simulate limb-scattered sunlight radiances from given vertical number density profiles and parameters describing the atmospheric

state and measurement conditions. Simulated optical depths are then determined and subjected to a DOAS analysis. The resulting effective column densities constitute the forward model. As described in Chapter 5 and Section 7.1.3.1, the forward model is used to invert ECD as a function of tangent height to number density as a function of altitude. In this work, the pseudo-spherical multiple scattering radiative transfer model LIMBTRAN is used. For further description of LIMBTRAN see *Griffioen and Oikarinen* (2000).

The temperature and pressure information used in LIMBTRAN is from the European Centre for Medium-range Weather Forecasts (ECMWF) analysis fields. O_3 and NO_2 mean state distributions (climatologies) are included and are discussed in Section 7.1.3.3. Aerosol information is also included and consists of the stratospheric aerosol extinction for 1999 as a function of latitude, month and wavelength from *Bauman et al.* (2003a,b) and a Henyey-Greenstein phase function (asymmetry parameter 0.7). The surface albedo as a function of latitude, longitude, month and wavelength is taken from the clear-sky database of *Koelemeijer et al.* (2003). The O_3 and NO_2 temperature-dependent absorption cross sections and the Rayleigh cross section used in LIMBTRAN are the same as those used for the DOAS spectral fits (see Section 7.1.2.5). Note that O_4 and H_2O are not included in the forward model.

As is discussed in detail in **Paper IV**, LIMBTRAN assumes horizontal homogeneity within its vertical layers, uses cross sections convolved to the OS resolution, and accounts for the variation of SZA and SSA with tangent height and along the viewing LOS. The forward model does not account for the vertical FOV of the OS (the calculations are carried out assuming a pencil-beam LOS).

7.1.3.3 A Priori Information

The a priori number density profiles for O_3 as a function of latitude, longitude and month are taken from the climatology of *Li and Shine* (1995), which was constructed from satellite and ozonesonde data sets. The O_3 climatology is assumed to follow a log-normal distribution, with standard deviations for the diagonal components of the covariance matrix of the a priori state, $\mathbf{S}_a$, set to 40%. The off-diagonal components are defined assuming an exponential correlation, where the value of element $S_a(i,j)$ is:

$$S_a(i,j) = \varepsilon_a(i)\varepsilon_a(j)\exp\left[-2\frac{|z(i)-z(j)|}{l_c(i)+l_c(j)}\right] \tag{7.13}$$

where ε_a is the standard deviation of the a priori and l_c is the correlation length. A correlation length of 4 km is assumed at all altitudes.

The NO_2 a priori number density profiles as a function of latitude, time of year (bi-weekly) and local time (SZA) are taken from a climatology constructed using the University of California, Irvine photochemical box model (*McLinden et al.*, 2000; *Prather*, 1992). A log-normal distribution and 4 km correlation length are also used to characterize the NO_2 a priori, but since the NO_2 climatology is assumed to be less accurate, ε_a is set to 60% (reduced from 80% in **Paper IV**).

7.1.3.4 Calculating F and K

As discussed in Chapter 5, the calculation of weighting functions requires knowledge of the derivatives of the forward model. In this work $\mathbf{K}$ is calculated using finite differences with sequential perturbation of the elements of $\mathbf{n}$. Perturbation in this

case refers to changing an element in $\mathbf{n}$ by some amount (5% in this work). The forward model is run with and without this perturbed $\mathbf{n}$. An element of the weighting function matrix can then be approximated as:

$$K(i,j) \approx \frac{F[\mathbf{n}^\star, h_t(i)] - F[\mathbf{n}, h_t(i)]}{n^\star[z(j)] - n[z(j)]} \tag{7.14}$$

where $F[\mathbf{n}, h_t(i)]$ is the forward model calculation for tangent height $h_t(i)$ and $n[z(j)]$ is the number density at altitude $z(j)$. $\mathbf{n}^\star$ denotes $\mathbf{n}$ perturbed in the region of $z(j)$.

Calculating $\mathbf{K}$ using sequential perturbations can be very time-consuming, and the various approximations used to reduce the computational requirements are discussed in detail in **Paper IV**. Since a non-linear inversion approach is used, $\mathbf{F}$ must be calculated at every iteration and some approximations are used in this calculation as well (see **Paper IV** for details).

7.1.3.5 Sample Results

Figure 7.13 shows retrieved O_3 and NO_2 number density profiles and the associated retrieval errors for a typical OS scan. As described in Section 5.3, each retrieved profile is characterized by the measurement response and the vertical resolution, and this information is also shown in Figure 7.13. Retrievals with high response (>0.75) and good vertical resolution (<5 km) are generally obtained between 12 km and 44 km for both O_3 and NO_2, though these ranges vary somewhat with latitude and season and, for NO_2, local time. However, the response and vertical resolution of the retrievals must be considered together since a high response at the extremes of the retrieval range can be associated with a degraded resolution, as can be seen in Figure

7.13.

Weighting functions calculated for the sample scan are shown in Figure 7.14. The non-uniformity in the weighting functions is due to the irregular measurement (tangent height) grid compared to the regular retrieval (altitude) grid. For comparison, weighting functions calculated for a regular measurement grid that matches the retrieval grid (i.e. where the tangent heights are located at the centres of the perturbed altitude layers) are shown in Figure 7.15. Note that the the NO_2 weighting function peaks above about 30 km are smaller than expected. The source of this underestimation is unknown and is under investigation, however, the impact on the retrieved NO_2 profiles is small.

Number density profiles retrieved from the ECDs in Figure 7.12 are shown in Figure 7.16. The retrieval error fields, given by panels (b) and (c) in Figure 7.16, are anti-correlated with the concentration of the retrieved species and increase at low and high altitudes, particularly for NO_2, primarily due to the smoothing error. The structure in the error fields is due to the irregular OS measurement grid. Note that Odin was pointing off of the orbital plane into the sunlit region for the second half of this particular orbit, explaining the unexpected measurement pattern (Figure 7.16, panel g) and SZAs (Figure 7.16, panel e). This off-plane mode is occasionally utilized to provide better global coverage.

Results from one entire day of measurements, spanning 1-2 October 2003, are shown in Figure 7.17 with maps of retrieved O_3 and NO_2 number densities at 16, 20 and 26 km. The NO_2 retrievals are divided based on local time in order to account for the strong NO_2 diurnal variation.

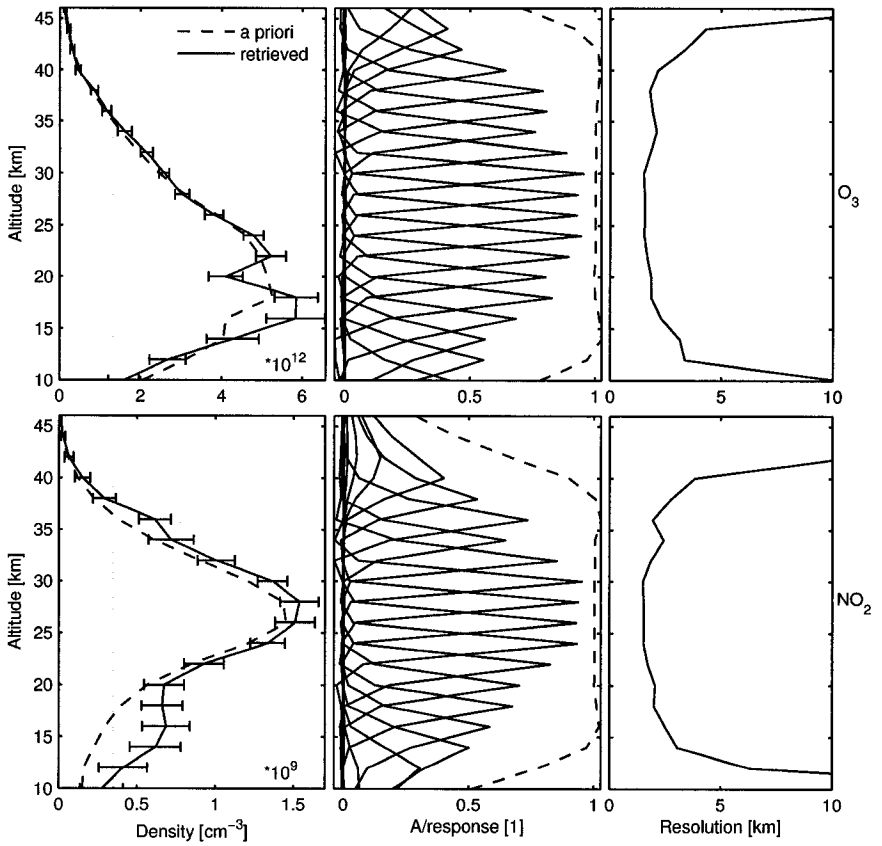

Figure 7.13: Retrieval characteristics of the O_3 (upper panels) and NO_2 (lower panels) retrievals for a typical OS scan (scan 6045012). The left panels show the retrieved and a priori profiles, with the error bars giving the 1-STD retrieval error. The middle panels show the averaging kernels (solid lines) and the measurement response (dashed line) and the right panels show the vertical resolution.

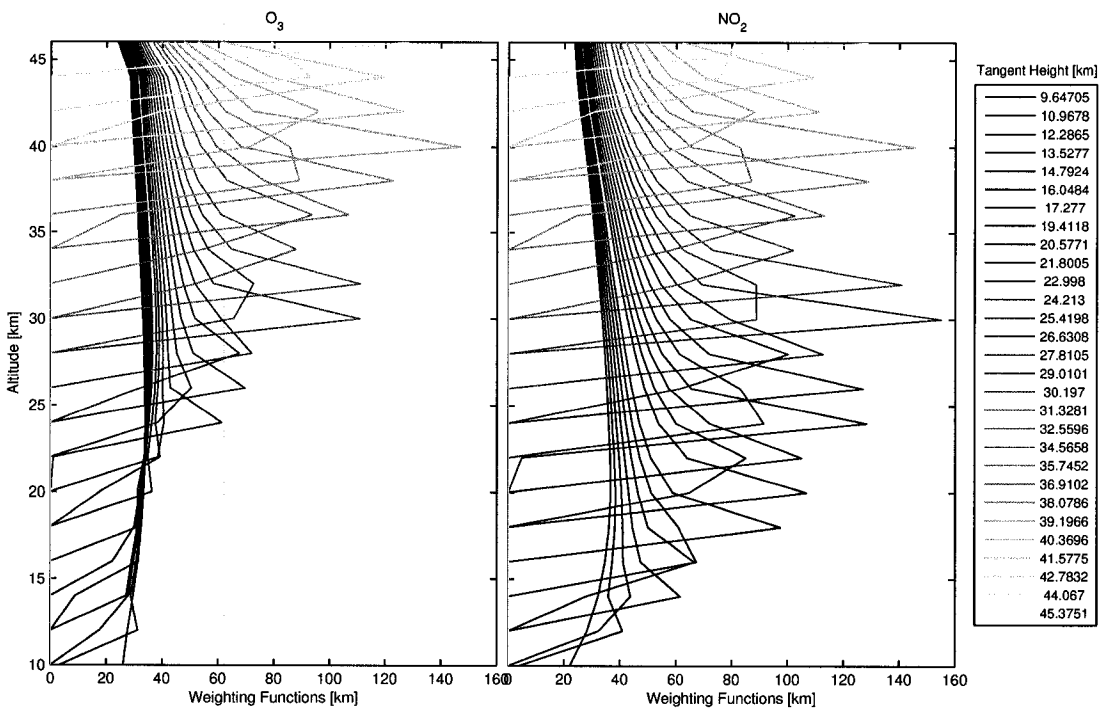

Figure 7.14: Weighting functions for O_3 (left panel) and NO_2 (right panel) calculated for a typical OS scan (scan 6045012). Each line represents the altitude-dependent weighting function for one of the tangent heights.

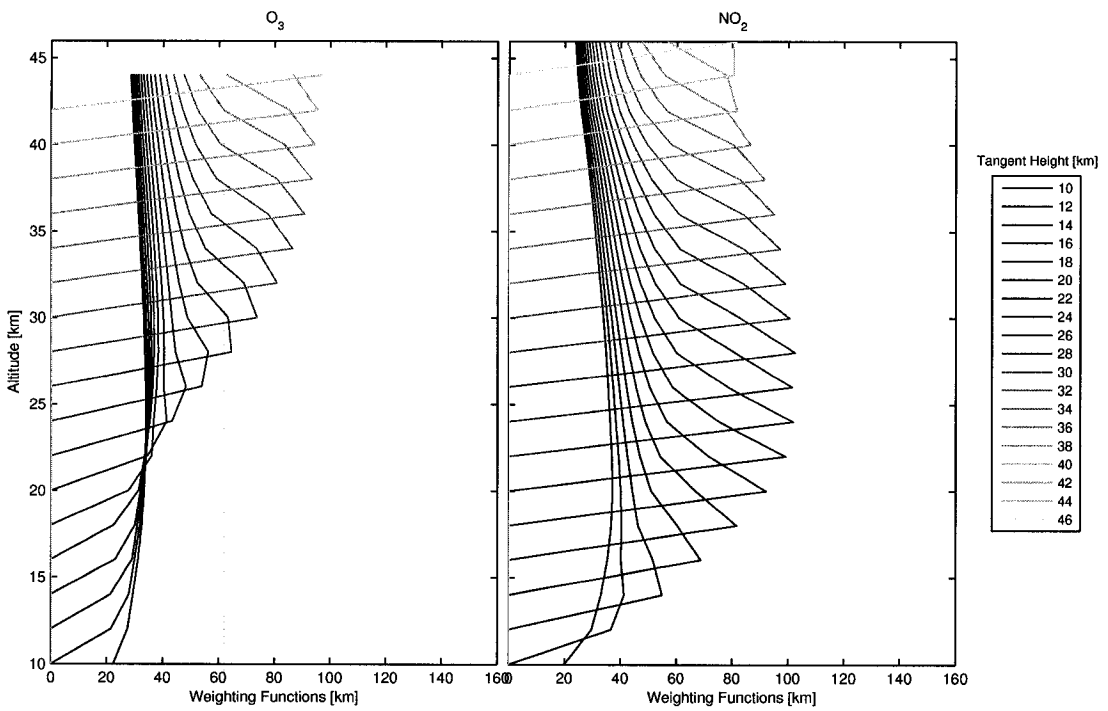

Figure 7.15: Same as Figure 7.14, but assuming a regular measurement (tangent height) grid that matches the retrieval (altitude) grid.

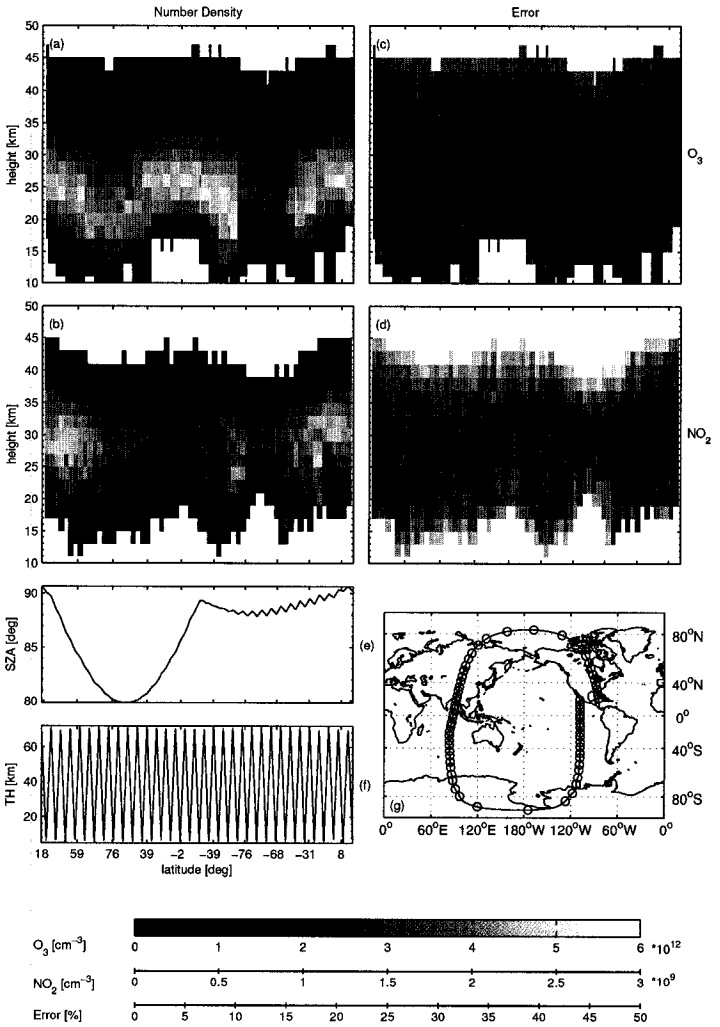

Figure 7.16: Retrieved profiles of O_3 (a) and NO_2 (b) for Odin orbit 14013 on 20 September 2003 as a function of latitude, with corresponding 1-STD retrieval errors, (c) and (d). Note that values with a measurement response less than 0.75 and non-converging or poorly-converged profiles are excluded. Also plotted is the SZA for each scan versus latitude (e), the tangent heights of the Odin/OSIRIS limb scanning (f) and the global map of the retrieved profile locations (g).

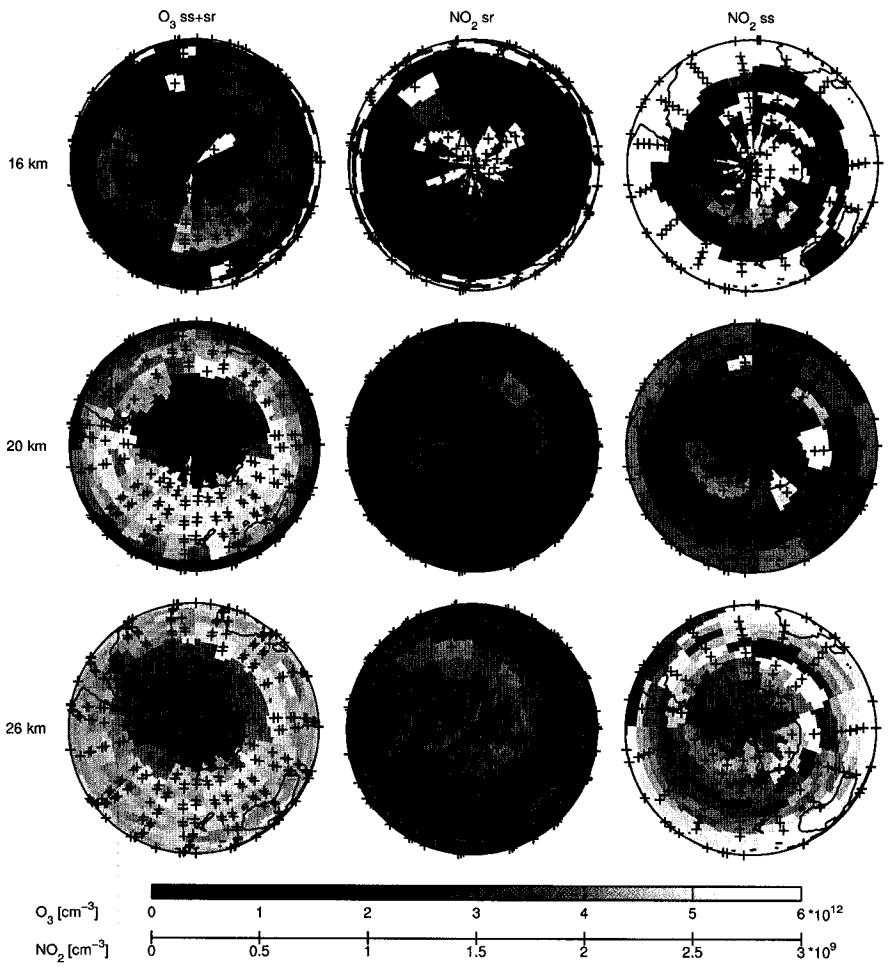

Figure 7.17: Retrieved O_3 and NO_2 number densities for the Southern Hemisphere on 1-2 October 2003 at 16, 20 and 26 km. Data has been binned to a 4° longitude by 2° latitude grid and interpolated to the nearest neighbour. The crosses denote the retrieved profile locations. Note that values with a measurement response less than 0.75 and non-converging or poorly-converged profiles are excluded. NO_2 has been separated into sunset (ascending) nodes (ss) and sunrise (descending) nodes (sr) due to the strong variations between daytime and nighttime chemistry.

7.2 Sensitivity Analyses

As discussed in Section 5.4, the total error of the solution can be separated into four separate components. The smoothing and measurement errors are statistically-based and straightforward to calculate. However, they require an understanding of the statistics of the measurements (in the case of the measurement error) and of the a priori state (in the case of the smoothing error). The latter can present a particular challenge, since the covariance of the a priori is often not known and must be estimated, with $\mathbf{S}_a$ frequently used as a tuning parameter in the retrievals rather than a true constraint. As a result, the smoothing error is often not reliable. The FM errors are evaluated by studying the various approximations taken in the forward model. The impact of most of these are addressed in **Paper IV**, with an additional contribution assessed in **Paper VII**. The FMP errors are more difficult to determine. The approach taken in this work is described in **Paper IV** and involves treating the systematic sources of error as independent error sources with assumed uncertainties. A comprehensive treatment of the FMP errors is contained in **Paper IV**, with some modifications and updates in **Papers V, VI and VII**.

7.2.1 Forward Model Error

In **Paper IV**, the FM error is estimated by considering the impact of simplifications and approximations used in the forward model, including the neglect of spectral convolution, the number of line-of-sight points used in LIMBTRAN, ignoring the effects of the OS vertical resolution and the choice of atmosphere grid in LIMBTRAN,

as well as any biases in the implementation of the retrieval method (retrieval bias). The impact of the neglect of polarization in the forward model is added to the analysis in **Paper VII**.

The individual components of the FM error are shown in Figure 7.18, along with the total FM error, given by the sum of the individual components. The total FM error is estimated at less than 2% for O_3 and less than 6% for NO_2, with the largest source of error being the atmosphere grid step size (1 km is used in both retrievals). Note that no attempt is made to estimate the error introduced by the use of a pseudo-spherical RTM.

7.2.2 Forward Model Parameter Error

The FMP error is estimated in **Paper IV** by performing perturbations (1-STD) to a number of forward model parameters, including: aerosol, neutral density, temperature, clear-sky surface albedo, spectral resolution, absorption cross sections and tangent height registration. In addition, the impact of cloud on the retrievals is estimated in a preliminary manner in **Paper VII** by perturbing the surface albedo to a value of 0.6 (reduced from 1.0 used in **Paper IV**, since this value was excessive). The sensitivity of the retrievals to interfering species was added to the analysis in **Paper VI**. The main interfering species for the O_3 retrievals is NO_2 and the main interfering species for the NO_2 retrievals is O_3.

Figure 7.19 shows the FMP errors for the O_3 and NO_2 retrievals for low-sun (SZA = 90°) and high-sun (SZA = 60°) scenarios. The error for the worst-case single

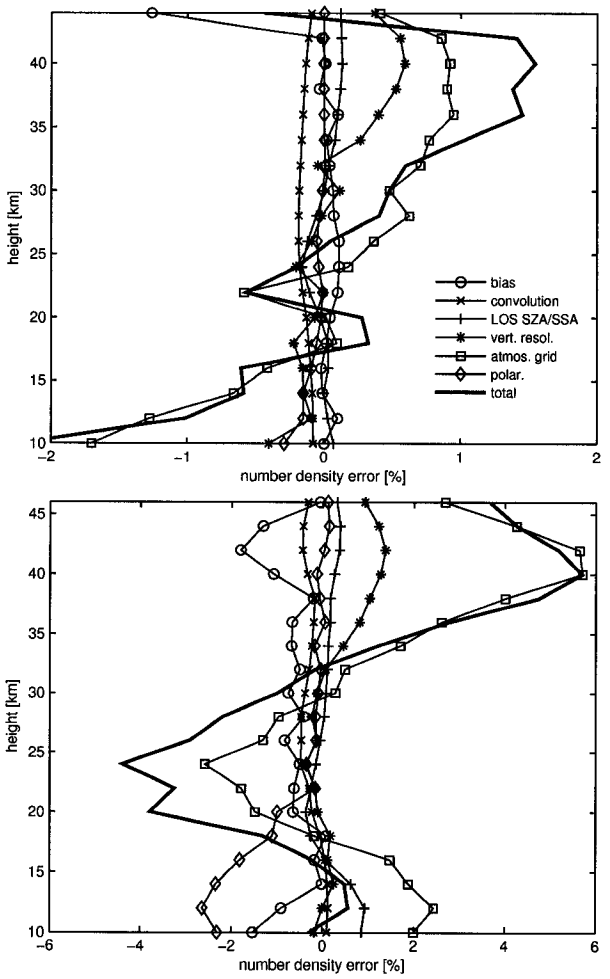

Figure 7.18: Forward model errors for O_3 (upper panel) and NO_2 (lower panel) due to retrieval bias, the use of convolved cross sections, approximations in the variation of SZA and SSA along the LOS, the neglect of taking the vertical resolution of the OS measurements into account, the use of a 1 km atmosphere grid in LIMBTRAN and the neglect of polarization. The total forward model error is given by the sum of the individual errors.

scattering angle was used in all cases. The total error, calculated as the square root of the sum of the individual variances under the assumption that the components are independent, is also shown. The total FMP error is estimated at less than 10% for O_3 and less than 15% for NO_2, with the largest source of error being the tangent height registration uncertainty (see Section 6.2.4).

7.2.3 Total Error

As discussed in Section 5.4, the total error is estimated by combining the smoothing error, measurement error, forward model error and forward model parameter error. The estimated total error is shown in Figure 7.20 for low-sun (SZA = 90°) and high-sun (SZA = 60°) scenarios. The estimated total error for the O_3 retrievals is 8% at 25 km, increasing roughly linearly to 20% at 10 km and 25% at 44 km. The NO_2 total error is estimated to be 10% at 25 km, increasing roughly linearly to 35% at 10 km and 50% at 46 km. In both cases the smoothing error is the largest error source at high and low altitudes, where the a priori begins to significantly impact the retrievals. As mentioned above, since the a priori covariance matrix is somewhat uncertain, and only technically relates to an ensemble of profiles, the inclusion of this component in the total error must be treated with caution, since it may tend to lead to an overestimation of the error for individual profiles.

An additional source of error in the NO_2 retrievals not included in the above error estimate is that due to the 'diurnal effect', which is discussed in **Papers V and VI**. This source of error is highly dependent on the observation conditions and thus

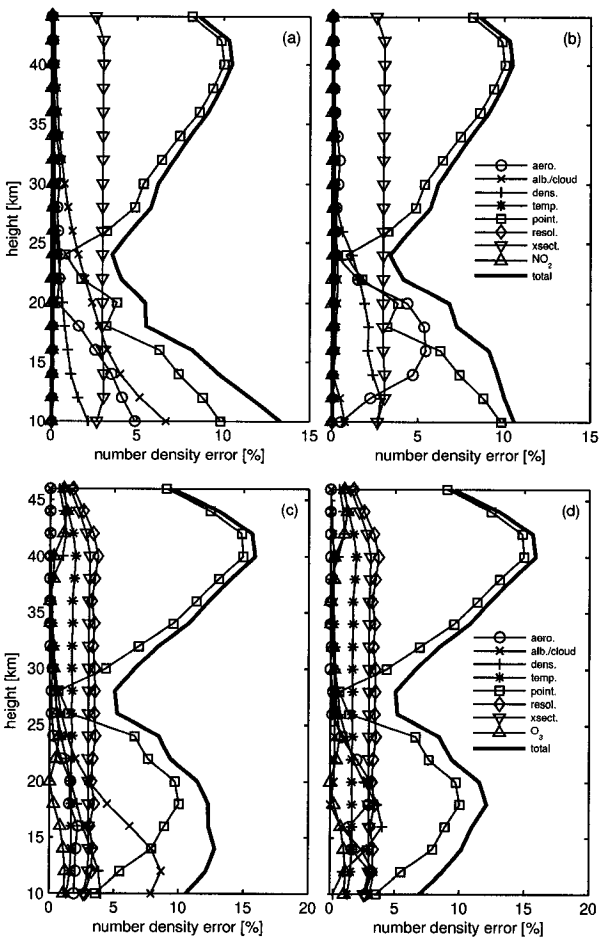

Figure 7.19: Forward model parameter errors (1-STD) for O_3 (upper panels) and NO_2 (lower panels) due to uncertainties in aerosol, albedo/cloud, neutral density, temperature, tangent height registration (pointing), spectral resolution, cross section, and interference from O_3 or NO_2. The total forward model parameter error is given by the square root of the sum of the individual variances. The calculations were carried out for high-sun (SZA=60°, panels a and c) and low-sun (SZA=90°, panels b and d) scenarios.

difficult to quantify generally. However, the error is relatively small (<10%) above 25 km and is at most 45%, with the maximum error located at the lowest altitudes, putting this error source on par with the estimated NO_2 total error. More importantly, the observation conditions where the diurnal errors are significant (>10%) below 25 km are only present for about 16% of OSIRIS data, primarily at the solstices in the tropics. The impact of other sources of horizontal inhomogeneities have not been considered in this work.

7.3 Geophysical Validation

A validation study for an older version of the OS NO_2 retrievals (version 2.4) in **Paper VI** estimated the OSIRIS random and systematic uncertainties through comparisons with a number of solar occultation instruments. This analysis was repeated in **Paper VII** on the current OS NO_2 data (version 3.0) with similar results. O_3 retrieved using the method presented in this work is not used as the operational O_3 data product. As such, no detailed validation studies have been carried out since the initial limited comparisons in **Papers III and IV**. The validation methodology described in **Paper VI** and updated in **Paper VII** is briefly described below and has been applied to O_3 produced using the retrieval method described in this work. The validation results for both species are summarized in Table 7.2 and Figure 7.21.

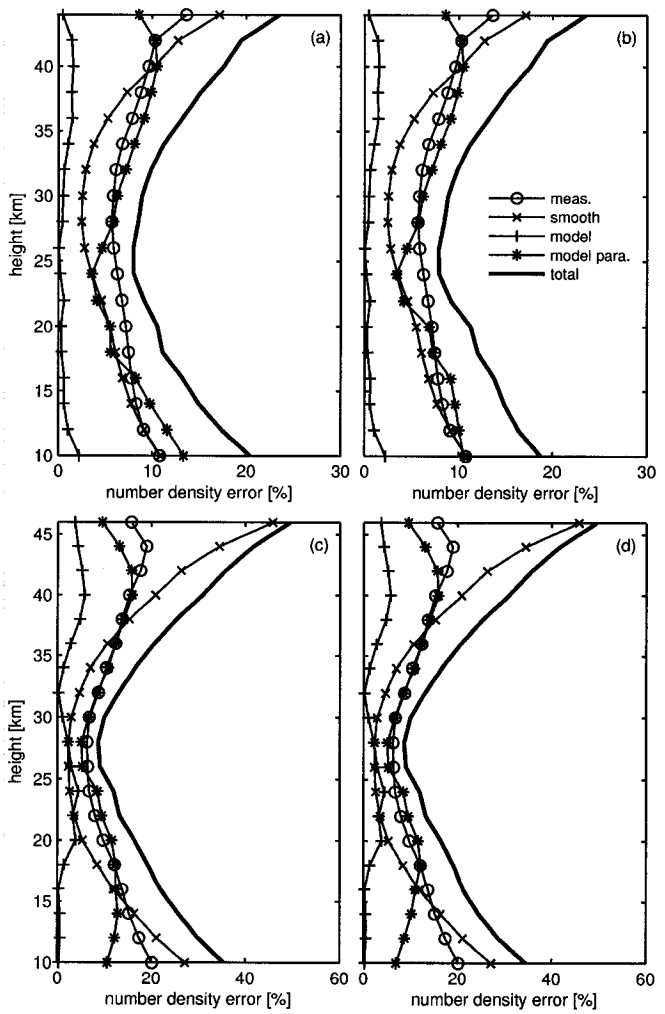

Figure 7.20: Total error estimates (1-STD) for O_3 (upper panels) and NO_2 (lower panels). The four main error sources are included; the smoothing error, the measurement error, the forward model error, and the forward model parameter error. The total error is given by the square root of the sum of the four variances. The calculations were carried out for high-sun (SZA=60°, panels a and c) and low-sun (SZA=90°, panels b and d) scenarios.

	Random		Systematic	
O_3:				
35-40 km	5%		6-12%	
25-35 km	3%		7-9%	
12-25 km†	4%		20-31%	
NO_2:	PM	AM	PM	AM
35-45 km	8%	10%	13-33%	30%
25-35 km	7%	9%	7-40%	22-29%
15-25 km‡	14%	-	20%	-

Table 7.2: Estimated systematic and random (1-STD) uncertainties of the OS O_3 and NO_2 profiles in percent, based on comparisons with SAGE II, SAGE III, HALOE and POAM III, as described in the text. †HALOE results have been excluded. ‡Only comparisons with SAGE III are included.

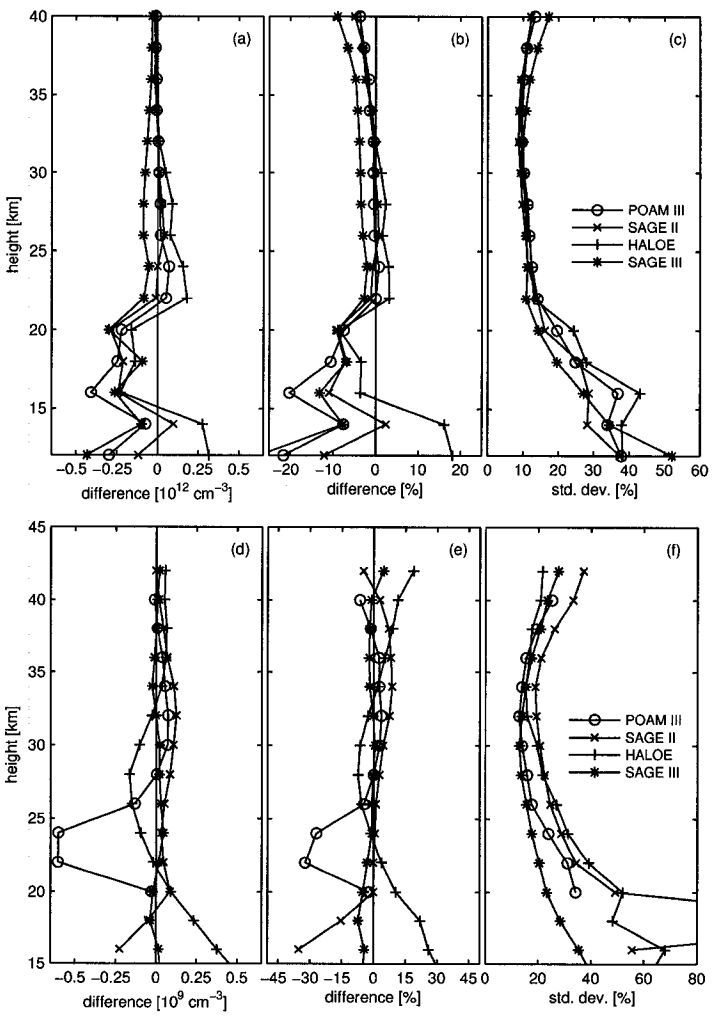

Figure 7.21: Results from all coincidences between OS O_3 (upper panels) and NO_2 (lower panels) profiles and HALOE, POAM III, SAGE II, and SAGE III from 2001 to 2006, expressed as the mean (panels a, b, d and e) and standard deviation (panels c and f) of the differences (OS-Instrument). The coincidence criteria used were 4 hours, 500 km and 20 DU, as described in the text.

7.3.1 Methodology

The validation methodology applied to the OS O_3 and NO_2 data is described in detail in **Paper VI**. Small changes to the approach were introduced in **Paper VII**. The methodology is briefly described below.

The coincidence criteria used are a difference in time of measurement of less than 4 hours and in distance between the measurements of less than 500 km. In addition, coincidences are restricted to cases where the total column O_3 at the two measurement locations differs by less than 20 DU, with the total ozone information taken from the Earth Probe TOMS (*McPeters et al.*, 1998) and OMI (*Levelt et al.*, 2006). When multiple coincidences with a particular OS measurement occur, the closest in distance is chosen. Only OS data with good response (>0.75) and vertical resolution (<5 km) are included. In addition, OS profiles where potentially large pointing offsets were indicated (flagged) are not considered. For NO_2, the coincidences are further constrained to cases where the local times of the measurements were both near sunrise (AM) or sunset (PM) in order to limit the impact of diurnal scaling errors (see below). The coincidences are separated into three latitude bins: 90°S-30°S, 30°S-30°N, and 30°N-90°N, and four season bins: November-December-January, February-March, April-May-June-July-August and September-October.

For NO_2 it is important that the coincident measurements not only occurred close in time and space, but also that they occurred under the same SZA conditions because of the strong diurnal cycle of NO_2. However, a tight constraint on the SZA differences would severely limit the number of coincidences. To remove the need for a specific

SZA constraint, the OS NO_2 measurements are scaled to 90° SZA using output from the University of California, Irvine photochemical box model (*McLinden et al.*, 2000; *Prather*, 1992). In addition, occultation measurements of NO_2 are strongly affected by the variation in NO_2 along the measurement line of sight (the solar beam), which adds a bias to the retrieved profiles. A correction similar to that described in **Paper VI** is applied to each occultation profile except for the Halogen Occultation Experiment (HALOE) (see below), which accounts for this variation (*Gordley et al.*, 1996). This differs from the treatment in **Paper VI**, where only representative corrections were determined for various latitude/season conditions. The OS NO_2 measurements are also affected by diurnal variations both along the measurement line of sight and along the incoming solar beam, as described in **Paper VI**. However, as noted in Section 7.2.3, this error is generally small and for the comparisons here is significantly smaller than the solar occultation correction, and no correction for this effect is applied.

In each latitude/season coincidence bin the mean and standard deviation of the differences between OSIRIS and each instrument are determined at every altitude. From these statistics the OS random and systematic uncertainties are estimated for three altitude regions: 12-25 km (15-25 km for NO_2), 25-35 km and 35-40 km (35-45 km for NO_2). The random uncertainties are estimated by assuming that the instrument and latitude/season bin with the smallest standard deviation represents an estimate of the random uncertainty, with OSIRIS and the other instrument contributing equally to the standard deviation. The systematic uncertainty is estimated from the range of the maximum absolute mean differences from all of the instruments.

Strictly speaking, any validation analysis should consider the averaging kernels

and the influence of the a priori (e.g. *Rodgers and Connor*, 2003). However, since all of the instruments considered here have similar vertical resolutions (~1-2 km) and generally have a low sensitivity to the a priori at the comparison altitudes, the analysis in this work did not account for the individual averaging kernels.

7.3.2 O_3 Results

Since the O_3 retrieval method presented here is not run operationally on the OSIRIS measurements, a selection of scans was processed for this work, based on a subset of the identified validation coincidences used for the O_3 (operational product) and NO_2 analyses in **Paper VII**. The methodology presented in Section 7.3.1 was then applied to this data and measurements from HALOE (*Russell et al.*, 1993), SAGE II (*Mauldin III et al.*, 1985) and III (*McCormick et al.*, 1991), and the Polar Ozone and Aerosol Measurement (POAM) III instrument (*Lucke et al.*, 1999). The OSIRIS measurements used covered the period from 2001 to 2006, providing 485 SAGE II coincidences, 1208 SAGE III coincidences, 1124 POAM III coincidences and 799 HALOE coincidences. Figure 7.21 and Table 7.2 summarize the results.

The results are similar to those for the current operational O_3 product (version 3.0), which were determined in **Paper VII**, and validation studies on previous versions of the operational O_3 product (e.g. *Petelina et al.*, 2004). In general, the retrievals using the method presented in this work produce smaller uncertainties (random and systematic) than does the operational product. In particular, the ~5% negative bias above 20 km in the operational product is not present.

The smaller random uncertainties are likely due to a reduced sensitivity to spectral outliers, due to the spectral fitting approach, and more vertical smoothing, due to a reduced sensitivity below the O_3 peak from a combination of the large optical depths and interference from O_4 and the polarization pseudo-absorber in the spectral fits. The smaller systematic uncertainties are likely due to the reduced impact of baffle scatter and other wavelength-dependent features that are not properly accounted for in the analysis for the operational product, including spectrally-varying albedo and aerosol extinction.

7.3.3 NO_2 Results

In **Paper VII** the OS NO_2 data (version 3.0) were compared with measurements from HALOE, SAGE II and III, and POAM III using the method described above. In total 1060 SAGE II coincidences, 2784 SAGE III coincidences, 1334 POAM III coincidences and 1548 HALOE coincidences were used, spanning 2001 to 2006. The results were similar to those in **Paper VI** on a previous version of the NO_2 data and are summarized in Figure 7.21 and Table 7.2.

In brief, the comparisons are very good overall, particularly above 25 km, with SAGE III clearly giving the best results, both in terms of the mean difference and the standard deviation. Below 25 km the results are mixed. However, this is expected since most of the instruments have difficulties retrieving NO_2 at these altitudes. In particular, the POAM III NO_2 profiles have a clear bias in the 20-25 km region. Note that although not shown here, larger random uncertainties were found in the AM and

are likely related to the small NO_2 abundances (compared to PM).

Chapter 8

Summary, Conclusions and Outlook

8.1 Summary and Conclusions

This dissertation has presented a method for retrieving stratospheric ozone and nitrogen dioxide number density profiles from measurements of limb-scattered sunlight made with the OSIRIS instrument on the Odin satellite. The retrieval method involves a combination of differential optical absorption spectroscopy, used to calculate effective column densities from the measured UV/visible/near-IR spectra, and optimal estimation, used to retrieve the optimal number density vertical profiles based on the effective column densities, their uncertainties and a priori information. The method has been described in detail in a series of publications included in this dissertation. The publications span work from initial studies based on simulated OSIRIS measurements through to the current method used for operational retrievals. It has

been shown that OSIRIS, and limb-scatter measurements in general, can be used to retrieve accurate and highly resolved (vertically) stratospheric ozone and nitrogen dioxide information with good spatial and temporal coverage. Data produced using the retrieval method presented here have been used to produce a stratospheric NO_2 climatology (*Brohede et al.*, 2007), to study stratospheric NO_y (*Brohede et al.*, 2008), and in a number of validation studies of other instruments (e.g. *Kerzenmacher et al.*, 2008; *Taylor et al.*, 2007). The retrieval method has also been applied to the OSIRIS measurements to retrieve additional species, including BrO (*Freedman*, 2005), OClO (*Krecl et al.*, 2006) and NO_3 (*McLinden and Haley*, 2008), as well as polarization information (*McLinden et al.*, 2004).

8.2 Outlook

Although the retrieval method presented here is very robust and produces good results, further work is required, with a focus on the parameters that affect the total retrieval error. The following issues need to be investigated and addressed:

1. The use of more accurate a priori information, in particular more representative a priori covariances.

2. The impact of retrieving to a fixed altitude grid, which introduces artifacts in the retrieved profiles.

3. The dependency of the retrievals on stratospheric aerosol and the impact of stratospheric aerosol variations on the use of the data in trend and variability

studies.

4. Approaches to deal with the remaining tangent height registration errors.

Additional issues include:

- Correlations in the effective column densities (caused by the use of the same reference for all tangent heights).
- A better treatment of albedo in the retrievals, in particular accounting for clouds and seasonal snow cover.
- The impact of horizontal inhomogeneities (other than the NO_2 diurnal effect) and approaches to accounting for them in the retrieval process.
- The error introduced by using a pseudo-spherical radiative transfer model.
- The error introduced by baffle (out-of-field) scatter and approaches to correcting for this.
- The application of the retrieval method to the UV to extend the ozone retrievals to the upper stratosphere and lower mesosphere.

List of Notation

α	aerosol Ångström coefficient
χ	angle of polarization
χ^2_{doas}	DOAS χ^2 value
χ^2_{inv}	inversion χ^2 value
δ	Dirac delta function
$\Delta\phi$	difference in azimuth angle
η	number of pixels in the fitting window
γ	Levenberg-Marquardt step size parameter
λ	wavelength
$\mathbf{1}$	identity matrix
$\hat{\mathbf{b}}$	forward model parameter best estimate
$\hat{\mathbf{S}}$	MAP expected or retrieval error covariance matrix
$\hat{\mathbf{x}}$	MAP expected value
$\mathbf{\Omega}$	direction vector
$\mathbf{\Omega}_0$	direction vector of the solar beam
$\mathbf{A}$	averaging kernel matrix
$\mathbf{b}'$	forward function parameters not included in $\mathbf{F}$
$\mathbf{B}$	basis function matrix

$\mathbf{b}$	forward function parameters included in $\mathbf{F}$
$\mathbf{c}$	effective column density vector
$\mathbf{c}_{lsq}$	least squares estimation of $\mathbf{c}$
$\mathbf{F}$	forward model
$\mathbf{f}$	forward function
$\mathbf{g}$	derivative of the cost function
$\mathbf{G}_y$	gain matrix
$\mathbf{I}$	Stokes vector
$\mathbf{K}$	weighting function matrix
$\mathbf{K}_b$	forward model parameter weighting function matrix
$\mathbf{K}_L$	linearisation weighting function matrix
$\mathbf{n}$	number density vector
$\mathbf{n}^\star$	perturbed number density vector
$\mathbf{r}$	position vector
$\mathbf{r}_{lsq}$	residual vector
$\mathbf{S}_\epsilon$	covariance of the measurement noise
$\mathbf{S}_b$	forward model parameter error covariance matrix
$\mathbf{S}_f$	forward model error covariance matrix
$\mathbf{S}_m$	measurement error covariance matrix
$\mathbf{S}_s$	smoothing error covariance matrix
$\mathbf{S}_\tau$	optical depth error covariance matrix
$\mathbf{S}_a$	a priori covariance matrix
$\mathbf{S}_c$	effective column density error covariance matrix
$\mathbf{S}_{lsq}$	$\mathbf{c}_{lsq}$ error covariance matrix

$\mathbf{S}_{tot}$	total error covariance matrix
$\mathbf{x}$	state vector
$\mathbf{x}_L$	linearisation state vector
$\mathbf{x}_a$	a priori state vector
$\mathbf{y}$	measurement vector
μ	cosine of the zenith angle
μ_0	cosine of the solar zenith angle
Φ	scattering phase function
ϕ	azimuth angle
ϕ_0	solar azimuth angle
ψ	internal stray light correction factor
σ	absorption cross section
σ'	differential cross section
σ^s	slowly varying component of the cross section
σ_a	absorption cross section
σ_e	extinction cross section
σ_M	Mie scattering cross section
σ_R	Rayleigh scattering cross section
σ_s	scattering cross section
τ	optical depth
τ'	differential optical depth
τ^s	slowly varying component of the optical depth
τ_M	Mie scattering optical depth
τ_R	Rayleigh scattering optical depth

τ_s	optical depth along the solar beam
τ_t	total vertical optical depth
Θ	single scattering angle
θ	zenith angle
θ_0	solar zenith angle
$\tilde{\omega}$	single scattering albedo
ε_ψ	standard deviation of the error in ψ
ε_a	standard deviation of the a priori
ε_B	standard deviation of the error in B
ε_D	standard deviation of the error in D
ε_I	standard deviation of the error in I
ε_R	standard deviation of the error in R
ε_S	standard deviation of the error in the Level 0 data
ε_τ	standard deviation of the error in τ
ε_{I_0}	standard deviation of the error in I_0
ε_{lin}	normal standard deviation
ε_{log}	log-normal standard deviation
ε_{ROE}	readout electronics noise
A	albedo
a	polynomial coefficient
B	bias correction
C	cost function
c	effective column density
c_{aer}	effective column density of aerosol

c_{air}	effective column density of air
D	dark current correction
d	degrees of freedom in the spectral fit
F_0	solar flux
G	reciprocal effective gain
g_{12}	Q grating efficiency
g_{13}	U grating efficiency
h_t	tangent height
h_t^{ref}	reference tangent height
I	radiance (intensity)
I_0	incident (unattenuated) reference radiance
I_0^s	slowly varying component of I_0
I_{diff}	diffuse (indirect) radiance
I_{dir}	direct radiance
I_{unpol}	equivalent unpolarized radiance
J	source function
J_{ms}	multiple scattering source function
J_{ss}	single scattering source function
k	absorption coefficient
k_a	absorption coefficient
k_e	extinction coefficient
k_M	Mie scattering coefficient
k_R	Rayleigh scattering coefficient
k_s	scattering coefficient

L	path length
l_c	correlation length
LP	degree of linear polarization
n	concentration or number density
N_{off}	off-chip binning
N_{on}	on-chip binning
P	probability density function
p	number of elements in $\mathbf{x}$ or $\mathbf{n}$
Q	linearly polarized light (parallel and perpendicular)
q	number of elements in $\mathbf{y}$ or $\mathbf{c}$
R	flat-field responsivity
r	radial distance from the centre of the Earth
r	residual
r_{rms}	root-mean-square residual
S	Level 0 data
T	temperature
t_{exp}	exposure/integration time
U	45° linear polarized light (45° and 135°)
V	circularly polarization light
w	spread (vertical resolution)
$\boldsymbol{\epsilon}_y$	total error in the measurement relative to $\mathbf{F}$
$\boldsymbol{\epsilon}$	measurement noise
$\boldsymbol{\epsilon}_\tau$	optical depth error vector
$\boldsymbol{\tau}$	optical depth vector

ACE	Atmospheric Chemistry Experiment
AS	albedo scattering
BUV	Backscatter Ultraviolet
CCD	charge-coupled device
CDI	Combined Differential-Integral
CDIPI	Combined Differential-Integral Picard Iterative
CFC	chlorofluorocarbon
dAZ	difference in azimuth angle
DN	data number
DOAS	differential optical absorption spectroscopy
DOD	differential optical depth
DU	Dobson unit
ECD	effective column density
ECMWF	European Centre for Medium-range Weather Forecasts
EESC	equivalent effective stratospheric chlorine
FM	forward model
FMP	forward model parameter
FOP	field-flattener/order-sorter/prism
FOV	field of view
FWHM	full-width at half maximum
GN	Gauss-Newton
GOMOS	Global Ozone Measurement by Occultation of Stars
GPS	Global Positioning System
GSLS	Gauss-Seidel Limb Spherical

HALOE	Halogen Occultation Experiment
HBFC	hydrobromofluorocarbon
HCFC	hydrochlorofluorocarbon
ILS	iterative least-squares
IR	infrared
IRI	Infrared Imager
LM	Levenberg-Marquardt
LORE	Limb Ozone Retrieval Experiment
LOS	line of sight
LOSU	level of scientific understanding
LSQ	least-squares
LST	local solar time
MAESTRO	Measurements of Aerosol Extinction in the Stratosphere and Troposphere Retrieved by Occultation
MAP	maximum a posteriori
MART	multiplicative algebraic reconstruction technique
MCC++	Monte Carlo C++
MIPAS	Michelson Interferometer for Passive Atmospheric Sounding
MLS	Microwave Limb Sounder
MS	multiple scattering
MSU	Microwave Sounding Unit
NASA	National Aeronautics and Space Administration
NAT	nitric acid trihydrate
NH	Northern Hemisphere

NOAA	National Oceanic and Atmospheric Administration
NPOESS	National Polar-Orbiting Operational Environmental Satellite System
NPP	NPOESS Preparatory Project
ODS	ozone depleting substances
OE	optimal estimation
OMI	Ozone Monitoring Instrument
OMPS	Ozone Mapping and Profiler Suite
OS	Optical Spectrograph
OSIRIS	Optical Spectrograph and Infrared Imager System
PDF	probability density function
PMC	polar mesospheric cloud
POAM	Polar Ozone and Aerosol Measurement
PSC	polar stratospheric cloud
QBO	quasi-biennial oscillation
RF	radiative forcing
RMS	root-mean-square
ROE	readout electronics
RTE	radiative transfer equation
RTM	radiative transfer model
SAGE	Stratospheric Aerosol and Gas Experiment
SAO	semi-annual oscillation
SBUV	Solar Backscatter Ultraviolet
SCIAMACHY	Scanning Imaging Absorption Spectrometer for Atmospheric Chartography

SH	Southern Hemisphere
SME	Solar Mesosphere Explorer
SMR	Submillimetre and Millimetre Radiometer
SNR	signal-to-noise ratio
SOLSE	Shuttle Ozone Limb Scattering Experiment
SS	single scattering
SSA	single scattering angle
SSU	Stratospheric Sounding Unit
STD	standard deviation
STEP	Stratosphere-Troposphere Exchange Processes
STS	supercooled ternary solutions
SZA	solar zenith angle
TH	tangent height
TOA	top of atmosphere
TOMS	Total Ozone Mapping Spectrometer
TTL	tropical tropopause layer
UTLS	upper troposphere/lower stratosphere
UV	ultraviolet
VECTOR	Vector Orders-of-Scattering Radiative Transfer Model

References

Aliwell, S. R., M. V. Roozendael, P. V. Johnston, A. Richter, T. Wagner, D. W. Arlander, J. P. Burrows, D. J. Fish, R. L. Jones, K. K. Tornkvist, J. C. Lambert, K. Pfeilsticker, and I. Pundt, Analysis for BrO in zenith-sky spectra: An intercomparison exercise for analysis improvement, *J. Geophys. Res.*, *107*(D14), 4199, doi:10.1029/2001JD000329, 2002.

Aruga, T., and D. F. Heath, Determination of vertical ozone distributions by spacecraft measurements using a limb-scan technique, *Appl. Opt.*, *21*, 3047–3054, 1982.

Auvinen, H., L. Oikarinen, and E. Kyrölä, Inversion algorithms for recovering minor species densities from limb scatter measurements at UV-visible wavelengths, *J. Geophys. Res.*, *107*(D13), 4172, doi:10.1029/2001JD000407, 2002.

Axelsson, H., H. Edner, B. Galle, P. Ragnarsson, and M. Rudin, Differential optical absorption spectroscopy (DOAS) measurements of ozone in the 280-290 nm wavelength range, *Appl. Spectrosc.*, *44*, 1654–1658, 1990.

Backus, G. E., and J. F. Gilbert, Uniqueness in the inversion of inaccurate gross Earth data, *Phil. Trans. R. Soc. Lond.*, *266*, 123–192, 1970.

Baldwin, M. P., L. J. Gray, T. J. Dunkerton, K. Hamilton, P. H. H. W. J. Randel, J. R. Holton, M. J. Alexander, I. Hirota, T. Horinouchi, D. B. A. Jones, J. S. Kinnersley, C. Marquardt, K. Sato, and M. Takahashi, The quasi-biennial oscillation, *Rev. Geophys.*, *39*, 179–230, 2001.

Bates, D. R., Rayleigh scattering by air, *Planet. Space Sci.*, *32*(6), 785–790, 1984.

Bates, D. R., and M. Nicolet, The photochemistry of the atmospheric water vapor, *J. Geophys. Res.*, *55*, 301–327, 1950.

Bauman, J. J., P. B. Russell, M. A. Geller, and P. Hamill, A stratospheric aerosol climatology from SAGE II and CLAES measurements: 1. Methodology, *J. Geophys. Res.*, *108*(D13), 4382, doi:10.1029/2002JD002992, 2003a.

Bauman, J. J., P. B. Russell, M. A. Geller, and P. Hamill, A stratospheric aerosol climatology from SAGE II and CLAES measurements: 2. Results and comparisons, 1984-1999, *J. Geophys. Res.*, *108*(D13), 4383, doi:10.1029/2002JD002993, 2003b.

Bernath, P. F., C. T. McElroy, M. C. Abrams, C. D. Boone, M. Butler, C. Camy-Peyret, M. Carleer, C. Clerbaux, P. F. Coheur, R. Colin, P. DeCola, M. DeMazière, J. R. Drummond, D. Dufour, W. F. J. Evans, H. Fast, D. Fussen, K. Gilbert, D. E. Jennings, E. Llewellyn, R. P. Lowe, E. Mahieu, J. C. McConnell, M. McHugh, S. D. McLeod, R. Michaud, C. Midwinter, R. Nassar, F. Nichitiu, C. Nowlan, C. P. Rinsland, Y. J. Rochon, N. Rowlands, K. Semeniuk, P. Simon, R. Skelton, J. J. Sloan, M. A. Soucy, K. Strong, P. Tremblay, D. Turnbull, K. A. Walker, I. Walkty, D. Wardle, V. Wehrle, R. Zander, and J. Zou, Atmospheric Chemistry Experiment (ACE): Mission overview, *Geophys. Res. Lett.*, *32*, L15S01, doi:10.1029/2005GL022386, 2005.

Bertaux, J., G. Mégie, T. Widemann, E. Chassefière, R. Pellinen, E. Kyrölä, S. Korpela, and P. Simon, Monitoring of ozone trend by stellar occultations: The GOMOS instrument, *Adv. Space Res.*, *11*, 237–242, 1991.

Bogumil, K., J. Orphal, T. Homann, S. Voigt, P. Spietz, O. C. Fleischmann, A. Vogel, M. Hartmann, H. Kromminga, H. Bovensmann, J. Frerick, and J. P. Burrows, Measurements of molecular absorption spectra with the SCIAMACHY pre-flight model: Instrument characterization and reference data for atmospheric remote-sensing in the 230-2380 nm region, *J. Photochem. Photobiol. A: Chem*, *157*, 167, doi:10.1016/S1010-6030(3)00062-5, 2003.

Bourassa, A. E., D. A. Degenstein, and E. J. Llewellyn, Climatology of the subvisual cirrus clouds as seen by OSIRIS on Odin, *Adv. Space Res.*, *36*, 807–812, doi:10.1016/j.asr.2005.05.045, 2005.

Bourassa, A. E., D. A. Degenstein, R. L. Gattinger, and E. J. Llewellyn, Stratospheric aerosol retrieval with optical spectrograph and infrared imaging system limb scatter measurements, *J. Geophys. Res.*, *112*, D10217, doi:10.1029/2006JD008079, 2007.

Bourassa, A. E., D. A. Degenstein, and E. J. Llewellyn, SASKTRAN: A spherical geometry radiative transfer code for efficient estimation of limb scattered sunlight, *J. Quant. Spectrosc. Radiat. Transfer*, *109*, 52–73, doi:10.1016/j.jqsrt.2007.07.007, 2008.

Bovensmann, H., J. P. Burrows, M. Buchwitz, J. Frerick, S. Noël, V. V. Rozanov, K. V. Chance, and A. P. H. Goede, SCIAMACHY: Mission objectives and measurement modes, *J. Atmos. Sci.*, *56*, 127–150, 1999.

Brasseur, G., and S. Solomon, *Aeronomy Of The Middle Atmosphere: Chemistry And Physics Of The Stratosphere And Mesosphere*, 3 ed., Springer, 2005.

Brewer, A. M., Evidence for a world circulation provided by the measurements of helium and water vapor distribution in the stratosphere, *Q. J. R. Meteorol. Soc.*, *75*, 351–363, 1949.

Brohede, S., Post-launch measurement of OSIRIS spectral resolution, *OSIRIS Technical Report*, Chalmers University of Technology, 2003.

Brohede, S., C. A. McLinden, G. Berthet, C. S. Haley, D. Murtagh, and C. E. Sioris, A stratospheric NO_2 climatology from Odin/OSIRIS limb-scatter measurements, *Can. J. Phys.*, *85*, 1253–1274, doi:10.1139/P07-141, 2007.

Brohede, S., C. A. McLinden, J. Urban, C. S. Haley, A. I. Jonsson, and D. Murtagh, Odin stratospheric proxy NO_y measurements and climatology, *Atmos. Chem. Phys.*, *8*, 5731–5754, 2008.

Burrows, J. P., M. Weber, M. Buchwitz, V. Rozanov, A. Ladstätter-Weißenmayer, A. Richter, R. deBeek, R. Hoogen, K. Bramstedt, K. U. Eichmann, M. Eisinger, and D. Perner, The global ozone monitoring experiment (GOME): Mission concept and first scientific results, *J. Atmos. Sci.*, *56*, 151–175, 1999.

Chahine, M. T., Inverse problems in radiative transfer: Determination of atmospheric parameters, *J. Atmos. Sci.*, *27*, 960–967, 1970.

Chandrasekhar, S., *Radiative Transfer*, Dover Publications, 1960.

Chapman, S., On ozone and atomic oxygen in the upper atmosphere, *Philos. Mag.*, *10*, 369–383, 1930.

Crutzen, P. J., The influence of nitrogen oxides on the atmospheric ozone content, *Q. J. R. Meteorol. Soc.*, *96*, 320–325, 1970.

Crutzen, P. J., and F. Arnold, Nitric acid cloud formation in the cold Antarctic stratosphere: A major cause for the springtime 'ozone hole', *Nature*, *324*, 651, 1986.

Cunnold, D. M., C. R. Gray, and D. C. Merritt, Stratospheric aerosol layer detection, *J. Geophys. Res.*, *78*, 920–931, 1973.

Dahlback, A., and K. Stamnes, A new spherical model for computing the radiation field available for photolysis and heating at twilight, *Planet. Space Sci.*, *39*, 671–683, 1991.

Degenstein, D., A. Bourassa, C. Roth, N. Lloyd, D. Gattinger, and E. J. Llewellyn, Yet another NO_2 retrieval from OSIRIS, in *Proc. 3rd International Atmospheric Limb Workshop, Montreal*, 2006.

Degenstein, D. A., E. J. Llewellyn, and N. D. Lloyd, Volume emission rate tomography from a satellite platform, *Appl. Opt.*, *42*(8), 1441–1450, 2003.

Degenstein, D. A., E. J. Llewellyn, and N. D. Lloyd, Tomographic retrieval of the oxygen infrared atmospheric band with the OSIRIS infrared imager, *Can. J. Phys.*, *82*, 501–515, doi:10.1139/P04-024, 2004.

Degenstein, D. A., A. Bourassa, C. Z. Roth, and E. J. Llewellyn, Limb scatter ozone retrieval from 10 to 60 km using a multiplicative algebraic reconstruction technique, *Atmos. Chem. Phys. Discuss.*, *8*(3), 11,853–11,877, 2008.

Dessler, A. E., *The Chemistry and Physics of Stratospheric Ozone*, Academic Press, 2000.

Dobson, G. M. B., Origin and distribution of the polyatomic molecules in the atmosphere, *Proc. R. Soc.*, *A236*, 187–193, 1956.

Dupuy, E., J. Urban, P. Ricaud, E. L. Flochmoën, N. Lautié, D. Murtagh, J. de la Nöe, L. E. Amraoui, P. Eriksson, P. Forkman, U. Frisk, F. Jégou, C. Jiménez, and M. Olberg, Strato-mesospheric measurements of carbon monoxide with the Odin sub-millimetre radiometer: Retrieval and first results, *Geophys. Res. Lett.*, *31*, L20101, doi:10.1029/2004GL020558, 2004.

Evans, W. F. J., and J. M. Alfred, Algorithm for correction of internal scattering and spectral cross-talk in the UV/vis band of the OSIRIS instrument flight model, *OSIRIS Technical Report*, Trent University, 1999.

Farman, J. C., B. G. Gardiner, and J. D. Shanklin, Large losses of total ozone in Antarctica reveal seasonal ClO_x/NO_x interaction, *Nature*, *315*, 207–210, 1985.

Fischer, H., and H. Oelhaf, Remote sensing of vertical profiles of atmospheric trace constituents with MIPAS limb emission spectrometers, *Appl. Opt.*, *35*, 2787–2796, 1996.

Flittner, D. E., P. Bhartia, and B. Herman, O_3 profiles retrieved from limb scatter measurements: Theory, *Geophys. Res. Lett.*, *27*, 2601–2604, 2000.

Freedman, R., Stratospheric minor species densities from satellite measurements of scattered light, M.Sc. Thesis, York University, Toronto, Canada, 2005.

Friess, U., K. Kreher, P. V. Johnston, and U. Platt, Ground-based DOAS measurements of stratospheric trace gases at two Antarctic stations during the 2002 ozone hole period, *J. Atmos. Sci.*, *62*(3), 765–777, 2005.

Frisk, U., M. Hagström, J. Ala-Laurinaho, S. Andersson, J. C. Berges, J. P. Chabaud, M. Dahlgren, A. Emrich, H. G. Florén, M. Gredrixon, T. Gaier, R. Haas, T. Hirvonen, A. Hjalmarsson, B. Jakobsson, P. Jukkala, P. S. Kildal, E. Kollberg, J. Lassing, A. Lecacheux, P. Lehikoinen, A. Lehto, J. Mallat, C. Marty, D. Michet, J. Narbonne, M. Nexon, M. Olberg, A. O. H. Olofsson, G. Olofsson, A. Origné, M. Petersson, P. Piironen, R. Pons, D. Pouliquen, I. Ristorcelli, C. Rosolen, G. Rouaix, A. V. Räisänen, G. Serra, F. Sjöberg, L. Stenmark, S. Torchinsky, J. Tuovinen, C. Ullberg, E. Vinterhav, N. Wadefalk, H. Zirath, P. Zimmermann, and R. Zimmermann, The Odin satellite I. Radiometer design and test, *Astron. Astrophys.*, *402*, L27–L34, doi:10.1051/0004-6361:20030335, 2003.

Gattinger, R. L., D. A. Degenstein, and E. J. Llewellyn, Optical Spectrograph and Infra-Red Imaging System (OSIRIS) observations of mesospheric OH $A^2\Sigma^+$-$X^2\Pi$ 0-0 and 1-1 band resonance emissions, *J. Geophys. Res.*, *111*, D13303, doi:10.1029/2005JD006369, 2006.

Goody, R. M., and Y. L. Yung, *Atmospheric Radiation: Theoretical Basis*, 2 ed., Oxford University Press, 1989.

Gordley, L. L., J. M. Russell III, L. J. Mickley, J. E. Frederick, J. H. Park, K. A. Stone, G. M. Beaver, J. M. McInemey, L. E. Deaver, G. C. Toon, F. J. Murcray, R. D. Blatherwick, M. R. Gunson, J. P. D. Abbatt, R. L. Mauldin III, G. H. Mount, B. Sen, and J. F. Blavier, Validation of nitric oxide and nitrogen dioxide measurements made by the Halogen Occultation Experiment for UARS platform, *J. Geophys. Res.*, *101*(D6), 10,241–10,266, 1996.

Grainger, J., and J. Ring, Anomalous Fraunhofer line profiles, *Nature*, *193*, 762, 1962.

Griffioen, E., and L. Oikarinen, LIMBTRAN: A pseudo three-dimensional radiative transfer model for the limb-viewing imager OSIRIS on the Odin satellite, *J. Geophys. Res.*, *105*, 29,717–29,730, 2000.

Gumbel, J., Z. Y. Fan, T. Waldemarsson, J. Stegman, E. J. Llewellyn, C. Y. She, and J. M. C. Plane, Retrieval of global mesospheric sodium densities from the Odin satellite, *Geophys. Res. Lett.*, *34*, L04813, doi:10.1029/2006GL028687, 2007.

Haley, C., and C. Sioris, OS Level 0→1 processing and error approximation, *OSIRIS Technical Report*, York University, 2001.

Haley, C., C. von Savigny, and C. Sioris, Internal scattering correction for the optical spectrograph, *OSIRIS Technical Report*, York University, 2001.

Haley, C. S., and S. Brohede, Status of the Odin/OSIRIS stratospheric O_3 and NO_2 data products, *Can. J. Phys.*, *85*(11), 1177–1194, doi:10.1139/P07-114, 2007.

Haley, C. S., S. M. Brohede, C. E. Sioris, E. Griffioen, D. P. Murtagh, I. C. McDade, P. Eriksson, E. J. Llewellyn, A. Bazureau, and F. Goutail, Retrieval of stratospheric O_3 and NO_2 profiles from Odin Optical Spectrograph and Infrared Imager System (OSIRIS) limb-scattered sunlight measurements, *J. Geophys. Res.*, *109*, D16303, doi:10.1029/2004JD004588, 2004.

Hansen, J. E., and L. D. Travis, Light scattering in planetary atmospheres, *Space Sci. Rev.*, *16*, 527–610, 1974.

Hilsenrath, E., Ozone variations observed during the international ozone rocket sonde intercomparison, *Adv. Space Res.*, *3*(7), 9–12, 1983.

Hirota, I., Observational evidence of the semiannual oscillation in the tropical middle atmosphere - A review, *Pure Appl. Geophys.*, *118*, 217–238, 1980.

Hutley, M. C., *Diffraction Gratings*, 165-193 pp., Academic Press, London, 1982.

Intergovernmental Panel on Climate Change, *Safeguarding the Ozone Layer and the Global Climate System: Issues Related to Hydrofluorocarbons and Perfluorocarbons*, Cambridge University Press, Cambridge, UK, 2005.

Intergovernmental Panel on Climate Change, *Climate Change 2007: The Physical Science Basis. Contribution of Working Group I to the Fourth Assessment Report of the Intergovernmental Panel on Climate Change*, Cambridge University Press, Cambridge, UK, 2007a.

Intergovernmental Panel on Climate Change, *Climate Change 2007: Impacts, Adaptation and Vulnerability. Contribution of Working Group II to the Fourth Assessment Report of the Intergovernmental Panel on Climate Change*, Cambridge University Press, Cambridge, UK, 2007b.

Johnston, H. S., Reduction of stratospheric ozone by nitrogen oxide catalysts from supersonic transport exhaust, *Science*, *173*, 517–522, 1971.

Kaiser, J. W., Atmospheric parameter retrieval from UV-vis-NIR limb scattering measurements, Ph.D. Dissertation, Institute of Environmental Physics/Institute of Remote Sensing, University of Bremen, Bremen, Germany, 2001.

Karlsson, B., and J. Gumbel, Challenges in the limb retrieval of noctilucent cloud properties from Odin/OSIRIS, *Adv. Space Res.*, *36*(5), 935–942, 2005.

Kerr, J. B., and C. T. McElroy, Total ozone measurements made with the Brewer ozone spectrophotometer during STOIC 1989, *J. Geophys. Res.*, *100*(D5), 9225–9230, 1995.

Kerzenmacher, T., M. A. Wolff, K. Strong, E. Dupuy, K. A. Walker, L. K. Amekudzi, R. L. Batchelor, P. F. Bernath, G. Berthet, T. Blumenstock, C. D. Boone, K. Bramstedt, C. Brogniez, S. Brohede, J. P. Burrows, V. Catoire, J. Dodion, J. R. Drummond, D. G. Dufour, B. Funke, D. Fussen, F. Goutail, D. W. T. Griffith, C. S. Haley, F. Hendrick, M. Höpfner, N. Huret, N. Jones, J. Kar, I. Kramer, E. J. Llewellyn, M. López-Puertas, G. Manney, C. T. McElroy, C. A. McLinden, S. Melo, S. Mikuteit, D. Murtagh, F. Nichitiu, J. Notholt, C. Nowlan, C. Piccolo, J.-P. Pommereau, C. Randall, P. Raspollini, M. Ridolfi, A. Richter, M. Schneider, O. Schrems, M. Silicani, G. P. Stiller, J. Taylor, C. Tétard, M. Toohey, F. Vanhellemont, T. Warneke, J. M. Zawodny, and J. Zou, Validation of NO_2 and NO from the Atmospheric Chemistry Experiment (ACE), *Atmos. Chem. Phys.*, *8*, 5801–5841, 2008.

Khabibrakhmanov, I. K., D. A. Degenstein, and E. J. Llewellyn, Mesospheric ozone: Determination from orbit with the OSIRIS instrument on Odin, *Can. J. Phys.*, *80*(4), 493–504, 2002.

Koelemeijer, R. B. A., J. F. de Haan, and P. Stammes, A database of spectral surface reflectivity in the range 335-772 nm derived from 5.5 years of GOME observations, *J. Geophys. Res.*, *108*(D2), 4070, doi:10.1029/2002JD002429, 2003.

Krecl, P., C. S. Haley, J. Stegman, S. M. Brohede, and G. Berthet, Retrieving the vertical distribution of stratospheric OClO from Odin/OSIRIS limb-scattered sunlight measurements, *Atmos. Chem. Phys.*, *6*, 1879–1894, 2006.

Lautié, N., J. Urban, D. P. Murtagh, E. L. Flochmoën, E. Dupuy, L. E. Amraoui, P. Eriksson, U. Frisk, C. Jiménez, J. de LaNoë, M. Olberg, and P. Richaud, Odin/SMR global measurements of water vapour and its isotopes in the stratosphere and the mesosphere, in *Proc. 20th Quadrenn. Ozone Symp.*, pp. 215–216, 2004.

Lenoble, J., and P. Pruvost, Inference of the aerosol Ångström coefficient from SAGE short-wavelength data, *J. Clim. Appl. Meteor.*, *22*, 1717–1725, 1983.

Lenoble, L., *Radiative Transfer in Scattering and Absorbing Atmospheres: Standard Computational Procedures*, A. Deepak Pub., 1985.

Levelt, P. F., G. H. J. van den Oord, M. R. Dobber, A. Mälkki, H. Visser, J. de Vries, P. Stammes, J. Lundell, and H. Saari, The ozone monitoring instrument, *IEEE Trans. Geosci. Remote Sensing*, *44*(5), 1093–1101, doi:10.1109/TGRS.2006.872333, 2006.

Li, D., and K. P. Shine, A 4-dimensional ozone climatology for UGAMP models, *Tech. rep.*, UGAMP Internal Report No. 35, 1995.

Lindzen, R. S., and J. R. Holton, A theory of the quasi-biennial oscillation, *J. Atmos. Sci.*, *25*, 1095–1107, 1968.

Livingston, J. M., B. Schmid, P. B. Russell, J. A. Eilers, R. W. Kolyer, J. Redemann, S. R. Ramirez, J.-H. Yee, W. H. Swartz, C. R. Trepte, L. W. Thomason, M. C. Pitts, M. A. Avery, C. E. Randall, J. D. Lumpe, R. M. Bevilacqua, M. Bittner, T. Erbertseder, R. D. McPeters, R. E. Shetter, E. V. Browell, J. B. Kerr, and K. Lamb, Retrieval of ozone column content from airborne Sun photometer measurements during SOLVE II: Comparison with coincident satellite and aircraft measurements, *Atmos. Chem. Phys.*, *5*, 2035–2054, 2005.

Llewellyn, E. J., and R. L. Gattinger, OSIRIS/UVIS optics bench temperature effects on wavelength stability and spectral resolution, *OSIRIS Technical Report*, University of Saskatchewan, 2000.

Llewellyn, E. J., W. F. J. Evans, J. C. McConnell, I. C. McDade, B. H. Solheim, and R. L. Gattinger, Odin aeronomy: An NSERC CSP grant application, *OSIRIS Technical Report*, University of Saskatchewan, 1995.

Llewellyn, E. J., R. L. Gattinger, D. L. Desaulniers, and G. Warshaw, Estimated OSIRIS UVIS baffle on-orbit performance, *OSIRIS Technical Report*, University of Saskatchewan, 1998.

Llewellyn, E. J., R. L. Gattinger, and L. Piché, The inspection of the OSIRIS slit to determine the apparent change in the OSIRIS performance during storage, *OSIRIS Technical Report*, University of Saskatchewan, 2001.

Llewellyn, E. J., N. D. Lloyd, D. A. Degenstein, R. L. Gattinger, S. V. Petelina, A. E. Bourassa, J. T. Wiensz, E. V. Ivanov, I. C. McDade, B. H. Solheim, J. C. McConnell, C. S. Haley, C. von Savigny, C. E. Sioris, C. A. McLinden, E. Griffioen, J. Kaminiski, W. F. J. Evans, E. Puckrin, K. Strong, V. Wehrle, R. H. Hum, D. J. W. Kendall, J. Matsushita, D. P. Murtagh, S. Brohede, J. Stegman, G. Witt, G. Barnes, W. F. Payne, L. Piché, K. Smith, G. Warshaw, D. L. Deslauniers, P. Marchand, E. H. Richardson, R. A. King, I. Wevers, W. McCreath, E. Kyrölä, L. Oikarinen, G. W. Leppelmeier, H. Auvinen, G. Mégie,

A. Hauchecorne, F. Lefèvre, J. de La Nöe, P. Ricaud, U. Frisk, F. Sjoberg, F. von Schéele, and L. Nordh, The OSIRIS instrument on the Odin spacecraft, *Can. J. Phys.*, *82*, 411–422, doi:10.1139/P04-005, 2004.

Lloyd, N., Dark current algorithm for the OSIRIS optical spectrograph, *OSIRIS Technical Report*, University of Saskatchewan, 2005a.

Lloyd, N., Internal scattering correction for the optical spectrograph: Update to original algorithm, *OSIRIS Technical Report*, University of Saskatchewan, 2005b.

Lloyd, N., OSIRIS level 1 absolute calibration: Derived from atmospheric modelling comparisons, *OSIRIS Technical Report*, University of Saskatchewan, 2007.

Loughman, R. P., E. Griffioen, L. Oikarinen, O. V. Postylyakov, A. Rozanov, D. E. Flittner, and D. F. Rault, Comparison of radiative transfer models for limb-viewing scattered sunlight measurements, *J. Geophys. Res.*, *109*, D06303, doi: 10.1029/2003JD003854, 2004.

Loughman, R. P., D. E. Flittner, B. M. Herman, P. K. Bhartia, E. Hilsenrath, and R. D. McPeters, Description and sensitivity analysis of a limb scattering ozone retrieval algorithm, *J. Geophys. Res.*, *110*, D19301, doi:10.1029/2004JD005429, 2005.

Lucke, R. L., D. R. Korwan, R. M. Bevilacqua, J. S. Hornstein, E. P. Shettle, D. T. Chen, M. Daehler, J. D. Lumpe, M. D. Fromm, D. Debrestian, B. Neff, M. Squire, G. König-Langlo, and J. Davies, The polar ozone and aerosol measurement (POAM) III instrument and early validation results, *J. Geophys. Res.*, *104*, 18,785–18,799, 1999.

Malchow, H. L., and C. K. Whitney, Inversion of scattered radiance horizon profiles and gaseous concentrations and aerosol parameters, in *Inversion Methods in Atmospheric Remote Sensing*, edited by A. Deepak, pp. 217–261, Academic, San Diego, 1977.

Marchuk, G. I., G. A. Mikhailov, M. A. Nazaraliev, R. A. Darbinjan, B. A. Kargin, and B. S. Elepov, *The Monte Carlo Methods in Atmospheric Optics*, Springer-Verlag, 1980.

Mauldin III, L. E., N. H. Zaun, M. P. McCormick, J. H. Guy, and W. R. Vaughn, Stratospheric aerosol and gas experiment II instrument: A functional description, *Opt. Eng.*, *34*, 307–312, 1985.

McCormick, M. P., W. P. Chu, J. M. Zawodny, L. E. Mauldin III, and L. R. McMaster, Stratospheric aerosol and gas experiment III (SAGE III) aerosol and trace gas measurements for earth observing system (EOS), in *Proc. SPIE Int. Soc. Opt. Eng.*, vol. 1491, pp. 125–141, 1991.

McDade, I. C., K. Strong, C. S. Haley, J. Stegman, D. P. Murtagh, and E. J. Llewellyn, A method for recovering stratospheric minor species densities from the Odin/OSIRIS scattered-sunlight measurements, *Can. J. Phys.*, *80*(4), 395–408, 2002.

McElroy, C. T., Stratospheric nitrogen dioxide concentrations as determined from limb brightness measurements made on June 17, 1983, *J. Geophys. Res.*, *93*, 7075–7083, 1988.

McElroy, C. T., C. R. Nowlan, J. R. Drummond, P. F. Bernath, D. V. Barton, D. G. Dufour, C. Midwinter, R. B. Hall, A. Ogyu, A. Ullberg, D. I. Wardle, J. Kar, J. Zou, F. Nichitiu, C. D. Boone, K. A. Walker, and N. Rowlands, The ACE-MAESTRO instrument on SCISAT: description, performance, and preliminary results, *Appl. Opt.*, *46*, 4341–4356, doi:doi:10.1364/AO.46.004341, 2007.

McElroy, M. B., R. J. Salawitch, S. C. Wofsy, and J. A. Logan, Reduction of Antarctic ozone due to synergistic interactions of chlorine and bromine, *Nature*, *321*, 759–762, 1986.

McLinden, C. A., and C. S. Haley, Odin/OSIRIS observations of stratospheric NO_3 through sunrise and sunset, *Atmos. Chem. Phys.*, *8*, 5529–5534, 2008.

McLinden, C. A., S. Olsen, B. Hannegan, O. Wild, M. J. Prather, and J. Sundet, Stratospheric ozone in 3-D models: A simple chemistry and the cross-tropopause flux, *J. Geophys. Res.*, *105*(D11), 14,653–14,665, 2000.

McLinden, C. A., J. C. McConnell, E. Griffioen, and C. T. McElroy, A vector radiative-transfer model for the Odin/OSIRIS project, *Can. J. Phys.*, *80*(4), 375–393, 2002a.

McLinden, C. A., J. C. McConnell, K. Strong, I. C. McDade, R. L. Gattinger, R. King, B. Solheim, E. J. Llewellyn, and W. F. J. Evans, The impact of the OSIRIS grating efficiency on radiance and trace-gas retrievals, *Can. J. Phys.*, *80*(4), 469–481, 2002b.

McLinden, C. A., C. S. Haley, and E. J. Llewellyn, Derivation of polarization from Odin/OSIRIS limb spectra, *Geophys. Res. Lett.*, *31*, L20112, doi:10.1029/2004GL020825, 2004.

McLinden, C. A., V. E. Fioletov, C. S. Haley, N. Lloyd, C. Roth, D. Degenstein, A. Bourassa, C. T. McElroy, and E. Llewellyn, An evaluation of Odin/OSIRIS limb pointing and stratospheric ozone through comparisons with ozonesondes, *Can. J. Phys.*, *85(11)*, 1125–1141, doi:10.1139/P07-112, 2007.

McPeters, R. D., P. K. Bhartia, A. J. Krueger, and J. R. Herman, Earth probe total ozone mapping spectrometer (TOMS) data products user's guide, *Tech. rep.*, NASA/IP-1998-206895, 1998.

McPeters, R. D., S. J. Janz, E. Hilsenrath, and T. L. Brown, The retrieval of O_3 profiles from limb scatter measurements: Results from the shuttle ozone limb sounding experiment, *Geophys. Res. Lett.*, *27*(17), 2597–2600, 2000.

Molina, L. T., and M. J. Molina, Production of the Cl_2O_2 from the self-reaction of the ClO radical, *J. Phys. Chem.*, *91*, 433–436, 1987.

Molina, M. J., and F. S. Rowland, Stratospheric sink for chlorofluoromethanes: Chlorine atom-catalysed destruction of ozone, *Nature*, *249*, 810–812, 1974.

Molina, M. J., T. L. Tso, L. T. Molina, and F. C. Y. Yang, Antarctic stratospheric chemistry of chlorine nitrate, hydrogen chloride, and ice: Release of active chlorine, *Science*, *238*, 1253, 1987.

Mount, G. H., D. W. Rusch, J. M. Zawodny, J. F. Noxon, C. A. Barth, G. J. Rottman, R. J. Thomas, G. E. Thomas, R. W. Sanders, and G. M. Lawrence, Measurements of NO_2 in the Earth's stratosphere using a limb scanning visible light spectrometer, *Geophys. Res. Lett.*, *10*(4), 265–268, 1983.

Mount, G. H., D. W. Rusch, J. F. Noxon, J. M. Zawodny, and C. A. Barth, Measurements of stratospheric NO_2 from the Solar Measosphere Explorer satellite 1. An overveiw of the results, *J. Geophys. Res.*, *89*(D1), 1327–1340, 1984.

Murtagh, D., U. Frisk, F. Merino, M. Ridal, A. Jonsson, J. Stegman, G. Witt, P. Eriksson, C. Jiménez, G. Megie, J. de la Noë, P. Ricaud, P. Baron, J. R. Pardo, A. Hauchcorne, E. J. Llewellyn, D. A. Degenstein, R. L. Gattinger, N. D. Lloyd, W. F. J. Evans, I. C. McDade, C. Haley, C. Sioris, C. von Savigny, B. H. Solheim, J. C. McConnell, K. Strong, E. H. Richardson, G. W. Leppelmeier, E. Kyrölä, H. Auvinen, and L. Oikarinen, An overview of the Odin atmospheric mission, *Can. J. Phys.*, *80*(4), 309–319, 2002.

Nordh, H. L., F. von Schéele, U. Frisk, K. Ahola, R. S. Booth, P. J. Encrenaz, A. Hjalmarson, D. Kendall, E. Kyrölä, S. Kwok, A. Lecacheux, G. Leppelmeier, E. J. Llewellyn, K. Mattila, G. Mégie, D. Murtagh, M. Rougeron, and

G. Witt, The Odin orbital observatory, *Astron. Astrophys.*, *402*, L21–L25, doi: 10.1051/0004-6361:20030334, 2003.

Noxon, J. F., Nitrogen dioxide in the stratosphere and troposphere measured by ground-based absorption spectroscopy, *Science*, *189*, 547–549, 1975.

Noxon, J. F., E. C. Whipple, and R. S. Hyde, Stratospheric NO_2. I. Observational method and behavior at mid-latitude, *J. Geophys. Res.*, *28*(8), 5047–5065, 1979.

Oikarinen, L., Polarization of light in UV-visible limb radiance measurements, *J. Geophys. Res.*, *106*(D2), 1533–1544, 2001.

Oikarinen, L., Effect of surface albedo variations on UV-visible limb-scattering measurements of the atmosphere, *J. Geophys. Res.*, *107*(D19), 4404, doi:10.1029/ 2001JD001492, 2002.

Oikarinen, L., E. Sihova, and E. Kyrölä, Multiple scattering radiance in limb-viewing geometry, *J. Geophys. Res.*, *104*, 31,261–31,274, 1999.

Perner, D., and U. Platt, Detection of nitrous acid in the atmosphere by differential optical absorption, *Geophys. Res. Lett.*, *6*(12), 917–920, 1979.

Perner, D., and U. Platt, Absorption of light in the atmosphere by collision pairs of oxygen $(O_2)_2$, *Geophys. Res. Lett.*, *7*(12), 1053–1056, 1980.

Petelina, S. V., E. J. Llewellyn, D. A. Degenstein, N. D. Lloyd, R. L. Gattinger, C. S. Haley, C. von Savigny, E. Griffioen, I. C. McDade, W. F. J. Evans, D. P. Murtagh, and J. de La Nöe, Comparison of the Odin/OSIRIS stratospheric ozone profiles with coincident POAM III and ozonesonde measurements, *Geophys. Res. Lett.*, *31*, L07104, doi:2003GL019299, 2004.

Petelina, S. V., E. J. Llewellyn, D. A. Degenstein, and N. D. Lloyd, Odin/OSIRIS limb observations of Polar Mesospheric Clouds in 2001-2003, *J. Atmos. Solar-Terr. Phys.*, *68*(1), 42–55, doi:doi:10.1016/j.jastp.2005.08.004, 2006.

Pfeilsticker, K., H. Bösch, C. Camy-Peyret, R. Fitzenberger, H. Harder, and H. Osterkamp, First atmospheric profile measurements of UV/visible O_4 absorption band intensities: Implications for the spectroscopy, and the formation enthalpy of the O_2-O_2 dimer, *Geophys. Res. Lett.*, *28*(24), 4595–4598, 2001.

Platt, U., Differential optical absorption spectroscopy (DOAS), in *Air monitoring by Spectroscopic Techiques*, edited by M. Sigrist, pp. 27–84, John Wiley & Sons, New York, 1994.

Platt, U., and J. Stutz, *Differential Optical Absorption Spectroscopy: Principles and Applications*, Springer, 2008.

Platt, U., D. Perner, and H. W. Pätz, Simultaneous measurement of atmospheric CH_2O, O_3 and NO_2 by differential optical absorption, *J. Geophys. Res.*, *84*(10), 6329–6335, 1979.

Platt, U., L. Marquad, and T. Wagner, Corrections for zenith scattered light DOAS, *Geophys. Res. Lett.*, *24*(14), 1759–1762, 1997.

Pommereau, J. P., F. Goutail, J. Piquard, L. Denis, and C. Phillips, The SAOZ balloon optical sonde for atmospheric chemistry study, in *Proc. 11th ESA Symp. Eur. Rocket & Balloon Prog.*, 1994.

Postylyakov, O. V., Linearized vector radiative transfer model MCC++ for spherical atmosphere, *J. Quant. Spectrosc. Radiat. Transfer*, *88*, 297–317, doi:10.1016/j.jqsrt.2004.01.009, 2004a.

Postylyakov, O. V., Radiative transfer model MCC++ with evaluation of weighting functions in spherical atmosphere for use in retrieval algorithms, *Adv. Space Res.*, *34*, 721–726, doi:10.1016/j.asr.2003.07.070, 2004b.

Postylyakov, O. V., Spherical radiative transfer model with computation of layer air mass factors, and some of its applications, *Izv. Atmos. Ocean. Phys.*, *40*, 276–290, 2004c.

Prather, M. J., Catastrophic loss of stratospheric ozone in dense volcanic clouds, *J. Geophys. Res.*, *97*(D9), 10,187–10,191, 1992.

Proffitt, M. H., M. J. Steinkamp, J. A. Powell, R. J. McLaughlin, O. A. Mills, A. L. Schmeltekopf, T. L. Thompson, A. F. Tuck, T. Tyler, R. H. Winkler, and K. R. Chan, In situ ozone measurements within the 1987 Antarctic ozone hole from a high-altitude ER-2 aircraft, *J. Geophys. Res.*, *94*(D14), 16,547–16,555, 1989.

Rault, D. F., Ozone profile retrieval from Stratospheric Aerosol and Gas Experiment (SAGE III) limb scatter measurements, *J. Geophys. Res.*, *110*, D09309, doi:10.1029/2004JD004970, 2005.

Reed, R. J., Some features of the annual temperature regime in the tropical stratosphere, *Mon. Wea. Rev.*, *90*, 211–215, 1962.

Reed, R. J., Zonal wind behavior in the equatorial stratosphere and lower mesosphere, *J. Geophys. Res.*, *71*, 4223–4233, 1966.

Reed, R. J., W. J. Campbell, L. A. Rassmussen, and D. G. Rogers, Evidence of a downward-propagating, annual wind reversal in the equatorial stratosphere, *J. Geophys. Res.*, *66*, 813–818, 1961.

Reinsel, G., G. Tiao, and R. Lewis, A statistical analysis of total ozone data from the Nimbus-4 BUV satellite experiment, *J. Atmos. Sci.*, *39*, 418–430, 1982.

Ricaud, P., D. Alexandre, B. Barret, E. L. Flochmöen, E. Motte, G. Berthet, F. Lefèvre, and D. Murtagh, Measurements of mid-stratospheric formaldehyde from the Odin/SMR instrument, *J. Quant. Spectrosc. Radiat. Transfer*, *107*, 91–104, doi: 10.1016/j.jqsrt.2007.01.058, 2007.

Rodgers, C. D., Retrieval of atmospheric temperature and composition from remote measurements of thermal radiation, *R. Geophys. Space Phys.*, *14*, 609–624, 1976.

Rodgers, C. D., Characterization and error analysis of profiles retrieved from remote sounding measurements, *J. Geophys. Res.*, *95*, 5587–5595, 1990.

Rodgers, C. D., *Inverse methods for atmospheric sounding: Theory and practice*, World Scientific Publishing, Singapore, 2000.

Rodgers, C. D., and B. J. Connor, Intercomparison of remote sounding instruments, *J. Geophys. Res.*, *108*(D3), 4116, doi:10.1029/2002JD002299, 2003.

Roth, C. Z., D. A. Degenstein, A. E. Bourassa, and E. J. Llewellyn, The retrieval of vertical profiles of the ozone number density using Chappuis band absorption information and a multiplicative algebraic reconstruction technique, *Can. J. Phys.*, *85(11)*, 1225–1243, doi:10.1139/P07-130, 2007.

Rothman, L. S., D. Jacquemart, A. Barbe, D. C. Benner, M. Birk, L. R. Brown, M. R. Carleer, C. C. Jr., K. Chance, L. H. Coudert, V. Dana, V. M. Devi, J. M. Flaud, R. R. Gamache, A. Goldman, J. M. Hartmannh, K. W. Jucks, A. G. Maki, J. Y. Mandin, S. T. Massie, J. Orphal, A. Perrin, C. P. Rinsland, M. A. H. Smith, J. Tennyson, R. N. Tolchenov, R. A. Toth, J. V. Auwera, P. Varanasi, and G. Wagner, The HITRAN 2004 molecular spectroscopic database, *J. Quant. Spectrosc. Radiat. Transfer*, *96*, 139–204, doi:10.1016/j.jqsrt.2004.10.008, 2005.

Rozanov, A., Modeling of radiative transfer through a spherical planetary atmosphere: Application to atmospheric trace gases retrieval from occultation- and limb-measurements in UV-Vis-NIR, Ph.D. Dissertation, Institute of Environmental Physics/Institute of Remote Sensing, University of Bremen, Bremen, Germany, 2001.

Rozanov, A., V. Rozanov, and J. P. Burrows, A numerical radiative transfer model for a spherical planetary atmosphere: Combined differential-integral approach involving the Picard iterative approximation, *J. Quant. Spectrosc. Radiat. Transfer*, *69*, 491–512, 2001.

Rozanov, A., V. Rozanov, M. Buchwitz, A. Kokhanovsky, and J. P. Burrows, SCIATRAN 2.0 - a new radiative transfer model for geophysical applications, *Adv. Space Res.*, *36*, 1015–1019, 2005.

Rozanov, A. V., V. V. Rozanov, and J. P. Burrows, Combined differential-integral approach for the radiation field computation in a spherical shell atmosphere: Nonlimb geometry, *J. Geophys. Res.*, *105*, 22,937–22,942, 2000.

Rusch, D. W., G. H. Mount, C. A. Barth, G. J. Rottmann, R. J. Thomas, G. E. Thomas, R. W. Sanders, G. M. Lawrence, and R. S. Eckman, Ozone densities in the lower mesosphere measured by a limb scanning ultraviolet spectrometer, *Geophys. Res. Lett.*, *10*, 241–244, 1983.

Rusch, D. W., G. H. Mount, C. A. Barth, R. J. Thomas, and M. T. Callan, Solar measospheric explorer ultraviolet spectrometer: Measurements of ozone in the 1.0-0.1 mbar region, *J. Geophys. Res.*, *89*(D7), 11,677–11,687, 1984.

Russell, J. M., L. L. Gordley, J. H. Park, S. R. Drayson, W. D. Hesketh, R. J. Cicerone, A. F. Tuck, J. E. Frederick, J. E. Harries, and P. J. Crutzen, The halogen occultation experiment, *J. Geophys. Res.*, *98*, 10,777–10,797, 1993.

Seftor, C. J., J. C. Larsen, Q. Remund, J. V. Rodriguez, L. E. Flynn, and E. Hilsenrath, The ozone mapping and profiler suite: Extending the BUV technique to meet future ozone measurement requirements, *Eos Trans. AGU*, *84*(46), Fall Meet. Suppl., Abstract A21D-1010, 2003.

Sioris, C. E., and W. F. J. Evans, Filling in of Fraunhofer and gas-absorption lines in sky spectra as caused by rotational Raman scattering, *Appl. Opt.*, *38*(12), 2706–2713, 1999.

Sioris, C. E., and C. S. Haley, Pixel-to-wavelength conversion for the optical spectrograph of OSIRIS, *OSIRIS Technical Report*, York University, 2001.

Sioris, C. E., C. von Savigny, R. L. Gattinger, J. C. McConnell, I. C. McDade, E. Griffioen, E. J. Llewellyn, and the ODIN Team, Attitude determination for limb-scanning satellites: The "knee" at 305 nm, *Eos Trans. AGU*, *82*(47), Fall Meet. Suppl., Abstract A32B-0056, 2001.

Sioris, C. E., W. F. J. Evans, R. L. Gattinger, I. C. McDade, D. A. Degenstein, and E. J. Llewellyn, Ground-based Ring-effect measurements with the OSIRIS development model, *Can. J. Phys.*, *80*(4), 483–491, 2002.

Sioris, C. E., C. S. Haley, C. A. McLinden, C. von Savigny, I. C. McDade, J. C. McConnell, W. F. J. Evans, N. D. Lloyd, E. J. Llewellyn, K. V. Chance, T. P. Kurosu, D. Murtagh, U. Frisk, K. Pfeilsticker, H. Bösch, F. Weidner, K. Strong, J. Stegman, and G. Mégie, Stratospheric profiles of nitrogen dioxide observed by OSIRIS on the Odin satellite, *J. Geophys. Res.*, *108*(D7), 4215, doi:10.1029/2002JD002672, 2003.

Sioris, C. E., C. A. McLinden, R. V. Martin, B. Sauvage, C. S. Haley, N. D. Lloyd, E. J. Llewellyn, P. F. Bernath, C. D. Boone, S. Brohede, and C. T. McElroy, Vertical profiles of lightning-produced NO_2 enhancements in the upper troposphere observed by OSIRIS, *Atmos. Chem. Phys.*, *7*, 4281–4294, 2007.

Solomon, S., R. R. Garcia, F. S. Rowland, and D. J. Wuebbles, On the depletion of Antarctic ozone, *Nature*, *321*, 755–758, 1986.

Stegman, J., OSIRIS spectral point spread function, *OSIRIS Technical Report*, Stockholm University, 1998.

Stegman, J., Absolute calibration for OSIRIS FM - ver 1.1, *OSIRIS Technical Report*, Stockholm University, 1999.

Stolarski, R. S., and R. J. Cicerone, Stratospheric chlorine: A possible sink for ozone, *Can. J. Chem.*, *52*, 1610–1615, 1974.

Stolarski, R. S., A. J. Krueger, M. R. Schoeberl, R. McPeters, P. Newman, and J. Alperr, Nimbus-7 satellite measurements of the springtime antarctic ozone decrease, *Nature*, *322*, 808–811, 1986.

Strong, K., B. Joseph, R. Dosanjh, I. C. McDade, C. A. McLinden, J. C. McConnell, J. Stegman, D. P. Murtagh, and E. J. Llewellyn, Retrieval of vertical concentration profiles from OSIRIS UV-visible limb spectra, *Can. J. Phys.*, *80*(4), 409–434, 2002.

Stutz, J., and U. Platt, Numerical analysis and estimation of the statistical error of differential optical absorption spectroscopy measurements with least-squares methods, *Appl. Opt.*, *35*(30), 6041–6053, 1996.

Taylor, J. R., K. Strong, C. A. McLinden, D. A. Degenstein, and C. S. Haley, Comparison of OSIRIS stratospheric NO_2 and O_3 measurements with ground-based Fourier transform spectrometer measurements at the Toronto Atmospheric Observatory, *Can. J. Phys.*, *85(11)*, 1301–1316, doi:10.1139/P07-144, 2007.

Thomas, G. E., and K. Stamnes, *Radiative Transfer in the Atmosphere and Ocean*, Cambridge University Press, 1999.

Thomas, G. E., C. A. Barth, E. R. Hansen, C. W. Hord, G. M. Mount, G. H. Rottmann, D. W. Rusch, A. I. Stewart, R. J. Thomas, J. London, P. L. Bailey, P. J. Crutzen, R. E. Dickenson, J. C. Gille, S. C. Liu, J. J. Noxon, and C. B. Farmer, Scientific objectives of the solar mesosphere explorer mission, *Pure Appl. Geophys.*, *118*, 591–615, 1980.

Thompson, A. M., J. C. Witte, R. D. McPeters, S. J. Oltmans, F. J. Schmidlin, J. A. Logan, M. Fujiwara, V. W. J. H. Kirchhoff, F. Posny, G. J. R. Coetzee, B. Hoegger, S. Kawakami, T. Ogawa, B. J. Johnson, H. Vömel, and G. Labow, Southern hemisphere additional ozonesondes (SHADOZ) 1998-2000 tropical ozone climatology 1. Comparison with total ozone mapping spectrometer (TOMS) and ground-based measurements, *J. Geophys. Res.*, *108*(D2), 8238, doi:10.1029/2001JD000967, 2003.

Tukiainen, S., S. Hassinen, A. Seppälä, H. Auvinen, E. Kyrölä, J. Tamminen, C. S. Haley, N. D. Lloyd, and P. T. Verronen, Description and validation of a limb scatter retrieval method for Odin/OSIRIS, *J. Geophys. Res.*, *113*, D04308, doi: doi:10.1029/2007JD008591, 2008.

Tung, K. K., M. K. W. Ko, J. M. Rodriguez, and N. D. Sze, Are Antarctic ozone variations a manifestation of dynamics or chemistry?, *Nature*, *333*, 811–814, 1986.

Urban, J., N. Lautié, E. Le Flochmoën, C. Jiménez, P. Eriksson, E. Dupuy, L. El Amraoui, M. Ekström, U. Frisk, D. Murtagh, J. de La Noë, M. Olberg, and P. Ricaud, Odin/SMR limb observations of stratospheric trace gases: Level 2 processing of ClO, N_2O, O_3, and HNO_3., *J. Geophys. Res.*, *110*, D14307, doi: 10.1029/2004JD005741, 2005.

Vandaele, A. C., C. Hermans, P. C. Simon, M. Carleer, R. Colin, S. Fally, M. F. Mérienne, A. Jenouvrier, and B. Coquart, Measurements of the NO_2 absorption cross-section from 42000 cm^{-1} to 10000 cm^{-1} (238-1000 nm) at 220 K and 294 K, *J. Quant. Spectrosc. Radiat. Transfer*, *59*(3–5), 171–184, 1998.

von Savigny, C., Retrieval of stratospheric ozone density profiles from OSIRIS scattered sunlight observations, Ph.D. Dissertation, York University, Toronto, Canada, 2002.

von Savigny, C., C. S. Haley, C. E. Sioris, I. C. McDade, E. J. Llewellyn, D. Degenstein, W. F. J. Evans, R. L. Gattinger, E. Griffioen, N. D. Lloyd, J. C. McConnell, C. A. McLinden, D. P. Murtagh, B. Solheim, and K. Strong, Stratospheric ozone

profiles retrieved from limb scattered sunlight radiance spectra measured by the OSIRIS instrument on the Odin satellite: Method and first results, *Geophys. Res. Lett.*, *30*(14), 1755, doi:10.1029/2002GL016401, 2003.

von Savigny, C., I. C. McDade, E. Griffioen, C. S. Haley, C. E. Sioris, and E. J. Llewellyn, Sensitivity studies and first validation of stratospheric ozone profile retrievals from Odin/OSIRIS observations of limb-scattered solar radiation, *Can. J. Phys.*, *83*, 957–972, doi:10.1139/P05-041, 2005.

von Schéele, F., The Swedish Odin satellite to eye heaven and Earth, in *Proc. 47th International Astronautical Congress*, 1996.

Warshaw, G., D. Desaulniers, and D. Degenstein, Optical design and performance of the Odin UV/visible spectrograph and infrared imager instrument, in *Proc. 12th Annual AIAA/USU Conference on Small Satellites*, 1998.

Watanabe, T., K. Suzuki, and K. Oyama, Observation of stratospheric ozone with MT-135 rockets in 1990-1999, *Inst. Space Astronaut. Sci. Rep.*, *679*, 1–81, 2001.

Waters, J. W., L. Froidevaux, R. S. Harwood, R. F. Jarnot, H. M. Pickett, W. G. Read, P. H. Siegel, R. E. Cofield, M. J. Filipiak, D. A. Flower, J. R. Holden, G. K. Lau, N. J. Livesey, G. L. Manney, H. C. Pumphrey, M. L. Santee, D. L. Wu, D. T. Cuddy, R. R. Lay, M. S. Loo, V. S. Perun, M. J. Schwartz, P. C. Stek, R. P. Thurstans, M. A. Boyles, S. Chandra, M. C. Chavez, G.-S. Chen, B. V. Chudasama, R. Dodge, R. A. Fuller, M. A. Girard, J. H. Jiang, Y. Jiang, B. W. Knosp, R. C. LaBelle, K. A. Lee, D. Miller, J. E. Oswald, N. C. Patel, D. M. Pukala, O. Quintero, D. M. Scaff, W. V. Snyder, M. C. Tope, P. A. Wagner, and M. J. Walch, The Earth Observing System Microwave Limb Sounder (EOS MLS) on the Aura satellite, *IEEE Trans. Geosci. Remote Sensing*, *44*(5), doi: 10.1109/TGRS.2006.873771, 2006.

Wofsy, S. C., and M. B. McElroy, HO_x, NO_x, and ClO_x: Their role in atmospheric photochemistry, *Can. J. Chem.*, *52*, 1582, 1974.

Wofsy, S. C., M. B. McElroy, and Y. L. Yung, OCLO diurnal photochemistry and implications for ozone destruction, *Geophys. Res. Lett.*, *2*, 215–218, 1975.

World Meteorological Organization, *Scientific Assessment of Ozone Depletion: 2006, Global Ozone Research and Monitoring Project, Report No. 50*, Geneva, Switzerland, 2007.

Appendix A

Paper I

A method for recovering stratospheric minor species densities from the Odin/OSIRIS scattered-sunlight measurements

Ian C. McDade, Kimberly Strong, Craig S. Haley, Jacek Stegman, Donal P. Murtagh, and Edward J. Llewellyn

Can. J. Phys.

80, 395-408, doi:10.1139/P01-152, 2002

A method for recovering stratospheric minor species densities from the Odin/OSIRIS scattered-sunlight measurements

Ian C. McDade, Kimberly Strong, Craig S. Haley, Jacek Stegman, Donal P. Murtagh, and Edward J. Llewellyn

Abstract: A method for recovering minor species density profiles in the stratosphere from observations made with the OSIRIS (optical spectrograph and infrared imager system) instrument on the Odin satellite is described. The OSIRIS instrument measures limb radiances of scattered sunlight over the spectral range 2800 to 8000 Å, for tangent heights ranging from 10 to 100 km. We describe how the limb spectra may be processed using the DOAS (differential optical absorption spectroscopy) technique to derive apparent column densities for the minor atmospheric constituents O_3, NO_2, OClO, and BrO. We also show how these column densities, measured over a range of tangent heights, may be inverted using an iterative least-squares technique to determine the local density profiles. The procedures are illustrated using simulated limb radiances generated with a realistic OSIRIS instrument model.

PACS Nos.: 42.68Mj, 94.10Dy

Résumé: Nous présentons une méthode pour recouvrer les profils de densité de composés mineurs de la stratosphère à partir des observations faites avec le détecteur OSIRIS (spectrographe optique et systéme d'imagerie infrarouge) à bord du satellite Odin. OSIRIS a pour mission de mesurer la radiance du limbe terrestre due à la diffusion de la lumière solaire dans le domaine de 2800 à 8000 Å pour des altitudes allant de 10 à 100 km. Nous montrons comment les spectres du limbe peuvent être analysés par DOAS (spectroscopie optique d'absorption différentielle) pour en déduire les variations verticales de densité des constituents mineurs de l'atmosphère, O3, NO2, OClO et BrO. Nous montrons aussi comment ces distributions verticales, mesurées pour une gamme d'altitudes, peuvent être inversées par une technique de moindres carrés pour déterminer les profils locaux de densité.

Received 7 June 1999. Accepted 15 January 2000. Published on the NRC Research Press Web site at http://cjp.nrc.ca/ on 4 April 2002.

I.C. McDade[1] **and C.S. Haley.** Centre for Research in Earth and Space Science, York University, 4700 Keele Street, Toronto, ON M3J 1P3, Canada.
K. Strong. Department of Physics, University of Toronto, 60 St. George Street, Toronto, ON M5S 1A7, Canada.
J. Stegman and D.P. Murtagh.[2] Department of Meteorology, University of Stockholm, S-106 91 Stockholm, Sweden.
E.J. Llewellyn. Department of Physics and Engineering Physics, University of Saskatchewan, 116 Science Place, Saskatoon, SK S7N 5E2, Canada.

[1] Corresponding author (email: mcdade@yorku.ca).
[2] Present Address: Department of Radio and Space Science, Chalmers University of Technology, SE-41296 Göteborg, Sweden.

 DOI: 10.1139/P01-152

Nous illustrons ici la procédure en utilisant des radiances de limbe générées par un modèle réaliste d'OSIRIS.

[Traduit par la Rédaction]

1. Introduction

OSIRIS (optical spectrograph and infrared imager system) is a Canadian instrument now flying on the Swedish–Canadian–French–Finnish Odin satellite [1, 2]. Odin is in a 97.8° inclination, Sun-synchronous near-terminator orbit, with ascending and descending nodes at 18:00 and 06:00 h, respectively. OSIRIS makes limb measurements of solar radiation scattered by the atmosphere during the daytime for the purposes of monitoring atmospheric composition and temperatures in the stratosphere and lower mesosphere. The OSIRIS measurements are made over the wavelength range of 2800 to 8000 Å, at a spectral resolution of about 10 Å, for tangent heights ranging from 10 to 100 km. One of the objectives of the OSIRIS instrument is to determine the local density profiles of the important minor atmospheric constituents O_3, NO_2, OClO, and BrO. In this paper, we describe one of the methods being developed to extract the O_3, NO_2, OClO, and BrO densities from the OSIRIS scattered-sunlight measurements. The method exploits (*i*) the DOAS (differential optical absorption spectroscopy) technique [3] to determine apparent column densities for each of the species as a function of tangent height, and (*ii*) an iterative least-squares (ILS) inversion algorithm to extract the O_3, NO_2, OClO, and BrO densities from the apparent column densities. An alternative method for extracting the O_3, NO_2, OClO, and BrO densities using the optimal estimation method of Rodgers [4] is described in a companion paper by Strong et al. [5].

2. DOAS processing of the Odin/OSIRIS observations

2.1. DOAS in a solar occultation case

To illustrate how the DOAS technique will be applied to the OSIRIS scattered-sunlight measurements, we first consider the related, but much more restrictive, observational technique of solar occultation. In solar occultation the intensity of the unattenuated solar radiation $I^o(\lambda)$ at wavelength λ is measured by a solar-pointing satellite instrument when the line of sight towards the Sun does not pass through the atmosphere. Subsequent measurements of the transmitted solar intensity, $I^{th}(\lambda)$, when the line of sight, defined by the tangent altitude th, passes through the atmosphere can be used to obtain the column density of any absorbing species along the line of sight. If only one species, with known absorption cross section $\sigma(\lambda)$ at wavelength λ, is responsible for the atmospheric attenuation of the sunlight, the column density along the line of sight, c^{th} (molecules/cm^2), can be readily obtained using the Beer–Lambert Law

$$\frac{I^{th}(\lambda)}{I^o(\lambda)} = \exp(-\sigma(\lambda)c^{th}) \quad \text{or} \quad c^{th} = \frac{\ln\left[\frac{I^o(\lambda)}{I^{th}(\lambda)}\right]}{\sigma(\lambda)} \tag{1}$$

where the dimensionless quantity $\sigma(\lambda)c^{th}$ is the optical depth, $D(\lambda)$. Note that in this discussion, we are ignoring instrumentation effects such as finite spectral resolution and are not including the effects of rotational Raman scattering.

Usually, more than one species absorbs at wavelength λ, and Rayleigh scattering by air molecules and scattering by atmospheric aerosols contribute to the extinction of the sunlight. This problem of having more than one absorbing species can be taken into account by making the observations over a range of wavelengths for which the individual absorption cross sections $\sigma_i(\lambda)$ vary. The effects of Rayleigh and aerosol extinction can be taken into account by recognizing that the Rayleigh and aerosol extinctions, represented by the Rayleigh and aerosol optical depths $e_R(\lambda)$ and $e_A(\lambda)$, are slowly varying functions of wavelength as opposed to the absorption cross sections $\sigma(\lambda)$, which are typically rich

in spectral structure. This is the basis of the DOAS approach [3], which assumes that the absorption cross-section spectrum, $\sigma(\lambda)$, can be represented by a component that varies slowly with wavelength, $\sigma^s(\lambda)$, and a differential component, $\sigma'(\lambda)$, which varies rapidly with wavelength, i.e.,

$$\sigma(\lambda) = \sigma^s(\lambda) + \sigma'(\lambda) \tag{2}$$

For a single absorbing species, the transmitted solar intensity $I^{th}(\lambda)$ can then be expressed as

$$I^{th}(\lambda) = I^o(\lambda) \exp\left\{-\left[\sigma^s(\lambda) + \sigma'(\lambda)\right] c^{th} - e_R^{th}(\lambda) - e_A^{th}(\lambda)\right\} \tag{3}$$

where $e_R^{th}(\lambda)$ and $e_A^{th}(\lambda)$ are the slowly varying Rayleigh and aerosol optical depths.

The total optical depth $D^{th}(\lambda)$, for a given tangent height, can then be written as

$$D(\lambda) = \ln\left[\frac{I^o(\lambda)}{I(\lambda)}\right] = \sigma'(\lambda)c + \left[\sigma^s(\lambda)c + e_R(\lambda) + e_A(\lambda)\right] \tag{4}$$

where the tangent height superscripts have been dropped for clarity.

If the measured total optical depth $D(\lambda)$ is resolved into its slowly and rapidly varying components $D^s(\lambda)$ and $D'(\lambda)$, the slowly varying component $D^s(\lambda)$ can be assigned to the slowly varying absorption and extinction components, i.e.,

$$D^s(\lambda) = \sigma^s(\lambda)c + e_R(\lambda) + e_A(\lambda) \tag{5}$$

and the rapidly varying, or differential, component $D'(\lambda)$ can be assigned to the rapidly varying component of the optical depth, i.e.,

$$D'(\lambda) = \sigma'(\lambda)c \tag{6}$$

The total column density of the absorbing species can then be obtained from

$$c = \frac{D'(\lambda)}{\sigma'(\lambda)} \tag{7}$$

where $D'(\lambda)$ is the rapidly varying component of the measured quantity $\ln[I^o(\lambda)/I(\lambda)]$.

For the case of more than one absorber, $D'(\lambda)$ can be expressed as

$$D'(\lambda) = \sigma_1'(\lambda)c_1 + \sigma_2'(\lambda)c_2 + \sigma_3'(\lambda)c_3 + \cdots \tag{8}$$

and the actual column density of each species, c_1, c_2, etc., can be obtained by fitting the observed $D'(\lambda)$ spectrum to the differential spectra of the individual species using standard linear regression.

2.2. DOAS in the Odin/OSIRIS case

In the case of OSIRIS, we do not make a direct solar transmission measurement, as in an occultation experiment, but continuously measure the sunlight scattered by the atmosphere on the dayside of the orbit, thus greatly enhancing the global coverage of the observations. The OSIRIS limb measurements are made within the orbital plane, and for a true terminator orbit the scattering angle and the solar zenith angle at the tangent point would both be 90°. However, since the Odin inclination is 97.8° the orbit only coincides with the terminator twice per year (once in October and once in February) and the scattering angle and solar zenith angle vary between 58.7° and 121.3°. Owing to this observing geometry, we do not have a simple external source of radiation against which to register transmission, rather, we have a continuum of internal Rayleigh-scattering sources along the instrument line of sight. This can be thought of as a collection of discretized sources along the line of sight. The spectral distribution and radiance of each of these discretized internal sources, $I_j^o(\lambda)$, for a single-scattering atmosphere is determined by

Fig. 1. Daytime limb-radiance spectra calculated for tangent heights of 20, 40, 60, and 80 km at 1 Å spectral resolution using MODTRAN [6].

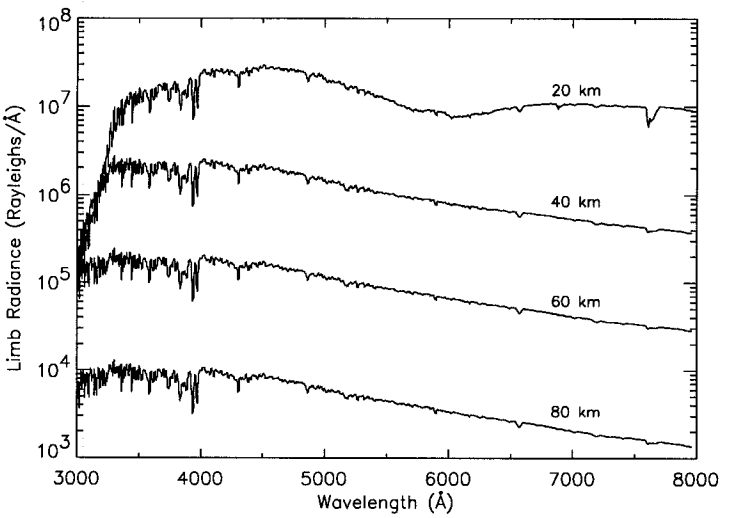

(*a*) the attenuation of the sunlight on its way in to each scattering point,

(*b*) the wavelength dependence of the Rayleigh-scattering cross section, and

(*c*) the density of the scattering molecules at point j.

For tangent heights above ~70 km the attenuation of the sunlight on its way in to each scattering point is negligible and the effective $I_j^o(\lambda)$ for each element along the line of sight for some lower tangent height can be characterized by a constant, B_j^{th}, times the spectral radiance $I^{\text{ref}}(\lambda)$ measured at a reference tangent height of say 70 km, i.e.,

$$I_j^o(\lambda) = B_j^{th} I^{\text{ref}}(\lambda) \tag{9}$$

where B_j^{th} depends on the tangent height and position of the jth source along the line of sight. By summing over all elements along a particular line of sight, we can define an effective $I^o(\lambda)$ for each tangent height as $I^o(\lambda) = B^{th} I^{\text{ref}}(\lambda)$. Then by analogy with the standard DOAS approach described above in Sect. 2.1, it can be shown that for a single absorbing species

$$\ln\left[\frac{B^{th} I^{\text{ref}}(\lambda)}{I^{th}(\lambda)}\right] = \sigma'(\lambda)c^{th} + \left[\sigma^{\text{s}}(\lambda)c^{th} + e_{\text{R}}^{th}(\lambda) + e_{\text{A}}^{th}(\lambda)\right] \tag{10}$$

where $I^{th}(\lambda)$ represents the radiance observed at tangent height th and c^{th} is the apparent column density of the absorbing species along the line of sight. This apparent column density is determined in part by absorption on the way in from the Sun to each scattering point and by absorption on the way out from each scattering point towards OSIRIS.

By rearrangement of (10) we obtain

$$R^{th}(\lambda) = \sigma'(\lambda)c^{th} + \left[\sigma^{\text{s}}(\lambda)c^{th} + e_{\text{R}}^{th}(\lambda) + e_{\text{A}}^{th}(\lambda) - \ln(B^{th})\right] \tag{11}$$

Fig. 2. Daytime limb-radiance spectra calculated with the MISU model for tangent heights of 20 and 70 km in the region where O_3, NO_2, OClO, and BrO are significant absorbers.

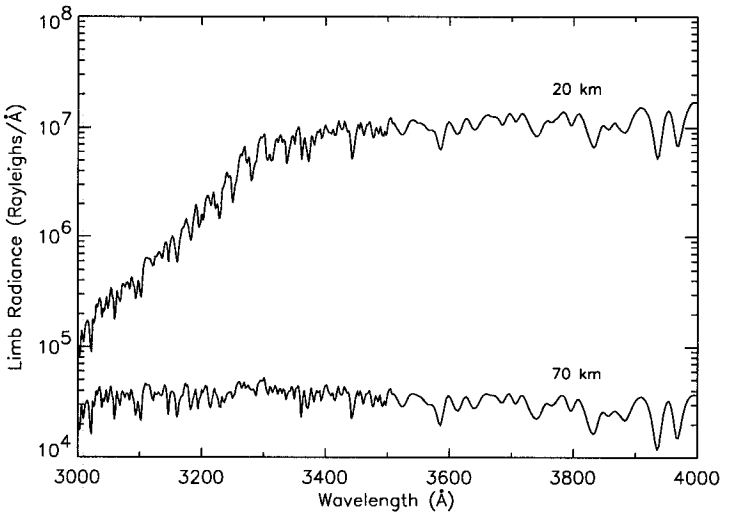

where $R^{th}(\lambda)$ is the natural logarithm of the ratio of $I^{\text{ref}}(\lambda)$, the radiance observed at the reference altitude, and the radiance $I^{th}(\lambda)$ observed at the lower tangent altitude th, that is

$$R^{th}(\lambda) = \ln\left[\frac{I^{\text{ref}}(\lambda)}{I^{th}(\lambda)}\right] \tag{12}$$

If $I^{\text{ref}}(\lambda)$ and $I^{th}(\lambda)$ are measured over a finite wavelength range then $R^{th}(\lambda)$ can be resolved into its components that vary rapidly and slowly with wavelength and we obtain

$$R(\lambda) = R'(\lambda) + R^{\text{s}}(\lambda) = \sigma'(\lambda)c + \left[\sigma^{\text{s}}(\lambda)c + e_{\text{R}}(\lambda) + e_{\text{A}}(\lambda) - \ln(B)\right] \tag{13}$$

where the $e_{\text{R}}(\lambda)$ and $e_{\text{A}}(\lambda)$ terms represent the apparent Rayleigh and aerosol optical depths and the th superscripts have again been omitted for clarity.

By assigning the rapidly varying component of $R(\lambda)$ to the rapidly varying component of the absorber optical depth, i.e., $R'(\lambda) = \sigma'(\lambda)c$, we can obtain the absorber apparent column density from $c = R'(\lambda)/\sigma'(\lambda)$ at any wavelength.

For the case of more than one absorbing species we have

$$R'(\lambda) = \sigma'_1(\lambda)c_1 + \sigma'_2(\lambda)c_2 + \sigma'_3(\lambda)c_3 + \cdots \tag{14}$$

and the individual species apparent column densities, c_1, c_2, etc., for each tangent height can be obtained by least-squares fitting the differential ratio $R'(\lambda)$ spectrum to the individual differential cross-section spectra using linear regression.

2.3. Illustration of DOAS recovery for OSIRIS observations

To demonstrate how the DOAS approach can be applied to the OSIRIS observations we show in Fig. 1 modelled daytime limb-radiance spectra calculated using the MODTRAN code [6] at a spectral resolution of 1 Å for a number of tangent heights. Figure 1 shows how the radiances generally increase exponentially with decreasing tangent height and shows how absorption features appear at lower tangent

Fig. 3. The natural logarithm of the ratio of the 70 and 20 km tangent height radiance spectra shown in Fig. 2.

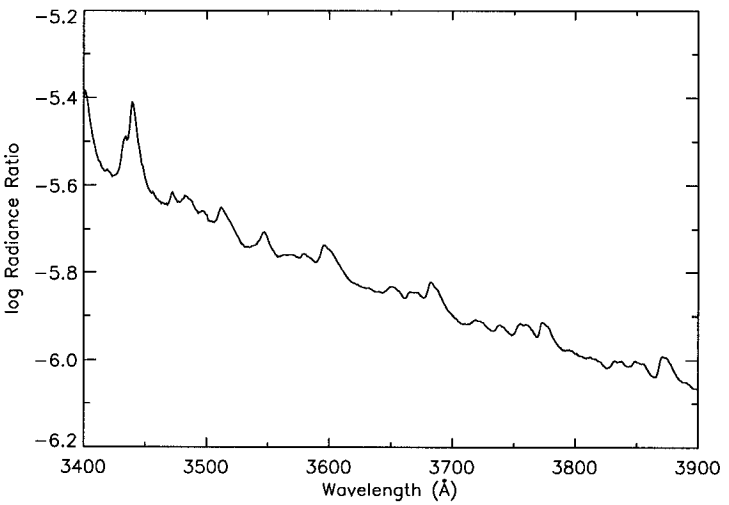

Table 1. DOAS fitting coefficients for a 20 km tangent height.

Absorber	Apparent column density
O_3	1.2×10^{20} molecules/cm^2
NO_2	1.3×10^{17} molecules/cm^2
OClO	4.2×10^{15} molecules/cm^2
BrO	4.0×10^{15} molecules/cm^2

heights. For example, in the 20 km spectrum, the broad O_3 Chappuis absorption between 5000 and 7000 Å and the narrower O_2 atmospheric (0-0) band absorption feature at 7620 Å are clearly evident.

Figure 2 shows more detailed 1 Å resolution 20 and 70 km tangent height spectra in the region where O_3, NO_2, OClO, and BrO are significant absorbers. The Fig. 2 spectra were obtained using the MISU (Meteorological Institute Stockholm University) single-scattering radiance model[3] which, unlike MODTRAN, incorporates absorption by O_3, NO_2, OClO, and BrO in the UV and visible regions. The radiances of Fig. 2 were calculated using a set of "standard" O_3, NO_2, OClO, and BrO density profiles for a nominal solar zenith angle of 80° and a scattering angle of 90°. For this study, aerosols were not included in the MISU model and a surface albedo of zero was adopted. Note that most of the obvious structure here arises from the structure in the solar spectrum and the decrease in the 20 km radiances below 3300 Å is due to strong absorption by O_3 and enhanced Rayleigh extinction.

In Fig. 3, we show the natural logarithm of the ratio of the 70 and 20 km radiances, i.e., $R(\lambda) = \ln[I^{\text{ref}=70}(\lambda)/I^{th=20}(\lambda)]$, for the 3400 to 3900 Å region. The high-frequency structure here is due to the absorption signatures of O_3, NO_2, OClO, and BrO and the general increase in the ratio towards shorter wavelengths is due to the effects of Rayleigh extinction in the 20 km radiances.

One simple way to perform a DOAS analysis of the Fig. 3 radiance ratios, and to resolve $R(\lambda)$ into its slowly and rapidly varying components, is to pass a simple boxcar filter across $R(\lambda)$. The resulting

[3] J. Stegman and D.P. Murtagh. Private communication.

Fig. 4. The differential component of the Fig. 3 log ratio spectrum obtained as described in the text (continuous line). The symbols show the fit obtained using the O_3, NO_2, OClO, and BrO differential absorption cross sections and the fitting coefficients listed in Table 1.

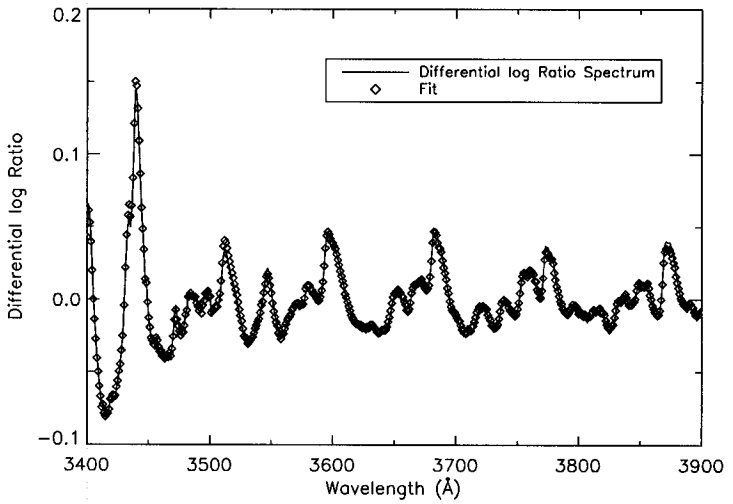

Fig. 5. The differential absorption spectra for O_3, NO_2, OClO, and BrO obtained as described in the text.

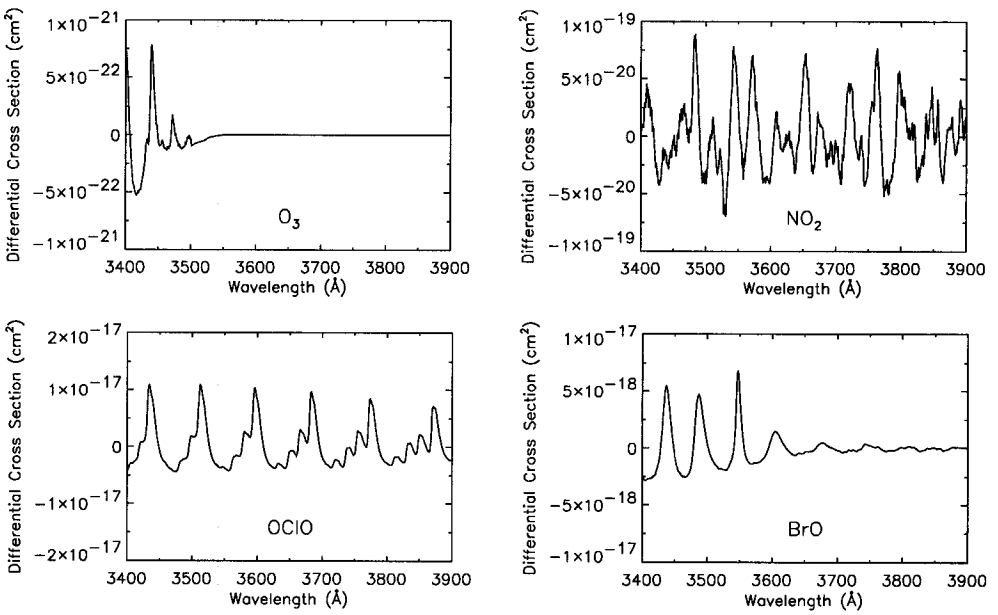

degraded spectrum is then subtracted from $R(\lambda)$ to obtain the differential component $R'(\lambda)$ required for the DOAS fit. The differential component thus obtained from the Fig. 3 values for $R(\lambda)$ using a 100 Å boxcar is shown in Fig. 4. The O_3, NO_2, OClO, and BrO differential absorption cross sections obtained in the same manner from the absolute cross sections of Molina and Molina [7], Schneider et al. [8], and Wahner et al. [9,10], respectively, are shown in Fig. 5.

Fig. 6. The line-of-sight geometric weighting functions appropriate to a solar occultation experiment for tangent heights of 20, 40, and 60 km (left panel) and the OSIRIS scattered-sunlight weighting functions (right panel).

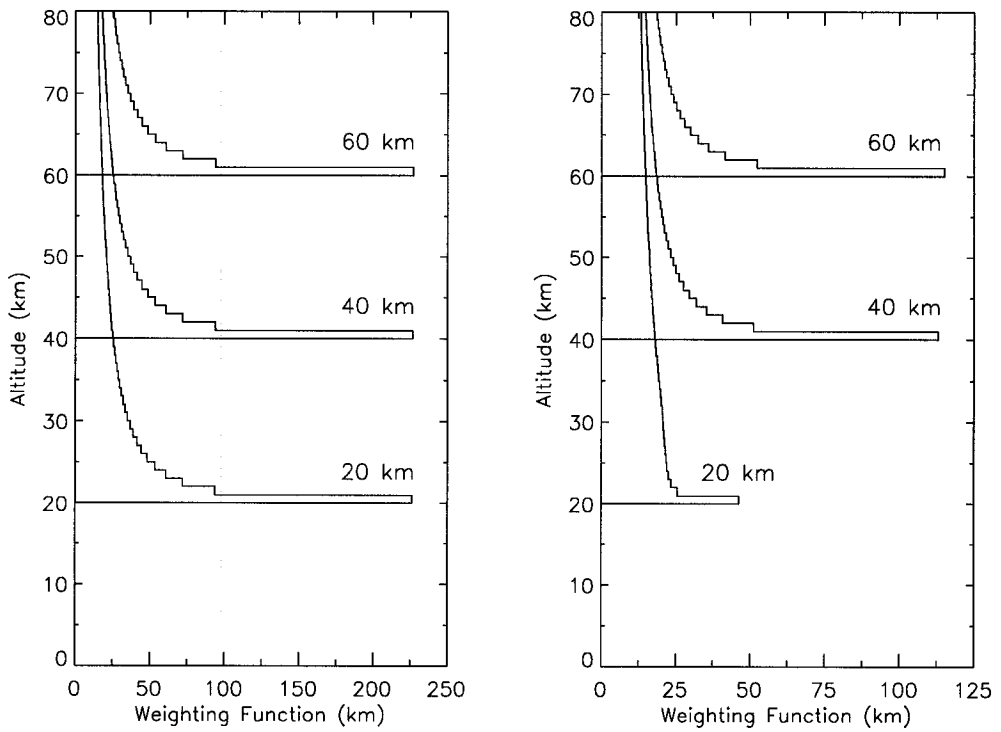

The final step in the DOAS process is to fit the differential log radiance ratios of Fig. 4 with the differential absorber cross sections of Fig. 5. The fitting coefficients from (14), obtained from a standard linear regression, provide the apparent column densities of O_3, NO_2, OClO, and BrO for the 20 km tangent height. The result of such a fit obtained with the O_3, NO_2, OClO, and BrO column densities listed in Table 1 is shown in Fig. 4.

By repeating this procedure using radiances measured at other tangent heights, profiles of the O_3, NO_2, OClO, and BrO apparent column densities can be obtained.

It should be noted that the apparent column densities thus obtained from scattered-sunlight limb radiances are not the same as the actual column densities along the instrument's geometric line of sight. The relationship between the apparent column densities and the line-of-sight column densities depends on the solar zenith angle and the spectral region used for the DOAS fit. For the case considered here, the actual column densities are about a factor of two larger than the apparent column densities.

3. Local density profiles from DOAS apparent column densities

To demonstrate how the O_3, NO_2, OClO, and BrO local number-density profiles can be extracted from a sequence of apparent column densities, obtained over a range of tangent heights, we again examine the problem in terms of the solar occultation analogue. For solar occultation, the relationship between the local density profiles and the measured sequence of column densities may be summarized as

$$\boldsymbol{C} = \boldsymbol{K}\boldsymbol{d} \tag{15}$$

where is $\boldsymbol{C}$ is an $m \times 1$ column vector representing the measured column densities of one specific species at m different tangent heights, $\boldsymbol{d}$ is an $n \times 1$ column vector representing the local densities of that species at n different altitudes, and $\boldsymbol{K}$ is an $m \times n$ weighting function matrix describing how the local densities at each altitude contribute to the column densities observed at each tangent height. For solar occultation, the K matrix is essentially made up of geometric path lengths through different atmospheric shells. For the case of $m = n$, the solution for the local number densities can formally be expressed as

$$\boldsymbol{d} = \boldsymbol{K}^{-1}\boldsymbol{C} \tag{16}$$

where $\boldsymbol{K}^{-1}$ is the inverse of the K matrix in (15).

In the case of the OSIRIS measurements, a similar relationship exists between the DOAS apparent column densities and the absorber density profiles. However, the K-matrix elements, or weighting functions, cannot be determined simply from geometric considerations.

3.1. The K-matrix elements

One approach for obtaining the K matrices for the OSIRIS observations is to use a forward radiance model such as the MISU model. The forward model is used to determine the apparent DOAS column densities that would be observed at each tangent height for known O_3, NO_2, OClO, and BrO density profiles. The density profile for one species is then perturbed by a small amount at some altitude, h, and the apparent column density of that species is redetermined for all tangent heights. The resulting change in column density for each tangent height, th, is divided by the absolute density perturbation made at height h to provide one column of the K matrix for that species. By repeating this procedure for all heights the entire K matrix can be obtained for each species.

A limitation of this approach is that an accurate and reliable forward model is required and this model should take into account all of the relevant physics including multiple scattering and surface albedo effects. A second limitation is that the K-matrix elements are not entirely independent of the minor species densities. The magnitude of this nonlinearity depends on the spectral region used for the DOAS recovery. For the simulations discussed here, the nonlinearity effects are relatively weak.

Examples of DOAS weighting functions for ozone calculated using the MISU forward model for a number of tangent heights are shown in Fig. 6, where they are compared with the line-of-sight geometric weighting functions appropriate to an occultation experiment. Note that the scattered-sunlight weighting functions are smaller than the geometric line-of-sight functions. This is consistent with the DOAS column densities being smaller than the line-of-sight column densities as discussed in Sect. 2.3. Also note that the peak value of the DOAS weighting function for a tangent height of 20 km is smaller than that for the 40 and 60 km cases. This is due to larger Rayleigh extinction at lower tangent heights, which leads to shorter effective optical paths.

3.2. The matrix inversion

In the ideal case of perfect linearity, (15) also holds for OSIRIS observations. The solution density vector $\boldsymbol{d}$ can then be found by direct matrix inversion, (16). Direct inversions, however, are notoriously prone to noise in the observational data. An alternative approach that is particularly robust, noise tolerant, and computationally efficient is based on the iterative least-squares (ILS) method originally due to Budinger and Gullberg [11] and applied to atmospheric problems by McDade and Llewellyn [12]. This method is also used for the tomographic inversion of the IR imager observations made with the OSIRIS instrument [13]. An alternative approach based on the optimal estimation method of Rodgers [4] is discussed by Strong et al. [5].

The ILS algorithm starts with an initial guess $\boldsymbol{d}'$ for the actual solution density vector $\boldsymbol{d}$ and iteratively adjusts $\boldsymbol{d}'$ until the reconstructed observation vector $\boldsymbol{C}' = \boldsymbol{K}\boldsymbol{d}'$ agrees with the actual observation vector $\boldsymbol{C}$ to within the observational errors through a χ^2 minimization technique. The final solution is quite

Fig. 7. Simulated DOAS apparent column densities for O_3, NO_2, OClO, and BrO as a function of tangent height. Note that the MISU model used identical OClO and BrO density profiles for this simulation.

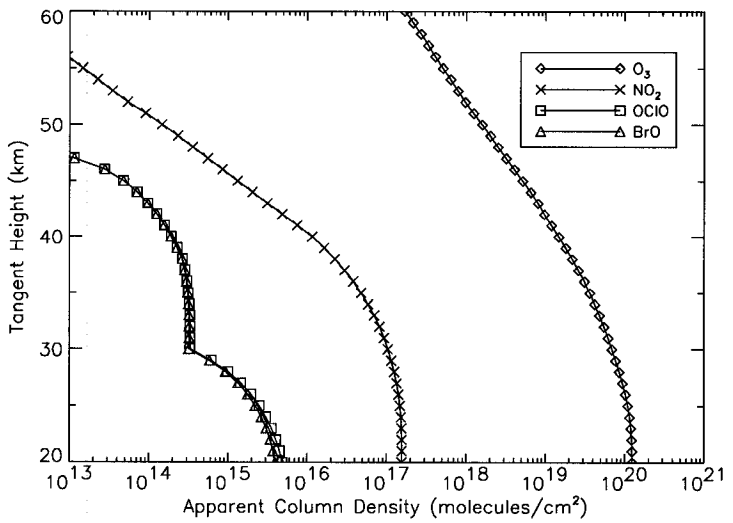

insensitive to the initial guess. Though the algorithm takes into account the estimated uncertainties in the observation vector, $\delta \boldsymbol{C}$, it should be noted that it does not provide useful statistics on the uncertainties in the solution vector.

To illustrate how the ILS inversion algorithm performs we consider the simulated O_3, NO_2, OClO, and BrO apparent column densities shown in Fig. 7. These column densities were obtained using the procedures described in Sect. 2 with radiances from the MISU forward model calculated at 1 Å resolution for a solar zenith angle of 80° and a scattering angle of 90°. The local number-density profiles recovered from the Fig. 7 apparent column densities using the ILS method are shown in Fig. 8 where they are compared with the actual O_3, NO_2, OClO, and BrO densities used in the MISU forward model. Note that for this simulation, OClO and BrO had identical density profiles within the MISU model. Clearly, for this high spectral resolution and noise-free simulation, the actual O_3, NO_2, OClO, and BrO densities are recovered with considerable fidelity, though small discrepancies, barely discernable in Fig. 8, do exist and arise from the weak nonlinearity.

4. OSIRIS simulations

The recoveries illustrated in the previous section do not take into account the effects of noise in the expected OSIRIS observations, nor do they include spectral degradation resulting from the actual instrument function. To assess how instrument noise and reduced spectral resolution will impact on the recoveries, a forward instrument model has been created to simulate the OSIRIS observations. Within this model, the MISU radiances are first convolved with a 10 Å boxcar to simulate the OSIRIS spectral resolution. The spectrally degraded radiances are then interpolated onto the nominal OSIRIS detector pixel wavelengths. The measured instrument flat-field responsivity (sensitivity to unpolarized light) is used to calculate the detected photon counts for each pixel assuming a specified integration time. Random Poisson noise is then added to each pixel count using the known detector characteristics – this allows for contributions from readout noise, photon shot noise, and dark current. As the OSIRIS instrument has 32 pixels for each wavelength bin, the individual pixel counts with noise added are summed in blocks of 32 to enhance the signal-to-noise ratio and to simulate the nominal OSIRIS operational mode. For each wavelength bin, uncertainties in the derived radiances are estimated using the procedures that will be

Fig. 8. The density profiles for O_3, NO_2, OClO, and BrO recovered from the ILS inversion of the Fig. 7 apparent column densities (symbols) and the actual densities used in the MISU forward model (continuous lines). Note that the actual OClO and BrO densities used for the simulation were the same.

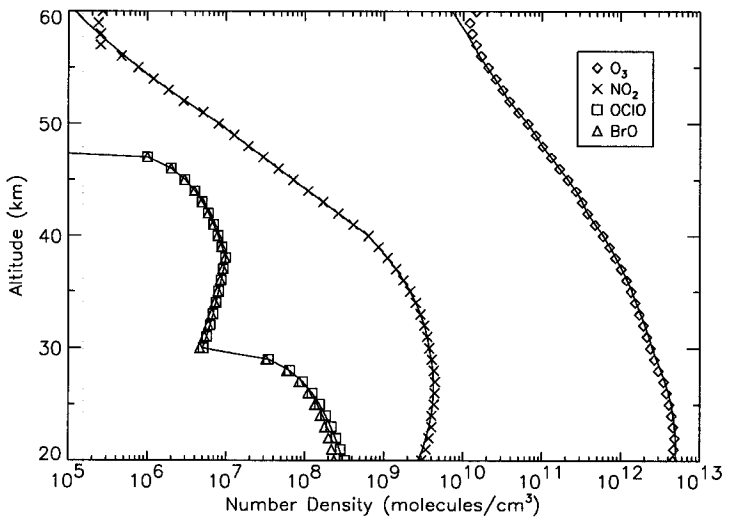

Fig. 9. A 30 km tangent height differential log ratio spectrum for the simulated OSIRIS radiances with noise and spectral resolution effects included (continuous line). The fit to the differential O_3, NO_2, OClO, and BrO absorption cross sections is shown by the symbols.

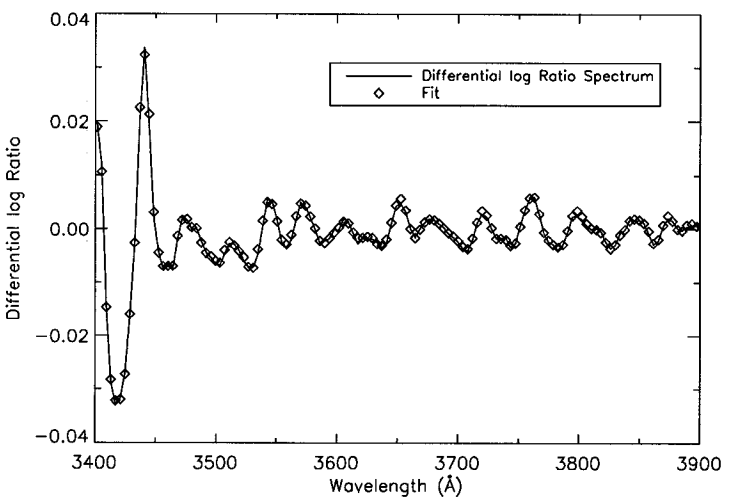

used for the processing of the actual OSIRIS data. Recoveries performed using the simulated OSIRIS radiances allow us to assess the precision with which O_3, NO_2, OClO, and BrO number densities may be obtained. For the DOAS processing of the simulated radiances, the absolute O_3, NO_2, OClO, and BrO absorption cross sections are also degraded to the instrument resolution and interpolated to the OSIRIS pixel wavelengths.

Figure 9 shows a typical simulated differential log ratio spectrum for a tangent height of 30 km together with the results of the DOAS fit to the O_3, NO_2, OClO, and BrO differential cross sections.

Fig. 10. The O_3, NO_2, OClO, and BrO apparent column density profiles obtained from the OSIRIS simulations that take into account the spectral resolution and noise characteristics of the instrument (symbols). The continuous lines show the column densities obtained without the effects of noise included.

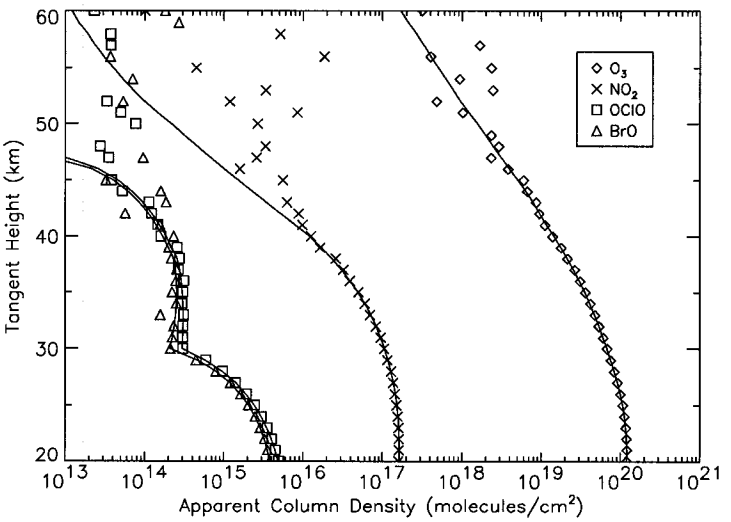

For this simulation, a noise-free 70 km spectrum was adopted as the reference. No noise was added to this 70 km spectrum since the reference spectra used for processing the actual OSIRIS data will be accumulated from a large number of high-altitude measurements. Note that the effects of noise are barely apparent in Fig. 9 but they do become apparent in the spectra for higher tangent heights. It should also be noted that Fig. 9 differs from Fig. 4 because of the lower spectral resolution of the former and different absorber signatures at 20 and 30 km. Figure 10 shows the O_3, NO_2, OClO, and BrO apparent column density profiles recovered from one complete simulated OSIRIS limb scan with DOAS processing of the limb radiances in the 3400 to 3900 Å region. These limb radiances were obtained for an integration time of 1 s at each tangent height and an Odin limb scan rate of 1 km/s.

Figure 11 shows the ozone number-density profile recovered from the ILS inversion of the ozone column densities shown in Fig. 10. Figure 11 also shows the actual ozone densities used in the MISU forward model. As noted above, the ILS algorithm does not provide error estimates for the recovered number densities. However, these errors may be estimated from the standard deviation of the densities recovered from a number of independent simulations performed using different sequences of random noise. The error bars on Fig. 11 indicate the estimated 1-σ uncertainties based on the standard deviation of the densities recovered at each height from 25 independent runs. Figure 11 shows that the ozone densities should be recoverable from a single OSIRIS limb scan with a precision of approximately $\pm 1\%$ between 20 and 30 km and better than $\pm 10\%$ between 30 and 40 km. This is more clearly illustrated in Fig. 12, which shows the 1-σ uncertainties expressed as a percentage of the actual ozone densities. At high altitudes the recovery is degraded due to reduced signal to noise in the measured radiance spectra and decreasing absorber signatures. It should be noted, however, that the precision at higher altitudes can be significantly improved with a separate DOAS analysis of radiances measured at shorter wavelengths where the ozone absorption signature is stronger. At lower altitudes, the uncertainties increase slightly because of increasing Rayleigh extinction, which reduces the magnitude of the weighting functions.

Figure 12 also shows the estimated percentage uncertainties associated with the NO_2 and OClO density recoveries. The BrO uncertainties are very similar to those for OClO and have, therefore, been omitted from Fig. 12 for clarity. In the case of NO_2, the recovery precision is not as good as for ozone. This is because even though the NO_2 differential cross sections are about a factor of 100 stronger, the

Fig. 11. The O_3 number densities recovered from the ozone apparent column densities of Fig. 10 that included noise (symbols) and the actual densities used in the MISU forward model (continuous line). The error bars show the 1-σ uncertainties based on the RMS deviation of the densities recovered at each altitude from 25 independent runs as described in the text.

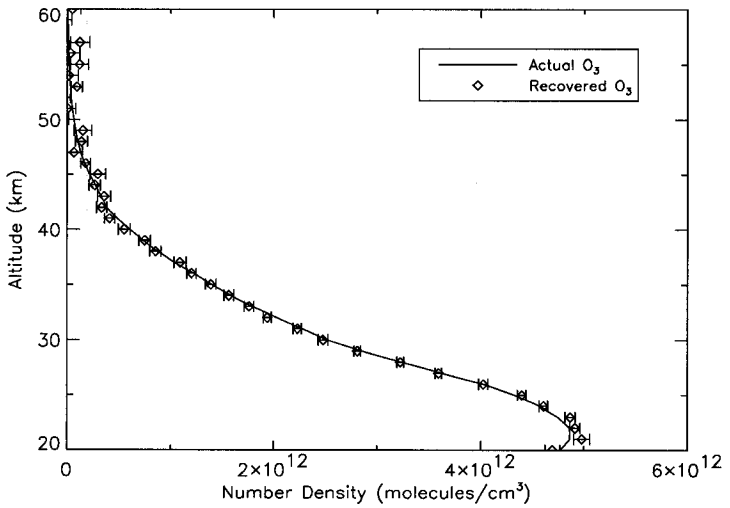

Fig. 12. The RMS deviation of the O_3, NO_2, and OClO densities recovered from 25 independent runs expressed as a percentage of the true densities at each height.

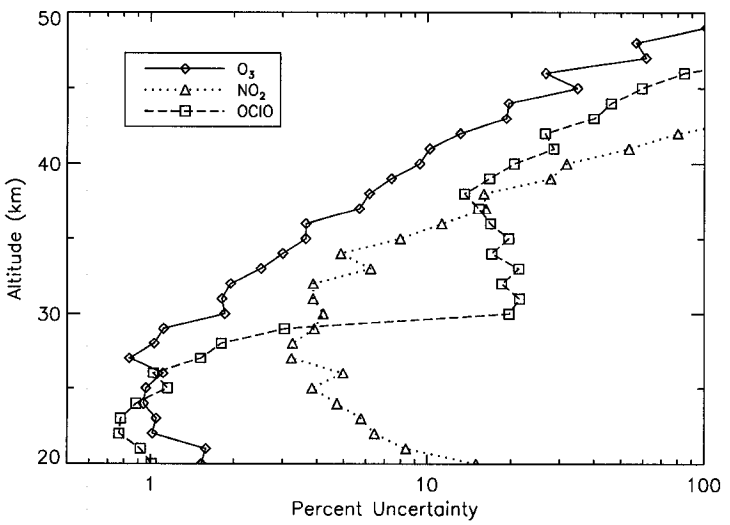

NO_2 densities used in the simulation are about a factor of 1000 smaller than ozone. As a result the NO_2 DOAS signature is about a factor of 10 smaller. For OClO and BrO the recovery precision is comparable to that for ozone in the 20 to 30 km region where their DOAS absorption signatures are similar to the ozone DOAS signature. At about 30 km the OClO and BrO uncertainties show a sharp increase which results from the sudden decrease in the OClO and BrO densities used in the MISU model (see Fig. 8). It should be noted that stratospheric OClO and BrO densities are highly variable and the ultimate precision with which the OClO and BrO densities will be recovered from the OSIRIS measurements will depend

on the actual densities encountered during the Odin mission.

5. Conclusions

A method for recovering O_3, NO_2, OClO, and BrO densities from OSIRIS scattered-sunlight measurements has been described. The method has been illustrated for the scenario of single scattering, no aerosols, and zero surface albedo. Procedures are presently being developed for dealing with multiple scattering, aerosols, and surface albedo effects using more sophisticated forward radiance models such as that described by McLinden et al. [14]. Preliminary results indicate that surface albedo and multiple-scattering effects introduce enhanced absorber signatures in the high-altitude reference spectrum. However, this effect is also reflected in the K-matrix elements obtained by perturbing a multiple-scattering forward radiance model and we find that the actual absorber density profiles can still be recovered when multiple-scattering effects are taken into account. Procedures are also being developed for dealing with nonlinearity, rotational Raman scattering (see ref. 15), and polarization effects.

Acknowledgements

Support for this work from the Canadian Space Agency and the Natural Sciences and Engineering Research Council of Canada is gratefully acknowledged.

References

1. E.J. Llewellyn, D.A. Degenstein, I.C. McDade et al. *In* Applications of photonic technology. *Edited by* G.A. Lampropoulos and R.A. Lessard. Plenum Press, New York. 1997. pp. 627–632.
2. D.P. Murtagh, U. Fisk, F. Merino et al. Can. J. Phys. **80** (2002). This issue.
3. U. Platt. *In* Air monitoring by spectroscopic techniques. *Edited by* M.W. Sigrist. John Wiley, New York. 1994. pp. 27–84.
4. C.D. Rodgers. Rev. Geophys. Space Phys. **14**, 609 (1976).
5. K. Strong, B.M. Joseph, R. Dosanjh, I.C. McDade, C.A. McLinden, J.C. McConnell, J. Stegman, D.P. Murtagh, and E.J. Llewellyn. Can. J. Phys. **80** (2002). This issue.
6. A. Berk, L. Bernstein, and D. Robertson. MODTRAN: A moderate resolution model for LOWTRAN 7. AFGL Tech. Rep. F19628-86-C-0079. Air Force Geophysics Laboratory, Hanscom AFB, Mass. 1989.
7. L.T. Molina and M.J. Molina. J. Geophys. Res. **91**, 14 501 (1986).
8. W. Schneider, G.K. Moortgat, G.S. Tyndall, and J.P. Burrows. J. Photochem. Photobiol. A: Chemistry **40**, 195 (1987).
9. A. Wahner, G.S. Tyndall, and A.R. Ravishankara. J. Phys. Chem. **91**, 2734 (1987).
10. A. Wahner, A.R. Ravishankara, S.P. Sander, and R.R. Friedl. Chem. Phys. Lett. **152**, 507 (1988).
11. T.F. Budinger and G.T. Gullberg. IEEE Trans. Nucl. Sci. **NS-21**, 2 (1974).
12. I.C. McDade and E.J. Llewellyn. Can. J. Phys. **69**, 1059 (1991).
13. D. Degenstein. Ph.D. thesis, University of Saskatchewan, Saskatoon, Sask. 1999.
14. C.A. McLinden, J.C. McConnell, E. Griffioen, and C.T. McElroy. Can. J. Phys. **80** (2002). This issue.
15. C.E. Sioris, W.F.J. Evans, R.L. Gattinger, I.C. McDade, D. Degenstein, and E.J. Llewellyn. Can. J. Phys. **80** (2002). This issue.

Appendix B

Paper II

Stratospheric profiles of nitrogen dioxide observed by Optical Spectrograph and Infrared Imager System on the Odin satellite

Christopher E. Sioris, Craig S. Haley, Chris A. McLinden, Christian von Savigny, Ian C. McDade, Jack C. McConnell, Wayne F.J. Evans, Nicholas D. Lloyd, Edward J. Llewellyn, Kelly V. Chance, Thomas P. Kurosu Donal P. Murtagh, Urban Frisk, Klaus Pfeilsticker, Hartmut Bösch, Frank Weidner, Kimberly Strong, Jacek Stegman, and Gérard Mégie

J. Geophys Res.

108(D7), 4215-4234, doi:10.1029/2002JD002672, 2003

JOURNAL OF GEOPHYSICAL RESEARCH, VOL. 108, NO. D7, 4215, doi:10.1029/2002JD002672, 2003

Stratospheric profiles of nitrogen dioxide observed by Optical Spectrograph and Infrared Imager System on the Odin satellite

Christopher E. Sioris,[1] Craig S. Haley,[2] Chris A. McLinden,[3] Christian von Savigny,[4] Ian C. McDade,[2] Jack C. McConnell,[2] Wayne F. J. Evans,[5] Nicholas D. Lloyd,[6] Edward J. Llewellyn,[6] Kelly V. Chance,[1] Thomas P. Kurosu,[1] Donal Murtagh,[7] Urban Frisk,[8] Klaus Pfeilsticker,[9] Hartmut Bösch,[9] Frank Weidner,[9] Kimberly Strong,[10] Jacek Stegman,[11] and Gérard Mégie[12]

Received 19 June 2002; revised 5 November 2002; accepted 19 December 2002; published 9 April 2003.

[1] Vertical profiles of nitrogen dioxide in the 19–40 km altitude range are successfully retrieved over the globe from Optical Spectrograph and Infrared Imager System (OSIRIS) limb scatter observations in late 2001 and early 2002. The inclusion of multiple scattering in the radiative transfer model used in the inversion algorithm allows for the retrieval of NO_2 down to 19 km. The slant column densities, which represent the observations in the inversion, are obtained by fitting the fine structure in normalized radiance spectra over the 435–449 nm range, where NO_2 electronic absorption is readily observable because of long light paths through stratospheric layers rich in this constituent. Details of the spectral fitting and inversion algorithm are discussed, including the discovery of a pseudo-absorber associated with pixelated detectors and a new method to verify altitude registration. Comparisons are made with spatially and temporally coincident profile measurements of this photochemically active trace gas. Better than 20% agreement is obtained with all correlative measurements over the common retrieval altitude range, confirming the validity of OSIRIS NO_2 profiles. Systematic biases in the number densities are not observed at any altitude. A "snapshot" meridional cross section between 40°N and 70°S is shown from observations during a fraction of an orbit. *INDEX TERMS:* 0340 Atmospheric Composition and Structure: Middle atmosphere—composition and chemistry; 0360 Atmospheric Composition and Structure: Transmission and scattering of radiation; 0394 Atmospheric Composition and Structure: Instruments and techniques; 3334 Meteorology and Atmospheric Dynamics: Middle atmosphere dynamics (0341, 0342); *KEYWORDS:* optical, Sun-synchronous, polar-orbiting, Fraunhofer, Ring effect, iterative onion peel

Citation: Sioris, C. E., et al., Stratospheric profiles of nitrogen dioxide observed by Optical Spectrograph and Infrared Imager System on the Odin satellite, *J. Geophys. Res.*, *108*(D7), 4215, doi:10.1029/2002JD002672, 2003.

1. Introduction

[2] *Crutzen* [1970] first discussed the importance of catalytic destruction of ozone by NO_x ($NO + NO_2$). Reactions involving NO_x dominate stratospheric ozone loss between 24 and ~45 km [*Garcia and Solomon*, 1994; *Crutzen*, 1971]. NO_x measurements in the lower stratosphere are also important because of the coupling with ClO_x and HO_x cycles. The loss of NO_2 through its conversion to HNO_3 can be used as a diagnostic of ozone hole heterogeneous chemistry. OSIRIS (Optical Spectrograph and Infrared Imager System) is capable of measuring not only profiles of stratospheric ozone [*von Savigny et al.*, 2003] but, as will be demonstrated here, the vertical

[1]Atomic and Molecular Physics Division, Harvard-Smithsonian Center for Astrophysics, Cambridge, Massachusetts, USA.
[2]Centre for Earth and Space Science, York University, Toronto, Ontario, Canada.
[3]Meteorological Service of Canada, Environment Canada, Toronto, Ontario, Canada.
[4]Institute of Environmental Physics, University of Bremen, Bremen, Germany.
[5]Department of Physics, Trent University, Peterborough, Ontario, Canada.
[6]Department of Physics and Engineering Physics, University of Saskatchewan, Saskatoon, Saskatchewan, Canada.
[7]Department of Radio and Space Science, Chalmers University, Göteberg, Sweden.
[8]Swedish Space Corporation, Solna, Sweden.
[9]Institute of Environmental Physics, University of Heidelberg, Heidelberg, Germany.
[10]Department of Physics, University of Toronto, Toronto, Ontario, Canada.
[11]Department of Meteorology, Stockholm University, Stockholm, Sweden.
[12]Service d'Aeronomie, Centre National de la Recherche Scientifique, Institut Pierre-Simon Laplace–Université Pierre et Marie Curie, Paris, France.

0148-0227/03/2002JD002672$09.00

distribution of nitrogen dioxide (NO_2) as well. It is one of two limb-viewing instruments onboard the Swedish Sun-synchronous satellite Odin. The other instrument is a sub-mm radiometer (SMR), which also observes the stratospheric limb.

[3] Odin is a small, low cost satellite that will split its expected lifetime of two years alternating between aeronomic and astronomic observation on a daily basis [*Murtagh et al.*, 2002]. As of February 20th of 2001, Odin ascends over the equator toward the North Pole at 6 pm local time in a near-terminator orbit at an inclination of 97.8°, providing 15 orbits/day. Its orbit is such that OSIRIS cannot make dayside measurements in the winter hemisphere near solstice. In terms of aeronomy, the main mission of Odin is to monitor the stratospheric ozone layer. This is achieved by spectral measurements of UV and visible limb radiance. The Odin satellite scans the limb at a rate of approximately 0.75 km/s and OSIRIS, which looks in the forward along-track direction, collects a spectral image every ~2 km in tangent height (TH). Scans usually cover the range from $7 \leq TH \leq 70$ km when Odin is in stratospheric mode and up to TH = 100 km in stratospheric-mesospheric (strat/meso) mode. One scan of the limb in stratospheric mode takes ~1.5 minutes, so the spacecraft will have covered ~600 km in the along-track direction (or ~5° in latitude).

[4] Thus far, the limb scatter technique from above the atmosphere has only been applied to the retrieval of two stratospheric gases: ozone (e.g., by SOLSE/LORE [*Flittner et al.*, 2000]) and NO_2 by the Solar Mesosphere Explorer (SME, [e.g., *Thomas et al.*, 1988, and references therein]). The SME was a two channel visible spectrometer with a 3.5 km field of view (FOV) that could only observe one NO_2 differential feature at a time. POAM (Polar Ozone and Aerosol Measurement) III and SAGE II also measure NO_2 profiles but only at twilight and thus have limited spatial and temporal coverage. Similarly to SME, both instruments use only one wavelength pair corresponding to one NO_2 spectral feature: 448 and 453 nm for SAGE II [*Cunnold et al.*, 1991], 439.6 and 442.2 nm for POAM III [*Lucke et al.*, 1999]. In contrast, the retrieval algorithm briefly described here uses 37 of the 1353 pixels in the part of the spectral range of OSIRIS where four of the most identifiable NO_2 vibronic absorption structures appear. Thus, for the above reasons, the NO_2 profiles retrieved from OSIRIS limb spectra rely on an improved technique in satellite remote sensing. The use of many wavelengths as compared to only an "on" and "off" wavelength pair allows for much better discrimination between optical depth due to NO_2 and that caused by ozone and scattering [*McElroy*, 1988].

[5] In this paper, we show an initial validation of NO_2 profile measurements for different times of day, year and for a variety of latitudes. Good limb scanning was first achieved in late June 2001. Fairly consistent limb scanning began in late July. Profile measurements presented here will come from August, October, and February data in particular. Sample profiles are validated with profiles from three other coincident instruments that possess equal or better vertical resolution than OSIRIS. This provides insight into the ability of OSIRIS and the inversion algorithm to retrieve the shape and magnitude of the number density profile. Validated global 3-D maps of NO_2 will be presented in future work.

2. Method

[6] A detailed description of the OSIRIS instrument is available elsewhere [*Warshaw et al.*, 1996; *Llewellyn et al.*, 1997]. Here we will highlight the important instrumental characteristics. OSIRIS has an instantaneous field of view (IFOV) of ~1 km in the vertical and 40 km in the across-track horizontal direction with the slit of the spectrograph being oriented parallel to the limb. Although spectral images of the limb are recorded presently every ~2 km in tangent height (TH), the vertical sampling can be improved at the expense of a lower signal to noise (S/N) ratio with simple software changes to the auto-exposure algorithm. Across-track horizontal inhomogeneities can be resolved as the 40 km swath is provided by 32 pixel rows in the spatial dimension of the 2-D charge-coupled device (CCD). These 32 rows are binned together by default to reduce the data flow and improve S/N. Thus, ~1 km horizontal sampling is achievable when OSIRIS images in the across-track dimension. The IFOV of OSIRIS compares favourably with that of the recently launched SCIAMACHY in limb viewing mode [*Bovensmann et al.*, 1999]. In the spectral dimension, OSIRIS measures electromagnetic radiation in the 280–800 nm range with ~1 nm spectral resolution (full-width at half-maximum) and each of its 1353 CCD detector pixels cover ~0.4 nm in the spectral domain, leading to a fairly well sampled spectrum.

[7] The retrieval of NO_2 profiles is considerably simplified by separating it into two smaller problems [*McDade et al.*, 2002]. The first step is to determine the observed slant column densities (SCDs) of NO_2 by linear least squares fitting of the observed differential spectral structure. The second step is the inversion of the slant column density profiles to obtain local number density profiles. A global fitting approach [*Carlotti*, 1988] where all spectra and all tangent heights in a limb scan are fit by varying concentrations of a number of different absorbing constituents at a number of different heights was judged to be too computationally expensive and more complicated with regards to troubleshooting.

2.1. Spectral Fitting

2.1.1. Fraunhofer Reference

[8] The differential optical absorption spectroscopy (DOAS) technique [*Noxon*, 1975] is used for the spectral fitting with some modifications. High TH spectra ($50 < TH < 70$ km, even in strat/meso mode) from the same limb scan are co-added and used as a Fraunhofer reference spectrum (I_0) as they contain only weak NO_2 absorption from multiply scattered contributions to the source function. The near-terminator orbit leads to high solar zenith angles (SZA > 57°), thereby significantly reducing the impact of clouds and surface reflection. The normalization with lower mesospheric spectra from the same limb scan further reduces the importance of any underlying tropospheric signature as it cancels out to a first approximation in the ratio because the multiple-scattering contribution is only weakly altitude-dependent above 20 km [*Sioris*, 2001]. This point will be readdressed below.

2.1.2. Spectral Fitting Window

[9] The fitting window is chosen to be 434.7–449.0 nm because the largest differential NO_2 absorption structures lie therein. Differential optical depths (DODs) are as large as 2% at the peak of the slant column density profile. The fitting window must be kept small enough that the extinction over the fitting window is roughly constant otherwise the SCD is wavelength (λ) dependent. However, the window must contain enough pixels that none of the absorbers (or pseudo-absorbers) are strongly correlated and S/N is improved. The chosen window also avoids major Fraunhofer lines at ~431 and 434 nm. Large solar absorption features do not cancel completely regardless of which reference is used.

2.1.3. Ring Effect

[10] One reason for the imperfect cancellation is that a lower mesospheric reference is expected to have a different Ring effect signature [*Grainger and Ring*, 1962] than stratospheric limb spectra since temperature, aerosols, and multiple scattering are a function of altitude [*Sioris*, 2001] (available from www.geocities.com/csioris/thesis3.zip). The impact of residual Ring structures due to the altitude dependence of multiple scattering and filling in of NO_2 lines is quite small (leads to residuals on the order of 6×10^{-4} or less) in the 353–387 nm OClO fitting window for OSIRIS as shown using radiative transfer model (RTM) simulations [*Sioris*, 2001]. The temperature dependence of the rotational Raman scattering (RRS) cross sections can produce residual structures one order of magnitude larger ($\sim 10^{-3}$) and is much more important for limb viewing than in other geometries where the Ring effect has been observed (i.e., satellite-nadir [*Joiner et al.*, 1995], ground-based [*Sioris et al.*, 2002]) because radiance contribution functions peak more sharply at a certain altitude (or temperature) for limb viewing, usually at the tangent height. The residual does not match the filling-in spectral structure itself and is largest when the difference in effective temperature between the reference TH and the TH of interest is a maximum. The dilution of the inelastic signature of molecular scattering by elastic scattering from aerosols can be the most important of these altitude-dependent effects, particularly at longer wavelengths [*Sioris*, 2001].

[11] Before the observed spectral structure is fitted with the various absorbers and pseudo-absorbers, the Ring effect is removed from limb spectra in the 15 < TH (km) < 70 range with a single iteration of the backward Ring model [*Sioris et al.*, 2002]. To correct the radiance spectrum (I) at a given tangent height, the temperature at the tangent height is assumed to be the effective temperature for the calculation of the RRS cross sections. The temperature profile is currently obtained as a function of latitude, longitude and time from the MSIS-E-90 model [*Hedin*, 1991] and only needs to be moderately accurate (i.e., ~8 K [*Sioris*, 2001]). The current implementation of the backward model assumes a purely molecular scattering atmosphere, although in the case of a significant injection of particulate matter into the stratosphere an iterative version of the model [*Sioris*, 2001] would be implemented.

2.1.4. Spectral Radiance Calibration

[12] Only one other step was required before beginning the spectral fitting. This involved recalibrating OSIRIS wavelengths by cross-correlation of a single normalized limb radiance spectrum from early in the mission (July 30th, 2001) with the NO_2 cross section [*Vandaele et al.*, 1998] convolved to OSIRIS resolution. No shifting or stretching has been applied subsequently and does not appear to be required based on analysis of spectral fits. This is consistent with the fact that the detector temperature has remained cool and steady throughout the period analyzed here. During an individual scan such as the down-scan containing the aforementioned spectrum, the detector temperature was -18.21 ± 0.05 °C. This suggests that wavelength stability should be very good over one limb scan and dark current should be minimal. Internal scattering, defined elsewhere [*Sioris et al.*, 2002], is extremely small (γ = 2e-6) based on analysis of in-flight radiance profiles at short wavelengths (<305 nm) and low TH where little signal is expected. This value of γ is slightly lower than the value measured in laboratory tests on the flight model [*Evans and Alfred*, 2001]. Thus, in the 435–450 nm interval, internal scattering is trivial relative to the signal. Wood's anomalies are another cause of artificial spectral structure. The closure polynomial adequately removes any instrumental sensitivity to the Q (and U) Stokes component of the polarization as fortunately OSIRIS has no Wood's anomalies in this spectral interval [*McLinden et al.*, 2002]. Also, baffle scattering does not appear to be a significant issue in the blue for TH < 70 km. This was confirmed by examining the linearity of a plot of ln(radiance) vs. TH above the stratospheric aerosol layer.

2.1.5. Absorbers

[13] For stratospheric tangent heights, the differential absorption in this fitting window is almost entirely caused by absorption by NO_2 and O_3. A known atmospheric feature due to water vapour at ~442.6 nm regularly observed from nadir and zenith-viewing geometry [e.g., *Johnston and MacKenzie*, 1989] has not appeared in the normalized limb radiance spectra. Water vapour reference spectra [*Camy-Peyret et al.*, 1985; *Zobov et al.*, 2000] have not helped fits. We have also not been able to match the absorption feature of the O_2-O_2 collisional complex at 446.7 nm [*Greenblatt et al.*, 1990] although this is not surprising considering that for similar observing geometry and path lengths, *Pfeilsticker et al.* [2001] only retrieved the vertical profile of the O_2-O_2 collisional complex up to 14 km. Thus, these are expected to be interfering species at lower tangent heights. The absolute absorption cross section of NO_2 at 220 K of *Vandaele et al.* [1998] is chosen because it is the current HITRAN standard and is accurate to <3%. Also, SCIAMACHY laboratory reference data at 203, 223, and 243 K [*Bogumil et al.*, 1999] are used because of the number of available temperatures and the known, albeit weak temperature dependence of NO_2 absorption in this spectral range [e.g., *Vandaele et al.*, 1998]. For ozone, the cross section of *Burrows et al.* [1999a] at 202 K was chosen although in the fitting window, the ozone differential absorption is spectrally smooth and/or weak enough that the SCD profile of this interfering trace gas cannot be recovered reliably and is correlated with the closure polynomial. These absorption cross sections are convolved and binned to instrumental parameters of the optical spectrograph (OS). The convolution takes into account the spectral resolution of the source instrument (e.g., SCIAMACHY) by assuming that all

instrument functions are well approximated by a gaussian line shape.

2.1.6. Differential Cross Sections

[14] The differential cross sections are obtained by fitting a low order polynomial to each of the absolute cross sections over a larger spectral range than the fitting window to ensure that the spectrally smooth component of the absorption is removed without fitting any of the fine structure with the polynomial. Polynomials are in terms of pixel number (n) starting with 1 at the blue end of the differential window and the increment is 1 per pixel. This allows a low order polynomial to be more flexible than a polynomial in wavelength. The difference between using differential and absolute cross sections was found to be trivial in this fitting window, as the polynomial closure term in equation (1) appears to compensate for the spectrally smooth component of the NO_2 and ozone absorption.

2.1.7. Temperature Dependence

[15] Intermediate temperatures (e.g., T = 216 K) are obtained by linear interpolation between differential forms of the *Bogumil et al.* [1999] set of NO_2 cross sections. The ensemble of different temperatures (e.g., 203, 216, 220, 223, 243) are tried sequentially (not simultaneously) with each normalized radiance spectrum and the SCD for that observation is the SCD obtained with the NO_2 cross section giving the smallest fitting residual. Differential cross sections linearly interpolated to an intermediate temperature (i.e., 216 K) did not work well. In general, the most effective cross section is that of *Vandaele et al.* [1998] at 220 K followed by that of Bogumil et al. at 203 K. It appears that the temperature dependence of NO_2 is secondary in importance to the quality of the reference spectra. The best method to handle this temperature dependence is still under investigation.

2.1.8. Fitting Equation

[16] The linear regression model is

$$\ln(I_0/I) = SCD_{NO_2} d\sigma_{NO_2}(T) + SCD_{O_3} d\sigma_{O_3}(T) + c_{tilt} dtilt + A n^2 + B n + C, \quad (1)$$

where I is the radiance spectrum at the tangent height of interest, $d\sigma$ are the differential absorber cross sections, and c_{tilt} is the fitting coefficient for the tilt differential pseudo-absorber cross section (dtilt) described below. At high optical depths, the normalized radiance is highly sloped (i.e., wavelength trended) even over a narrow fitting window and up to a 4th order polynomial may be required. The optimal handling of the closure polynomial remains under investigation. The direct fitting method [*Chance*, 1998], in which $-\ln(I_0)$ is used as a basis function in fitting $-\ln I$, gives slightly larger uncertainties and residuals than simultaneous fitting of $\ln(I_0/I)$ for the cases we have attempted. We are unsure of the reason for this and further testing is required.

2.1.9. Tilt

[17] Fraunhofer structure does not cancel out in the normalization for a second reason, which to our knowledge, has not been discussed previously. It results partly from spectral undersampling. A sampling ratio of $\geq$4.5 pixels/FWHM is typically required in fitting NO_2 [*Roscoe et al.*, 1996]. This is almost twice the sampling ratio of OSIRIS and more than twice the sampling ratio of GOME in this window [*Burrows et al.*, 1999a]. It was noticed that, in OSIRIS limb radiance profiles, the pixel with the local minimum in radiance corresponding to a Fraunhofer line centre is a function of tangent height. The effect is partially attributable to the physical discretization of the spectral radiance by pixelated detectors and also due to the differently sloped continua of I and I_0. Spectral fine structure is introduced in the wings of Fraunhofer lines when the spectrum of interest and the spectrum used for normalization (i.e., TH = 70 km) do not have the same slope. The largest spectral structure is introduced when the core of a Fraunhofer line lies near the boundary between two adjacent pixels and is further compounded by instruments with "dead space" between pixels. The differences in slope are due to atmospheric processes; Rayleigh extinction, and Mie scattering are functions of altitude and either process can explain this effect. The difference in slope results in a different partitioning of the Fraunhofer line in the adjacent pixels. Because of the strong wavelength dependence of Rayleigh scattering, this phenomenon is most pronounced in the blue and UV and is aggravated by the long paths provided by limb viewing geometry. Hγ is an example of a Fraunhofer line for which the pixel with the minimum radiance actually depends on TH. The difference in superimposed NO_2 absorption between the pixels is not significant to the apparent line depth of Hγ. RRS also cannot cause this effect because the filling in is quite symmetrical about the line centre, especially for narrow (<0.9 nm) lines [*Sioris et al.*, 2002]. At low tangent heights, the pixel with the minimum radiance at Hγ shifts to the blue by one pixel due to Rayleigh extinction.

[18] To remove this atmospheric/instrumental spectral artefact we have dubbed 'tilt', we have used a combination of atmospheric and instrumental radiative transfer modelling to generate a pseudo-absorber spectrum to be used in the NO_2 fitting. Using MODTRAN4 [*Berk et al.*, 1999], the first step involved calculating highly resolved and sampled (1 cm^{-1}) spectral radiances at a low and high TH (16 and 70 km, respectively) for a non-absorbing atmosphere. We then convolved both these spectra and binned them according to the OSIRIS pixel-to-wavelength mapping and spectral resolution. After taking the ratio of the two spectra, and removing trending in the ratio with a quadratic, the fine structure introduced by this phenomenon was revealed (Figure 1). This pseudo-absorber has reduced fit residuals by a factor of two. In general, it appears to be important when: (1) spectral fitting windows include strong Fraunhofer lines; (2) the slope of the reference spectrum and spectrum of interest are not identical; and (3) detectors have pixels with intermediate spectral widths. When pixels or bandpasses are much wider than the apparent Fraunhofer line width, Fraunhofer structure becomes less important, e.g., NO_2 channels of POAM III. When pixels are much narrower than a strong Fraunhofer line, there are a sufficient number of bins over its width leading an adequate representation of its shape. This is the case for GOME channel 2 where a pixel is 0.11 nm wide and the equivalent width of the Fe I line at 358 nm is 0.21 nm [*Moore et al.*, 1966] even prior to convolution with the 0.17 nm FWHM instrument function of GOME [*Burrows et al.*, 1999b].

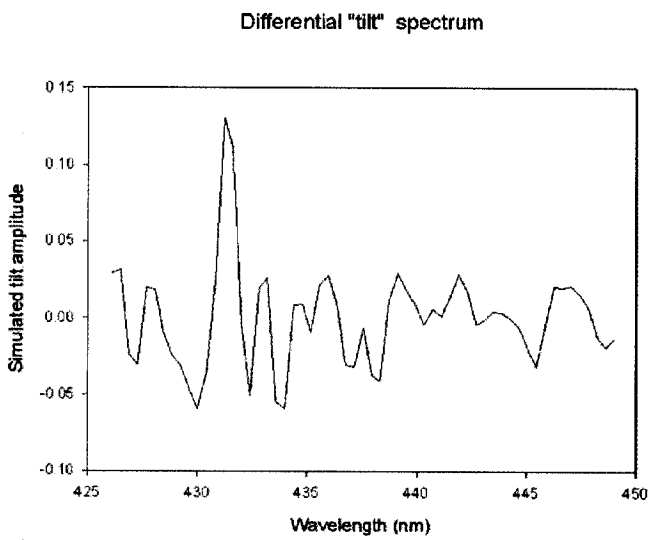

Figure 1. Simulated differential 'tilt' spectrum, appropriate for OSIRIS spectral resolution and binning in the 426–449 nm interval (see text for details).

[19] Based on simulations for the GOME BrO fitting window [*Chance*, 1998] with a solar reference and nadir radiance spectrum, we have calculated the importance of the pseudo-absorber and it is negligible (rms DOD of 7.7e-5) due partly to the narrower spectral binning of this instrument, whereas for OSIRIS, in the same fitting window, the 'tilt' rms DOD is 3.5e-4. In the NO_2 window, the 'tilt' rms DOD of OSIRIS is 1.0e-4. It is quite surprising that this effect was not discovered previously from observations made with detector pixels of intermediate spectral width, although an undersampling pseudo-absorber [e.g., *Chance*, 1998] or a shift and/or stretch algorithm [e.g., *Platt et al.*, 1997; *Sioris et al.*, 2002] could be partially compensating for the structure without including the essential physics of the phenomenon, as could smoothing of differential spectral structure. Fortunately NO_2, O_3 and 'tilt' are not strongly correlated with each other for OSIRIS in this fitting window so the inclusion of the tilt reference spectrum reduces the uncertainty of the retrieved NO_2 SCD but has no impact on the SCD itself.

2.2. Vertical Fitting: Inversion Algorithm

[20] After the SCDs of NO_2 are obtained as a function of tangent height, they are inverted to a yield a number density profile using a novel, iterative onion peeling (IOP) approach.

[21] The inversion consists of simulating SCDs in 2 km increments in TH and iteratively adjusting the number density profile until the simulated and measured SCDs converge at all tangent heights (18–40 km). In terms of vertically fitting the observed SCD profile with a simulated one, the method resembles the iterative least-squares inversion of *McDade et al.* [2002].

[22] The number densities are adjusted on the same 2 km grid. The grid is chosen to be comparable to the expected vertical resolution determined from averaging kernel calculations [*Strong et al.*, 2002]. A finer grid for the retrieval results in a zigzagging profile because the problem becomes underdetermined. The measured SCDs are interpolated onto the same grid using linear interpolation between the nearest two sampled THs or when vertical sampling is poor (ΔTH > 4.0 km), a 6th order polynomial fit (with typical $r^2 > 0.99$) to SCDs at THs sampled between 18–40 km is used. Interpolating the measured radiances onto the standard grid rather than the SCDs obscures the impact of satellite jitter in the retrieved SCD profile. Jitter during a down-scan affects S/N as the auto-exposure algorithm sets an exposure time appropriate for a lower (i.e., brighter) TH. The SCD uncertainties or χ^2 values from the linear least-squares fit can be used to determine which images were affected by jitter. These are omitted from the sextic fit to the SCD profile. Linear interpolation of SCDs is insufficient when the vertical sampling is poor (i.e., 4 km) due to irregular scanning (jitter) and results in an artefact in the retrieved number density at the height of the interpolation (and poor sampling).

[23] The OSIRIS tangent heights that are provided by the attitude control system (ACS) of Odin are verified independently (and occasionally corrected) using the 305 nm limb radiance profile. The quoted accuracy of the THs from the Odin ACS is <1.5 km. The tangent altitude of the 305 nm limb radiance maximum or 'knee' [*McPeters et al.*, 2000] is known from radiative transfer modeling and is insensitive to tropospheric clouds, surface albedo, and stratospheric aerosol because the upwelling radiation from the troposphere and lower stratosphere has been absorbed by stratospheric ozone. Using sensitivity studies, we have established that the knee is also very insensitive to temperature-related changes in number density and ozone absorption due to the weak temperature dependence at 305 nm. O_3

absorption is the main cause of the 305 nm knee. At 45 km, the overlying ozone column is largely governed by photochemistry, except at high latitudes [*Hilsenrath*, 1980], making it quite predictable. Observations over several orbits with OSIRIS and model calculations show the knee at 305 nm is at ~45 km. The insensitivity of the knee to these spatially variable geophysical parameters implies that the instrument measuring the limb radiance profile need not be a vertical imager for this technique to be applicable. Although the 305 nm knee exhibits some sensitivity to SZA, pressure, and mesospheric ozone, it is predictable using appropriate model atmospheres and scattering geometry. The precision of this technique is drastically improved by using spectral sampling to overcome Odin's vertical undersampling. A randomly chosen example from June 19th, 2001, at lat = 82°, and SZA = 59° will be presented to illustrate this technique. The first step is to find a set of pixel wavelengths that share the same knee TH using radiances on the measured TH grid such that the median wavelength is <305 nm. For this limb scan, there are exactly 6 pixel wavelengths ranging from 303.72–305.67 nm for which the knee is at TH = 45.589 km. For $\lambda < 303.7$ nm, the respective 'knees' are at higher THs and for $\lambda > 305.7$ nm, the 'knees' are at lower THs. The median wavelength of those six is 304.70 nm. Using vertically well-sampled simulations at 304.70 nm with MODTRAN4 for high-latitude summer and the appropriate geometry gives 45.6 km, indicating a difference between OSIRIS and MODTRAN4 of −11 m. After repeating this exercise at mid-latitudes over several orbits of data, the difference between the simulated and measured knee has a mean and standard deviation of 550 and 480 m, respectively. The non-zero mean is expected because the THs provided by the ACS do not include an accurate adjustment for the difference between the OSIRIS viewing angle and the Odin control frame. At high latitudes, it appears that due to its variability on timescales shorter than seasonal, the mesospheric O_3 column must be retrieved before or simultaneously with TH. Assuming accurate knowledge of pressure and mesospheric O_3, the overall accuracy of the technique approaches the limit imposed by the finite spectral sampling and resolution of OSIRIS and is <220 m.

[24] MODTRAN4 is the forward RTM used to simulate limb radiances in the $40 \geq$ TH (km) ≥ 16 range over the 22700–23000 cm^{-1} (434.8–440.5 nm) range at 20 cm^{-1} sampling and 45 cm^{-1} resolution (both appropriate for OSIRIS in this window). These spectra are then normalized with a simulated reference spectrum at the median TH used in the co-added observed reference spectrum (nominally TH = 60 km). MODTRAN4 includes refraction, and azimuthally varying higher order scattering [*Berk et al.*, 1999]. The solar geometry near the tangent point is used for the plane-parallel multiple-scattering calculation. The solar illumination on each layer is determined with spherical geometry. The DISORT 4-stream approximation is used thereby reducing the computational time significantly. The sensitivity of this assumption is quantified below (section 2.3). Then the simulated normalized spectra are fitted analogously to the measured normalized spectra using differential versions of the absolute cross sections of O_3 and NO_2 provided by MODTRAN4 (at 220 K) simultaneously with a linear closure term. The simulated slant column densities do not require any correction for tilt features since MODTRAN4 samples instead of binning.

[25] The onion peel starts at the highest tangent height grid point for which the r^2 of the spectral fit is >0.5 (usually at TH = 40km). The source of the NO_2 profile outside the retrieval range is the MODTRAN4 database from which the appropriate season and latitude band are selected. The number density profile outside the altitude range generally has a small impact on the retrieved profile (see section 2.3) because there is very little NO_2 above 40 km and OSIRIS is fairly insensitive to NO_2 below the tangent height. This is discussed further after the description of the inversion algorithm and in section 2.3. The retrieved profile from the previous scan in the orbit is used as the first guess in the altitude range of the retrieval or, in the absence of this, the scan for the same latitude from the previous orbit is used. The retrieved profile is not sensitive to this first guess; it is used simply to speed up the convergence between model and measurement.

[26] A first guess of the number density ($x_{i=0,z=40}$) begins the iterative retrieval process. The subscripts indicate the iteration number (i) and the altitude (z, in km). This results in a simulated SCD ($y_{0,40}$), which is compared with the measured SCD ($y_{t,40}$). The number density at this altitude is updated ($x_{1,z} = x_{0,z} + \Delta x_{1,z}$) using *Chahine*'s [1970] method

$$x_{1,z} = x_{0,z}(y_{t,z}/y_{0,z}), \tag{2}$$

i.e.,

$$\Delta x_{1,z} = x_{0,z}\frac{y_{t,z} - y_{0,z}}{y_{0,z}},$$

which ensures that number densities remain positive. This is usually not a good update at low tangent heights where the SCD and number density are not related so simply. However, this iteration provides us with $y_{1,z}$ and then

$$\Delta x_{2,z} = \Delta x_{1,z}\frac{y_{t,z} - y_{1,z}}{|y_{1,z} - y_{0,z}|} \tag{3}$$

usually improves the agreement between model and measurement significantly. In general, the correction $\Delta x_{i+1,z}$ is then, for $i \geq 1$:

$$\Delta x_{i+1,z} = \Delta x_{i,z}\frac{y_{t,z} - y_{i,z}}{|y_{i,z} - y_{i-1,z}|}. \tag{4}$$

In words, the algorithm linearly interpolates or extrapolates the modeled number density based on the preceding two guesses (at most) and consequent local SCD until the modeled SCD approaches the measured SCD. The model and measured SCD profiles are considered to agree when they are within the greater of 3% (i.e., the NO_2 cross section uncertainty [*Vandaele et al.*, 1998]) or the NO_2 SCD fitting uncertainty at each TH, at which point the retrieval terminates. The uncertainty is the 1-σ standard error of the SCD and is provided by the least-squares fitting program. At the NO_2 SCD peak in the scan, the SCD uncertainty is typically 2%. A typical SCD profile with uncertainties is shown below.

[27] To optimize the retrieval algorithm, only the newest (lowest) layer is checked until the SCD at the height of the layer converges with the measured SCD. The impact of adjusting underlying layer densities on the higher THs is not assessed until after the model and measured SCDs have converged at each TH moving sequentially downward. Then the entire SCD profile is modeled to confirm that it has not diverged from the measurement at any altitude. If it has, appropriate layer densities are updated using equations (2) and (4). Five iterations are typically required at each shell.

[28] Two conditional operations are used to either improve the accuracy of the retrieved profile or speed up the convergence between the measurement and the model. In order of implementation, they are as follows: (1) If after update ($\Delta x_{i,z}$), SCD at adjacent TH is more affected than targeted SCD, i.e., $(y_{i,z\pm2} - y_{i-1,z\pm2}) > (y_{i,z} - y_{i-1,z})$, undo update and update other adjacent layer ($\Delta x_{i,z\mp2}$). (2) Regularization: if $x_{i,z} > 2\ x_{i,z\pm1}$, smooth profile using average of two number densities for both layers and then continue (flag and do not re-regularize). However, a doubling in retrieved number density over a 2 km range can occur even with instruments with moderate vertical resolution (see Observations section below). Because the a priori NO_2 profile is, on occasion, quite different from the true profile above the retrieval range, the algorithm does not allow a local maximum or minimum in number density to exist at the upper end of the retrieved profile (i.e., z = 40 km). Instead, the number density in that layer is decreased and the number densities in the immediately overlying layers are increased to yield a profile which increases exponentially with decreasing altitude down to z = 38 km.

[29] With respect to the retrieval of NO_2 from limb scatter, optimal estimation (OE) [*Rodgers*, 1976] is only as robust as the algorithm presented above when the logarithm of both the independent and dependent variable (in this case, SCDs and number densities, respectively) are used in OE. This adaptation of OE is used to recover ozone profiles from OSIRIS [*von Savigny*, 2002]. The algorithm used here reduces computational time because the entire weighting function matrix need not be calculated. OE needs to calculate this matrix at least twice as it iterates toward a solution of comparable accuracy.

2.3. Analysis of Uncertainties and Sensitivities

[30] Number density precision is estimated for each profile by propagating SCD fitting uncertainties through the IOP algorithm. This is achieved by perturbing the tangent layer density until the consequent change in the SCD at that TH exceeds its uncertainty. The magnitude of the perturbation is the random error of the local number density and error bars are assumed symmetrical about the retrieved number density. The precision calculated in this way agrees well with that calculated using OE. Number density uncertainties are a function of the SZA and the NO_2 profile itself but tend to be ~20% at z = 20 and ~30% at z = 40 km and as low as 5% between these two altitudes. At z = 40 km, the uncertainty is dominated by the uncertainty in the first step of the inversion, namely the SCD fitting. At z = 20 km, the uncertainty is dominated by the inability of the inversion algorithm to distinguish small changes in local number density because the bulk of the NO_2 column lies above and because the atmosphere is optically thick with respect to Rayleigh scattering.

[31] The profile uncertainty in the vertical direction is <1.5 km assuming errors in TH translate to equivalent errors in altitude, which is to be expected since the retrieval is insensitive to realistic errors in neutral density as shown below and by *von Savigny* [2002]. There is also an uncertainty in the effective latitude and longitude of the profile due to two effects: (1) spatial sampling and resolution, and (2) near-side dominance in the contribution to the observed radiance. The spatial sampling is dictated by the displacement of the Odin satellite while OSIRIS is limb scanning the stratosphere. This can lead to a longitude range of 6° during stratospheric limb scanning in the worst case scenario at the poles and a latitude range of up to ~5° at the equator. However, the spatial sampling is only ~2° over the retrieval altitude range. The spatial resolution is comparable to the spatial sampling in the along-track direction as the NO_2 absorption signature can come from up to 3° away from the tangent point assuming single scattering only and that the NO_2 lies below z = 40 km. The case which results in the largest spatial range occurs during a down-scan where the spectral image at TH = 40 km is observed ~2° along-track before the spectrum at TH = 18 km. The latter spectrum contains useful information on the NO_2 number density at z = 40 km but from ~1.3° beyond the tangent point of the image at TH = 18 km. Thus, the spatial range in the along-track direction of the NO_2 number density in general is given by the spatial sampling over the retrieval range plus $\frac{1}{2}$ the spatial resolution and amounts to <3.5° in this worst case scenario (z = 40km). The spatial range is smaller for lower altitudes and for up-scans.

[32] We have performed quantitative tests to determine the relative contributions of the near and far side of the limb. The near side of the limb encompasses the atmospheric volume between the observing instrument and plane formed by the radial vector that passes through the tangent point and the vector normal to this and to the line-of-sight (LOS). The far side is the volume lying beyond this plane from the vantage point of the observing instrument. The possible errors introduced by assuming horizontal homogeneity along the LOS were investigated using the radiative transfer model of *McLinden et al.* [2002]. The model has been extended to now include variations of the number density profile of the given constituent along the LOS of the tangent ray. This is achieved by performing many plane-parallel calculations at different SZAs and for different atmospheres. A final LOS integration is then performed over the tangent path using plane-parallel source functions appropriate for that altitude, SZA, and atmosphere. For these tests, SCDs from the 2-D simulation represent the true case and the inversion relies on the 1-D model. The number density profile is scaled by user-defined multiplicative factors 10° away from the tangent point in the LOS direction and linear interpolation is used between the two extreme profiles. In Figure 2, we show the error in the NO_2 profile at the tangent point for a simulated retrieval (neglecting satellite motion) in which a strong gradient exists along the LOS. The magnitude of the near and far side NO_2 profiles have been scaled to 0.5 and 1.5 times the

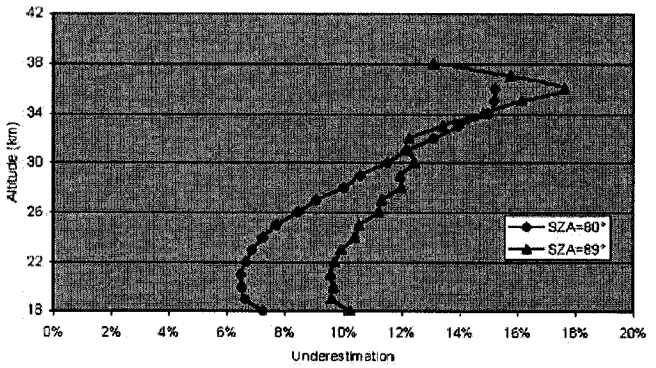

Figure 2. Impact of neglecting near-side dominance to the radiance contribution in the presence of horizontal inhomogeneity in the NO_2 profile along the line-of-sight. Near and far side NO_2 profiles are scaled to 0.5 and 1.5 times the profile at the tangent point and the difference in azimuth angle ($d\phi$) between the instrument and the Sun is 118°.

magnitude at the tangent point, respectively. Alternatively, from these calculations, it is possible to express the error in terms of geo-location. The error is on the order of 0.5° in the LOS direction in a worst-case scenario of high SZA (i.e., 89°). Thus, using the geo-location of the tangent point at a TH in the middle stratosphere (i.e., 30 km), should result in a representative geo-location of the profile.

[33] The sensitivity to the a priori NO_2 profile outside the retrieval range was tested by perturbing the number densities above and below the retrieval range ($z < 19$ km) at SZA = 89° for a profile retrieved below on February 28th, 2002 (see section 3). The a priori contribution, expressed as a percentage and shown in Figure 3, is the absolute magnitude of the % change in the retrieved number density relative to the absolute magnitude of the % perturbation in the a priori profile. For SZA = 57°, the retrieved NO_2 profile only shows a sensitivity to the a priori below the retrieval range. The a priori contribution is 2.3% at z = 19 km and decreases monotonically above that. There is no sensitivity to the a priori above the retrieval range (i.e., $z > 39$ km) because the NO_2 signature above this altitude is negligible for this SZA and because the algorithm recognizes that the layers above 39 km need updating and does so with sufficient accuracy. There is also no sensitivity to the first guess in the retrieval range because the method is iterative and several updates are required at each altitude to meet the convergence criteria.

[34] The effect of clouds (or a bright underlying surface) has been investigated and appears to be small in the blue when limb viewing at TH $\geq$ 18 km and SZA > 57°. This conclusion is reached by looking at the assigned weight (or effective path length) below the tangent altitude using the perturbation method of *McDade et al.* [2002] for the calculation. It is 1–2 orders of magnitude smaller than the magnitude (Figure 4) at the tangent height but increases as one looks into the troposphere. This clearly shows one of the benefits of OSIRIS/Odin being in an orbit where the Sun remains low. To quantitatively establish the sensitivity of the stratospheric NO_2 profile on clouds, a retrieval using simulated (noise-free) data was performed for 4 SZAs (30, 57, 79, and 89°) with an optically thick cumulus cloud (top at 3 km, base at 0.66km) used to calculate the 'true' SCD profile but with clouds excluded in the inversion and surface albedo (Λ) of 0.04. A sub-arctic winter NO_2 profile was assumed. Results are shown in Figure 5. The error due to neglecting the presence of clouds in the inversion is systematic and,

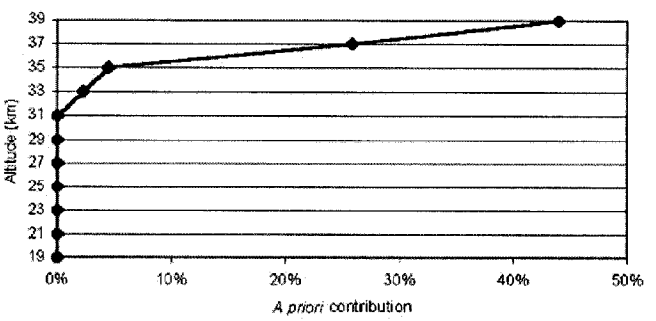

Figure 3. A priori contribution at SZA = 89° (details given in Figure 11d below).

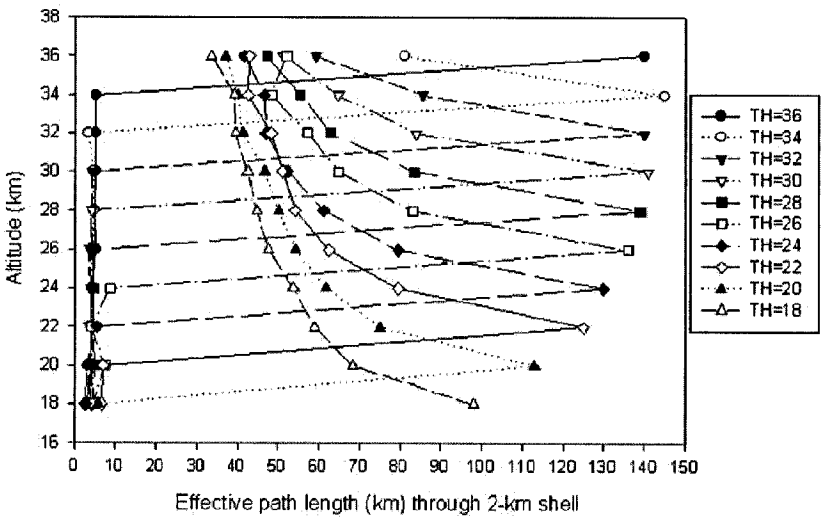

Figure 4. Effective path length for NO_2 absorption in 2-km shell for SZA = 72°, cumulus cloud deck with top and base at 3 and 0.66 km, respectively and extinction of 92.6 km^{-1} (at λ = 550 nm). The effective path length as a function of altitude is the weighting function for a given TH.

strangely, leads to an underestimation of the NO_2 profile. The underestimation cannot be explained by boundary layer NO_2 being screened off by the overlying cloud deck since after removing the boundary layer NO_2 entirely, the underestimation remains practically unchanged. We presume the underestimation is due to the fact that the path enhancement to the high-altitude reference is greater than that for the tangent height of interest. At SZA = 57°, the underestimation of the vertical column density approaches 5% but it is only 2% at 79° and 0% at SZA = 89°. The largest underestimation in local number density tends to occur at either end of the retrieval range. This can be explained as follows: at the upper end of the retrieval range a local maximum occurs because the NO_2 signature in the radiation upwelling through the underlying stratosphere becomes comparable to the single scattering NO_2 signature. At the lower end of the retrieval range, the error tends to be a local maximum because the multiple-scattering contribution is greater than at higher altitudes. Raising the a priori Λ (e.g., Λ = 0.2) can further minimize the sensitivity to clouds since the effects of clouds and bright surfaces should be somewhat interchangeable. Thus, the current assumption of a low surface reflectivity in the inversion maximizes the cloud sensitivity. The sensitivity of the NO_2 profile to high cloud has been tested by introducing a cirrus cloud with top at 10 km and base at 3 km, 64 μm mode radius, and an optical depth of 7. Since high clouds occur mostly in the tropics, we set the SZA to 81° since this is the lowest SZA for the Odin orbit in the

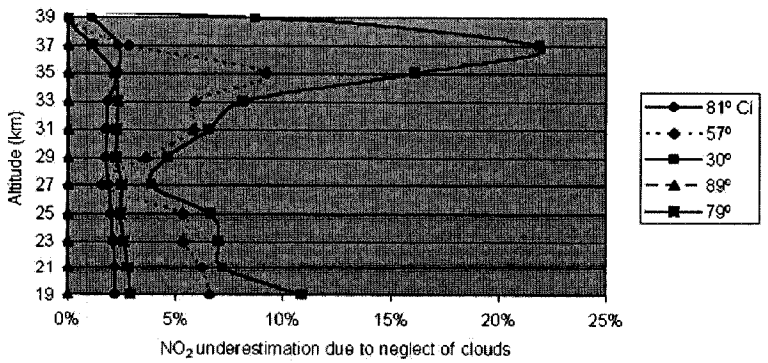

Figure 5. Impact of cloud as a function of SZA (see Figure 4 for details on the cumulus cloud). The cirrus cloud described in the text is labelled 'Ci'.

tropics. Even if cloud tops are as high as 10 km, high cirrus introduces a small, systematic error to the stratospheric NO_2 profile retrieval (Figure 5).

[35] The sensitivity of stratospheric aerosols also appears to be small for OSIRIS. In the retrieval algorithm, the assumed vertical distribution of aerosol optical properties and number densities are obtained from the MODTRAN4 database for the appropriate latitude and season. For SZA = 80°, and a scattering angle of 71°, the error in the retrieved NO_2 profile at all heights when the assumed aerosol profile is changed from background to moderate volcanic is <5% and the NO_2 column error was 0.2%. This aerosol perturbation amounts to more a doubling in the 20–30 km altitude range. However, the largest absolute and relative increase in aerosol number density is at 15 km, and decreases monotonically above this altitude. The largest impact on the NO_2 profile (19–39 km) occurred at 21 km.

[36] There is almost no sensitivity to the assumed pressure profile. This was determined by switching only the pressure profile from mid-latitude summer to mid-latitude winter and verifying that the vertical fitting convergence criterion had been met at all tangent heights using the resulting set of simulated limb radiances. Analogous tests were performed to establish a lack of sensitivity to temperature (mid-latitude summer vs. winter) and to the DISORT 4-stream approximation as to compared to using 8 quadrature points for SZA = 79°, with background aerosols, and Λ = 0.08. A 2-stream approximation results in very large differences (>10%) in the retrieved NO_2 profile as compared to the 8-stream and is thus inadequate.

[37] Correlation in NO_2 number density between layers is yet another source of error. A partial correlation matrix was established numerically using simulated noise-free data for layers at z = 21, 29, and 37 km, representing layers in the upper, middle and lower portion of the retrieval range. A mid-latitude summer atmosphere was used, with SZA = 72° and Λ = 0.04. A layer is perturbed by 3e9 molec/cm^3 and then the perturbed profile is retrieved assuming the unperturbed a priori profile. When the 2-km layer whose bottom is at 21 km was perturbed, the retrieved profile agreed with the true (perturbed) profile to better than 2% at all heights, indicating that the other layers are not significantly correlated to the layer at 21 km. The same conclusion was reached upon perturbing the layer at 29 km. The number density at the perturbed layer was retrieved to <0.8% in both cases. Finally, when the layer at 37 km was perturbed, some correlation was observed. This may be partly due to the fact that the perturbation, although constant in absolute magnitude is larger relative to the number density at 37 km than at 29 and 21 km. The 3e9 molec/cm^3 perturbation led to a retrieval error at 35 km of 2.5e8 molec/cm^3. Thus the correlation is the ratio of these values and amounts to 8.5%. The correlation at 39 km is 0.5% and is <0.5% at all other layers. The perturbed layer was underestimated by 4%. The correlation test provides support that the vertical grid size of the retrieval is adequate and that the vertical resolution of the NO_2 profile is clearly $\leq$2 km from 21–29 km, in agreement with *Strong et al.* [2002]. These simulations show the ability of the retrieval algorithm to retrieve sharply peaked profiles.

[38] In summary, only pointing appears to be a significant (>10%) systematic source of error. The magnitude of pointing errors depends directly on the sharpness of the profile. However, errors in the number density profile due to pointing appear to cancel out when vertical column densities are compared (see Validation section below).

[39] Random errors due to instrument noise have been quantified by *McDade et al.* [2002] and *Strong et al.* [2002] and range from 3% at best to 13–20% at 20 km and 30% at 39 km.

3. Observations and Discussion

[40] In this section, the observed differential structure and corresponding spectral fits (Figure 6) are shown along with SCD profiles (Figure 7) and fit residuals (Figures 8a and 8b). Vertical profiles are also presented below. Limb radiance spectra observed by OSIRIS as a function of TH have been illustrated elsewhere [*von Savigny et al.*, 2003].

[41] At the SCD peak, only 2% of the differential optical depth (DOD) is unexplained (Figure 7). The SCD percentage uncertainty increases rapidly above the NO_2 SCD peak and is on the order of 20% at TH = 40 km, but is highly variable because of the sharp gradient in NO_2 at this altitude so uncertainties can range from 10 to 300%. Below the SCD peak, the uncertainties are relatively TH-independent (i.e., 2–3%).

[42] The residuals as a function of TH show a repeating pattern (Figures 8a and 8b), indicating that the fits are not at the shot noise limit. The largest residual occurs at 438 nm, in the wings of Fe I, the largest Fraunhofer lines in the fitting window. The residual appears to increase in magnitude with decreasing TH. This feature and others are likely due to an imperfect 'tilt' correction.

[43] The fitting residuals are not systematically larger at pixels corresponding to Fraunhofer line cores whether the Ring effect correction is performed or not (see Figures 8a and 8b) indicating that in this NO_2 fitting window, the Ring effect cancels out quite well using a high TH reference. This is probably due to a combination of reasons: the fairly low spectral resolution of OSIRIS (1 nm), the fact that the effective temperature of the lower mesospheric reference spectrum is sufficiently close to the temperatures found in the lower and middle stratosphere, and that, during the period of the observations presented here, the stratosphere was extremely clean as can be seen from POAM III aerosol observations www.cpi.com/products/poam/download.html) thus the aerosol dilution effect was small in the blue (~440 nm). NO_2 SCDs are typically 3% larger when the backward model is applied than if the Ring effect is ignored altogether, presumably due to the removal of weak filling in of NO_2 features as has been discussed for other geometries [e.g., *Vountas et al.*, 1998].

[44] To illustrate the unique spatial and temporal coverage of OSIRIS NO_2 observations, a half-orbit of data was analyzed. We chose Odin's 3446th orbit on Oct 10th when the satellite, moving southward over the Pacific, scanned the limb starting from 40°N (NW USA). The data analysis is limited to SZA < 90°, allowing for coverage into the Antarctic circle (tangent point at 67° S). This orbit was selected for a number of reasons: (1) This is one of two times of the year when OSIRIS is spatially and temporally coincident with the satellite-borne occultation instruments (POAM III and HALOE). This orbit features a HALOE

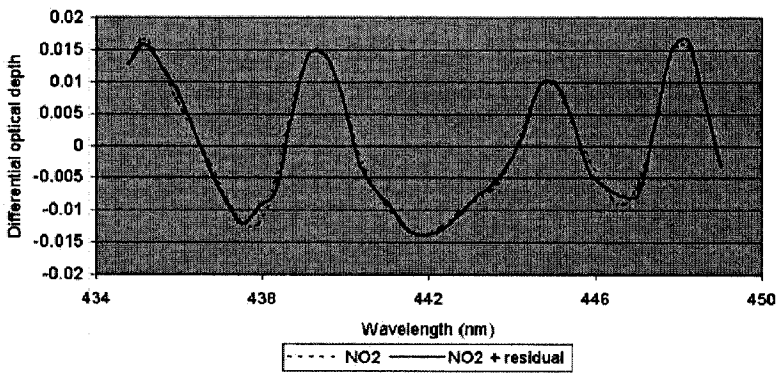

Figure 6. Natural logarithm of the reciprocal of the observed normalized radiance (ln [I_0/I]) on July 30th, 2001, 1 pm UT (lat: 33.5°, lon: 69°), SZA = 75°, TH ≅ 30 km. NO_2 SCD is 6.72e16 molecules/cm^2.

coincidence shown below. (2) Both the southern and northern hemispheres are sunlit on the descending phase of the orbit allowing for coverage from northern mid-latitudes to southern high-latitudes and an investigation of hemispheric asymmetry in NO_2. (3) The SZA is roughly constant during this segment of the orbit (Figure 9) so that the diurnal variation of NO_2 at 30 km is $\leq$10% over the SZA range according to photochemical modeling [*McLinden et al.*, 2001]. The NO_2 is known to vary rapidly between 90 and 92°, but not at SZA < 90°. Thus, this orbit allows latitudinal and diurnal variations to be separated as the entire orbit occurs just after local sunrise, whereas SZAs are much lower at the pole than the equator for Odin at other times of the year. (4) To test the forward RT model (and inversion algorithm) at high SZA.

[45] The Canadian Middle Atmosphere Model (CMAM) [*de Grandpré et al.*, 1997] is used to confirm the altitudinal and latitudinal distribution of NO_2 retrieved by OSIRIS. OSIRIS number densities are interpolated to CMAM pressures using the latitude-dependent pressure profiles assumed in the inversion. Figure 10 shows that the observations are consistent with the CMAM model in most respects, including: (1) In the tropics, the peak is shifted upward and is narrower and the total column is a latitudinal minimum. (2) In the northern hemisphere, the profile is shifted upward relative to the southern hemisphere presumably due to greater tropopause flux in the former. (3) At southern high-latitudes (e.g., 60° S), the NO_2 concentrations in the lower stratosphere are high as the peak shifts downward by 8 km over a narrow latitude range at the edge of the polar vortex.

[46] In contrast to Figure 10b, Figure 10a shows the variability commonly observed in the winter hemisphere at mid-latitudes [*Zawodny*, 1986] where the effect of

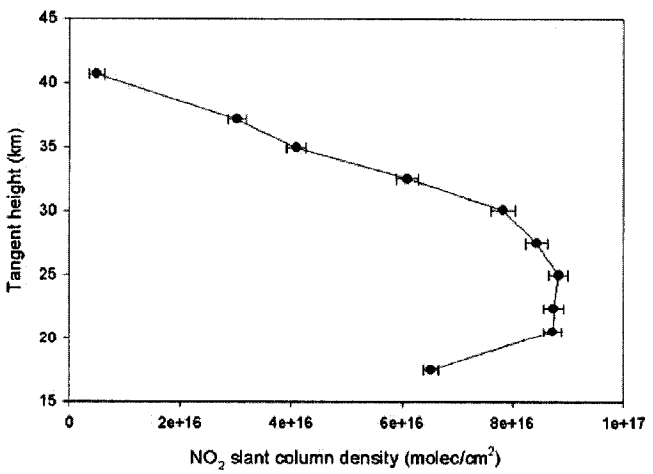

Figure 7. Measured SCD profile (see Figure 6 for details of geo-location).

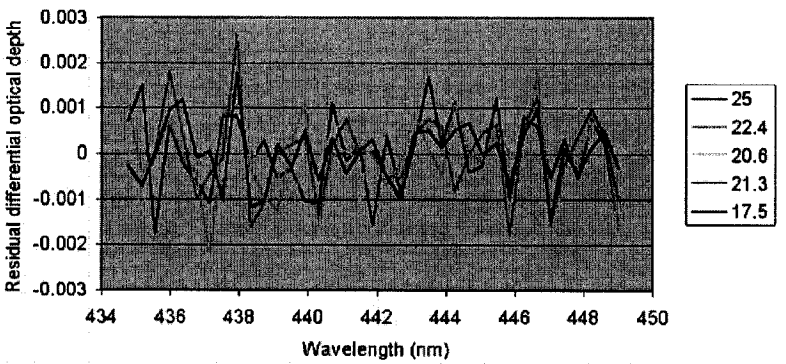

Figure 8a. Fit residuals (435–449 nm) from same scan as in Figure 6. THs (km) are indicated in legend. Ordinate scale shows residual of fit of ln $[I_0/I]$ (see Figure 6).

dynamics is largely responsible for the shape of the profile whereas in equatorial regions, the profile shape is governed by photochemistry.

[47] At the time of the observations, the annual Antarctic ozone hole is well apparent in OSIRIS O_3 profiles. The polar vortex appears to begin at about 63°S for Odin's longitude on this orbit (220°) based on the 220 DU contour on the EarthProbe-TOMS O_3 map for this day. At 67°S, there is ~200 DU of O_3, a far greater vertical column amount than the <100 DU that lies at the pole. Thus, OSIRIS may not have sampled much of the NO_2 depleted air inside the polar vortex on this orbit.

[48] OSIRIS NO_2 profiles are compared with correlative measurements by a variety of validated NO_2 profiling instruments such as HALOE [*Gordley et al.*, 1996], POAM III [e.g., *Randall et al.*, 2002], and LPMA/DOAS [*Ferlemann et al.*, 2000] as a function of season (summer and winter), latitude (high, low, and mid-latitude) and time of day (sunrise, midday, sunset). Coincidence criteria, following *Randall et al.* [2002] are ±4° in latitude, ±12° longitude, and ±2 hours in time. An additional criterion is included: the SZA of the coincident measurements must be comparable so that the NO_2 profile at that time and place does not change by >15% according to photochemical modeling [*McLinden et al.*, 2001]. Retrieved profiles from the instrument with superior vertical resolution are not convolved to match the vertical resolution of the other coincident instrument.

[49] The flight of LPMA/DOAS (Laboratoire Physique Moléculaire et Applications/Differential Optical Absorption Spectroscopy) balloon payload at Kiruna (67.9°N, 21.2°E) on August 21–22, 2001 allowed for the validation of the coincident daytime NO_2 profile observed by OSIRIS. The azimuth-controlled LPMA/DOAS payload carries two UV/vis balloon-borne spectrometers and a FT-IR instrument that measured NO_2 profiles in direct sun during balloon ascent (SZA = 77° to 88°). The profile measured by the visible DOAS instrument (420–465 nm) during the ascent phase of the LPMA/DOAS balloon flight (Figure 11) is typically within 15% of OSIRIS and the vertical columns are within 14% with very good agreement on the peak altitude (~25 km) during this northern high-latitude afternoon coincidence in late summer. The difference in the profile between 25–30 km may be explained by noting that the ascent profile takes place after the OS limb scan and that

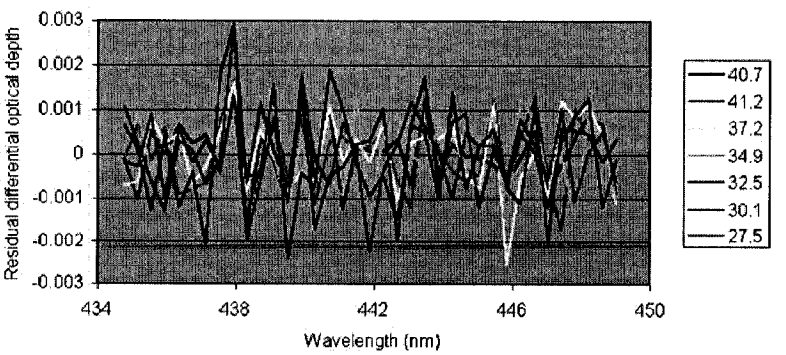

Figure 8b. Same as Figure 8a, except for higher THs. At TH ≅ 40 km, the rms residual is typically on the order of 6e-4.

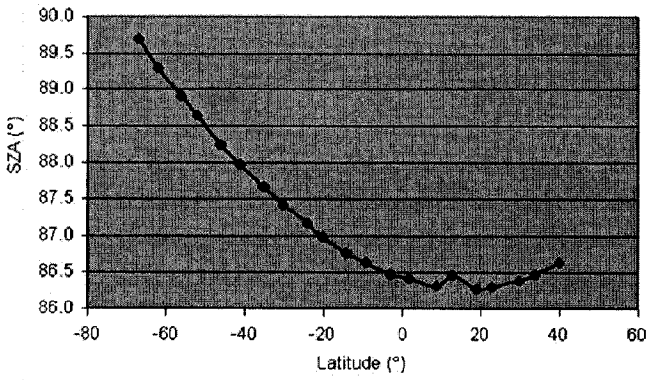

Figure 9. SZA (at tangent point for TH = 30 km) vs. latitude during orbit 0D76 on October 10th, 2001.

N_2O_5 dissociation, primarily by photolysis [*McLinden et al.*, 2002], continues throughout the day mostly at these altitudes. After correcting for the diurnal variation through the use of a photochemical model [*McLinden et al.*, 2002], OSIRIS and LPMA/DOAS agree to 10% on the vertical profile and 6% on the vertical column.

[50] In general, agreement with HALOE (Figures 12a–12d) is 18% on profiles in the 19–39 km range and the agreement on the stratospheric column is excellent (2%) as pointing errors appear to cancel out when integrated vertically. HALOE finds a slightly higher column abundance in cases shown in Figures 12a–12b and 12d, which is consistent with the fact that the NO_2 abundance should increase slightly with SZA from ~87° to 90° (see captions of Figures 12a, 12b, and 12d). The profile that includes photochemical forward modeling in Figure 12c was used in the aforementioned column and profile statistics for the three correlative HALOE measurements. OSIRIS and HALOE columns at SZA = 90° in Figure 12c agree to 1%. The agreement with HALOE in Figure 12d demonstrates that the assumption of horizontal homogeneity in the vicinity of the tangent point in the along-track direction appears to be adequate even though a large diurnal NO_2 gradient is expected beyond the terminator Furthermore, at high SZA (e. g. 89.5°, $d\phi$ = 93°, TH = 30 km, Λ = 0.04 and 440.5 nm), single scattering accounts for 98.5% of the total radiance. The measured radiance therefore contains the NO_2 signature of the sunlit atmosphere and thus does not contain significant signature from multiple scattering in the twilit NO_2-rich side of the terminator. Also, OSIRIS does not look normal to the terminator instead it roughly looks along it (±33°), minimizing the expected diurnal gradient.

[51] The comparison with POAM III again showed the ability of OSIRIS to accurately measure the shape and peak altitude of a given NO_2 profile as the coincident satellite observations agree to 14% on average between 21 and 37 km. Since the SZA approached 90° and atmospheric sphericity becomes increasingly important, the variation in SZA during the scan is taken into account (to 3 significant digits)

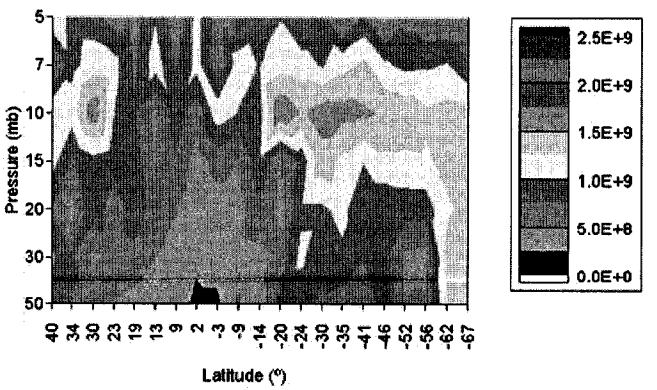

Figure 10a. Snapshot of latitudinal distribution of NO_2 number density (cm^{-3}) on Oct 10th (14:30 to 15 pm UT), At lat = 40°, lon = 254° and at lat = −67°, lon = 220°.

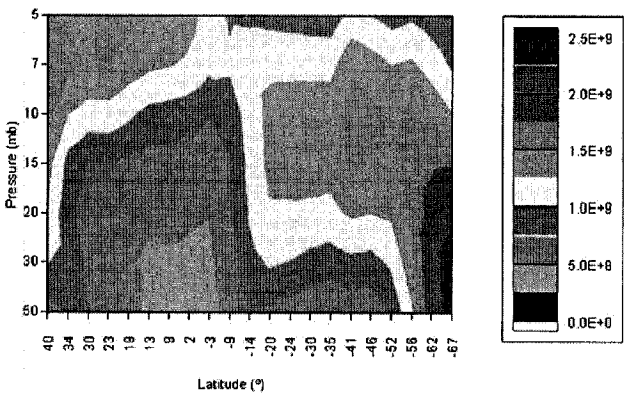

Figure 10b. CMAM contour plot of NO_2 number density (cm^{-3}) over same latitude range and solar conditions: October average.

in the OSIRIS inversion algorithm. The peak altitude is lower than in Figure 11 which shows a similar latitude band ~2 months earlier (August). This seasonal variation in peak height is consistent with CMAM.

[52] These comparisons with solar-occulting instruments show the ability of the retrieval algorithm (including MODTRAN4, its forward RTM) to accurately invert slant column densities in these difficult cases. Thus, it appears thus far that OSIRIS will be an excellent choice to validate future NO_2 profiling instruments, such as recently launched SAGE III [*McCormick et al.*, 1991] and SCIAMACHY.

4. Conclusions and Future Work

[53] A new pseudo-absorber is found which should be important for a variety of viewing geometries and fitting windows. This spectral artefact results from a combination

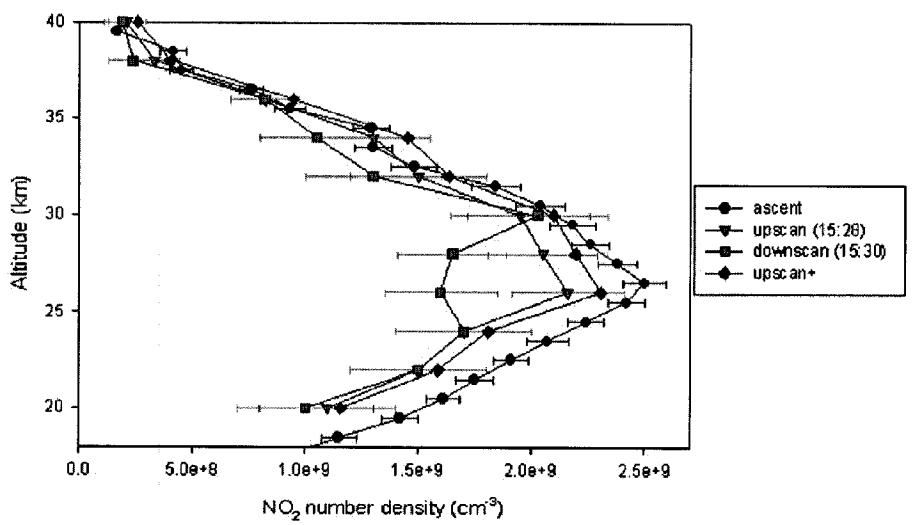

Figure 11. 'Upscan' and 'downscan' are consecutive OSIRIS limb scans southeast (lat = 64°, lon = 23°, SZA = 72°) and northwest (lat = 70°, lon = 16°, SZA = 71°) respectively of balloon ascent location (lat = 68°, lon = 21.2°). Odin was scanning above the stratosphere as it passed over the ascent location. 'Upscan+' contains forward modeling of the diurnal variation of NO_2 due to photochemistry from OSIRIS local time to LPMA/DOAS local time. Error bars are omitted for clarity on the latter profile.

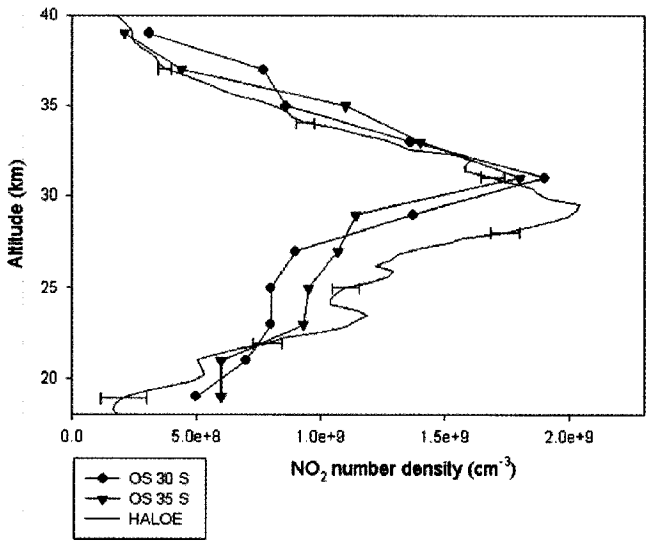

Figure 12a. Spot comparison of NO_2 observed during OSIRIS/HALOE spatial and temporal coincidence at sunrise on Oct 10th, 2001 (contains two successive OSIRIS profiles from Figure 10a). OSIRIS tangent point at TH = 30 km and lat = −30.4°: SZA = 87.4°, lon = 237.4° and time = 13:51 UT; OSIRIS tangent point at TH = 30 km and lat = −35°: SZA = 87.7°, lon = 236°, and time = 13:52 UT; HALOE coordinates are lat = −32.7°, lon = 248.7°, time = 12:54 UT, and SZA = 90°. OSIRIS error bars are omitted for clarity.

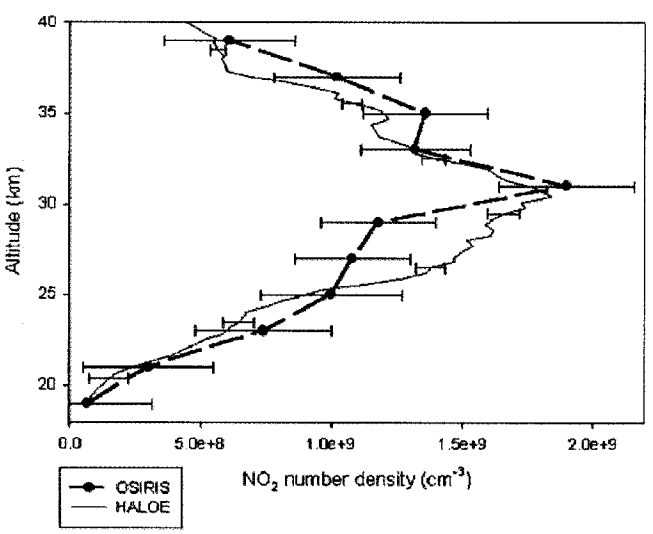

Figure 12b. Comparison of tropical NO_2 profile with HALOE during a sunset coincidence on Feb. 15th, 2002. OSIRIS lat = −1.9°, SZA = 86.63°, lon = 62.3° and time = 13:50 UT; HALOE coordinates were lat = −2.64°, lon = 68.87°, time = 13:40 UT, and SZA = 90°. HALOE also has a vertical resolution of ~2 km [*Gordley et al.*, 1996].

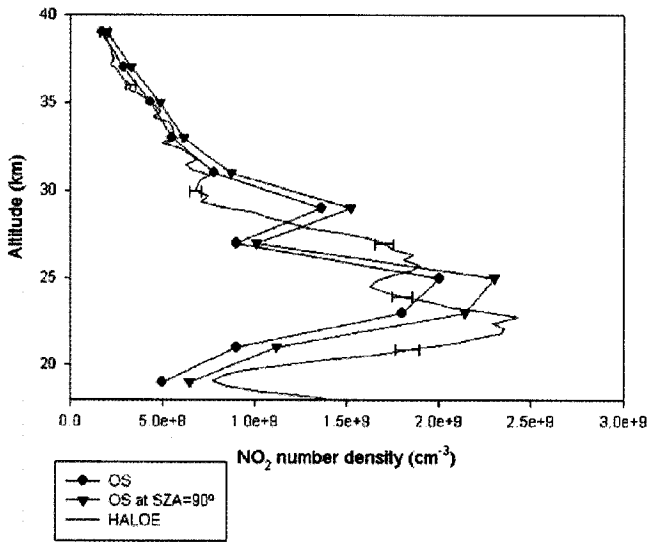

Figure 12c. Comparison of NO_2 profile in Antarctic ozone hole conditions with HALOE during a sunrise "coincidence" on Oct. 24th, 2001. OSIRIS lat = −67.7°, lon = 3.4°, SZA = 85.2°, and time = 4:25 UT; HALOE coordinates are lat = −69.0°, lon = 5.1°, time = 3:13 UT, and SZA = 90°. Yellow triangles include altitude-dependent forward modeling of OSIRIS profile from SZA = 85° to 90° based on photochemical calculations (without heterogeneous chemistry) for October a.m. at 80° S [*McLinden et al.*, 2001]. Error bars are omitted for clarity.

of spectral undersampling and convolution, Fraunhofer structure, and Rayleigh extinction and cannot be removed by a polynomial. Also with regard to the spectral fitting, the spectral resolution of OSIRIS in this fitting window needs to be pinpointed to reduce uncertainties in the retrieved profiles.

[54] The inclusion of multiple scattering has allowed NO_2 profiles retrieved from OSIRIS limb spectra to extend

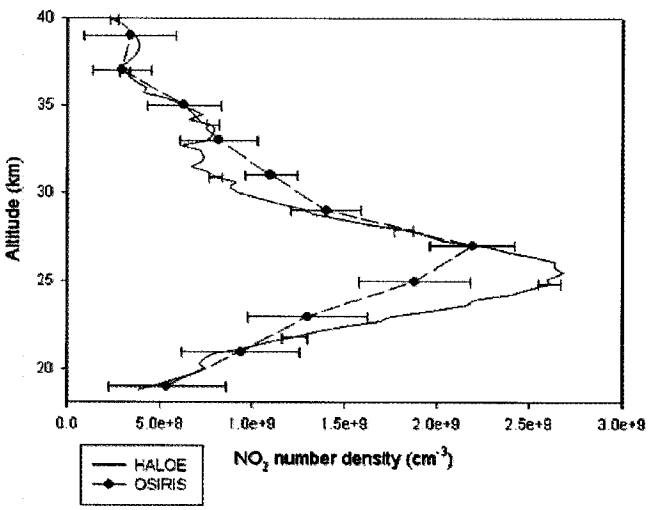

Figure 12d. Mid-latitude winter (28.02.2002) sunset coincidence between HALOE and OSIRIS (lat = 59.7°).

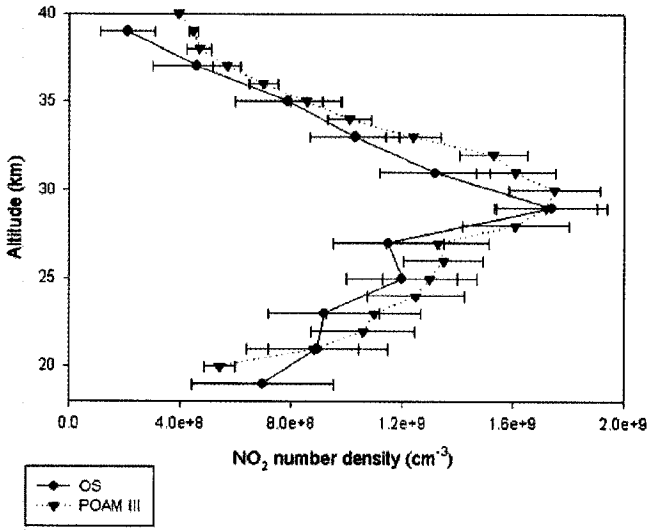

Figure 13. Spot comparison of NO2 observed during OSIRIS/POAM III spatial and temporal coincidence at sunset on Oct 10th, 2001. OSIRIS SZA (at tangent point) varies in the range 89.947–89.868° for 18 < TH(km) < 41.09, with lat = 74°, lon = 353° and time = 16:28 UT at TH = 30 km. POAM III coordinates are lat = 71°, lon = 2°, time = 16:17 UT, and SZA = 90°.

into the lower stratosphere (i.e., 17.5 km for low SZA) whereas previous work with the SME was limited to a lower altitude of 26 ± 2 km [*Thomas et al.*, 1988; *Mount et al.*, 1984] because of the single scattering approximation in the forward RTM. Non-linearity, caused by primarily by Rayleigh scattering, necessitates an iterative retrieval algorithm. A single iteration of optimal estimation [*Rodgers*, 1976] or a simple onion peel using the same weighting function matrix generated with an a priori profile has been tried and is not sufficient. Studies have been performed to quantify the sensitivity to a priori NO_2, stratospheric aerosols, pressure, and temperature and clouds. The validity of the 4-stream approximation has been confirmed. Other systematic sources of error that have been considered include pointing, baffle scattering, polarization, internal scattering, wavelength drift. The retrieval is sensitive near the retrieval altitude limits to the a priori NO_2 information from outside the retrieval range. In conclusion, shot noise is comparable to the systematic sources of error in the inversion algorithm.

[55] The novel algorithm presented above is stable and consistently returns profiles that are in good agreement with correlative measurements. These include spot comparisons with POAM III for northern high-latitude winter (Figure 13), with LPMA/DOAS for northern high-latitude summer (Figure 11), with HALOE for southern high and mid-latitude summer, northern mid-latitude winter and in the tropics (Figures 12c, 12a, 12d, and 12b, respectively). As mentioned in the introduction, the southern hemisphere cannot be viewed in austral winter. Where necessary, comparisons include photochemical forward modeling to the SZA of the correlative data.

[56] In summary, OSIRIS appears to measure stratospheric NO_2 columns with a 1-σ accuracy of 6% (typically) and profiles to <20% at all times of day and all seasons and latitudes in the 20–39 km range. Preliminary statistical analysis of the validated profiles indicates that OSIRIS does not show a systematic bias in any part of the retrieval range. These comparisons with instruments capable of equal or greater vertical resolution have also shown that OSIRIS can partially resolve some small-scale NO_2 structures.

[57] Based on the results presented here, OSIRIS will be invaluable in the early validation of NO_2 profiles from the recently launched SCIAMACHY and SAGE III satellite instruments. Moreover, OSIRIS provides stratospheric NO_2 monitoring with an unprecedented combination of accuracy, spatial coverage and resolution (vertically and latitudinally), and temporal coverage. Together with subsequent instruments, OSIRIS will give a more complete picture of trends in NO_2 and NO_y.

[58] **Acknowledgments.** Odin is a Swedish-led satellite project funded jointly by the Swedish National Space Board (SNSB), the Canadian Space Agency (CSA), the National Technology Agency of Finland (Tekes) and Centre National d'Etudes Spatiales (CNES). The Swedish Space Corporation has been the industrial prime contractor. This work was also supported by the National Sciences and Engineering Research Council (Canada). We are extremely grateful to the entire Odin team. We are indebted to the POAM III, HALOE and Earth Probe-TOMS teams for making their data readily available.

References

Berk, A., G. P. Anderson, P. K. Acharya, J. H. Chetwynd, L. S. Bernstein, E. P. Shettle, M. W. Matthew, and S. M. Adler-Golden, MODTRAN4 User's manual: Software manual, Air Force Res. Lab., Space Vehicles Dir., Air Force Mater. Command, Hanscom Air Force Base, Mass., 1999.

Bogumil, K., J. Orphal, S. Voigt, H. Bovensmann, O. C. Fleischmann, M. Hartmann, T. Homann, P. Spietz, A. Vogel, and J. P. Burrows, Reference spectra of atmospheric trace gases measured the SCIAMACHY PFM satellite spectrometer, paper presented at European Symposium on Atmospheric Measurements From Space, Eur. Space Res. and Technol. Cent., Noordwijk, Netherlands, 1999.

Bovensmann, H., J. P. Burrows, M. Buchwitz, J. Frerick, S. Noël, V. V. Rozanov, K. V. Chance, and A. P. H. Goede, SCIAMACHY: Mission objectives and measurement modes, *J. Atmos. Sci.*, *56*, 127–150, 1999.

Burrows, J. P., A. Richter, A. Dehn, B. Deters, S. Himmelmann, S. Voigt, and J. Orphal, Atmospheric remote sensing reference data from GOME, 2, Temperature dependent absorption cross sections of O_3 in the 234–794 nm range, *J. Quant. Spectrosc. Radiat. Transfer*, *61*, 509–517, 1999a.

Burrows, J. P., et al., The Global Ozone Monitoring Experiment (GOME): Mission concept and first scientific results, *J. Atmos. Sci.*, *56*, 151–175, 1999b.

Camy-Peyret, C., J.-M. Flaud, J.-Y. Mandin, J.-P. Chevillard, J. Brault, D. A. Ramsay, M. Vervloet, and J. Chauville, The high-resolution spectrum of water vapor between 16500 and 25250 cm^{-1}, *J. Mol. Spectrosc.*, *113*, 208–228, 1985.

Carlotti, M., Global-fit approach to the analysis of limb-scanning atmospheric measurements, *Appl. Opt.*, *27*, 3250–3254, 1988.

Chahine, M. T., Inverse problems in radiative transfer: Determination of atmospheric parameters, *J. Atmos. Sci.*, *27*, 960–967, 1970.

Chance, K., Analysis of BrO measurements from the Global Ozone Monitoring Experiment, *Geophys. Res. Lett.*, *25*, 3335–3338, 1998.

Crutzen, P. J., The influence of nitrogen oxides on the atmospheric ozone content, *Q. J. R. Meterol. Soc.*, *96*, 320–325, 1970.

Crutzen, P. J., Ozone production rates in an oxygen-hydrogen-nitrogen oxide atmosphere, *J. Geophys. Res.*, *76*, 7311–7327, 1971.

Cunnold, D. M., et al., Validation of SAGE II NO_2 measurements, *J. Geophys. Res.*, *96*, 12,913–12,925, 1991.

de Grandpré, J., J. W. Sandilands, J. C. McConnell, S. R. Beagley, P. C. Croteau, and M. Y. Danilin, Canadian Middle Atmosphere Model: Preliminary results from the chemical transport module, *Atmos. Ocean*, *35*, 385–431, 1997.

Evans, W. F. J., and J. M. Alfred, Algorithm for correction of internal scattering and spectral cross-talk in the UV/vis band of the OSIRIS instrument flight model, OSIRIS internal report, Trent Univ., Peterborough, Ont., Canada, 2001.

Ferlemann, F., N. Bauer, R. Fitzenberger, H. Harder, H. Osterkamp, D. Perner, U. Platt, M. Schneider, P. Vradelis, and K. Pfeilsticker, Differential optical absorption spectroscopy instrument for stratospheric balloon trace-gas studies, *Appl. Opt.*, *39*, 2377–2386, 2000.

Flittner, D. E., P. K. Bhartia, and B. M. Herman, O_3 profiles retrieved from limb scatter measurements: Theory, *Geophys. Res. Lett.*, *27*, 2601–2604, 2000.

Garcia, R. R., and S. Solomon, A new numerical model of the middle atmosphere, 2, Ozone and related species, *J. Geophys. Res.*, *99*, 12,937–12,951, 1994.

Gordley, L. L., et al., Validation of nitric oxide and nitrogen dioxide measurements made by the Halogen Occultation Experiment for UARS platform, *J. Geophys. Res.*, *101*, 10,241–10,266, 1996.

Grainger, J. R., and J. Ring, Anomalous Fraunhofer line profiles, *Nature*, *193*, 7621962.

Greenblatt, G. D., J. J. Orlando, J. B. Burkholder, and A. R. Ravishankara, Absorption measurements of oxygen between 330 and 1140 nm, *J. Geophys. Res.*, *95*, 18,577–18,582, 1990.

Hedin, A. E., Extension of the MSIS Thermospheric Model into the middle and lower atmosphere, *J. Geophys. Res.*, *96*, 1159–1172, 1991.

Hilsenrath, E., Rocket observations of the vertical distribution of ozone in the polar night and during a mid-winter stratospheric warming, *Geophys. Res. Lett.*, *7*, 581–584, 1980.

Johnston, P. V., and R. L. MacKenzie, NO_2 observations at 45°S during the decreasing phase of solar cycle 21, from 1980 to 1987, *J. Geophys. Res.*, *94*, 3473–3486, 1989.

Joiner, J., P. K. Bhartia, R. P. Cebula, E. Hilsenrath, R. D. McPeters, and H. Park, Rotational Raman scattering (Ring effect) in satellite ultraviolet measurements, *Appl. Opt.*, 4513–4525, 1995.

Llewellyn, E. J., et al., OSIRIS-an application of tomography for absorbed emissions in remote sensing, in *Applications of Photonic Technology*, edited by G. A. Lampropoulos and R. A. Lessard, pp. 627–632, Plenum, New York, 1997.

Lucke, R. L., et al., The Polar Ozone and Aerosol Measurement (POAM) II instrument and early validation results, *J. Geophys. Res.*, *104*, 18,785–18,799, 1999.

McCormick, M. P., W. P. Chu, J. M. Zawodny, L. E. Mauldin, and L. R. McMaster, Stratospheric Aerosol and Gas Experiment III (SAGE III) aerosol and trace gas measurements for Earth Observing System (EOS), *Proc. SPIE Int. Soc. Opt. Eng.*, *1491*, 125–141, 1991.

McDade, I. C., K. Strong, C. S. Haley, J. Stegman, D. P. Murtagh, and E. J. Llewellyn, A method for recovering stratospheric minor species densities from the ODIN/OSIRIS scattered sunlight measurements, *Can. J. Phys.*, *80*, 395–408, 2002.

McElroy, C. T., Stratospheric nitrogen dioxide concentrations as determined from limb brightness measurements made on June 17th, 1983, *J. Geophys. Res.*, *93*, 7075–7083, 1988.

McLinden, C. A., S. C. Olsen, M. J. Prather, and J. B. Liley, Understanding trends in stratospheric NO_y and NO_2, *J. Geophys. Res.*, *106*, 27,787–27,793, 2001.

McLinden, C. A., J. C. McConnell, K. Strong, I. C. McDade, R. L. Gattinger, R. King, B. Solheim, and E. J. Llewellyn, The impact of the OSIRIS grating efficiency on total radiance and trace-gas retrievals, *Can. J. Phys.*, *80*, 469–481, 2002.

McPeters, R. D., S. J. Janz, E. Hilsenrath, T. L. Brown, D. E. Flittner, and D. F. Heath, The retrieval of O_3 profiles from limb scatter measurements: Results from the Shuttle Ozone Limb Sounding Experiment, *Geophys. Res. Lett.*, *27*, 2597–2600, 2000.

Moore, C. E., M. G. J. Minnaert, and J. Houtgast, The solar spectrum: 2935 Å to 8770 Å: Second revision to Rowland's preliminary table of solar spectrum wavelengths, *Monogr. 61*, Natl. Bur. of Stand., U.S. Dep. of Comm., Washington, D. C., 1966.

Mount, G. H., D. W. Rusch, J. F. Noxon, J. M. Zawodny, and C. A. Barth, Measurements of stratospheric NO_2 from the Solar Mesosphere Explorer Satellite, 1, An overview of the results, *J. Geophys. Res.*, *89*, 1327–1340, 1984.

Murtagh, D., et al., An overview of the Odin atmospheric mission, *Can. J. Phys.*, *80*, 309–318, 2002.

Noxon, J. F., Nitrogen dioxide in the stratosphere and troposphere measured by ground-based absorption spectroscopy, *Science*, *189*, 547–549, 1975.

Pfeilsticker, K., H. Bösch, C. Camy-Peyret, R. Fitzenberger, H. Harder, and H. Osterkamp, First atmospheric measurements of UV/visible absorption intensities: Implications for the spectroscopy, and formation enthalpy of the O_2-O_2 dimer, *J. Geophys. Res.*, *28*, 4595–4598, 2001.

Platt, U., L. Marquard, T. Wagner, and D. Perner, Corrections for zenith scattered light DOAS, *Geophys. Res. Lett.*, *24*, 1759–1762, 1997.

Randall, C. E., et al., Validation of POAM III NO_2 measurements, *J. Geophys. Res.*, *107*(D20), 4432, doi:10.1029/2001JD001520, 2002.

Rodgers, C. D., Retrieval of atmospheric temperature and composition from remote measurements of thermal radiation, *Rev. Geophys.*, *14*, 609–624, 1976.

Roscoe, H. K., D. J. Fish, and R. L. Jones, Interpolation errors in UV-visible spectroscopy for stratospheric sensing: implications for sensitivity, spectral resolution, and spectral range, *Appl. Opt.*, *35*, 427–432, 1996.

Sioris, C. E., The filling in of absorption lines in sky spectra due to rotational Raman scattering, Ph. D. thesis, 135 pp., York Univ., Toronto, May 2001.

Sioris, C. E., W. F. J. Evans, R. L. Gattinger, I. C. McDade, D. A. Degenstein, and E. J. Llewellyn, Ground-based Ring effect measurements with the OSIRIS DM, *Can. J. Phys.*, *80*, 483–491, 2002.

Strong, K., B. M. Joseph, R. Dosanjh, I. C. McDade, C. A. McLinden, J. C. McConnell, J. Stegman, D. P. Murtagh, and E. J. Llewellyn, Retrieval of concentration profiles from OSIRIS UV-visible limb spectra, *Can. J. Phys.*, *80*, 409–434, 2002.

Thomas, R. J., K. H. Rosenlof, R. T. Clancy, and J. Zawodny, Stratospheric NO_2 over Antarctica as measured by the Solar Mesosphere Explorer during austral spring, 1986, *J. Geophys. Res.*, *93*, 12561–12568, 1988.

Vandaele, A. C., C. Hermans, P. C. Simon, M. Carleer, R. Colin, S. Fally, M. F. Mérienne, A. Jenouvrier, and B. Coquart, Measurements of NO_2 absorption cross-section from 42000 cm^{-1} to 10000 cm^{-1} (238–1000 nm) at 220 K and 298 K, *J. Quant. Spectrosc. Radiat. Transfer*, *59*, 171–184, 1998.

von Savigny, C., Retrieval of stratospheric ozone density profiles from OSIRIS scattered sunlight observations, Ph.D. thesis, 156 pp., York Univ., Toronto, April 2002.

von Savigny, C., et al., Stratospheric ozone profiles retrieved from limb scattered sunlight radiance spectra measured by the OSIRIS instrument on the Odin satellite, *Geophys. Res. Lett.*, *30*, doi:10.1029/2002GL016401, in press, 2003.

Vountas, M., V. V. Rozanov, and J. P. Burrows, Ring effect: Impact of rotational Raman scattering on radiative transfer in Earth's atmosphere, *J. Quant. Spectrosc. Radiat. Transfer*, *60*, 943–961, 1998.

Warshaw, G. D., D.-L. Desaulniers, and D. Degenstein, Optical design and performance of the performance of the ODIN UV/visible spectrograph and infrared imager system, paper presented at Technical Session XII, paper presented at 10th Annual AIAA/Utah State University Conference on Small Satellites, Am. Inst. of Aeronaut. and Astronaut., Logan, Utah, 1996.

Zawodny, J. M., Short-term variability of nitrogen dioxide in the winter stratosphere, *J. Geophys. Res.*, *91*, 5439–5450, 1986.

Zobov, N. F., et al., The near-ultraviolet rotation-vibration spectrum of water, *J. Chem. Phys.*, *113*, 1546–1552, 2000.

H. Bösch, K. Pfeilsticker, and F. Weidner, Institute of Environmental Physics, University of Heidelberg, INF 229, D-69120 Heidelberg, Germany. (pf@iup.uni-heidelberg.de)

K. Chance, T. P. Kurosu, and C. E. Sioris, Atomic and Molecular Physics Division, Harvard-Smithsonian Center for Astrophysics, Cambridge, MA 02138, USA. (kchance@cfa.harvard.edu; tkurosu@cfa.harvard.edu; csioris@cfa.harvard.edu)

W. F. J. Evans, Department of Physics, Trent University, Peterborough, Canada K9J 7B8. (wevans@trentu.ca)

U. Frisk, Swedish Space Corporation, P. O. Box 4207, Solna SE-171 04, Sweden.

C. S. Haley, J. C. McConnell, and I. C. McDade, Centre for Research in Earth and Space Science, York University, 113 Petrie Building, 4700 Keele Street, Toronto, Ontario, Canada M3J 1P3. (jack@nimbus.yorku.ca; mcdade@yorku.ca)

E. J. Llewellyn and N. D. Lloyd, Department of Physics and Engineering Physics, University of Saskatchewan, 116 Science Place, Saskatoon, Saskatchewan, Canada S7N 5E2. (llewellyn@skisas.usask.ca)

C. A. McLinden, Air Quality Research Branch, Meteorological Service of Canada, 4905 Dufferin Street, Toronto, Ontario, Canada M3H 5T4. (chris.mclinden@ec.gc.ca)

G. Mégie, Service d'Aeronomie du CNRS, IPSL-Université Pierre et Marie Curie, F-75252 Paris Cedex 05, France.

D. Murtagh, Department of Radio and Space Science, Chalmers University, Göteberg SE-41296, Sweden. (donal@rss.chalmers.se)

J. Stegman, Department of Meteorology, Stockholm University, Stockholm SE-106 91, Sweden. (jacek@misu.su.se)

K. Strong, Department of Physics, University of Toronto, Room MP 710A, 60 St. George Street, Toronto, Ontario, Canada M5S 1A7. (strong@atmosp.physics.utoronto.ca)

C. von Savigny, Institute of Environmental Physics, University of Bremen, NW1, Otto-Hahn-Allee 1, Bremen D-28359, Germany. (csavigny@iup.physik.uni-bremen.de)

Appendix C

Paper III

A comparison of methods for retrieving stratospheric ozone profiles from OSIRIS limb-scatter measurements

Craig S. Haley, Christian von Savigny, Samuel M. Brohede, Christopher E. Sioris, Ian C. McDade, Edward J. Llewellyn, and Donal P. Murtagh

Adv. Space Res.

34(4), 769-774, doi:10.1016/j.asr.2003.08.058, 2004

Available online at www.sciencedirect.com
SCIENCE DIRECT®
Advances in Space Research 34 (2004) 769–774
ADVANCES IN SPACE RESEARCH (a COSPAR publication)
www.elsevier.com/locate/asr

A comparison of methods for retrieving stratospheric ozone profiles from OSIRIS limb-scatter measurements

C.S. Haley [a,*], C. von Savigny [b], S. Brohede [c], C.E. Sioris [d], I.C. McDade [a], E.J. Llewellyn [e], D.P. Murtagh [c]

[a] Centre for Research in Earth and Space Science, York University, 4700 Keele Street, Toronto, ON M3J 1P3, Canada
[b] Institute of Environmental Physics, University of Bremen, Otto-Hahn-Allee 1, 28359, Bremen, Germany
[c] Department of Radio and Space Science, Chalmers University of Technology, Göteborg, SE-41296, Sweden
[d] Harvard-Smithsonian Center for Astrophysics, 60 Garden Street, Cambridge, MA 02138, USA
[e] Department of Physics and Engineering Physics, University of Saskatchewan, 116 Science Place, Saskatoon, SK S7N 5E2, Canada

Received 21 January 2003; received in revised form 6 August 2003; accepted 11 August 2003

Abstract

Vertical profiles of stratospheric ozone number density derived from optical spectrograph and infrared imager system (OSIRIS) measurements of limb-scattered sunlight are presented. Ozone profiles are inferred using a method based on the analysis of normalised and paired limb radiance profiles at a set of wavelengths covering the Chappuis–Wulf bands of ozone, and using differential optical absorption spectroscopy (DOAS) in the Chappuis region. Both methods incorporate the pseudo-spherical multiple scattering radiative transfer model LIMBTRAN and an optimal estimation (OE) approach. The results of both methods are compared with ozone sonde and other satellite measurements.

Keywords: Stratospheric ozone; Odin/OSIRIS; Limb scattering; DOAS

1. Introduction

Several satellite-based nadir-viewing spectrometers, including the total ozone mapping spectrometer (TOMS) (McPeters et al., 1998) and the global ozone monitoring experiment (GOME) (Burrows et al., 1999), currently provide global maps of total O_3 columns on a daily basis, but yield O_3 profiles with only limited vertical resolution. Solar occultation instruments, including the halogen occultation experiment (HALOE) (Russell et al., 1993) and the polar ozone and aerosol measurement III (POAM III) instrument (Lucke et al., 1999), on the other hand, allow for the retrieval of O_3 profiles with high vertical resolution, but their coverage is limited to about 15 sunset and 15 sunrise profiles per day.

A new generation of satellite instruments measures profiles of limb-scattered sunlight spectra to provide vertical profiles of O_3 and other minor constituents with a vertical resolution of 1–3 km and (near) global coverage. One instrument that employs the limb-scatter technique is the optical spectrograph and infrared imager system (OSIRIS) (Warshaw et al., 1998), which was launched aboard the Odin satellite in February 2001. Other instruments currently employing this technique include the scanning imaging absorption spectrometer for atmospheric chartography (SCIAMACHY) (Bovensmann et al., 1999), the global ozone monitoring by occultation of stars (GOMOS) instrument (Bertaux et al., 1991), and the stratospheric aerosol and gas experiment III (SAGE III) (McCormick et al., 1991).

In this paper, stratospheric O_3 profiles retrieved from OSIRIS limb-scatter measurements are presented. Two different retrieval methods are compared. Vertical profiles of O_3 are retrieved using a method based on the analysis of normalised and paired limb radiance profiles and using differential optical absorption spectroscopy (DOAS). Ozone profiles retrieved with these two

* Corresponding author. Tel.: +1-416-736-2100x33517; fax: +1-416-736-5626.
E-mail address: cshaley@yorku.ca (C.S. Haley).

0273-1177/$30 © 2004 COSPAR. Published by Elsevier Ltd. All rights reserved.
doi:10.1016/j.asr.2003.08.058

methods are compared to each other and to ozone sonde and POAM III measurements.

2. OSIRIS on Odin

OSIRIS was launched aboard the Odin satellite into a circular, sun-synchronous, near-terminator orbit with an inclination of 97.8° and an ascending node at 1800 local solar time (LST). Odin is a joint aeronomy and astronomy mission developed by Sweden, Canada, France, and Finland (Murtagh et al., 2002). OSIRIS is dedicated to aeronomy studies while a second instrument, the submillimeter and millimeter radiometer (SMR), carries out both aeronomy and astronomy studies. OSIRIS and SMR are co-aligned, and scan the limb of the atmosphere over a tangent height range of 7–70 km in the normal stratospheric mode through controlled nodding of the satellite.

OSIRIS consists of: (i) a UV–Visible imaging spectrograph designed to measure the spectrum of sunlight scattered by the limb in the spectral range 280–820 nm at a resolution of about 1 nm, and (ii) a 3-channel IR imager designed to measure atmospheric airglow emissions near 1.27 and 1.53 μm in a limb-viewing tomographic mode. The scattered sunlight measurements are used to provide vertical profiles of minor stratospheric constituents including O_3, NO_2, and aerosols, and the IR images are used to provide high resolution three dimensional distributions of O_3 in the mesosphere (Degenstein et al., 2003).

3. Paired radiance method

One O_3 retrieval method being applied to OSIRIS UV–Visible measurements closely follows the method successfully applied by Flittner et al. (2000) and McPeters et al. (2000) to limb radiance profiles measured by the shuttle ozone limb sounding experiment/limb ozone retrieval experiment (SOLSE/LORE) instruments, which were flown on NASA's space shuttle in 1997. In this method, limb-scatter measurements in the Chappuis–Wulf bands of O_3 are used to retrieve O_3 number density profiles between about 14 and 40 km. Below about 14 km the optical depths become quite large and the sensitivity of the method to O_3 at these heights decreases. This lower limit varies with latitude and season. Above 40 km, the method becomes insensitive to O_3 because of the small O_3 number densities and relatively weak absorption in the Chappuis–Wulf region. Additional measurements in the O_3 Hartley and Huggins bands can be incorporated to extend the retrievals above 40 km, but are not included in this study.

In the first step of the retrieval scheme, the limb radiance profiles are normalised with respect to a reference tangent height, i.e. $I_n(\lambda, \mathrm{TH}_i) = I(\lambda, \mathrm{TH}_i)/I(\lambda, \mathrm{TH}_{\mathrm{ref}})$, where $I(\lambda, \mathrm{TH}_i)$ is the limb radiance measured at wavelength λ and tangent height TH_i, and $I(\lambda, \mathrm{TH}_{\mathrm{ref}})$ is the limb radiance measured at wavelength λ and the reference tangent height $\mathrm{TH}_{\mathrm{ref}}$. The normalised radiances at the three wavelengths are then combined to produce the *Chappuis retrieval vector:*

$$y_c(\mathrm{TH}_i) = \frac{I_n(\lambda_2, \mathrm{TH}_i)}{\sqrt{I_n(\lambda_1, \mathrm{TH}_i) \times I_n(\lambda_3, \mathrm{TH}_i)}} \quad (1)$$

with $i = 1, \ldots, N_{\mathrm{TH}}$, where N_{TH} is the number of measurements in each limb radiance profile. Through normalisation, the sensitivity to ground albedo is reduced and the measurements are self-calibrated, analogous to the occultation technique. For this study, measurements centered about the wavelengths $\lambda_1 = 532$ nm, $\lambda_2 = 602$ nm, and $\lambda_3 = 672$ nm and a reference tangent height $\mathrm{TH}_{\mathrm{ref}} \approx 50$ km are used.

To derive vertical profiles of O_3 from the retrieval vectors, a non-linear Newtonian iteration version of optimal estimation (OE) (Rodgers, 1976) is used. The radiative transfer (RT) model used as the forward model in the inversion is LIMBTRAN (Griffioen and Oikarinen, 2000), operating in a pseudo-spherical, full multiple scattering mode. The required weighting functions are calculated through a perturbation technique (5% perturbations). The RT model incorporates O_3 and NO_2 absorption cross-sections (including temperature dependence) from Bogumil et al. (2003) and Vandaele et al. (1998). The a priori and reference atmosphere information is obtained from the climatology of McLinden et al. (2002a) and the ground albedo database of Matthews (1983) is utilised. The a priori covariance matrix is chosen to be diagonal, and the standard deviation for each altitude is assumed to be 100% of the a priori value.

The application of this method to OSIRIS measurements is discussed in greater detail by von Savigny et al. (2003), and a detailed sensitivity study has been carried out by von Savigny (2002).

4. Differential optical absorption spectroscopy (DOAS)

The retrieval of O_3 profiles through a DOAS analysis of limb-scatter measurements (McDade et al., 2002) is similar to the method routinely applied to ground-based (zenith) and space-based (nadir) measurements.

A spectral fit is first carried out using the standard DOAS approach of Platt (1994), where *effective column densities* of O_3 are determined by carrying out a linear regression against the measured *optical density:*

$$D(\lambda, \mathrm{TH}_i) = \ln\left[\frac{I(\lambda, \mathrm{TH}_i)}{I(\lambda, \mathrm{TH}_{\mathrm{ref}})}\right] = -\sum_{n=1}^{\#\mathrm{species}} C_n(\mathrm{TH}_i) \times \sigma_n(\lambda) + \mathrm{POLY}(\lambda, \mathrm{TH}_i), \quad (2)$$

where $D(\lambda, \mathrm{TH}_i)$ are the measured optical densities, $C_n(\mathrm{TH}_i)$ are the effective column densities, $\sigma_n(\lambda)$ are the absorption cross-sections, and $\mathrm{POLY}(\lambda, \mathrm{TH}_i)$ are polynomial terms to account for the low frequency structure in the optical density and cross-sections. The reference spectrum is taken to be a high (≈50 km) tangent height measurement from the same scan.

For this study, the spectral range 571–617 nm is used, thus avoiding the strong temperature dependence of the O_3 cross-sections in the Huggins and Wulf bands, but limiting the retrievals to below about 40 km. Measurements in the region of the Na Fraunhofer/airglow feature near 590 nm are not included in the spectral fitting. For this spectral window, absorption cross-sections of NO_2 and O_4, and the Rayleigh scattering cross-section are included along with O_3 in the spectral fit and a 2nd order polynomial is used. The absorption cross-sections are from Bogumil et al. (2003), Vandaele et al. (1998), and Greenblatt et al. (1990) at fixed temperatures (223 K for O_3, 220 K for NO_2, and 298 K for O_4). The polarisation sensitivity of the spectrograph is taken into account through the inclusion of a pseudo-absorber, as described by McLinden et al. (2002b). Residuals from the spectral fitting are typically about 2.5×10^{-3} rms (root-mean-square) and vary little with tangent height.

Vertical O_3 profiles are retrieved from the effective column densities using OE and the LIMBTRAN model in a similar manner to that described in the previous section, though whereas in the previous section the RT model is used to produce weighting functions and modelled retrieval vectors using Eq. (1), here the RT model radiances (perturbed and unperturbed) are passed through the same DOAS spectral fit as the measurements via Eq. (2). To speed up the processing, wavelengths at 6 nm steps covering the spectral window are modelled rather than OSIRIS pixel steps, and the OSIRIS spectral resolution is not fully taken into account. It was found that these simplifications have little effect on O_3 profiles retrieved from this spectral window, but this may not be the case for other windows containing narrower absorption features.

A detailed study is currently in progress to examine the sensitivity of this retrieval method to issues including albedo, clouds, and a priori information. A similar method has been used to retrieve stratospheric profiles of NO_2 from OSIRIS measurements by Sioris et al. (2003).

5. Results

Figs. 1 and 2 show the O_3 number density profiles retrieved using both retrieval methods for coincident ozone sonde profiles measured at Ny-Ålesund and Santa Cruz. Note that the ozone sonde results have not been smoothed. Clearly the methods are in good agreement with each other and with the sonde measurements,

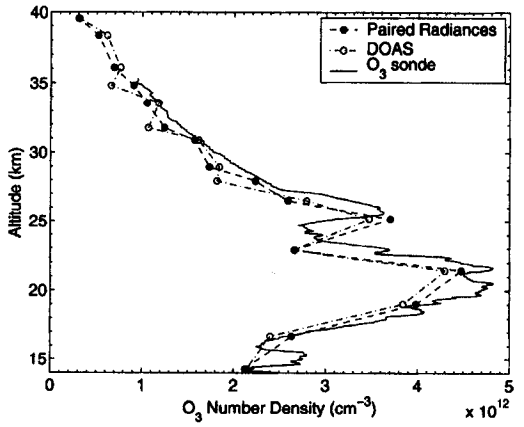

Fig. 1. August 8, 2001 O_3 profiles retrieved from OSIRIS (lat: 76.8°N, lon: 12.7°E, 7:33 UTC) and an ozone sonde launched from Ny-Ålesund, Norway (lat: 78.9°N, lon: 11.9°E, 10:59 UTC).

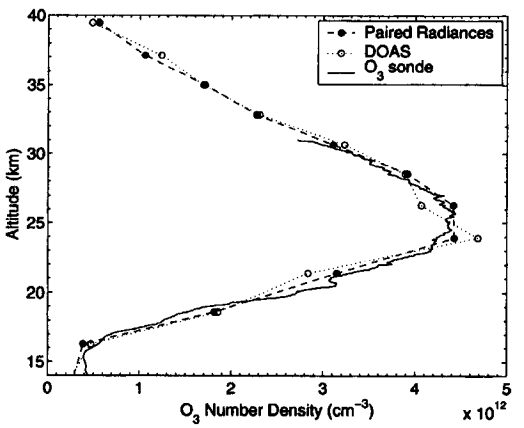

Fig. 2. August 22, 2001 O_3 profiles retrieved from OSIRIS (lat: 29.5°N, lon: 16.0°W, 18:48 UTC) and an ozone sonde launched from Santa Cruz, Spain (lat: 28.3°N, lon: 16.5°W, 11:17 UTC).

though Fig. 1 suggests an offset of about 1 km in the attitude reconstruction for this scan. The instabilities in the DOAS retrievals in both figures are due to the relatively broad absorption signatures in the chosen spectral window, which are not well-suited to a DOAS analysis.

In Figs. 3 and 4, OSIRIS results are compared with results from the POAM III instrument. Again there is good agreement between the two methods and with the POAM III measurements, though some differences between the two methods are evident, particularly in the region of the peak.

For a more detailed comparison of the two techniques, two days of OSIRIS measurements were

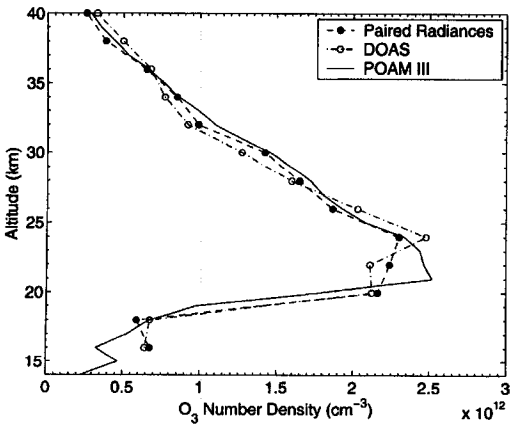

Fig. 3. November 18, 2001 O_3 profiles retrieved from OSIRIS (lat: 64.8° S, Ion: 33.8° E, 16:53 UTC) and POAM III (lat: 68.6° S, Ion: 30.0° E, 19:59 UTC).

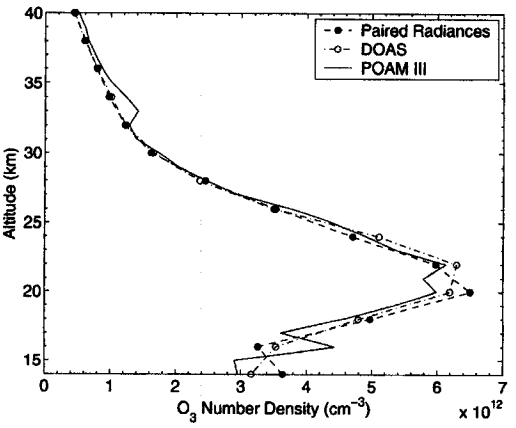

Fig. 4. March 3, 2002 O_3 profiles retrieved from OSIRIS (lat: 68.1°N, Ion: 10.5°W, 17:23 UTC) and POAM III (lat: 67.5°N, Ion: 20.5°W, 18:27 UTC).

processed: November 18, 2001 and March 3, 2002. The retrievals for each day were combined to produce the zonally averaged O_3 number density profiles presented in Figs. 5 and 6, where the results from both methods show the general features of stratospheric O_3 climatology. Also shown are the percent differences between the two techniques for the two days. In general, the differences are less than 5% in most regions, with the limb radiance retrievals giving larger densities. Large differences exist in regions that correlate with the intertropical convergence zone (ITCZ) on both days, where the DOAS retrievals give densities on the order of 20–30%

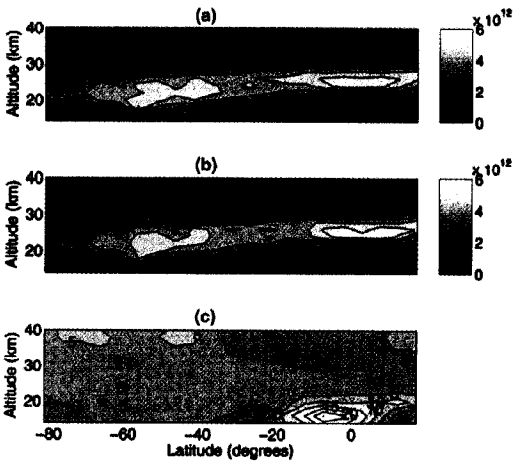

Fig. 5. Zonally averaged November 18, 2001 O_3 field (cm^{-3}) retrieved from OSIRIS limb radiance profiles with a paired radiance analysis (panel a) and a DOAS analysis (panel b) and the percent difference ($[1 - b/a] * 100\%$) (panel c).

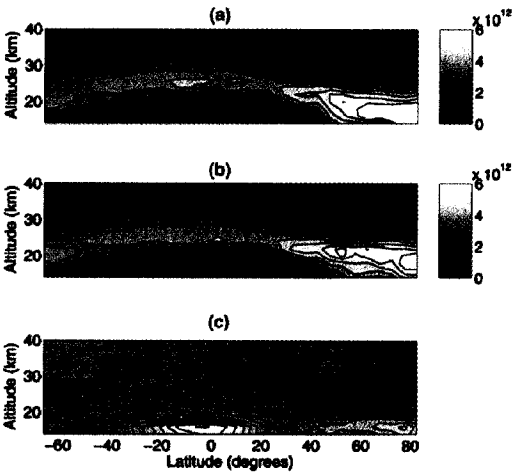

Fig. 6. Zonally averaged March 3, 2002 O_3 field (cm^{-3}) retrieved from OSIRIS limb radiance profiles with a paired radiance analysis (panel a) and a DOAS analysis (panel b) and the percent difference ($[1 - b/a] * 100\%$) (panel c).

smaller than those retrieved from the limb radiance method below 20 km. The differences in terms of absolute number density, however, are small ($\approx 2 \times 10^{11}$ cm^{-3}), and partial vertical columns (14–40 km) derived from the retrievals differ by less than 5%. Large differences also exist at high northern latitudes in Fig. 6, with the DOAS method retrieving smaller densities below 20 km and larger densities above.

The differences between the two methods in the ITCZ region may be related to a number of issues. The sensitivity of each method to O_3 decreases at low altitudes in the tropics, and clouds, surface albedo and the a priori O_3 estimate begin to affect the retrievals from each method to different extents. Also, the sensitivity of the spectrograph to polarised light is accounted for in the DOAS analysis but is ignored in the paired radiance retrievals. As well, a weak water vapour feature exists within the DOAS window, but is not accounted for in the spectral fitting and may be interfering at low altitudes in the tropics. The wavelengths chosen for the paired radiance analysis avoid this feature. Further studies into the sensitivities of the DOAS method to each of these issues are required.

At high northern latitudes the DOAS retrievals had difficulty converging. It must be noted again that the spectral window chosen for the DOAS retrievals is not ideal for O_3 retrievals due to the broad spectral features and contamination from O_4 and potentially water vapour. The removal of data near the Na feature and the inclusion of polarisation also complicate the retrievals.

6. Summary

Retrievals of vertical profiles of stratospheric O_3 from OSIRIS limb-scatter measurements have been presented. Two retrieval methods were compared, one based on a paired radiance approach and one based on a DOAS approach. Both methods use a non-linear OE scheme and incorporate the pseudo-spherical multiple scattering radiative transfer model LIMBTRAN. The main features of the O_3 climatology over a wide range of conditions are retrieved by both methods and are in good agreement with ozone sonde and POAM III measurements. The DOAS retrievals appear somewhat unstable, likely due to the particular spectral region being used, and seem to underestimate O_3 number densities at low altitudes in the tropics. Further investigation into the sensitivities of the DOAS retrievals is required.

Acknowledgements

This work has been supported by the Canadian Space Agency, the Natural Sciences and Engineering Research Council (Canada), and the Swedish National Space Board. Odin is a Swedish-led satellite project funded jointly by Sweden (SNSB), Canada (CSA), Finland (Tekes), and France (CNES). We would like to thank P. van der Gathen (AWI Potsdam) and E. Cuevas (INM Spain) for providing the ozone sonde data, and the POAM III processing team for making their data available.

References

Bertaux, J.L., Mégie, G., Widemann, T., et al. Monitoring of ozone trend by stellar occultations: the GOMOS instrument. Adv. Space Res. 11 (3), 237–242, 1991.

Bogumil, K., Orphal, J., Homann, T., et al. Measurements of molecular absorption spectra with the SCIA-MACHY pre-flight model: instrument characterization and reference data for atmospheric remote-sensing in the 230–2380 nm region. J. Photochem. Photobiol. A: Chem. 157, 167–184, 2003, doi:10.1016/S1010-6030(03)00062-5.

Bovensmann, H., Burrows, J.P., Buchwitz, M., et al. SCIAMACHY: mission objectives and measurement modes. J. Atmos. Sci. 56, 127–150, 1999.

Burrows, J.P., Weber, M., Buchwitz, M., et al. The global ozone monitoring experiment (GOME): mission concept, and first scientific results. J. Atmos. Sci. 56, 151–175, 1999.

Degenstein, D.A., Llewellyn, E.J., Lloyd, N.D. Volume emission rate tomography from a satellite platform. Appl. Opt. 42, 1441–1450, 2003.

Flittner, D.E., Bhartia, P.K., Herman, B.M. O_3 profiles retrieved from limb scatter measurements: theory. Geophys. Res. Lett. 27, 2601–2604, 2000.

Greenblatt, G.D., Orlando, J.J., Burkholder, J.B., et al. Absorption measurements of oxygen between 330 and 1140 nm. J. Geophys. Res. 95, 18,577–18,582, 1990.

Griffioen, E., Oikarinen, L. LIMBTRAN: a pseudo three-dimensional radiative transfer model for the limb-viewing imager OSIRIS on the Odin satellite. J. Geophys. Res. 105, 29,717–29,730, 2000.

Lucke, R.L., Korwan, D.R., Bevilacqua, R.M., et al. The polar ozone and aerosol measurement (POAM) III instrument and early validation results. J. Geophys. Res. 104, 18,785–18,799, 1999.

Matthews, E. Global vegetation and land use: new high-resolution databases for climate studies. J. Clim. Appl. Meteor. 22, 474–487, 1983.

McCormick, M.P., Chu, W.P., Zawodny, J.M., et al. Stratospheric aerosol and gase experiment III (SAGE III) aerosol and trace gas measurements for earth observing system (EOS), in: Proc. SPIE Int. Soc. Opt. Eng., 1491, pp. 125–141, 1991.

McDade, I.C., Strong, K., Haley, C.S., et al. A method for recovering stratospheric minor species densities from the Odin/OSIRIS scattered-sunlight measurements. Can. J. Phys. 80, 395–408, 2002.

McLinden, C.A., McConnell, J.C., Griffioen, E., et al. A vector radiative transfer model for the Odin/OSIRIS project. Can. J. Phys. 80, 375–393, 2002a.

McLinden, C.A., McConnell, J.C., Strong, K., et al. The impact of the OSIRIS grating efficiency on radiance and trace-gas retrievals. Can. J. Phys. 80, 469–481, 2002b.

McPeters, R.D., Bhartia, P.K., Krueger, A.J., et al. Earth Probe Total Ozone Mapping Spectrometer (TOMS) Data Products User's Guide, NASA Technical Publication, 1998-206895, 1998.

McPeters, R.D., Janz, S.J., Hilsenrath, E., et al. The retrieval of O_3 profiles from limb scatter measurements: results from the shuttle ozone limb sounding experiment. Geophys. Res. Lett. 27, 2597–2600, 2000.

Murtagh, D., Frisk, U., Merino, F., et al. An overview of the Odin atmospheric mission. Can. J. Phys. 80, 309–319, 2002.

Platt, U. Differential optical absorption spectroscopy (DOAS), in: Sigrist, M.W. (Ed.), Air Monitoring by Spectroscopic Techniques. Wiley, New York, pp. 27–84, 1994.

Rodgers, C.D. Retrieval of atmospheric temperature and composition from remote measurements of thermal radiation. Rev. Geophys. Space Phys. 14, 609–624, 1976.

Russell III, J.M., Gordley, L.L., Park, J.H., et al. The halogen occultation experiment. J. Geophys. Res. 98, 10,777–10,797, 1993.

von Savigny, C. Retrieval of Stratospheric Ozone Density Profiles from OSIRIS Scattered Sunlight Observations, Ph.D. Thesis, York University, Toronto, 2002.

von Savigny, C., Haley, C.S., Sioris, C.E., et al. Stratospheric ozone profiles retrieved from limb scattered sunlight radiance spectra measured by the OSIRIS instrument on the Odin satellite. Geophys. Res. Lett. 30 (14), 1755–1758, 2003, doi:10.1029/2002GL016401.

Sioris, C.E., Haley, C.S., McLinden, C.A., et al. Stratospheric profiles of nitrogen dioxide observed by OSIRIS on the Odin satellite. J. Geophys. Res. 108 (D7), 4215–4234, 2003, doi:10.1029/2002JD002672.

Vandaele, A.C., Hermans, C., Simon, P.C., et al. Measurements of the NO_2 absorption cross-section from 42000 to 10000 cm^{-1} (238–1000 nm) at 220 K and 294 K. J. Quant. Spectrosc. Radiat. Transfer 59, 171–184, 1998.

Warshaw, G.D., Desaulniers, D.-L., Degenstein, D. Optical design and performance of the Odin UV/Visible spectrograph and infrared imager instrument, in: Proc. 12th Annual AIAA/USU Conference on Small Satellites, 1998.

Appendix D

Paper IV

Retrieval of stratospheric O_3 and NO_2 profiles from Odin Optical Spectrograph and Infrared Imager System (OSIRIS) limb-scattered sunlight measurements

Craig S. Haley, Samuel M. Brohede, Christopher E. Sioris, Erik Griffioen, Donal P. Murtagh, Ian C. McDade, Patrick Eriksson, Edward J. Llewellyn, Arianne Bazureau, and Florence Goutail

J. Geophys. Res.

109, D16303, doi:10.1029/2004JD004588, 2004

JOURNAL OF GEOPHYSICAL RESEARCH, VOL. 109, D16303, doi:10.1029/2004JD004588, 2004

Retrieval of stratospheric O_3 and NO_2 profiles from Odin Optical Spectrograph and Infrared Imager System (OSIRIS) limb-scattered sunlight measurements

Craig S. Haley,[1] Samuel M. Brohede,[2] Christopher E. Sioris,[1,3] Erik Griffioen,[1,4] Donal P. Murtagh,[2] Ian C. McDade,[1] Patrick Eriksson,[2] Edward J. Llewellyn,[5] Ariane Bazureau,[6] and Florence Goutail[6]

Received 30 January 2004; revised 3 April 2004; accepted 3 June 2004; published 20 August 2004.

[1] Scientific studies of the major environmental questions of global warming and ozone depletion require global data sets of atmospheric constituents with relevant temporal and spatial resolution. In this paper, global number density profiles of O_3 and NO_2 are retrieved from Odin Optical Spectrograph and Infrared Imager System (Odin/OSIRIS) limb-scattered sunlight measurements, using the maximum a posteriori estimator. Differential optical absorption spectroscopy is applied to OSIRIS radiances as an intermediate step, using the wavelength windows 571–617 nm for O_3 and 435–451 nm for NO_2. The method is computationally efficient for processing OSIRIS data on an operational basis. Results show that a 2–3 km height resolution is generally achievable between about 12 km and 45 km for O_3 with an estimated accuracy of 13% at the peak and between about 15 km and 40 km for NO_2 with an estimated accuracy of 10% at the peak. First validations of the retrieved data indicate a good agreement both with other retrieval techniques applied to OSIRIS measurements and with the results of other instruments. Once the validation has reached a confident level, the retrieved data will be used to study important stratospheric processes relevant to global environmental problems. The unique NO_2 data set will be of particular interest for studies of nitrogen chemistry in the middle atmosphere. *INDEX TERMS:* 0340 Atmospheric Composition and Structure: Middle atmosphere—composition and chemistry; 0394 Atmospheric Composition and Structure: Instruments and techniques; 0360 Atmospheric Composition and Structure: Transmission and scattering of radiation; *KEYWORDS:* Odin/OSIRIS, limb scattering, DOAS

Citation: Haley, C. S., S. M. Brohede, C. E. Sioris, E. Griffioen, D. P. Murtagh, I. C. McDade, P. Eriksson, E. J. Llewellyn, A. Bazureau, and F. Goutail (2004), Retrieval of stratospheric O_3 and NO_2 profiles from Odin Optical Spectrograph and Infrared Imager System (OSIRIS) limb-scattered sunlight measurements, *J. Geophys. Res.*, *109*, D16303, doi:10.1029/2004JD004588.

1. Introduction

[2] A number of satellite instruments have been launched recently that measure limb-scattered sunlight radiances with the goal of deriving vertical profiles of stratospheric minor species. These instruments include Optical Spectrograph and Infrared Imager System (OSIRIS) on the Odin satellite [*Warshaw et al.*, 1998; *Llewellyn et al.*, 2004] and Scanning Imaging Absorption Spectrometer for Atmospheric Chartography (SCIAMACHY) on Envisat [*Bovensmann et al.*, 1999]. Global Ozone Measurement by Occultation of Stars (GOMOS) on Envisat [*Bertaux et al.*, 1991] and Stratospheric Aerosol and Gas Experiment III (SAGE III) on the Meteor-3M spacecraft [*McCormick et al.*, 1991] also have limb-scatter measurement capabilities. The Ozone Mapping and Profiler Suite (OMPS) on the National Polar-Orbiting Operational Environmental Satellite System (NPOESS) Preparatory Project (NPP) [*Seftor et al.*, 2003], due to be launched in 2006, will also contain a limb profiler measuring scattered sunlight to provide stratospheric O_3 profiles on an operational basis.

[3] The limb-scatter technique was first applied by Ultraviolet Spectrometer (UVS) on the Solar Mesosphere Explorer (SME) satellite to retrieve mesospheric O_3 profiles [*Rusch et al.*, 1984] and stratospheric NO_2 profiles [*Mount et al.*, 1984]. The Shuttle Ozone Limb Sounding Experiment/Limb Ozone Retrieval Experiment (SOLSE/LORE)

[1]Centre for Research in Earth and Space Science, York University, Toronto, Ontario, Canada.
[2]Department of Radio and Space Science, Chalmers University of Technology, Göteborg, Sweden.
[3]Now at Atomic and Molecular Physics Division, Harvard-Smithsonian Center for Astrophysics, Cambridge, Massachusetts, USA.
[4]Now at Juravinski Cancer Centre, Hamilton, Ontario, Canada.
[5]Department of Physics and Engineering Physics, University of Saskatchewan, Saskatoon, Saskatchewan, Canada.
[6]Service d'Aéronomie, Centre National de la Recherche Scientifique, Verrières le Buisson, France.

0148-0227/04/2004JD004588$09.00

instrument package that flew on NASA's space shuttle also used the limb-scatter technique to successfully derive stratospheric O_3 profiles [*McPeters et al.*, 2000].

[4] The interest in the limb-scatter technique lies in a demand for atmospheric information with both global coverage and relatively high vertical resolution. The traditional source of global stratospheric minor species information has been satellite instruments such as Total Ozone Mapping Spectrometer (TOMS) [*McPeters et al.*, 1998], Global Ozone Monitoring Experiment (GOME) [*Burrows et al.*, 1999], Halogen Occultation Experiment (HALOE) [*Russell et al.*, 1993] and Polar Ozone and Aerosol Measurement (POAM) [*Lucke et al.*, 1999]. The measurements provided by these instruments are limited by either poor or no vertical information (TOMS and GOME) or restricted spatial coverage (HALOE and POAM). The advantage of the limb-scatter technique is the provision of vertical profiles of stratospheric and mesospheric minor constituents with high vertical resolution (1–3 km) and near-global coverage. A limitation to the technique is that only the measurements from the sunlit portion of each orbit can be utilized. Passive thermal emission instruments provide the same benefits as the limb-scatter technique and are not limited to measuring the sunlit atmosphere. Such instruments include Microwave Limb Sounder (MLS) on Upper Atmosphere Research Satellite (UARS) [*Barath et al.*, 1993], MIPAS (Michelson Interferometer for Passive Atmospheric Sounding) on Envisat [*Fischer and Oelhaf*, 1996] and Submillimeter and Millimeter Radiometer (SMR) on the Odin satellite [*Frisk et al.*, 2003].

[5] A number of methods for retrieving stratospheric minor species profiles from limb-scattered radiances have been proposed, including methods which retrieve information directly from the limb measurements [*Kaiser*, 2001; *Auvinen et al.*, 2002] and methods that apply a spectral analysis technique to simplify the problem [*Flittner et al.*, 2000; *Rozanov*, 2001; *McDade et al.*, 2002; *Strong et al.*, 2002; *Sioris et al.*, 2003]. This study focuses on the application of differential optical absorption spectroscopy (DOAS) [*Platt*, 1994] in combination with an optimal estimation (OE) method, more specifically the maximum a posteriori estimator (MAP) [*Rodgers*, 2000], to OSIRIS limb-scatter measurements for the retrieval of stratospheric O_3 and NO_2 number density profiles. A brief overview of OSIRIS is followed by a detailed description of the retrieval technique and an analysis of the various sources of error. Some first comparisons with other measurements are then shown to illustrate that the technique is appropriate and produces reasonable results.

2. Instrument Description

[6] OSIRIS, the Optical Spectrograph and Infrared Imager System [*Warshaw et al.*, 1998; *Llewellyn et al.*, 2004], is one of two instruments on board the Odin satellite [*Nordh et al.*, 2003]. Odin was launched in February 2001 into a 600 km circular Sun-synchronous near-terminator orbit with inclination 97.8° and ascending node at 1800 hours local solar time (LST). Odin is a combination of astronomy and aeronomy missions, with OSIRIS dedicated to aeronomy studies [*Murtagh et al.*, 2002]. A second instrument, the Submillimeter and Millimeter Radiometer (SMR) [*Frisk et al.*, 2003], carries out both aeronomy and astronomy studies. The instruments are coaligned and scan the limb of the atmosphere over a tangent height range of 7–70 km in approximately 85 s in a sawtooth pattern during normal stratospheric operations through controlled nodding of the satellite.

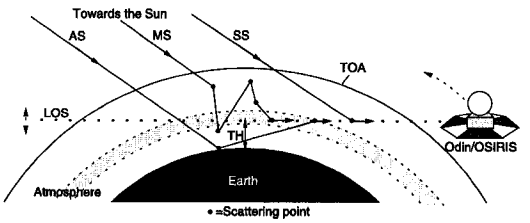

Figure 1. Viewing geometry of the OSIRIS instrument on board the Odin satellite. Most information comes from the tangent height region (shaded).

[7] OSIRIS contains two optically independent components, the Optical Spectrograph (OS) and the Infrared Imager (IRI). The OS is a grating spectrometer that measures limb-scattered sunlight spectra in the spectral range 280 nm to 800 nm at a resolution of ~1 nm at tangent height intervals of roughly 2 km. The IRI is a three channel camera, imaging the atmospheric airglow emissions near 1.27 μm and 1.53 μm in a limb-viewing tomographic mode [*Degenstein et al.*, 2003]. The OS scattered sunlight measurements are used to provide vertical profiles of minor stratospheric constituents including O_3, NO_2, BrO, OClO and aerosol, and the IRI images are used to provide high-resolution three-dimensional distributions of O_3 in the mesosphere [*Khabibrakhmanov et al.*, 2002]. The SMR complements OSIRIS, providing simultaneous measurements of O_3, N_2O, ClO and HNO_3 in the normal stratospheric mode. The Optical Spectrograph is the focus of this study.

[8] The instantaneous field of view (FOV) of the OS is 1 km in the vertical and 40 km in the horizontal at the tangent point. When the nodding of the spacecraft and the varying exposure time of the OS (~0.01 s at 10 km increasing to ~2 s at 50 km) are considered, the vertical resolution of the measured limb radiances is found to range from approximately 1 km at 10 km to 2 km at 50 km.

[9] The limb-viewing geometry is illustrated in Figure 1, the typical coverage resulting from the near-terminator orbit is shown in Figure 2 and spectra from a typical limb scan are shown in Figure 3.

3. Methodology

[10] The full method for retrieving number density profiles from limb-scattered sunlight can be subdivided into several steps including spectral analysis, radiative transfer modeling and the inversion technique, as outlined in Figure 4.

3.1. Spectral Analysis

[11] Vertical profiles of number density can in principle be retrieved directly from limb-scattered sunlight radiances, though accurate and complete models of both the instrument and the atmosphere are then required. To simplify the

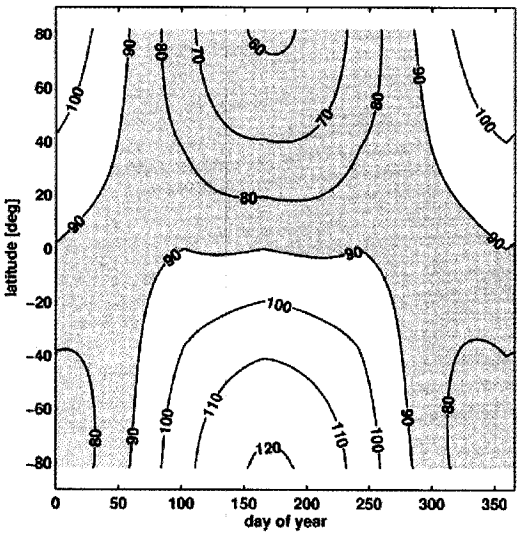

Figure 2. Global coverage of the OS DOAS retrievals for normal stratospheric operations (shaded) and the SZAs at ground level (contours).

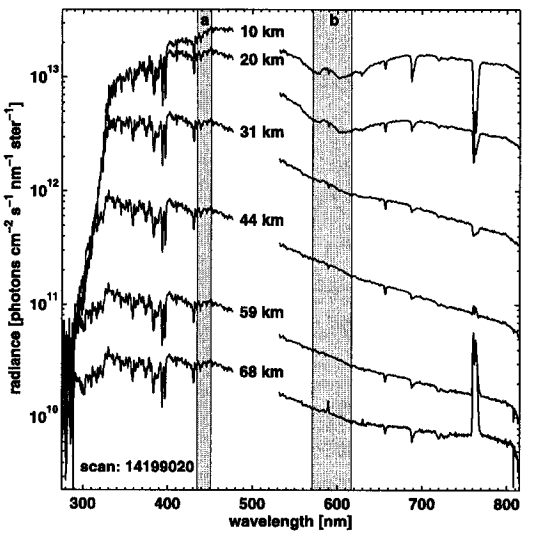

Figure 3. A sample of limb-scatter radiances at different tangent heights as measured by the OS. Shaded area a is the NO_2 retrieval window, and shaded area b is the O_3 window. The data gap near 500 nm is in the region of an order-sorter where the data are not recorded.

inversion problem, it is advantageous to use an intermediate spectral analysis. In this study, the DOAS technique is chosen.

[12] The DOAS technique was first described by *Noxon* [1975], *Noxon et al.* [1979], *Platt et al.* [1979], and *Perner and Platt* [1980]. In general, DOAS is a spectral fitting technique, analyzing broadband spectra of ultraviolet (UV) and visible light that have been transmitted through long open paths. Different atmospheric species leave their absorption "fingerprints" in the spectra, from which concentrations can be retrieved. DOAS has been used in ground-based and satellite applications, for both active and passive instruments [i.e., *Axelsson et al.*, 1990; *Platt*, 1994; *Burrows et al.*, 1999; *Pfeilsticker et al.*, 2001]. The application of DOAS to scattered sunlight limb radiances is described in detail below.

[13] The basic equation of absorption spectroscopy, describing pure absorption of a single species in a homogeneous medium, is the Beer-Lambert Law:

$$I(\lambda) = I_0(\lambda)e^{-L\sigma(\lambda)n}, \tag{1}$$

where $I(\lambda)$ is the measured intensity, $I_0(\lambda)$ is the unattenuated reference intensity, L is the pathlength, $\sigma(\lambda)$ is the wavelength-dependent absorption cross section, and n is the number density of the species. The dimensionless quantity $L\sigma n$ is often referred to as the optical depth, denoted τ. The Beer-Lambert Law is applicable in cases where atmospheric emissions can be neglected, such as UV/visible limb-scattered sunlight measurements. Note that the Beer-Lambert Law is not perfectly valid for averaged (convolved) spectra unless the optical depth is small (i.e., $\tau \ll 1$).

[14] For limb-scattered sunlight measurements, the pathlength is not well defined and the medium is not homogeneous along the line of sight (LOS). As such, instead of number density and pathlength, the "effective column density along the LOS," c, is used. The optical depth is then simply σc. In atmospheric conditions, Rayleigh (molecular)

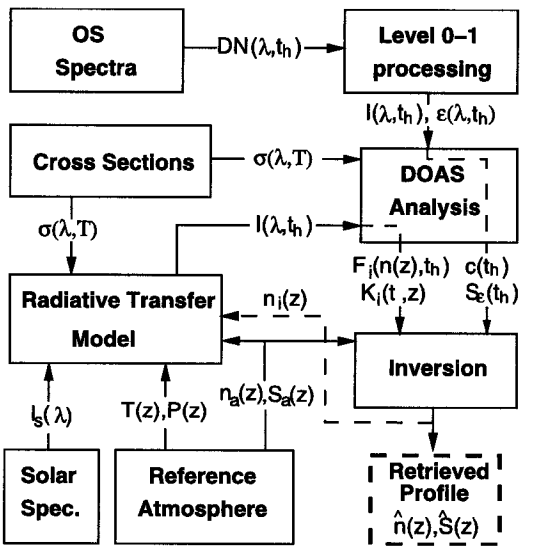

Figure 4. Overview of the retrieval process.

and Mie (aerosol) scattering also contributes to the radiation extinction. Rayleigh and Mie scattering can simply be added to equation (1), and with some rearrangement the optical depth can be expressed as

$$\tau(\lambda) = \ln\left[\frac{I_0(\lambda)}{I(\lambda)}\right] = \sigma(\lambda)c + \varepsilon_R(\lambda) + \varepsilon_M(\lambda), \quad (2)$$

where $\varepsilon_R(\lambda)$ is the Rayleigh optical depth, which is the product of the Rayleigh cross section, $\sigma_R(\lambda)$, and the effective column density of air, c_{air}. Similarly, the Mie optical depth, $\varepsilon_M(\lambda)$, corresponds to $\sigma_M(\lambda)c_{\text{aer}}$, where c_{aer} is the effective column density of aerosol and $\sigma_M(\lambda)$ is the Mie cross section.

[15] The limb scanning action of Odin allows the OS to measure spectra from a sample of different tangent heights, h_t. In addition, multiple absorbing species, denoted with index i, usually need to be included, and the Beer-Lambert Law must be further extended. The different species can be added and equation (2) becomes

$$\tau(\lambda, h_t) = \ln\left[\frac{I_0(\lambda)}{I(\lambda, h_t)}\right] = \sum_i \sigma_i(\lambda)c_i(h_t) + \varepsilon_R(\lambda, h_t) + \varepsilon_M(\lambda, h_t).$$

[16] The key principle of the DOAS approach is the separation of the total cross section of each species, $\sigma_i(\lambda)$, into two components, one slowly varying with wavelength, $\sigma_i^s(\lambda)$, and another rapidly varying, $\sigma_i'(\lambda)$:

$$\sigma_i(\lambda) = \sigma_i^s(\lambda) + \sigma_i'(\lambda). \quad (4)$$

The slowly varying component, describing the general slope, corresponds to a smoothing of the total cross section and can be calculated, for example, with a low-order polynomial or a running average. A running average requires additional spectral points; thus polynomial smoothing is advantageous and a second-order polynomial is used in this study. The rapidly varying component of the cross section, commonly referred to as the differential cross section, corresponds to the difference between the smoothed and the total cross section. Inserting equation (4) into equation (3) and separating the rapidly and slowly varying components gives

$$\tau(\lambda, h_t) = \underbrace{\sum_i \sigma_i'(\lambda)c_i(h_t)}_{\text{rapid},\tau'} + \underbrace{\sum_i \sigma_i^s(\lambda)c_i(h_t) + \varepsilon_R(\lambda, h_t) + \varepsilon_M(\lambda, h_t)}_{\text{slow},\tau^s}. \quad (5)$$

Note that both Rayleigh and Mie scattering are slowly varying with λ and are assigned to the slowly varying component of the optical depth, τ^s. Assigning the measured differential optical depth (the rapidly varying component), $\tau'(\lambda, h_t)$, to the absorption due to differential cross sections, $\sigma'(\lambda)$, gives

$$\tau'(\lambda, h_t) = \sum_i \sigma_i'(\lambda)c_i(h_t) + E_{\tau'}(\lambda, h_t), \quad (6)$$

where $E_{\tau'}(\lambda, h_t)$ is the error in the differential optical depth resulting from the measurement error (noise) of the OS. $E_{\tau'}(\lambda, h_t)$ has a mean of zero and standard deviation (STD) $\epsilon_{\tau'}(\lambda, h_t)$. Recalling that $\tau(\lambda, h_t) = \ln[I_0(\lambda)/I(\lambda, h_t)]$, $\epsilon_\tau(\lambda, h_t)$ can be approximated by

$$\epsilon_\tau(\lambda, h_t) = \sqrt{\left[\frac{\epsilon_{I_0}(\lambda)}{I_0(\lambda)}\right]^2 + \left[\frac{\epsilon(\lambda, h_t)}{I(\lambda, h_t)}\right]^2}, \quad (7)$$

where $\epsilon_{I_0}(\lambda)$ is the estimated error of the reference spectrum and $\epsilon(\lambda, h_t)$ is the estimated error in spectrum $I(\lambda, h_t)$. When differential optical depth is considered, an additional error contribution due to the spectral smoothing, ϵ_{τ^s}, is required:

$$\epsilon_{\tau'}(\lambda, h_t) = \epsilon_\tau(\lambda, h_t) + \epsilon_{\tau^s}. \quad (8)$$

The magnitude of ϵ_{τ^s} depends on the chosen smoothing technique. When a polynomial is used for the spectral smoothing, ϵ_{τ^s} is small and is thus ignored in this study.

[17] It is convenient to express equation (6) in vector form:

$$\underbrace{\begin{bmatrix}\tau'(\lambda_1, h_t)\\ \tau'(\lambda_2, h_t)\\ \vdots \\ \tau'(\lambda_N, h_t)\end{bmatrix}}_{\boldsymbol{\tau}'} = \underbrace{\begin{bmatrix}\sigma'_{O_3}(\lambda_1) & \sigma'_{NO_2}(\lambda_1)\\ \sigma'_{O_3}(\lambda_2) & \sigma'_{NO_2}(\lambda_2)\\ \vdots & \vdots \\ \sigma'_{O_3}(\lambda_N) & \sigma'_{NO_2}(\lambda_N)\end{bmatrix}}_{\mathbf{D}} \underbrace{\begin{bmatrix}c_{O_3}(h_t)\\ c_{NO_2}(h_t)\end{bmatrix}}_{\mathbf{c}} + \underbrace{\begin{bmatrix}E_{\tau'}(\lambda_1, h_t)\\ E_{\tau'}(\lambda_2, h_t)\\ \vdots \\ E_{\tau'}(\lambda_N, h_t)\end{bmatrix}}_{\mathbf{E}_{\tau'}}, \quad (9)$$

where λ_j are the sampled wavelengths in the selected spectral window. Note that equation (9) includes O_3 and NO_2 as an example, but should include all significant absorbers. Effective column densities are calculated through a least squares (LSQ) fit of equation (9) with respect to $\mathbf{c}$. The LSQ solution with a known error covariance matrix in the differential optical depth, $\mathbf{S}_{\epsilon_{\tau'}}$, is given by

$$\mathbf{c}_{\text{lsq}} = \left[\mathbf{D}^T\mathbf{S}_{\epsilon_{\tau'}}^{-1}\mathbf{D}\right]^{-1}\mathbf{D}^T\mathbf{S}_{\epsilon_{\tau'}}^{-1}\boldsymbol{\tau}', \quad (10)$$

$$\mathbf{S}_{\text{lsq}} = \left[\mathbf{D}^T\mathbf{S}_{\epsilon_{\tau'}}^{-1}\mathbf{D}\right]^{-1}, \quad (11)$$

$$\mathbf{r}_{\text{lsq}} = \boldsymbol{\tau}' - \mathbf{D}\mathbf{c}_{\text{lsq}}, \quad (12)$$

where $\mathbf{c}_{\text{lsq}}$ is the least squares estimation of $\mathbf{c}$, $\mathbf{r}_{\text{lsq}}$ is the fitting residual, and $\mathbf{S}_{\text{lsq}}$ is the $m \times m$ covariance matrix of the LSQ fit, where m is the number of species. The fit is done independently for each tangent height. Note that $\mathbf{S}_{\epsilon_{\tau'}}$ is a diagonal matrix because of the independence of the elements in $\epsilon_{\tau'}$ when ϵ_{τ^s} is neglected. Examples of DOAS fits to OS measurements are shown in Figure 5. The estimated effective column densities for the target species (NO_2 or O_3 in this study) are later inverted to number densities (see section 3.4). The lsq notation is omitted in further discussions for clarity.

3.1.1. I_0 for Limb Measurements

[18] If the intensity of the unattenuated reference spectrum, $I_0(\lambda)$, is not available, as is the case for the OS, either a limb-scatter spectrum from another tangent height or a modeled or measured exoatmospheric spectrum can be

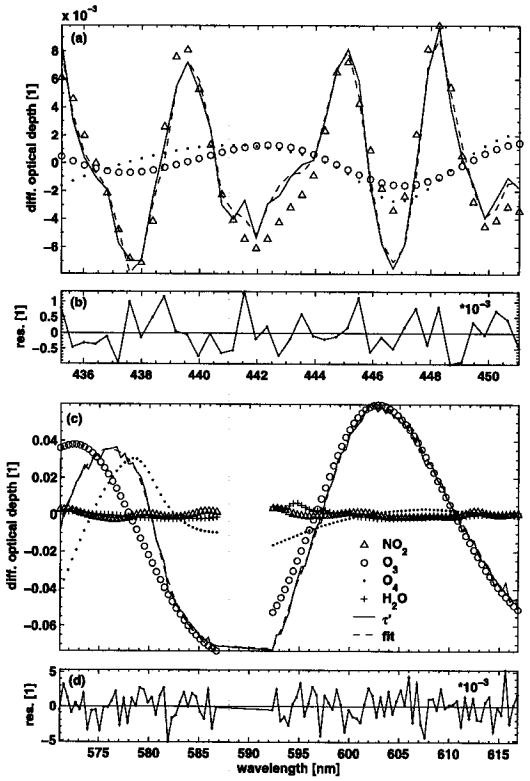

Figure 5. Differential optical depths and residuals in the (a and b) NO_2 and (c and d) O_3 retrieval regions for a 8.5 km tangent height measurement from a typical OS limb scan (solid line). The circles correspond to the O_3 fit ($\sigma'_{O_3} \cdot c_{O_3}$), triangles correspond to the NO_2 fit ($\sigma'_{NO_2} \cdot c_{NO_2}$), dots correspond to the O_4 fit ($\sigma'_{O_4} \cdot c_{O_4}$), and crosses correspond to the H_2O fit ($\sigma'_{H_2O} \cdot c_{H_2O}$). The total fit ($\Sigma\sigma'_i \cdot c_i$) is given by the dashed line.

used. Using another OS limb-scatter spectrum is preferable because it removes the need for absolute calibration. However, a spectrum at some reference tangent height, h_t^{ref}, will contain some absorption from minor species, denoted $c_i(h_t^{ref})$, and Rayleigh and Mie scattering extinction, $\varepsilon_R(\lambda, h_t^{ref})$ and $\epsilon_M(\lambda, h_t^{ref})$, respectively. Replacing $I_0(\lambda)$ with $I(\lambda, h_t^{ref})$ in equation (3) gives

$$\tau(\lambda, h_t) = \ln\left[\frac{I(\lambda, h_t^{ref})}{I(\lambda, h_t)}\right] = \sum_i \sigma_i(\lambda)\left[c_i(h_t) - c_i(h_t^{ref})\right] + \left[\varepsilon_R(\lambda, h_t) - \varepsilon_R(\lambda, h_t^{ref})\right] + \left[\varepsilon_M(\lambda, h_t) - \varepsilon_M(\lambda, h_t^{ref})\right], \quad (13)$$

where $\tau(\lambda, h_t)$ is now the optical depth between h_t^{ref} and h_t. The expression for the differential optical depth is then

$$\tau'(\lambda, h_t) = \sum_i \sigma'_i(\lambda)\left[c_i(h_t) - c_i(h_t^{ref})\right]. \quad (14)$$

In this case, equations (10)–(12) still hold, where **c** is now interpreted as the effective column densities relative to the reference tangent height.

[19] It is usually desirable to choose a limb-scatter spectrum from a high tangent height, containing little absorption, as the reference in order to maximize the differential structure, hence maximizing the signal-to-noise ratio. The measurement closest to 50 km is chosen as the reference for the O_3 retrievals, while the average of measurements between 46 km and 65 km is used as the reference for the NO_2 retrievals to reduce noise. No averaging is carried out for the O_3 reference because of contamination from out of field radiation (baffle scattering) at high tangent heights. This contamination is negligible below ~70 km in the NO_2 window and below ~50 km in the O_3 window.

3.1.2. Spectral Windows

[20] Spectral windows used for DOAS must be chosen such that the species of interest have highly structured absorption features in the region, while avoiding interfering species as much as possible. In addition, the differential absorption must be strong enough to achieve a high signal-to-noise ratio, but the total absorption must be weak enough to avoid large optical depths.

[21] Although it is theoretically possible to retrieve multiple species simultaneously from the same window using DOAS, it is often unsuitable to do so. To decrease uncertainties, it is advantageous to use separate windows where the target species is the dominant absorber. The chosen windows for O_3 and NO_2 are specified in Table 1 and illustrated in Figures 3 and 6. For O_3 retrievals, the spectral range 571–617 nm in the Chappuis region is chosen, thus avoiding the temperature dependence of the O_3 cross section in the Huggins and Wulf bands. Measurements in the region of the Na Fraunhofer/airglow feature (~590 nm) are not included in the spectral fitting. For this spectral window, absorption cross sections of NO_2, the O_2·O_2-dimer (O_4) and water vapor (H_2O(g)) are included along with O_3 in the spectral fit. Note that the selected O_3 window is not ideal for a DOAS analysis because of the broad nature of the spectral features and the potential contamination from O_4 and polarization (see section 3.2.6). A more suitable window that provides large differential structure while also avoiding the temperature dependence of the O_3 cross section would be near 500 nm, but OS data in this spectral region are not recorded because of an order-sorter.

[22] The window chosen for NO_2 is 435–451 nm. In this window the NO_2 differential absorption cross section is large compared to that of O_3 and there are no strong

Table 1. Summary of the Specifications of the Spectral Windows Used for O_3 and NO_2

Retrievals	O_3 Window	NO_2 Window
Wavelengths	571–617 nm	435–451 nm
Fitted species	O_3, NO_2, O_4, H_2O	O_3, NO_2, O_4
Corrections	polarization	tilt, I_0, λ-shift
Retrieval range	10–48 km	10–46 km
Reference height	~50 km	46–65 km average
Estimating **K**	2λ, SS, no aerosol	2λ, SS, no aerosol
Estimating **F**	4-nm grid	2-nm grid
Response > 0.75	~12–45 km	~15–40 km
Resolution at 30 km	~2 km	~2 km
Retrieval error at 30 km	~13%	~10%

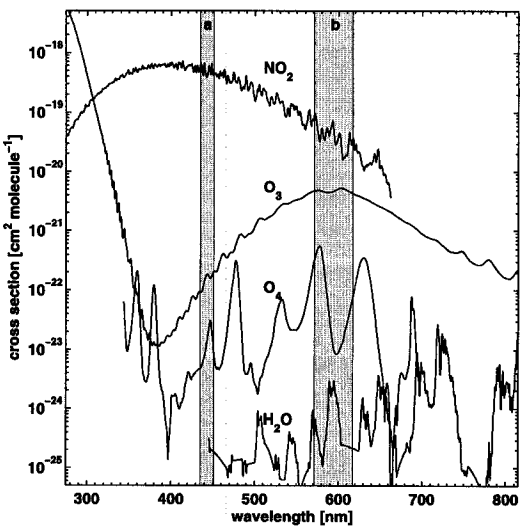

Figure 6. Cross sections of O_3 [*Bogumil et al.*, 2003], NO_2 [*Vandaele et al.*, 1998], O_4 [*Greenblatt et al.*, 1990], and H_2O [*Rothman et al.*, 2003] convolved to the OS resolution. The O_4 cross sections have been multiplied by 10^4 to decrease the y axis interval. Shaded area a is the NO_2 retrieval window, and shaded area b is the O_3 window.

Fraunhofer features. For this spectral window, absorption cross sections of O_3 and O_4 are included along with NO_2 in the spectral fit. A Rayleigh cross section [from *Bates*, 1984] is also included in both windows to account for atmospheric molecular scattering since the spectral smoothing may not completely remove this fourth-order polynomial structure. Residuals from the least squares DOAS fitting are typically less than 3×10^{-3} root mean square (RMS) for the O_3 window and less than 1×10^{-3} RMS for the NO_2 window, as illustrated in Figure 5. These residuals represent approximately 3% and 7% of the peak differential optical depths in the O_3 and NO_2 windows, respectively.

3.2. Spectral Corrections

[23] In order to correctly apply the DOAS analysis described above to retrieve number densities of atmospheric species like O_3 and NO_2, some corrections must be applied to the OS spectra and absorption cross sections [*Platt et al.*, 1997]. The effects of instrument resolution and sampling, polarization response, wavelength shifts, temperature dependence and Ring contributions are considered in the following sections. Table 1 summarizes the corrections applied in each DOAS window.

3.2.1. Cross Sections and the I_0 Effect

[24] No useful measurements of O_3, NO_2, O_4 or H_2O absorption cross sections were conducted with the OS instrument. Hence cross sections used in the DOAS analysis must be taken from the literature. These cross sections, usually highly resolved and denoted σ_i^{hr}, must be convolved to the OS resolution. The convolution is done using a Gaussian filter function, which is found to best represent the OS instrument function (J. Stegman, personal communication, 1998). The standard deviation of this filter function, denoted s_g to avoid confusion with cross section, is

$$s_g(\lambda) = \sqrt{[s^{os}(\lambda)]^2 - [s^{hr}(\lambda)]^2}, \tag{15}$$

where $s^{os}(\lambda)$ is the standard deviation of the resolution of the OS (the instrument function) and $s^{hr}(\lambda)$ is the resolution of the highly resolved cross section. The convolved cross sections, denoted σ_i^*, are given by

$$\sigma_i^*(\lambda) = \int_{-\infty}^{\infty} g(\lambda', s_g)\sigma_i^{hr}(\lambda - \lambda')d\lambda', \tag{16}$$

where g is the Gaussian filter function.

[25] The limited resolution of the OS (~1 nm full width at half maximum (FWHM)) can lead to interference of highly structured Fraunhofer features in scattered sunlight with the absorption cross sections. Dividing measured spectra with I_0, as in the DOAS procedure of section 3.1, can therefore lead to interfering spectral structure. This effect is usually referred to as the I_0 effect because it results from structure in the I_0 spectrum [*Aliwell et al.*, 2002]. To deal with the I_0 effect, the convolution of reference absorption cross sections to the OS resolution must include structures in a highly resolved reference, I_0^{hr}. A solar exoatmospheric spectrum provided by R. L. Kurucz (unpublished data, 1997), denoted I_s, is used in place of this highly resolved I_0. This approximation is valid since I_0 and I_s differ primarily by only a Rayleigh trending. Using the Beer-Lambert Law for the limb geometry, equation (2), a more accurate estimation of σ_i^* is

$$\begin{aligned}\sigma_i^*(\lambda) &= \frac{1}{c_i(h_t)} \cdot \ln\left[\frac{I_0^{hr}(\lambda)*}{I^{hr}(\lambda, h_t)*}\right] \\ &\approx \frac{1}{c_i(h_t)} \cdot \ln\left\{\frac{I_s^{hr}(\lambda)*}{[I_s^{hr}(\lambda)\exp(-\sigma_i^{hr}(\lambda)c_i(h_t))]*}\right\},\end{aligned} \tag{17}$$

where $*$ denotes convolution and I_s^{hr} is the solar spectrum at a resolution identical to that of σ_i^{hr}. For small optical depths, i.e., $\sigma_i^{hr}(\lambda)c_i(h_t) \ll 1$, equation (17) can be approximated as

$$\begin{aligned}\sigma_i^*(\lambda) &\approx \frac{[I_s^{hr}(\lambda)\sigma_i^{hr}(\lambda)]*}{I_s^{hr}(\lambda)*} \\ &= \frac{\int_{-\infty}^{\infty} g(\lambda', s_g)I_s^{hr}(\lambda - \lambda')\sigma_i^{hr}(\lambda - \lambda')d\lambda'}{\int_{-\infty}^{\infty} g(\lambda', s_g)I_s^{hr}(\lambda - \lambda')d\lambda'},\end{aligned} \tag{18}$$

with $5 \cdot s_g$ substituted for ∞ in this study. If the optical depth is not small, the effective column densities, $c_i(h_t)$, should be included in the convolution. This requires an accurate estimate of $c_i(h_t)$ or time consuming iterations. Note that the I_0 effect is only important in regions with deep Fraunhofer lines and highly structured differential cross sections. Thus the I_0 effect is taken into account in the NO_2 window, but not in the O_3 window.

[26] In addition to the wavelength convolution of cross sections, the discrete mapping of wavelengths onto the charge-coupled device (CCD) detector must be considered. Each pixel, denoted j, integrates incoming radiation over a

wavelength interval, $\lambda(j)$ to $\lambda(j+1)$. Hence the final cross sections, σ_i^{os}, are

$$\sigma_i^{os}(j) = \int_{\lambda(j)}^{\lambda(j+1)} \sigma_i^*(\lambda')d\lambda'. \quad (19)$$

[27] The following high-resolution and temperature-dependent cross sections, as recommended by *Orphal* [2003] (O_3 and NO_2), are treated as above and used in this work: (1) O_3 from *Bogumil et al.* [2003] at temperatures 293 K, 273 K, 243 K, 223 K and 203 K with quadratic interpolation and resolution (FWHM) of 0.47 nm at 600 nm and 0.21 nm at 440 nm; (2) NO_2 from *Vandaele et al.* [1998] at temperatures 294 K and 220 K with linear interpolation and resolution (FWHM) of 0.072 nm at 600 nm and 0.039 nm at 440 nm; (3) O_4 from *Greenblatt et al.* [1990] at temperature 298 K and resolution (FWHM) of 0.6 nm; (4) H_2O(g) from HITRAN [*Rothman et al.*, 2003] line-by-line calculation at pressure 500 hPa, temperature 246 K and partial water vapor pressure 0.03 hPa.

3.2.2. Wavelength Shift

[28] Wavelength calibration discrepancies between the measured spectra and the cross sections can affect the spectral fitting. A relative shift in wavelength is accounted for through Levenberg-Marquardt (L-M) [*Levenberg*, 1944; *Marquardt*, 1963] nonlinear iterations of equation (10) with respect to a wavelength shift, similar to the approach of *Stutz and Platt* [1996]. The converged L-M iteration gives $\mathbf{c}$ with a wavelength shift that minimizes the residuals, $\mathbf{r}$, with an emphasis on the dominant absorber (O_3 in the O_3 window and NO_2 in the NO_2 window). Any higher-order distortion of the wavelength calibration, such as stretching and squeezing of the spectra, is not accounted for.

[29] Ozone retrievals are insensitive to wavelength shift errors because of the broad cross section features in the chosen window (see Figure 6) and no L-M wavelength shift algorithm is required. However, because of the fine structure in the NO_2 cross section, the NO_2 retrievals are sensitive to wavelength shifts. It is not expected that the OS pixel wavelengths vary during the duration of a scan because of the short time period and the temperature stability of the OS. As such, the L-M algorithm is only used to derive the wavelength shift at one tangent height in each scan (~10 km) and the shift is then applied to all measurements in the scan.

3.2.3. Temperature Dependence

[30] Any temperature dependence of the absorption cross sections can affect the DOAS fit since the derived effective column densities depend on the specific cross sections used in the spectral fit. If there is significant temperature dependence, it is necessary to use cross sections appropriate to the temperature at which the absorption occurred in the fitting procedure in order to calculate the correct column densities. In this case, the differential cross sections $\sigma_i'(\lambda)$ should be denoted $\sigma_i'(\lambda, T_{spec})$, where T_{spec} is the atmospheric temperature appropriate to the spectrum $\tau'(\lambda)$. Since limb radiances contain information from many heights (temperatures), T_{spec} is not well defined. T_{spec} can be approximated using prior knowledge about the atmospheric temperature, for example by assuming that T_{spec} for tangent height h_t is equal to the atmospheric temperature at that height. A nonlinear technique that finds the temperature at which the fit residuals are minimized could also be used to determine T_{spec}.

[31] Fortunately, the temperature dependence of the O_3 cross section in the chosen windows is small, and the temperature dependence can be ignored in the DOAS fits, with the absorption cross section for one temperature (223 K from *Bogumil et al.* [2003]) used in all cases. The NO_2 cross section exhibits some temperature dependence in the selected windows and this can lead to errors in the derived column densities as mentioned above. However, as is discussed in section 3.3, a forward model is utilized in the inversion of column density to number density. If the technique used to determine T_{spec} for the measurements is also applied in the forward model, errors resulting from the choice of T_{spec} are minimized as long as any resulting residual structure does not correlate strongly with other species in the window. In other words, any systematic error in the column densities derived from the measurements resulting from an incorrect T_{spec} will be compensated for when column densities are derived from the model radiances, providing that the radiative transfer model properly accounts for the temperature dependence through the use of both the correct atmospheric temperature profile and the correct cross section. As a result, it is also appropriate to select a cross section at one temperature for all cases in the NO_2 retrievals, and the 220 K cross section from *Vandaele et al.* [1998] is used in all cases.

3.2.4. Ring Effect

[32] The Ring effect refers to the "filling-in" (broadening and reduction of depth) of spectral features compared to the unattenuated spectrum. This effect was first described by *Grainger and Ring* [1962] and its primary cause is proposed to be rotational Raman scattering (RRS), that is, inelastic scattering by atmospheric species (mostly N_2 and O_2) [*Brinkmann*, 1968]. The magnitude of RRS is a function of pressure, temperature, aerosol, surface albedo and scattering angle [*Hunten*, 1970; *Harrison*, 1976; *Pallamraju et al.*, 2000], and the RRS signature in the OS radiance spectra thus varies with tangent height. As a result, Fraunhofer structures in the radiances do not cancel out entirely when two limb radiance spectra are ratioed, with some RSS structure remaining as residual structure that may interfere with the fit. In addition, filling-in of O_3 and NO_2 features can affect the derived column densities.

[33] The Ring effect is negligible in the O_3 window because of the broad absorption features and lack of strong Fraunhofer structures. However, the impact is potentially important in the NO_2 window. Two different methods of dealing with the Ring effect in the NO_2 retrievals were examined: iterative backward modeling of the measured spectra, as proposed by *Sioris et al.* [2002], and the introduction of a pseudoabsorber in the DOAS LSQ fit, as suggested by *Chance and Spurr* [1997]. Neither method resulted in improved DOAS fits compared to the results when the Ring effect is ignored (i.e., smaller residuals or significant changes to the derived effective columns). The reason for this may be the lack of strong Fraunhofer lines in the NO_2 window, in combination with imperfections of the methods. Also, the use of a high tangent height spectrum from each scan as the reference minimizes the Ring contamination.

3.2.5. Tilt Effect

[34] Undersampling of Fraunhofer structures in combination with different slopes (tilts) of the measured limb-scatter spectra can lead to a skewed partitioning of the wings of Fraunhofer lines. The slope differences are largely due to Rayleigh scattering extinction. The effect, denoted tilt effect, was discovered when the location of Fraunhofer minima in the OS spectra were found to vary with tangent height, leading to differential structures in the derived optical depths when a high tangent height measurement is used as the reference in the DOAS fit [*Sioris et al.*, 2003].

[35] The strongest influences from the tilt effect are found in regions of strong Fraunhofer lines and in the blue part of the spectrum because of Rayleigh trending. Hence the tilt effect is negligible in the O_3 window but can be important in the NO_2 window. The tilt effect can be compensated for by representing it as a pseudoabsorber in the DOAS LSQ fit, as proposed by *Sioris et al.* [2003]. If atmospheric absorption is ignored, the ratio of highly resolved and sampled spectra, I^{hr}, and the ratio of spectra convolved to the OS resolution and sampling, I^{os}, can be related by a factor $1 + t(\lambda, h_t)$, i.e.,

$$\frac{I^{os}(\lambda, h_t^{ref})}{I^{os}(\lambda, h_t)} = \frac{I^{hr}(\lambda, h_t^{ref})}{I^{hr}(\lambda, h_t)}[1 + t(\lambda, h_t)], \quad (20)$$

where t is the tilt contribution and I is modeled with pure Rayleigh scattering and no absorbers. Assuming that the spectral structure of the tilt contribution is independent of h_t for tangent heights below the reference, $t(\lambda, h_t)$ can be expressed as $k_{tilt}(h_t)t(\lambda)$. Taking the logarithm of equation (20) with this substitution gives

$$\ln\left[\frac{I^{os}(\lambda, h_t^{ref})}{I^{os}(\lambda, h_t)}\right] = \ln\left[\frac{I^{hr}(\lambda, h_t^{ref})}{I^{hr}(\lambda, h_t)}\right] + \ln[1 + k_{tilt}(h_t)t(\lambda)] \approx \ln\left[\frac{I^{hr}(\lambda, h_t^{ref})}{I^{hr}(\lambda, h_t)}\right] + k_{tilt}(h_t)t(\lambda), \quad (21)$$

where the approximation holds when the tilt contribution is small ($k_{tilt}t \ll 1$). Equation (21) shows that t can be included as a pseudoabsorber in the DOAS LSQ fit. The tilt pseudoabsorber can be calculated with equation (20) by convolving limb radiances modeled at high resolution and sampling to OS resolution and sampling. In this study, the tilt pseudoabsorber is calculated from limb radiances modeled at 10 km and 50 km with the LIMBTRAN radiative transfer model (see section 3.3). The tilt pseudoabsorber calculated for the NO_2 window is shown in Figure 7. Introducing this pseudoabsorber decreases residuals from the LSQ fit by as much as a factor of 2. The influence in the fitting decreases with height, as h_t approaches h_t^{ref}.

3.2.6. Polarization

[36] The efficiency (response) of any diffraction grating shows wavelength-dependent features for different polarization states of incident light due to complex interactions between the grooves of the grating and the electromagnetic field [*Hutley*, 1982; *Solimeno et al.*, 1986]. These features, first described by R. W. Woods in 1902, are referred to as Woods' anomalies and are found to be greatest for incident light polarized perpendicular to the grooves. Limb-scattered sunlight always contains a plane-polarized fraction because

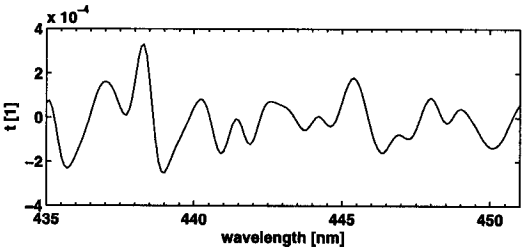

Figure 7. Tilt pseudoabsorber calculated for the NO_2 region.

of a Rayleigh scattering atmosphere. The relative strength of the parallel and perpendicular components, denoted $I_\parallel$ and $I_\perp$, respectively, is a function of wavelength, tangent height, solar zenith angle (SZA), single scattering angle (SSA) and the atmospheric composition [*Oikarinen*, 2001; *McLinden et al.*, 2002]. With the OSIRIS viewing geometry, the scattering angle is often close to 90°, hence maximizing the relative contribution of the perpendicular component.

[37] The presentation of DOAS in section 3.1 assumed unpolarized light. When linearly polarized light is taken into account, the optical depth becomes

$$\ln\left[\frac{I^P(\lambda, h_t^{ref})}{I^P(\lambda, h_t)}\right] = \ln\left[\frac{R_\parallel(\lambda)I_\parallel(\lambda, h_t^{ref}) + R_\perp(\lambda)I_\perp(\lambda, h_t^{ref})}{R_\parallel(\lambda)I_\parallel(\lambda, h_t) + R_\perp(\lambda)I_\perp(\lambda, h_t)}\right], \quad (22)$$

where I^P is the measured polarized limb-scatter radiance and $R_\parallel$ and $R_\perp$ are the response of the OS for parallel and perpendicular light, respectively. $I_\parallel$ can be exchanged with $(1 - I \cdot \mathrm{LP} \cos 2\chi)/2$ and $I_\perp$ with $(1 + I \cdot \mathrm{LP} \cos 2\chi)/2$, where LP is the fraction of linearly polarized light and χ is the angle of polarization. Also, the orthogonal components $R_\parallel$ and $R_\perp$ can be expressed in terms of the response for unpolarized light R: $R_\parallel = (1 - p)R$ and $R_\perp = (1 + p)R$, where p is the OS efficiency parameter. Equation (22) can then be written as

$$\ln\left[\frac{I^P(\lambda, h_t^{ref})}{I^P(\lambda, h_t)}\right] = \ln\left[\frac{I(\lambda, h_t^{ref})}{I(\lambda, h_t)}\right] + \ln\left\{\frac{1 + p(\lambda)[\mathrm{LP}(\lambda, h_t^{ref})\cos 2\chi(\lambda, h_t^{ref})]}{1 + p(\lambda)[\mathrm{LP}(\lambda, h_t)\cos 2\chi(\lambda, h_t)]}\right\}. \quad (23)$$

The use of a single efficiency parameter p (which is equivalent to g_{12} given by *McLinden et al.* [2002]), is appropriate since the second efficiency parameter (given as g_{13} by *McLinden et al.* [2002]) is small (<0.01) and varies slowly with wavelength in the chosen spectral windows. For the conditions considered here, $p(\mathrm{LP} \cos 2\chi) \ll 1$, and equation (23) can be approximated as

$$\ln\left[\frac{I^P(\lambda, h_t^{ref})}{I^P(\lambda, h_t)}\right] = \ln\left[\frac{I(\lambda, h_t^{ref})}{I(\lambda, h_t)}\right] + p(\lambda)[\mathrm{LP}(\lambda, h_t^{ref})\cos 2\chi(\lambda, h_t^{ref}) - \mathrm{LP}(\lambda, h_t)\cos 2\chi(\lambda, h_t)]. \quad (24)$$

For optically thin conditions and no significant Ring contributions, as is the case for the chosen spectral

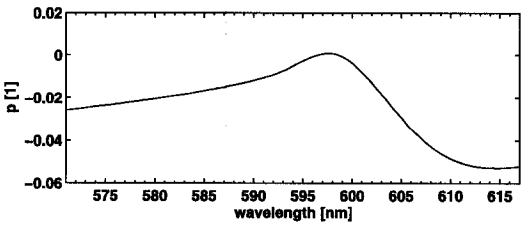

Figure 8. OS polarization efficiency parameter in the O_3 window.

windows, LP and χ are slowly varying functions of λ and it is clear that polarization can be treated as a pseudoabsorber in the DOAS LSQ fit, where p is the polarization pseudoabsorber cross section. According to *McLinden et al.* [2002], in these spectral windows the difference in linear polarization for limb spectra within the same scan is generally less than 0.1, with most of the variation occurring through the aerosol layer. Above the aerosol layer (~30 km), LP is almost constant. Thus it is mainly at the lower tangent heights that the differential structure in p can interfere in the DOAS fits. This interference will be exacerbated during periods of enhanced aerosol loading.

[38] In the NO_2 retrieval window the OS efficiency parameter varies slowly with wavelength and polarization can be neglected. However, in the O_3 window the differential structure of p is significant (see Figure 8) and can interfere with the spectral fitting and thus the polarization pseudoabsorber must be included in the DOAS fits. The interference is stronger for low tangent heights and decreases with increasing tangent height. Above 20 km the impact is negligible.

3.3. Forward Model

[39] A radiative transfer model (RTM) is used to simulate limb-scattered sunlight radiances, $\tilde{I}(\lambda, h_t)$, from known vertical number density profiles, **n**, and parameters describing the atmospheric state and measurement conditions, **b**. Simulated optical depths, $\tilde{\tau}(\lambda, h_t)$, are then calculated and subjected to a DOAS analysis. The resulting effective column densities constitute the forward model, F. The forward model is used in section 3.4 to invert effective column density as a function of tangent height to number density as a function of height. The RTM should simulate the conditions at the measurement positions in time and space as accurately as possible. However, not every feature of the atmosphere can be included because of the increasing CPU time resulting from the mathematical complexity. Hence a compromise has to be made between complexity and computational time. In addition, many physical properties of the atmosphere, such as clouds and aerosols, are difficult to model accurately.

[40] According to *Oikarinen et al.* [1999], multiple scattering constitutes 10–50% of the total radiance in the limb viewing geometry, depending on SZA, SSA and albedo. Furthermore, multiple scattering is wavelength dependent and reflects atmospheric absorption features. Because of this, a single scattering RTM is not sufficient for general atmospheric conditions. In this study, the pseudospherical multiple scattering radiative transfer model LIMBTRAN is used. For further description of LIMBTRAN, see *Griffioen and Oikarinen* [2000]. LIMBTRAN has been compared extensively with other pseudospherical and fully spherical (Monte Carlo) models in calculating UV/visible limb radiances under a broad range of atmospheric, solar and viewing conditions [*Loughman et al.*, 2004]. The agreement with other similar pseudospherical models is generally within 1–2% and is within 8–10% compared to fully spherical models (and typically much better). LIMBTRAN thus provides limb radiances with similar accuracy to fully spherical models at a fraction of the computational cost.

[41] Temperature and pressure information used in LIMBTRAN is from the European Centre for Medium-Range Weather Forecasts (ECMWF) analysis fields. O_3 and NO_2 mean a priori state distributions (climatologies) are included and are described in section 3.4.1. The O_3 and NO_2 temperature-dependent absorption cross sections used in LIMBTRAN are the same as those used for the DOAS spectral fits (see section 3.2.1). Aerosol information is also included and consists of the stratospheric aerosol extinction climatology for 1999 from *Bauman et al.* [2003a, 2003b] and a Heney-Greenstein phase function (asymmetry parameter 0.7). The surface albedo is taken from *Koelemeijer et al.* [2003].

[42] An important aspect of LIMBTRAN is that the variation of SZA and SSA along the LOS can be taken into account. This is important for the OSIRIS viewing conditions. For example, when SZA = 90° and SSA = 60° at the tangent point, the solar zenith angle varies between about 85° and 95° along the LOS and ignoring this variation can lead to large errors in the retrievals (>20% at some heights). The variation is taken into account by computing the source function at a number of points along the LOS. The number of points is varied depending on the solar conditions in order to provide accurate results while minimizing the computational cost. Some error is introduced in the retrieved profiles by this approximation, but is limited to less than 2% for the NO_2 retrievals and 1% for the O_3 retrievals.

[43] It is also important that the variation of SZA and SSA with tangent height (due to the Odin scanning) is taken into account in the RTM calculations (X. Liu, personal communication, 2003). However, LIMBTRAN currently only supports a fixed SZA and SSA for all tangent heights within each run of the model. To avoid running separate instances of LIMBTRAN for each tangent height (requiring significant CPU time), the variation is taken into account by running LIMBTRAN for all tangents heights for the solar conditions at the top, bottom and middle of each scan, and interpolating the three resulting sets of limb radiance profiles to the true conditions at each tangent height. This approximation leads to a negligible difference (in terms of errors in the retrieved profiles) from taking to full variation into account.

[44] LIMBTRAN assumes horizontal homogeneity within its vertical layers. This can lead to errors in the retrieved profiles at times when horizontal variations in the true O_3 or NO_2 distributions exist, such as at the edge of the polar vortex. Such variations also exist in the NO_2 distribution near the terminator because of photochemistry. The retrieval of horizontal variation has been studied for passive thermal emission measurements [*Livesey and Read*, 2000; *Kemnitzer*

et al., 2002] but generally does not apply for the OSIRIS measurement geometry. The photochemical variations of NO_2 at the terminator can be modeled and included in the RTM in order to reduce the impact of this predictable variation on the retrievals, as suggested by *Sioris et al.* [2003]. This functionality is not presently included in LIMBTRAN and has not been studied in this work. However it should be noted that for limb-scatter measurements it is important to not only model the variation along the LOS, but also to take the variation along the path of the incoming sunlight into account, requiring a full three-dimensional treatment. There is also some question as to how the results are influenced by the specifics of the photochemical model.

[45] Ideally, the RTM should be run at high spectral resolution to calculate $\tilde{I}$, and the results should then be convolved to the OS resolution and sampling. This is, however, very time-consuming and instead cross sections convolved to the OS resolution and sampling are input to LIMBTRAN, introducing some systematic error. The error in the derived number density profiles is negligible for O_3, as is expected because of the broad nature of the cross sections in the Chappuis band. For NO_2 retrievals the error introduced by this approximation is larger, leading to an underestimation of ~1.5%, which is acceptable given the reduced computational requirements and other error sources.

[46] The RTM should also account for the vertical resolution of the effective OS FOV, which ranges from ~1 km at 10 km to ~2 km at 50 km. This is also a time-consuming operation and instead LOS radiances are used. This assumption leads to errors of less than 1% in the derived number density profiles for both O_3 and NO_2. To further reduce the computational requirements, LIMBTRAN is run with a 1 km vertical grid, leading to errors of about 1% and 7% in the retrieved O_3 and NO_2 profiles, respectively.

3.4. Inversion

[47] Effective column densities of the target species from the DOAS fit must be converted to number densities as a function of height, $n(z)$, where z is the vertical retrieval grid. This conversion is an inverse problem, which uses the forward model, the measured quantities and some a priori information. The forward model, consisting of the results of applying DOAS to RTM simulated radiances, maps measurement space into the state space. In this study, the retrieval grid is chosen to be a 2 km grid from 10 km to 48 km for O_3 and from 10 km to 46 km for NO_2.

[48] In the linear case with no measurement noise, the problem consists of solving a linear system of equations:

$$\mathbf{c} = \mathbf{F}(\mathbf{n}, \mathbf{b}) = \mathbf{K}\mathbf{n}, \tag{25}$$

where $\mathbf{n}$ is the number density state vector and $\mathbf{c}$ represents a vector of effective column densities for the target species (O_3 or NO_2) for all tangent heights. Furthermore, $\mathbf{F}$ is the forward model, $\mathbf{b}$ are the model parameters that are not retrieved and $\mathbf{K}$ is the $q \times r$ weighting function matrix (the Jacobian), with q denoting the number of tangent heights in the measurement grid and with r denoting the number of heights in the retrieval grid. $\mathbf{K}$ describes the forward model response to changes in the true atmospheric state (its derivation for this work is given in section 3.4.4). When measurement noise and the measurement conditions are considered, it is clear that a unique solution to equation (25) does not exist (there are an infinite number of states that can give the same measurement, within the measurement error), so the inversion algorithm must estimate the optimum solution in some way.

[49] Because of the long atmospheric pathlengths involved in limb-scatter measurements, optical depths can be large. For the ozone retrievals, ozone absorption itself leads to large optical depths, particularly at the peak of the ozone profile. For NO_2, the absorption is much weaker, but the increased Rayleigh scattering at low tangent heights can lead to large total optical depths in some viewing orientations, masking the contributions of NO_2 from beyond the tangent point. Because of these nonlinear effects a nonlinear approach is necessary.

[50] The inversion algorithm used in this work is optimal estimation (OE) or more specifically the maximum a posteriori (MAP) estimator from *Rodgers* [2000], solved in a Gauss-Newton iterative way. MAP is a Bayesian estimator giving the most probable solution based on the measurements and a priori information and the associated covariances. The Gauss-Newton iterative solution, assuming Gaussian statistics, is given by

$$\mathbf{n}_{i+1} = \mathbf{n}_a + \mathbf{G}_i[\mathbf{c} - \mathbf{F}(\mathbf{n}_i) + \mathbf{K}_i(\mathbf{n}_i - \mathbf{n}_a)], \tag{26}$$

$$\mathbf{S}_{i+1} = \mathbf{S}_a - \mathbf{G}_i(\mathbf{K}_i\mathbf{S}_a), \tag{27}$$

$$\mathbf{G}_i = \mathbf{S}_a\mathbf{K}_i^T\left(\mathbf{K}_i\mathbf{S}_a\mathbf{K}_i^T + \mathbf{S}_\epsilon\right)^{-1}, \tag{28}$$

where $\mathbf{n}_a$ is the a priori state, $\mathbf{S}_a$ is the a priori covariance matrix, $\mathbf{S}_\epsilon$ is the covariance matrix of the measurement error, $\mathbf{S}$ is the covariance matrix of the solution, and $\mathbf{G}$ is the gain matrix. In this study, the iteration is started at $\mathbf{n}_0 = \mathbf{n}_a$. The measurement error is assumed to be uncorrelated in tangent height, making $\mathbf{S}_\epsilon$ a diagonal matrix, and is taken from the diagonal component of $\mathbf{S}_{\text{lsq}}$ from equation (11) for the target species at each tangent height.

[51] A positive constraint is applied to the retrievals by inverting the natural logarithm of $\mathbf{n}$, $\ln(\mathbf{n})$, instead of $\mathbf{n}$ directly. This positive constraint is required since LIMBTRAN does not accept negative densities, but must be treated with caution since it may introduce a bias when averaging retrieved profiles, for example to form a climatology. To minimize this bias, the logarithm of the retrieved profiles should be averaged. Note that the positive constraint necessitates a nonlinear retrieval.

[52] Following *Rodgers* [2000], equation (26) is said to have converged to some value $\hat{\mathbf{n}}$ with corresponding $\hat{\mathbf{K}}$, $\hat{\mathbf{G}}$ and $\hat{\mathbf{S}}$ when

$$d_i^2 = (\mathbf{n}_{i+1} - \mathbf{n}_i)^T\hat{\mathbf{S}}^{-1}(\mathbf{n}_{i+1} - \mathbf{n}_i) < r/1000, \tag{29}$$

with $\hat{\mathbf{S}}^{-1}(\mathbf{n}_{i+1} - \mathbf{n}_i) \simeq \mathbf{K}_i^T\mathbf{S}_\epsilon^{-1}[\mathbf{c} - \mathbf{F}(\mathbf{n}_i)] - \mathbf{S}_a^{-1}(\mathbf{n}_i - \mathbf{n}_a)$. Correct convergence is determined with

$$\chi^2[\mathbf{c} - \mathbf{F}(\hat{\mathbf{n}})] = [\mathbf{c} - \mathbf{F}(\hat{\mathbf{n}})]^T\mathbf{S}_{\mathbf{c}\hat{\epsilon}}^{-1}[\mathbf{c} - \mathbf{F}(\hat{\mathbf{n}})] \simeq q, \tag{30}$$

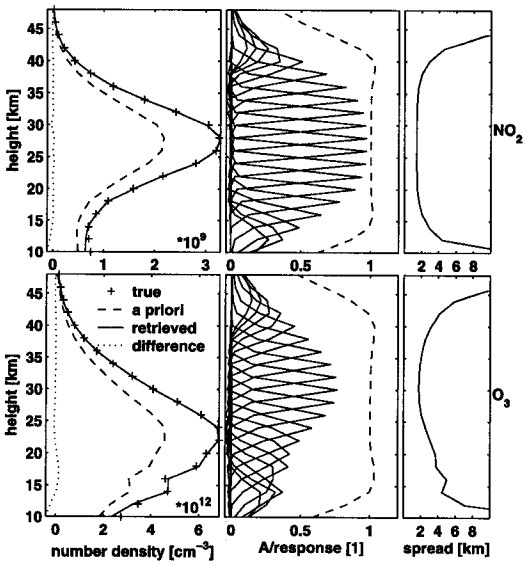

Figure 9. Retrieval characteristics in the NO_2 (upper panels) and O_3 (lower panels) regions for a modeled noise-free OSIRIS midlatitude limb scan (SZA = 85°, SSA = 90°). The left panels show the true, a priori (66% of the true), and retrieved profiles and the absolute difference between the true and retrieved profiles, the middle panels show the averaging kernels (solid lines) and the measurement response (dashed line), and the right panels show the resolution ("spread").

where $\mathbf{S}_{\hat{\epsilon}} = \mathbf{S}_\epsilon(\hat{\mathbf{K}}\mathbf{S}_a\hat{\mathbf{K}}^T + \mathbf{S}_\epsilon)^{-1}\mathbf{S}_\epsilon$. Profiles that have not converged after eight iterations or have converged with $\chi^2/q > 4$ are discarded. The χ^2 condition corresponds to the probability of rejecting one profile in a million belonging to a theoretical χ^2 distribution with 30 degrees of freedom. Sample retrievals of O_3 and NO_2 number density profiles from a modeled noise-free OS limb scan are shown in Figure 9.

3.4.1. A Priori Information

[53] The a priori information for O_3 is taken from the four-dimensional climatology of *Li and Shine* [1995], which was constructed from satellite and ozonesonde data sets. The NO_2 a priori information is taken from a climatology constructed using a photochemical box model [*Prather and Jaffe*, 1990; *McLinden et al.*, 2000], constrained with ozone and temperature climatologies (C. A. McLinden, personal communication, 2003), and accounts for the diurnal variation.

[54] The covariance matrix of the a priori state, $\mathbf{S}_a$, is also required for the retrievals. O_3 is assumed to follow a lognormal distribution, with standard deviations for the diagonal components of $\mathbf{S}_a$ of 40% and an exponential off-diagonal correlation length of 4 km. This information is based on ozonesonde data statistics from 1970 to 1996 retrieved at 17 stations situated around 35°N, 50°N and 75°N, as reported by *Eriksson and Chen* [2002]. The 4 km correlation length and lognormal distribution are also used to characterize the NO_2 a priori, but since the NO_2 climatology is assumed to be less accurate, the diagonal elements of $\mathbf{S}_a$ are set to 80%.

3.4.2. Error Estimation

[55] Error estimation of the retrieved profile is a crucial part of any inversion technique. As described by *Rodgers* [2000], four different sources of error can be identified: (1) smoothing error, (2) retrieval noise, (3) forward model error, and (4) forward model parameter error. The smoothing error arises because of the limited vertical resolution of the retrieval. The covariance of the smoothing error can be expressed as

$$\mathbf{S}_s = (\mathbf{A} - \mathbf{I}_r)\mathbf{S}_a(\mathbf{A} - \mathbf{I}_r)^T, \tag{31}$$

where $\mathbf{A} = \mathbf{GK}$ is the averaging kernel matrix and $\mathbf{I}_r$ is an identity matrix ($r \times r$). Including the smoothing error in the total error estimate means that the retrieval can be considered an estimate of the true state with an error contribution from average kernel smoothing, rather than an estimate of a smoothed true state. The covariance matrix corresponding to the retrieval noise is given by

$$\mathbf{S}_m = \mathbf{G}\mathbf{S}_\epsilon\mathbf{G}^T. \tag{32}$$

Forward model error, with covariance $\mathbf{S}_f$, occurs because of imperfections and approximations within the forward model. This error is difficult to estimate, requiring a perfect forward model containing the correct physics. However, as was mentioned in previous sections, some approximations are made in order to decrease the computational requirements and the error resulting from these approximations is assigned to the forward model error. Forward model parameter error, with covariance $\mathbf{S}_b$, relates to uncertainties in the parameters specified within the RTM including albedo, aerosol, temperature, and cross sections. This error can also be difficult to estimate, requiring knowledge about the true state and expected variation of each parameter. Forward model error and forward model parameter error will be discussed in more detail in section 4.

[56] The total retrieval error is the sum of the four error sources

$$\mathbf{S}_{tot} = \mathbf{S}_s + \mathbf{S}_m + \mathbf{S}_f + \mathbf{S}_b. \tag{33}$$

Note that this is not the same as the covariance matrix of the solution, $\hat{\mathbf{S}}$, which only contains the first two terms of equation (33), i.e., the smoothing error and retrieval noise.

3.4.3. Characterization

[57] Resolution and measurement response can be derived to characterize the retrievals. The resolution of the retrieved profile is usually defined as the "width" of the averaging kernels, that is the rows of $\mathbf{A}$. A quantity called "spread" [*Backus and Gilbert*, 1970], denoted s, is used to determine this width:

$$s(z_0) = 12\frac{\int(z_0 - z')^2\mathbf{A}^2(z_0, z')dz'}{\left[\int|\mathbf{A}(z_0, z')|dz'\right]^2}, \tag{34}$$

where z_0 is the nominal altitude of the peak of the related averaging kernel. The measurement response is given by the area of the averaging kernels and gives the relative

contribution of the measurements and a priori information to the retrieved profile. These two statistics are shown for the sample retrievals in Figure 9.

3.4.4. Calculating K and F

[58] The calculation of weighting functions requires knowledge about the derivatives of the forward model in a multivariate sense, i.e.,

$$\mathbf{K} = \frac{\partial \mathbf{F}(\mathbf{n})}{\partial \mathbf{n}} = \nabla_{\mathbf{n}} \mathbf{F}(\mathbf{n}). \tag{35}$$

When the natural logarithm of $\mathbf{n}$ is inverted, the weighting functions are given by

$$\mathbf{K}_{\log} = \frac{\partial \mathbf{F}(\mathbf{n})}{\partial \ln(\mathbf{n})} = \frac{\partial \mathbf{F}(\mathbf{n})}{\partial \mathbf{n}} \cdot \frac{\partial \mathbf{n}}{\partial \ln(\mathbf{n})} = \mathbf{K}\mathbf{n}. \tag{36}$$

For clarity, only the linear version of $\mathbf{K}$ is derived. LIMBTRAN does not include analytical expressions for the derivatives of the limb-scatter radiances. Also, the relationship between the derivatives of the RTM and the derivatives of $\mathbf{F}$ is not obvious because of the intermediate DOAS step. Hence any calculation of $\mathbf{K}$ has to be done numerically. Remember that $\mathbf{K}$ is a $q \times r$ matrix, where q is the number of tangent heights in $\mathbf{c}$ and r is the number of heights in $\mathbf{n}$. An element in $\mathbf{K}$ can be expressed as

$$K(i,j) = \frac{\partial F[\mathbf{n}, h_t(i)]}{\partial n[z(j)]}, \tag{37}$$

where $F[\mathbf{n}, h_t(i)]$ is the forward model for tangent height $h_t(i)$ and $n[z(j)]$ is the number density at height $z(j)$. One method of calculating $\mathbf{K}$ is using finite differences with sequential perturbation of the elements of $\mathbf{n}$. Perturbation in this case refers to changing an element $n[z(j)]$ in $\mathbf{n}$ by some amount (5% in this study). The forward model is run with and without this perturbed $\mathbf{n}$. An element of the weighting function matrix can then be approximated as

$$K(i,j) \approx \frac{F[\mathbf{n}^*, h_t(i)] - F[\mathbf{n}, h_t(i)]}{n^*[z(j)] - n[z(j)]}, \tag{38}$$

where $\mathbf{n}^*$ denotes an $\mathbf{n}$ vector perturbed in the region of $z(j)$.

[59] Sequential perturbation is very time consuming because the RTM has to be run r times in order to estimate $\mathbf{K}$ for every iteration. Thus it is desirable to find approximations that can be used in the calculation of $\mathbf{K}$. One option is to reduce the number of spectral elements by using a two wavelength DOAS approach that exploits the differential absorption between one strongly absorbing wavelength, λ_{on}, and one weakly absorbing wavelength, λ_{off}:

$$c_i(h_t) \approx \frac{\ln\left[\frac{I(\lambda_{off}, h_t^{ref})}{I(\lambda_{off}, h_t)}\right] - \ln\left[\frac{I(\lambda_{on}, h_t^{ref})}{I(\lambda_{on}, h_t)}\right]}{\sigma_i(\lambda_{off}) - \sigma_i(\lambda_{on})}. \tag{39}$$

This simplification is applicable when no other species are interfering significantly with the target species at the two selected wavelengths. In addition, the wavelengths must be close enough to minimize the impact of slowly varying features such as Mie and Rayleigh scattering. The two wavelength approach is sufficient in the determination of $\mathbf{K}$ for O_3 and NO_2 retrievals using the spectral windows of this study and leads to negligible differences from using a full DOAS analysis. In this study, the wavelengths 602 nm and 615 nm are used for O_3 and 431 nm and 440 nm are used for NO_2.

[60] The computational requirements for calculating $\mathbf{K}$ can be further reduced by assuming single scattering and an aerosol-free atmosphere in the RTM. The approximation that $\mathbf{K}$ can be calculated with single scattering leads to negligible error in both the NO_2 and O_3 retrievals. The error resulting from the assumption of an aerosol-free atmosphere is also negligible for both NO_2 and O_3.

[61] The nonlinear solution requires calculations of $\mathbf{F}$ as well as $\mathbf{K}$ for every iteration. Thus it is also desirable to make approximations in the calculation of $\mathbf{F}$. Systematic errors in $\mathbf{F}$ do not necessarily lead to errors in $\mathbf{K}$, since only derivatives are considered in the latter, and as a result the approximations discussed above are found to not be appropriate for calculating $\mathbf{F}$. An approximation that can be made is to use just a selection of wavelengths in the retrieval window rather than the full OS sampling. This sparse wavelength grid is treated in the same way as the regular grid in the DOAS analysis. The use of a 4 nm wavelength grid for O_3 and a 2 nm wavelength grid for NO_2 leads to negligible differences from using a full DOAS analysis. Larger step sizes can lead to interference with the spectral smoothing since the differential structure becomes poorly sampled.

4. Error Analysis

[62] As was discussed in section 3.4.2, the smoothing error and measurement noise components of the total retrieval error are easily calculated. However, the forward model and forward model parameter errors are more difficult to evaluate. In this section, the various contributions to each error source are analyzed and an estimate of the total retrieval error is presented.

4.1. Forward Model Error

[63] The forward model error is estimated by analyzing the impact of the various approximations discussed in sections 3.3 and 3.4.4 on the retrievals. The error introduced by each of the approximations is determined by comparing retrievals that incorporate the approximation to retrievals in which no approximation is used. Some additional error exists because of truncation and interpolation within the forward model and inversion code. This error term is evaluated by comparing retrievals using simulated noise-free measurements of the a priori state computed with the forward model to the a priori. Since the forward model errors are not independent, the error terms are added together to produce the total forward model error. The individual error terms and the total forward model error for the O_3 and NO_2 retrievals are shown in Figure 10. The forward model errors, calculated for a midlatitude atmosphere with SZA = 85° and SSA = 90° and surface albedo 0.3, are generally independent of the measurement conditions, with any variations primarily due to the influence of the a priori at the top and bottom of the retrieval range. The

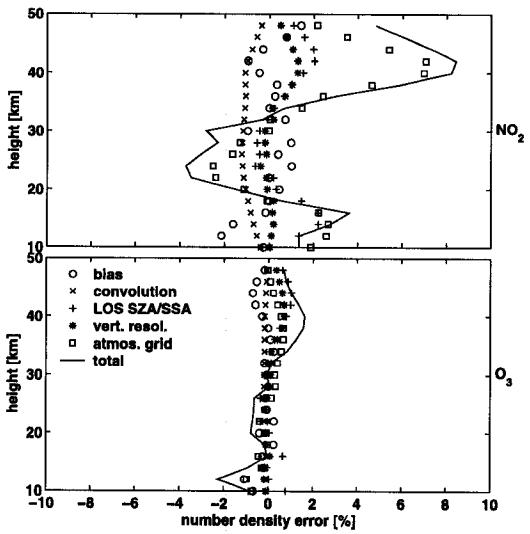

Figure 10. Forward model errors due to model bias, the use of convolved cross sections, approximations in the variation of SZA and SSA along the LOS, the neglect of taking the vertical resolution of the OS measurements into account and the use of a 1 km atmosphere grid in LIMBTRAN, and the total forward model error, given by the sum of the errors.

LOS SZA/SSA variation approximation has a small dependence on the solar conditions, and the worst case is shown in the figure. Note that no attempt is made to estimate the error introduced by the use of a pseudospherical RTM or by the horizontal homogeneity assumption.

4.2. Forward Model Parameter Error

[64] To estimate the forward model parameter error, the approach of *Dudhia et al.* [2002] is followed. In this approach the systematic errors are treated as independent error sources with an assumed uncertainty. The systematic errors are estimated by performing perturbations of 1 standard deviation to a number of forward model parameters about a midlatitude atmosphere with surface albedo 0.3: uncertainties in aerosol (30%), neutral density (10%) and temperature (5 K); a 10% uncertainty in the surface albedo (with no clouds); uncertainties of 10% in the instrument spectral resolution and 3% in the O_3 and NO_2 cross sections; and a 500 m uncertainty in the tangent height registration.

[65] The relatively large instrument resolution uncertainty is based on the fact that the OS does not carry any spectral calibration sources, making the spectral resolution of the OS difficult to monitor. This is compounded by some contamination of the OS entrance slit prior to launch [*Llewellyn et al.*, 2004] that has led to some uncertainty as to the true spectral resolution, and an uncertainty of 10% is assumed. The tangent height registration uncertainty in the OS measurements is also difficult to estimate. There are periods when the pointing of the SMR telescope is reportedly accurate to 200 m at the tangent point, however, there are times when the uncertainty just fulfills the 1.5 km design requirement. There is also some question as to the relative alignment of OSIRIS on the Odin platform since this is difficult to measure on orbit. The relative alignment has been estimated by using measurements of Jupiter (N. D. Lloyd, personal communication, 2002), but the accuracy of this method is limited and determining the alignment to better than 500 m has been difficult. It is also possible that the alignment is not static. Methods have been proposed for determining and correcting pointing offsets in limb-scatter measurements. A technique similar to that of *Janz et al.* [1996] has been applied to OS data with some success by *Sioris et al.* [2001, 2003]. The accuracy of this technique is limited and the technique is currently only used to monitor the tangent height registration. For the purpose of this error analysis it is assumed that the corrected tangent heights are accurate to 500 m.

[66] In addition to the above error sources, the impact of cloud on the retrievals is estimated in a preliminary way by perturbing the surface albedo to a value of 1.0. Though crude, this gives a sense of the impact that can be expected when cloud is present in the measurements (below the FOV of the lowest measurement), but is not taken into account in the retrievals. No estimation of the impact of clouds within the FOV of the instrument is included.

[67] Assuming that each of the errors are independent and that vertical correlations can be ignored, the total forward model retrieval error is calculated by adding the error variances. Each of the error sources and the total are shown in Figure 11. Four scenarios are illustrated for each species: high-Sun (SZA = 60°, SSA = 90°) and low-Sun (SZA = 90°, SSA = 90°) cases for both cloud and cloud-free conditions. As the figure shows, tangent height registration uncertainty is the largest source of error, introducing errors of ~10% for O_3 and ~15% for NO_2 away from the profile peaks. Clouds can also have a large effect on the retrievals, leading to errors of ~10% for O_3 and ~20% for NO_2 below 20 km.

4.3. Total Retrieval Error

[68] The total retrieval error is estimated by combining the smoothing error, measurement noise, forward model error and forward model parameter error (see section 3.4.2), and is shown in Figure 12 for the four cases mentioned in the previous section. As the figure shows, the estimated total error is about 10% at 30 km for NO_2 and 13% at 30 km for O_3. Note that the smoothing error is the dominant error source at high and low altitudes for both species, where the a priori begins to significantly impact the retrievals. Since the a priori covariance matrix is somewhat uncertain, and only relates to an ensemble of profiles, the inclusion of this component in the total error must be treated with caution, since it may tend to lead to an overestimation of the error for individual profiles. This is particularly the case for the NO_2 error estimation, where the a priori covariance is potentially overestimated.

5. Validation

[69] The intention of this section is not to make a full validation of the O_3 and NO_2 DOAS retrievals, but rather to give some justification that the retrieval method is appropriate, producing reasonable results.

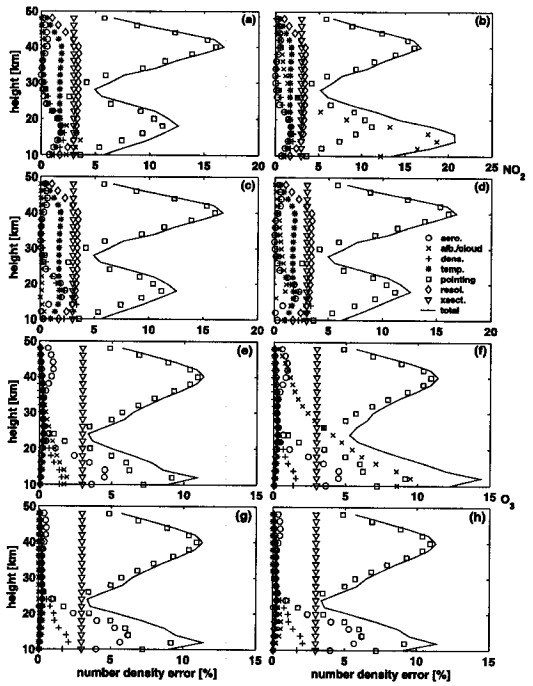

Figure 11. Forward model parameter errors due to uncertainties in aerosol, surface albedo/cloud, neutral density, temperature, pointing, spectral resolution, and cross section given as 1 STD, and the total forward model parameter error, given by the sum of the variances. Four scenarios are illustrated for each species: (a and e) high Sun (SZA = 60°, SSA = 90°) with cloud-free conditions, (b and f) high Sun with clouds, (c and g) low Sun (SZA = 90°, SSA = 90°) with cloud-free conditions, and (d and h) low Sun with clouds.

[70] A first step in justifying the DOAS approach is to compare the results to other retrieval approaches that have been applied to OSIRIS data. Figure 13 shows a comparison between O_3 profiles retrieved using the DOAS approach and results from the paired-radiance approach of *Flittner et al.* [2000] that has been applied to OSIRIS data by *von Savigny et al.* [2003] for two OSIRIS limb scans. Note that error bars are only displayed for the DOAS retrievals for clarity. The results of the two retrieval techniques agree quite well, with the paired-radiance results generally contained within the DOAS error bars. A more detailed comparison of the two methods is given by *Haley et al.* [2004], who found that the two techniques agree to within 5% in most cases. The paired-radiance approach is the algorithm that is used to produce operational O_3 profiles from OSIRIS and has been compared extensively to POAM III and ozonesonde data with favorable results [*Petelina et al.*, 2004]. Figure 14 compares NO_2 profiles retrieved using the DOAS approach described here with results from a different DOAS approach used by *Sioris et al.* [2003]. Again, the two approaches are in good agreement, demonstrating that the retrieval technique presented here produces results that are consistent with other OSIRIS data analyses.

[71] OSIRIS results can also be compared with the results of other instruments, such as data from balloon campaigns or other satellite measurements. When making these comparisons, one must bear in mind that the geometry of limb-scattered sunlight measurements is fundamentally different than that of other techniques (i.e., occultation). Also, any deviation in local solar time and the location of the measurements can affect any comparison. This is particularly true for NO_2, which has a short atmospheric lifetime and strong variations between daytime and nighttime chemistry, enhanced by Odin's near-terminator orbit.

[72] Comparisons of O_3 retrievals with coincident electrochemical concentration cell (ECC) ozonesonde measurements for two OS limb scans are shown in Figure 13. The ozonesondes make in situ measurements of the concentration of ozone with very high vertical sampling. Since the atmospheric lifetime of O_3 (odd oxygen) is long, the effect of any SZA and location differences between the sonde and OSIRIS is not crucial. In both cases the agreement is quite

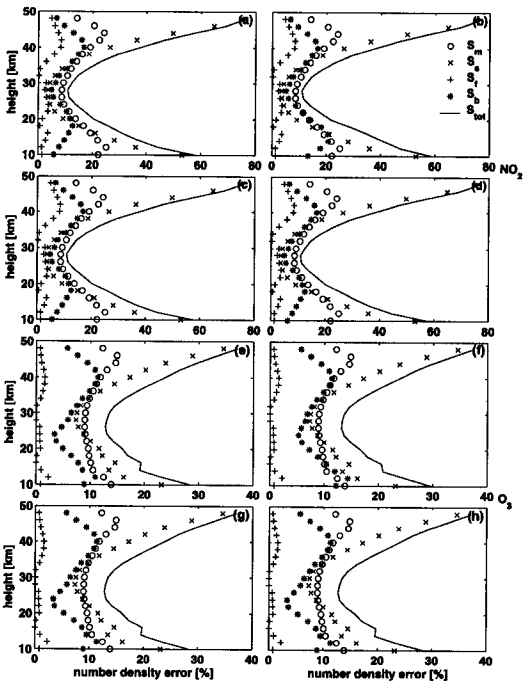

Figure 12. Total error estimate (1 STD) for the NO_2 and O_3 retrievals, S_{tot}, calculated from the sum of the variances of the smoothing error, S_s, retrieval noise, S_m, forward model error, S_f, and forward model parameter error, S_b. Four scenarios are illustrated for each species: (a and e) high Sun (SZA = 60°, SSA = 90°) with cloud-free conditions, (b and f) high Sun with clouds, (c and g) low Sun (SZA = 90°, SSA = 90°) with cloud-free conditions, and (d and h) low Sun with clouds.

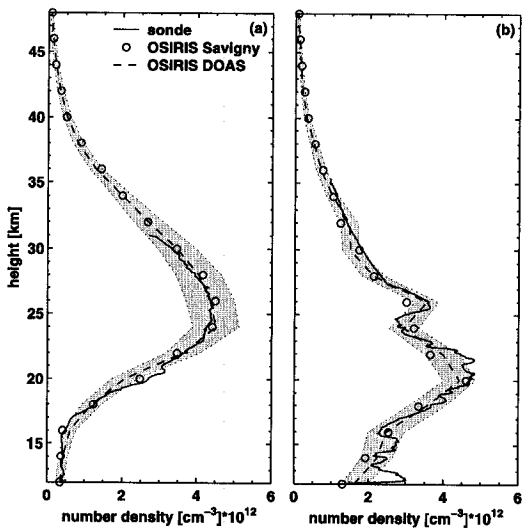

Figure 13. Comparisons of DOAS O_3 retrievals (dashed lines) with paired-radiance (circles) and sonde (solid lines) results. (a) O_3 profiles retrieved from OSIRIS measurements on 22 August 2001 (scan 2722001, latitude 29.8°N, longitude 16.1°W, 1849 UT) and an ozonesonde launched from Santa Cruz, Spain (latitude 28.5°N, longitude 16.3°W, 1117 UT). (b) O_3 profiles retrieved from OSIRIS measurements on 8 August 2001 (scan 2507009, latitude 77.2°N, longitude 14.1°E, 0733 UT) and an ozonesonde launched from Ny lesund, Norway (latitude 78.9°N, longitude 12.0°E, 1059 UT). The shaded regions give the 1-STD error calculated from the square root of the diagonals of the retrieval covariance matrices ($\mathbf{S}_m + \mathbf{S}_s$).

good, particularly considering that only a smoothed ozone profile (~2–3 km resolution) is retrieved from OSIRIS measurements.

[73] Profiles of NO_2 retrieved from OSIRIS measurements are compared to Systeme d'Analyse par Observation Zenithale (SAOZ) balloon measurements in Figure 14. The SAOZ UV/visible spectrometer makes solar occultation measurements at sunrise and sunset at float and during ascent and descent. Measuring between 290 nm and 640 nm, SAOZ provides the vertical distribution of O_3, NO_2 and atmospheric extinction at a resolution of 1.4 km with accuracies better than 3% for O_3 and 10% for NO_2 [*Pommereau and Piquard*, 1994]. Figure 14 shows that the general NO_2 features of the SAOZ data are consistent with the DOAS retrievals performed in this study. The agreement is quite good considering the different measurement geometries and conditions and the considering the differences between the SOAZ ascent and occultation measurements, particularly at low altitudes in the 16 March comparison.

6. Results and Conclusions

[74] To give a better picture of the potential of the limb-scatter technique, one complete orbit and one entire day of OS measurements were analyzed. Results from Odin orbit 14013 on 19 September 2003 are shown in Figure 15. Note that Odin was pointing off of the orbital plane into the sunlit region for the second half of this orbit, explaining the unexpected measurement pattern (Figure 15g) and SZAs (Figure 15e). This off-plane mode is occasionally utilized to provide better global coverage. The expected Antarctic O_3 hole, at altitudes between 15 and 30 km, together with the tropopause uplift in the equatorial region are clearly visible in the figure. In the interpretation of the NO_2 fields, the near-terminator orbit must be considered. The low NO_2 concentrations at the descending (sunrise) node of the orbit are associated with the prevailing nighttime chemistry, where the photolysis of N_2O_5 and NO_3 to form NO_2 and NO has only taken place for a short period of time, leading to low NO_2 densities. As the time in which the atmosphere has been in sunlight increases, the concentration of NO_2 increases. This can be seen in the regions of long periods of sunlight toward the South Pole and near the ascending (sunset) nodes of the orbit. Low NO_2 concentrations in the ozone hole region are expected because of

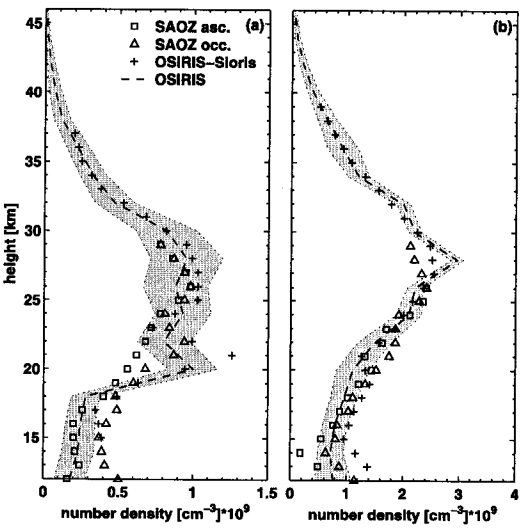

Figure 14. Comparisons of DOAS NO_2 retrievals (dashed lines) with results from a different DOAS technique (crosses) and SAOZ results (squares and triangles). (a) NO_2 profiles retrieved from OSIRIS measurements on 16 March 2003 (scan 11219006, latitude 66.2°N, longitude 10.5°E, 1613 UT) and data from a SAOZ sonde launched at Kiruna, Sweden (ascent, latitude 67.5°N, longitude 22.0°E, 1548 UT; occultation, latitude 67.3°N, longitude 14.3°E, 1654 UT). (b) NO_2 profiles retrieved from OSIRIS measurements on 1 October 2002 (scan 8745006, latitude 47.2°N, longitude 11.8°E, 1642 UT) and data from a SAOZ sonde launched at Aire sur l'Adour, France (ascent, latitude 43.8.5°N, longitude 0.1°E, 1700 UT; occultation, latitude 43.7°N, longitude 3.9°E, 1754 UT). The shaded regions give the 1-STD error calculated from the square root of the diagonals of the retrieval covariance matrices ($\mathbf{S}_m + \mathbf{S}_s$).

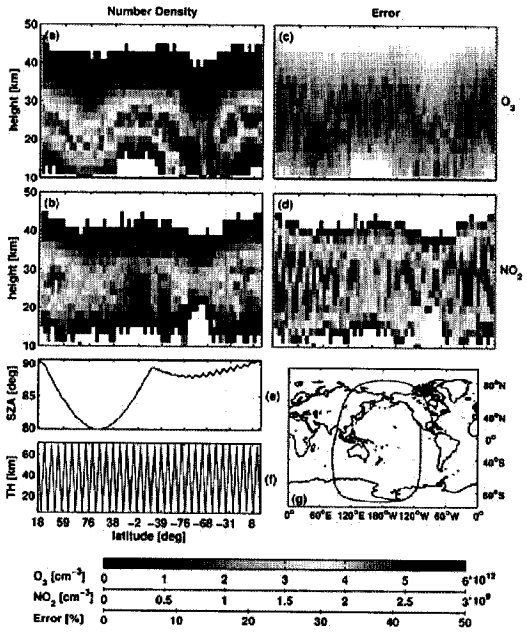

Figure 15. Retrieved profiles of (a) O_3 and (b) NO_2 for Odin orbit 14013 on 20 September 2003 as a function of latitude, with (c and d) corresponding retrieval errors ($S_m + S_s$), in percent. Note that values with a measurement response less than 0.75 are excluded. Also plotted is (e) SZA versus latitude for each scan, (f) the tangent heights of the Odin/OSIRIS limb scanning, and (g) the global map of the limb scan locations. Note that Odin was pointing off of the orbit plane toward the South Pole during the second half of the orbit to achieve better coverage.

denitrification processes resulting from the deposition of nitrogen-rich polar stratospheric cloud (PSC) particles and the formation of reservoir species. The retrieval error fields, given by Figures 15b and 15c, are correlated with the concentration of the retrieved species and increase at low and high altitudes, particularly for NO_2, primarily due to the smoothing error. Note that forward model parameter error and forward model error are not included in the displayed error. The structure in the error fields is due to the irregular OS measurement grid. Since the figure only shows data where the response is greater than 0.75, it gives an indication that the retrievals are largely free of a priori contamination between about 12 km and 45 km for O_3 and between about 15 km and 40 km for NO_2. One must be careful, however, to consider the response and vertical resolution of the retrievals together since a high response at the extremes of the retrieval range can be associated with a degraded resolution, as can be seen in Figure 9.

[75] Results from one entire day, spanning 1–2 October 2003 (1200 UT to 1200 UT), are shown in Figure 16 with maps of retrieved O_3 and NO_2 number densities at 16, 20 and 26 km. The NO_2 retrievals are divided on the basis of local time in order to separate the diurnal effects. The extension of the ozone hole and the associated denitrification are clearly evident in the global figure.

[76] As the error analysis has shown, the retrieval method described here has a large sensitivity to cloud that could be significantly reduced if cloud information was included in the retrievals. TOMS reflectivity data or other similar data sets could be utilized to provide information about the presence of cloud or perhaps some albedo information could be derived from the OSIRIS measurements to give an indication of the presence of clouds. The retrievals are also sensitive to tangent height registration uncertainties, and an accurate correction technique could significantly reduce these uncertainties and reduce the associated error in the retrievals. Further study of the impact of horizontal inhomogeneities on the retrievals, in particular in regard to retrievals near the edge of the polar vortex, is also required.

[77] In conclusion, a method for retrieving stratospheric O_3 and NO_2 profiles from limb-scattered sunlight measurements has been presented and applied to OSIRIS measurements. It has been shown that O_3 profiles are generally retrieved with a measurement response above 0.75 and a

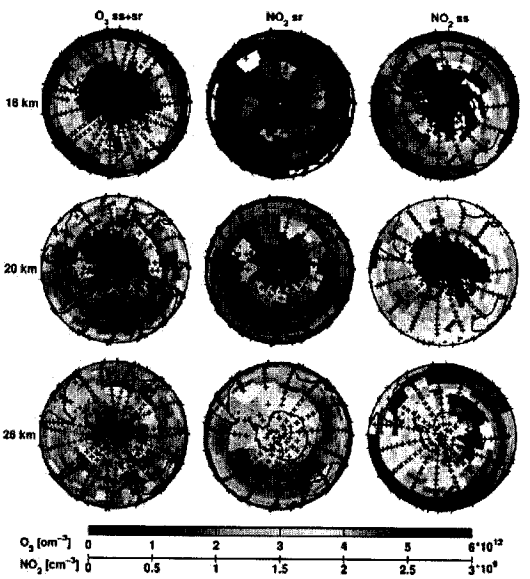

Figure 16. Retrieved number densities (molecules cm^{-3}) for the Southern Hemisphere on 1–2 October 2003 (1200 UT to 1200 UT) at 16, 20, and 26 km. Data have been binned to a 4° longitude and 2° latitude grid and interpolated to the nearest neighbor. Crosses denote the position of OSIRIS scans. Note that values with a measurement response less than 0.75 are excluded. NO_2 has been separated into sunset (ascending) nodes (ss) and sunrise (descending) nodes (sr) because of the strong variations between daytime and nighttime chemistry. Note that Odin was pointing off of the orbit plane toward the South Pole during this period to achieve better coverage.

vertical resolution of 2–3 km in the range 12–45 km, and NO_2 profiles are retrieved with a measurement response above 0.75 and a vertical resolution of 2–3 km in the range 15–40 km. It is difficult to determine the total uncertainty in the retrievals, but given the various sources of error and initial validation studies, the retrieved number densities should be generally accurate to about 13% for O_3 and 10% for NO_2 at the peak of the profiles. Future application of a DOAS analysis to the UV region may be able to provide stratospheric BrO and OClO density profiles and mesospheric O_3 densities.

Notation

$*$	convolution.
$\star$	perturbation.
$\hat{}$	MAP estimate.
$\tilde{}$	modeled.
λ	wavelength, nm.
σ	absorption cross section, cm^2 $molecule^{-1}$.
σ'	differential cross section, cm^2 $molecule^{-1}$.
τ	optical depth.
τ'	differential optical depth.
ϵ	measurement error of the OS (STD), photons cm^{-2} s^{-1} nm^{-1} $ster^{-1}$.
ϵ_{I_0}	error in I_0 (STD).
$\epsilon_{\tau'}$	error in τ' (STD).
ε_R	Rayleigh optical depth.
ε_M	Mie optical depth.
$\mathbf{A}$	averaging kernel matrix.
$\mathbf{b}$	forward model parameters.
c	effective column density, molecules cm^{-2}.
$\mathbf{c}$	effective column density profile.
$\mathbf{F}$	forward model vector.
g	Gaussian filter function.
$\mathbf{G}$	gain matrix.
hr	highly resolved.
h_t	tangent height, km.
h_t^{ref}	tangent height of reference, km.
I	radiance, photons cm^{-2} s^{-1} nm^{-1} $ster^{-1}$.
I_0	radiance of unattenuated spectrum.
$\mathbf{K}$	weighting function matrix ($q \times r$).
n	number density, molecules cm^{-3}.
$\mathbf{n}$	number density profile.
$\mathbf{n}_a$	a priori number density profile.
p	polarization pseudoabsorber.
q	number of tangent heights in $\mathbf{c}$.
r	number of heights in $\mathbf{n}$.
$\mathbf{S}$	covariance matrix of the solution ($r \times r$).
$\mathbf{S}_a$	covariance matrix of a priori ($r \times r$).
$\mathbf{S}_\epsilon$	covariance matrix of measurement ($q \times q$).
$\mathbf{S}_{\epsilon_{\tau'}}$	covariance matrix of τ'.
t	tilt pseudoabsorber.
z	height/retrieval grid, km.
AS	albedo scattering.
DN	data number.
DOAS	differential optical absorption spectroscopy.
IRI	infrared imager.
FOV	field of view.
FWHM	full width at half maximum.
L-M	Levenberg-Marquardt.
LOS	line of sight.
LSQ	least squares.
LST	local solar time, hours.
MAP	maximum a posteriori estimator.
MS	multiple scattering.
OE	optimal estimation.
OS	optical spectrograph.
OSIRIS	Optical Spectrograph and Infrared Imager System.
RMS	root mean square.
RRS	rotational Raman scattering.
RTM	radiative transfer model.
SMR	Submillimeter and Millimeter Radiometer.
SS	single scattering.
SSA	single scattering angle.
STD	standard deviation.
SZA	solar zenith angle.
TH	tangent height.
TOA	top of atmosphere.
UT	universal time.
UV	ultraviolet.

[78] **Acknowledgments.** This work is supported by the Natural Sciences and Engineering Research Council (Canada), the Canadian Space Agency, the Swedish National Space Board, and Chalmers University of Technology. Odin is a Swedish-led satellite project, funded jointly by Sweden (SNSB), Canada (CSA), Finland (Tekes), and France (CNES). The authors thank P. van der Gathen (AWI Potsdam) and E. Cuevas (INM Spain) for providing the ozonesonde data and the anonymous reviewers for their constructive comments.

References

Aliwell, S. R., et al. (2002), Analysis for BrO in zenith-sky spectra: An intercomparison exercise for analysis improvement, *J. Geophys. Res.*, *107*(D14), 4199, doi:10.1029/2001JD000329.

Auvinen, H., L. Oikarinen, and E. Kyrölä (2002), Inversion algorithms for recovering minor species densities from limb scatter measurements at UV-visible wavelengths, *J. Geophys. Res.*, *107*(D13), 4172, doi:10.1029/2001JD000407.

Axelsson, H., H. Edner, B. Galle, P. Ragnarsson, and M. Rudin (1990), Differential optical absorption spectroscopy (DOAS) measurements of ozone in the 280–290 nm wavelength range, *Appl. Spectrosc.*, *44*(10), 1654–1658.

Backus, G. E., and J. F. Gilbert (1970), Uniqueness in the inversion of inaccurate gross Earth data, *Philos. Trans. R. Soc. London, Ser. A*, *266*, 123–192.

Barath, F. T., et al. (1993), The Upper Atmosphere Research Satellite Microwave Limb Sounder instrument, *J. Geophys. Res.*, *98*(D6), 10,751–10,762.

Bates, D. R. (1984), Rayleigh scattering by air, *Planet. Space Sci.*, *32*(6), 785–790.

Bauman, J. J., P. B. Russell, M. A. Geller, and P. Hamill (2003a), A stratospheric aerosol climatology from SAGE II and CLAES measurements: 1. Methodology, *J. Geophys. Res.*, *108*(D13), 4382, doi:10.1029/2002JD002992.

Bauman, J. J., P. B. Russell, M. A. Geller, and P. Hamill (2003b), A stratospheric aerosol climatology from SAGE II and CLAES measurements: 2. Results and comparisons, 1984–1999, *J. Geophys. Res.*, *108*(D13), 4383, doi:10.1029/2002JD002993.

Bertaux, J., G. Mégie, T. Widemann, E. Chassefière, R. Pellinen, E. Kyrölä, S. Korpela, and P. Simon (1991), Monitoring of ozone trend by stellar occultations: The GOMOS instrument, *Adv. Space Res.*, *11*(3), 237–242.

Bogumil, K., et al. (2003), Measurements of molecular absorption spectra with the SCIAMACHY pre-flight model: Instrument characterization and reference data for atmospheric remote-sensing in the 230–2380 nm region, *J. Photochem. Photobiol. A: Chem*, *157*(2–3), 167–184, doi:10.1016/S1010-6030(3)00062-5.

Bovensmann, H., J. P. Burrows, M. Buchwitz, J. Frerick, S. Noël, V. V. Rozanov, K. V. Chance, and A. P. H. Goede (1999), SCIAMACHY: Mission objectives and measurement modes, *J. Atmos. Sci.*, *56*(2), 127–150.

Brinkmann, R. T. (1968), Rotational Raman scattering in planetary atmospheres, *Astrophys. J.*, *154*, 1087–1093.

Burrows, J. P., et al. (1999), The Global Ozone Monitoring Experiment (GOME): Mission concept and first scientific results, *J. Atmos. Sci.*, *56*(1), 151–175.

Chance, K. V., and R. J. D. Spurr (1997), Ring effect studies: Rayleigh scattering, including molecular parameters for rotational Raman scattering, and the Fraunhofer spectrum, *Appl. Opt.*, *36*(21), 5224–5230.

Degenstein, D. A., E. J. Llewellyn, and N. D. Lloyd (2003), Volume emission rate tomography from a satellite platform, *Appl. Opt.*, *42*(8), 1441–1450.

Dudhia, A., V. L. Jay, and C. D. Rodgers (2002), Microwindow selection for high-spectral-resolution sounders, *Appl. Opt.*, *41*(18), 3665–3673.

Eriksson, P., and D. Chen (2002), Statistical parameters derived from ozonesonde data of importance for passive remote sensing of ozone, *Int. J. Remote Sens.*, *23*(22), 4945–4963.

Fischer, H., and H. Oelhaf (1996), Remote sensing of vertical profiles of atmospheric trace constituents with MIPAS limb emission spectrometers, *Appl. Opt.*, *35*(16), 2787–2796.

Flittner, D. E., P. Bhartia, and B. Herman (2000), O_3 profiles retrieved from limb scatter measurements: Theory, *Geophys. Res. Lett.*, *27*(17), 2601–2604.

Frisk, U., et al. (2003), The Odin satellite I: Radiometer design and test, *Astron. Astrophys.*, *402*(3), L27–L34, doi:10.1051/0004-6361:20030335.

Grainger, J., and J. Ring (1962), Anomalous Fraunhofer line profiles, *Nature*, *193*, 762.

Greenblatt, G. D., J. J. Orlando, J. B. Burkholder, and A. R. Ravinshankara (1990), Absorption measurements of oxygen between 300 and 1140 nm, *J. Geophys. Res.*, *95*(D11), 18,577–18,582.

Griffioen, E., and L. Oikarinen (2000), LIMBTRAN: A pseudo three-dimensional radiative transfer model for the limb-viewing imager OSIRIS on the Odin satellite, *J. Geophys. Res.*, *105*(D24), 29,717–29,730.

Haley, C. S., C. von Savigny, S. Brohede, C. E. Sioris, I. C. McDade, E. J. Llewellyn, and D. P. Murtagh (2004), A comparison of methods for retrieving stratospheric ozone from OSIRIS limb-scatter measurements, *Adv. Space. Res.*, *34*(4), 769–774, doi:10.1016/j.asr.2003.08.058.

Harrison, A. W. (1976), Diurnal variation of the Ring effect, *Can. J. Phys.*, *54*, 1000–1005.

Hunten, D. M. (1970), Surface albedo and the filling-in of Fraunhofer lines in the day sky, *Astrophys. J.*, *159*, 1010–1107.

Hutley, M. C. (1982), *Diffraction Gratings*, pp. 165–193, Academic, San Diego, Calif.

Janz, S. J., E. Hilsenrath, D. Flittner, and D. Heath (1996), Rayleigh scattering attitude sensor, *Proc. SPIE Int. Soc. Opt. Eng.*, *2831*, 146–153.

Kaiser, J. W. (2001), Atmospheric parameter retrieval from UV-vis-NIR limb scattering measurements, Ph.D. thesis, Inst. of Environ. Phys.-Inst. of Remote Sens., Univ. of Bremen, Bremen, Germany.

Kemnitzer, H., S. Hilgers, G. Schwarz, T. Steck, T. v. Clarmann, M. Höpfner, and K. Ressel (2002), Trace gas retrieval including horizontal gradients, *Adv. Space. Res.*, *29*(11), 1631–1636.

Khabibrakhmanov, I. K., D. A. Degenstein, and E. J. Llewellyn (2002), Mesospheric ozone: Determination from orbit with the OSIRIS instrument on Odin, *Can. J. Phys.*, *80*(4), 493–504.

Koelemeijer, R. B. A., J. F. de Haan, and P. Stammes (2003), A database of spectral surface reflectivity in the range 335–772 nm derived from 5.5 years of GOME observations, *J. Geophys. Res.*, *108*(D2), 4070, doi:10.1029/2002JD002429.

Levenberg, K. (1944), A method for the solution of certain problems in least-squares, *Q. Appl. Math.*, *2*, 164–168.

Li, D., and K. P. Shine (1995), A 4-dimensional ozone climatology for UGAMP models, UGAMP internal report 35, UK Univ. Global Atmos. Modell. Programme, Reading.

Livesey, N. J., and W. G. Read (2000), Direct retrieval of line-of-sight atmospheric structure from limb sounding observations, *Geophys. Res. Lett.*, *27*(6), 891–894.

Llewellyn, E. J., et al. (2004), The OSIRIS instrument on the Odin spacecraft, *Can. J. Phys.*, *82*(6), 411–422, doi:10.1139/P04-005.

Loughman, R. P., E. Griffioen, L. Oikarinen, O. V. Postylyakov, A. Rozanov, D. E. Flittner, and D. F. Rault (2004), Comparison of radiative transfer models for limb-viewing scattered sunlight measurements, *J. Geophys. Res.*, *109*, D06303, doi:10.1029/2003JD003854.

Lucke, R. L., et al. (1999), The polar ozone and aerosol measurement (POAM) III instrument and early validation results, *J. Geophys. Res.*, *104*(D15), 18,785–18,799.

Marquardt, D. (1963), An algorithm for least-squares estimation on nonlinear parameters, *SIAM J. Appl. Math.*, *11*, 431–441.

McCormick, M. P., W. P. Chu, J. M. Zawodny, L. E. Mauldin III, and L. R. McMaster (1991), Stratospheric Aerosol and Gas Experiment III (SAGE III) aerosol and trace gas measurements for Earth Observing System (EOS), *Proc. SPIE Int. Soc. Opt. Eng.*, *1491*, 125–141.

McDade, I. C., K. Strong, C. S. Haley, J. Stegman, D. P. Murtagh, and E. J. Llewellyn (2002), A method for recovering stratospheric minor species densities from the Odin/OSIRIS scattered-sunlight measurements, *Can. J. Phys.*, *80*(4), 395–408.

McLinden, C. A., S. Olsen, B. Hannegan, O. Wild, M. J. Prather, and J. Sundet (2000), Stratospheric ozone in 3-D models: A simple chemistry and the cross-tropopause flux, *J. Geophys. Res.*, *105*(D11), 14,653–14,665.

McLinden, C. A., J. C. McConnell, K. Strong, I. C. McDade, R. L. Gattinger, R. King, B. Solheim, E. J. Llewellyn, and W. J. F. Evans (2002), The impact of the OSIRIS grating efficiency on radiance and trace-gas retrievals, *Can. J. Phys.*, *80*(4), 469–481.

McPeters, R. D., P. K. Bhartia, A. J. Krueger, and J. R. Herman (1998), Earth Probe Total Ozone Mapping Spectrometer (TOMS) data products user's guide, *NASA Tech. Publ., NASA/TP-1998-206895*.

McPeters, R. D., S. J. Janz, E. Hilsenrath, and T. L. Brown (2000), The retrieval of O_3 profiles from limb scatter measurements: Results from the shuttle ozone limb sounding experiment, *Geophys. Res. Lett.*, *27*(17), 2597–2600.

Mount, G. H., D. W. Rusch, J. F. Noxon, J. M. Zawodny, and C. A. Barth (1984), Measurements of stratospheric NO_2 from the Solar Mesosphere Explorer satellite: 1. An overveiw of the results, *J. Geophys. Res.*, *89*(D1), 1327–1340.

Murtagh, D., et al. (2002), An overview of the Odin atmospheric mission, *Can. J. Phys.*, *80*(4), 309–319.

Nordh, H. L., et al. (2003), The Odin orbital observatory, *Astron. Astrophys.*, *402*(3), L21–L25, doi:10.1051/0004-6361:20030334.

Noxon, J. F. (1975), Nitrogen dioxide in the stratosphere and troposphere measured by ground-based absorption spectroscopy, *Science*, *189*, 547–549.

Noxon, J. F., E. C. Whipple, and R. S. Hyde (1979), Stratospheric NO_2. I. Observational method and behavior at mid-latitude, *J. Geophys. Res.*, *28*(8), 5047–5065.

Oikarinen, L. (2001), Polarization of light in UV-visible limb radiance measurements, *J. Geophys. Res.*, *106*(D2), 1533–1544.

Oikarinen, L., E. Sihova, and E. Kyrölä (1999), Multiple scattering radiance in limb-viewing geometry, *J. Geophys. Res.*, *104*(D24), 31,261–31,274.

Orphal, J. (2003), A critical review of the aborption cross-sections of O_3 and NO_2 in the 240–740 nm region, *J. Photochem. Photobiol. A: Chem.*, *157*(2–3), 185–209, doi:10.1016/S1010-6030(03)00061-3.

Pallamraju, D., J. Baumgardner, and S. Chakrabarti (2000), A mulitwavelength investigation of the Ring effect in the day sky spectrum, *Geophys. Res. Lett.*, *27*(13), 1875–1878.

Perner, D., and U. Platt (1980), Absorption of light in the atmosphere by collision pairs of oxygen $(O_2)_2$, *Geophys. Res. Lett.*, *7*(12), 1053–1056.

Petelina, S. V., et al. (2004), Comparison of the Odin/OSIRIS stratospheric ozone profiles with coincident POAM III and ozonesonde measurements, *Geophys. Res. Lett.*, *31*, L07104, doi:10.1029/2003GL019299.

Pfeilsticker, K., H. Bösch, C. Camy-Peyret, R. Fitzenberger, H. Harder, and H. Osterkamp (2001), First atmospheric profile measurements of UV/visible O_4 absorption band intensities: Implications for the spectroscopy, and the formation enthalpy of the O_2-O_2 dimer, *Geophys. Res. Lett.*, *28*(24), 4595–4598.

Platt, U. (1994), Differential optical absorption spectroscopy (DOAS), in *Air Monitoring by Spectroscopic Techiques*, edited by M. Sigrist, pp. 27–84, John Wiley, Hoboken, N. J.

Platt, U., D. Perner, and H. W. Pätz (1979), Simultaneous measurement of atmospheric CH_2O, O_3 and NO_2 by differential optical absorption, *J. Geophys. Res.*, *84*(10), 6329–6335.

Platt, U., L. Marquad, and T. Wagner (1997), Corrections for zenith scattered light DOAS, *Geophys. Res. Lett.*, *24*(14), 1759–1762.

Pommereau, J. P., and J. Piquard (1994), Ozone and nitrogen dioxide vertical distributions by UV-visible solar occultation from balloons, *Geophys. Res. Lett.*, *21*(13), 1227–1230.

Prather, M., and A. H. Jaffe (1990), Global impact of the Antarctic ozone hole: Chemical propagation, *J. Geophys. Res.*, *95*(D4), 3473–3492.

Rodgers, C. D. (2000), *Inverse Methods for Atmospheric Sounding: Theory and Practice*, 1st ed., World Sci., River Edge, N. J.

Rothman, L. S., et al. (2003), The HITRAN molecular spectroscopic database: Edition of 2000 including updates of 2001, *J. Quant. Spectrosc. Radiat. Transfer*, *82*(1–4), 5–44, doi:10.1016/S0022-4073(03)00146-8.

Rozanov, A. (2001), Modeling of radiative transfer through a spherical planetary atmosphere: Application to atmospheric trace gases retrieval from occultation- and limb-measurements in UV-Vis-NIR, Ph.D. thesis, Inst. of Environ. Phys.–Inst. of Remote Sens., Univ. of Bremen, Bremen, Germany.

Rusch, D. W., G. H. Mount, C. A. Barth, R. J. Thomas, and M. T. Callan (1984), Solar measospheric explorer ultraviolet spectrometer: Measurements of ozone in the 1.0–0.1 mbar region, *J. Geophys. Res.*, *89*(D7), 11,677–11,687.

Russell, J. M., et al. (1993), The Halogen Occultation Experiment, *J. Geophys. Res.*, *98*(D6), 10,777–10,797.

Seftor, C. J., J. C. Larsen, Q. Remund, J. V. Rodriguez, L. E. Flynn, and E. Hilsenrath (2003), The Ozone Mapping and Profiler Suite: Extending the BUV technique to meet future ozone measurement requirements, *Eos Trans. AGU*, *84*(46), Fall Meet. Suppl., F86.

Sioris, C. E., C. von Savigny, R. L. Gattinger, J. C. McConnell, I. C. McDade, E. Griffioen, E. J. Llewellyn, and the ODIN Team (2001), Attitude determination for limb-scanning satellites: The "knee" at 305 nm, *Eos Trans. AGU*, *82*(47), Fall Meet. Suppl., F78.

Sioris, C. E., W. F. J. Evans, R. L. Gattinger, I. C. McDade, D. A. Degenstein, and E. J. Llewellyn (2002), Ground-based Ring-effect measurements with the OSIRIS development model, *Can. J. Phys.*, *80*(4), 483–491.

Sioris, C. E., et al. (2003), Stratospheric profiles of nitrogen dioxide observed by OSIRIS on the Odin satellite, *J. Geophys. Res.*, *108*(D7), 4215, doi:10.1029/2002JD002672.

Solimeno, S., B. Crosignani, and P. D. Porto (1986), *Guiding, Diffraction and Confinement of Optical Radiation*, Academic, San Diego, Calif.

Strong, K., B. Joseph, R. Dosanjh, I. McDade, C. McLinden, J. McConnell, J. Stegman, D. Murtagh, and E. Llewellyn (2002), Retrieval of vertical concentration profiles from OSIRIS UV-visible limb spectra, *Can. J. Phys.*, *80*(4), 409–434.

Stutz, J., and U. Platt (1996), Numerical analysis and estimation of the statistical error of differential optical absorption spectroscopy measurements with least-squares methods, *Appl. Opt.*, *35*(30), 6041–6053.

Vandaele, A., C. Hermans, P. Simon, M. Carleer, R. Colin, S. Fally, M. F. Mérienne, A. Jenouvrier, and B. Coquart (1998), Measurements of the NO_2 absorption cross-section from 42,000 cm^{-1} to 10,000 cm^{-1} (238–1000 nm) at 220 K and 294 K, *J. Quant. Spectrosc. Radiat. Transfer*, *59*(3–5), 171–184.

von Savigny, C., et al. (2003), Stratospheric ozone profiles retrieved from limb scattered sunlight radiance spectra measured by the OSIRIS instrument on the Odin satellite, *Geophys. Res. Lett.*, *30*(14), 1755, doi:10.1029/2002GL016401.

Warshaw, G., D. Desaulniers, and D. Degenstein (1998), Optical design and performance of the Odin UV/visible spectrograph and infrared imager instrument, paper presented at 12th Annual AIAA/USU Conference on Small Satellites, Am. Inst. of Aeronaut. and Astronaut., Logan, Utah.

A. Bazureau and F. Goutail, Service d'Aéronomie, Centre National de la Recherche Scientifique, Reduit de Verrières–BP3, F-91371 Verrières le Buisson Cedex, France. (ariane.bazureau@aerov.jussieu.fr; florence.goutail@aerov.jussieu.fr)

S. M. Brohede, P. Eriksson, and D. P. Murtagh, Department of Radio and Space Science, Chalmers University of Technology, SE-412 96 Göteborg, Sweden. (brohede@rss.chalmers.se; patrick.eriksson@rss.chalmers.se; donal.murtagh@rss.chalmers.se)

E. Griffioen, Juravinski Cancer Centre, 699 Concession Street, Hamilton, Ontario, Canada L8V 5C2. (erik@nimbus.yorku.ca)

C. S. Haley and I. C. McDade, Centre for Research in Earth and Space Science, York University, 4700 Keele Street, Toronto, Ontario, Canada M3J 1P3. (cshaley@yorku.ca; mcdade@yorku.ca)

E. J. Llewellyn, Department of Physics and Engineering Physics, University of Saskatchewan, 116 Science Place, Saskatoon, Saskatchewan, Canada S7N 5E2. (edward.llewellyn@usask.ca)

C. E. Sioris, Atomic and Molecular Physics Division, Harvard-Smithsonian Center for Astrophysics, Cambridge, MA 02138, USA. (csioris@cfa.harvard.edu)

Appendix E

Paper V

Diurnal effects in limb scatter observations

Christopher A. McLinden, Craig S. Haley, and Christopher E. Sioris

J. Geophys. Res.

111, D14302, doi:10.1029/2005JD006628, 2006

JOURNAL OF GEOPHYSICAL RESEARCH, VOL. 111, D14302, doi:10.1029/2005JD006628, 2006

Diurnal effects in limb scatter observations

Chris A. McLinden,[1] Craig S. Haley,[2] and Christopher E. Sioris[3,4]

Received 27 August 2005; revised 21 December 2005; accepted 24 March 2006; published 19 July 2006.

[1] Instruments that measure UV/visible scattered light from the Earth's limb are emerging as an important class of sensors capable of providing high-quality profiles of aerosols and trace gases from the upper troposphere to the mesosphere. Critical to the inversion of limb scatter observations is the forward radiative transfer model. A fast and accurate radiative transfer model, VECTOR (Vector Orders-of-scattering Radiative transfer model), is presented that is able to account for the diurnal variation of species such as NO_2 and BrO along the observing line of sight and the incoming solar beam. VECTOR has been used to quantify for the first time diurnal effect errors in NO_2 and BrO with application to OSIRIS (Optical Spectrograph and Infra-Red Imager System) and SCIAMACHY (Scanning Imaging Absorption Spectrometer for Atmospheric Chartography), two limb viewing satellite instruments. For a solar zenith angle near 90° at the tangent point, errors can exceed 50% for NO_2 and 100% for BrO in the lower stratosphere, with the largest errors generally occurring when viewing across, and at large angles to, the terminator. These results applied to OSIRIS NO_2 and SCIAMACHY BrO reveal that diurnal effect errors are generally small (<10%). Yet 1 out of every 6 OSIRIS NO_2 profiles experiences large (10–35%) errors and 1 out of every 11 SCIAMACHY BrO profiles experiences large (10–100%, or larger) errors in the lower stratosphere.

Citation: McLinden, C. A., C. S. Haley, and C. E. Sioris (2006), Diurnal effects in limb scatter observations, *J. Geophys. Res.*, *111*, D14302, doi:10.1029/2005JD006628.

1. Introduction

[2] The remote sensing technique of limb scanning [*Rusch et al.*, 1983; *McElroy*, 1988] in which profiles of stratospheric and mesospheric constituents are derived from measurements of sunlight scattered from the Earth's limb has recently come of age. In the "limb scatter" technique, a moderate (0.1 to 1 nm) resolution spectrometer is used to measure UV-visible-near IR spectra scattered from the Earth's limb at multiple tangent heights to infer number density profiles of important constituents. It is a method complimentary to solar occultation and may measure continuously as long as there is sufficient scattered sunlight (i.e., daytime only). One of the primary drawbacks of limb scanning is that the inversions require complex radiative transfer models to account for the multiple scattering.

[3] Proof of the recent success of limb scattering can be gleaned by the number of studies appearing in the literature using data from limb scatter satellite instruments such as OSIRIS (Optical Spectrograph and Infra-Red Imager System) [*Llewellyn et al.*, 2004] and SCIAMACHY (Scanning Imaging Absorption Spectrometer for Atmospheric Chartography) [*Bovensmann et al.*, 1999]. These instruments have been successfully retrieving stratospheric profiles of ozone [*von Savigny et al.*, 2003, 2005a; *Palm et al.*, 2005] and NO_2 [*Sioris et al.*, 2003; *Haley et al.*, 2004] for several years, with aerosol [*von Savigny et al.*, 2005b; *McLinden et al.*, 2004], BrO [*Sioris et al.*, 2006], OClO [*Krecl et al.*, 2006], and mesospheric ozone [*Rohen et al.*, 2005] presently on the cusp. Success has also been achieved by space shuttle [*McPeters et al.*, 2000], balloon-borne [*Weidner et al.*, 2005], and aircraft [*McElroy*, 1995] limb scanners. Further, instruments such as OMPS (Ozone Mapping and Profiler Suite), planned for later this decade, will lead the next generation of limb scatter satellite instruments.

[4] Despite the tremendous success of limb scanning some complications remain unresolved. Among them is the issue of how to handle retrievals of species that vary diurnally when the measurement is made near twilight, the period in which large diurnal gradients are encountered. The problem arises as the limb sensor is measuring light that has passed through a range of solar zenith angles (SZAs), and hence sampled species at different points in their diurnal cycle. Yet the inversions schemes, and in particular the radiative transfer models that are required to unravel the multiple scattering, do not account for this and as a result systematic errors may be introduced into the retrieved profile.

[5] Figure 1 illustrates the root source of the problem by showing the diurnal cycle for NO_2 and BrO at 20 km (on 15 June at 0°N) as calculated using a photochemical box model (discussed below). A very rapid change in number density is evident for SZAs of 90 ± 5°. Thus a limb scatter instrument

[1]Environment Canada, Toronto, Ontario, Canada.
[2]Centre for Research in Earth and Space Science, York University, Toronto, Ontario, Canada.
[3]Harvard-Smithsonian Center for Astrophysics, Cambridge, Massachusetts, USA.
[4]Now at Institute of Space and Atmospheric Studies, University of Saskatchewan, Saskatoon, Saskatchewan, Canada.

0148-0227/06/2005JD006628$09.00

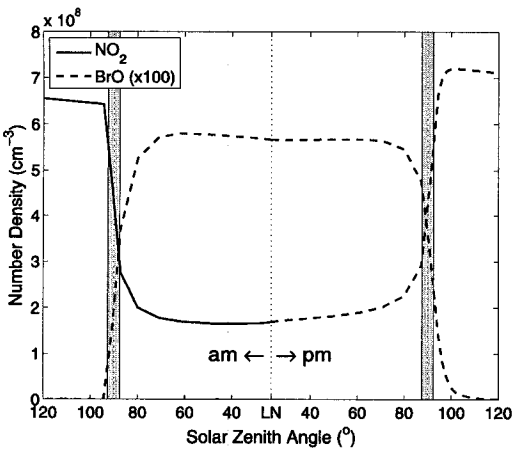

Figure 1. Photochemical box model calculations of the diurnal cycles of NO_2 and BrO at 20 km on 15 June at 0°N. "LN" refers to local noon (SZA = 23.3°). In this plot BrO has been increased by a factor of 100. Dashed vertical lines represent SZAs at LN and 90°. The shaded areas denote the variation in SZA along the line of sight for altitudes within one scale height (taken as 8 km) of the tangent altitude. Shown for observing geometry of SZA = 90° and the change in azimuth is 30° at the tangent point (see section 2 and Figure 3).

sampling over a range of SZAs of just 2 or 3° would be sensing NO_2 varying by a factor of 2 or 3 and BrO varying by an order of magnitude. Detailed discussions of the underlying chemistry driving these diurnal variations can be found in numerous other sources [e.g., *Chartrand et al.*, 1999]. In short, it is the rapid change in the rates of photodissociation during sunrise and sunset that produces these sharp gradients at twilight. For NO_2 it is its own photolysis rate that is important while for BrO, it is the rate at which the nighttime reservoir species photolyze (mainly $BrONO_2$ and HOBr, and BrCl if chlorine is activated). The rate at which the transition of NO_2 and BrO between day and night (or night and day) time levels occurs is accelerated as NO_2, $BrONO_2$, HOBr, and BrCl all photolyze into the visible and so sufficient light to drive photolysis is present in the stratosphere at SZAs near 90°.

[6] While this diurnal effect has been acknowledged as a potential error source [*Sioris et al.*, 2003], to date little quantitative analysis has been carried out. It is the goal of the present study to (1) introduce a new radiative transfer code capable of modeling the diurnal effect and (2) to conduct a preliminary analysis of its effect on retrieved profiles.

2. Description of the Limb Scatter Diurnal Effect

[7] The geometry of limb scattering is shown in Figure 2. The limb radiance measured at the sensor has contributions from all points along the line of sight (LOS) due to scattering into the LOS, with the maximum contribution generally originating near the tangent point where path lengths are the longest and the background density is the largest. (The fact that the optical depths along the LOS may be large enough that the sensor may not "see" down to the tangent point is taken into account by the forward model.) As such the retrieved profile is assigned to the location of the subtangent point. Current limb scatter inversion schemes assume horizontal homogeneity; that is, the properties at a particular altitude are constant over the entire atmospheric region contributing to the measurement. One measure of this, the horizontal distance spanning the altitude range within a scale height of the tangent point, is about 650 km. If a particular constituent does vary then the retrieved

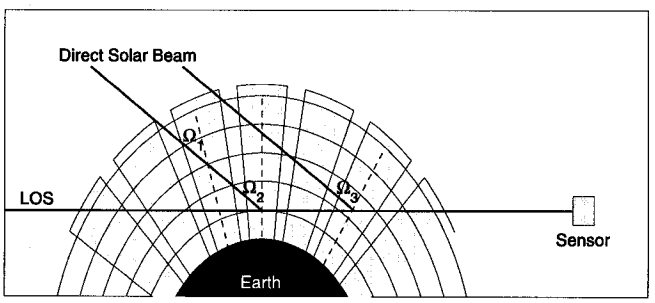

Figure 2. Depiction of limb scatter geometry in a spherical-shell atmosphere. The intersection of the line of sight (LOS) with the shells is divided into a number of sectors, in this example, seven. The shaded sectors each represent the region over which source function vectors from a plane-parallel calculation are used. The solar zenith angle, $\theta_{0,i}$, and change in azimuth angle, $\Delta\phi_i$, pair is denoted by Ω_i, where $\Omega_i = (\theta_{0,i}, \Delta\phi_i)$. As the local SZA is defined relative to the local vertical, it is clear that the SZA changes along the LOS and so $\theta_{0,2} \neq \theta_{0,3}$. While not evident from this figure, dAZ may also vary along the LOS and so $\Delta\phi_2 \neq \Delta\phi_3$. In addition, the local SZA changes along the path of the direct solar beam and so $\theta_{0,1} \neq \theta_{0,2}$. The SZA and dAZ at the tangent point are prescribed, and on the basis of this the local SZA and dAZ along the LOS are calculated. In each sector a different atmosphere and/or surface albedo may be prescribed.

profile will be some complex weighted average of the profiles sampled.

[8] As is evident from Figure 2, the SZA may vary along the LOS. (The change in azimuthal angle between the solar direction and the viewing direction (dAZ) may also vary but this variation is much less important.) This can radically affect the scattering source along the LOS, particularly when the SZA (at the tangent point) is near 90°. Forward models used in limb scatter inversions need to account for this. A second effect of this SZA variation along the LOS is that the profiles of species such as NO_2 and BrO, which vary diurnally, will also vary along the LOS. In this case the assumption of horizontal homogeneity fails to hold automatically, and it fails to hold in a predictable way (at least to the extent the photochemistry may be predicted). Variations of NO_2 and BrO along the LOS have only a small (<1%) impact on the limb radiances, and so this effect is insignificant for retrievals of, e.g., ozone or aerosols. However, it may lead to significant changes in the absorption signals of these species, particularly during twilight where their diurnal gradients are largest. This diurnal variation along the LOS is the first component of the so-called "diurnal effect." The second component is the variation in SZA along the path of the incoming solar beam, also shown in Figure 2. As the solar beam penetrates into the atmosphere, the local SZA increases, and so the profile of NO_2 and BrO it samples also varies. Similar to the LOS component, the diurnal variation of NO_2 and BrO along the direct solar beam is not large enough to significantly alter the incoming transmittance and so it only impacts the absorption signature of diurnally varying species. Taken together these two components constitute the limb scatter diurnal effect.

[9] A quantification of the change in SZA along the LOS and direct solar beam is shown in Figure 3. For the LOS, the range shown represents the difference between the maximum and minimum SZA within one scale height (taken as 8 km) of the tangent point along the LOS. For the direct solar beam, the range is the difference in SZA between the tangent point and one scale height above the tangent point. One scale height is used as this roughly represents the region over which most of the scattered signal is originating. Note that the LOS variation is roughly independent of the SZA at the tangent point (hence it is plotted as a function of dAZ), whereas the variation of SZA along the direct beam is independent of dAZ (and is plotted as a function of SZA at the tangent point). For a SZA of 90° the change in SZA along the direct solar beam is 2.9°, exactly half of the LOS SZA range when dAZ is 0 or 180°. For SZA > 90° the change in SZA along the direct solar beam increases rapidly, with a value of 7.5 for SZA = 93°. The LOS SZA range is clearly a strong function of dAZ with no range in SZA for dAZ = 90° and nearly 6° for dAZ = 0 or 180°. Thus for SZA = 90° and large excursions from 90° in dAZ any limb measurement will be sampling air over a large range of SZAs.

[10] The variation in dAZ along the LOS is much less important for several reasons. For a SZA near 90° this variation is small, a fraction of a degree within a scale height. For high Sun its variation will increase but this is artificial as the radiation field becomes increasingly independent of dAZ for symmetry reasons. Finally, there is no "problematic region" analogous to SZAs near 90°. While its variation is accounted for, it is not discussed further.

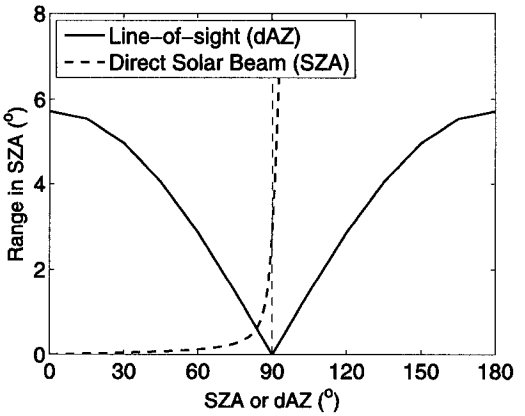

Figure 3. Range in solar zenith angle (SZA) along the line of sight (LOS) and the direct solar beam. The range over the LOS is shown as a function of the change in azimuthal angle between the solar direction and the viewing direction (dAZ) for a SZA of 90° at the tangent point. The range along the direct solar beam is plotted as a function of SZA at the tangent point. In each case the range refers to the altitudes between the tangent point and one scale height (8 km) above the tangent point.

[11] We note that an analogous diurnal effect problem exists for occultation instruments as the solar beam passes through a range of SZAs as it is transmitted through the atmosphere [*Newchurch et al.*, 1996; *Natarajan et al.*, 2005]. The primary difference between the occultation diurnal effect and the limb scatter diurnal effect is that the impact of the limb scatter diurnal effect varies with the SZA and dAZ of the observation (as will become evident below). For occultation, only the range in SZAs sampled may vary (depending on latitude, day of year, and beta angle) and thus its impact will not be as variable. The dependence on viewing geometry, together with the complex paths of multiple-scattered light, make any correction for the limb scatter diurnal effect more complicated.

3. Radiative Transfer Model

[12] In an effort to both quantify diurnal effect errors and account for the diurnal effect as part of the retrieval, a new radiative transfer (RT) model has been developed, VECTOR (Vector Orders-of-scattering Radiative transfer model). VECTOR is based on the RT model of *McLinden et al.* [2002] and has been successfully applied to modeling of the limb radiance and polarization [e.g., *McLinden et al.*, 2004]. Details on its numerics are given by *McLinden et al.* [2002]. VECTOR calculates the limb radiance, including polarization, (or equivalently, the full Stokes vector) in two stages. The first involves multiple plane-parallel solutions and the second is a solution in a spherical shell atmosphere. At each point of intersection of the LOS with the spherical shell atmosphere the local SZA and dAZ are calculated (on the

basis of the prescribed values at the tangent point). A subset of these is selected, shown schematically in Figure 2 as shaded sections. The number of sections, from 1 to 21, is determined on the basis of the SZA at the tangent point and how fast it is varying along the LOS. For each SZA and dAZ section, a solution to the vector radiative transfer equation is obtained in a plane-parallel (PP) atmosphere using the successive orders of scattering solutions technique [e.g., *Hansen and Travis*, 1974]. The resultant Stokes vectors are then used to generate the multiple-scattered source function vectors along the LOS. These, along with the LOS extinction coefficients, are used in the second step in which the vector RT equation is integrated along the LOS through the spherical shell atmosphere to obtain the limb Stokes vector. The width of each PP section decreases closer to the tangent point, and linear interpolation is employed to transition between them. This multiple PP calculation approach to limb RT modeling has been shown to be in good agreement, generally within 2%, with fully spherical limb radiance calculations [*Griffioen and Oikarinen*, 2001].

[13] The unique feature of VECTOR is that for each PP calculation, or section, a different atmosphere and/or surface albedo may be prescribed. Thus a localized aerosol layer or ozone hole can be modeled by specifying it for one or some of the sections. Furthermore, VECTOR has been linked to the University of California, Irvine photochemical box model [*Prather*, 1992; *McLinden et al.*, 2000]. This combination enables species such as NO_2 and BrO to be varied from section to section as predicted by the photochemistry according to the local SZA of the section. Analogous to this, VECTOR also calculates the attenuation of the incoming solar beam according to the species concentrations at the local SZA. In this way both components of the limb scatter diurnal effect are modeled. One caveat to this is when the SZA at the tangent point is very close to local noon. In this case the calculated local SZA along the direct solar beam may be smaller than the local noon SZA and when this occurs the model must use densities at local noon. This problem arises as VECTOR does not account for the change in latitude (and hence the change in SZA at local noon) along the path of the direct solar beam. In this rare circumstance the direct beam diurnal effect will be underestimated.

[14] To eliminate the need for online integrations of the photochemical box model to calculate diurnal cycles, large "climatological" lookup tables have been compiled for NO_2, BrO, OClO, and NO_3 as a function of latitude (2.5° increments), Julian day (two week increments), altitude (2 km increments from 10 to 58 km), and SZA (34 per day, concentrated around twilight). These atmospheres represent an update to those presented by *McLinden et al.* [2002]. Box model input data are obtained from climatologies (O_3, T), three-dimensional model output (N_2O, NO_y), or tracer-tracer correlations (Cl_y, Br_y, CH_4, H_2O). Profiles are taken from the lookup table using the nearest latitude and Julian day and interpolated onto the vertical grid of VECTOR, and to the required local SZA as necessary. Photochemical rate data are taken from the JPL 2002 compendium [*Sander et al.*, 2003].

[15] VECTOR is also able to calculate internal Stokes vectors for arbitrary viewing geometry. Thus a balloon or aircraft instrument could be simulated for limb or nadir viewing, and likewise a ground-based instrument could be simulated. As is the case for the top-of-atmosphere (TOA) limb Stokes vector, these may be calculated with the diurnal effect turned on or off. Additionally, VECTOR is coupled to a line-by-line code (Y. Rochon, personal communication, 2003) with the option for the full numerical calculation of the Voigt line shape or one of several Voigt approximations [e.g., *Humlíček*, 1982]. These features, combined with its low CPU requirements (since VECTOR is essentially a one-dimensional model), make it ideal for use operationally with limb scatter inversions.

4. Diurnal Effect Errors

[16] VECTOR is used to quantify the diurnal effect errors introduced into retrieved profiles. The diurnal effect error, ε (defined below), is a measure of the systematic error introduced into the retrieved profile (at the tangent point) when the retrieval algorithm neglects the diurnal variation of the target species. The procedure to calculate ε is quite straightforward. Noise-free, synthetic spectra are generated with the diurnal effect turned on. These spectra are then used in a limb scatter retrieval code (that does not account for any diurnal variability) and a profile is retrieved. As a consistency check, this procedure is repeated with the diurnal effect turned off in VECTOR to ensure that the retrieved profile is identical to the true profile. The diurnal effect error is simply the relative difference between these two profiles, as follows,

$$\varepsilon(z) = 100 \times [n_{on}(z) - n_{off}(z)]/n_{off}(z)\ [\%] \quad (1)$$

where z is altitude, n_{on} is the number density profile retrieved from the spectra generated with the diurnal effect turned on, and n_{off} is the number density profile from the spectra generated with the diurnal effect turned off. This definition may seem backward but recall the "on" and "off" refer to the forward calculation, not the inversion, and that n_{off} is identical to the true or input profile. In other words: n_{off} represents the truth, n_{on} represents what is retrieved, or "measured," and their difference is the systematic error in the measurement.

[17] In this work diurnal effect errors are assessed for NO_2 and BrO. Some other UV-visible candidate species that may incur diurnal effect errors include OClO, NO_3, and mesospheric O_3.

4.1. NO_2

[18] Synthetic limb spectra between 43–451 nm at tangent heights from 10–48 km are inverted to obtain profiles of NO_2 using the OSIRIS operational retrieval code [*Haley et al.*, 2004]. OSIRIS is a Canadian instrument on board the Odin satellite launched in 2001 into a sun synchronous orbit (an ascending node at 1800 local time (LT)) and measures limb-scattered sunlight between 280 and 800 nm at about 1 nm resolution [*Llewellyn et al.*, 2004]. The retrieval is a two step process involving first a spectral fit to obtain apparent slant column densities (SCDs) and second an inversion of the apparent column densities to number density profiles using optimal estimation [*Haley et al.*, 2004]. An operational algorithm was employed as it should

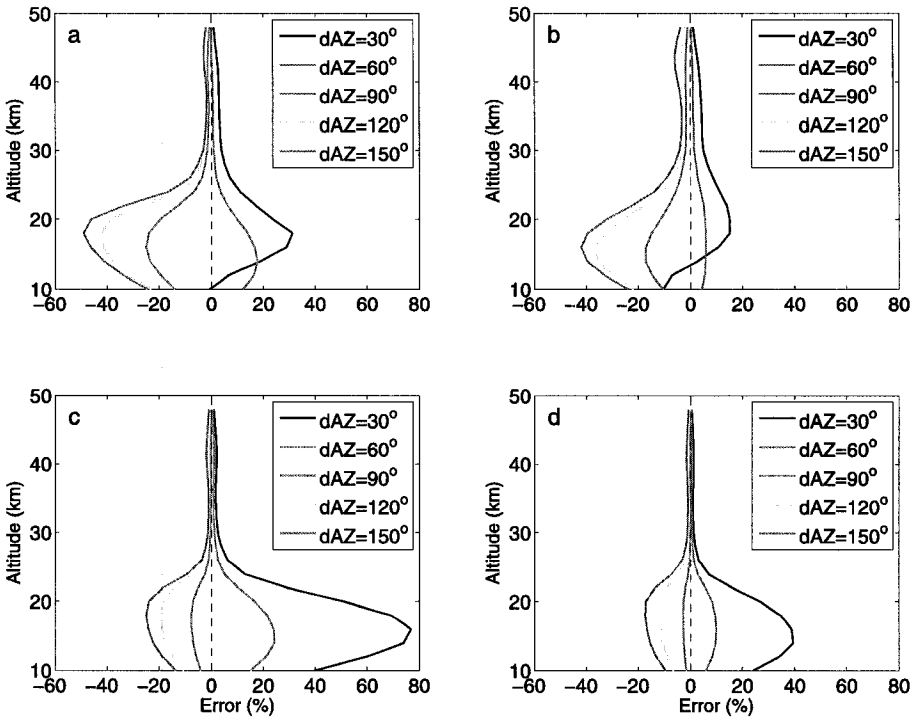

Figure 4. Percent error introduced into retrieved NO_2 profiles by neglecting the diurnal effect. The simulations were performed for 15 June at 0°N at dAZ = 30°, 60°, 90°, 120°, and 150° and (a) SZA = 90°, PM; (b) SZA = 90°, AM; (c) SZA = 87.5°, PM; and (d) SZA = 85°, PM.

more precisely reflect how diurnal effect errors propagate through into OSIRIS profiles. Note that for this work, the retrieval algorithm utilized VECTOR as the forward radiative transfer model (as opposed to LIMBTRAN [*Griffioen and Oikarinen*, 2001]).

[19] One issue that arose when conducting this study was the error level that should be assigned to the synthetic observations. Decreasing the assumed error level led to a small decrease in diurnal error in the middle stratosphere and a substantial increase in the diurnal effect error in the lower stratosphere. This is the result of the retrieval fitting the "observations" too closely in the midstratosphere where the sensitivity is high at the expense of the lower stratosphere where there is a reduced sensitivity. In the end the simulated radiances were prescribed a signal-to-noise ratio (SNR) of 1400 to be consistent with actual OSIRIS observations.

[20] Spectra were simulated for 15 June at 0°N using the following geometries: dAZ = 30°, 60°, 90°, 120°, and 150° for SZAs between 60° and 90° near sunset, or PM. The SZA = 90° case was repeated for sunrise, or AM. The differences between AM or PM simulations arise because of the differences in the diurnal cycle of NO_2 (see Figure 1). The time and location of the simulations were chosen as they are consistent with the time and location when OSIRIS should experience maximum diurnal effect errors. Note that when dAZ > 90° the sensor is on the day side of the tangent point while for dAZ < 90° the sensor is on the night side.

[21] Diurnal effect errors are presented in Figure 4. Key to understanding these results is the interpretation of where the signal is originating. Above 25 km where LOS optical depths are relatively small, there are roughly equal contributions from the near and far side of the tangent point. The smaller errors in the midstratosphere are the result of a weaker diurnal gradient and a degree of cancellation of near and far side errors (which have opposite signs). The small increase in errors near 40 km in Figure 4b, and to a lesser extent in Figure 4a, is due to larger diurnal gradients. Overall, diurnal effect errors above 25 km are small, not exceeding 10%.

[22] Below 20 km the LOS optical depths become large and the signal generally originates from the nearside as light scattered into the LOS on the far side is scattered out before reaching the sensor. One result of this is reduced cancellation of near and far side errors. Furthermore, below 20 km diurnal gradients tend to increase, also promoting larger errors. The overall result of this is a rapid increase in diurnal effect errors below 25 km with a maximum at 14–18 km. The SZA = 90°, PM case (Figure 4a) is considered first. For dAZ = 90° the entire error is driven by the diurnal variation along the incoming solar beam since there is no variation along the LOS. Errors are negative, implying the retrieved

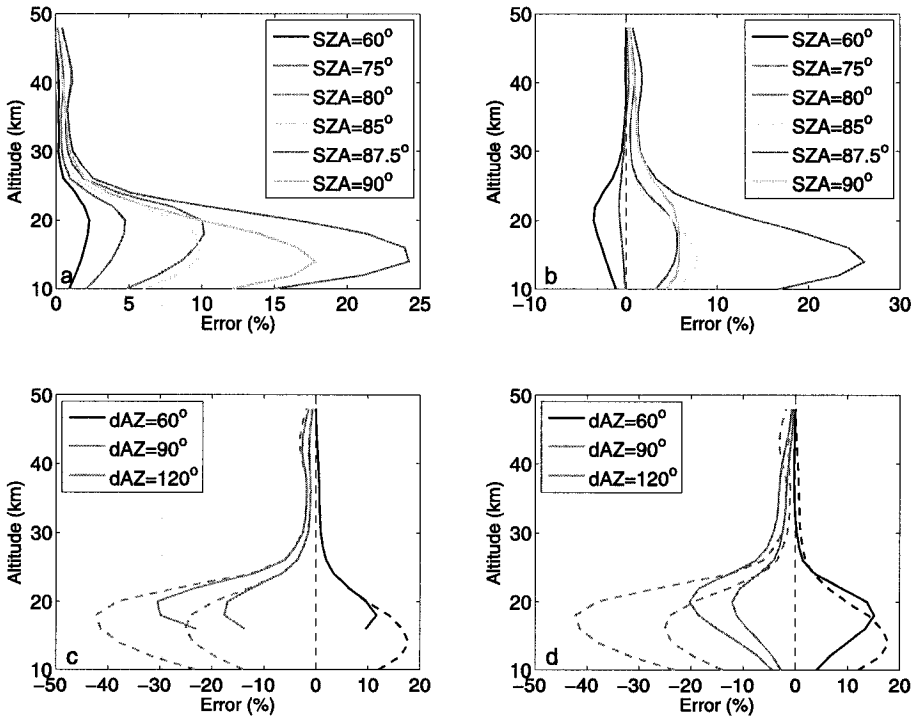

Figure 5. Percent error introduced into retrieved NO_2 profiles by neglecting the diurnal effect. The simulations were performed for 15 June at 0°N (unless stated otherwise). (a) dAZ = 60°, PM, for SZAs from 60 to 90°; (b) dAZ = 60°, AM, for SZAs from 60 to 90°; (c) SZA = 90°, PM for selected dAZs for retrieved down to 10 km (dashed) and 16 km (solid); and (d) SZA = 90°, PM for selected dAZs at a latitude of 60°S (solid) and 0°N (dashed).

profile is underestimated, as the incoming beam samples less NO_2 (as local SZAs are smaller than 90°). As dAZ departs from 90° there is an additional effect from variation along the LOS. When dAZ > 90°, OSIRIS is on the day side and the signal originates primarily on the nearside. These photons traverse smaller NO_2 abundances (since SZA is <90°) and this acts in concert with the direct beam effect and results in even larger underestimates of the NO_2, reaching a maximum of −50% for dAZ = 150°. For dAZ < 90° OSIRIS is on the night side. Since the scattering source is small on the nearside (as SZA > 90°) most of the signal originates near the tangent point and these photons must pass through NO_2 at SZAs larger then 90° and thus acquire a larger NO_2 absorption signature. This overcomes the direct beam effect and NO_2 is overestimated by up to 30% for dAZ = 30°. For a SZA of 90° at sunrise (Figure 4b), diurnal errors display the same general behavior but tend to be 10–20% smaller as diurnal gradients are not as steep.

[23] At a SZA of 87.5° (Figure 4c) the dAZ = 90° error is small as the SZA range being sensed is ~85–87.5°. The situation is similar for dAZ > 90° where NO_2 is being sampled only at SZAs smaller than 87.5° (assuming there is no signal from the far side of the tangent point because of LOS optical depth considerations). However, for dAZ = 30° and 60° the errors are larger than for the analogous SZA = 90° case (Figure 4a), reaching +75%, as SZAs greater than 87.5° are being sampled. Additionally, there is less of a direct beam error component to compensate. Errors are found to be smaller for SZA = 85° (Figure 4d) and are below 10% at SZA = 80° (not shown).

[24] Some additional results are shown in Figure 5. Figure 5a shows the diurnal effect errors for all the SZAs simulated at dAZ = 60°, PM. Maximum errors range from 2% for SZA = 60° to 25% at SZA = 87.5°. Analogous results for dAZ = 60°, AM are shown in Figure 5b with again the largest errors occurring for SZA = 87.5°. Figure 5c explores the impact of increasing the lower altitude limit used in the retrieval from 10 km to 16 km. This led a reduction in errors in the 16–20 km region by up to 5–10%. By removing the "worst" part of the retrieval (<16 km) errors were reduced at the altitudes immediately above as they were not forced as far away from the true answer in order to achieve convergence, which is based on the entire range of tangent heights. Figure 5d examines the difference in error between an observation at the equator and 60°S (on 15 June). Overall errors at 60°S tend to be smaller as local noon occurs at SZA = 80° and this leads to

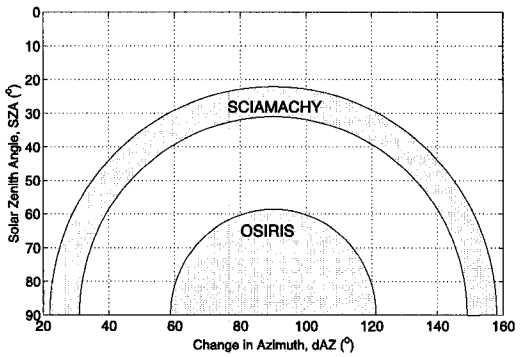

Figure 6. Approximate domain of solar zenith angles (SZAs) and change in azimuths (dAZs) mapped out by OSIRIS and SCIAMACHY over a year, on the basis of their orbits and viewing directions.

smaller differences between day and nighttime values. The situation is not quite this straightforward as the SZA at which diurnal gradients peak may also vary and this may explain why errors are slightly larger at 60°S at some altitudes when the SZA is 90°.

4.2. Application to OSIRIS NO_2

[25] The range of SZA and dAZ swept out by OSIRIS is shown in Figure 6. Extremes in dAZ are 58° and 122° occurring on 21 June in the tropics, when the SZA is near 90° (corresponding to PM and AM, respectively). This represents the worst case and errors can be as large as −35% for dAZ = 120°, SZA = 90° (from Figure 4b) and +25% for dAZ = 60°, SZA = 87.5° (from Figure 4c). On the basis of Figure 2 the range in SZA (within one scale height of the tangent point) along the LOS and the incoming solar beam is about 3° for these cases. Examining all NO_2 profiles from 2004 (obtained from the OSIRIS data server, http://osirus.usask.ca/), 24% were made with a SZA at the tangent point of 86° or larger and 13% were made with a SZA of 88° or larger.

[26] Using the results presented in Figures 4 and 5 the OSIRIS NO_2 profiles were crudely characterized as being subject to "large" (>10%) diurnal effect errors when (1) SZA > 88° or (2) SZA > 86° and dAZ < 75° or dAZ > 105°. A value of 10% was chosen as it is comparable to, but smaller than, the minimum uncertainty in the retrieved profile, 15% [*Haley et al.*, 2004]. On the basis of these criteria and the observation geometry for 2004, of the 55,000 NO_2 profiles about 16% have a diurnal effect error between 10–35%. A summary of this analysis is presented in Table 1. Because of the 1800 LT ascending node, the tropics are always observed at a SZA near 90° and so large errors arise in 30% of all profiles in the tropics. The frequency of profiles with large errors in the extratropics is 10%. Further, occurrences of large errors were more frequent for profiles on the ascending node (the PM side, or LST > 1200) due in part to the gradual precession since 2001 away from a true dusk-dawn orbit.

[27] While a sizable fraction (16%) of all OSIRIS NO_2 profiles in 2004 possess a "large" (10–35%) diurnal effect error, it must be kept in mind this is the maximum and it occurs only below 25 km. Above 25 km the maximum error is <10%. Below 20 km the OSIRIS NO_2 total error estimate is 20–40% [*Haley et al.*, 2004] and so the diurnal effect represents an error source, albeit a systematic one, roughly on par with this 16% of the time. Further, studies such as this enable it to be a predictable error source. Considering all this, our overall characterization of the diurnal effect on OSIRIS NO_2 is that it is a small-to-moderate error source. In the short term it is recommended that retrievals performed at unfavorable geometry be flagged. In the longer term a retrieval algorithm that accounts for the diurnal effect should be implemented.

[28] Any uncertainties in the photochemistry or assumed model profiles (e.g., temperature or ozone) will lead to uncertainties in the diurnal effect error. At this point no attempt is made to quantify them.

4.3. BrO With Application to SCIAMACHY

[29] Diurnal effect errors in BrO are assessed in an analogous fashion, but using the inversion code of *Sioris et al.* [2003] which has most recently been applied to SCIAMACHY limb spectra [*Sioris et al.*, 2006]. SCIAMACHY was launched on the EnviSat platform in March 2002 into a sun-synchronous orbit with a descending node at 1015 LT. SCIAMACHY possesses a 0.2 nm resolution in the BrO fitting region around 350 nm. The *Sioris et al.* [2003, 2006] algorithm is also a two-step process where the first step is spectral fit in the 344–360 window and the second inverts the fitted SCDs using an iterative, Chahine-like procedure. This algorithm also uses the VECTOR model in both forward and inverse calculations and so the retrieved profile is identical to the true profile (with the diurnal effect turned off).

[30] Diurnal effect errors for BrO are presented in Figure 7 on the basis of simulations performed for 15 April at 0°N (unless stated otherwise). The behavior of the diurnal effect error with dAZ is shown in Figure 7a for a SZA of 88°, AM. As with NO_2, errors tend to be small (<5%) above 25 km and increase rapidly below 20 km. Errors are at a minimum for dAZ = 90°, and with a sign opposite to that observed for NO_2. This is because BrO increases with decreasing SZA (see Figure 1) and thus there is additional absorption along the incoming beam, not accounted for in the inversion, resulting in an overestimate of the profile. Moving away

Table 1. Summary of OSIRIS NO_2 Profiles for 2004[a]

	All	LST < 1200	LST > 2400
Total profiles	54,818	34,253	20,565
% of total	100	62.5	37.5
Fraction Subject to Large Diurnal Effect Errors, %			
Globe	16.1	13.5	20.5
Tropics	29.4	23.6	51.9
Extratropics	9.8	7.0	13.2
Fraction of Total Profiles With Large Errors, %			
Globe	100	52.3	47.7
Tropics	58.9	36.1	22.8
Extratropics	41.1	16.2	24.9

[a]The definition of "large" diurnal effect errors is given in the text. LST, local standard time.

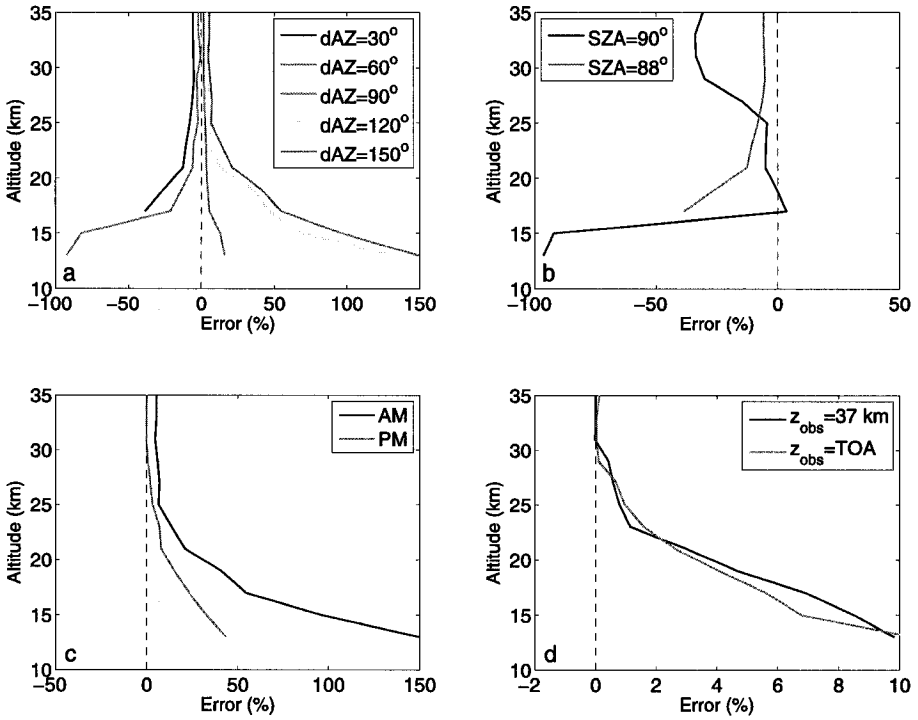

Figure 7. Percent error introduced into retrieved BrO profiles by neglecting the diurnal effect. The simulations were performed for 1 April at 0°N (unless stated otherwise). (a) SZA = 88°, AM, for multiple values of dAZ (see text for explanation on dAZ = 30° error profile); (b) dAZ = 30°, AM and SZA = 88° and 90°; (c) SZA = 88°, dAZ = 150° for AM and PM; and (d) SZA = 89°, dAZ = 90°, PM, at 45°N for observing altitudes at 37 km and TOA (top-of-atmosphere, for a satellite instrument).

from dAZ = 90° leads to larger errors due to the LOS component, again with signs opposite that of NO_2. At and below 15 km errors reached 100–150%. For dAZ = 30° diurnal effect errors initially led to number densities that were a factor of 20–30 too small below 15 km. This is due to the extremely rapid formation of BrO at sunrise in the lower stratosphere, as indicated by Figure 1. This inversion was repeated using a lower altitude limit of 17 km and this result is shown in Figure 7a. This result suggests that restrictions should be placed on inversions of BrO for this extreme geometry.

[31] A comparison of dAZ = 30° errors at a SZA of 88°, AM and 90°, AM is shown in Figure 7b. The SZA = 90° error curve has a peculiar shape with large negative errors at 30 km. This result, which underscores the complexity of the real world, is thought to be a result of a radical change in the shape of the BrO profile between a SZA of 94° and 90° (the altitude of BrO peak decreases from 41 km to 25 km). With the diurnal variation on the simulated measurements will have sampled both shape regimes, but the inversion will converge on a solution that is some average shape. The AM-PM difference is explored in Figure 7c. Errors are roughly a factor of three smaller in the PM case (for SZA = 88° and dAZ = 150°). This is the result of a much smaller diurnal gradient as is evident from Figure 1. Figure 7d compares diurnal effect errors for a sensor in space and at an altitude of 37 km, as would be appropriate for a balloon-borne sensor. Errors tend to be very similar. In fact, as long as the sensor is above the bulk of the absorber and scattering source there should be little difference in the error for an internal sensor and one in space. As such most of these results should be transferable to balloon-borne instruments and suggest that dAZ of 90° be used to minimize diurnal effect errors. For an aircraft instrument (which would be at a lower altitude) or a sensor that uses observations made at positive elevation angles (i.e., looking above the local horizon) this is not necessarily true. These cases would require their own assessment.

[32] Figure 6 also shows the SZAs and dAZs swept out by SCIAMACHY. The majority of SCIAMACHY limb observations are made for high Sun where diurnal effect errors are minimal. However, twice each orbit, near the northern most and southern points, the SZA passes through 90° as SCIAMACHY crosses the terminator and dAZ takes on values of 27 ± 4° and 153 ± 4°, respectively. However, because of the ~7.5° latitudinal sampling and time sharing between limb, nadir, and occultation observing modes, SCIAMACHY does not always obtain a limb scan near a

SZA of 90°. Several SCIAMACHY orbits have been examined throughout a year and about 9% (about 1 in 11) of all limb observations are made for SZAs between 86° and 90°. As for OSIRIS, this range of SZAs is used to crudely characterize errors as being "large." More work is required to comprehensively characterize BrO diurnal effect errors but on the basis of Figure 7 it is clear that values as large as 100% at 15 km will not be uncommon. The density of BrO in the 14–18 km layer is of particular interest since it is critical for quantifying the levels of inorganic bromine source gases entering the stratosphere [*Salawitch et al.*, 2005; *Sioris et al.*, 2006].

[33] Finally, we comment briefly on expected diurnal effect errors in SCIAMACHY NO_2, on the basis of the results from Figure 4. Maximum errors are between −50% (SZA = 90°, dAZ = 150°, PM) and +20% (SZA = 90°, dAZ = 30°, AM), slightly worse than for OSIRIS. A more thorough evaluation would require using the SCIAMACHY retrieval algorithm and limb radiance SNR.

5. Conclusions

[34] As the role of limb scatter instruments increases it becomes vital that systematic errors be identified and quantified. One such source of error is the limb scatter diurnal effect affecting species that vary diurnally and arising from a changing solar zenith angle along the observing line of sight and incoming solar beam. A new radiative transfer model, VECTOR (Vector Orders-of-scattering Radiative transfer model), has been developed that is able to simulate the diurnal effect in NO_2, BrO, and other diurnally varying species. Using synthetic spectra from VECTOR an initial analysis of diurnal effect errors has been conducted. Errors, even in the worst case, are small in the mid to upper stratosphere. In the lower stratosphere errors can reach 60% when the SZA is near 90° and the change in azimuth departs significantly from 90°.

[35] On the basis of these results the implications for OSIRIS NO_2 and SCIAMACHY BrO were assessed. In the worst case errors of up to 35% in OSIRIS NO_2 are possible and it is estimated that 16% of all NO_2 profiles experience a diurnal effect error in excess of 10%. Errors for SCIAMACHY BrO, while less frequent, were found to sometimes exceed 100%, and, in the worst case, a solution may not even be possible over the entire retrieval range. These results also serve as a guide for future limb scatter missions to minimize, or at least quantify beforehand, potential diurnal effect errors.

[36] This study does not solve the greater problem of how to remove the diurnal effect errors from profiles (assuming it should be removed as any such process will surely be model-dependent). It does, however, represent an important first step in this process by identifying when diurnal effect errors will be problematic. Further, it provides a guide as to their sign and magnitude. In the case of NO_2, an algorithm to remove diurnal effects might use the simultaneously measured ozone profile (as most limb scatter instruments also measure ozone) and a temperature profile from reanalysis as input into a photochemical model to obtain the actual NO_2 diurnal cycle. *Newchurch et al.* [1996] concluded that knowledge of ozone and temperature is sufficient to accurately capture the NO_2 diurnal cycle. Such an algorithm would then be used to retrieve the profile at the subtangent point. BrO is more complicated as capturing its diurnal cycle requires additional information (such as total reactive nitrogen which could be constrained by NO_2) but the principle is the same. There is also potential application to other diurnally varying species such as OClO and mesospheric O_3.

[37] **Acknowledgments.** The authors thank the anonymous referees for their helpful comments. This work is supported by the Natural Sciences and Engineering Research Council (Canada) and the Canadian Space Agency. Odin is a Swedish-led satellite project funded jointly by Sweden (SNSB), Canada (CSA), France (CNES) and Finland (Tekes). OSIRIS level 2 data products may be downloaded from the OSIRIS web server at http://osirus.usask.ca/.

References

Bovensmann, H., et al. (1999), SCIAMACHY: Mission objectives and measurement modes, *J. Atmos. Sci.*, *56*, 127–150.

Chartrand, D. J., J. de Grandpré, and J. C. McConnell (1999), An introduction into atmospheric chemistry, *Atmos. Ocean*, *37*, 309–367.

Griffioen, E., and L. Oikarinen (2001), LIMBTRAN: A pseudo-three dimensional radiative transfer model for the limb-viewing imager OSIRIS on the ODIN satellite, *J. Geophys. Res.*, *105*, 29,717–29,730.

Haley, C. S., S. M. Brohede, C. E. Sioris, E. Griffioen, D. P. Murtagh, I. C. McDade, P. Eriksson, E. J. Llewellyn, A. Bazureau, and F. Goutail (2004), Retrieval of stratospheric O_3 and NO_2 profiles from Odin/OSIRIS limb-scattered sunlight measurements, *J. Geophys. Res.*, *109*, D16303, doi:10.1029/2004JD004588.

Hansen, J. E., and L. D. Travis (1974), Light scattering in planetary atmospheres, *Space Sci. Rev.*, *16*, 527–610.

Humlíček, J. (1982), Optimized computation of the voigt and complex probability functions, *J. Quant. Spectrosc. Radiat. Trans.*, *27*, 434–437.

Krecl, P., C. S. Haley, J. Stegman, S. M. Brohede, and G. Berthet (2006), Retrieving the vertical distribution of stratospheric OClO from Odin/OSIRIS limb-scattered sunlight measurements, *Atmos. Chem. Phys.*, *6*, 1879–1894.

Llewellyn, E. J., et al. (2004), The OSIRIS instrument on the Odin satellite, *Can. J. Phys.*, *82*, 411–422.

McElroy, C. T. (1988), Stratospheric nitrogen dioxide concentrations as determined from limb brightness measurements made on June 17th, 1983, *J. Geophys. Res.*, *93*, 7075–7083.

McElroy, C. T. (1995), A spectroradiometer for the measurement of direct and scattered solar irradiance from on board the NASA ER-2 high-altitude research aircraft, *Geophys. Res. Lett.*, *22*, 1361–1364.

McLinden, C. A., S. Olsen, B. Hannegan, O. Wild, M. J. Prather, and J. Sundet (2000), Stratospheric ozone in 3-D models: A simple chemistry and the cross-tropopause flux, *J. Geophys. Res.*, *105*, 14,653–14,665.

McLinden, C. A., J. C. McConnell, E. Griffioen, and C. T. McElroy (2002), A vector radiative transfer model for the Odin/OSIRIS project, *Can. J. Phys.*, *80*, 375–393.

McLinden, C. A., C. S. Haley, and E. J. Llewellyn (2004), Derivation of polarization from Odin/OSIRIS limb spectra, *Geophys. Res. Lett.*, *31*, L20112, doi:10.1029/2004GL020825.

McPeters, R. D., S. J. Janz, E. Hilsenrath, T. L. Brown, D. E. Flittner, and D. F. Heath (2000), The retrieval of ozone profiles from limb scatter measurements: Results from the Shuttle Ozone Limb Sounding Experiment, *Geophys. Res. Lett.*, *27*, 2597–2600.

Natarajan, M., L. E. Deaver, E. Thompson, and B. Magill (2005), Impact of twilight gradients on the retrieval of mesospheric ozone from HALOE, *J. Geophys. Res.*, *110*, D13305, doi:10.1029/2004JD005719.

Newchurch, M. J., et al. (1996), Stratospheric NO and NO_2 abundances from ATMOS solar-occultation measurements, *Geophys. Res. Lett.*, *23*, 2373–2376.

Palm, M., C. von Savigny, T. Warneke, V. Velazco, J. Notholt, K. Künzi, J. Burrows, and O. Schrems (2005), Intercomparison of O_3 profiles observed by SCIAMACHY and ground based microwave instruments, *Atmos. Chem. Phys.*, *5*, 2091–2098.

Prather, M. J. (1992), Catastrophic loss of stratospheric ozone in dense volcanic clouds, *J. Geophys. Res.*, *97*, 10,187–10,191.

Rohen, G. J., C. von Savigny, E. J. Llewellyn, J. W. Kaiser, K.-U. Eichmann, A. Bracher, H. Bovensmann, and J. P. Burrows (2005), First results of ozone profiles between 35 and 65 km retrieved from SCIAMACHY limb spectra and observations of ozone depletion during the solar proton event in Oct./Nov. 2003, *Adv. Space Res.*, doi:10.1016/j.asr.2005.03.160, in press.

Rusch, D. W., G. H. Mount, C. A. Barth, G. J. Rottman, R. J. Thomas, G. E. Thomas, R. W. Sanders, G. M. Lawrence, and R. S. Eckman (1983), Ozone densities in the lower mesosphere measured by a limb scanning ultraviolet spectrometer, *Geophys. Res. Lett.*, *10*, 241–244.

Salawitch, R. J., C. E. Sioris, D. K. Weisenstein, P. O. Wennberg, L. J. Kovalenko, K. Chance, M. K. W. Ko, and C. A. McLinden (2005), Sensitivity of ozone to bromine in the lower stratosphere, *Geophys. Res. Lett.*, *32*, L05811, doi:10.1029/2004GL021504.

Sander, S. P., et al. (2003), Chemical kinetics and photochemical data for use in stratospheric modeling, *Eval. 14, JPL Publ. 02-025*, Jet Propul. Lab., Pasadena, Calif.

Sioris, C. E., et al. (2003), Stratospheric profiles of nitrogen dioxide observed by Optical Spectrograph and Infrared Imager System on the Odin satellite, *J. Geophys. Res.*, *108*(D7), 4215, doi:10.1029/2002JD002672.

Sioris, C. E., et al. (2006), Latitudinal and vertical distribution of bromine monoxide in the lower stratosphere from SCIAMACHY limb scattering measurements, *J. Geophys. Res.*, *111*, D14301, doi:10.1029/2005JD006479.

von Savigny, C., et al. (2003), Stratospheric ozone profiles retrieved from limb scattered sunlight radiance spectra measured by the OSIRIS instrument on the Odin satellite, *Geophys. Res. Lett.*, *30*(14), 1755, doi:10.1029/2002GL016401.

von Savigny, C., A. Rozanov, H. Bovensmann, K.-U. Eichmann, S. Noël, V. Rozanov, B.-M. Sinnhuber, M. Weber, J. P. Burrows, and J. W. Kaiser (2005a), The ozone hole breakup in September 2002 as seen by SCIAMACHY on ENVISAT, *J. Atmos. Sci.*, *62*, 721–734.

von Savigny, C., S. V. Petelina, B. Karlsson, E. J. Llewellyn, D. A. Degenstein, N. D. Lloyd, and J. P. Burrows (2005b), Vertical variation of NLC particle sizes retrieved from Odin/OSIRIS limb scattering observations, *Geophys. Res. Lett.*, *32*, L07806, doi:10.1029/2004GL021982.

Weidner, F., et al. (2005), Balloon-borne limb profiling of UV/vis skylight radiances, O_3, NO_2, and BrO: Technical set-up and validation of the method, *Atmos. Chem. Phys.*, *5*, 1409–1422.

C. S. Haley, Centre for Research in Earth and Space Science, York University, Toronto, ON, Canada M3J 1P3.

C. A. McLinden, Environment Canada, Toronto, ON, Canada M3H 5T4. (chris.mclinden@ec.gc.ca)

C. E. Sioris, Institute of Space and Atmospheric Studies, University of Saskatchewan, Saskatoon, SK, Canada S7N 5E2.

Appendix F

Paper VI

Validation of Odin/OSIRIS stratospheric NO_2 profiles

Samuel M. Brohede, Craig S. Haley, Chris A. McLinden, Christopher E. Sioris, Donal P. Murtagh, Svetlana V. Petelina, Edward J. Llewellyn, Ariane Bazureau, Florence Goutail, Cora E. Randall, Jerry D. Lumpe, Ghassan Taha, Larry W. Thomasson, and Larry L. Gordley

J. Geophys. Res.

112, D07310, doi:10.1029/2006JD007586, 2007

JOURNAL OF GEOPHYSICAL RESEARCH, VOL. 112, D07310, doi:10.1029/2006JD007586, 2007

Validation of Odin/OSIRIS stratospheric NO_2 profiles

Samuel M. Brohede,[1] Craig S. Haley,[2] Chris A. McLinden,[3] Christopher E. Sioris,[3,4] Donal P. Murtagh,[1] Svetlana V. Petelina,[4] Edward J. Llewellyn,[4] Ariane Bazureau,[5] Florence Goutail,[5] Cora E. Randall,[6] Jerry D. Lumpe,[7] Ghassan Taha,[8] Larry W. Thomasson,[9] and Larry L. Gordley[10]

Received 31 May 2006; revised 25 October 2006; accepted 20 November 2006; published 12 April 2007.

[1] This paper presents the validation study of stratospheric NO_2 profiles retrieved from Odin/OSIRIS measurements of limb-scattered sunlight (version 2.4). The Optical Spectrograph and Infrared Imager System (OSIRIS) NO_2 data set is compared to coincident solar occultation measurements by the Halogen Occultation Experiment (HALOE), Stratospheric Aerosol and Gas Experiment (SAGE) II, SAGE III, and Polar Ozone and Aerosol Measurement (POAM) III during the 2002–2004 period. Comparisons with seven Systeme d'Analyse par Observation Zenithal (SAOZ) balloon measurements are also presented. All comparisons show good agreement, with differences, both random and systematic, of less than 20% between 25 km and 35 km. Inconsistencies with SAGE III below 25 km are found to be caused primarily by diurnal effects from varying NO_2 concentrations along the SAGE III line-of-sight. On the basis of the differences, the OSIRIS random uncertainty is estimated to be 16% between 15 km and 25 km, 6% between 25 km and 35 km, and 9% between 35 km and 40 km. The estimated systematic uncertainty is about 22% between 15 and 25 km, 11–21% between 25 km and 35 km, and 11–31% between 35 km and 40 km. The uncertainties for AM (sunrise) profiles are generally largest and systematic deviations are found to be larger at equatorial latitudes. The results of this validation study show that the OSIRIS NO_2 profiles are well behaved, with reasonable uncertainty estimates between 15 km and 40 km. This unique NO_2 data set, with more than hemispheric coverage and high vertical resolution will be of particular interest for studies of nitrogen chemistry in the middle atmosphere, which is closely linked to ozone depletion.

Citation: Brohede, S. M., et al. (2007), Validation of Odin/OSIRIS stratospheric NO_2 profiles, *J. Geophys. Res.*, *112*, D07310, doi:10.1029/2006JD007586.

1. Introduction

[2] A number of satellite instruments have been launched recently that measure limb-scattered sunlight radiances with the goal of deriving vertical profiles of stratospheric minor species. These instruments include OSIRIS (Optical Spectrograph and Infrared Imager System) on the Odin satellite [*Warshaw et al.*, 1998; *Llewellyn et al.*, 2004] and SCIAMACHY (Scanning Imaging Absorption Spectrometer for Atmospheric Chartography) on Envisat [*Bovensmann et al.*, 1999]. GOMOS (Global Ozone Measurement by Occultation of Stars) on Envisat [*Bertaux et al.*, 1991] and SAGE (Stratospheric Aerosol and Gas Experiment) III on the Meteor-3M spacecraft [*McCormick et al.*, 1991] are primarily occultation instruments that also have limb-scatter measurement capabilities.

[3] The interest in the limb-scatter technique lies in a demand for atmospheric information with both global coverage and relatively high vertical resolution. The traditional sources of global stratospheric minor species information have largely been limited to either poor or no vertical information (nadir mapping instruments) or restricted spatial coverage (solar occultation instruments). The advantage of the limb-scatter technique is the provision of vertical profiles of stratospheric and mesospheric minor constituents with high vertical resolution (1–3 km) and near global coverage. A limitation to the technique is that only the measurements from the sunlit portion of each orbit can be utilized (i.e., daytime only). Passive emission instruments

[1]Department of Radio and Space Science, Chalmers University of Technology, Göteborg, Sweden.
[2]Centre for Research in Earth and Space Science, York University, Toronto, Ontario, Canada.
[3]Environment Canada, Toronto, Ontario, Canada.
[4]Department of Physics and Engineering Physics, University of Saskatchewan, Saskatoon, Saskatchewan, Canada.
[5]Service d'Aéronomie, Centre National de la Recherche Scientifique, Verrières le Buisson, France.
[6]Laboratory for Atmospheric and Space Physics and Department of Atmospheric and Oceanic Science, University of Colorado, Boulder, USA.
[7]Computational Physics Inc., Springfield, Virginia, USA.
[8]Science Systems and Applications Inc., Lanham, Maryland, USA.
[9]NASA Langley Research Center, Hampton, Virginia, USA.
[10]GATS Inc., Newport News, Virginia, USA.

0148-0227/07/2006JD007586$09.00

provide similar benefits as the limb-scatter technique and are not limited to measuring the sunlit atmosphere. The Michelson Interferometer for Passive Atmospheric Sounding (MIPAS) on Envisat [*Fischer and Oelhaf*, 1996] provides NO_2 profiles with a vertical resolution of about 4 km, but the retrievals require extensive non-LTE (Local Thermodynamic Equilibrium) calculations [*Funke et al.*, 2005].

[4] *Haley et al.* [2004] describe how NO_2 and O_3 can be successfully retrieved from OSIRIS limb-scatter measurements in the stratosphere using a combination of Differential Optical Absorption Spectroscopy (DOAS) [*Platt*, 1994] and Optimal Estimation (OE) [*Rodgers*, 2000]. OSIRIS provides a unique data set of NO_2 with a slightly more than hemispheric coverage and a vertical resolution of about 2 km between 15 and 40 km. A detailed error analysis was carried out by *Haley et al.* [2004] and the major sources of uncertainty were identified as pointing offset (tangent height registration), aerosols and cloud and concluded that the OSIRIS NO_2 profiles have an accuracy of 10% at the peak of the profiles.

[5] The purpose of this study is to validate the OSIRIS NO_2 product (version 2.4) and determine the systematic and random uncertainties. Four solar occultation instruments, HALOE (Halogen Occultation Experiment), POAM (Polar Ozone and Aerosol Measurement) III, SAGE (Stratospheric Aerosol and Gas Experiment) II, and SAGE III, are used for comparisons with coincident OSIRIS NO_2 measurements from 2002 to 2004. OSIRIS NO_2 profiles are also compared with SAOZ (Systeme d'Analyse par Observation Zenithale) balloon instrument measurements. Stratospheric NO_2 is an important species to measure because it is part of the NO_x chemistry, which is closely linked to ozone depletion; see section 2.

[6] Section 2 gives a brief description of nitrogen chemistry in the stratosphere and is followed by a brief overview of each instrument in section 3 and a short description of the OSIRIS retrieval process in section 4. Thereafter the validation process is described (section 5) and the results are presented (section 6). An analysis of the results is presented in section 7, followed by major conclusions and suggested future work in section 8.

2. Stratospheric NO_x Chemistry

[7] This section gives a brief introduction to stratospheric NO_x chemistry based on *Brasseur and Solomon* [1986] and references therein. The term NO_x refers to the sum of NO and NO_2 and is used due to the strong interaction between these species according to reactions (1) to (3) below. The term NO_y is reserved for all reactive nitrogen oxides, including NO, N_2O, NO_2, NO_3, N_2O_5, and HNO_3.

$$NO_2 + h\nu \rightarrow NO + O \quad (1)$$

$$NO_2 + O \rightarrow NO + O_2 \quad (2)$$

$$NO + O_3 \rightarrow NO_2 + O_2 \quad (3)$$

[8] The lifetime of NO_x is too short for it to cross the tropopause barrier in any significant amount, and the dominant sources of NO_x in the stratosphere are rather the more inert N_2O crossing the tropopause and to a small extent the polar winter descent of NO_y created by auroral processes.

[9] NO_x species are photochemically active, and the availability of solar radiation determines the relative abundance of NO and NO_2 as seen in reaction (1). During daytime conditions, the NO_x equilibrium is pushed toward NO. As the Sun sets the NO_2 concentration rapidly increases at the cost of NO (see Figure 1). In the nighttime chemistry an additional, but slower, processes take place, converting NO_x into NO_y:

$$NO_2 + O_3 \rightarrow NO_3 + O_2 \quad (4)$$

$$NO_2 + NO_3 + M \rightarrow N_2O_5 + M \quad (5)$$

The NO_3 and N_2O_5 are photolyzed during the daytime, creating NO_x again. The NO_3 concentration drops rapidly at sunrise, while N_2O_5 is more slowly photolyzed at stratospheric temperatures, which explains the positive NO_2 gradient during the day in Figure 1.

[10] NO_x chemistry is crucial to many stratospheric processes, including ozone depletion. Ozone (odd oxygen) is catalytically destroyed through the reaction cycle (2) and (3). In fact, photochemical loss of O_3 is dominated by NO_x between 25 km and 40 km altitude [*Dessler*, 2000]. In addition, NO_x is an important factor in the formation of reservoir species and in the creation of HNO_3-rich PSC (Polar Stratospheric Cloud) particles. The most important sink of stratospheric nitrogen inside the polar vortex is deposition of these particles to the troposphere (denitrification).

3. Instrument Descriptions

[11] Brief descriptions of the satellite orbit, instrument parameters, NO_2 retrieval method, and error estimation for each of the instruments are found below. An overview of the important parameters is found in Table 1. The viewing geometries of solar occultation and solar scattering instruments are illustrated in Figure 2.

3.1. OSIRIS Instrument

[12] The Optical Spectrograph and Infrared Imager System [*Llewellyn et al.*, 2004] is one of two instruments on board the Odin satellite [*Nordh et al.*, 2003]. Odin was launched in February 2001 into a 600 km circular Sun-synchronous near-terminator orbit with a 97.8° inclination and the ascending node at 1800 hours LST (Local Solar Time). Odin is a combination of astronomy and aeronomy missions with equal time disposition. OSIRIS is dedicated to aeronomy studies [*Murtagh et al.*, 2002] and a second instrument, the Submillimeter and Millimeter Radiometer (SMR) [*Frisk et al.*, 2003] carries out both aeronomy and astronomy studies. The instruments are coaligned and scan the limb of the atmosphere over a tangent height range 7 km to 70 km in approximately 85 seconds during normal stratospheric operations through controlled nodding of the satellite. Every 8th day in general and every 1–3 days

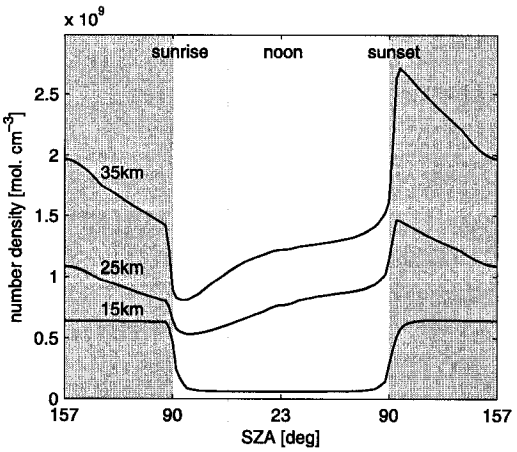

Figure 1. NO_2 concentrations as a function of solar zenith angle (SZA) and altitude based on simulations from the PRATMO chemical box model [*Prather*, 1992; *McLinden et al.*, 2000] for equatorial conditions (June, albedo = 0). The NO_2 concentration drops rapidly at sunrise due to photolyzation and increases similarly at sunset as NO_2 reforms from NO reacting with ozone (reaction (3)).

during the northern hemisphere summer, the scans are extended up to 100 km to cover the entire mesosphere.

[13] OSIRIS contains two optically independent components, the Optical Spectrograph (OS) and the Infrared Imager (IRI). The OS is a grating spectrometer that measures limb-scattered sunlight spectra in the spectral range 280 nm to 800 nm at a resolution of about 1 nm at tangent height intervals of roughly 2 km. The IRI is a three channel camera, imaging the atmospheric airglow emissions near 1.27 μm and 1.53 μm in a limb-viewing tomographic mode [*Degenstein et al.*, 2002]. The OS scattered sunlight measurements are used to provide vertical profiles of minor stratospheric constituents including O_3, NO_2, BrO, OClO, and aerosol, and are the focus of this study.

[14] The instantaneous field of view (FOV) of the OS is 1 km in the vertical and 40 km in the horizontal at the tangent point. When the nodding of the spacecraft and the varying exposure time of the OS ($\sim$0.01 s at 10 km increasing to $\sim$2 s at 50 km) are considered, the vertical resolution of the measured limb radiances is found to range from approximately 1 km at 10 km to 2 km at 50 km.

[15] The retrieval of NO_2 profiles from OSIRIS (version 2.4 data product) is discussed in section 4. Full global coverage of the OSIRIS NO_2 data is achieved around the equinoxes and hemispheric coverage is obtained during the rest of the year, as seen in Figure 3 (top). Data gaps are mainly due to Odin being in astronomy mode.

3.2. HALOE Instrument

[16] The Halogen Occultation Experiment [*Russell et al.*, 1993] was launched on the Upper Atmosphere Research Satellite (UARS) in September 1991 into a precessing 585 km altitude and 57° inclination orbit.

[17] HALOE is a solar occultation instrument with four radiometer channels and four dual radiometer/gas-filter correlation channels. It views the atmosphere in transmission with 15 sunrises and 15 sunsets per day. The occultation events occur in daily latitude bands, covering all latitudes between from 80°S and 80°N in approximately 36 days (see Figure 3). Vertical profiles of temperature, O_3, HCl, HF, CH_4, H_2O, NO, and NO_2 are retrieved from the measurements.

[18] The radiometer channels at 1015, 1510, and 1600 cm^{-1} are used for the NO_2 retrievals. Profiles are calculated with a modified onion-peeling approach using the High-Resolution Transmission (HITRAN) molecular absorption database (www.hitran.com). Interfering species include H_2O and CH_4 (both retrieved using separate channels) and O_2 (known). Extrapolated aerosol extinctions from the 1900 cm^{-1} vacuum-path channel are used to compensate for Mie scattering. NO_2 number densities are retrieved over the altitude range 10–50 km at a vertical resolution of 2 km and are reported at 300 m intervals. NO_2 gradients along the line of sight (LOS) are present due to the NO_x diurnal photochemistry discussed in section 2. This is compensated for in the HALOE retrievals by introducing a solar zenith angle (SZA) parameter in the forward model. The retrieved profile is then consistent with the atmospheric state at the subtangent point (STP); see Figure 2. The HALOE version 19 data product is used in this study.

Table 1. Summary of the Specifications of the Satellite Instruments in This Study[a]

Specification	OSIRIS	SAGE II	SAGE III	POAM III	HALOE
Geometry	solar scat.	solar occ.	solar/lunar occ.	solar occ.	solar occ.
Meas. type	full spectr.	7 channels	full spectr.	9 channels	4 rad.+4 gas corr.
Satellite	Odin	ERBS	Meteor-3M	SPOT-4	UARS
Launch	Feb 2001	Oct 1984	Dec 2001	Mar 1998	Sep 1991
Orbit type	sun synchr.	precessing	sun synchr.	sun synchr.	precessing
Eq. cross. time	18:00	-	09:00	22:30	-
NO_2 data					
Version	2.4	6.20	3	4	19
Alt. range, km	10–46	15–60	10–50	20–45	10–50
Sampling, km	2	0.5	0.5	1	0.3
Res.@30 km, km	2	1.5	2	1.5	2
Uncert.@30 km, %	10	15	10–15	5–10	10

[a]The resolution and uncertainty is generally a function of height for all instruments with a minimum at about 30 km. Note that the reported uncertainties are not entirely comparable since they are defined differently for each instrument.

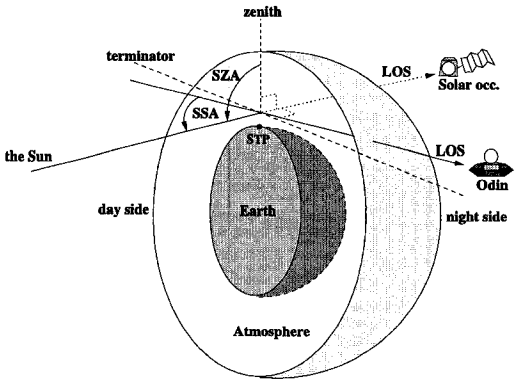

Figure 2. Viewing geometries of limb-scatter (OSIRIS) and solar occultation instruments. The OSIRIS viewing direction is usually close to parallel to the terminator, and the solar zenith angles (SZAs) and single scattering angles (SSAs) vary with season and geographical position. Solar occultation instruments always look perpendicular to the terminator. The figure is not to scale. LOS = line of sight, STP = subtangent point.

[19] According to *Gordley et al.* [1996], aerosol scattering dominates the extinction at low altitudes leading to poor NO_2 retrieval accuracy in the lower stratosphere (below 25 km). Other major error terms include random noise, pressure registration, interfering species, and spectral parameters. The total uncertainty, except aerosol extinction which is varying rapidly in time and space and thus difficult to quantify generally, is estimated to be about 10% at 30 km, increasing rapidly to 20% at 25 km and 40 km, and more than 60% at 15 km and 45 km. Infrequently, sunspots and Sun tracking errors can cause biased retrievals.

[20] Extensive correlative comparisons conducted by *Gordley et al.* [1996] on an older version of the HALOE NO_2 data (version 17) show good agreement (within 10–15%) in the middle stratosphere (25–35 km), but poor agreement below 25 km, especially for heavy aerosol conditions, where a low bias is evident. Between 35 km and 40 km a low bias of up to 5% was also indicated. *Randall et al.* [2002] compared the version 19 data product to NO_2 profiles from the Atmospheric Trace Molecule Spectroscopy experiment (ATMOS) [*Gunson*, 1996] and confirmed the good behavior of the HALOE data above 25 km (within 10%) and a low bias below 25 km of as much as 40%. The low bias between 35 km and 40 km was fixed in the new version.

3.3. POAM III Instrument

[21] The Polar Ozone and Aerosol Measurement III instrument [*Lucke et al.*, 1999] was launched on the SPOT (Satellite Probatoire d'Observation de la Terre) 4 satellite in March 1998 into a Sun-synchronous orbit (ascending node at 2230 hours LST) with an altitude of 833 km and a 98.7° inclination.

[22] POAM III is a solar occultation instrument with nine radiometer channels between 353 nm and 1018 nm. The instrument nominally makes 14 sunrise and 14 sunset measurements per day occurring in a latitude band from 55° to 71° in the northern hemisphere and from 63° and 88° in the southern hemisphere (see Figure 3). All POAM NH measurements are made during spacecraft sunrise but correspond to local sunset. SH observations are obtained during spacecraft sunset, and correspond to local sunrise from mid-April through mid-September and local sunset at other times. Vertical profiles of O_3, NO_2, and H_2O as well as aerosol extinction are measured.

[23] NO_2 is retrieved using Optimal Estimation and the differential absorption between two channels: 439.6 nm (on) and 442.2 nm (off) [*Lumpe et al.*, 2002]. NO_2 number densities are retrieved between 20 km and 45 km at 1 km intervals with a vertical resolution of 1.5–2.5 km below 40 km. Spherical symmetry is assumed and no SZA corrections are made. The POAM III version 4 data product is used in this study.

[24] The random error in the retrieved NO_2 profiles is estimated as 6% at 20 km, 3% at 30 km, and 7% at 40 km. The total error is estimated to be 5–10%, though conditions with dense PSCs are reported to induce large biases below 23 km.

[25] A validation study of version 3 of the POAM III data using HALOE data [*Randall et al.*, 2002] shows agreement to within 6% between 22 km and 33 km with no bias. Above 33 km a positive POAM III bias of up to 17% is indicated and is partly attributed to errors in the HALOE data. A hemispheric bias at 20 km (POAM III higher in the NH and lower in the SH by up to 30%) due in part to POAM III not accounting for SZA variations and individual instrument errors is also found. NO_2 values above 35 km are not significantly different in the version 4 data. Between

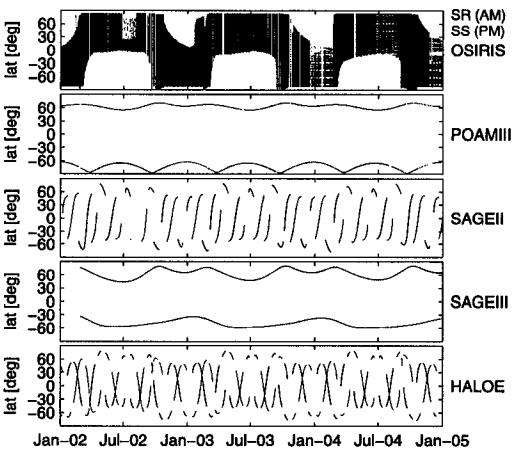

Figure 3. The latitudinal coverage of the satellite instruments in this study for sunrise (AM) and sunset (PM) measurements. POAM III and SAGE III provide measurements at small latitude bands around 60°, whereas the latitude coverage of SAGE II and HALOE varies from day to day in a repeatable pattern. OSIRIS gives near global coverage, which means all latitudes, near the equinoxes in addition to the summer hemisphere.

27 km and 33 km the values in version 4 are about 5–15% lower than in version 3. Below 25 km the version 4 data are significantly larger than in version 3, varying from 5% or less in the summer to up to 50% in the winter, where the NO_2 abundances are small (C. E. Randall et al., Comparison of solar occultation NO_2 measurements, manuscript in preparation, 2007).

3.4. SAGE II Instrument

[26] The Stratospheric Aerosol and Gas Experiment II instrument [*Mauldin et al.*, 1985] was launched on board the Earth Radiation Budget Satellite (ERBS) in October 1984 into a precessing orbit with an altitude of 610 km and a 56° inclination.

[27] SAGE II is a solar occultation photometer with a holographic grating and 7 channels between 385 nm and 1020 nm. The latitude coverage of SAGE II varies from day to day in a 1-year repeatable pattern, similar to HALOE, extending from approximately 70°S to 70°N (see Figure 3). SAGE II produces vertical profiles of aerosols, O_3, NO_2, and H_2O.

[28] Slant columns of NO_2 are calculated from the 448 nm and 453 nm channels using a differential technique [*Chu and McCormick*, 1989]. Vertical profiles are then retrieved between 15 km and 60 km using an onion peeling procedure, where the NO_2 slant columns are smoothed prior to peeling. The altitude sampling is 1 km and the vertical resolution for NO_2 is about 1.5 km below 39 km and 5 km above 39 km. As with POAM III, spherical symmetry is assumed and no SZA correction is applied. The SAGE II version 6.20 data product is used in this study, and compensates for the slight drift in the NO_2 channels after launch.

[29] The random error associated with the NO_2 retrievals between 27 km and 36 km is approximately 5%. The overall accuracy is estimated to be 15%, with the increase mostly due to NO_2 cross section uncertainties. Difficulties in separating NO_2, O_3, and aerosols below 23 km make measurements in that region highly uncertain.

[30] A validation study carried out by *Cunnold et al.* [1991] on an older version of data found the SAGE II NO_2 to be in agreement with balloon instruments to within 10% between 23 km and 32 km. Comparisons between SAGE II and HALOE by *Gordley et al.* [1996], also using an older version of data, indicated a significant bias in the SAGE II data due to aerosol contamination below 27 km, good agreement (10%) from 27 km to 33 km, and a negative bias of up to 25% above 33 km. *Taha et al.* [2004] analyzed the version 6.20 data product and found that the agreement with SAGE III NO_2 is within 5–9% in the altitude range 20–36 km.

3.5. SAGE III Instrument

[31] The Stratospheric Aerosol and Gas Experiment III instrument [*Thomason and Taha*, 2003] was launched on board the Russian Meteor-3M platform in December 2001 into a Sun-synchronous orbit with ascending node at 0900 hours LST. It is primarily designed to make solar and lunar occultation measurements but also has a limb-scatter measurement capability.

[32] The SAGE III instrument is a spectrometer covering wavelengths from 280 nm to 1040 nm with a 1–2 nm spectral resolution. An additional photodetector at 1550 nm is included. SAGE III provides 30 measurement events per day, 15 sunrises at high northern latitudes (45–80°N) and 15 sunsets at southern midlatitudes (25–60°S). All satellite sunrise measurements are at local sunset, while observations obtained during satellite sunset are also at local sunset except from mid-September through February, as seen in Figure 3. SAGE III measures O_3, NO_2, aerosol extinction, H_2O, NO_3 (lunar), OClO, cloud information, pressure, and temperature.

[33] Profiles of NO_2 are derived using a multiple linear regression (MLR) technique for two spectral channels (433–450 nm and 563–622 nm) [*NASA Langley Research Center*, 2002]. MLR simultaneously solves for O_3 and NO_2, which absorb significantly in both spectral regions. The uncertainty is estimated to be 10–15% (systematic) and 10–15% (random). Smoothing is applied to the NO_2 slant columns, giving an effective vertical resolution of about 2 km throughout the 10–50 km retrieval range (for other products the resolution is about 1 km). Number densities are reported at 0.5 km intervals and no SZA correction is applied. The SAGE III version 3 data product is used in this study.

[34] According to *Taha et al.* [2004], the agreement with SAGE II NO_2 is within 5–9% in the altitude range 20–36 km. Agreement with POAM III is within 10% above 22 km and with HALOE is within 5% between 25 km and 34 km. Large differences between SAGE III and HALOE below 25 km (up to 60%) are found and are likely due to SAGE III not accounting for SZA variations.

3.6. SAOZ Instrument

[35] The SAOZ (Systeme d'Analyse par Observation Zenithale) UV/visible spectrometer makes solar occultation measurements during the ascent/descent of the balloon and during sunset/sunrise from float. The balloon version of the SAOZ instrument is very similar to the one used for ground-based measurements of total ozone and NO_2 [*Pommereau and Goutail*, 1988]. Measurements are recorded between 290 nm and 640 nm with an average spectral resolution of 0.8 nm. Using an onion peeling method, SAOZ provides the vertical distribution of O_3, NO_2, and atmospheric extinction at a vertical resolution of 1.4 km with accuracies of better than 3% for O_3 and 10% for NO_2 [*Pommereau and Piquard*, 1994].

[36] The SAOZ NO_2 profiles are reported to agree to within 20% with POAM III from 23 km to 27 km, where SAOZ has a negative bias at 27 km and a positive positive bias at 23 km [*Randall et al.*, 2002]. At 20 km the mean difference is larger (50%). The SAOZ NO_2 data used in this study have not been corrected for diurnal variations along the line of sight.

4. OSIRIS NO_2 Retrievals

[37] A thorough description of the OSIRIS NO_2 retrievals can be found in the work of *Haley et al.* [2004]. Only a simplified description is given here.

4.1. DOAS Step

[38] Instead of retrieving NO_2 vertical profiles directly from the OSIRIS limb-scattered radiance measurements, an intermediate step is applied where effective column densities,

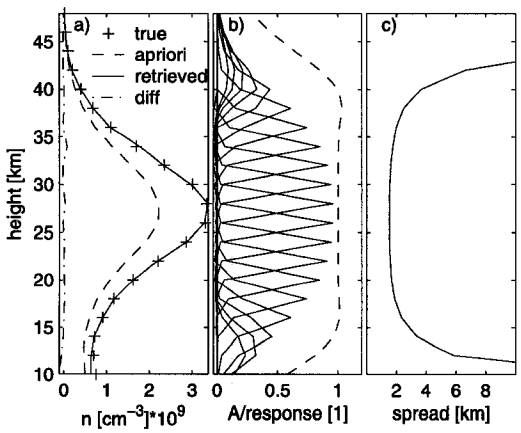

Figure 4. Typical NO_2 retrieval characteristics for a modeled, noise-free OSIRIS midlatitude limb scan (SZA = 85°, SSA = 90°). (a) The true, a priori (66% of the true), and retrieved profiles and the absolute difference between the true and retrieved profiles, (b) the averaging kernels (solid lines) and the measurement response (dashed line), and (c) the vertical resolution ("spread") are shown. High response (> 0.75) is usually found between 15 km and 40 km and the vertical resolution is about 2 km near 30 km.

ECD, (sometimes referred to as slant column densities) are calculated using Differential Optical Absorption Spectroscopy (DOAS) [*Platt*, 1994]. The DOAS step is performed to reduce the sensitivity to phenomena that vary slowly with wavelength such as aerosol (Mie) scattering.

[39] The wavelength region used for retrieving NO_2 is 435–451 nm, where the absorption is large compared with O_3 and strong Fraunhofer lines are avoided. An average of spectra measured between 46 km and 65 km tangent height from each limb scan is used as the reference spectrum, effectively reducing any Ring-effect and Fraunhofer signatures. O_3 and O_4 are included together with NO_2 in the nonlinear, least-squares fit, and the I_0-effect, wavelength shifts, and different trending in the reference and the measurement spectra (tilt-effect) are compensated for. The NO_2 absorption cross sections from *Vandaele et al.* [1998] are used.

4.2. Forward Model

[40] The pseudo-spherical multiple scattering radiative transfer model LIMBTRAN [*Griffioen and Oikarinen*, 2000] is used to invert ECD as a function of tangent height to number density as a function of height. Temperature and pressure information used in LIMBTRAN is from the European Centre for Medium-Range Weather Forecasts (ECMWF) analysis fields. Aerosol information is also included and consists of the stratospheric aerosol extinction climatology for 1999 from *Bauman et al.* [2003a, 2003b] and a Heney-Greenstein phase function (asymmetry parameter 0.7). The surface albedo is taken from *Koelemeijer et al.* [2003].

[41] LIMBTRAN assumes horizontal homogeneity within its vertical layers, and the retrieved profile is assigned to the location of the STP; see Figure 2. This can lead to errors in the retrieved profiles at times when horizontal variations in the true NO_2 distribution exists. Such variations exist in the NO_2 distribution near the terminator due to photochemistry and can affect the retrieved profiles, as will be discussed in section 4.5.

4.3. Inversion Process

[42] The inversion algorithm used to deduce vertical profiles of NO_2 from ECDs is Optimal Estimation (OE) or more specifically the nonlinear Maximum A Posteriori (MAP) estimator from *Rodgers* [2000], solved in a Gauss-Newton iterative manner. MAP is a Bayesian estimator giving the most probable solution based on the measurements and a priori information and the associated covariances. A positive constraint is applied to the retrievals by inverting in logarithm space. Profiles that have not converged after eight iterations or have converged with a high χ^2-value are discarded.

[43] A fixed retrieval grid is chosen, stretching from 10 to 46 km at 2 km intervals. It was found that the weighting functions can be calculated using only two wavelengths, single scattering, and no aerosol without significantly reducing accuracy. Good response (>0.75), i.e., low a priori contamination, is usually found between 15 km and 40 km and the resolution at 30 km is about 2 km, but this varies slightly from profile to profile depending on the measurement conditions.

[44] The NO_2 a priori information is taken from precalculated look-up tables constructed using a photochemical box model [*Prather*, 1992; *McLinden et al.*, 2000], initialized with input fields derived from climatology (O_3, T, aerosol surface area), three-dimensional model output (NO_2, NO_y), and tracer correlations (CH_4, HO_2, Cly, Bry). The a priori profile is chosen to be the nearest neighbor based on profiles tabulated bimonthly and every 2.5° in latitude and then interpolated in SZA to the value at the OSIRIS scan location. The covariance matrix of the a priori state is also required for the retrievals. NO_2 is assumed to follow a log-normal distribution, with standard deviations for the diagonal components of 60% and an exponential off-diagonal correlation length of 4 km. The measurement covariance matrix is a diagonal matrix with the variance of the propagated measurement noise in the diagonal. Measurements from different tangent altitudes are assumed uncorrelated. A sample NO_2 number density profile retrieved from a modeled noise-free OSIRIS limb scan is shown in Figure 4.

4.4. Error Budget

[45] The error estimation of the retrieved profiles is the crucial part of any inversion technique. As described by *Rodgers* [2000], four sources of error can be identified: (1) smoothing error, (2) retrieval noise, (3) forward model error, (4) forward model parameter error. The smoothing error and measurement noise components of the total retrieval error are easily calculated. However, the forward model and forward model parameter errors are more difficult to evaluate.

[46] The smoothing error arises due to the limited vertical resolution of the retrieval compared to the true atmospheric state. If the retrieved profile is said to represent a smoothed

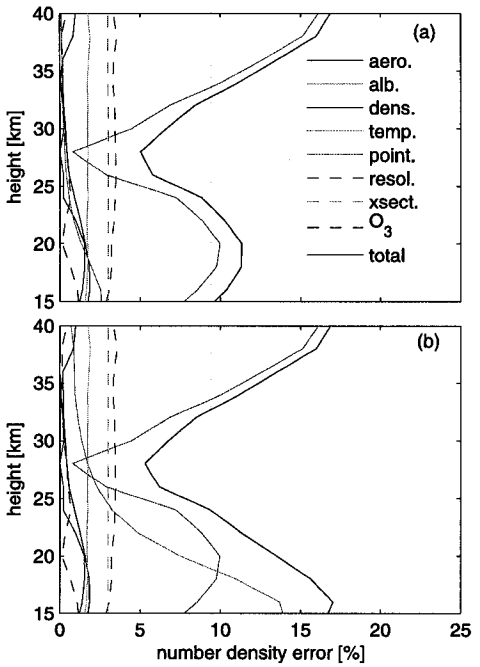

Figure 5. Forward model parameter errors for the OSIRIS NO_2 retrievals due to uncertainties in aerosol, surface albedo/cloud, neutral density, temperature, tangent height registration or pointing, spectral resolution, cross section, and ozone, given as 1σ, and the total forward model parameter error, given by the square root of the sum of the variances. Two scenarios are shown: (a) high-Sun (SZA = 60°, SSA = 90°) with cloud-free conditions and (b) high-Sun with clouds. Tangent height registration and albedo/cloud are the most significant errors and their influence increases below 27 km.

version on the true state, this error term can be ignored. Furthermore, when comparing retrieved profiles to profiles from another instrument with similar vertical resolution, the smoothing error becomes irrelevant. Henceforth, the OSIRIS smoothing error will not be included in the error budget for this validation study, where the vertical resolution of the various instruments only differs by a factor of two at most (see Table 1).

[47] Retrieval noise is the measurement noise propagated through the inversion process. This is a pure random error which is easily computed and verified.

[48] The forward model error is estimated by analyzing the impact of various approximations on the retrievals. The total forward model error for OSIRIS NO_2 retrievals was assessed by *Haley et al.* [2004] and found to be small (<5%), between 15 and 40 km, and generally independent of the measurement conditions. This type of error is mostly systematic. Note that no attempt was made to estimate the error introduced by the use of a pseudo-spherical forward model.

[49] The forward model parameter error concerns the uncertainty in input parameters to the forward model such as aerosol, neutral density, temperature, surface albedo, instrument spectral resolution, absorption cross sections, and the tangent height registration. *Haley et al.* [2004] studied these errors by treating them as independent error sources, each with an assumed uncertainty. The errors were estimated by performing perturbations of one standard deviation to a number of forward model parameters about a midlatitude atmosphere with surface albedo 0.3. In addition to the above error sources, the impact of cloud on the retrievals is estimated in a preliminary way by perturbing the surface albedo to a value of 1.0. Though crude, this gives a sense of the impact that can be expected when cloud is present in the measurements (below the FOV of the lowest measurement) but is not taken into account in the retrievals. An additional error that was not considered by *Haley et al.* [2004] was the impact of nonretrieved species (i.e., O_3), but this has now been included and has been found to be small (<1%). Assuming that each of the errors are independent and that vertical correlations can be ignored, the total forward model parameter error is given by the square root of the sum of the error variances of the individual errors. Note that no attempt was made to estimate the error introduced by the assumption of spherical homogeneity.

[50] Each of the forward model parameter error sources and the total are shown in Figure 5 for high-Sun (SZA = 60°) and for both cloudy and cloud-free conditions. Errors for low-Sun conditions (SZA $\approx$ 90°) are comparable to those of high-Sun cloud-free conditions and are not significantly sensitive to clouds. As the figure shows, tangent height registration (pointing) uncertainty is the largest source of error, potentially introducing errors of about 15% away from the peak. Clouds (albedo) can also have a large effect on the retrievals, leading to errors of about 15% below 20 km. Note that the tangent height registration uncertainty in the OS measurements is difficult to determine, but for this analysis it was estimated that the corrected tangent heights are accurate to 500 m (see section 4.6). The error due to cloud is also difficult to assess since the effective albedo of cloud depends on the characteristics of the cloud (e.g., thickness and patchiness) and on the solar conditions. The analysis here is essentially a worst-case scenario.

[51] If the three different error sources can be treated independently, the standard deviation of the total error is the square root of the sum of the three error variances. The total error is presented in Figure 6 for the two high-Sun cases mentioned above. As the figure shows, the estimated total error is about 10% at 30 km and increases to about 20% at 15 km and 40 km for cloud-free conditions. The error at 15 km increases to about 25% for cloudy conditions. These error levels are comparable to the occultation instruments.

4.5. Diurnal-Effect Error

[52] As noted above, one forward model parameter error source that was not evaluated by *Haley et al.* [2004] was the impact of the horizontal homogeneity assumption. When making near-terminator limb measurements related to photochemically active species with strong diurnal cycles, such as NO_2, the signal received at the sensor is an integration

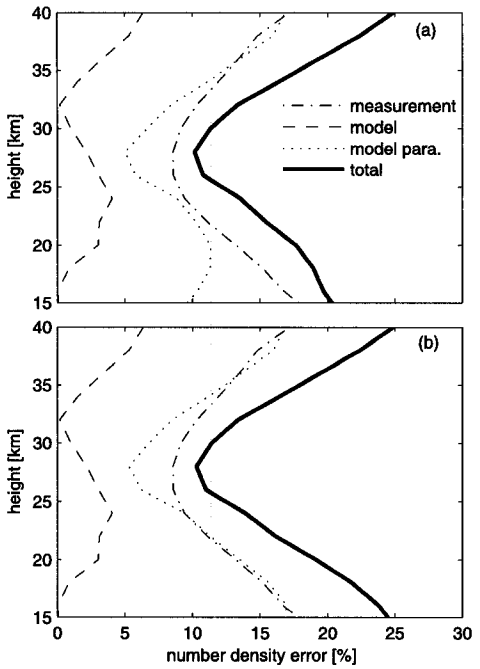

Figure 6. Error estimates (1σ) for OSIRIS NO_2 retrievals. Three main error sources are recognized; the measurement error (retrieval noise), the forward model error, and the forward model parameter error. The total error corresponds to the square root of the sum of the three variances. Two different scenarios are shown: (a) high-Sun (SZA = 60°, SSA = 90°) with cloud-free conditions and (b) high-Sun with clouds. Measurement error and forward model parameter error are the most significant and the total error adds up to 25% at 15 and 40 km at cloudy conditions and 10% at 27 km.

over a range of SZAs representing different atmospheric states with a potentially large variation in the number density of the target species. This so-called "diurnal effect" is not accounted for in the OSIRIS retrievals, where spherical homogeneity is assumed.

[53] The error introduced by not accounting for the diurnal effect will vary with the SZA and the angle between the incoming solar beam and the viewing direction (LOS) of the measurement, the so-called single scattering angle (SSA). For occultation measurements (with SZA = 90° and SSA = 0°) and limb-scatter measurements when SSA = 90°, the error is only related to variations along the incoming beam (see Figure 2). As the SSA deviates from 90° for limb-scatter measurements, variations along the LOS must also be considered. The OSIRIS SZA and SSA vary with latitude and season (see Figure 7) so that the SZA is always large in equatorial regions and small at high latitudes near the solstices. The SSA variation shows the largest deviations from 90° at the equator around the solstices and smaller deviations at high latitudes and around the equinoxes.

[54] Generally speaking, diurnal effect errors for limb-scatter instruments are expected to be largest below 25 km where the atmosphere is becoming optically thick and the signal is weighted toward the satellite (near) side of the LOS. At higher altitudes, errors from the far and near side will roughly cancel out because they have opposite signs. The diurnal effect errors are also linked to the magnitude of the diurnal NO_2 cycle, which is a function of altitude with stronger gradients at 15 km and 35 km than at 25 km, as seen in Figure 1.

[55] A model study conducted by *McLinden et al.* [2006] has shown that the overall diurnal effect errors do not exceed 10% above 25 km and reach a maximum at 14–18 km for OSIRIS viewing conditions (SZA = 60–90°, SSA = 60–120°). The magnitude and sign of the error below 25 km varies substantially with the viewing conditions as seen in Figure 8. For SZA = 90° and SSA = 90° (i.e., LOS exactly along the terminator) OSIRIS underestimates NO_2 by at most 25% for sunset conditions (PM) and slightly less at sunrise (AM). SSA > 90° gives further underestimation (up to 45% at 120°) while SSA < 90° introduces an overestimation of up to 20% at SSA = 60°. At SZA = 87.5°, the overestimation is about 25% at SSA = 60° but the corresponding underestimation at SSA = 120° is only about 20%. At SZA = 80° (and smaller), the diurnal effect errors are below 10% for all SSAs. Considering all of the OSIRIS NO_2 measurements over a 1-year period, *McLinden et al.* [2006] estimates that about 16% of all OSIRIS NO_2 profiles have diurnal effect errors of between 10% and 35% below 25 km, which is comparable to the size of the OSIRIS NO_2

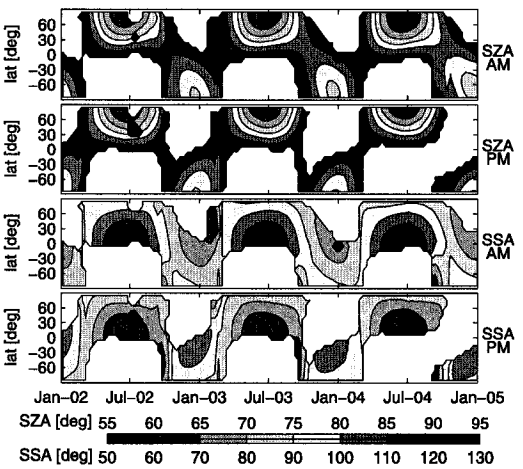

Figure 7. Solar zenith angle (SZA) and single scattering angle (SSA) for OSIRIS AM and PM measurements during the validation period 2002–2004. White regions indicate no OSIRIS measurements. The smallest SZAs are found in high-latitude summer conditions, whereas the SZA is close to 90° for all latitudes at the equinoxes. The SSA deviates furthest from 90° in the equatorial region in the northern latitude summer.

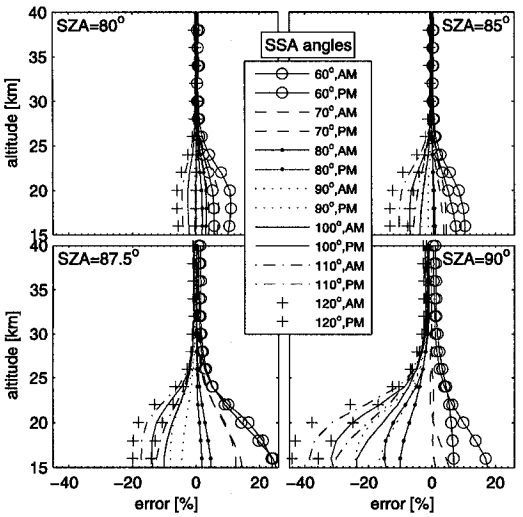

Figure 8. Estimated NO_2 limb-scatter diurnal errors for a range of typical OSIRIS SZA and SSA (the angles indicated in the legend) conditions based on equatorial conditions (June) with a ground albedo of 0.3. Diurnal errors arise due to inhomogeneous NO_2 concentrations along the scattering paths in conjunction with increasing optical depth at low tangent altitudes, see section 4.5. Generally, the diurnal error increases as the SZA approaches 90° and as the SSA departes from 90°. Above 25 km this error is insignificant regardless of the SZA and SSA.

total error estimate in this region (see Figure 6). The worst-case error, with extreme SSA, occurs at the solstices near the equator.

[56] The impact of the diurnal effect on solar occultation instruments also has to be considered in this validation study, except for HALOE which corrects for this. The error for occultation measurements has been assessed by applying the method of *McLinden et al.* [2006] to modeled occultation spectra. An OSIRIS-like instrument was assumed, with a retrieval approach using a DOAS spectral fit and a simple onion-peel inversion. The calculated errors for a few selected cases are found in Figure 9. The diurnal effect error for solar occultation instruments depends strongly on latitude and season and is generally consistent with the results of *Newchurch et al.* [1996]. A predicted systematic overestimation of about 20% for both AM and PM profiles is seen at 20 km, except for equatorial latitudes where the PM overestimation reaches 50%. The errors for December at 60°N and June at 60°S were not calculated because of limitations with the technique employed by the radiative transfer model (VECTOR) for varying the atmospheres along the LOS. Above 25 km the diurnal error is small (equatorial latitudes) or insignificant (high latitudes).

[57] In general, the diurnal effect error for occultation instruments is larger than that for OSIRIS except for equatorial latitudes at solstice where AM errors are larger and PM errors have similar magnitudes (and opposite signs). Unlike in limb-scatter, where most of the information comes from near the tangent point, the occultation measurements are sensitive to variations all along the LOS, with a weighting dependent on the contribution to the total optical depth (i.e., combination of path length and density). Hence whereas the limb-scatter measurements are affected by just the "local" diurnal error, the occultation error is affected by the variation in all layers above the tangent point, leading to the larger errors shown in Figure 9.

4.6. OSIRIS Pointing Offset Correction

[58] An approximate correction is used to account for a long-term Odin pointing drift (due to a satellite timing error) that has been identified, but is not accounted for in the OSIRIS version 2.4 NO_2 data product. A linear fit of the resulting retrieval altitude offset, z_{offset}, based on all scans up to 11 July 2004 (when the problem was corrected) gives

$$z_{offset} = t_{mjd} * \left(8.543 \cdot 10^{-4}\right) - 43.95; \quad (6)$$

where t_{mjd} is the modified Julian date (MJD) of the measurement. This offset value is added to the retrieval altitude grid. This correction approximately transforms the systematic pointing drift into a random pointing uncertainty of about 500 m, corresponding to a 10% uncertainty at 20 km, 5% at 30 km, and 15% at 40 km, as shown in Figure 5. Note that some additional error is introduced when correcting retrieved profiles, rather than correcting the

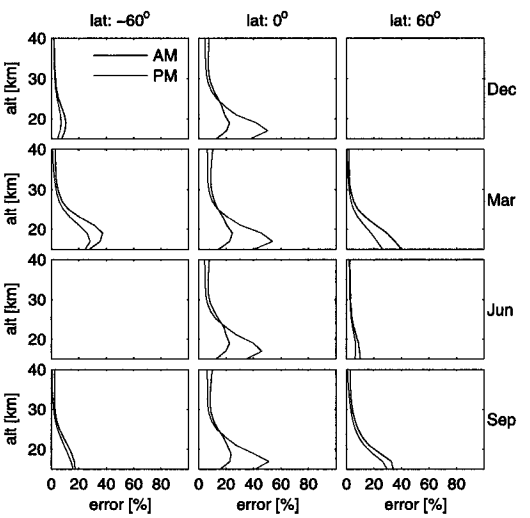

Figure 9. Estimated NO_2 diurnal errors for a typical occultation instrument for a selection of latitudes and months. Diurnal errors arise due to inhomogeneous NO_2 concentrations along the line of sight in conjunction with increasing optical depth at low tangent altitudes, see section 4.5. This error increases rapidly below 25 km and is significantly larger in PM at low latitudes. At high latitudes the diurnal error is largest around the equinoxes and AM values are slightly larger than at PM.

OSIRIS measurements prior to the retrieval process, due to nonlinearities.

5. Intercomparison Methodology

[59] When comparing limb-scattered sunlight measurements to solar occultation measurements, it is important to remember that the viewing geometries are quite different, as is seen in Figure 2, and can lead to differences even for measurements in which the STPs are colocated in time and space. Also, any deviation in the LST and location of the measurements can make the result difficult to interpret. This is particularly true for NO_2, which has a short atmospheric lifetime and strong variations between daytime and nighttime chemistry, enhanced by Odin's near-terminator orbit. An approach to compensate for different LSTs is described in section 5.2.

5.1. Finding Coincidences

[60] The validation period in this study stretches from January 2002 to December 2004, avoiding the first months of the Odin mission where there were satellite pointing problems, and excluding the more recent period where Odin's orbit has deviated significantly from the initial 1800 hour ascending node.

[61] A distance tolerance of 500 km is used in this study. This tolerance is loose enough to give a sufficient number of coincidences for an extensive statistical analysis, but tight enough to not impact significantly on the results of the analysis. The time tolerance is selected to be 2 hours UT. Owing to the diurnal variation of NO_2, a small time tolerance is needed, although 2 hours is not nearly small enough without SZA scaling (as described in section 5.2). Also, the different chemistry during sunrise (AM) and sunset (PM) necessitates that these categories are treated separately. For the SAOZ balloon comparisons, the distance tolerance was relaxed to 1000 km and the time tolerance was relaxed to 6 hours due to the small SAOZ data set. When more than one coincidence is found within the tolerances, the one which is closest in time (UT) is selected.

[62] All coincidences are further divided into three latitude bands: southern latitudes ($-90 \leq \text{lat} < -30$), equatorial latitudes ($-30 \leq \text{lat} \leq 30$), and northern latitudes ($30 < \text{lat} \leq 90$). This division is done to limit the impact of different atmospheric conditions on the comparisons, including cloudiness and tropopause height. In addition, the data is divided into four seasons: November–December–January (NDJ), February–March (FM), April–May–June–July–August (AMJJA), and September-October (SO). This division is logical when considering the OSIRIS latitude coverage over the year, where the northern hemisphere is covered between April and August, the southern hemisphere is covered from November to January, and full global coverage is achieved only close to the equinoxes (September/October and February/March) (see Figure 3).

[63] When interpreting the results, the altitudes have been divided into three regimes; high altitudes (35–40 km), midaltitudes (25–35 km), and low altitudes (15–25 km). The low-altitude regime is characterized by large uncertainties, including diurnal effect errors, SZA scaling biases, OS tangent height registration errors, cloud, aerosol, albedo, and a priori contamination. In the high-altitude regime, the signal to noise ratio for all instruments is generally declining and there is potential a priori contamination, depending on the retrieval technique. The midaltitude regime is presumed to contain the highest data quality for all instruments.

[64] The OSIRIS data are filtered based on measurement response (only >0.75 accepted) and vertical resolution (only <5 km accepted) to ensure that the a priori contamination is minimized. The other instrument data are filtered based on available data flags (any flagged data points are removed) and error estimate (any data points with an error estimate >100% are removed). To calculate differences, the OSIRIS data is interpolated to the altitude grid of the solar occultation instrument.

[65] To be entirely consistent, the vertical resolution of the instruments must be similar. If not, the resolution of one instrument must be transformed to the resolution of the other. This is omitted in this study since the resolution of all of the instruments is similar, only varying between 1 and 2 km (see Table 1), and resulting differences would only produce small errors that do not justify the effort of and potential errors introduced by the transformation.

5.2. SZA Scaling

[66] Owing to the sharp concentration gradients of NO_2 around sunset and sunrise (see Figure 1), even small deviations in SZA (or equivalently LST) of the coincident measurements can have a large impact on the results. Near the terminator, a SZA difference of a few degrees can lead to a change in the NO_2 concentration by a factor of 2 or 3 due to only photochemistry. Since the intention is to study differences in the general NO_2 field, meaningful comparisons can demand a very small SZA (or LST) tolerance, perhaps within a degree or a few minutes. Such strict requirements would reduce the number of coincidences dramatically, making a statistical analysis impossible.

[67] One solution to this problem is to use a photochemical model to scale the OSIRIS profile to the SZA of the other instrument, as is discussed by *Bracher et al.* [2005]. A tabulated photochemical box model (PRATMO) [*Prather*, 1992; *McLinden et al.*, 2000], driven by climatological ozone and temperatures, is used for this purpose. The look-up tables are given as a function of latitude (2.5° increments), time (2-week increments), altitude (2 km increments from 10 to 58 km), and SZA (up to 34 per day).

[68] The OSIRIS number density profiles at 90° SZA, $n_{OS}(90, z)$, are estimated by multiplying the profiles at the measured SZA, $n_{OS}(\theta_{OS}, z)$, by the model-based scaling factor s_θ;

$$n_{OS}(90,z) = \underbrace{\frac{n_{mod}(90,z)}{n_{mod}(\theta_{OS},z)}}_{s_\theta} n_{OS}(\theta_{OS},z), \tag{7}$$

where z is the altitude and n_{mod} are the model profiles obtained from the look-up tables. Points where s_θ is greater than 2 or less than 2/3 are discarded since the scaling is believed to lose accuracy at the extremes.

[69] Uncertainties in the SZA scaling for OSIRIS measurement conditions are shown in Figure 10 and have been estimated by repeating the calculation of s_θ after varying one of the assumed geophysical parameters by estimate of its uncertainty. The parameters considered (and their

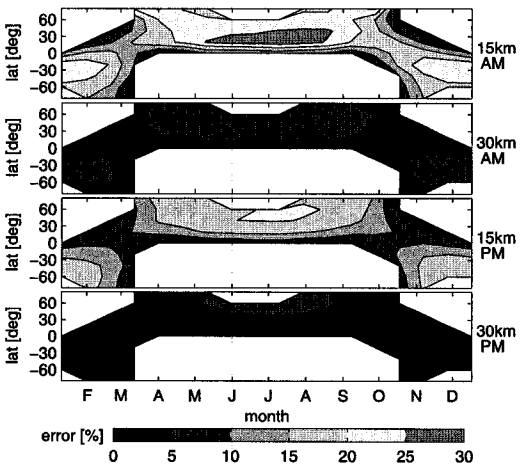

Figure 10. SZA scaling error for OSIRIS AM and PM measurements from estimated uncertainties in PRATMO parameters. The scaling error is insignificant at 30 km but substantial at 15 km with values up to 25% in midlatitude summer at AM.

uncertainties) are O_3 (30%), temperature (4 K), surface albedo (0.2), NOy (30%), Cly (30%), Bry (30%), and aerosol surface area (factor of 3). Additionally, uncertainties in the rates of NO + O_3 (30%) and NO_2 + hν (20%), two key rates controlling the NO_2 diurnal cycle, are considered. All individual uncertainties are added in quadrature to obtain an overall uncertainty estimate for s_θ. The uncertainties increase as the SZA departs from 90° (see Figure 7), as expected, and peak in the lower stratosphere (~15 km). The large uncertainties in this region are due to the assumed uncertainties in ozone and the rate of NO + O_3 (each contributing about equally) and are on par with the OSIRIS NO_2 profile retrieval uncertainty (~20%). Above 30 km the error is small (<5%) for all seasons and latitudes.

5.3. Statistical Analysis

[70] A statistical analysis is carried out when more than 12 coincidences are found within a latitude/season category (profiles and individual altitudes). The most relevant statistical parameter for studying systematic differences is the mean of the individual differences:

$$\bar{\Delta}(z) = \frac{1}{n}\sum_{i=1}^{n}\left[\frac{OS_i(z) - X_i(z)}{OS_i(z)}\right], \quad (8)$$

where n is the number of coincidences, X is the intercomparing instrument (i.e., POAM III, HALOE, or SAGE II/III), and z is the altitude. Random differences are studied through the standard deviation of the differences:

$$\Delta_\sigma(z) = \left\{\frac{1}{n-1}\sum_{i=1}^{n}\left[\left(\frac{OS_i(z) - X_i(z)}{OS_i(z)}\right) - \bar{\Delta}(z)\right]^2\right\}^{\frac{1}{2}}. \quad (9)$$

Within each category, systematic differences between the instruments appear as deviations in the mean of the differences from zero and random differences will contribute to the standard deviation. Scatterplots with fitted linear regression lines are complementary to these calculations, where systematic differences appear as deviations from the 1-1 line and random differences will contribute to the spread of the points, quantified by the r^2 value for the fit.

5.4. Random and Systematic Uncertainties

[71] The total uncertainty of an instrument includes both a systematic and a random part, sometimes referred to as accuracy and precision. A theoretical estimation of the total uncertainty of OSIRIS NO_2 is presented by *Haley et al.* [2004] (see also section 4.4) and found in Figure 6. A method of estimating the OSIRIS random and systematic uncertainties from the measured differences is described below.

[72] Systematic uncertainties in both instruments contribute to the observed mean differences, $\bar{\Delta}(z)$. In a perfect scenario where it could be assumed that the other instrument provides an unbiased measurement of the true atmospheric state, the OSIRIS NO_2 systematic uncertainty could be determined as the maximum of $|\bar{\Delta}(z)|$ found in all latitude/season categories. However, this is rarely the case and may never be the case since remote measurements can never perfectly retrieve the true state since the problem is constrained by both the measurement and retrieval technique. In addition, the comparison of two instruments that contain biases relative to the true state does not necessarily give insight into the systematic uncertainty, since similar biases will cancel. Comparing with an ensemble of instruments, like in this study, can help minimize this problem. An estimate of the OSIRIS systematic uncertainty is expressed as the range of max $|\bar{\Delta}(z)|$ from all four occultation comparisons. Note that the approximate combined diurnal error (from both the scattering and occultation instrument except for HALOE where only scattering is considered), is calculated for representative conditions (latitude, longitude, season, SZA, and SSA) of each latitude/season category and subtracted from $\bar{\Delta}$ when calculating the systematic uncertainties.

[73] The instrument random uncertainties, i.e., the repeatability of the measurements, are related to the measured random differences, Δ_σ, although the true values are smaller since real differences between the probed air masses and SZA scaling errors will contribute to Δ_σ. An upper limit of the random uncertainty can however be estimated from Δ_σ. If it is assumed that the instruments OS and X are independent with random uncertainties ϵ_{OS} and ϵ_X having standard deviations σ_{OS} and σ_X, respectively, then the standard deviation of the differences, Δ_σ equals $\sqrt{\sigma_{OS}^2 + \sigma_X^2}$. If both instruments are assumed to have equal uncertainty (i.e., $\sigma_{OS} = \sigma_X$), then ϵ_{OS} is given by

$$\epsilon_{OS}(z) = \sqrt{\frac{\Delta_\sigma^2(z)}{2}} \quad (10)$$

The theoretical random uncertainty (1σ) is about 10% at 30 km for all instruments, as seen in Table 1, which supports the assumption on which equation (10) is based. From each instrument, latitude/season category, and altitude

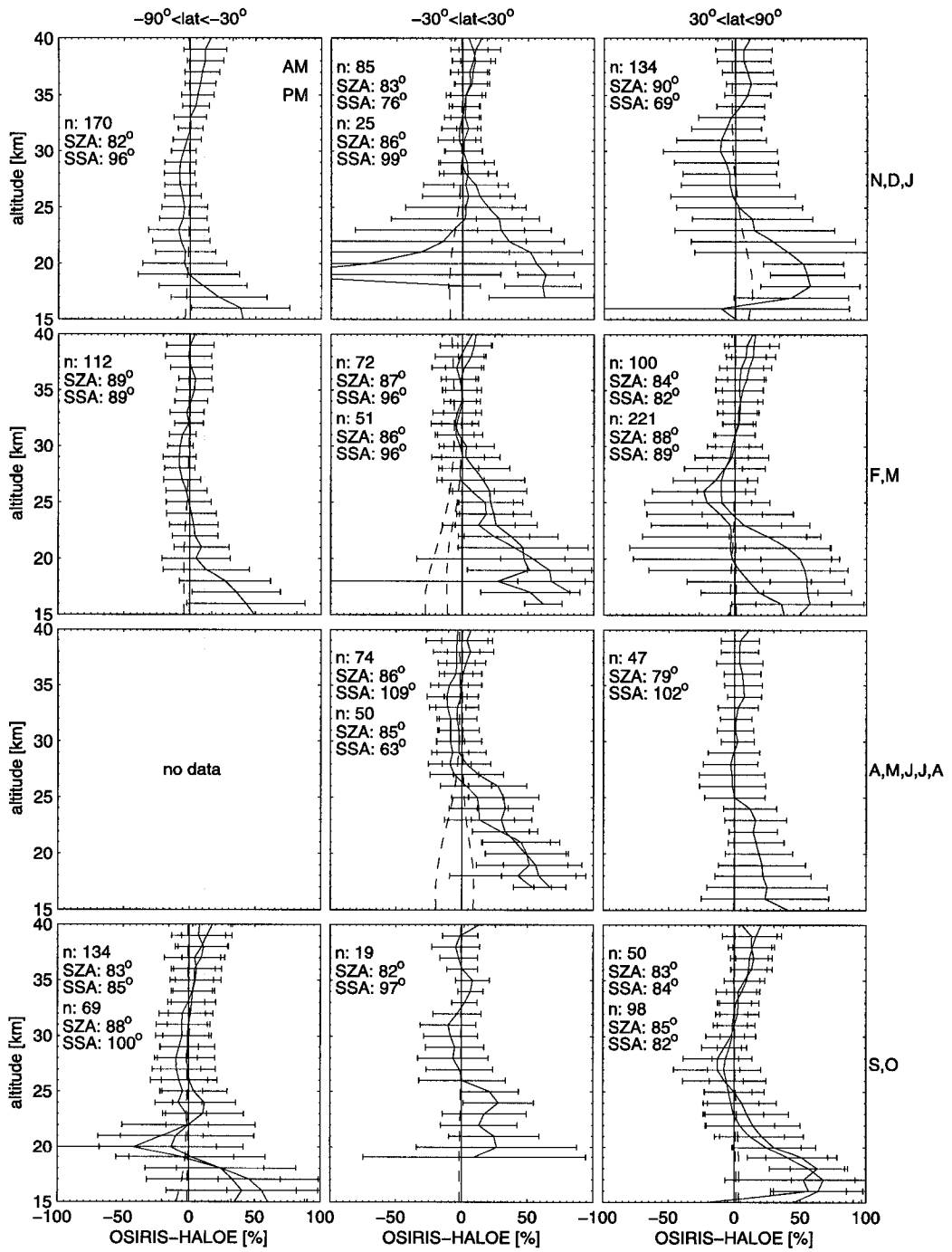
−90°<lat<−30°
−30°<lat<30°
30°<lat<90°
AM
PM
n: 170
SZA: 82°
SSA: 96°
n: 85
SZA: 83°
SSA: 76°
n: 25
SZA: 86°
SSA: 99°
n: 134
SZA: 90°
SSA: 69°
N,D,J
n: 112
SZA: 89°
SSA: 89°
n: 72
SZA: 87°
SSA: 96°
n: 51
SZA: 86°
SSA: 96°
n: 100
SZA: 84°
SSA: 82°
n: 221
SZA: 88°
SSA: 89°
F,M
no data
n: 74
SZA: 86°
SSA: 109°
n: 50
SZA: 85°
SSA: 63°
n: 47
SZA: 79°
SSA: 102°
A,M,J,J,A
n: 134
SZA: 83°
SSA: 85°
n: 69
SZA: 88°
SSA: 100°
n: 19
SZA: 82°
SSA: 97°
n: 50
SZA: 83°
SSA: 84°
n: 98
SZA: 85°
SSA: 82°
S,O
altitude [km]
OSIRIS−HALOE [%]

Figure 11

range, a value of ϵ_{OS} is calculated. The best estimate of the true instrument random uncertainty of OSIRIS is assumed to be the lowest value since this emanates from a category with the smallest atmospheric variation and the occultation instrument with lowest random uncertainty.

6. Results

[74] The intercomparison methodology presented in the previous section results in 7711 coincidences between OSIRIS and the other four satellite instruments. Figures 11 to 14 show the mean differences and the 1σ standard deviation of the mean differences for the four intercomparisons in each of the twelve categories, while Figure 15 shows scatter plots for all coincidences with each of the four instruments at five altitudes. Figure 16 shows additional comparisons between OSIRIS and four SAOZ balloon flights.

[75] Also shown in Figures 11 to 14 is the estimated diurnal effect error for each category. The diurnal effect error was simulated as discussed in section 4.5 and includes both the limb-scatter and the occultation components except for the HALOE comparisons, where only the limb-scatter component is shown since the HALOE retrievals include a diurnal effect correction. The error was simulated for the representative conditions in each category (average SZA, SSA, latitude, and day of year of the coincidences). The occultation component generally dominates this error in the conditions studied here.

[76] Detailed results from each instrument intercomparison are presented in the following sections and are summarized in Table 2. The results are given in three different altitude regions: high altitudes (35–40 km), midaltitudes (25–35 km), and low altitudes (15–25 km). Δ_σ values refer to one standard deviation (1σ). Results for individual years are not shown, but are consistent with the results from the full 3-year comparison period.

6.1. HALOE

[77] Altogether 830 sunrise (AM) and 687 sunset (PM) coincidences are found for OSIRIS and HALOE during the validation period. The results of these comparisons are shown in Figure 11. Coincidences are found in all latitude/season categories except for southern latitudes in AMJJA. The HALOE coincidences in the northern hemisphere in NDJ are the only coincidences for high latitudes around the winter solstice in the entire study.

[78] The Δ_σ for PM categories varies from 22–33% at low altitudes, 12–17% at midaltitudes, and 12–18% at high altitudes. The systematic differences, $\bar{\Delta}$, are within 70% at low altitudes, 11% at midaltitudes, and 20% at high altitudes, if equatorial categories, where the systematic difference increases rapidly below 30 km, are excluded. All categories show similar patterns, where OSIRIS is increasingly larger than HALOE below 20 km. The systematic differences below 25 km are not consistent with the estimated limb-scatter diurnal error.

[79] For AM profiles, Δ_σ varies from 24–60% at low altitudes, 13–35% at midaltitudes, and 14–20% at high altitudes, if the large values (>100%) at equatorial latitudes in NDJ are excluded. Northern latitudes in NDJ and equatorial latitudes in NDJ and SO tend to have the largest values. The systematic differences, $\bar{\Delta}$ are within 60% at low altitudes, 23% at midaltitudes, and 18% at high altitudes, again if the equatorial categories, where the difference is larger, are excluded. The OSIRIS NO_2 densities are significantly larger than HALOE at the lower altitudes for almost all categories. The equatorial region in NDJ in the AM is a clear exception, showing OSIRIS values that are smaller by more than 100%. The diurnal error estimates do not correlate with the AM systematic differences.

[80] The HALOE/OSIRIS scatter plots (Figure 15a) show very close fits to the 1-1 line (high r^2) at 25 km and 30 km, while OSIRIS shows larger NO_2 densities at 35 km and 40 km. The 15 km and 20 km plots show many outliers. The correlations are higher for PM comparisons at all altitudes.

[81] HALOE mean profiles and their corresponding standard deviations are not presented, but show very significant increases in NO_2 concentration and variability below 18 km, particularly for equatorial categories and in the AM. This pattern is not visible in the OSIRIS data set, the OSIRIS a priori data, or in the other instrument data sets except for SAGE II.

6.2. SAGE II

[82] For the OSIRIS and SAGE II data sets, 860 AM and 386 PM coincidences are found. The results of these comparisons are shown in Figure 12. The coincidences cover all latitude/season categories except southern latitudes in AMJJA and northern latitudes in NDJ.

[83] The PM Δ_σ varies from 17–86% at low altitudes, 9–17% at midaltitudes, and 15–22% at high altitudes, if equatorial latitudes and southern latitudes in FM, where the magnitudes reach several hundred percent at low altitudes, are excluded. The OSIRIS NO_2 densities are lower than SAGE II for most categories and the systematic differences ($\bar{\Delta}$) are within 26% at low altitudes, 17% at midaltitudes, and 31% at high altitudes, again if the equatorial latitudes and southern latitudes in FM are excluded. Southern latitudes have the smallest systematic differences and equatorial regions have the largest. The systematic differences are to some extent consistent with the estimated diurnal error in shape and sign, although the magnitude seems incorrect, especially for the equatorial regions.

[84] For AM coincidences, Δ_σ varies from 23–47% at low altitudes, 13–23% at midaltitudes, and 20–26% at high altitudes. The systematic differences, $\bar{\Delta}$, are within 56% at low altitudes, 21% at midaltitudes, and 25% at high altitudes, if the low-altitude range is constrained to 18–25 km, since values below 18 km deviate considerably. All

Figure 11. Results from OSIRIS and HALOE coincidences in 2002–2004, divided into 12 latitude/season categories and expressed as the mean (solid line) and 1σ standard deviation (error bars) of the differences. Sunrise (AM) and sunset profiles (PM) profiles are treated and plotted separately. The average solar zenith angle (SZA) and solar scattering angle (SSA) are given together with the number of coincidences (n) in each category. Estimated diurnal error biases (sum of occultation and limb-scatter) are plotted as dashed lines.

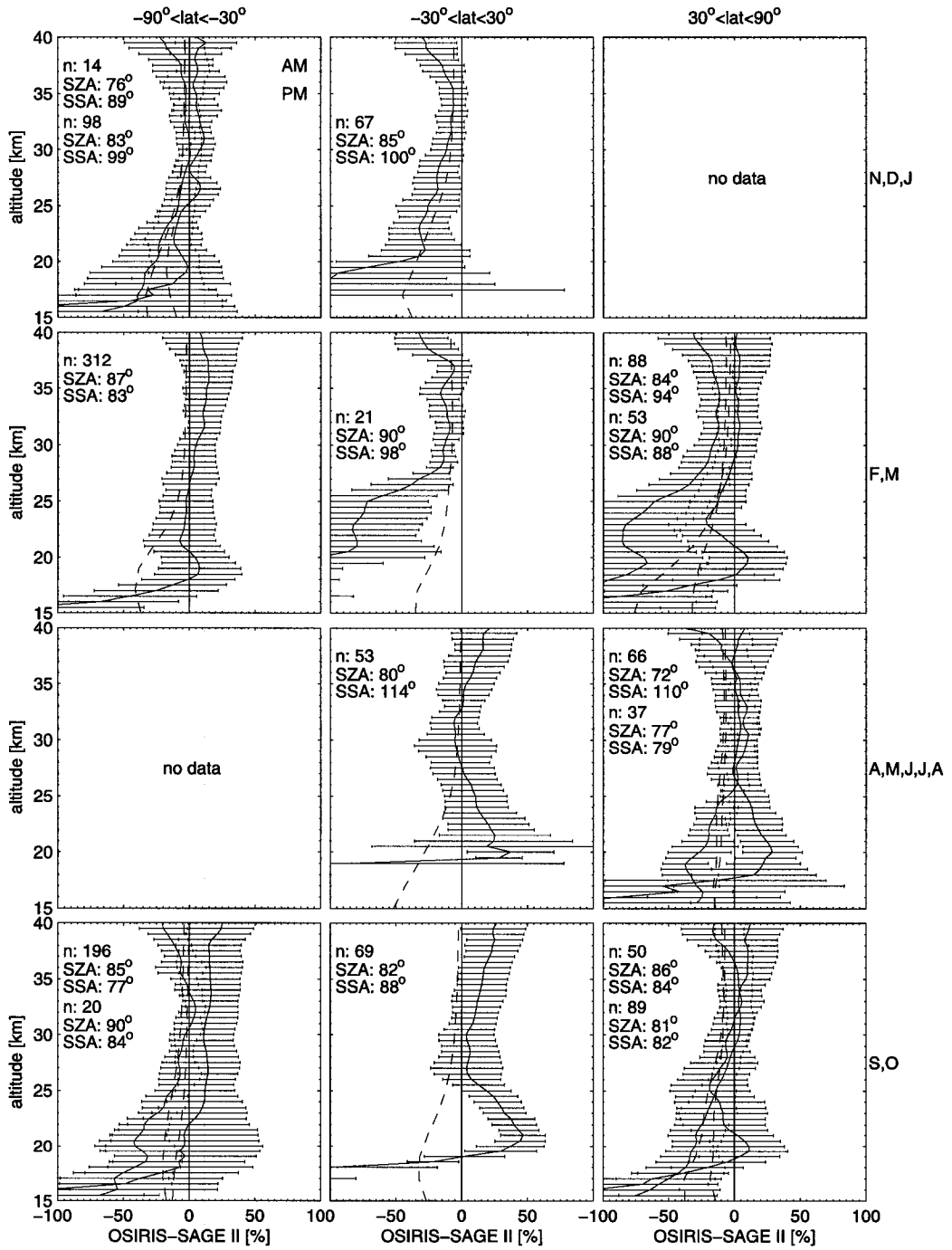

Figure 12. Same as Figure 11, but for SAGE II.

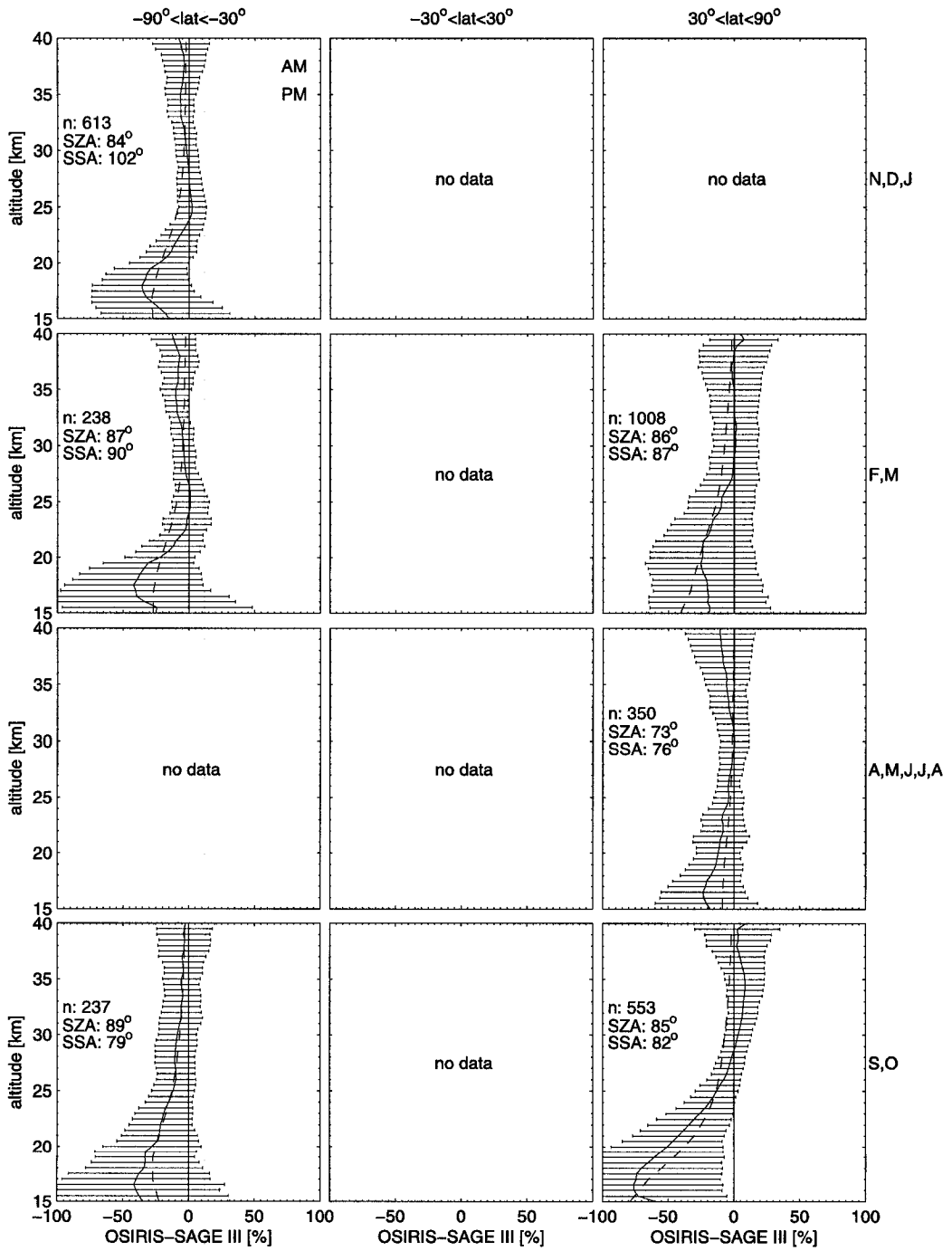

Figure 13. Same as Figure 11, but for SAGE III.

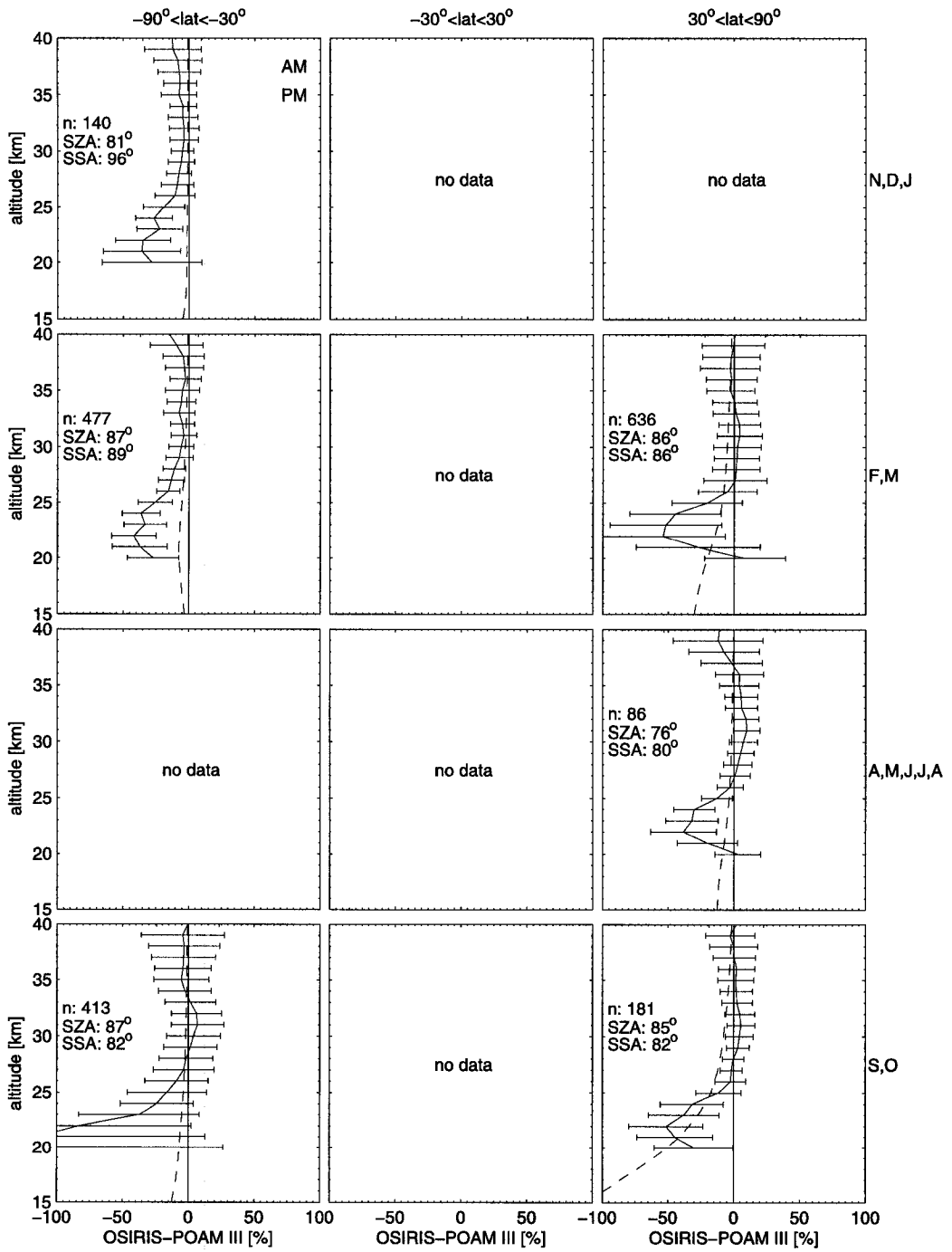

Figure 14. Same as Figure 11, but for POAM III.

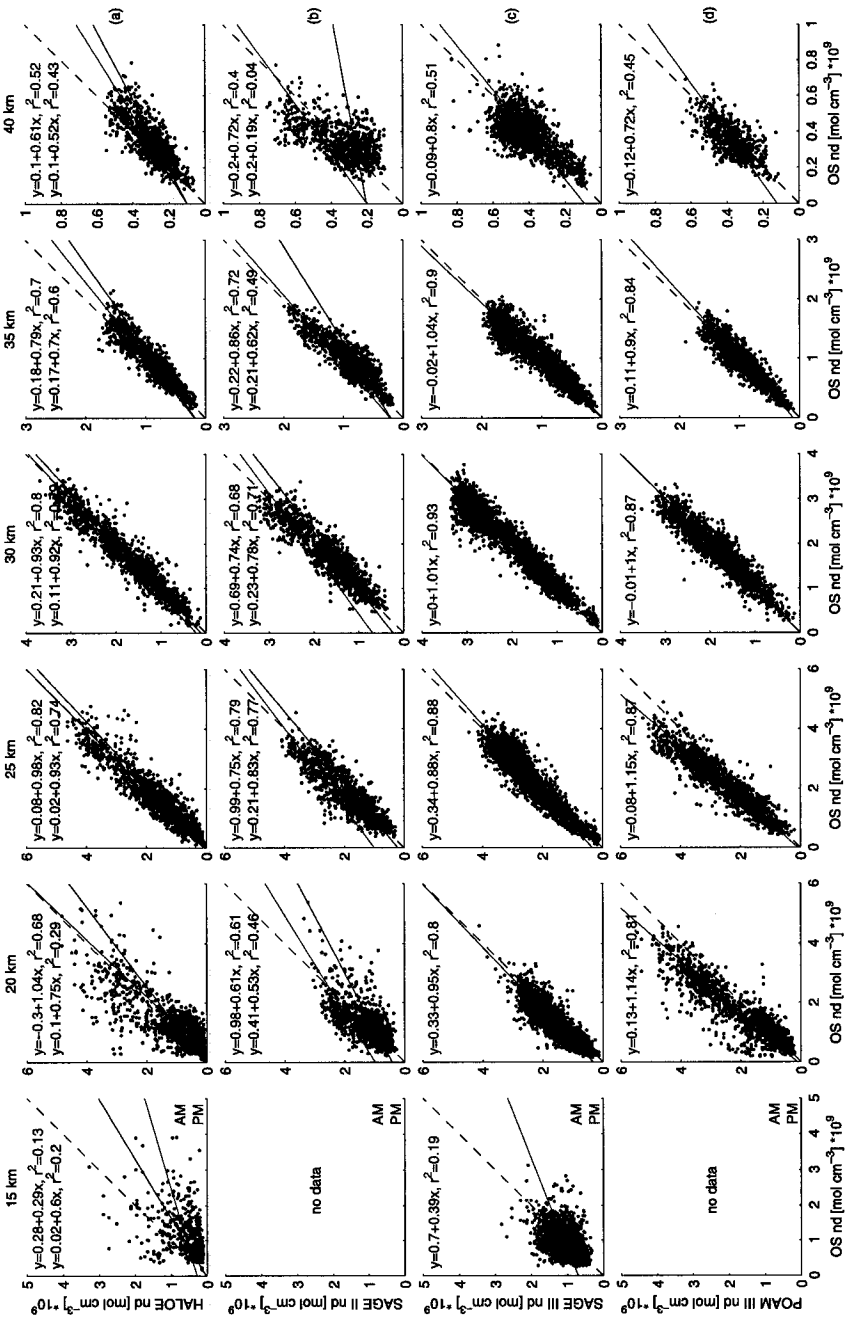

Figure 15. Scatterplots of OSIRIS versus the four solar occultation instruments ((a) = HALOE, (b) = SAGE II, (c) = SAGE III, (d) = POAM III) for all the coincidences in 2002–2004 at six altitudes. Sunrise (AM) and sunset profiles (PM) profiles are treated and plotted separately. Linear regression lines and their corresponding equations are included for each height The 1-1 line is given by the black dashed line.

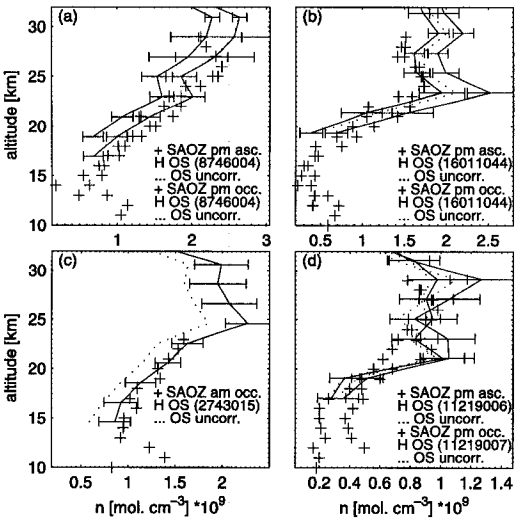

Figure 16. Comparisons of OSIRIS NO_2 profiles (solid and dotted lines) with results from four SAOZ flights (crosses). The closest coincidences in time and space for ascent (asc.) and occultation (occ.) are shown, with (solid lined with 1σ standard deviation uncertainties) and without (dotted lines) photochemical scaling of the OSIRIS profiles to the solar zenith angle of the respective SAOZ measurement. (a) NO_2 profiles retrieved from OSIRIS measurements on 1 October 2002 (scan:8745004, lat:39.2°N, lon:10°W, 1817 UT) and data from a SAOZ sonde launched at Aire sur l'Adour, France (PM ascent: lat:43.8°N, lon:0.1°W, 1700 UT, PM occultation: lat:43.7°N, lon:3.9°W, 1754 UT). (b) OSIRIS measurements on 31 January 2004 (scan:16011044, lat:24.6°S, lon:58.7°W, 2220 UT) and data from a SAOZ sonde launched at Bauru, Brazil (PM ascent: lat:22.4°S, lon:49°W, 2118 UT, PM occultation: lat:23.5°S, lon:53.4°W, 2206 UT). (c) OSIRIS measurements on 24 August 2001 (scan:2743015, lat:63.9°S, lon:29.5°W, 0508 UT) and data from a SAOZ sonde launched at Kiruna, Sweden (AM occultation: lat:67.9°N, lon:23.5°E, 0230 UT). (d) OSIRIS measurements on 16 March 2003 (scan:11218006, lat:66.1°N, lon:10.6°E, 16:12 UT, scan:11219007, lat:71.0°N, lon:4.9°E, 1614 UT) and data from a SAOZ sonde launched at Kiruna, Sweden (PM ascent: lat:67.5°N, lon:22.0°E, 1548 UT, PM occultation: lat:67.3°N, lon:14.3°E, 1654 UT).

categories show large negative systematic differences below 20 km, reaching up to several hundred percent at 15 km at equatorial latitudes. The estimated diurnal effect bias does not correlate with the measured AM bias at low altitudes.

[85] The SAGE II/OSIRIS scatterplots (Figure 15b) show close fits to the 1-1 line, with few extreme outliers, from 25 km to 35 km except for an OSIRIS high bias in the 35 km AM points. The fits at 20 km and 40 km are poor with a large number of outliers. PM comparisons show generally higher correlations, especially at the highest and lowest altitudes.

[86] The SAGE II mean profiles and their corresponding standard deviations are not presented but show a very significant increase in NO_2 concentration and variability below 20 km, especially for midlatitude categories and in the AM, similar to what is seen in the HALOE data.

[87] There seems to be a significant systematic difference between SAGE II SR and SS measurements at around 20 km for many categories, even though it is smaller than expected from the observed bias between SAGE II satellite SR and SS events [*Randall et al.*, 2005]. Note that for SAGE II and OSIRIS coincidences, local sunrise corresponds to satellite sunrise, except for a few cases in northern latitudes in NDJ.

6.3. SAGE III

[88] Owing to the latitude coverage of the Sun-synchronous orbits of SAGE III and OSIRIS, close coincidences in time and space only occur in southern and northern latitudes almost entirely at local sunset (PM). Altogether 3005 coincidences are found of which only six are in the AM, too few to make any statistical analysis. The coincidences appear in the northern and southern latitudes in all seasons except the winter solstices, as seen in Figure 13.

[89] All available latitude/season categories show similar patterns with a Δ_σ of 22–45% at low altitudes, 9–19% at midaltitudes, and 14–25% at high altitudes. Northern latitudes in FM stand out with significantly larger Δ_σ at middle and high altitudes. OSIRIS is systematically low by about 50%, peaking between 15 km and 20 km, which corresponds very well to the estimated diurnal errors in both magnitude and shape. If the estimated diurnal error is subtracted, the $\bar{\Delta}$ is within 21% at low altitudes, 12% at midaltitudes, and 11% at high altitudes.

[90] The SAGE III/OSIRIS scatterplots (Figure 15c) show generally good fits to the 1-1 line from 20 km to 35 km and a reasonable fit at 40 km, particularly at smaller concentrations. At 15 km, the fit is poor. The SAGE III mean profiles and corresponding standard deviations are not presented but are consistent with OSIRIS and do not show the low-altitude features seen in the HALOE and SAGE II data sets.

6.4. POAM III

[91] For OSIRIS and POAM III, close coincidences only occur in the southern and northern latitude regions, almost entirely at local sunset (PM). A total of 1943 coincidences are found of which only 10 are AM coincidences (again too few to make any statistical analysis). The categories around the winter solstices contain no coincidences due to the lack of OSIRIS data, as seen in Figure 14.

[92] The mean Δ_σ varies from 18–40% at low altitudes, 10–19% at midaltitudes, and 16–27% at high altitudes, if the southern latitude category in SO, which shows significantly larger Δ_σ, is excluded. Systematic differences, $\bar{\Delta}$, after the diurnal error is subtracted, are within 40% at low altitudes, 21% at midaltitudes, and 14% at high altitudes, again if the southern latitudes in SO are excluded. OSIRIS has systematically lower values by about 40% for southern latitudes and 50% for northern latitudes, peaking at about 22 km. The only exception is the southern latitudes in SO,

Table 2. Systematic and Random Differences (1σ) of OSIRIS Versus SAGE II, SAGE III, HALOE, and POAM III NO_2 Profiles (AM and PM) in Percent

	HALOE				SAGE II				SAGE III		POAM III	
Altitudes, km	AM rand.	PM rand.	AM syst.	PM syst.	AM rand.	PM rand.	AM syst.	PM syst.	PM rand.	PM syst.	PM rand.	PM syst.
35–40	14–20	12–18	18	20	20–26	15–22	25	31	14–25	11	16–27	14
25–35	13–35	12–17	23	11	13–23	9–17	21	17	9–19	12	10–19	21
15–25	24–60	22–33	60	70	23–47	17–86	56	26	22–45	22	18–40	40

where OSIRIS is lower by above 80%. The OSIRIS systematic low peak does not correspond to the estimated diurnal error.

[93] The scatterplots of POAM III/OSIRIS (Figure 15d) show a good fit to the 1-1 line only at 30 km and 35 km. Below 30 km, OSIRIS are clearly lower than POAM III, especially at high concentrations. At 20 km and 40 km the fit is fair due to many outlayers.

[94] The mean profiles of POAM III are not presented but show a typical sharp peak or double peak at 20 km, which roughly corresponds to the atmospheric NO_2 maximum. The OSIRIS mean NO_2 peak is smaller and much smoother. The sharp peak structure appears in almost all POAM III profiles and is not due to a few outliers in the data set. This behavior is not seen in any of the other instruments.

6.5. SAOZ

[95] Only four coincidences between OSIRIS and SAOZ balloon flights are found, even with the relaxed coincidence tolerances; hence no statistical analysis can be performed. However, as is shown in Figure 16, the four profiles generally agree to within the combined OSIRIS and SAOZ error bars (SAOZ error bars are not plotted for clarity) down to 15 km for most occasions except for the SAOZ PM occultation during the 31 January 2004 Bauru flight at altitudes above 20 km, where the OSIRIS SZA scaling correction appears to lead to an overestimate of the NO_2 concentrations, and for the PM ascent during the 1 October 2002 Aire sur l'Adour flight, where the SZA scaling appears to lead to an underestimation.

6.6. OSIRIS Uncertainties

[96] Estimated OSIRIS random and systematic uncertainties for AM and PM NO_2 profiles in the three altitude regimes are presented in Table 3. The values are estimated from the measured Δ_σ and $\bar{\Delta}$ of all latitude/season categories and instruments as described in section 5.4.

[97] SAGE II and HALOE have reported difficulties measuring NO_2 in the low-altitude regime, mainly due to problems with separating the NO_2 signal from other strong signals including aerosols and water vapor (see section 3.2 and 3.4), which makes these instruments less useful for estimating the OSIRIS uncertainty at low altitudes. The large and unexplained discrepancy between POAM III and OSIRIS below 25 km (which is traced to the POAM III data set since it does not appear in the other comparisons) makes also this data set inappropriate at low altitudes. Fortunately, the SAGE III data set appears to be well behaved down to 15 km (see Figure 13). Hence only SAGE III data have been used in the low-altitude regime. Furthermore, equatorial latitudes (for SAGE II and HALOE) are excluded from the calculations since they show major systematic uncertainties also at midaltitudes. SAGE II PM northern latitudes in FM and POAM III southern latitudes in SO have also been excluded due to strongly deviating results.

[98] As seen in Table 3, the OSIRIS random uncertainty for PM measurements is estimated to be 16% at low altitudes, 6% at midaltitudes, and 9% at high altitudes and is slightly higher for AM measurements. The systematic PM uncertainty is estimated to be about 22% at low altitudes, 11–21% at midaltitudes, and 11–31% at high altitudes, after correction for diurnal effect errors. The AM systematic uncertainty is estimated to be 21–23% at midaltitudes and 18–25% at high altitudes. Equatorial latitudes, which are excluded in the calculations, appear to have higher uncertainties; however, this is not quantified.

7. Discussion

[99] As is shown in Figure 6, the theoretical total uncertainty in the OSIRIS NO_2 profiles is smallest (~10%) near 30 km. At 15 km and 40 km, the uncertainty increases to 20–25%. The results of this study show a minimum in the random and systematic differences for all instruments near 30 km and increasing differences at high and low altitudes, which is consistent with the theoretical estimation.

[100] The agreement below 25 km is quite variable and generally poor, however, this is expected. At low altitudes, the signal to noise ratio of the NO_2 absorption signature in the measurements declines sharply due to the small NO_2 abundances. Furthermore, the atmosphere becomes optically thick (opaque) in the lower stratosphere at the wavelengths used by all of the instruments except HALOE. This tends to push the measurement focus toward the satellite side of the LOS since the contribution from the far side is decreased, increasing the diurnal effect errors and reducing the sensitivity of the instruments to NO_2 in the lower stratosphere. In addition, the SZA scaling error and many forward model parameter errors such as cloud, aerosol and albedo become

Table 3. Estimated Systematic and Random (1σ) Uncertainties of OSIRIS NO_2 AM and PM Profiles Based on the Mean and Standard Deviations of the Differences With SAGE II, SAGE III, HALOE, and POAM III

	Random		Systematic	
Altitudes, km	PM	AM	PM	AM
35–40	9%	10%	11–31%	18–25%
25–35	6%	9%	11–21%	21–23%
15–25[a]	16%	-	22%	-

[a]Only comparisons with SAGE III are used in this altitude regime.

important below 20 km. Decreasing signal to noise and possibly increasing pointing offset errors are the main reasons for the worse agreement at high altitudes (above 35 km). The generally larger random uncertainties for AM profiles are likely related to the small AM NO_2 abundances (as compared to PM profiles).

[101] One thing to notice is that solar scattering and solar occultation techniques probe different air masses even if a measurement corresponds to the very same STP. Solar occultation instruments sample NO_2 along the solar beam, but the scattering instruments sample partly along the solar beam and partly along the instrument LOS (considering single scattering only, the multiple scattering component of the signal further complicates the picture). If the atmospheric NO_2 concentration is truly spherically homogeneous, as is assumed in the retrievals, this is not a problem. The true concentration can, however, vary horizontally, due to photochemistry and near the vortex edge, for example. The two different techniques, then, should not be expected to give exactly the same result even if the measurements are perfect with no noise or other errors. However, a large number of coincidences will tend to minimize this problem (in terms of a systematic effect).

[102] As was mentioned in section 5.3, random uncertainties in the various instruments will contribute to the observed Δ_σ. In a perfect scenario, where no other sources of error contribute and where both instrument have exactly equal uncertainties, the real OSIRIS NO_2 random uncertainty can be calculated. However, coincidence issues, random errors in the SZA scaling factor, OSIRIS pointing error, vertical/horizontal resolution differences, a priori contamination and any other nonretrieved parameters that can affect the retrievals in a random way within each category (i.e., cloud, aerosols, and albedo) will potentially lead to an overestimation of the random uncertainty. This is particularly true at low altitudes where the various contributions are generally most significant. Nevertheless, the estimated OSIRIS random uncertainty, as seen in Table 3, is consistent with the theoretical measurement error (Figure 6). This indicates that the potential overestimation is small (or that the theoretical measurement error is underestimated).

[103] OSIRIS SZA scaling errors could possibly explain some of the differences at altitudes below 25 km. From Figure 10, the error should be more pronounced in the summer solstice periods (i.e., NH in AMJJA and SH in NDJ) and less significant around the time of the equinoxes where the SZA is close to 90° (i.e., in FM and SO). In addition, AM profiles should be more affected. However, nothing in the results indicates that the SZA scaling is a major random error source. To confirm this, the comparisons were repeated while limiting the included OSIRIS measurements to those where the SZA was within 2° of 90°, thus making the SZA scaling factor negligible). Very similar patterns to those presented in the previous section were found, indicating that indeed the SZA scaling is not a major source of the observed differences.

[104] OSIRIS uses a climatological albedo in the NO_2 retrievals (assuming no clouds) which may introduce systematic errors of up to 15% at 15 km for high Sun conditions (SZA = 60°) in the presence of clouds, as seen in Figure 5, and small errors in low Sun conditions. The largest albedo errors (due to the presence of clouds) are then expected in the summer high latitudes. However, this pattern is not evident in the comparisons.

[105] Systematic and random differences may also be related to aerosols since OSIRIS has some sensitivity to the accuracy of the aerosol climatology used in the retrievals, and the other instruments (HALOE, SAGE II, and POAM III in particular) are known to have significant aerosol-related errors at low altitudes. This error should generally be largest in the equatorial region. Peaks at the lowest altitudes in the NO_2 mean profiles exist in the HALOE and SAGE II data but not in SAGE III and POAM III data. Such peaks also do not exist in the OSIRIS NO_2 profiles or the aerosol climatology used in the OSIRIS retrievals. These peaks in the lower altitudes are likely the cause of the large mean difference values and are likely due to, for example, the LOS passing directly through clouds. This should mostly occur in the tropical region where tropical convective clouds may extend into the lower stratosphere or in regions of polar stratospheric clouds.

[106] The ad hoc OSIRIS tangent height registration correction that has been applied to the NO_2 data could also be a source of the systematic differences at low altitudes since in this region a simple shift of the retrieved profiles in height can lead to large errors due to a priori contamination and nonlinearities in the retrievals. However, this would be expected to impact the comparisons with all instruments. The remaining OSIRIS pointing uncertainty of approximately 500 m is expected to introduce random errors of about 10% at 20 km, 5% at 30 km, and 15% at 40 km and is likely contributing to the observed standard deviations of the differences.

[107] The combined diurnal effect error (both occultation and scattering) explains most of the systematic differences between OSIRIS and SAGE III at low altitudes. Both the magnitude and the shape of the error is consistent with the differences in all of the categories. In the POAM III and SAGE II PM data the diurnal effect error may explain part of the observed differences at low altitudes. For the other comparisons the contribution of the diurnal error to the observed systematic differences at low altitudes remains unclear. The approximation of the combined diurnal error for representative conditions (as plotted in the result Figures 11 to 14) are believed to be more accurate for POAM III and SAGE III where the latitudes are restricted to a small latitude band. A more accurate approach is to simulate the diurnal error for each profile within a category, not just for a representative case. However, this involves extensive computer runs and is left for future studies.

[108] It is difficult to make any quantitative assessment of the OSIRIS data quality based on the SAOZ comparisons due to the small number of coincidences and since the distance and time criteria are large. However, it can be said that the results are consistent and that no obvious biases exist.

[109] The assumption of independence made in the calculation of the random uncertainties can be questioned since the same NO_2 cross sections, and atmospheric parameters such as temperature and pressure are sometimes used in the retrievals for the various instruments. However, since the viewing geometries and the retrieval techniques are fundamentally different (except for OSIRIS and POAM III, which both use OE) the measurements should be largely independent.

Furthermore, HALOE measurements are made in the infrared and are consistent with OSIRIS measurements in the visible.

8. Conclusions

[110] Stratospheric NO_2 profiles retrieved from OSIRIS limb-scatter measurements (version 2.4) have been compared with NO_2 profiles measured with the HALOE, SAGE II, SAGE III, and POAM III satellite occultation instruments. All together 7711 coincidences were found within 2 hours and 500 km tolerances, between 1 January 2002 and 31 December 2004. Comparisons were also made with the SAOZ balloon occultation instrument.

[111] The agreement between OSIRIS and the satellite instruments is excellent between 25 km and 35 km, where both the random and systematic differences are within 20%. This is true for all instruments, seasons, and latitudes, except for a few exceptional cases. From 35 km to 40 km, the agreement is within 30%. The systematic agreement is slightly better for high latitudes than for equatorial latitudes. Below 25 km only OSIRIS and SAGE III are consistent. Model simulations indicate that the systematic difference between OSIRIS and SAGE III at low altitudes to a large extent can be attributed to diurnal effects in the SAGE III measurements from varying NO_2 concentrations along the line of sight. The SAOZ comparisons, though limited in number, show good agreement with OSIRIS down to 15 km, which further indicates high-quality OSIRIS measurements throughout the entire altitude range (15–40 km).

[112] On the basis of on the measured differences, the OSIRIS random uncertainty (~precision) is estimated to be 9% from 35 km to 40 km, 6% from 25 km to 35 km, and 16% from 15 km to 25 km. The systematic uncertainty (~accuracy) is estimated to be 11–31% from 35 km to 40 km, 11–21% from 25 km to 35 km, and around 22% from 15 km to 25 km. The AM uncertainties are found to be slightly higher than the PM uncertainties. These results correspond well to the theoretical uncertainties.

[113] Given the results of this validation study, the OSIRIS NO_2 profiles are well behaved, with reasonable uncertainty estimates throughout the entire retrieval range of 15–40 km. This unique NO_2 data set, with more than hemispheric coverage and high vertical resolution will be of particular interest for studies of nitrogen chemistry in the middle atmosphere, which is closely linked to ozone depletion.

[114] **Acknowledgments.** This work is supported by the Natural Sciences and Engineering Research Council (Canada), the Canadian Space Agency, the Swedish National Space Board, and Chalmers University of Technology. Odin is a Swedish-led satellite project, funded jointly by Sweden (SNSB), Canada (CSA), Finland (Tekes), and France (CNES). POAM III analyses are supported by the NASA data buy program and by the NASA Solar Occultation Satellite Science Team program. The SAGE II, SAGE III, and POAM III data were obtained from the NASA Langley Research Center EOSDIS Distributed Active Archive Center. Thanks also goes to the HALOE and SAOZ teams for providing data and support.

References

Bauman, J. J., P. B. Russell, M. A. Geller, and P. Hamill (2003a), A stratospheric aerosol climatology from SAGE II and CLAES measurements: 1. Methodology, *J. Geophys. Res.*, *108*(D13), 4382, doi:10.1029/2002JD002992.

Bauman, J. J., P. B. Russell, M. A. Geller, and P. Hamill (2003b), A stratospheric aerosol climatology from SAGE II and CLAES measurements: 2. Results and comparisons, 1984–1999, *J. Geophys. Res.*, *108*(D13), 4383, doi:10.1029/2002JD002993.

Bertaux, J., G. Mégie, T. Widemann, E. Chassefiè, R. Pellinen, E. Kyrölä, S. Korpela, and P. Simon (1991), Monitoring of ozone trend by stellar occultations: The GOMOS instrument, *Adv. Space. Res.*, *11*, 237–242.

Bovensmann, H., J. P. Burrows, M. Buchwitz, J. Frerick, S. Noël, V. V. Rozanov, K. V. Chance, and A. P. H. Goede (1999), SCIAMACHY: Mission objectives and measurement modes, *J. Atmos. Sci.*, *56*, 127–150.

Bracher, A., M. Sinnhuber, A. Rozanov, and J. P. Burrows (2005), Using a photochemical model for the validation of NO_2 satellite measurements at different solar zenith angles, *Atmos. Chem. Phys.*, *5*, 393–408.

Brasseur, G., and S. Solomon (1986), *Aeronomy of the Middle Atmosphere*, 2nd ed., Springer, New York.

Chu, W. P., and M. P. McCormick (1989), SAGE II inversion algorithm, *J. Geophys. Res.*, *94*, 8339–8351.

Cunnold, D. M., et al. (1991), Validation of SAGE II NO_2 measurements, *J. Geophys. Res.*, *96*, 12,913–12,925.

Degenstein, D. A., E. J. Llewellyn, and N. D. Lloyd (2002), Volume emission rate tomography from a satellite platform, *Appl. Opt.*, *42*(8), 1441–1450.

Dessler, A. E. (2000), *The Chemistry and Physics of Stratospheric Ozone*, Elsevier, New York.

Fischer, H., and H. Oelhaf (1996), Remote sensing of vertical profiles of atmospheric trace constituents with MIPAS limb emission spectrometers, *Appl. Opt.*, *35*, 2787–2796.

Frisk, U., et al. (2003), The Odin satellite I. Radiometer design and test, *Astron. Astrophys.*, *402*, L27–L34, doi:10.1051/0004-6361:20030335.

Funke, B., et al. (2005), Retrieval of stratospheric NOx from 5.3 and 6.2 Mm nonlocal thermodynamic equilibrium emissions measured by Michelson Interferometer for Passive Atmospheric Sounding (MIPAS) on Envisat, *J. Geophys. Res.*, *110*, D09302, doi:10.1029/2004JD005225.

Gordley, L. L., et al. (1996), Validation of nitric oxide and nitrogen dioxide measurements made by the halogen occulation experiment for uars platform, *J. Geophys. Res.*, *101*, 10,241–10,266.

Griffoen, E., and L. Oikarinen (2000), LIMBTRAN: A pseudo three-dimensional radiative transfer model for the limb-viewing imager OSIRIS on the Odin satellite, *J. Geophys. Res.*, *105*, 29,717–29,730.

Gunson, M. R. (1996), The atmospheric trace molecule spectroscopy (ATMOS) experiment: Deployment on the ATLAS space shuttle missions, *Geophys. Res. Lett.*, *23*, 2333–2336.

Haley, C. S., et al. (2004), Retrievals of stratospheric O_3 and NO_2 profiles from Odin Optical Spectrograph and InfraRed Imager System (OSIRIS) limb-scattered sunlight measurements, *J. Geophys. Res.*, *109*, D16303, doi:10.1029/2004JD004588.

Koelemeijer, R. B. A., J. F. de Haan, and P. Stammes (2003), A database of spectral surface reflectivity in the range 335–772 nm derived from 5.5 years of GOME observations, *J. Geophys. Res.*, *108*(D2), 4070, doi:10.1029/2002JD002429.

Llewellyn, E. J., et al. (2004), The OSIRIS instrument on the Odin spacecraft, *Can. J. Phys.*, *82*, 411–422.

Lucke, R. L., et al. (1999), The polar ozone and aerosol measurement (POAM) III instrument and early validation results, *J. Geophys. Res.*, *104*, 18,785–18,799.

Lumpe, J. D., R. M. Bevilacqua, K. W. Hoppel, and C. E. Randall (2002), POAM III retrieval algorithm and error analysis, *J. Geophys. Res.*, *107*(D21), 4575, doi:10.1029/2002JD002137.

Mauldin, L. E., III, N. H. Zaun, M. P. McCormick, J. H. Guy, and W. R. Vaughn (1985), Stratospheric aerosol and gas experiment II instrument: A functional description, *Opt. Eng.*, *34*, 307–312.

McCormick, M. P., W. P. Chu, J. M. Zawodny, L. E. Mauldin III, and L. R. McMaster (1991), Stratospheric aerosol and gas experiment III (SAGE III) aerosol and trace gas measurements for earth observing system (EOS), *Proc. SPIE Int. Soc. Opt. Eng.*, *1491*, 125–141.

McLinden, C. A., S. Olsen, B. Hannegan, O. Wild, M. J. Prather, and J. Sundet (2000), Stratospheric ozone in 3-D models: A simple chemistry and the cross-tropopause flux, *J. Geophys. Res.*, *105*, 14,653–14,665.

McLinden, C. A., C. S. Haley, and C. E. Sioris (2006), Diurnal effects in limb scatter observations, *J. Geophys. Res.*, *111*, D14302, doi:10.1029/2005JD006628.

Murtagh, D., et al. (2002), An overview of the Odin atmospheric mission, *Can. J. Phys.*, *80*, 309–319.

NASA Langley Research Center (2002), SAGE III algorithm theoretical basis document (ATBD) solar and lunar algorithm, *Tech. Rep. LaRC-475-00-109, Version 2.1*, Hampton, Va.

Newchurch, M. J., et al. (1996), Stratospheric NO and NO_2 abundances from atmos solar-occultation measurements, *J. Geophys. Res.*, *23*, 2373–2376.

Nordh, H. L., et al. (2003), The Odin orbital observatory, *Astron. Astrophys.*, *402*, L21–L25, doi:10.1051/0004-6361:20030334.

Platt, U. (1994), Differential optical absorption spectroscopy (DOAS), in *Air Monitoring by Spectroscopic Techiques*, edited by M. Sigrist, pp. 27–84, John Wiley, Hoboken, N. J.

Pommereau, J. P., and F. Goutail (1988), O_3 and NO_2 ground-based measurements by visible spectrometry during arctic winter and spring 1988, *Geophys. Res. Lett.*, *15*, 891–894.

Pommereau, J. P., and J. Piquard (1994), Ozone, nitrogen dioxide and aerosol vertical distribution by UV-visible solar occultation from balloons, *Geophys. Res. Lett.*, *21*, 1227–1230.

Prather, M. J. (1992), Catastrophic loss of stratospheric ozone in dense volcanic clouds, *J. Geophys. Res.*, *97*, 10,187–10,191.

Randall, C. E., et al. (2002), Validation of POAM III NO_2 measurements, *J. Geophys. Res.*, *107*(D20), 4432, doi:10.1029/2001JD001520.

Randall, C. E., et al. (2005), Update on the SOSST Unified Data Base and Occultation Intercomparisons, paper presented at Solar Occultation Satellite Science Team Meeting, NASA, Washington, D. C.

Rodgers, C. D. (2000), *Inverse Methods for Atmospheric Sounding: Theory and Practise*, 1st ed., World Sci., Tokyo.

Russell, J. M., et al. (1993), The halogen occultation experiment, *J. Geophys. Res.*, *98*, 10,777–10,797.

Taha, G., L. W. Thomason, C. R. Trepte, and W. P. Chu (2004), Validation of SAGE III data products version 3.0, paper presented at Quadrennial Ozone Symposium, Int. Ozone Comm., Kos, Greece. (Available at http://ioc.atmos.uiuc.edu)

Thomason, L. W., and G. Taha (2003), SAGE III aerosol extinction measurements: Initial results, *Geophys. Res. Lett.*, *30*(12), 1631, doi:10.1029/2003GL017317.

Vandaele, A., et al. (1998), Measurements of the NO_2 absorption cross-section from 42000 cm^{-1} to 10000 cm^{-1} (238–1000 nm) at 220 K and 294 K, *J. Quant. Spectrosc. Radiat. Transfer*, *59*, 171–184.

Warshaw, G., D. Desaulniers, and D. Degenstein (1998), Optical design and performance of the Odin UV/visible spectrograph and infrared imager instrument, paper presented at 10th Annual Conference on Small Satellites, Am. Inst. of Aeronaut. and Astronaut., Logan, Utah. (Available at http://www.smallsat.org/proceedings)

A. Bazureau and F. Goutail, Service d'Aéronomie-Centre National de la Recherche Scientifique, Reduit de Verrières-BP3, 91371 Verrières le Buisson Cedex, France. (ariane.bazureau@aerov.jussieu.fr; florence.goutail@aerov.jussieu.fr)

S. M. Brohede and D. Murtagh, Department of Radio and Space Science, Chalmers University of Technology, SE-412 96 Göteborg, Sweden. (samuel.brohede@chalmers.se; donal.murtagh@chalmers.se)

L. Gordley, GATS Inc., 11864 Canon Boulevard, Suite 101, Newport News, VA 23606, USA. (larry@gats-inc.com)

C. Haley, Centre for Research in Earth and Space Science, York University, 4700 Keele Street, Toronto, Ontario, M3J 1P3, Canada. (cshaley@yorku.ca)

J. Lumpe, Computational Physics Inc., 1650 38th Street, Suite 105, Boulder, CO 80301, USA. (lumpe@cpi.com)

C. McLinden and C. Sioris, Environment Canada, 4905 Dufferin Street, Toronto, Ontario, M3H 5T4, Canada. (chris.mclinden@ec.gc.ca; csioris@cfa.harvard.edu)

S. Petelina and E. Llewellyn, Department of Physics and Engineering Physics, 116 Science Place, University of Saskatchewan, Saskatoon, Saskatchewan, S7N 5E2, Canada. (svetlana@osirus.usask.ca; edward.llewellyn@usask.ca)

C. Randall, Laboratory for Atmospheric and Space Physics, University of Colorado, Boulder, CO 80309-0392, USA. (cora.randall@lasp.colorado.edu)

G. Taha, Science Systems and Applications Inc., 10210 Greenbelt Road, Suite 400, Lanham, MD 20706, USA. (ghassan_taha@ssaihq.com)

L. Thomasson, Science Directorate, NASA Langley Research Center, Mail Stop 475, Hampton, VA 23681-2199, USA. (l.w.thomasson@nasa.gov)

Appendix G

Paper VII

Status of the Odin/OSIRIS stratospheric O_3 and NO_2 data products

Craig S. Haley and Samuel Brohede

Can. J. Phys.

85, 1177-1194, doi:10.1139/P07-114, 2007

Status of the Odin/OSIRIS stratospheric O_3 and NO_2 data products[1]

Craig S. Haley and Samuel Brohede

Abstract: This paper describes the status of the stratospheric ozone and nitrogen dioxide data products from the Optical Spectrograph and InfraRed Imager System (OSIRIS) instrument on the Odin satellite. The current version of the data products is 3.0, covering the period from November 2001 to the present. The O_3 and NO_2 retrieval methods are reviewed along with an overview of the error analyses and geophysical validation status.

PACS Nos.: 07.05.Kf, 07.87.+v, 42.68.Mj, 92.60.hd, 92.60.Ta, 92.60.Vb, 92.70.Cp, 95.75.Fg, 95.75.Rs

Résumé : Nous décrivons ici l'état des données sur l'ozone et le dioxyde d'azote dans la stratosphère, tels qu'obtenus par l'instrument de spectrographie optique et d'imagerie infrarouge (OSIRIS) embarqué à bord du satellite Odin. La présente version des données est notée 3.0 et couvre la période allant de novembre 2001 jusqu'à maintenant. Nous décrivons les méthodes pour extraire les données sur O_3 et NO_2 et passons en revue l'analyse d'erreurs ainsi que l'assignation géophysique des données.

[Traduit par la Rédaction]

1. Introduction

The Optical Spectrograph and InfraRed Imager System (OSIRIS) instrument on the Odin satellite has been in orbit since February 2001 and has been operating nominally since November 2001 [1, 2]. Since launch, great effort has gone into retrieving stratospheric species information from the OSIRIS measurements. To date, stratospheric O_3, NO_2, and aerosol number density profiles have been successfully retrieved and other species, including BrO and OClO, are under investigation.

The initial OSIRIS O_3 retrievals were undertaken by von Savigny et al. [3]. The retrieval technique was adapted from the O_3 retrieval algorithm used for the SOLSE/LORE instrument that flew on the NASA shuttle [4], and involves measurements at three wavelengths in the Chappuis band of O_3 combined with a Maximum A Posteriori (MAP) solver [5]. The initial OSIRIS NO_2 retrievals were carried

Received 23 February 2007. Accepted 9 July 2007. Published on the NRC Research Press Web site at http://cjp.nrc.ca/ on 17 October 2007.

C.S. Haley.[2] Centre for Research in Earth and Space Science, York University, 4700 Keele Street, Toronto, ON M3J 1P3, Canada.
S. Brohede. Department of Radio and Space Science, Chalmers University of Technology, SE-412 96 Göteborg, Sweden.

[1]This original article is from work that highlights some of the science that has been produced in the last couple of years using the Odin satellite.

[2]Corresponding author (e-mail: cshaley@yorku.ca).

 doi: 10.1139/P07-114

out by Sioris et al. [6] using Differential Optical Absorption Spectroscopy (DOAS) [7] combined with a Chahine-type solver [8]. These initial analyses were carried out on relatively small samples of preliminary OSIRIS data. Following the initial studies, a data retrieval software package for OSIRIS was developed for MATLAB® [9, 10] and became the operational software, producing the official Level 2 O_3 and NO_2 products. More recently, the software package has been used to retrieve OClO [11] and BrO [12] and to study polarization [13], diurnal effects [14], and NO_3.[3] Alternative processing algorithms for stratospheric O_3 and NO_2 have been developed at the University of Saskatchewan [15][4] and the Finnish Meteorological Institute (FMI) [16][5].

The O_3 and NO_2 data products are publicly available at http://osirus.usask.ca and have been used in a number of intercomparison activities [17–24] and scientific studies [25–30]. The version 3.0 data set currently contains approximately 318 000 O_3 profiles and 312 000 NO_2 profiles.

The purpose of this paper is to present the status of the version 3.0 OSIRIS O_3 and NO_2 data products, including a brief description of the retrieval techniques and an overview of the current error estimates and validation status.

2. OSIRIS Instrument

The OSIRIS instrument has been described in detail elsewhere (see, for example, refs. 1, 31) and is only briefly introduced here.

OSIRIS was launched in February 2001 on the Odin spacecraft [2] into a 610 km Sun-sychronous, near-terminator orbit with a 97.8° inclination and a 18:00 ascending node. Odin divides its time equally between aeronomy and astronomy studies [32]. OSIRIS is only used for aeronomy studies, while the other instrument on Odin, the Sub-millimetre and Millimetre Radiometer (SMR) [33] is used for both aeronomy and astronomy.

OSIRIS consists of two optically independent components, the Optical Spectrograph (OS) and the InfraRed Imager (IRI). The OS is a grating spectrometer that primarily measures sunlight scattered from the Earth limb over the spectral range 280 to 800 nm with a resolution of about 1 nm, sampled at 0.4 nm intervals. OS measurements are obtained over a tangent height range of 7 to 70 km in the normal stratosphere mode, through controlled nodding of the Odin spacecraft. Other modes include a mesospheric mode, in which the scanning covers 60–110 km, and a stratosphere–mesosphere mode, in which the scanning covers 7–110 km. OS measurements from the stratosphere and stratosphere–mesosphere modes are used for the stratospheric retrievals. The OS measurements are made with an instantaneous vertical resolution of about 1 km and a horizontal (cross-track) resolution of about 40 km. The OS operates with a quasi auto-exposure technique, where the detector exposure times are varied autonomously to account for the strong change in limb-scatter radiance with tangent height. Due to the varying exposure times combined with the nodding motion of the spacecraft, the effective vertical resolution of the limb-scatter measurements varies from about 1 km at 7 km to 2.5 km at 70 km.

Since the OS generally measures limb-scattered sunlight and the Odin spacecraft is in a near-terminator orbit, the measurements (which are normally made in the orbit plane) are hemispheric in nature, with the northern hemisphere sampled between mid-February and mid-October and the southern hemisphere sampled between mid-October and mid-February. There are short periods in February and October where near-global coverage is obtained (82.2°N to 82.2°S). In addition, scheduled off-plane pointing provides measurements all the way to the pole in the southern hemisphere at certain time

[3] C.A. McLinden and C.S. Haley. Odin/OSIRIS observations of stratospheric NO_3 through sunrise and sunset. Manuscript in preparation.

[4] D. Degenstein, A. Bourassa, C. Roth, N. Lloyd, D. Gattinger, and E.J. Llewellyn. Yet another NO_2 retrieval from OSIRIS. Third International Atmospheric Limb Workshop, Montréal, 25-28 April 2006.

[5] S. Tukiainen, S. Hassinen, A. Seppälä, H. Auvinen, E. Kyrölä, J. Tamminen, C.S. Haley, N.D. Lloyd, and P.T. Verronen. Description and validation of a limb scatter retrieval method for Odin/OSIRIS. Manuscript in preparation.

Fig. 1. The latitudinal and temporal coverage of the OSIRIS version 3.0 data products from November 2001 to December 2006, where sunrise measurements (AM) are shown in the upper panel and sunset measurements (PM) are shown in the lower panel. White regions indicate no OSIRIS measurements. Full global coverage is achieved near the equinoxes and hemispheric (summer hemisphere) coverage is achieved elsewhere. Note the gradual loss of PM measurements as the equator-crossing time of the Odin orbit drifts over time.

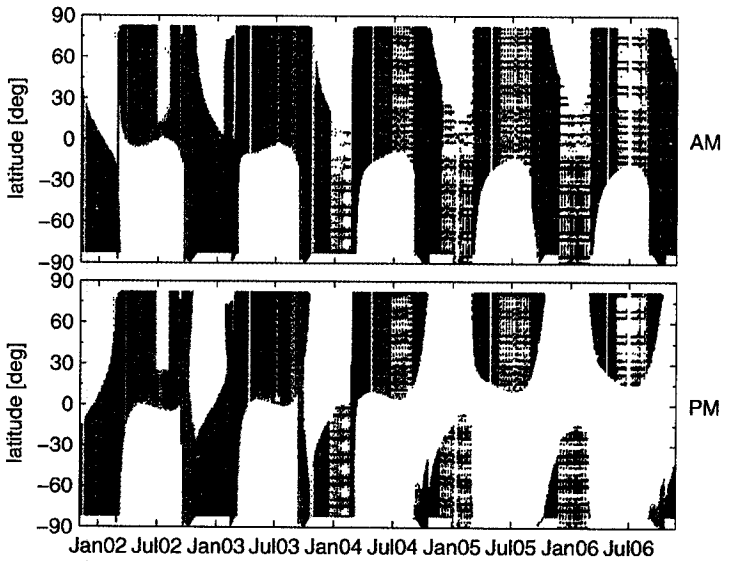

periods. The actual latitudinal coverage of OSIRIS from November 2001 to December 2006 is shown in Fig. 1. The impact of the precession of the Odin orbit through the mission is clear in Fig. 1, leading to better coverage in the AM, and poorer coverage in the PM. This is of particular importance for NO_2.

3. Retrieval method

Retrieving stratospheric minor species concentrations directly from the absolute limb-scattered radiance measurements is challenging. This is largely due to the strong sensitivity of the measured signal to many parameters, including neutral density, aerosol, albedo, and instrument calibration. The solution used for OSIRIS has been to transform the radiance measurements to intermediate quantities prior to the inversion to number density profiles. These intermediate quantities are designed to maximize the sensitivity to the target species (O_3 or NO_2) while minimizing the sensitivity to other parameters. An overview of the O_3 and NO_2 retrieval specifications is given in Table 1.

3.1. Measurement transformation functions

All OSIRIS Level 1 data (calibrated limb-scattered radiances) in which the Solar Zenith Angle (SZA) at the tangent point is less than 92° are processed. A large amount of data filtering and checking is carried out on the Level 1 data prior to the application of the transformation functions. In particular, the Level 1 data are checked for processing flags, large gaps in the tangent height sampling, and any other scanning problems. Scans where the satellite was in the South Atlantic Anomaly (SAA) and where the Moon was in or near the instrument Field of View (FOV) are flagged. In addition, scans where the temperature of the instrument optics was not within the nominal range (generally during the period where the Odin spacecraft experiences eclipse) are flagged since this leads to errors in the assumed

Table 1. Summary of the O_3 and NO_2 retrieval specifications.

	O_3	NO_2
Method	Chappuis triplet	DOAS
Wavelengths	540.2, 602.0, 663.9 nm†	435–451 nm
Corrections	n/a	Tilt, I_0, λ-shift
Fitted species	n/a	O_3, NO_2, O_4
Reference height	nearest above 46 km	46–65 km avg.
Retrieval range	10–46 km‡	10–46 km‡
Estimating $\boldsymbol{K}$	SS, no aerosol	2 λ, SS, no aerosol
Estimating $\boldsymbol{F}$	no pixel averaging	2 nm grid
a priori uncert.	40%	60%
Response > 0.75	~10–42 km	~12–44 km
Resolution at 25 km	~2 km	~2 km
Total error at 25 km	~6%	~10%

†3-pixel averages centred at each wavelength are used.
‡If no cloud is detected, otherwise the cloud top is used to set the lower limit.

instrument spectral resolution.[6] The spacecraft attitude information (pointing) is also checked using the so-called "knee" method [6], and scans where large tangent height offsets (>2 km) are found are flagged. However, no correction is applied due to uncertainties in the knee method, which are on the order of the nominal Odin attitude control performance.

Each scan is analyzed for clouds using the OS radiances near 807 nm. The radiance scale height is determined and the highest tangent height at which the scale height is less than 4.5 km is identified as the cloud top if the tangent height is no more than 3 km above a climatological tropopause [34] (to prevent the misidentification from polar stratospheric clouds or stratospheric aerosol). The derived cloud top is used to define the lower altitude limit of the retrievals. Scans in which clouds have been identified are also flagged to indicate that the climatological surface albedo used in the processing may not be accurate. The scale height threshold value of 4.5 km was determined to be overly sensitive and often results in an over-estimation of both cloud occurrence and cloud height in the version 3.0 products. Future versions will use a value of 3.84 km, as suggested by Sioris et al. [30].

The effect of atmospheric refraction on the limb radiances is addressed in the retrievals. The most important effect is the shift of the tangent point downwards compared to the geometric case, generally leading to larger radiances. A secondary effect is the shift of the tangent point horizontally combined with the modification of the paths through the atmospheric layers. The vertical shift is addressed by determining the refracted tangent heights, t_h^{refr}, from the geometric tangent heights, t_h, provided in the OS Level 1 data by solving

$$(R_e + t_h^{refr}) \times n_{tp}(t_h^{refr}, \lambda) = R_e + t_h \tag{1}$$

for t_h^{refr}, with

$$n_{tp}(z, \lambda) - 1 = [n_{air}(\lambda) - 1] \times \frac{P(z)}{96095.43} \times \frac{1 + 10^{-8} \times [0.601 - 0.00972 \times T(z)] \times P(z)}{1 + 0.003661 \times T(z)} \tag{2}$$

[6]E.J. Llewellyn and R.L. Gattinger. OSIRIS/UVIS Optics Bench Temperature Effects On Wavelength Stability and Spectral Resolution. OSIRIS Technical Note (2000).

and

$$n_{\text{air}}(\lambda) - 1 = 10^{-4} \times \left[0.7041 + \frac{3.159}{157.39 - (\lambda * 10^{-3})^{-2}} + \frac{8.4127}{50.429 - (\lambda * 10^{-3})^{-2}}\right] \quad (3)$$

where λ is the wavelength (nm), R_e is the Earth radius, n_{air} is the index of refraction for dry standard air [35], and n_{tp} is the index of refraction at pressure P (Pa) and temperature T (°C) at altitude z [36, 37]. The effect of the horizonal shift and path length modifications are not addressed, but are expected to be small.

The measurement transformation functions for the O_3 and NO_2 retrievals are different, largely because the former has strong absorption signatures and can benefit from a more direct approach than can the latter.

3.1.1. O_3 Chappuis Triplet

For the O_3 retrievals, the method described by von Savigny et al. [3] is used. In this method, radiances measured at three wavelengths in the Chappuis–Wolf bands of O_3 are transformed into the so-called Chappuis Triplet, C_T:

$$C_T(t_h) = \ln\left[\frac{I(t_h, \lambda_2)}{I_0(\lambda_2)}\right] - \left\{w_1 \times \ln\left[\frac{I(t_h, \lambda_1)}{I_0(\lambda_1)}\right] + w_3 \times \ln\left[\frac{I(t_h, \lambda_3)}{I_0(\lambda_3)}\right]\right\} \quad (4)$$

where $I(t_h, \lambda)$ is the limb radiance measured at tangent height t_h and wavelength λ and I_0 is the reference taken from a high tangent height within the scan. w_1 and w_3 are weighting factors determined from the selected wavelengths, i.e.,

$$w_1 = \frac{\lambda_3 - \lambda_2}{\lambda_3 - \lambda_1} \quad (5a)$$

$$w_3 = 1 - w_1 \quad (5b)$$

The limb radiance measurement errors are propagated through equation 4 to determine the uncertainties in C_T, which are assumed to be independent for each tangent height. This formulation and the use of a reference measurement from within the scan significantly reduce the sensitivity of the retrievals to parameters including absolute instrument calibration, albedo, polarization, and aerosol [3, 4, 38, 39].

The application of the triplet method here differs somewhat from that presented in ref. 3. Instead of single-pixel measurements at 532.2, 602.0 and 671.2 nm, 3-pixel averages centred at 540.2, 602.0, and 663.9 nm are used. These wavelengths minimize possible impacts from O_4 and H_2O absorption at the lowest tangent heights and the pixel-averaging reduces the sensitivity to radiance outliers. The lower limit of the retrieval range is selected as the higher of 10 km or the lowest cloud-free tangent height. The upper limit is chosen as 46 km and the reference is taken as the nearest measurement above 46 km. The triplet errors are adjusted above 30 km by increasing the errors (in quadrature) by a linearly increasing amount (0–1%) up to 35 km and a fixed 1% above. It was found that this additional error was necessary to reduce a systematic underestimation in the retrieved number density profiles at the corresponding altitudes. This is a compromise between the desire to base the uncertainties on the Level 1 limb radiance errors and the original application in ref. 3, where an uncertainty of 1% was used at all tangent heights. The exact cause of the underestimation is not known, but it is believed to be due to baffle (or out-of-field) scattering,[7] where light from outside of the nominal FOV contaminates the

[7] E.J. Llewellyn, R.L. Gattinger, D.-L. Desaulniers, and G. Warshaw. Estimated OSIRIS UVIS Baffle On-Orbit Performance. OSIRIS Technical Note (1998).

measurement. At high tangent heights and at the red end of the spectrum this source can dominate the true signal. No satisfactory correction for this contamination has been found. The baffle scatter causes a positive bias in the triplet, leading to an underestimation in the retrieved O_3. More discussion on the impact of baffle scatter follows in Sect. 5.

3.1.2. NO_2 effective column density

For NO_2, the Differential Optical Absorption Spectroscopy (DOAS) technique of Platt [7] is used to calculate effective column densities (ECDs), also referred to as Slant Column Densities (SCDs), as a function of tangent height from the measured limb radiances in the 435–451 nm region. In the DOAS approach, the differential optical depth, τ, can be expressed as

$$\tau(t_h, \lambda) = \ln\left[\frac{I(t_h, \lambda)}{I_0(\lambda)}\right] = \sum_{i=1}^{n} \sigma_i(\lambda) c_i(t_h) + P_n(t_h, \lambda) \tag{6}$$

where σ_i is the absorption cross section of species i, c_i is the ECD of species i, I_0 is the reference and P_n is the polynomial used to effectively remove the smoothly varying components of τ and σ. Equation (6) is solved using a least-squares approach to determine c and the associated uncertainties. The reference is taken as the average of all measurements between 46 and 65 km to reduce noise. Again, the use of a reference from within the scan proves extremely beneficial, removing the need for an absolute calibration of the instrument. The sensitivity to aerosol and other parameters that vary slowly with wavelength is reduced by the DOAS approach itself, but the reference also reduces sensitivity to other issues, including the Ring effect.

The determination of NO_2 ECDs from OSIRIS measurements is described in detail in ref. 9. Some minor modifications have been made for version 3.0, including accounting for the tangent height variation of the tilt or undersampling effect [11] and checking the χ^2 of the DOAS fits, where tangent heights with values of $\chi^2 > 4$ are discarded from further analysis. Also, the lower limit of the retrieval range is selected as the higher of 10 km or the lowest cloud-free tangent height (the upper limited is chosen as 46 km).

3.2. Inversion algorithm

The O_3 triplets and NO_2 ECDs, as a function of tangent height, are inverted to number density profiles using the Maximum A Posteriori (MAP) optimal estimation solver [5]. In this solver, the measurements are combined with a priori information to compute the optimal solution, $\hat{\boldsymbol{n}}$, and covariance matrix, $\hat{\mathbf{S}}$, which are found by iterating

$$\boldsymbol{n}_{i+1} = \boldsymbol{n}_a + \mathbf{G}_i\left[\boldsymbol{y} - \boldsymbol{F}(\boldsymbol{n}_i) + \boldsymbol{K}_i(\boldsymbol{n}_i - \boldsymbol{n}_a)\right] \tag{7}$$

$$\mathbf{S}_{i+1} = \mathbf{S}_a - \mathbf{G}_i(\boldsymbol{K}_i\mathbf{S}_a) \tag{8}$$

$$\mathbf{G}_i = \mathbf{S}_a\boldsymbol{K}_i^T(\boldsymbol{K}_i\mathbf{S}_a\boldsymbol{K}_i^T + \mathbf{S}_\epsilon)^{-1} \tag{9}$$

where $\boldsymbol{n}_a$ is the a priori state, $\mathbf{S}_a$ is the a priori covariance matrix, $\mathbf{S}_\epsilon$ is the covariance matrix of the measurement uncertainty, $\mathbf{G}$ is the gain matrix, $\boldsymbol{F}$ is the forward model calculation, and $\boldsymbol{K}$ are the weighting functions. $\boldsymbol{y}$ represents either the O_3 triplet, $C_T(t_h)$, or the NO_2 ECDs, $c(t_h)$. The radiative transfer model LIMBTRAN [40] is used to calculate $\boldsymbol{F}$ and $\boldsymbol{K}$.

A detailed description of the solver configuration, including convergence criteria and additional constraints used for both retrievals, is given in ref. 9. In brief, the O_3 triplet retrievals are carried out with the approximation of an aerosol-free, single-scattering (SS) atmosphere in the calculations of $\boldsymbol{K}$. In addition, the pixel-averaging is not simulated in the determination of $\boldsymbol{F}$ and $\boldsymbol{K}$ and an a priori uncertainty of 40% is assumed. The NO_2 retrievals also assume an aerosol-free, single-scattering atmosphere when calculating $\boldsymbol{K}$. A two wavelength DOAS approach is used in the weighting function calculations, while

wavelengths at 2 nm steps over the wavelength region are used when calculating $\boldsymbol{F}$. The NO_2 a priori uncertainty is set at 60% (reduced from 80% in ref. 9). Changes from the description in ref. 9 include the application of a Levenberg–Marquardt iterative solution if 7 fails to converge, as described in ref. 11, and the variation of the SZA with tangent height in LIMBTRAN when conditions warrant.

Though not mentioned in ref. 9, it should be noted that for the NO_2 retrievals the reference averaging is not simulated. Instead, a representative tangent height is determined considering the radiance scale height and sampling, and simulated radiances at this representative tangent height are used as the reference in the determination of $\boldsymbol{F}$ and $\boldsymbol{K}$. It should also be noted that no albedo and aerosol wavelength dependence is accounted for in LIMBTRAN, i.e., all wavelengths in a particular simulation use the same aerosol extinction and albedo values.

3.3. Retrieval characterization

Each retrieved profile is characterized by the measurement response (approximately the inverse of the level of a priori contamination) and the vertical resolution as described in [9], and this information is provided in the data product. Retrievals with high response (>0.75) and good vertical resolution (<5 km) are generally obtained between 10 and 42 km for O_3 and 12 and 44 km for NO_2, though these ranges vary somewhat with latitude and season. Figure 2 shows retrieval and characterization information for a typical OSIRIS scan.

3.4. Data set issues

The version 3.0 O_3 and NO_2 products contain all retrievals that are found to meet the convergence criteria and the version 3.0 retrievals are well behaved with few outliers. However, the following issues have been identified in the version 3.0 data:

- Infrequent periods of bad pointing, particularly in August/September 2005 (these are flagged).
- Effects of radiation hits on the detector (only those in the SAA are flagged).
- Oversensitive cloud algorithm, leading to misidentifications.
- Missing data in the tropics due to an overly stringent data filtering.
- Missing 10 km altitude level in some profiles due to an overly stringent data filtering.
- Pointing issue (~200–500 m offset) in the Odin eclipse season (May–July) [41].
- Variable vertical resolution due to the inversion from a variable tangent height grid to a fixed altitude grid.

There are also potential issues with retrievals in the vortex regions due to poor a priori information, in particular, the assumed a priori covariance. Retrievals in regions of strong horizontal gradients, for example, across the vortex edge, are also suspect due to the horizontal homogeneity assumption in the retrievals.

4. Error estimates

An analysis of the sensitivity to the various sources of error is an essential part of any retrieval technique. Following ref. 5, four sources of error are considered;

- smoothing error
- measurement error

Fig. 2. Retrieval characteristics for the O_3 (upper panels) and NO_2 (lower panels) version 3.0 retrievals for a typical OSIRIS scan (6045012). The error bars in panels (*a*) and (*d*) show the 1σ standard deviation of the combined smoothing and measurement errors.

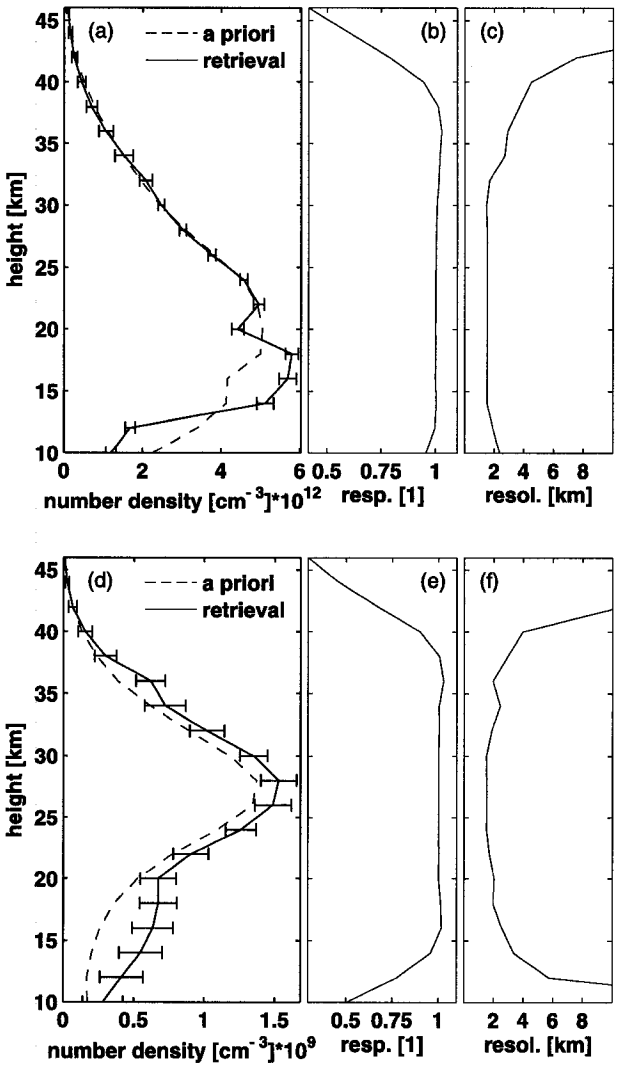

- forward model error
- forward model parameter error

The smoothing error is the error due to the limited resolution of the retrieval compared to the true state. The measurement error is the measurement noise propagated through the retrieval process. The forward model error is the error due to approximations made in the forward model. The forward model parameter error is the error due to uncertainties in the various input parameters of the forward model. The total error is estimated as the square root of the sum of the four variances. The retrieval error, or the combination of the smoothing error and the measurement error, is easily determined and is given

by equation 8. The forward model (FM) error and forward model parameter (FMP) error, however, are more difficult to determine.

A detailed analysis of the errors in the NO_2 retrievals is presented in ref. 9. A similar analysis was performed on the initial OSIRIS O_3 retrievals in ref. 38 and on the triplet technique in general in ref. 39. Here, the results of ref. 9 are summarized and the same methodology is applied to the version 3.0 triplet O_3 retrievals.

The FM error is estimated by considering the impact of simplifications and approximations used in the forward model, including the neglect of spectral convolution, the number of line-of-sight (LOS) points used in LIMBTRAN, the neglect of the OSIRIS vertical resolution, and the choice of atmosphere grid in LIMBTRAN, as well as any biases in the retrieval algorithm. In this study, the impact of the neglect of polarization in the retrievals was added to the analysis, and was found to be small ($<1\%$ for O_3 and $<3\%$ for NO_2), consistent with the findings of ref. 38. The individual components of the FM error are not presented here, since this component of the total error is relatively small, with the total FM error found to be $<2\%$ for O_3 and $<6\%$ for NO_2, and the dominant sources of error being the atmosphere grid step size (1 km is used in both retrievals).

The FMP error is estimated by performing perturbations (one standard deviation) to a number of forward model parameters about a mid-latitude atmosphere with surface albedo 0.3 with the following assumptions:

- Uncertainties in aerosol (30%), neutral density (10%) and temperature (5 K);
- A 10% uncertainty in the surface albedo (with no clouds);
- Uncertainties of 10% in the instrument spectral resolution and 3% in the O_3 and NO_2 cross sections;
- A 500 m uncertainty in the tangent height registration.

In addition, the impact of cloud on the retrievals is estimated in a preliminary way by perturbing the surface albedo to a value of 0.6 (reduced from 1.0 in ref. 9, since this value was excessive). The sensitivity of the retrievals to interfering species was added to the analysis in ref. 42. The main interfering species for the O_3 retrievals is NO_2 and the main interfering species for the NO_2 retrievals is O_3. In both cases, an uncertainty of 50% was assumed, resulting in errors of less than 1%. In this study, the signal-to-noise ratio used in the calculations was updated to better reflect the OSIRIS performance.

Figures 3 and 4 show the FMP errors and the total errors, respectively, for the O_3 and NO_2 retrievals for low-sun (SZA = 90°) and high-sun (SZA = 60°) scenarios. The error for the worst-case single-scattering angle (SSA) was used in all cases. From Fig. 3 the largest source of FMP error is the pointing uncertainty. The total error for the O_3 retrievals is estimated to be 6% at about 24 km, increasing roughly linearly to 12–14% at 10 km and 33% at 44 km. The total error for the NO_2 retrievals is estimated to be 10% at 25 km, increasing roughly linearly to 33–35% at 10 km and 50% at 46 km.

A source of error in the NO_2 retrievals not included in the above error estimate is that due to diurnal variations [14, 42]. This source of error is highly dependent on the observation conditions and thus difficult to quantify generally. However, the error is relatively small ($<10\%$) above 25 km and is at most 45%, with the maximum error located at the lowest altitudes, putting this error source on par with the estimated NO_2 total error. More importantly, the observation conditions where the diurnal errors are significant below 25 km ($>10\%$) are only present for about 16% of OSIRIS data [14], primarily at the solstices near the equator.

5. Validation results

A validation study of the version 2.4 NO_2 data [42] estimated the OSIRIS random and systematic uncertainties through comparisons with a number of solar occultation instruments. For O_3, validation

Fig. 3. Forward model parameter errors for the OSIRIS O_3 (upper panels) and NO_2 (lower panels) retrievals due to uncertainties in aerosol, albedo/cloud, neutral density, temperature, tangent height registration (pointing), spectral resolution, cross section, and interference from O_3 or NO_2, given as 1σ, and the total forward model parameter error, given by the square root of the sum of the individual variances. The calculations were carried out for high-sun (SZA=60°, panels *a* and *c*) and low-sun (SZA=90°, panels *b* and *d*) scenarios.

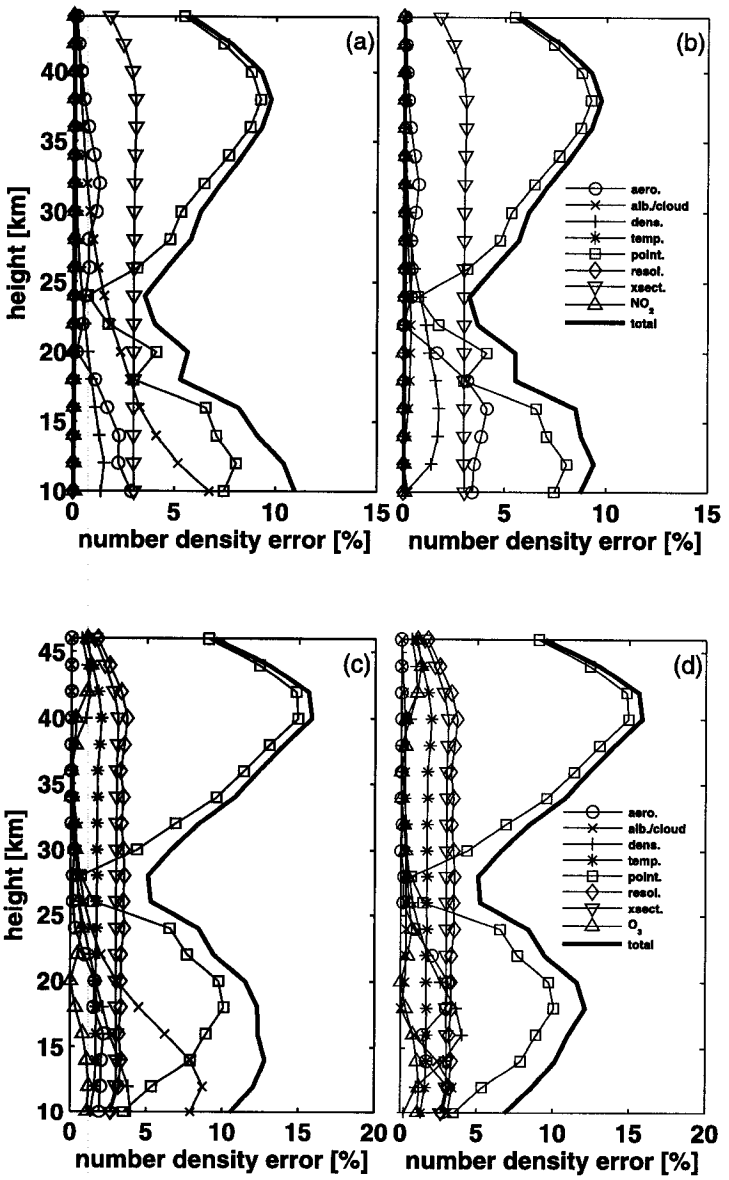

studies were carried out on an older version (1.2) of data in refs. 43 and 17. A detailed geophysical validation of the version 3.0 O_3 and NO_2 data is beyond of the scope of this study. Instead, the analysis

Fig. 4. Total error estimates (1σ) for OSIRIS O_3 (upper panels) and NO_2 (lower panels) retrievals. The four main error sources are included; the smoothing error, the measurement error, the forward model error, and the forward model parameter error. The total error corresponds to the square root of the sum of the four variances. The calculations were carried out for high-sun (SZA=60°, panels *a* and *c*) and low-sun (SZA=90°, panels *b* and *d*) scenarios.

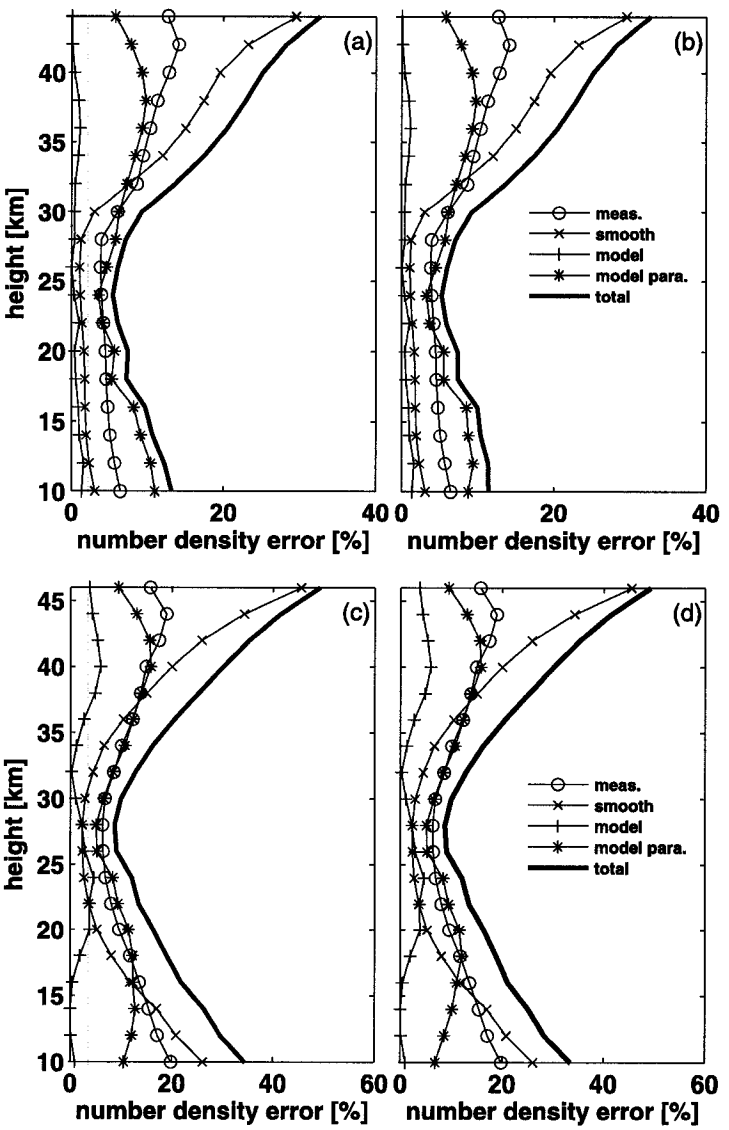

methodology used in ref. 42 has been applied to the version 3.0 data to provide estimates of the OSIRIS random and systematic uncertainties.

The O_3 and NO_2 data sets were compared with measurements from the Halogen Occultation Experiment (HALOE) [44], the Stratospheric Aerosol and Gas Experiment (SAGE) II [45] and III [46], and the Polar Ozone and Aerosol Measurement (POAM) III instrument [47]. Table 2 gives details on these

Table 2. Summary of the specifications of the satellite instruments in this study.

	HALOE	SAGE II	SAGE III	POAM III
Geometry	solar occ.	solar occ.	solar/lunar occ.	solar occ.
Meas. type	4 rad. + 4 gas corr.	7 channels	full spectr.	9 channels
Satellite	UARS	ERBS	Meteor-3M	SPOT-4
Launch	Sep. 1991	Oct. 1984	Dec. 2001	Mar. 1998
Orbit type	precessing	precessing	sun synchr.	sun synchr.
Eq. cross. time	—	—	09:00	22:30
Data version	19	6.20	3	4

measurements. Comparisons with ozonesonde data from the World Ozone and Ultraviolet Radiation Data Centre (WOUDC) were also included. The coincidence criteria used were a difference in time of measurement of less than 4 h and in distance between the measurements of less than 500 km. In addition, coincidences were restricted to cases where the total column O_3 at the two measurement locations was less than 20 Dobson Units (DU), with the total ozone information taken from the Earth Probe Total Ozone Mapping Spectrometer (EP-TOMS) [48] and the Ozone Monitoring Instrument (OMI) [49]. This differs from the analysis of ref. 42, where a time criterion of 2 h was used and no total ozone restriction was applied. When multiple coincidences with a particular OSIRIS measurement occurred, the closest in distance was chosen. Only OSIRIS data with good response (>0.75) and resolution (<5 km) were included. In addition, OSIRIS profiles where potentially large tangent height offsets were indicated (flagged) in the data sets were not considered. For NO_2, the coincidences were further constrained to cases where the local times of the measurements were both near sunrise (AM) or sunset (PM) to limit the impact of diurnal scaling errors (see below). All OSIRIS measurements from 2001 to 2006 were considered, providing 1290 SAGE II coincidences, 3306 SAGE III coincidences, 2444 POAM III coincidences, 1501 HALOE coincidences, and 535 coincidences with the WOUDC ozonesondes for O_3. For NO_2, 1060 SAGE II coincidences, 2784 SAGE III coincidences, 1334 POAM III coincidences, and 1548 HALOE coincidences were found.

For NO_2, it is important that the comparisons not only occur close in time and space, but also that they occur under the same SZA conditions because of the strong diurnal cycle of NO_2. To aid in this, the OSIRIS NO_2 measurements were scaled to 90° SZA using output from the University of California, Irvine, photochemical (stacked) box model [50, 51] (more details can be found in ref. 42). In addition, occultation measurements of NO_2 are strongly affected by the variations in NO_2 along the measurement line of sight, which adds a bias to the retrieved profiles. A correction similar to that described in ref. 42 was applied to each occultation profile except for HALOE, which accounts for this variation [52]. This differs from the treatment in ref. 42, where only representative corrections were determined for various latitude/season conditions. The OSIRIS NO_2 measurements are also affected by diurnal variations both along the measurement line of sight and along the incoming solar beam [14]. However, as noted in Sect. 4, this error is generally small and for the comparisons here is dominated by the solar occultation correction, and was thus not considered. Because of the large differences in concentraion, the AM and PM NO_2 measurements were treated separately in the analysis.

The coincidences were separated into the three latitude bins: 90°S–30°S, 30°S–30°N, and 30°N–90°N, and four season bins: November–December–January (NDJ), February–March (FM), April–May–June–July–August (AMJJA), and September–October (SO) used in ref. 42. In each latitude/season bin the mean and standard deviation of the differences between OSIRIS and each instrument were determined at every altitude. The mean and standard deviation of the differences for all coincidences are shown in Fig. 5. From these statistics the OSIRIS random and systematic uncertainties were estimated for three altitude regions: 12–25 km (15–25 km for NO_2), 25–35 km, and 35–40 km (35–45 km for NO_2). Following ref. 42, the random uncertainties were estimated by assuming that the instrument and

Fig. 5. Results from all coincidences between OSIRIS O_3 (upper panels) and NO_2 (lower panels) and HALOE, POAM III, SAGE II, SAGE III, and WOUDC ozonesondes from 2001 to 2006, expressed as the mean (panels *a*, *b*, *d*, and *e*) and standard deviation (panels *c* and *f*) of the differences (Instrument–OSIRIS). The coincidence criteria used were 4 h, 500 km, and 20 DU.

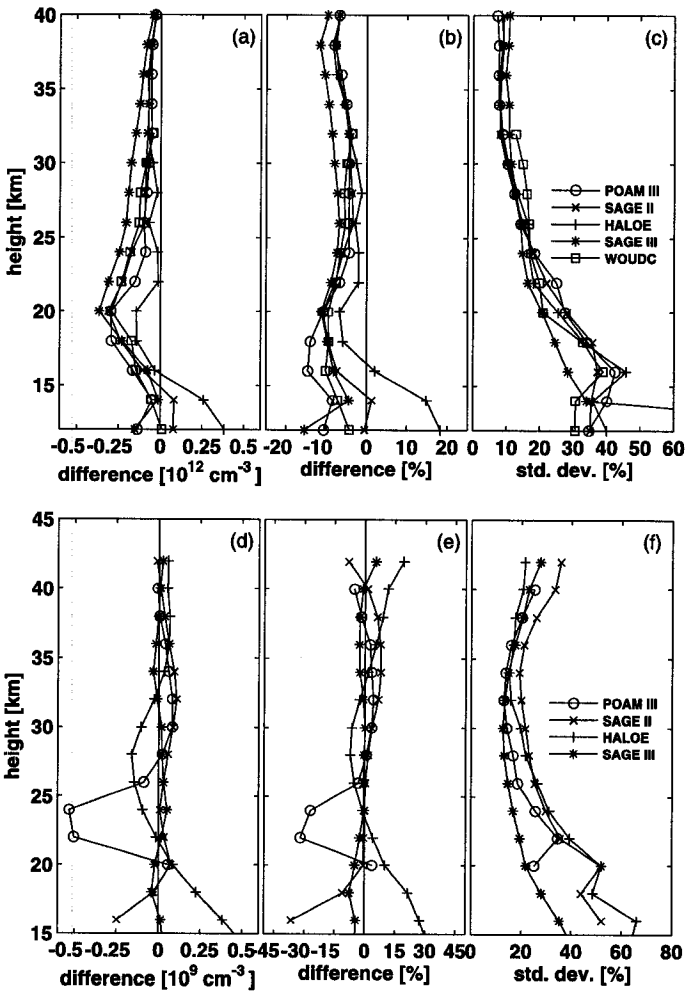

latitude/season bin with the smallest standard deviation represents an estimate of the random uncertainty, with OSIRIS and the other instrument contributing equally to the standard deviation. The random uncertainty is then given by:

$$\epsilon_{OS}(z) = \sqrt{\frac{\Delta_\sigma^2(z)}{2}} \tag{10}$$

where $\Delta_\sigma(z)$ is the standard deviation of the differences at altitude z. The systematic uncertainty is estimated from the range of the maximum absolute mean differences from all of the instruments. More discussion of the methodology can be found in ref. 42. The results of the analysis are presented in Table 3.

Table 3. Estimated systematic and random (1σ) uncertainties of the OSIRIS O_3 and NO_2 version 3.0 data products in percent, based on comparisons with SAGE II, SAGE III, HALOE, POAM III, and WOUDC ozonesondes as described in the text.

(km)	Random (%)		Systematic (%)	
O_3				
35–40	4		10–18	
25–35	5		8–15	
12–25†	9		17–36	
NO_2	PM	AM	PM	AM
35–45	8	10	13–33	30
25–35	7	9	7–40	22–29
15–25‡	14	—	20	—

†HALOE results have been excluded.
‡Only comparisons with SAGE III are included.

As mentioned above, validation studies have been carried out on the version 1.2 O_3 data product. In ref. 43 the version 1.2 O_3 product was compared with POAM III and ozonesonde data for the period November 2001 to October 2002. Only mean differences were assessed in this study, finding differences of 7–25% between 12 and 15 km, 5–7% between 15 and 32 km, and ~15% between 32 and 40 km. Larger differences were found in the May–July 2002 period, due to an apparent downward vertical shift in the OSIRIS profiles. In ref. 17 the version 1.2 O_3 product was compared with SAGE III for the period February–August 2004. Both mean differences and the standard deviation of the differences were assessed, but only over the 22–28 km altitude range, where mean differences of 5–10% and standard deviations of 5–14% were found. Though not mentioned in ref. 17, the OSIRIS profiles were shifted by ~0.7–1.3 km to account for an apparent spacecraft pointing drift error. In both studies, the OSIRIS profiles were found to have a fairly substantial negative bias (up to 20%) above 32 km.

The O_3 retrieval algorithm has changed in a number of areas between version 1.2 and version 3.0, with the primary changes being new spacecraft attitude data (correcting the pointing drift error), the use of the Level 1 OSIRIS radiance uncertainties (a fixed 1% uncertainty was assumed in version 1.2), different a priori information (a diagonal covariance matrix with uncertainties of 100% was assumed in version 1.2), a lower reference height (50 km was used in version 1.2), and significantly more quality control.

It is difficult to compare the current results for the version 3.0 data set directly with the previous results due to different coincidence criteria and analysis methodology. However, the results of the analysis here are in general agreement with the previous studies. The version 3.0 data set shows improved overall performance, particularly at high altitudes where the reported underestimation above 32 km appears to have been reduced by the use of a lower reference tangent height (thus reducing the impact of baffle scatter, discussed below), and with the resolution of the pointing drift error. Note that the HALOE results were not included in determining the random and systematic uncertainties in the 12–25 km region because of inconsistent results in some latitude and (or) season bins. The results are also consistent with the detailed comparison of the version 3.0 data with ozonesondes in ref. 41, where the OSIRIS O_3 uncertainties are found to be 20–25% at 12 km, about 4–6% in the middle-stratosphere, and 7–9% at 35 km. Note that the uncertainties presented in ref. 41 were derived from the OSIRIS and ozonesonde standard deviations, and the standard deviation of their differences, and thus should be compared with the random uncertainties presented here. It was also confirmed in ref. 41 that the pointing of OSIRIS

has a random variation of ~400 m and a systematic offset of ~100 m, which is consistent with the 500 m assumed in the error estimates (Sect. 4).

The main discrepancies between the OSIRIS version 3.0 O_3 and that of the other instruments are a systematic underestimation of up to 15% above ~30 km, a systematic ~2–5% low bias in the lower stratosphere, and a general downward shift in the profiles in the Odin eclipse seasons (May–July) that was first noted in ref. 43. The eclipse season issue has been studied in detail in ref. 41, where it is concluded that the source is a ~200–400 m tangent height registration error likely caused by thermal effects on the Odin spacecraft structure. The cause of the systematic underestimation above ~30 km is believed to be due to contamination by baffle (or out-of-field) scatter, particularly the effects on the reference, I_0. This is supported by preliminary results from a new OSIRIS O_3 retrieval algorithm that combines measurements in the Chappuis region below ~30 km (where the baffle scatter contamination is not significant) with measurements in the Hartley–Huggins region above ~30 km (where there is no significant baffle scatter contamination), and shows no obvious bias[8].

For NO_2, the results are very similar to those of ref. 42 for the version 2.4 data set. This is expected since the changes between version 2.4 and version 3.0 were generally minor in nature. The largest change was new attitude information in version 3.0 that corrected the spacecraft-pointing drift error that affected previous versions. However, this pointing drift error was accounted for in ref. 42 by applying a time-dependent altitude shift to the retrieved NO_2 profiles. A detailed discussion of the results can be found in ref. 42, but overall the comparisons are very good, particularly above 25 km, with SAGE III clearly giving the best results, both in terms of the mean difference and the standard deviation. Below 25 km, the results are mixed, but this is expected since most of the instruments have difficulties with retrievals in this region. In particular, the POAM III NO_2 profiles have a clear bias in the 20–25 km region. In determining the random and systematic uncertainties in the 15–25 km region only SAGE III data was used. As in ref. 42, larger random uncertainties were found in the AM and are likely related to the small NO_2 abundances (compared to PM). Though ref. 42 found generally better agreement at high latitudes than at low latitudes, the analysis here gives similar results at all latitudes and seasons.

6. Summary

The status of the OSIRIS stratospheric O_3 and NO_2 data products, version 3.0, has been presented. The data products, that cover the period from November 2001 to present, were described with respect to their retrieval methodology, error analyses, and geophysical validation status. The data products are well-behaved and in good agreement with other instruments. Given the good health of the OSIRIS instrument and the Odin spacecraft, the continuation of operations into the foreseeable future will provide an important long-term record of stratospheric O_3 and NO_2.

Acknowledgements

This work is supported by the Natural Sciences and Engineering Research Council (Canada), the Canadian Space Agency, the Swedish National Space Board, and Chalmers University of Technology. Odin is a Swedish-led satellite project, funded jointly by Sweden (SNSB), Canada (CSA), Finland (Tekes), and France (CNES). The authors thank N. Lloyd at the University of Saskatchewan for producing the OSIRIS Level 1 data and for managing the Level 2 processing. Contributions to the software package from C. von Savigny, C. Sioris, C. McLinden, P. Eriksson, P. Krecl, and N. Lloyd are gratefully acknowledged. The SAGE II/III data were obtained from the NASA Langley Research Center EOSDIS Distributed Active Archive Center. The EP-TOMS and OMI data were provided by the NASA/GSFC TOMS Ozone Processing Team (OPT). The ozonesonde data were obtained from the World Ozone

[8]C. Roth. Atmospheric Ozone Retrieval using Chappuis and Hartley–Huggins Data. Third International Atmospheric Limb Workshop, Montréal, QC. 25–28 April 2006.

and Ultraviolet Radiation Data Centre (WOUDC) operated by Environment Canada, Toronto, Ontario, Canada under the auspices of the World Meteorological Organization. The POAM III and HALOE teams are thanked for making their data publicly available.

References

1. E.J. Llewellyn, N.D. Lloyd, D.A. Degenstein, R.L. Gattinger, S.V. Petelina, A.E. Bourassa, J.T. Wiensz, E.V. Ivanov, I.C. McDade, B.H. Solheim, J.C. McConnell, C.S. Haley, C. von Savigny, C.E. Sioris, C.A. McLinden, E. Griffioen, J. Kaminski, W.F.J. Evans, E. Puckrin, K. Strong, V. Wehrle, R.H. Hum, D.J.W. Kendall, J. Matsushita, D.P. Murtagh, S. Brohede, J. Stegman, G. Witt, G. Barnes, W.F. Payne, L. Piché, K. Smith, G. Warshaw, D.-L. Deslauniers, P. Marchand, E.H. Richardson, R.A. King, I. Wevers, W. McCreath, E. Kyrölä, L. Oikarinen, G.W. Leppelmeier, H. Auvinen, G. Mégie, A. Hauchecorne, F. Lefévre, J. de La Noë, P. Ricaud, U. Frisk, F. Sjoberg, F. von Schéele, and L. Nordh. Can. J. Phys. **82**, 411 (2004); doi:10.1139/P04-005.
2. H.L. Nordh, F. von Schéele, U. Frisk, K. Ahola, R.S. Booth, P.J. Encrenaz, Å. Hjalmarson, D. Kendall, E. Kyrölä, S. Kwok, A. Lecacheux, G. Leppelmeier, E.J. Llewellyn, K. Mattila, G. Mégie, D. Murtagh, M. Rougeron, and G. Witt. Astron. Astrophys. **402**, L21 (2003); doi:10.1051/0004-6361:20030334.
3. C. von Savigny, C.S. Haley, C.E. Sioris, I.C. McDade, E.J. Llewellyn, D. Degenstein, W.F.J. Evans, R.L. Gattinger, E. Griffioen, E. Kyrölä, N.D. Lloyd, J.C. McConnell, C.A. McLinden, G. Mégie, D.P. Murtagh, B. Solheim, and K. Strong. Geophys. Res. Lett. **30**, 1755 (2003); doi:10.1029/2002GL016401.
4. D.E. Flittner, P.K. Bhartia, and B.M. Herman. Geophys. Res. Lett. **27**, 2601 (2000); doi:10.1029/1999GL011343.
5. C.D. Rodgers. Inverse methods for atmospheric sounding: Theory and practice. 1 ed. World Scientific Publishing, Singapore. 2000.
6. C.E. Sioris, C.S. Haley, C.A. McLinden, C. von Savigny, I.C. McDade, J.C. McConnell, W.F.J. Evans, N.D. Lloyd, E.J. Llewellyn, K.V. Chance, T.P. Kurosu, D. Murtagh, U. Frisk, K. Pheilsticker, H. Bösch, F. Weidner, K. Strong, J. Stegman, and G. Mégie. J. Geophys. Res. **108**, 4215 (2003); doi:10.1029/2002JD002672.
7. U. Platt. *In* Air monitoring by spectroscopic techniques. *Edited by* M.W. Sigrist. John Wiley, New York. 1994. pp. 27–84.
8. M.T. Chahine. J. Atmos. Sci. **27**, 960 (1970).
9. C.S. Haley, S.M. Brohede, C.E. Sioris, E. Griffioen, D.P. Murtagh, I.C. McDade, P. Eriksson, E.J. Llewellyn, A. Bazureau, and F. Goutail. J. Geophys. Res. **109**, D16303 (2004); doi:10.1029/2004JD004588.
10. C.S. Haley, C. von Savigny, S. Brohede, C.E. Sioris, I.C. McDade, E.J. Llewellyn, and D.P. Murtagh. Adv. Space Res. **34**, 769 (2004); doi:10.1016/j.asr.2003.08.058.
11. P. Krecl, C.S. Haley, J. Stegman, S.M. Brohede, and G. Berthet. Atmos. Chem. Phys. **6**, 1879 (2006).
12. R. Freedman. M.Sc. thesis, York University, Toronto, Ont. 2005.
13. C.A. McLinden, C.S. Haley, and E.J. Llewellyn. Geophys. Res. Lett. **31**, L20112 (2004); doi:10.1029/2004GL020825.
14. C.A. McLinden, C.S. Haley, and C.E. Sioris. J. Geophys. Res. **111**, D14302 (2006); doi:10.1029/2005JD0066282005.
15. C.Z. Roth, D.A. Degenstein, A.E. Bourassa, and E.J. Llewellyn. Can. J. Phys. **85** (2007). This issue.
16. H. Auvinen, L. Oikarinen, and E. Kyrölä. J. Geophys. Res. **107**, 4172 (2002); doi:10.1029/2001JD000407.
17. S.V. Petelina, E.J. Llewellyn, K.A. Walker, D.A. Degenstein, C.D. Boone, P.F. Bernath, C.S. Haley, C. von Savigny, N.D. Lloyd, and R.L. Gattinger. Geophys. Res. Lett. **32**, L15S06 (2005); doi:10.1029/2005GL022377.
18. F. Borchi and J.-P. Pommereau. Atmos. Chem. Phys. **7**, 2671 (2007).
19. D.F. Rault. J. Geophys. Res. **110**, D09309 (2005); doi:10.1029/2004JD004970.
20. J. Kuttippurath, H. Bremer, J. Burrows, A. Kleinböhl, H. Küllmann, H. Künzi, J, Notholt, M. Sinnhuber, C. von Savigny, N. Lautié, D. Murtagh, J. Urban, M. Milz, G. Stiller, S. Petelina, J. de La Noë, E. Le Flochmoën, and P. Ricaud. J. Geophys. Res. **112**, D09311 (2006); doi:10.1029/2006JD007830.

21. C.E. Sioris, T.P. Kurosu, R.V. Martin, and K. Chance. Adv. Space Res. **34**, 780 (2004); doi:10.1016/j.asr.2003.08.066.
22. D.F. Rault and G. Taha. J. Geophys. Res. **112**, D13309 (2007); doi:10.1029/2006JD007679 (2007).
23. J.R. Taylor, K. Strong, C.A. McLinden, D.A. Degenstein, and C.S. Haley. Can. J. Phys. **85** (2007). This issue.
24. S. Brohede and A. Jones. Can. J. Phys. **85** (2007). This issue.
25. M.N. Juckes. Atmos. Chem. Phys. **6**, 1549 (2006).
26. P. Ricaud, F. Lefèvre, G. Berthet, D. Murtagh, E.J. Llewellyn, G. Mégie, E. Kyrölä, G.W. Leppelmeier, H. Auvinen, C. Boonne, S. Brohede, D.A. Degenstein, J. de La Noë, E. Dupuy, L. El Amraoui, P. Eriksson, W.F.J. Evans, U. Frisk, R.L. Gattinger, F. Girod, C.S. Haley, S. Hassinen, A. Hauchecorne, C. Jiménez, E. Kyrö, N. Lautié, E. Le Flochmoën, N.D. Lloyd, J.C. McConnell, I.C. McDade, L. Nordh, M. Olberg, A. Pazmino, S.V. Petelina, A. Sandqvist, A. Seppälä, C.E. Sioris, B.H. Solheim, J. Stegman, K. Strong, P. Taalas, J. Urban, C. von Savigny, F. von Schéele, and G. Witt. J. Geophys. Res. **110**, D05302 (2005); doi:10.1029/2004JD005018.
27. C.E. Randall, V.L. Harvey, G.L. Manney, Y. Orsolini, M. Codrescu, C. Sioris, S. Brohede, C.S. Haley, L.L. Gordley, J.M. Zawodny, and J.M. Russell III. Geophys. Res. Lett. **32**, L05802 (2005); doi:10.1029/2004GL022003.
28. S.M. Brohede, C.A. McLinden, G. Berthet, C.S. Haley, D. Murtagh, and C.E. Sioris. Can. J. Phys. **85** (2007). This issue.
29. C.E. Sioris, S. Chabrillat, C.A. McLinden, C.S. Haley, R. Ménard, M. Charron, and C.T. McElroy. Can. J. Phys. **85** (2007). This issue.
30. C.E. Sioris, C.A. McLinden, R.V. Martin, B. Sauvage, C.S. Haley, N.D. Lloyd, E.J. Llewellyn, P.F. Bernath, C.D. Boone, S. Brohede, and C.T. McElroy. Atmos. Chem. Phys. **7**, 4281 (2007).
31. G. Warshaw, D. Desaulniers, and D. Degenstein. Optical design and performance of the Odin UV/visible spectrograph and infrared imager instrument. 10th Annual AIAA/USU Small Satellite Conference, Logan, Utah. 1996.
32. D. Murtagh, U. Frisk, F. Merino, M. Ridal, A. Jonsson, J. Stegman, G. Witt, P. Eriksson, C. Jiménez, G. Mégie, J. de La Noë, P. Ricaud, P. Baron, J.R. Pardo, A. Hauchcorne, E.J. Llewellyn, D. A. Degenstein, R.L. Gattinger, N.D. Lloyd, W.F.J. Evans, I.C. McDade, C.S. Haley, C. Sioris, C. von Savigny, B.H. Solheim, J.C. McConnell, K. Strong, E.H. Richardson, G.W. Leppelmeier, E. Kyrölä, H. Auvinen, and L. Oikarinen. Can J. Phys. **80**, 309 (2002).
33. U. Frisk, M. Hagström, J. Ala-Laurinaho, S. Andersson, J.-C. Berges, J.-P. Chabaud, M. Dahlgren, A. Emrich, H.-G. Florén, G. Florin, M. Fredrixon, T. Gaier, R. Haas, T. Hirvonen, Å. Hjalmarsson, B. Jakobsson, P. Jukkala, P.S. Kildal, E. Kollberg, J. Lassing, A. Lecacheux, P. Lehikoinen, A. Lehto, J. Mallat, C. Marty, D. Michet, J. Narbonne, M. Nexon, M. Olberg, A.O.H. Olofsson, A. Origné, M. Petersson, P. Piironen, R. Pons, D. Pouliquen, I. Ristorcelli, C. Rosolen, G. Rouaix, A.V. Räisänen, G. Serra, F. Sjöberg, L. Stenmark, S. Torchinsky, J. Tuovinen, C. Ullberg, E. Vinterhav, N. Wadefalk, H. Zirath, P. Zimmermann, and R. Zimmermann. Astron. Astrophys. **402**, L27 (2003); doi:10.1051/0004-6361:20030335.
34. M.P. McCormick, P.-H. Wang, and M.C. Pitts. Adv. Space Res. **13**, 7 (1993).
35. K.V. Chance and R.J.D. Spurr. Appl. Opt. **36**, 5224 (1997).
36. K.P. Birch and M.J. Downs. Metrologia, **30**, 155 (1993).
37. K.P. Birch and M.J. Downs. Metrologia, **31**, 315 (1994).
38. C. von Savigny, I.C. McDade, E. Griffioen, C.S. Haley, C.E. Sioris, and E.J. Llewellyn. Can. J. Phys. **83**, 957 (2005); doi:10.1139/P05-04.
39. R.P. Loughman, D.E. Flittner, B.M. Herman, P.K. Bhartia, E. Hilsenrath, and R.D. McPeters. J. Geophys. Res. **110**, D19301 (2005); doi:10.1029/2004JD005429.
40. E. Griffoen and L. Oikarinen. J. Geophys. Res. **105**, 29717 (2000).
41. C.A. McLinden, V.E. Fioletov, C.S. Haley, N. Lloyd, C. Roth, D. Degenstein, A. Bourassa, C.T. McElroy, and E.J. Llewellyn. Can. J. Phys. **85** (2007); This issue.
42. S.M. Brohede, C.S. Haley, C.A. McLinden, C.E. Sioris, D.P. Murtagh, S.V. Petelina, E.J. Llewellyn, A. Bazureau, F. Goutail, C.E. Randall, J.D. Lumpe, G. Taha, L.W. Thomasson, and L.L. Gordley. J. Geophys. Res. **112**, D07310 (2007); doi:10.1029/2006JD007586.
43. S.V. Petelina, E.J. Llewellyn, D.A. Degenstein, N.D. Lloyd, R.L. Gattinger, C.S. Haley, C. von Savigny,

E. Griffioen, I.C. McDade, W.F.J. Evans, D.P. Murtagh, and J. de La Noë. Geophys. Res. Lett. **31**, L07104 (2004); doi:10.1029/2003GL019299.
44. J.M. Russell, III, L.L. Gordley, J.H. Park, S.R. Drayson, D.H. Hesketh, R.J. Cicerone, A.F. Tuck, J.E. Frederick, J.E. Harries, and P.J. Crutzen. J. Geophys. Res. **98**, 10777 (1993).
45. L.E. Mauldin, III, N.H. Zaun, M.P. McCormick, J.H. Guy, and W.R. Vaughn. Opt. Eng. **34**, 307 (1985).
46. M.P. McCormick, W.P. Chu, J.M. Zawodny, L.E. Mauldin, III, and L.R. McMaster. Proc. SPIE Int. Soc. Opt. Eng. **1491**, 125 (1991).
47. R.L. Lucke, D. Korwan, R.M. Bevilacqua, J.S. Hornstein, E.P. Shettle, D.T. Chen, M. Daehler, J.D. Lumpe, M.D. Fromm, D. Debrestian, B. Neff, M. Squire, G. König-Langlo, and J. Davies. J. Geophys. Res. **104**, 18785 (1999).
48. R.D. McPeters, P.K. Bhartia, A.J. Krueger, J.R. Herman, C.G. Wellemeyer, C.J. Seftor, G.Jaross, O. Torres, L. Moy, G. Labow, W. Byerly, S.L. Taylor, T. Swissler, and R.P. Cebula. Earth Probe Total Ozone Mapping Spectrometer (TOMS) Data Products User's Guide. NASA/TP-1998-206895. 1998.
49. P.F. Levelt, G.H.J. van den Oord, M.R. Dobber, A. Mälkki, H. Visser, J. de Vries, P. Stammes, J. Lundell, and H. Saari. IEEE Trans. Geo. Rem. Sens. **44**, 1093 (2006); doi:10.1109/TGRS.2006.872333.
50. M.J. Prather. J. Geophys. Res. **97**, 10187 (1992).
51. C.A. McLinden, S. Olsen, B. Hannegan, O. Wild, M.J. Prather, and J. Sundet. J. Geophys. Res. **105**, 14653 (2000).
52. L.L. Gordley, J.M. Russell, III, L.J. Mickley, J.E. Frederick, J.H. Park, K.A. Stone, G.M. Beaver, J.M. McInerney, L.E. Deaver, G.C. Toon, F.J. Murcray, R.D. Blatherwick, M.R. Gunson, J.P.D. Abbatt, R.L. Mauldin, III, G.H. Mount, B. Sen, and J.-F. Blavier. J. Geophys. Res. **101**, 10241 (1996).